

MCLOEB 25(1-4) 1-508 (2000) ISSN: 1058-7268 Volume 25, Numbers 1-4 (2000)

**MCLC S & T**

**SECTION B**

# **Nonlinear Optics**

## **Principles, Materials, Phenomena, and Devices**

*Editor: Takayoshi Kobayashi, University of Tokyo, Japan*

*Consultant Editors: M M Labes, A F Garito*

*East European and CIS Editor: Vladilen S Letokhov*

*North American Editor: Jerome D Swalen*

*West European Editor: François Kajzar*

Proceedings of

### **The Fifth International Conference on Organic Nonlinear Optics**

**ICONO'5**

Davos, Switzerland  
12 – 16 March, 2000

*Guest Editors*

P. Günter and Ch. Bosshard  
ETH Zurich, Switzerland

[http://www.gbhap.com/Nonlinear\\_Optics/](http://www.gbhap.com/Nonlinear_Optics/)



GORDON AND BREACH SCIENCE PUBLISHERS

*MCLC S & T – Section B:*  
**NONLINEAR OPTICS**

**PRINCIPLES, MATERIALS, PHENOMENA, AND DEVICES**

**Editor**

*Takayoshi Kobayashi*, Department of Physics, University of Tokyo, Hongo, Tokyo 113, Japan

**Consultant Editors**

*MM Labes*, Department of Chemistry, Temple University, Philadelphia, Pennsylvania 19122, USA

*A F Garito*, Department of Physics, University of Pennsylvania, Philadelphia, Pennsylvania 19104, USA

**East European and CIS Editor:** *Vladilen S Letokhov*, Institute of Spectroscopy of Russian Academy of Sciences, Laser Spectroscopy Department, Troitsk, Moscow Region, 142092, Russian Federation

**North American Editor:** *Jerome D Swalen*, 16231, Matilija Drive, Los Gatos, CA 95030, USA

**West European Editor:** *François Kajzar*, DEIN/LPEM, CEN Saclay, Gif-sur-Yvette, 91191, France

**Editorial Advisory Board**

East Europe and CIS. *V V Ragul'skii*, Institute of Problems of Mechanics, Moscow, Russia • *V V Smirnov*, General Physics Institute, Moscow, Russia

**North America.** *Daniel S Chemla*, University of California, Berkeley, California, USA • *Stephen T Kowel*, University of Alabama, Huntsville, Alabama, USA • *RS Lytel*, AMP Corporation, Palo Alto, California, USA • *Gerald R Meredith*, E I Dupont de Nemours and Co, Wilmington, Delaware, USA • *Nasser Peyghambarian*, University of Arizona, Tucson, Arizona, USA • *Y R Shen*, University of California, Berkeley, California, USA • *Kenneth Singer*, Case Western Reserve University, Cleveland, Ohio, USA • *Eric W Van Stryland*, CREOL, University of Florida, Orlando, Florida, USA • *David J Williams*, Eastman Kodak Company, Rochester, New York, USA

**West Europe.** *David Bloor*, Durham University, Durham, UK • *Allan D Boardman*, University of Salford, UK • *Jean-Luc Brédas*, Université den Mons, Mons, Belgium • *David Cotter*, British Telecom Research Laboratories, Ipswich, UK • *Christos Flytzanis*, Laboratoire d'Optique Quantique du CNRS, Palaiseau, France • *Peter Günter*, Institute of Quantum Electronics, Zürich, Switzerland • *Yves L'évy*, Institut d'Optique, Orsay, France • *Gerd Marowsky*, Laser Laboratorium Göttingen e. V., Göttingen, Germany • *Arnold Migus*, Ecole Polytechnique ENSTA, Palaiseau, France • *Jean-Paul Pocholle*, Thomson CSF, Orsay, France • *Joseph Zyss*, CNET, Bagneux, France

**Japan.** *Kazuhiro Ema*, Sophia University, Tokyo • *Tadashi Itoh*, Osaka University, Osaka • *Yuzo Ito*, Hitachi Ltd, Hitachi-shi • *Toshikuni Kaino*, NTT Optoelectronics Laboratory, Tokai • *Ken'ichi Kubodera*, NTT Science and Core Technology Laboratory Group, Atsugi • *Arao Nakamura*, Nagoya University, Nagoya • *Hachiro Nakanishi*, Tohoku University, Sendai • *Hiroki Nakatsuka*, University of Tsukuba, Tsukuba • *Hiroyuki Sasabe*, RIKEN, Wako • *Shinsuke Umegaki*, Keio University, Yokohama • *Masamichi Yamanishi*, Hiroshima University, Hiroshima

**Korea.** *Jang-Joo Kim*, Kwangju Institute of Science and Technology, Kwangju • *Kwang-Sup Lee*, Hannam University, Taejon • *Jeong-Weon Wu*, Ewha Womans University, Seoul

**Aims and Scope**

*Nonlinear Optics* publishes primary papers reporting original research, review articles, and rapid communications. The journal is divided into four main sections. 1. Principles – covering studies into the fundamental theoretical understanding of the origins and mechanisms of nonlinear optical processes, such as squeezing, phase conjugation, and optical bistability, and theoretical calculations of susceptibilities either by band theory or by quantum mechanical theory. 2. Materials – including work on the solid state physics of semiconductors and dielectrics, and organic and polymer compounds exhibiting nonlinear and electrooptical behaviour. 3. Phenomena – devoted to papers on: the discovery of new nonlinear optical phenomena; measurement of nonlinear optical processes; determination of nonlinear optical constants and figures of merit; observation of ultrafast and fast nonlinear optical processes; and the characterization of nonlinear optical materials by new measurement methods. 4. Device – featuring fundamental research articles on applications to devices, optical switches, optical bistable devices, phase conjugation, and optical logics. The journal recognizes the multidisciplinary nature of this field, and will include materials science and device implementation material, as well as the physiochemical aspects. The editors place great emphasis on the importance of the development of applications of nonlinear optical materials to practical devices.

Notes for contributors can be found at the back of the journal.

©2000 OPA (Overseas Publishers Association) N.V. Published by license under the Gordon and Breach Science Publishers imprint. All rights reserved.

Except as permitted under national laws or under the Photocopy License described below, no part of this publication may be reproduced or transmitted in any form or by any means, electronic, mechanical, photocopying or otherwise, or stored in a retrieval system of any nature, without the advance written permission of the Publisher.

**World Wide Web Addresses**

Additional information is also available through the Publisher's web home page site at <http://www.gbhap.com>. Full text on-line access and electronic author submissions may also be available.

Editorial enquiries by e-mail: <editlinkgbhap.com>.

**Order Information**

Four issues per volume. Subscriptions are renewed on an annual basis. 2000 Volume (s): 25

Orders may be placed with your usual supplier or at one of the addresses shown below. Journal subscriptions are sold on a per volume basis only; single issues of the current volume are not available separately. Claims for

(Continued on inside back cover)

**REPORT DOCUMENTATION PAGE**

Form Approved OMB No. 0704-0188

Public reporting burden for this collection of information is estimated to average 1 hour per response, including the time for reviewing instructions, searching existing data sources, gathering and maintaining the data needed, and completing and reviewing the collection of information. Send comments regarding this burden estimate or any other aspect of this collection of information, including suggestions for reducing this burden to Washington Headquarters Services, Directorate for Information Operations and Reports, 1215 Jefferson Davis Highway, Suite 1204, Arlington, VA 22202-4302, and to the Office of Management and Budget, Paperwork Reduction Project (0704-0188), Washington, DC 20503.

1. AGENCY USE ONLY (Leave blank)		2. REPORT DATE November 2000		3. REPORT TYPE AND DATES COVERED 12-16 March 2000 Conference Proceedings - Final Report	
4. TITLE AND SUBTITLE International Conference on Organic Nonlinear Optics (5 <sup>th</sup> ) ICONO'5 Held in Davos, Switzerland, on 12-16 March, 2000				5. FUNDING NUMBERS F61775-00-WF	
6. AUTHOR(S) Takayoshi Kobayashi, Editor					
7. PERFORMING ORGANIZATION NAME(S) AND ADDRESS(ES) Institute of Quantum Electronics ETH Honggerberg, HPF E7 Zurich CH-8093 Switzerland				8. PERFORMING ORGANIZATION REPORT NUMBER ISSN: 1058-7268	
9. SPONSORING/MONITORING AGENCY NAME(S) AND ADDRESS(ES) US Department of the Air Force European Office of Aerospace Research and Development (EOARD) PSC 802 Box 14 FPO AE 09499-0039				10. SPONSORING/MONITORING AGENCY REPORT NUMBER CSP 00-5039	
11. SUPPLEMENTARY NOTES Published in MCLC S&T-Section B: Nonlinear Optics: Principles, Phenomena, and Devices, Vol. 24, No.1-4, 2000. Published by Gordon and Breach Science Publishers. This work relates to a Department of Air Force contract/grant issued by the European Aerospace Office of Research and Development. The United States has a royalty free license throughout the world in all copyrightable material contained herein.					
12a. DISTRIBUTION/AVAILABILITY STATEMENT Approved for Public Release. U.S. Government Rights License. All other rights reserved by the copyright holder. (Code 1, 20)				12b. DISTRIBUTION CODE A	
12. ABSTRACT (Maximum 200 words) The International Conference on Organic Nonlinear Optics ICONO'5 was interdisciplinary. Topics included: Crystal growth of organics, Poled polymers, Optical amplification, Wave mixing and phase conjugation, Fibers and wave guides, Photorefractive effects, Nonlinear optical information storage, Optical parallel processing, and Display applications of organic LEDs and spatial light modulators.					
13. SUBJECT TERMS EOARD, Foreign reports, Organic nonlinear optical materials.				15. NUMBER OF PAGES	
				16. PRICE CODE	
17. SECURITY CLASSIFICATION OF REPORT UNCLASSIFIED	18. SECURITY CLASSIFICATION OF THIS PAGE UNCLASSIFIED	19. SECURITY CLASSIFICATION OF ABSTRACT UNCLASSIFIED		20. LIMITATION OF ABSTRACT UL	

NSN 7540-01-280-5500

Standard Form 298 (Rev. 2-89)  
Prescribed by ANSI Std. Z39-18  
298-102

# CONTENTS

Volume 25(1-4)

Committees	xi
Sponsors	xiii
Preface	xv

## Invited Papers

M. SCHADT: Optics and Applications of Photo-aligned Liquid Crystalline Surfaces	1
X. WEI, D. KIM, M. O-HE and Y. R. SHEN: Nonlinear Vibrational Spectroscopy on Rubbed Polymer Surfaces	13
L. DALTON, B. ROBINSON and W. STEIER: Production of High Bandwidth Polymeric Electro-optic Modulators with $V_{\pi}$ Voltages of Less than 1 Volt	23
T. KOBAYASHI: Sub-5-fs Nonlinear Optical Processes in Polydiacetylenes	35
S. OKADA, K. TSUJI, ANWAR, H. NAKANISHI, H. OIKAWA and H. MATSUDA: Molecular Engineering of the DAST Family	45
G. I. STEGEMAN, A. GALVAN-GONZALES, M. CANVA, R. TWIEG, A. C. KOWALCZYK, X. Q. ZHANG, H. S. LACKRITZ, S. MARDER, S. THAYUMANAVAN, K. P. CHAN, A. K.-Y. JEN and X. WU: Photodegradation of Various Electro-optic Polymer Families	57
N. KIM, H. CHUN, W. S. JAHNG, S. SONG, D.-H. SHIN and M. JOO: Nonlinear Optics and Photorefractivity of Polymer Composites	67
L. ROCHA, V. DUMARCHER, C. DENIS, P. RAIMOND, C. FIORINI, J.-M. NUNZI, F. SOBEL, D. GINDRE and B. SAHRAOUI: Periodically Structured Polymer Films and Applications	77



C. BUBECK, K. UEBERHOFEN, J. ZIEGLER, F. FITRILAWATI, U. BAIER, H. EICHNER, C. FORMER, K. MÜLLEN, S. PFEIFFER, H. TILLMANN and H.-H. HÖRHOLD: Waveguides of Conjugated Polymers with Large Cubic Nonlinearities .....	93
---	----

S. VAN ELSHOCHT, T. VERBIEST, T. J. KATZ, C. NUCKOLLS, B. BUSSON, M. KAURANEN and A. PERSOONS: Molecular Chirality as a Tool for Second-order Nonlinear Optics .....	105
---	-----

M. HE AND R. J. TWIEG: Synthesis and Mesogenic Properties of Liquid Crystals Containing a Methylene-1,4-di-tetra or Hexahydropyridine Core Unit .....	117
---	-----

P.-Y. HAN, M. TANI, F. PAN and X.-C. ZHANG: Organic Crystal (DAST) for THz Applications .....	123
--	-----

### **Session A: Novel Nonlinear Optical Phenomena and Applications**

C. ANDRAUD and P. L. BALDECK: Enhanced Two-photon Absorption with Polyphenyl Oligomers .....	133
---	-----

X.-L. YANG, C. ANDRAUD and J. ZYSS: Tensorial Analysis of First-order Hyperpolarizabilities of $C_{2v}$ Molecules .....	139
--	-----

R. ANEMIAN, C. ANDRAUD, A. COLLET, J.-M. NUNZI, Y. MOREL AND P. L. BALDECK: Molecular Engineering Around Diaminobiphenyls for Optical Limiting at Visible Wavelengths .....	145
--	-----

F. HACHE, M. C. SCHANNE-KLEIN and H. MESNIL: Theoretical Investigation of the Nonlinear Circular Dichroism in a Liquid of Chiral Molecules .....	153
--	-----

N. V. KAMANINA and L. N. KAPORSKII: New Properties of COANP and PNP Compounds: Optical Limiting Effect .....	159
---	-----

N. V. KAMANINA and L. N. KAPORSKII: Optical Limiting Effect in Polymer Organic Systems .....	165
---	-----

N. KATO, K. SAITO and Y. UESU: <i>In-situ</i> Observation of Thermochromic Behavior in Merocyanine J-aggregate Monolayers using the Multipurpose Nonlinear Optical Microscope .....	171
--	-----

## CONTENTS

v

P. MACAK, Y. LUO, P. NORMAN, and H. ÅGREN: Semi-classical  
Modeling of Medium Effects in NLO Molecular Properties . . . . . 177

L. MOREAUX, O. SANDRE, M. BLANCHARD-DESCE  
and J. MERTZ: Simultaneous Second-harmonic Generation  
and Two-photon Excited Fluorescence Microscopy . . . . . 183

### Session B: Photorefractive Effects

M. A. DIAZ-GARCIA, D. WRIGHT, J. D. CASPERSON,  
B. SMITH, E. GLAZER, W. E. MOERNER,  
L. I. SUKHOMLINOVA and R. J. TWIEG:  
High Speed PVK-based Photorefractive Polymer Composites . . . . . 189

M. DUMONT: Modelization of the Angular Redistribution  
in Optical Ordering Processes in dye Containing Polymers . . . . . 195

T. FUJIHARA, M. TOKUUE, T. SASSA, K. OZAWA,  
S. UMEGAKI, M. YOKOYAMA, T. WADA  
and H. SASABE: Formation of an Anti-guide Structure  
in a Photorefractive Polymer by a Pump-light Beam . . . . . 201

N. V. KAMANINA and N. A. VASILENKO:  
LC SLM Based on Fullerene Doped Polyimide . . . . . 207

A. MINIEWICZ, P. SIKORSKI, A. JANUSZKO, S. BARTKIEWICZ,  
J. PARKA and F. KAJZAR: Optical Image Correlators Based  
on Nematic Liquid Crystals . . . . . 213

D. VAN STEENWINCKEL, E. HENDRICKX,  
K. VAN DEN BROECK, C. SAMYN  
and A. PERSOONS: Influence of the Chromophore  
Ionization Potential on the Magnitude of Photorefractive  
Effects in PVK-based Polymer Composites . . . . . 219

### Session C: Poled Polymers for SHG and Electro-optic Devices

R. BLUM, K. PFEIFER and M. EICH: Numerical Analysis  
of the Three Dimensional Polarization Distribution  
in Poled Nonlinear Optical Polymers . . . . . 225

S. HORINOUCI, M. FUKUDA, K.-S. LEE, J.-H. LEE, K. MITO and K. SASAKI: Second Harmonic Generation in Photo-bleached PU1-C4B Film Channel Waveguides .....	231
---	-----

N. LEMAITRE, A.-J. ATTIAS, I. LEDOUX and J. ZYSS: New Mesogenic 3,3'-bipyridine Derivatives for Side-chain Liquid Crystal Polymers - Second-order NLO Properties .....	235
---	-----

I. LIAKATAS, M. JÄGER, CH. BOSSHARD, P. GÜNTER and T. KAINO: Photobleaching Mechanism Studies of Side-chain Polyimides .....	241
--	-----

C. FLUERARU, S. SCHRADER, B. DIETZEL, V. ZAULS, H. MOTSCHMANN, B. SCHULZ and G. DECHER: Organized Organic Multilayer Structures for Frequency Doubling and Electro-Optics .....	247
--	-----

N. S. LAGALI, D. J. W. KLUNDER, G. J. GERRITSMA and A. DRIESSEN: Ultra-efficient Electro-optic Polymer Modulators for Short-distance High-speed Optical Interconnects ...	253
---	-----

V. RODRIGUEZ and C. SOURISSEAU: SHG at Near Resonance and Chromophore Orientational Distribution Function in p(DR1M) Thin Films Oriented by Corona Poling .....	259
---	-----

#### **Session D: Nonlinear Optical Organic Crystals**

J. M. COLE, C. C. WILSON and J. A. K. HOWARD: Rationalising the SHG Response in DCNP through Anomalous Atomic Thermal Motion .....	265
--	-----

A. FELDNER, TH. FEHN, TH. VOGTMANN and M. SCHWOERER: Preparing Polydiacetylene Single Crystal Thin Films .....	271
--	-----

H. KOBAYASHI, H. OKUYAMA and M. KOTANI: SHG-active p-nitroaniline Thin Films Grown by Dip-coating .....	277
--	-----

I. WANG, N. SANZ, A. IBANEZ and P. L. BALDECK: Observation of Second-harmonic Generation in Sol-gel Glass Doped with N-4-nitrophenyl-(L)-prolinol Nanocrystals .....	283
---	-----

M. RINI, G. P. BANFI, V. DEGIORGIO and J. N. SHERWOOD: Phase-matching Properties of the Organic Crystal (S)-3-Methyl-5-nitro-N- (1-phenylethyl)-2-pyridinamine .....	289
---	-----

### Session E: Fundamental Studies

A. ERIKSSON, C. LOPES, M. LINDGREN, S. SVENSSON, T. MCKAY and J. DAVY: Modelling and Characterisation of Nonlinear Materials for Optical Limiting. Mononuclear and Binuclear Platinum Ethynyls .....	297
---	-----

E. HENDRICKX, B. KIPPELEN, S. THAYUMANAVAN, S. R. MARDER, A. P. PERSOONS and N. PEYGHAMBARIAN: Improved Photogeneration Efficiency of Charge-transfer Complexes Between C <sub>60</sub> and Low Ionization Potential Arylamines .....	303
---	-----

S. HOUBRECHTS, T. WADA, H. SASABE and Y. KUBO: Control of the First Hyperpolarizability of Functionalized Mesostructures Through Cation Binding .....	309
---	-----

M. JOO, H. CHUN and N. KIM: Ellipsometric Polarization Contour Measurement for Anisotropy in Organic Materials .....	315
---	-----

G. MESHULAM, P. SHAIER, G. BERKOVIC, A. BEN-ASULY, R. MAZOR, L. SHAPIRO, V. KHODORKOVSKY and Z. KOTLER: Second-order Nonlinear Optical Response at the Two-photon Resonance in a Two-dimensional NLO Molecule .....	321
---	-----

Y. MOREL, C. ANDRAUD and P. L. BALDECK: Large Two-photon Absorption in Tetra and Penta Phenyl Compounds .....	327
---	-----

Y. OKADA-SHUDO: Polarization Recording and Reconstruction in a Photoinduced Anisotropic Medium .....	333
---	-----

Y. UESU, N. KATO and K. SAITO: Second Harmonic Spectroscopy and SHG Microscopic Observation of J-aggregate Domains in Merocyanine at Air–Water Interface .....	339
--	-----

R. VALLEE, P. DAMMAN, M. DOSIERE, E. TOUSSAERE and J. ZYSS: Orientation and Non Linear Optical Properties of DAN Crystals on PTFE Substrates .....	345
--	-----

K. WOSTYN, G. OLBRECHTS, K. CLAYS, A. PERSOONS, A. WATANABE, K. NOGI, X.-M. DUAN, S. OKADA, H. OIKAWA, H. NAKANISHI, H. VOGEL, D. BELJONNE and J.-L. BREDAS: Influence of Conjugation Length on First Hyperpolarizability of Fluorescent Hemicyanine (DAST) Homologues . . . . .	353
--	-----

T. TANO, T. KODZASA, H. USHIJIMA and T. KAMATA: Preparation of the Anisotropic Thin Film of a One-dimensional Material on an ITO Electrode . . . . .	359
--	-----

## **Session F: Ultrafast Nonlinear Optics in Organics**

R. V. MARKOV, P. A. CHUBAKOV, A. I. PLEKHANOV, Z. M. IVANOVA, N. A. ORLOVA, T. N. GERASIMOVA, V. V. SHELKOVNIKOV and J. KNOESTER: Optical and Nonlinear Optical Properties of Low-dimensional Aggregates of Amphiphilic Cyanine Dyes . . . . .	365
--	-----

R. MOUNTASSER, H. MAILLOTTE, F. CHÉRIOUX and M. AYADI: Picosecond Optical Limiting Action Through a Thin MMA-octupole Copolymer Layer near the Total Reflection State . . . . .	373
--	-----

R. RANGEL-ROJO, H. MATSUDA, H. KASAI and H. NAKANISHI: Resonant Nonlinearities in an Organic Material: Irradiance Dependence . . . . .	379
--	-----

S. SOTTINI, G. MARGHERI, E. GIORGETTI, F. GELLI, A. CRAVINO, D. COMORETTO, C. CUNIBERTI, C. DELL'ERBA, I. MOGGIO and G. DELLEPIANE: Thin Films of a Novel Polydiacetylene for Applications to All-optical Signal Processing . . . . .	385
---	-----

## **Session G: Fibers and Waveguides**

P. LABBÉ, A. CLOUQUEUR, R. HIERLE, E. TOUSSAERE and J. ZYSS: Drift Correction of Polymer Based Mach-Zehnder Modulators . . . . .	393
--	-----

M. A. BADER and G. MAROWSKY: Gaussian Profile Bragg Gratings in Polydiacetylene Waveguides: Characterization and Application in Integrated Optics . . . . .	399
---	-----

M. E. PIETRZYK: Compression of Self-trapping Pulses in Kerr-type Planar Waveguides .....	407
---	-----

K. TAKAYAMA, M. YOSHIDA, H.-H. DENG, K. KOMATSU and T. KAINO: Channel Waveguide Fabrication of the Organic Nonlinear Optical Crystal, DAST, by using Oxygen RIE ....	413
--	-----

### **Session H: Novel Molecular Design and Synthesis**

F. CHERIOUX, S. BRASSELET, P. AUDEBERT and J. ZYSS: New Octupolar Star-shaped Molecules with Non-resonant Quadratic Optical Nonlinearities .....	419
--	-----

J. KAWAMATA, T. AKUTAGAWA, T. HASEGAWA, K. INOUE and T. NAKAMURA: Nonlinear Optical Properties of the Langmuir-Blodgett Films of an Intermolecular Charge Transfer Complex .....	425
---	-----

J. KAWAMATA, Y. OGATA, A. YAMAGISHI and K. INOUE: Structural Analyses of Clay-Metal Complex Hybrid Films by Observation Optical Second Harmonic Generation .....	431
---	-----

Y. SAKURAI, H. SHIOZAKI, S. NAKAO and M. KIMOTO: MO Calculations of Dyes for the Solid State Absorption Spectra ...	437
--	-----

M. SIGALOV, A. BEN-ASULY, L. SHAPIRO and V. KHODORKOVSKY: Novel N-aryl Carbazole Derivatives for Two-photon Absorption Applications .....	443
---	-----

Y. TABUCHI, K. ASAI, M. RIKUKAWA, K. SANUI and K. ISHIGURE: Organic/Inorganic Quantum Confinement Structures based on Lead Halide Perovskites .....	449
---	-----

### **Session I: Organic Light Emitting Materials**

P. IMPERIA, S. SCHRADER, M. B. CASU, M. JANDKE and P. STROHRIEGL: Quinoxaline Films for Hetero-layer Light Emitting Devices .....	455
---	-----

M. KIY, I. BIAGGIO and P. GÜNTHER: Photoelectron Spectroscopy on a Running Organic Light Emitting Diode .....	461
--	-----

Z. LIU, J. PINTO, J. SOARES and E. PEREIRA: Influence of Hole Transport Materials on the Emission of Organic LED .....	467
---	-----

F. MICHELOTTI, S. BUSSI, Z. BAO and M. BERTOLOTTI: Probing Space Charge Distributions in Polymer LEDs by Means of an Electro-optic Technique .....	473
R. ONO, P. LOSIO, I. BIAGGIO and P. GÜNTER: Impedance Spectroscopy of ALQ <sub>3</sub> based Organic Light Emitting Diodes in Ultra High Vacuum .....	479
O. STÉPHAN and Y. KERVELLA: Bluegreen Light-emitting Electrochemical Cells Based on a Copolymer Derived from Fluorene .....	485
Y. TAO, M. D'IORIO, M. S. WONG, Z. H. LI, I. LEVESQUE and J. LAM: Luminescent and Electronic Properties of End-substituted Distylbenzen Derivatives .....	491
A. TAPPONNIER, I. BIAGGIO, M. KIY, R. ONO and P. GÜNTER: Transient photocurrent Investigation of Charge Transport in Electroluminescent Organic Thin Films .....	497
Z. LIU, J. PINTO, H. NAZARÉ and S. XU: Injection and Transport of Carriers in Single Layer Light Emitting Device .....	503

## **COMMITTEES**

### **Conference Chair**

Peter Günter (ETH Zürich, Switzerland)

### **Co-Chairs**

François Kajzar, European Chair	(LETI, CEA, France)
Mark Kuzyk, American Chair	(Washington State U., USA)
Hiroyuki Sasabe, Pacific Chair	(CIST, Japan)

## **INTERNATIONAL ADVISORY COMMITTEE**

Fernando Agullo-Lopez	(Spain)	André Persoons	(Belgium)
Werner Blau	(Ireland)	Nasser Peyghambarian	(USA)
Donald C. Bradley	(UK)	Paras Prasad	(USA)
Christoph Bräuchle	(Germany)	Takatomo Sasaki	(Japan)
Jean-Luc Brédas	(USA)	Ron Shen	(USA)
Vittorio Degiorgio	(Italy)	Ken Singer	(USA)
Christos Flytzanis	(France)	George I. Stegeman	(USA)
Toshikuni Kaino	(Japan)	Carlo Taliani	(Italy)
Nakjoong Kim	(Korea)	Sukant Tripathy	(USA)
Takayoshi Kobayashi	(Japan)	Robert Twieg	(USA)
Charles Lee	(USA)	Shinsuke Umegaki	(Japan)
Seth Marder	(USA)	Kenneth Wynne	(USA)
Seizo Miyata	(Japan)	Joseph Zyss	(France)
Hachiro Nakanishi	(Japan)		

## **LOCAL ORGANIZING COMMITTEE**

Ivan Biaggio (ETH)	Conference Program and Information
Christian Bosshard (ETH)	Secretary General
François Diederich (ETH)	
Peter Günter (ETH)	Conference Chair
Carolina Medrano (ETH)	Treasurer
Germano Montemezzani (ETH)	Local Arrangements
Ulrich Suter (ETH)	



## SPONSORS

We wish to thank the following for their contribution to the success of this Conference:

European Office of Aerospace Research and Development  
U.S. Air Force Office of Scientific Research  
United States Air Force Research Laboratory  
U.S. Office of Naval Research - European Office

Swiss National Science Foundation  
Wildhainweg 20, P.O. Box, CH-3001 Berne, Switzerland  
<http://www.snf.ch/>

Swiss Federal Institute of Technology (ETH)  
<http://www.ethz.ch/>

Nonlinear Optics Laboratory  
ETH Zürich, Switzerland  
<http://nlo-serv.ethz.ch/>

Bayer AG  
Werk Leverkusen, 51368 Leverkusen, Germany  
<http://www.bayer.com/>

Gordon and Breach Science Publishers  
<http://www.gbhap.com/>

GMP SA  
19, av. de Baumettes/CP, CH-1020 Renens 1, Switzerland  
<http://www.gmp.ch/>

Rainbow Photonics AG  
Einsteinstrasse HPF E7, CH-8093 Zürich, Switzerland  
<http://www.rainbowphotonics.ethz.ch/>

## **EXHIBITORS**

The following companies have agreed to take part in the exhibition:

Gordon and Breach Science Publishers

<http://www.gbhap.com/>

Sopra SA (Non-Linear Optical Spectrometer)

26 rue Pierre Joigneaux, F-92170 Bois Colombe, France

<http://www.sopra-sa.com/>

Springer-Verlag

Tiergartenstrasse 17, D-69121 Heidelberg, Germany

<http://www.springer.de/>

## PREFACE

Optical wave manipulation is one of the future technologies for optical processing and communication. Organic nonlinear optical materials are thought to have a key role in those technologies, and a lot of effort to develop new molecules/materials as well as fundamental understanding is under way throughout the world.

This special issue of *Nonlinear Optics* provides a current status of this very active field of research. It covers new experimental and theoretical results that were presented through invited lectures and poster sessions at the *International Conference on Organic Nonlinear Optics'5* (ICONO'5) that took place in Davos, Switzerland, from March 12–16, 2000.

ICONO'5 provided an excellent opportunity for an international exchange of information and cooperation among researchers in academia, government laboratories, and industries, and to stimulate growth in the field of organic nonlinear optics. The conference was a great success (over 200 attendees from universities, governmental laboratories, and industry) and provided a forum for discussion of all aspects of nonlinear optics, *e.g.*, new phenomena, novel optoelectronic devices, and advanced organic materials.

More specifically, the conference was divided into ten oral sessions, three extended evening poster sessions, and a round table discussion on *The Future of Electro-Optic Polymers*. Additionally, several social events provided ideal opportunities for further discussions among the participants. All oral contributions were presented by invited speakers that gave overviews on the current status of their field of expertise. The oral sessions were organized according to different topics. The first full day was devoted to *Future Photonic Applications*, *Electro-Optic Polymers*, and *Optical Memories*, treating more application oriented subjects. On the second day the fascinating topics of *Highly Nonlinear Organic Crystals* and *Nonlinear Optical Polymers* were covered in detail. In the evening, *The Future of Electro-Optic Polymers* was thoroughly discussed by experts from universities, industry, and funding agencies. Novel exciting trends in the fields of *Third-Order Nonlinear Optics*, *Organic Light Emitting Diodes*, and *Novel Molecules* were presented on Wednesday. The last day of the conference was devoted to *Fundamental Investigations* and *New Phenomena* (THz

*Spectroscopy*), two topics that were of prime importance to show further research directions in the area of organic nonlinear optics.

To summarize, a total of 33 invited talks and 143 poster presentations with many new and exciting results made ICONO'5 a great success and we are looking forward to ICONO'6 which will be held in Tuscon, Arizona, in 2001.

We gratefully acknowledge the support of M. Bösch, R. Ono and A. Schneider during the preparation of these proceedings.

Zürich, July 2000.

P. Günter and  
Ch. Bosshard

---

## **INVITED PAPERS**

## **Optics and Applications of Photo-Aligned Liquid Crystalline Surfaces**

MARTIN SCHADT  
ROLIC Research Ltd, 4123 Allschwil, Switzerland

### **Abstract**

Photo-alignment and photo-patterning of monomeric and polymeric liquid crystals renders a plethora of new birefringent optical elements and improved LCDs possible. Linear photo-polymerization (LPP) is shown to enable photo-alignment of multi-domain VAN-LCDs with very broad field of view. Moreover, novel LPP-aligned thin-film stacks of polymeric liquid crystals with controllable spatial uniaxiality, non-absorbing, bright interference color filters, photo-structured polarizers, positive and negative optical retarders and wide-view films are presented.

Key words: liquid crystal displays, photo-alignment, liquid crystal polymers, wide-view optical films

### **Introduction**

Without external aligning forces the long axes of liquid crystal (LC)-molecules align spontaneously only over microscopic domains. Since LC-alignment is a prerequisite for rendering any liquid crystal display (LCD) operable, functional display boundaries are essential. Conventionally, display alignment is achieved by sandwiching a liquid crystal layer between two brushed polyimide coated display substrates. LC-molecules align parallel at the discrete, uniaxial brushing traces, whereas the aligning information between traces is communicated via the long range elastic coupling forces of liquid crystals. With increasing distance between traces and/or decreasing aligning strength, thermal LC-director fluctuations reduce display contrast and in the extreme –under thermal or optical stress – lead to display failure.

Uniaxiality of LC-alignment at the boundaries of field-effect LCDs – such as in twisted nematic (TN)-, supertwisted nematic (STN)-, or vertically aligned nematic (VAN)-LCDs – is only one of two essential prerequisites for proper display operation. The other is the generation of display-specific bias tilt angles  $0 < \Theta < 90^\circ$  between substrate(s) and LC-director(s)  $\hat{n}(\Theta, \varphi)$  at the LCD boundaries;  $\varphi$  = azimuthal angle. Without defined bias tilt, director dislocations occur and display appearance deteriorates [1]. LC-alignment must be thermally and optically stable.

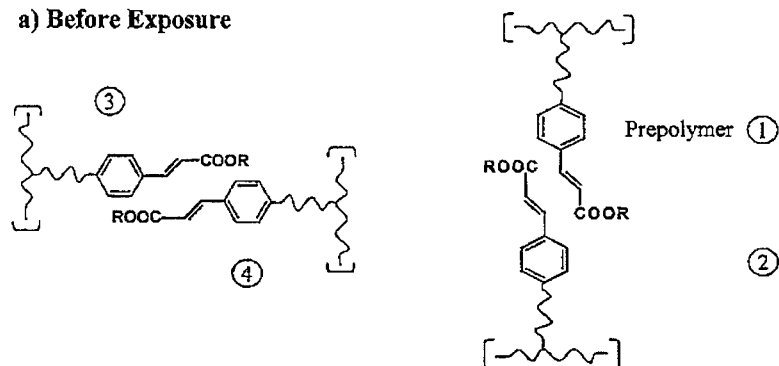
There are a number of drawbacks associated with brushing LCD substrates, such as: the generation of dust and electrostatic charges, reduced contrast of weakly brushed micro-displays due to thermal LC-director fluctuations between brushing traces, or defects which become visible when projected. Moreover, multi-domain LC-alignment to improve the field of view of displays requires alignment patterning within individual pixels which cannot be achieved by brushing.

In the 1980's first attempts were made to induce molecular reorientation in guest host materials by exposing LC-polymers, comprising mainly azo guest molecules, to linearly polarized light [2-4]. In the early 1990's two research groups showed that it is possible to align monomeric liquid crystals at surfaces not by mechanical means but optically [5,6]. Two fundamentally different aligning strategies were pursued, namely (i) *single-molecular* processes such as photo-alignment in azo-type guest host systems [5] which reorients LCs through optically induced cis-trans isomerization by linear polarized light, or by directional bleaching of polyimide layers by linear polarized light [7] versus (ii) *bi-molecular* photo-alignment by linear photo-polymerization (LPP) developed at ROLIC [6,8]. LPP-photo-alignment generates alignment in adjacent liquid crystal layers via exposing LPP-surfaces to linear polarized UV-light *and simultaneously* cross-links pairs of pre-polymer LPP-molecules, thus fixing the alignment in-situ. The LPP-process is inherently photo-stable [8] and capable to simultaneously align *and* induce tilt angles in monomeric as well as in polymeric liquid crystals [9,10]. The following photo-aligned devices and novel thin-film optical elements are based on the LPP technology developed in our labs.

Reviewed are the broadening effect of LPP photo-patterned alignment on the field of view of multi-domain LCDs, such as twisted nematic (TN)- and vertically aligned nematic (VAN)-LCDs [8,10]. Moreover, LPP photo-aligned thin-film stacks of liquid crystal polymers (LCPs) with controllable spatial uniaxiality on *single* substrates are shown to render virtually any

optical retarder configuration feasible, namely planar, tilted or homeotropic retarders with positive as well as negative birefringence. This enables the realization of such diverse optical thin-film devices as wide-view films, optical compensation films or interference color filters on plastic substrates for any type of LCD by a single technology [11-13].

**a) Before Exposure**



**b) After Exposure**

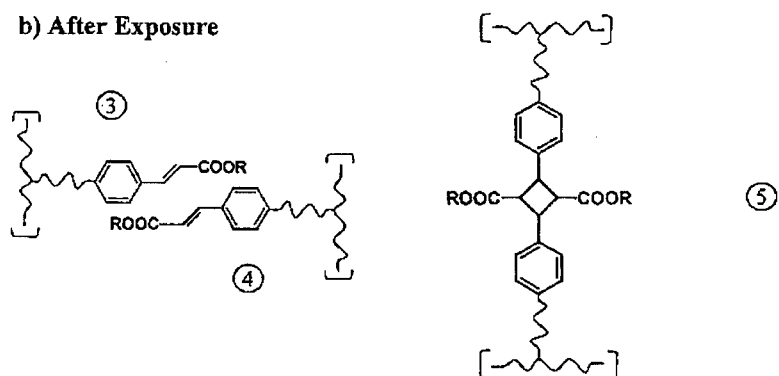


**Fig.1** Schematic of ROLIC's LPP-photo-aligning- and simultaneous cross-linking mechanism.



### LPP-Photo-Alignment and Dual-Domain VAN-LCDs

Fig.1 schematically depicts our LPP photo-aligning model [10] for the case of two adjacent pairs of novel endo cinnamic ester LPP-pre-polymer molecules which are isotropically aligned prior to exposure with linearly polarized uv-light  $h\nu(P_{uv})$ ; i.e. the number of pre-polymers in x- and y- direction in a given plane are equal before exposure. The LPP-molecules are designed such that the directional 2+2 cross-linking photo-reaction generates (i) an anisotropic LPP pre-polymer distribution:  $1,2,3,4 \Rightarrow 3,4$  (ii) anisotropically aligned cycloadditioned new molecules 5 and (iii) simultaneously fixes and cross-links the photo-induced alignment (Fig.1). Fig.1 depicts the bi-molecular character of our LPP-process which in-situ stabilizes photo-alignment [8]. Fig.1 also indicates the non-degenerate alignment symmetry of the LPP-process which causes the LC-director  $\hat{n}$  to align parallel to the polarization direction  $P_{uv}$ , thus enabling the generation of bias tilt angles in adjacent LC-layers [9].

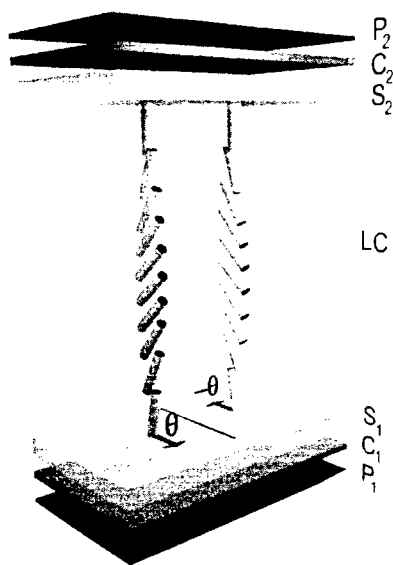


**Fig.2** Single pixel of a LPP-aligned dual-domain VAN-LCD with integrated LPP/LCP wide-view compensators C.

Fig.2 illustrates the two most important features of photo-alignment of displays namely (a) alignment and (b) photo-patterning in a very demanding molecular display configuration, namely a dual-domain VAN-LCD which requires slightly tilted vertical boundaries. Fig.2 shows a single pixel of the first homeotropically photo-aligned VAN-LCD which we recently presented [13]. On a macroscopic scale, the optical anisotropies of the differently aligned central LC-directors of the sub-pixels compensate each other which broadens the field of view of the display. Apart from photo-aligned boundaries, the VAN-LCD in Fig.2 comprises two integrated planar photo-aligned LPP/LCP retarders on each display substrate which further enhance the field of view of the dual-domain VAN configuration in the off-state [13]. The retarders will be discussed later.

The measurements in Fig.3 show the remarkably broad field of view of the dual-domain VAN-LCD of Fig.2 versus the strong angular dependence of a non-compensated, single-domain VAN-LCD [13]. Also shown is the further possible improvement of the field of view of the compensated versus the non-compensated dual-domain VAN-LCD in its on-state. Fig. 2 shows that additional compensation mainly further improves the off-state of the display.

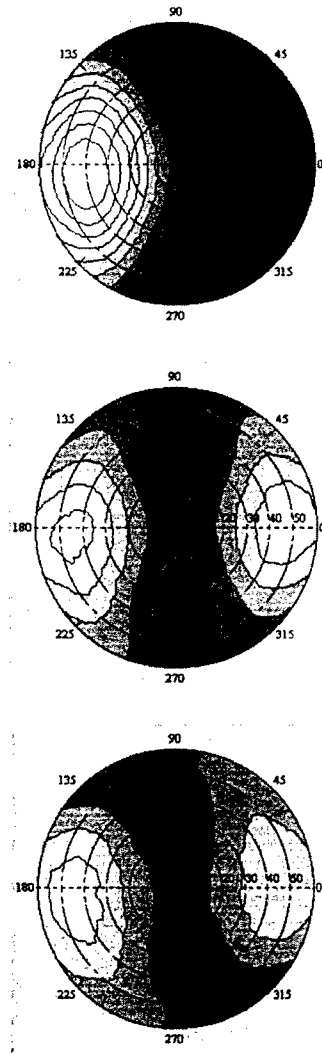
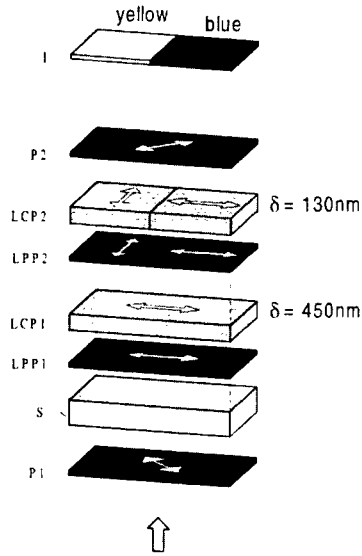


**Fig.3** From top to bottom: angular brightness dependence of (i) single domain VAN-LCD, (ii) LPP-aligned dual-domain VAN-LCD and (iii) LPP-aligned dual-domain VAN-LCD with integrated wide-view LPP/LCP films.

### LPP-Photo-Aligned Birefringent Optical Thin Film Stacks

Apart from monomeric liquid crystals we have shown that the LPP technology also permits to photo-align and photo-pattern polymeric liquid crystal (LCP) layers on *single* substrates of glass, plastic, metal, etc., such, that the LC-directors  $\hat{n}(\Theta, \varphi)$  of an LCP-film at it's respective boundaries; i.e. substrate/LCP and LCP/air<sub>0</sub> are independently adjustable in any spatial direction  $\hat{n}(\varphi = 0 \dots 360^\circ, \Theta = 0 \dots 90^\circ)$  [8,10-14]. Because of their optical anisotropy  $\Delta n = (n_e - n_o)$ , LCP films [15] are birefringent with a slow optical axis  $n_e \parallel \hat{n}(\Theta, \varphi)$  and therefore exhibit an optical retardation  $\delta = \Delta n d$ ; where  $d$  = film thickness. Moreover, we have shown that LPP- and LCP-films can be stacked [10]; where the  $\approx 30\text{nm}$  thin LPP-layers comprise the photo-aligning and photo-patterning information which adjacent LCP films copy and convert into optical phase information. ROLIC's LPP/LCP optical thin-film building block system enables the generation of virtually any optically anisotropic film stack. Since the films are non-absorptive and optically highly stable and because of their diverse phase retarder properties, LPP/LCP stacks are ideal optical thin film- elements to control the phase of light in polarization sensitive optical devices such as in LCDs, projection engines, etc.. The following examples illustrate some of their many applications.

Fig.4 shows a stack of two LPP- and LCP- layers which act as interference color filters between crossed polarizers P [10]. The LPP layers induce zero bias tilt in the adjacent LCP layers which therefore act as planar, uniaxial optical retarders whose film thickness is chosen such that LCP1 and LCP2 exhibit different optical retardations  $\delta$ . The alignment of layer LPP2 is photo-pixelated such that the respective slow optical axes of the LCP2 pixels align perpendicular to each other. The resulting total optical retardation of the left pixel-stack is therefore subtractive ( $\delta_{\text{tot}} = 320\text{nm}$ ), whereas the right stack is additive ( $\delta_{\text{tot}} = 580\text{nm}$ ). This generates yellow (left) and blue (right) interference colors when exposing the stack to white polarized input light.



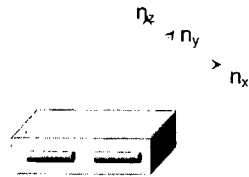
**Fig.4** LPP/LCP polarization interference color filter stack.

Fig.5 schematically depicts three examples to configure LPP/LCP optical thin-film retarders with very diverse optical functions [16]. The stacks are designed to meet the optical requirements of different types of LCDs. For simplicity the LPP photo-aligning layers which induce the respective boundary conditions in the LCP films of Fig.5 are not shown. From top to bottom: (i) zero-tilt, uniaxial retarder; (ii) retarder which consists of two orthogonally aligned uniaxial LCP films and acts as a negative birefringence retarder [13] as well as (iii) a wide-view retarder for TN-LCDs whose orthogonally aligned LCP directors are tilted [11]. Negative retarders of the type depicted in Fig.5 (middle) were used to further enhance the field of view of the dual-domain VAN-LCD of Figs.2,3. The respective optical retardations of the top- and bottom VAN wide-view retarder of Fig.2 are  $\delta_{C1} = 200 + 200 \text{ nm}$  and  $\delta_{C2} = 130 + 130 \text{ nm}$  [13]. We have recently shown [11] that the tilted LPP/LCP retarder configuration at the bottom of Fig.5 enhances the field of view of TN-LCDs to the same degree as discotic wide-view films [17]. Moreover, and because the dispersion of our LPP/LCP wide-view film can be matched with the dispersion of the monomeric liquid crystals in the TN-LCD the chromaticity of the LPP/LCP wide-view film is much improved; i.e. no yellow tint occurs at large viewing angles.

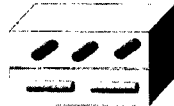
**Uniaxial Retarder**

$$n_x = n_z; \quad n_y = n_z = n_o$$

$$n_x > n_y = n_z$$

**Retarder with Negative Birefringence**

$$n_x = n_y > n_z$$

**Wide View Retarder**

**Fig.5** Three different LPP/LCP optical retarder configurations.

Conventionally, polarization interference color filters are made by vacuum deposition of many layers of dielectric thin-films. As shown in Fig.4 photo-alignment and photo-patterning of LPP/LCP-films enables the realization of such filters by spin coating or by tandem wet-coating. These non-vacuum deposition techniques are compatible with roll-to-roll processes [11,12]. Moreover, the unique optical properties and the broad range of material design parameters of the LPP/LCP technology enable to realize high quality polarization interference filters with only very few LPP/LCP layers. Fig.6 shows the C.I.E. color coordinates of our first R, G, B, LPP/LCP interference color filter stack which consists of only five LPP and LCP layers each. The total film thickness is 12.3  $\mu\text{m}$  and the surface of the film stack is flat. From Fig.6 it follows that five properly photo-aligned LPP/LCP layers lead to color coordinates which meet the PAL/SECAM standard [16].

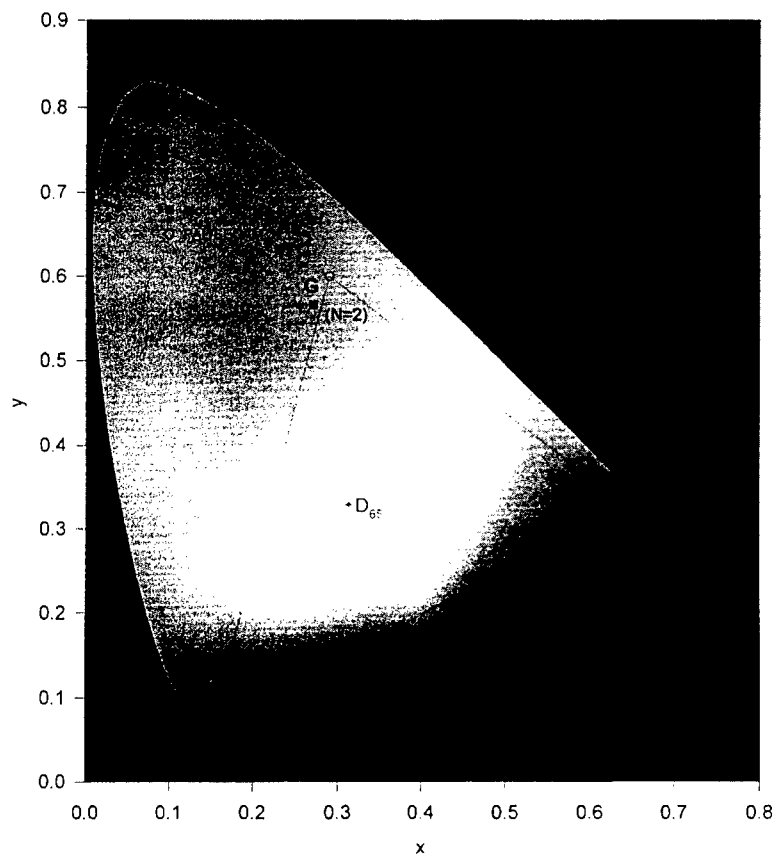


**Fig.6** Color coordinates of 5-layer r, g, b LPP/LCP-polarization interference color filter stack.

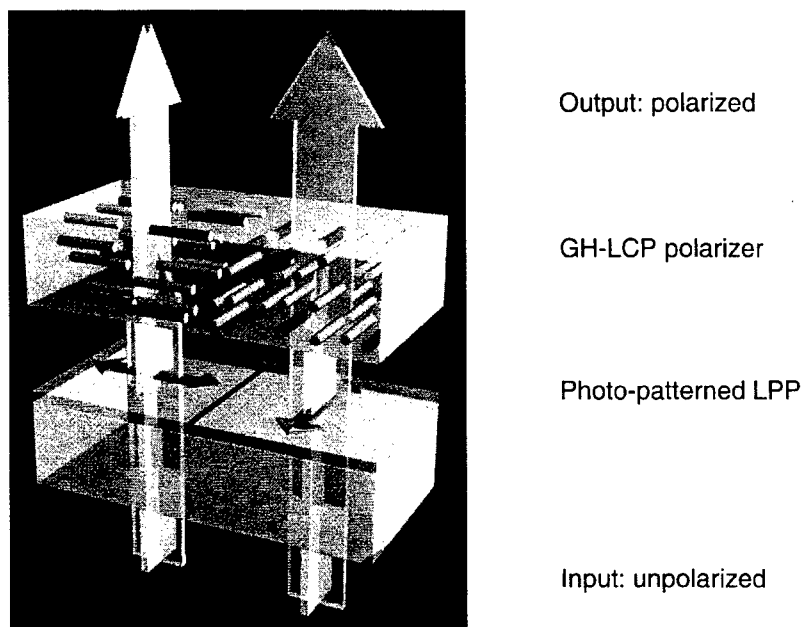


**Fig.7** Two pixels of a photo-structured LPP/LCP dichroic linear polarizer with orthogonal output polarization directions.

To conclude, Fig.7 shows an LPP/LCP guest-host optical device, namely a photo-structured linear polarizer. We photo-patterned and photo-aligned the LPP layer such that adjacent LCP film pixels, which are doped with dichroic dye guest-molecules, align orthogonally. The photo-aligning information is transferred from the LPP surface to the LC-molecules in the LCP layer which acts as a host and transfers the alignment information to the dichroic dye molecules. Due to their dichroism the guest-molecules selectively absorb one of the two linear components of unpolarized input light such that s- and p-polarized light occurs at the output of the structured polarizer in Fig.7. When using the black-white dichroic molecules described in ref. [18] a polarization contrast of 20:1 results for the polarizer in Fig.7. An interesting application for photo-structured polarizers are 3D- LCDs.



## References

- [1] D. W. Berreman, Phys. Rev. Lett. **28**, 1683 (1972)
- [2] M. Eich and J. H. Wendorff, Macromol. Chem. Rapid Commun. **8**, 467 (1987)
- [3] T. Todorov, L. Nikolova and N. Tomova, Appl. Optics **23**, 4309 (1984)
- [4] K. Ichimura, Y. Suzuki, T. Seki et al. Langmuir **4**, 1214 (1988)
- [5] W. M. Gibbons, P. J. Shannon, S. T. Sun et al. Nature **351**, 49 (1991)
- [6] M. Schadt, K. Schmitt, V. Kozenkov et al. Jpn. J. Appl. Phys. **31**, 2155 (1992)
- [7] J. Chen, D. L. Johnson, P. J. Bos et al. Phys. Rev. **54E**, 54 (1996)
- [8] M. Schadt and H. Seiberle, Digest **SID97**, 367 (1997)
- [9] M. Schadt, H. Seiberle and A. Schuster, Nature **381**, 212 (1996)
- [10] M. Schadt, H. Seiberle, A. Schuster et al. Jpn. J. Appl. Phys. **34**, 3240 (1995)
- [11] J. Chen, K. C. Chang, J. DelPico et al. Digest **SID99**, 98 (1999)
- [12] C. Chiulli, J. DelPico, W. Vetterling et al. Digest **SID99**, 1054 (1999)
- [13] H. Seiberle and M. Schadt, Digest **ASIA Display98**, 193 (1998)
- [14] C. Benecke, H. Seiberle and M. Schadt, Jpn. J. Appl. Phys. **39**, 525 (2000)
- [15] D. J. Broer, R. M. Hickmet and G. Challa, Makromol. Chem. **190**, 3201 (1989)
- [16] M. Schadt, H. Seiberle and F. Moia, Proc. Int. Display Workshop **IDW99**, 1013 (1999)
- [17] H. Mori et al. Digest **AMLCD96**, 189 (1996)
- [18] M. Schadt and P. Gerber, Mol. Cryst. Liq. Cryst. **65**, 241 (1980)

## Nonlinear Vibrational Spectroscopy on Rubbed Polymer Surfaces

X. WEI, D. KIM, M. O-HE, and Y. R. SHEN

Department of Physics, University of California, Berkeley, CA 94720, USA

**Abstract** Sum-frequency vibrational spectroscopy is an effective tool for probing polymer surfaces and interfaces. This is demonstrated here by its application on rubbed polymer surfaces. The spectroscopic results show that rubbing preferentially aligns the surface polymer chains along the rubbing direction. The modified polymer surface then acts as a template to align the liquid crystal molecules adsorbed on it.

Polymer surfaces have played an increasingly important role in modern science and technology. For example, many electronic [1] and biomedical [2] applications of polymers depend critically on the interfacial properties of the polymers. Hence possible characterization of polymer interfaces at the molecular level has attracted a great deal of attention. Various spectroscopic techniques such as infrared and Raman spectroscopy [3], X-ray spectroscopy [4], and ellipsometry [5] have been used to probe polymer surfaces and interfaces. They often suffer from not being very surface-specific. Atomic force microscopy [6] is more surface-specific but it does not have sufficient resolution to probe microscopic structure of polymer surfaces and is not suitable for buried polymer interfaces.

In recent years, sum-frequency generation (SFG) vibrational spectroscopy has been demonstrated to be an effective tool to study polymer surfaces and interfaces [7]. As a second-order nonlinear optical process, SFG is highly surface-specific and sensitive in media with inversion symmetry [8]. Being capable of providing spectroscopic information about a surface or interface, it is ideally suited for surface studies of polymers. Indeed, it has been used successfully to probe surface composition and

structure of polymers and their changes in different environments [7]. Even polymers as complex as biopolymers can be studied [9].

An important application of polymers in the electronic industry is its use as an alignment layer for liquid crystal (LC) displays [10]. To construct a homogeneously aligned LC display cell, the commonly adopted method is to use substrates coated with a polymer film that is mechanically rubbed. The LC film sandwiched between such substrates will have its molecules aligned along the rubbing direction. It has been shown that the LC ordering and alignment throughout the film are controlled by the orientation and alignment of the LC monolayers adsorbed at the polymer surfaces of the substrates [11]. For better understanding of LC alignment by rubbed polymer surfaces, it is obvious that we must understand how rubbing induces structural alignment of a polymer surface and then how the adsorbed LC molecules interact with polymer molecular units at the surface.

We have used SFG vibrational spectroscopy to study surfaces of polyvinyl alcohol (PVA) and polyimides, both rubbed and unrubbed [12, 13]. The results clearly show that rubbing aligns the main polymer chains along the rubbing direction. Analysis of the data allows a quantitative determination of the alignment. The LC monolayer deposited on a rubbed polymer surface appears to be oriented and aligned by the surface via an orientational epitaxy-like mechanism.

The theory and the experimental arrangement for SFG spectroscopy have been described elsewhere [14]. With the beam geometry described in the inset of Fig. 1, the experiment measures the effective surface non-linear optical susceptibility  $\chi_{\text{eff}}^{(2)}(\omega_{\text{SF}} = \omega_{\text{vis}} + \omega_{\text{IR}})$  for different sample orientations (defined by the azimuthal angle  $\gamma$  in Fig. 1) and different polarization orientations

$$\chi_{\text{eff}}^{(2)} = [\mathbf{L}(\omega_{\text{SF}}) \cdot \mathbf{e}_{\text{SF}}] \cdot \chi^{(2)} : [\mathbf{L}(\omega_{\text{vis}}) \cdot \mathbf{e}_{\text{vis}}][\mathbf{L}(\omega_{\text{IR}}) \cdot \mathbf{e}_{\text{IR}}] \quad (1)$$

where  $\mathbf{e}_i$  is the unit polarization vector of the field at  $\omega_i$ ; and  $\mathbf{L}(\omega_i)$  is the tensorial transmission Fresnel factor at  $\omega_i$ . If  $\omega_{\text{IR}}$  is scanned over a surface vibrational resonance,  $\chi_{\text{eff}}^{(2)}$  is resonantly enhanced yielding a surface vibrational spectrum. We have the SFG spectrum described by

$$S(\omega_{\text{IR}}) = |\chi_{\text{eff}}^{(2)}|^2 \quad (2)$$

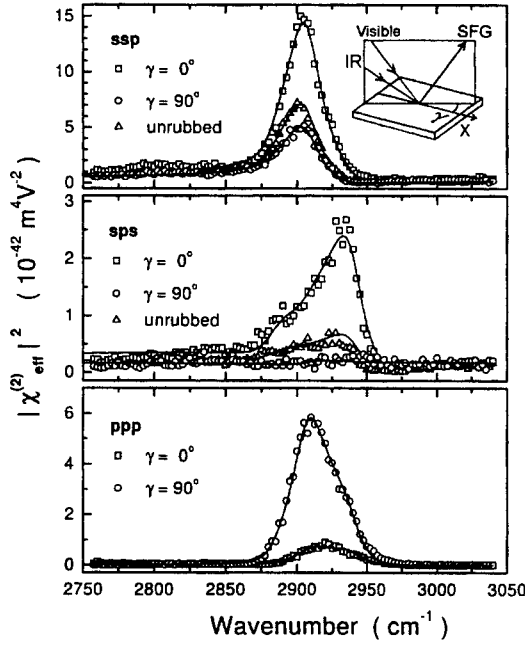


Figure 1: SFG spectra of a PVA surface, rubbed (circles and squares) and unrubbed (triangles) for three different polarization combinations. The lines are fits from Eqs. (1)-(3). The inset describes the experimental geometry with  $x$  being along the rubbing direction and  $\gamma$  the azimuthal angle between  $x$  and the incident plane.

with  $\chi_{\text{eff}}^{(2)}$  given in Eq. (1) and

$$\chi^{(2)}(\omega_{\text{IR}}) = \chi_{\text{NR}}^{(2)} + \sum_q \frac{A_q}{\omega_{\text{IR}} - \omega_q + i\Gamma_q} \quad (3)$$

where  $A_q$ ,  $\omega_q$  and  $\Gamma_q$  are the strength, resonant frequency, and damping coefficient of the  $q$ th vibrational mode, respectively, and  $\chi_{\text{NR}}^{(2)}$  is the nonresonant contribution. As an example, Fig. 1 shows the SFG spectra of PVA ( $[-\text{CH}_2-\text{CHOH}]_n$ ) for various beam polarization combinations. Three CH stretch modes appear in the spectra: a stretch mode at  $2882 \text{ cm}^{-1}$  for the CH group, and a symmetric stretch at  $2907 \text{ cm}^{-1}$  and

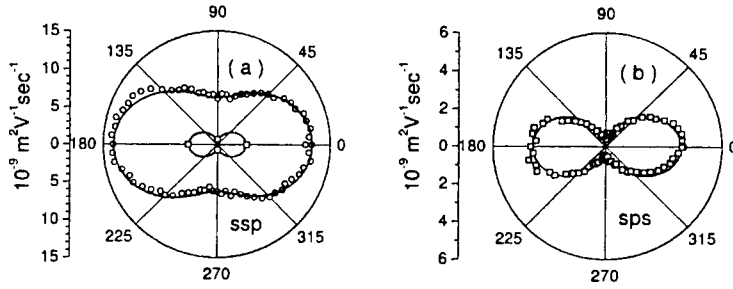


Figure 2: Polar plots of  $A_{q,\text{eff}}$  of the  $\text{CH}_2$  symmetric (circles) and antisymmetric (squares) stretch modes as functions of  $\gamma$  for two polarization combinations (a) *ssp* and (b) *sps*. Lines are obtained from fits.

an antisymmetric stretch at  $2940\text{ cm}^{-1}$  for the  $\text{CH}_2$  group. As shown in Fig. 1, the experimental data can be well fit by Eqs. (1)-(3). From the fit, we can deduce  $A_q$  for each case.

The spectra in Fig. 1 show clearly that there is an induced anisotropy in the structure of the rubbed PVA surface. For example, the antisymmetric stretch mode of  $\text{CH}_2$  in the *sps* spectra (denoting *s*-, *p*-, and *s*-polarized sum-frequency, visible, and infrared beams, respectively) is strong for  $\gamma = 0^\circ$  but absent for  $\gamma = 90^\circ$ . Since this mode can only be excited with an IR field component in the  $\text{CH}_2$  plane, the observed spectra immediately suggest that the  $\text{CH}_2$  plane at the PVA surface must be perpendicular to the rubbing direction. Now that  $\text{CH}_2$  must be perpendicular to the PVA backbone, the result indicates that the PVA chains must be oriented along the rubbing direction.

In the complete experiment on PVA, we measured  $\chi_{\text{eff}}^{(2)}$  for the rubbed PVA surface for many different sample orientations ( $\gamma$ ) with *sps* and *ssp* polarization combinations. The quantities  $A_{q,\text{eff}} = [\mathbf{L}(\omega_{\text{SF}}) \cdot \mathbf{e}_{\text{SF}}] \cdot \mathbf{A}_q : [\mathbf{L}(\omega_{\text{vis}}) \cdot \mathbf{e}_{\text{vis}}][\mathbf{L}(\omega_{\text{IR}}) \cdot \mathbf{e}_{\text{IR}}]$  versus  $\gamma$  deduced from  $\chi_{\text{eff}}^{(2)}$  for  $q = s$  (symmetric  $\text{CH}_2$  stretch) and  $q = a$  (antisymmetric  $\text{CH}_2$  stretch) are plotted in Fig. 2. It is easy to see that  $A_{q,\text{eff}}(\gamma)$  can be described in terms of a linear combination of  $(A_q)_{ijk}$ . By symmetry, there are only 10 nonvanishing independent elements of  $(A_q)_{ijk}$  for a rubbed surface, namely,  $xxz$ ,  $yyz$ ,  $zzz$ ,  $xxz = zxx$ ,  $yyz = zyy$ ,  $xxx$ ,  $yyx$ ,  $zzx$ ,  $xyy = yxy$ , and  $xzz = zxz$  for the subindices with  $x$  along the rubbing direction and  $z$  the surface

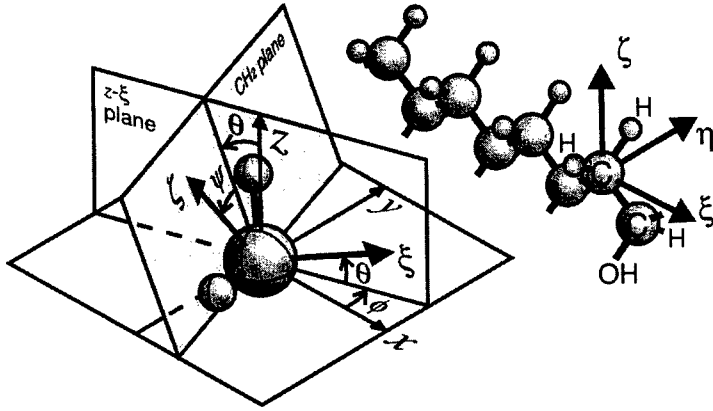


Figure 3: Molecular structure of PVA and orientational geometry of a  $\text{CH}_2$  group on PVA at a rubbed surface. Axis  $x$  is along the rubbing direction, and  $z$  is along the surface normal. Axis  $\xi$  is normal to the  $\text{CH}_2$  plane or along the PVA chain, and  $\zeta$  is along the symmetry axis of  $\text{CH}_2$ .

normal. Fitting the data of  $A_{q,\text{eff}}(\gamma)$  in Fig. 2 then allows us to deduce all these nonvanishing elements with good accuracy. This is particularly true because the very weak forward-backward asymmetry in the data of Fig. 2 renders the last five independent elements in the above list nearly vanishing. We now realize that  $(A_q)_{ijk}$  is related to the strength  $\mathbf{a}_q$  of the molecular polarizability of the  $q$ th vibrational mode by a coordinate transformation and an orientational average

$$(A_q)_{ijk} = N_S \int \sum_{\lambda\mu\nu} (\mathbf{a}_q)_{\lambda\mu\nu} (\hat{\lambda} \cdot \hat{i})(\hat{\mu} \cdot \hat{j})(\hat{\nu} \cdot \hat{k}) f(\Omega) d\Omega \quad (4)$$

where  $N_S$  is the surface molecular density and  $f(\Omega)$  is the orientational distribution for the  $\text{CH}_2$  groups at the surface. For the  $\text{CH}_2$  stretch vibrations, the only nonvanishing elements of  $\mathbf{a}_q$  are  $(a_s)_{\xi\xi\xi}$ ,  $(a_s)_{\eta\eta\xi}$ ,  $(a_s)_{\zeta\zeta\xi}$ , and  $(a_a)_{\eta\zeta\eta} = (a_a)_{\zeta\eta\eta}$  with  $\zeta$  along the symmetry axis of  $\text{CH}_2$  and  $\eta$  in the  $\text{CH}_2$  plane. The values of these  $\mathbf{a}_q$  elements can be calculated from the known values for a single CH bond using the bond additivity model [15]. With  $(A_q)_{ijk}$  ( $q = s, a$ ) given, Eq. (4) can then be used to deduce an approximate form for  $f(\Omega)$ .

For  $\text{CH}_2$  at the rubbed PVA surface, we can assume a Gaussian dis-

tribution for  $f(\Omega)$

$$f(\Omega) = C \exp \left[ -\frac{(\theta - \theta_0)^2}{2\sigma_\theta^2} - \frac{(\phi - \phi_0)^2}{2\sigma_\phi^2} - \frac{(\psi - \psi_0)^2}{2\sigma_\psi^2} \right] \quad (5)$$

where  $\theta$ ,  $\phi$  and  $\psi$  define the orientation of a  $\text{CH}_2$  group described in Fig. 3;  $C$  is a normalization constant;  $\theta_0$ ,  $\phi_0$ ,  $\psi_0$ ,  $\sigma_\theta$ ,  $\sigma_\phi$ , and  $\sigma_\psi$  are parameters to be determined. From the mirror symmetry about the rubbing direction, we have  $\phi_0 = \psi_0 = 0^\circ$ . The remaining four parameters can be determined consistently with good accuracy from the known values of more than 10  $(A_q)_{ijk}$  elements. We found in our case of a relatively strongly rubbed PVA surface,  $\theta_0 = 2.5^\circ \pm 0.7^\circ$ ,  $\sigma_\theta = 26^\circ \pm 5^\circ$ ,  $\sigma_\phi = 27^\circ \pm 5^\circ$ , and  $\sigma_\psi = 35^\circ \pm 5^\circ$  for  $\text{CH}_2$  orientation. Accordingly, the PVA chains must be well aligned along the rubbing direction with a narrow angular distribution and on average, a  $2.5^\circ$  backward tilt.

To see how adsorbed LC molecules orient on a rubbed PVA surface, we deposited a monolayer of octyl-cyanobiphenyl (8CB) on it and used optical second-harmonic generation (SHG) to probe its orientational distribution [11]. The results appear as SHG intensity versus sample azimuthal rotation for various input/output polarizations [15]. In an analysis similar to the one described above, we could obtain an orientational distribution for the LC monolayer.

$$g(\Omega) = C \exp \left[ -\frac{(\theta - \theta_0)^2}{2\sigma_\theta^2} \right] [1 + d_1 \cos \phi + d_2 \cos(2\phi) + d_3 \cos(3\phi)] \quad (6)$$

with  $\theta$  and  $\phi$  denoting the polar and azimuthal angles of the 8CB core, respectively, and  $\theta_0 = 75^\circ$ ,  $\sigma_\theta = 9^\circ$ ,  $d_1 = 0.07$ ,  $d_2 = 0.85$ , and  $d_3 = 0.04$ . From  $f(\Omega)$  and  $g(\Omega)$  we can calculate  $F(\phi) = \int f(\Omega) \sin \theta d\theta d\psi$  and  $G(\phi) = \int g(\Omega) \sin \theta d\theta$  for PVA and 8CB, respectively. The results show that the two match closely. This provides strong evidence that the rubbed polymer indeed serves as a template to align the LC monolayer through short-range interaction.

We also studied polyimide surfaces, rubbed and unrubbed, with SFG vibrational spectroscopy. The samples were prepared by the spin coating method described in Ref. [13]. Fig. 4 presents the *ssp* spectra of a rubbed poly-n-alkyl-pyromellitic imide surface ( $[-\text{N}(\text{CO})_2\text{C}_6\text{H}_2(\text{CO})_2\text{N}(\text{CH}_2)_n-]$  with  $n=6$  (P6), whose chemical structure is depicted in the inset). The two peaks at  $1729$  and  $1777 \text{ cm}^{-1}$  are associated with the antisymmetric and symmetric stretch modes of the coupled CO groups on the imide ring,

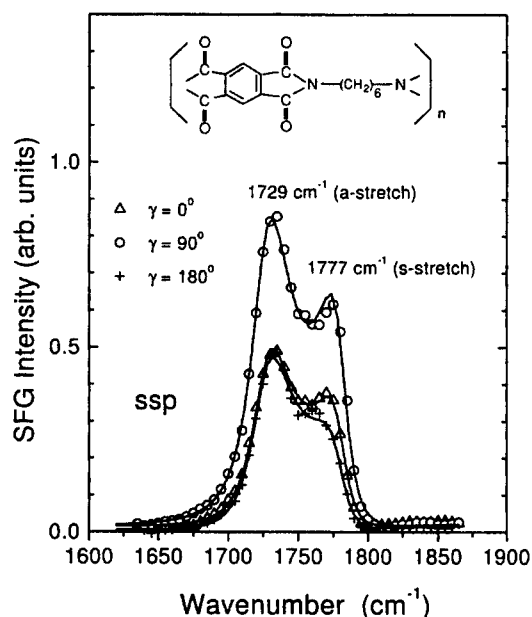


Figure 4: SFG vibrational spectra of a rubbed polyimide surface with the *ssp* polarization combination for  $\gamma = 0^\circ, 90^\circ$ , and  $180^\circ$ . The inset shows the chemical structure of the polyimide.

respectively. Again, the spectra show explicitly the existence of rubbing-induced anisotropy in the surface structure of P6 polyimide. While the spectra taken with the incident plane parallel and anti-parallel to the rubbing direction are nearly the same, they are significantly weaker than the one taken with the incident plane perpendicular to the rubbing direction. This indicates that the CO plane or the imide ring is preferentially oriented along the rubbing direction. Analysis of results obtained with different polarization combinations show that the spectra originated from the two CO groups on the same side of the imide ring projecting out of the surface. The induced orientation of the CO groups is a direct manifestation of the induced alignment of the polyimide main chains at the surface by rubbing.



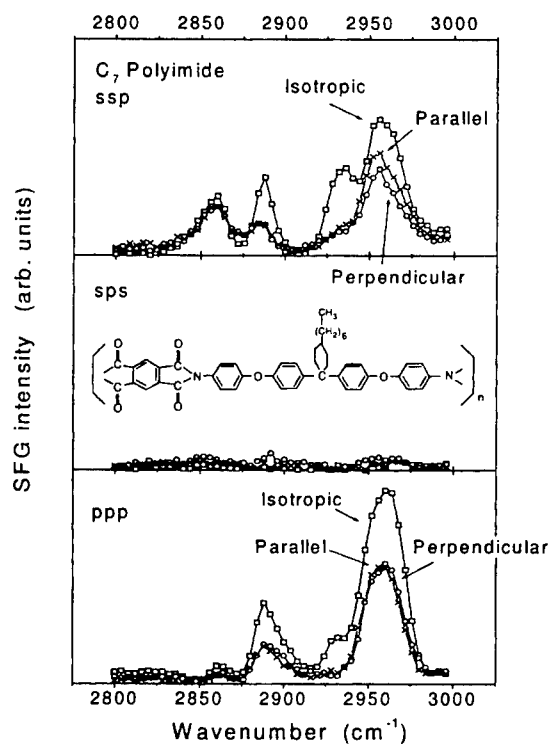


Figure 5: SFG spectra of the rubbed surface of a polyimide with side alkyl chain. The inset shows the chemical structure of the polyimide.

We have also studied the surfaces of polyimides with side chains (chemical structure of one such polyimide is shown in the inset of Fig. 5). The SFG spectra for CO stretches in the  $1750 \text{ cm}^{-1}$  region are similar to those of P6 polyimide. Again they exhibit an anisotropy induced by rubbing that arises from alignment of the main chains along the rubbing direction. The CH stretch modes associated with the alkyl side chains, however, show very little induced anisotropy, as seen from the spectra of Fig. 5. Analysis of spectra with various polarization combinations indicates that the side chains protrude out from the surface with a broad angular distribution about the surface normal. Alignment of the main chains can

hardly affect the orientational distribution of the side chains. This then explains the lack of induced anisotropy by rubbing.

In conclusion, we have demonstrated that SFG vibrational spectroscopy is an effective tool to probe rubbing-induced modification of a polymer surface. It is found that rubbing preferentially aligns the surface polymer chains along the rubbing direction. The modified surface structure then acts as a template that effectively aligns the LC monolayer adsorbed on it and consequently the bulk LC film. Such a template effect is clearly not restricted to LC on polymer. The spectroscopic technique described here is also generally useful for studies of polymer surface structures and their changes by external perturbations.

#### Acknowledgments

This work was supported by NSF Grant No. DMR-9704384.

#### References

- [1] J. Dinardo, J. E. Demuth and T. C. Clarke, J. Chem. Phys. **85**, 6739 (1986).
- [2] J. B. Park and R. S. Lakes, Biomaterials: an Introduction, (Plenum Press, New York, 1992).
- [3] K. C. Cole, J. Guevremont, A. Ajji, and M. M. Dumoulin, Appl. Spectrosc. **48**, 1513 (1994); N. Yiu, Y. Suzuki, H. Mori, and M. Terano, J. Polymer **27**, 614 (1995); B. J. Kip and M. C. P. van Eijk, J. Polymer Sci. B **29**, 99 (1991).
- [4] K. B. Lewis, and D. R. Ratner, J. Colloid Interface Sci. **159**, 77 (1993); K. Weiss, et al, Macromolecules **31**, 1930 (1998); J. Stohr, et al, Macromolecules **31**, 1942 (1998).
- [5] I. Hirose, Jpn. J. Appl. Phys. **35**, 5873 (1996).
- [6] A. J. Pidduck, et al, J. Vac. Sci. Technol. A **14**, 1723 (1996); Y. B. Kim, et al, Appl. Phys. Lett. **66**, 2218 (1995); Y. M. Zhu, et al, Appl. Phys. Lett. **65**, 49 (1994).

- 
- [7] D. Zhang, et al, J. Phys. Chem. **101**, 9060 (1997); D. Zhang, et al, J. Phys. Chem. **102**, 6225 (1998); D. H. Gracias, et al, Tribology Lett. **4**, 231 (1998).
  - [8] Y. R. Shen, Nature **337**, 519 (1998).
  - [9] Z. Chen, et al, J. Phys. Chem. (to be published).
  - [10] J. M. Geary, et al, J. Appl. Phys. **62**, 4100 (1987).
  - [11] X. Zhuang, L. Marrucci, and Y. R. Shen, Phys. Rev. Lett. **73**, 1513 (1994).
  - [12] X. Wei, et al, Phys. Rev. Lett. **82**, 4256 (1999).
  - [13] D. Kim, and Y. R. Shen, Appl. Phys. Lett.
  - [14] Y. R. Shen, in Frontiers in Laser Spectroscopy, Proc. of the International School of Physics, "Enrico Fermi", Course CXX, edited by T. W. Hansch and M. Inguscio (North Holland, Amsterdam, 1994), p.139.
  - [15] X. Wei, et al, (submitted to Phys. Rev. B)

## Production of High Bandwidth Polymeric Electro-Optic Modulators With $V_{\pi}$ Voltages of Less Than 1 Volt

LARRY DALTON, BRUCE ROBINSON AND WILLIAM STEIER  
Department of Chemistry, University of Washington, Seattle, WA  
98195-1700 and Department of Electrical Engineering, University of  
Southern California, Los Angeles, CA 90089-0483

**ABSTRACT:** Structure/function relationships crucial to realization of broad bandwidth, low halfwave voltage, high stability polymeric electro-optic modulators are discussed. Particular attention is given a family of chromophores containing cyanofuran acceptors. Such chromophores permit the simultaneous realization of large molecular hyperpolarizability and thermal stability. The role of intermolecular electrostatic interactions in limiting maximum achievable macroscopic electro-optic activity is discussed within the frameworks of both equilibrium and Monte Carlo statistical mechanical calculations. The processing of polymeric electro-optic materials into low optical loss, 3-D optical circuits is discussed. Finally, the use of polymeric electro-optic circuits for realization of phased array radar, time stretching, and other device applications is reviewed.

**Keywords** Electro-optic polymers, intermolecular interactions, Monte Carlo calculations, phased array radar, high bandwidth modulators, 3-D integration, optical loss

## INTRODUCTION

Five quite different types of materials have attracted attention for use in external modulation; namely, crystalline lithium niobate, crystalline organic materials such as DAST, multilayer organic materials fabricated by sequential self-assembly methods, electro-absorptive gallium arsenide materials, and electrically-poled polymeric electro-optic (EO) materials. The inorganic materials, lithium niobate and gallium arsenide, have certain advantages. For example, lithium niobate can be used as a low loss material over a

wide range of wavelengths. Gallium arsenide permits polarization insensitive modulation to be carried out. It is doubtful that one material will ever be the material of choice for every application of external modulators.

Electrically-poled, chromophore-containing polymeric materials have attracted attention because of their potential for yielding low drive voltage, broad bandwidth electro-optic materials that can be readily integrated with very large scale integration (VLSI) semiconductor electronics and passive optical circuitry. Conceivably, these materials could also permit low cost fabrication of multiple modulator opto-chips characterized by low crosstalk and low optical loss at telecommunication wavelengths. Although a number of chromophores with large dipole moments and hyperpolarizabilities have been synthesized over the past several years, it is only recently that polymeric electro-optic materials have been produced that exhibit large electro-optic activity at telecommunication wavelengths [1]. Indeed, only in the past several months, have  $V_{\pi}$  voltages on the order of 1 volt been demonstrated for polymeric materials with push-pull Mach Zehnder devices [2,3]. The reason for failure to translate ever-improving molecular optical nonlinearity into macroscopic optical nonlinearity can be appreciated from a consideration of Figure 1.

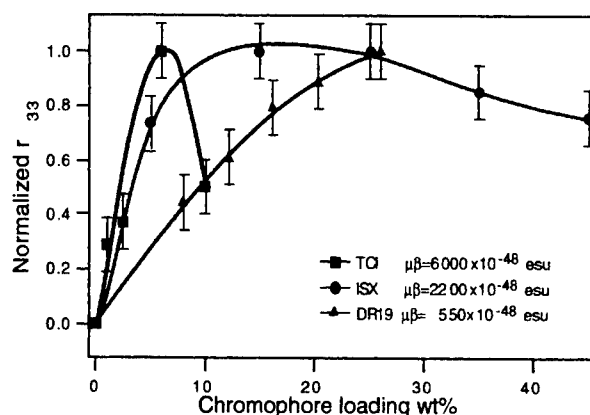


Figure 1. The variation of electro-optic activity with chromophore concentration is shown. The structures of the chromophores are given in [1].

From Figure 1, we see that although increasing dipole moment ( $\mu$ ) and molecular hyperpolarizability ( $\beta$ ) leads to greater initial slope of the dependence of electro-optic coefficient upon chromophore loading, the curves roll over at ever lower loading values as  $\mu\beta$  increases. Thus, little or no increase in macroscopic electro-optic activity is achieved by development of chromophores with larger  $\mu\beta$  values.

In Figure 2, different structural forms of chromophores containing the same electro-optically active  $\pi$ -electron core are shown.

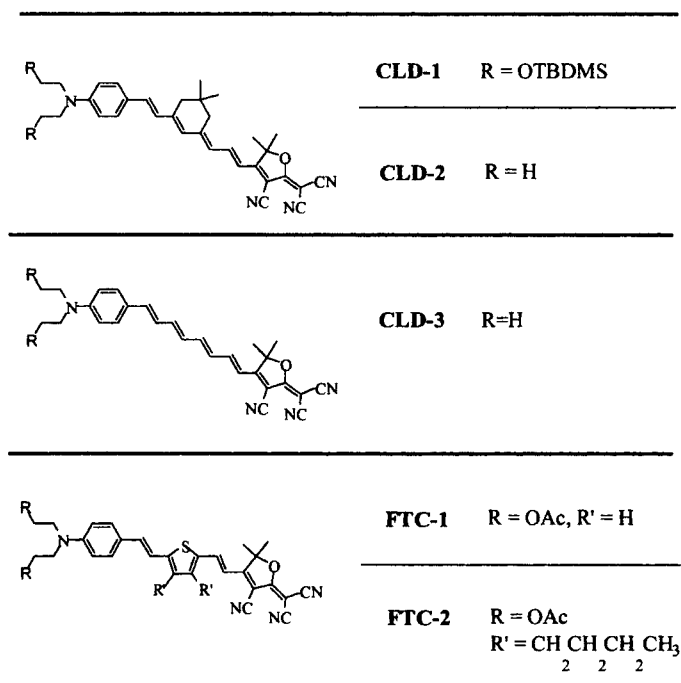


Figure 2. Variants of CLD and FTC type chromophores are shown.

In Figure 3, we show the effect of adding an isophorone group to the  $\pi$ -electron bridge of CLD-type chromophores. This figure clearly

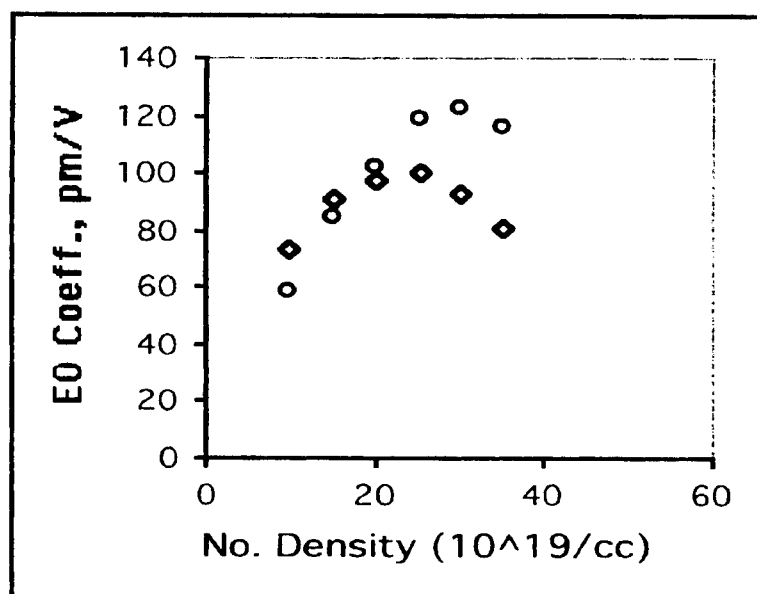


Figure 3. Electro-optic coefficients are shown as a function of chromophore number density for CLD-2 (circles) and CLD-3 (diamonds) chromophores in polymethylmethacrylate (PMMA).

demonstrates that maximum achievable electro-optic activity also depends upon chromophore shape. The dependence on chromophore dipole moment and shape shown in Figures 1 and 3 suggest that spatially-anisotropic intermolecular electrostatic interactions influence the translation of microscopic hyperpolarizability into macroscopic electro-optic activity. Clearly, the linear dependence of electro-optic coefficient on chromophore number density that would be expected for non-interacting particles is not observed. Let us consider the competition of poling field and intermolecular electrostatic interactions within the frameworks of both equilibrium and Monte Carlo statistical mechanical methods. These two approaches involve quite different approximations and comparison of the results should provide useful insight into the validity of approximations made with each approach. Moreover, molecular dynamical methods should provide useful insight into aggregation phenomena that can lead to light scattering and unacceptable optical loss.

THEORY AND RESULTS

Electro-optic activity is approximately given by  $r = 2N\beta f(\omega) \langle \cos^3 \theta \rangle / n^4$ , so our objective must be the evaluation of the acentric order parameter  $\langle \cos^3 \theta \rangle$ . In the equation for electro-optic coefficient,  $r$ , number density is denoted by the symbol  $N$ ,  $n$  is the index of refraction,  $\beta$  is the first molecular hyperpolarizability, and  $f(\omega)$  takes into account medium dielectric effects. The order parameter can be calculated by equilibrium statistical mechanics according to

$$\langle \cos^n(\theta) \rangle = \frac{\int_{\cos(\theta)=-1}^1 \cos^n(\theta) \exp\{-U/kT\} d\cos\theta}{\int_{\cos(\theta)=-1}^1 \exp\{-U/kT\} d\cos\theta}$$

where  $U = U_1 + U_2$  is the potential energy describing the interaction of chromophores with the poling field ( $U_1$ ) and with each other ( $U_2$ ). For non-interacting chromophores,  $U = -\mu F \cos\theta$ , where  $F$  is the poling field felt by the chromophore. For this case,  $\langle \cos^n \theta \rangle = L_n(f)$  where  $L_n$  is the  $n^{\text{th}}$  order Langevin function and  $f = \mu F/kT$ . Consider chromophores interacting through a mean distance,  $R$ , which is related to number density by  $N = R^{-3}$ . Let us follow Piekara [4] and write the effective field at a given chromophore from surrounding chromophores as  $U_2 = -W \cos(\theta_2)$ . The position with respect to the poling field is defined by Euler angles,  $\Omega_1 = \{\theta_1, \phi_1\}$  and by the trigonometric relationship  $\Omega_1 = \Omega \oplus \Omega_2$  or  $\cos\theta_1 = \cos\theta \cos\theta_2 + \sin\theta \sin\theta_2 \cos(\phi - \phi_2)$ . Averaging is done over the two variables  $\Omega$  and  $\Omega_2$ . Explicitly,

$$\langle \langle \cos^n(\theta) \rangle \rangle = \frac{1}{4\pi} \int_{\phi=0}^{2\pi} \int_{\cos(\theta)=-1}^1 \frac{\int_{\cos(\theta_2)=-1}^1 \int_{\phi_2=0}^{2\pi} \cos^n(\theta_1) \cdot \exp\{-U/kT\} d\cos\theta_2 d\phi_2}{\int_{\cos(\theta)=-1}^1 \int_{\phi=0}^{2\pi} \exp\{-U/kT\} d\cos\theta_2 d\phi_2} d\cos\theta d\phi$$



The total potential is taken as  $-f\cos(\theta) - W\cos(\theta_2)$ . In the high temperature approximation,  $\exp(-U_1/kT) = 1 - f\cos(\theta_1)$ .

$$\langle\langle\cos^n(\theta)\rangle\rangle = \left\langle \frac{\langle\cos^n(\theta_1)\rangle_2 - f\langle\cos^{n+1}(\theta_1)\rangle_2}{1 - f\langle\cos(\theta_1)\rangle_2} \right\rangle$$

$$\langle\langle\cos^n(\theta)\rangle\rangle = \langle\langle\cos^n(\theta_1)\rangle_2 - f\{\langle\cos^{n+1}(\theta_1)\rangle_2 - \langle\cos^1(\theta_1)\rangle_2\langle\cos^n(\theta_1)\rangle_2\}\rangle$$

These integrals can be evaluated analytically giving

$$\langle\cos^n(\theta)\rangle = L_n(f)\{1 - L_1^2(w/kT)\}$$

Equilibrium statistical mechanical calculations are easily modified to take into account nuclear repulsive effects (in the hard shell limit, by simply adjusting the limits of integration). Below we show simulation data for a typical CLD-type chromophore in PMMA, where we separate (shape) and purely intermolecular electronic effects.

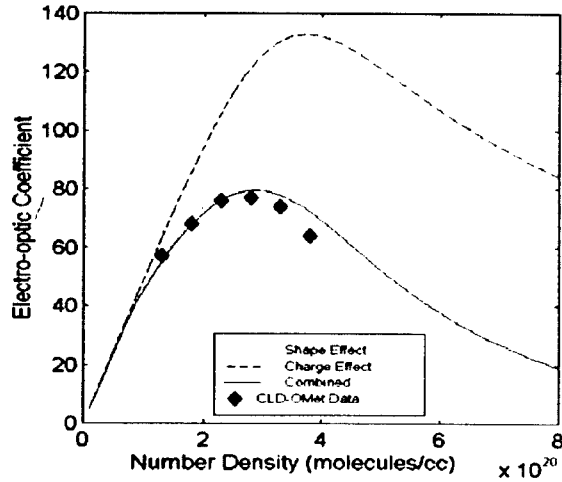


Figure 4. Experimental (solid diamonds) and theoretical (lines) data are compared for the CLD-OMet chromophore in PMMA.

The chromophore of Figure 4 is simply CLD-1 (see Figure 2) with the TBDMS (tetra-butyl-dimethylsilyl) group replaced by a Met (methyl) group.

Several features of Figure 4 merit comment. As we have noted elsewhere [2,5-7], consideration of both nuclear repulsive and longer-range purely electronic interactions are necessary for quantitative simulation of experimental results. Note that the functional dependence of these two effects on chromophore number density is different. The agreement of theory with experiment is not perfect, which in the present case reflects the neglect of higher order self-consistent dielectric corrections (see Figure 5 for inclusion of these effects).

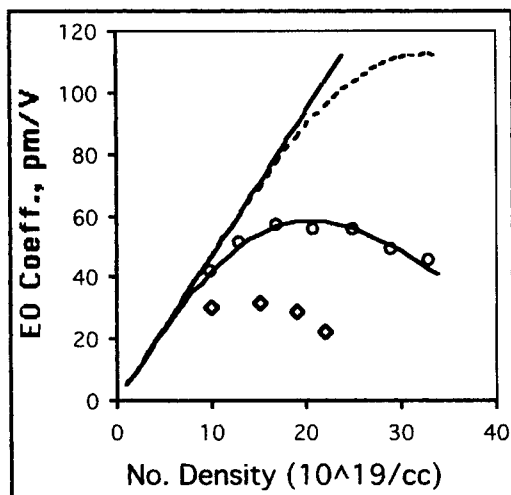


Figure 5. Theoretical (lines) and experimental (symbols) results are shown for FTC-type chromophores in PMMA. Diamonds are for FTC-1 and circles are for FTC-2 (see Figure 2). The dashed line is obtained treating chromophores as hard spheres. The straight line is for total neglect of intermolecular electrostatic interactions.

Actually, that good agreement can be obtained neglecting these corrections is at first surprising but reflects the fact both negative and positive terms are associated with these corrections. That is, the medium dielectric attenuates the poling field felt by a chromophore

but also attenuates intermolecular electrostatic interactions (which themselves act to attenuate the effective poling field). With neglect of higher order self-consistent dielectric iterations, calculations can be carried out on personal computers.

The equilibrium statistical mechanical calculations, such as shown in Figure 4, tell us two things. First, theoretical results tell us that we want to make chromophores as spherical as possible because the close packing of prolate ellipsoidal structures will favor centrosymmetric chromophore order. Second, theoretical results tell what chromophore concentration will lead to optimum electro-optic activity for a given chromophore structure (shape). As discussed elsewhere, these theoretical suggestions have been tested and found valid for a number of chromophore/polymer systems [2,5-7]. From a device standpoint, the important result is that a number of chromophores have been designed that, when examined as components of simple polymer composites of PMMA or amorphous polycarbonate (APC, Aldrich Chemicals), lead to electro-optic coefficients greater than 100 pm/V at 1.06  $\mu\text{m}$ . When extended protection of polyene bridges or dithiophene units [8] are incorporated, values approaching 130 pm/V have been obtained. The chromophores leading to these high values of electro-optic activity also exhibit thermal stability (chromophore decomposition temperatures) on the order of 300°C. These materials hold considerable promise for permitting devices with 1 volt or lower halfwave voltages to be routinely fabricated.

It would seem as if the theoretical and experimental status of polymeric electro-optic materials is in good shape but in point of fact this conclusion is premature. A number of critical details, including (1) rigorous justification of theoretical approximations, and (2) critical evaluation of device performance characteristics under harsh operating conditions, remain to be convincingly demonstrated. The remainder of this article is devoted to consideration of these issues, which cannot be definitively put to rest at this time.

The approximation of Piekara [4], describing the potential felt by a reference chromophore from surrounding chromophores as  $-W\cos\theta$ , greatly facilitates the treatment of long-range, many-body chromophore interactions. Unfortunately, it is not simple to justify this approximation from first principles. Moreover, equilibrium statistical mechanical methods do not facilitate the consideration of non-uniform chromophore distributions arising from kinetic phenomena such as chromophore aggregation. Thus, to test the

approximation of Piekara and to consider non-equilibrium as well as equilibrium phenomena, we undertook Monte Carlo simulations of the competition of poling field and intermolecular electrostatic interactions. Monte Carlo calculations are carried out with rigorous consideration of intermolecular electrostatic (e.g., dipole-dipole, etc.) interactions and calculations extend over non-nearest neighbor interactions. Indeed, calculations are limited only by the finite size of the 3-dimensional chromophore lattice, which in our case is taken as 1000 interacting chromophores. Our Monte Carlo results are discussed in much greater detail elsewhere [7] and we will make only a couple of salient points here. The first is that Monte Carlo results lead to the same functional dependence as found with the Piekara approximation (see Figure 6).

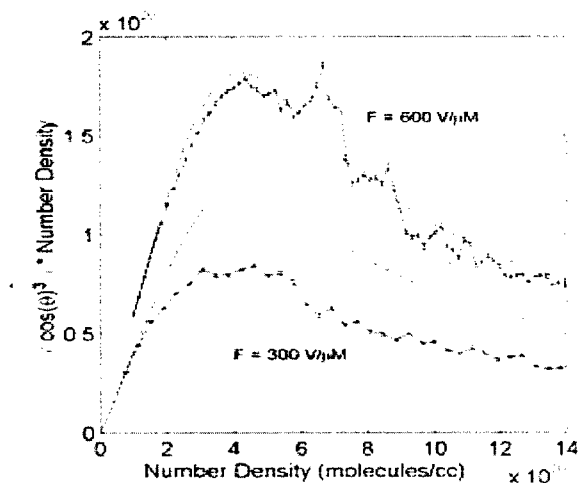


Figure 6. Comparison of the functional dependence of  $r/\beta$  upon  $N$  is given for the Piekara approximation (solid and dashed lines) and for Monte Carlo methods (connected error bars). The two methods are in good agreement.

Monte Carlo calculations reproduce all of the experimentally observed trends, e.g., the dependence of  $r/\beta$  curves upon chromophore dipole moment shown in Figure 7. Note that strong dependence on dipole moment is observed only for values greater than 7 Debye.

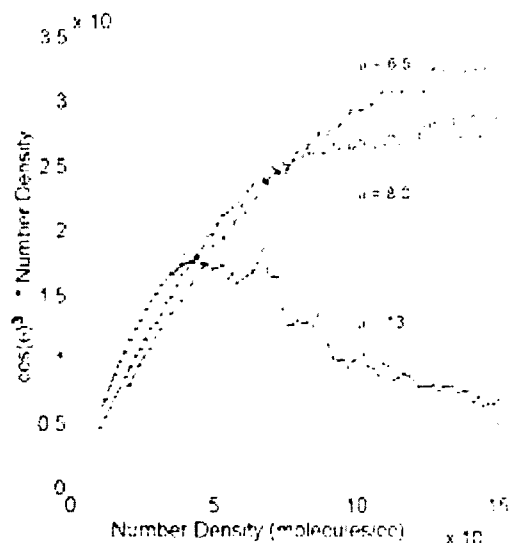


Figure 7. The variation of theoretical (Monte Carlo calculation) curves of  $r/\beta$  versus  $N$  with chromophore dipole moment is shown.

Theoretically-predicted trends are in good agreement with experimental results (e.g., see Figure 1). The agreement between equilibrium statistical mechanical and Monte Carlo calculations provides support for Piekara approximation. Moreover, Monte Carlo calculations suggest that chromophore aggregation and phase separation should not be a problem for corona poling of chromophores considered here. However, if the poling field strength is reduced or if chromophore dipole moments are further increased, aggregation is predicted to become problematic. Monte Carlo results do explain a number of experimentally-observed kinetic effects including electric field dependent phenomena. Indeed, Monte Carlo results send a strong warning to pay attention to the details of processing and to properties such as the dielectric constant of the host polymer. Failure to do so can lead to chromophore aggregation and unacceptably high optical loss. On the positive side, Monte Carlo calculations are starting to provide insight even to the details of poling dynamics and to the interaction of chromophores with the host matrix [9].

## DISCUSSION

Our attention to this point has focused on improving electro-optic activity. Such improvement is crucial to the realization of a number of special applications including lossless optical links [2,3], time stretching [10] and ultrafast analog-to-digital conversion, ultrastable oscillators, optical gyroscopes, and phased-array radar systems [11]. Low  $V_{\pi}$  is certainly a critical consideration for some applications including those involving radiofrequency (RF) photonics.

However, auxiliary properties such as optical loss (including material and mode-mismatch or insertion loss), thermal stability, photochemical stability, and ease of integration with other systems components and circuitry are also crucial. Failure in any area can be fatal for device application.

Just as electro-optic activity will depend upon detailed material structure, so will photochemical and thermal stability. Simply attaching the second end of a chromophore to a crosslinked polymer lattice can improve photochemical stability (for irradiation with 1.3 micron light) from nonexistent even for 50 mW power levels and low fluence to capable of withstanding 250 mW power radiation to fluences of 700 gigajoules per cubic centimeter or higher [1]. In like manner, such chromophore attachment can improve the thermal stability of electro-optic activity from 50-80°C to greater than 170°C [1]. In like manner, material optical loss can be systematically reduced by isotopic substitution; we have realized loss values on the order of 0.7 dB/cm at 1.3  $\mu\text{m}$  and 1 dB/cm at 1.55  $\mu\text{m}$ . Even lower values are likely in the future with further structural modifications.

What is not typically appreciated is that polymeric EO materials represent an evolving technology. Improvement in one area usually results in a temporary set-back in other properties but not always so. The chromophores, which have lead to large electro-optic activity for composite materials [2,3], have already been incorporated into hardened lattices with the result of greatly improved thermal and photochemical stability with only modest sacrifice of electro-optic activity. While the ultimate utility of these materials can only be ascertained after extended beta testing of devices, there is every reason to believe that stability comparable to lithium niobate will be realized for operation at telecommunication wavelengths. As we have already shown [1], it is unreasonable to expect such stability for composite materials or for chromophores having a single point of attachment to a

low glass transition polymer such as PMMA [1]; this point is also made by others in this volume.

### ACKNOWLEDGEMENTS

The authors gratefully acknowledge support of this work by the National Science Foundation and by the Air Force Office of Scientific Research.

### REFERENCES

1. L. R. Dalton, W. H. Steier, B. H. Robinson, C. Zhang, A. Ren, S. Garner, A. Chen, T. Londergan, L. Irwin, B. Carlson, L. Fifield, G. Phelan, C. Kincaid, J. Amend, and A. Jen, J. Mater. Chem. **9**, 1905 (1999) and references contained therein.
2. Y. Shi, C. Zhang, H. Zhang, J. H. Bechtel, L. R. Dalton, B. H. Robinson, and W. H. Steier, Science in press (2000).
3. S. Ermer, D. G. Girtton, L. S. Dries, R. E. Taylor, W. Eades, T. E. Van Eck, A. S. Moss, and W. W. Anderson, Proc. SPIE **3949**, in press (2000).
4. A. Piekara, Proc. R. Soc. London **A172**, 360 (1939).
5. L. R. Dalton, A. W. Harper, and B. H. Robinson, Proc. Natl. Acad. Sci. USA **94**, 4842 (1997).
6. B. H. Robinson, L. R. Dalton, A. W. Harper, A. Ren, F. Wang, C. Zhang, G. Todorova, M. Lee, R. Aniszfeld, S. M. Garer, A. Chen, W. H. Steier, S. Houbrecht, A. Persoons, I. Ledoux, J. Zyss, and A. K. Y. Jen, Chem. Phys. **245**, 35 (1999).
7. B. H. Robinson and L. R. Dalton, J. Phys. Chem. in press (2000).
8. I Liakatas, C. Cai, M. Bosch, M. Jager, Ch. Bosshard, P. Gunter, C. Zhang, and L. R. Dalton, Appl. Phys. Lett. in press (2000); Dalton, Gutner, and coworkers, unpublished results.
9. W. K. Kim and L. M. Hayden, J. Chem. Phys. **111**: 5212 (1999).
10. D. H. Chang, H. Erlig, H. R. Fetterman, M. C. Oh, W. H. Steier, and L. R. Dalton, IEEE Photon. Tech. Lett. in press (2000).
11. W. H. Steier, A. Chen, S. S. Lee, S. Garner, H. Zhang, V. Chuyanov, L. R. Dalton, F. Wang, A. S. Ren, C. Zhang, G. Todorova, A. W. Harper, H. R. Fetterman, D. Chen, A. Udupa, D. Bhattacharya, and B. Tsap, Chem. Phys. **245**, 487 (1999).

## Sub-5-fs Nonlinear Optical Processes in Polydiacetylenes

TAKAYOSHI KOBAYASHI

*Department of Physics, University of Tokyo, Hongo, Bunkyo-ku, Tokyo  
113-0033, Japan*

*Tell. +81-3-58414227, Fax. +81-3-5841-4240*

*(Received 13 March 2000)*

Using sub-5-fs visible pulses the real-time observation of the formation of a self-trapped exciton in polydiacetylenes has been observed for the first time. The stretching mode vibration (C-C, 27 fs, C=C, 23 fs and C≡C, 16 fs) coupled with the excitonic transition drives the coherent vibration of the conjugated backbone structure from an acetylene(A)-like ( $=\text{CR}-\text{C}\equiv\text{C}-\text{CR}'=$ )<sub>n</sub> to a butatriene(B)-like ( $-\text{CR}=\text{C}=\text{C}=\text{CR}'-$ )<sub>n</sub> configuration. The former two modes are coupled through C-C=C bending mode with an oscillation period of 145 fs.

**Keywords:** real-time spectroscopy, polydiacetylene, mode-coupling, self-trapped exciton

### 1. INTRODUCTION

Optical and transport properties of conjugated polymers have been attracting many scientists because they have potentiality for application to electronics such as flexible conductors, optoelectronics devices such as light-emitting diode, and photonics such as all-optical switches. The polymers are of interest not only in the applications but also in basic physics, because they are models of one-dimensional system with outstanding characteristic features including optical and spectroscopic properties. These are due to the formation of localized nonlinear excitations such as a pair of solitons, polarons, and a self-trapped exciton (STE) formed via a strong coupling between electronic excitations and



lattice vibrations. From previous extensive studies [1-6] the initial kinetics after photo-excitation can be explained by a relaxation of a free exciton (FE) to a self-trapped exciton (STE) within 150 fs. The recent achievement of sub-5-fs visible pulse generation based on a novel noncollinear optical parametric amplification (NOPA) [7,8] has enabled the real-time observation of the formation of a STE in a PDA for the first time. The stretching mode vibration (C-C, 27 fs, C=C, 23 fs, and C≡C, 16 fs) coupled with the excitonic transition drives the coherent relaxation of the backbone structure from an acetylene (A)-like ( $=\text{CR}-\text{C}\equiv\text{C}-\text{CR}'=$ )<sub>n</sub> to a butatriene (B)-like ( $-\text{CR}=\text{C}=\text{C}=\text{CR}'-$ )<sub>n</sub> configuration.

## 2. EXPERIMENTAL

The pulse-front-matched NOPA generates transform-limited (TL) 4.7-fs, 5-μJ 1-kHz pulses centered at 650nm with a 250-nm bandwidth [7,8]. The PDA studied is a novel ladder-polymer, poly [5,7,17,19-tetracosatetraynylene bis (N-butoxycarbonylmethyl) carbamate](PDA-4BCMU4A(8)), with two PDA-backbones linked with methylene chains [9]. The transition energy to an  $1^1\text{B}_u$  FE is peaked at 1.96eV, which is classified to a typical blue-phase A-like PDA [1-6]. The 370-nm-thick film sample prepared by spin coating was pumped and probed with the visible sub-5-fs pulses at room temperature.

## 3. RESULTS AND DISCUSSION

The time dependence of population change is analyzed at first by removing the oscillatory structures in the Fourier transform of the normalized transmittance change using a low-pass filter and back transformation to the time domain. The traces  $\Delta T(t)/T$  can be fitted to the following equation:

$$\Delta T(t)/T = \int_{-\infty}^t dt' I(t') [A_0 \delta(t-t') + A_1 e^{-(t-t')/\tau_1} + A_2 e^{-(t-t')/\tau_2} (1 - e^{-(t-t')/\tau_1})].$$

(1)

The first term in parentheses is due to the instantaneous interaction induced by coherent coupling and extremely fast

internal conversion (IC) process from the  $1^1B_u$  free exciton (FE) state to the  $2^1A_g$  state. The second term represents the geometrically relaxed  $2^1A_g$  state with a shorter time constant  $\tau_1$ . The third term corresponds to IC from the  $2^1A_g$  state to the  $1^1A_g$  ground state by the quantum mechanical tunneling with a longer time constant,  $\tau_2$ , which is insensitive to temperature. The shorter time constant  $\tau_1$  ranges between 50 and 150 fs depending on the probe photon energy. This dependence can be explained by the differences in the relative amounts of the following three different contributions to the signal: (1) internal conversion from the  $1^1B_u$  FE state to the  $2^1A_g$  state, (2) geometrical relaxation (GR) from acetylene type to butatriene type, (3) thermalization in the main chain. It is difficult to separate the three processes by the spectroscopic data available. However from the extremely low quantum yield of fluorescence and the natural lifetime estimated from the absorption coefficient, the time needed for the IC process from  $1^1B_u$  FE state to the  $2^1A_g$  state is estimated to be shorter than 10 fs. The GR process takes place within an oscillation period of relevant vibrational mode to the configuration change because of the lack of the potential barrier [3-6,10]. In the case of PDAs, the C=C and C-C stretching modes are considered to be most strongly coupled to the GR process, it is considered to be terminated in 30 fs, since the oscillation periods of the stretching modes are 22 fs (C=C) and 27 fs (C-C). However the GR processes fully completed only after intrachain thermalization, which is the energy redistribution process among various vibrational modes of the main chain. The time needed for this process is estimated as several tens to a hundred femtoseconds because of the low-frequency main-chain modes involved. Therefore the rate-determining step is the intrachain thermalization. Because of the reduction of the average energy of the thermalization of the geometrically relaxed  $2^1A_g$  state, the lifetime is longer for higher probe photon energy in the case of induced absorption and vice versa in the stimulated emission case [3-6,10].

The traces in Fig. 1 clearly exhibit a complex oscillatory

behavior in the normalized transmittance change. The oscillation is ascribed to a wave packet motion composed of several modes as is seen in molecular systems. From the complex features it is clear that more than two modes are contributing to the time-dependent transmittance change. In spite of the complexity, there are systematic features in the phases of the oscillations. For example, there are eight peaks at 23, 44, 90, 154, 180, 200, 260, and 308 fs among the eleven prominent peaks in the trace of 2.12 eV and the signal intensity is minimum at these delay times in the trace of 1.75 eV. This result indicates that there are constant phase relation among the observed modes and that the coherence times of the relevant modes are substantially longer than 300fs.

The real-time spectrum is given by the transient differential transmittance, which clearly shows a coherent molecular motion composed of several modes over the whole probe spectral range[Fig.1]. The integrated Fourier analysis of the real-time spectrum reveals two main modes of  $C=C(\sim 1455\text{cm}^{-1})$  and  $C\equiv C(\sim 2080\text{cm}^{-1})$  stretching, in addition to weaker modes around 220, 700, and  $1220\text{cm}^{-1}$ , of which intensities are dependent on the probe wavelength. These modes are also observed in the static Raman spectrum. The vibration persists for longer than 1ps.

Recent experimental and theoretical studies manifest the lowest singlet state in a blue-phase PDA to be an optically forbidden  $2^1A_g$  state lying  $\sim 0.1\text{eV}$  below an  $1^1B_u$  FE state [3-6]. The fast 60-fs decay observed around  $E_{\text{probe}}=1.96\text{eV}$  is attributed to the internal conversion(IC) from a photoexcited  $1^1B_u$  FE to a  $2^1A_g$  FE. The long-lived wavepacket in the bleaching signal is thus exclusively assigned to a ground-state motion driven by impulsive stimulated Raman scattering. The stimulated emission from an  $1^1B_u$  FE observed at  $E_{\text{probe}}<1.8\text{eV}$  is suppressed rapidly by the IC, followed by the relaxation to a STE that causes the excited-state absorption of the biexcitons $\leftarrow$ STE transition [3-6]. The net formation time of STE is determined to be about 80fs and the lifetime is 1.5ps.

The wavepacket motion in a STE is transferred coherently from the  $1^1B_u$  FE via IC, which indicates the coherent motions of the C=C and C $\equiv$ C stretching along the backbone act as the driving force of the geometrical relaxation to a localized B-like structure where the exciton is self-trapped. The A $\rightarrow$ B isomerization and following thermalization of STE is clearly visualized by a real-time frequency analysis using a spectrogram [10]. The interesting feature is the  $\sim 200\text{-cm}^{-1}$  oscillation of the mode frequency, which strongly indicates the diabatic coupling of the stretching modes with the wagging mode of C-C-C bending in the backbone. After the energy exchange the STE is thermalized, and the  $\sim 20\text{-cm}^{-1}$  red shift of each mode indicates the thermal B-like backbone creation.

Very recently, it was reported that the ground-state vibrational motion and energy flow was found in a PDA by coherent anti-Stokes Raman scattering (CARS) [11]. However the beat frequencies in CARS signals between neighboring vibrational modes and isotope-shifted modes have already been observed for neat liquids of  $\text{CCl}_4$  and  $\text{SnBr}_4$  [12]. This phenomenon must be explained in terms of the beating of the same mode even between two different isotopic molecules. In the CARS experiment, signal detected is proportional to the squared absolute values of the CARS fields and beating appears between the CARS field from different molecules like isotopes. Therefore the beating in [11] is not related to the energy flow. While in our experiment the difference transmittance signal is proportional to the vibrational amplitude and change in the transmission frequency directly represents the change in the instantaneous mode frequency.

Therefore this is the first real-time observation of vibrational energy flow due to non-adiabatic coupling between vibrational modes via another mode. This phenomenon is expected widely for such a photoexcited molecular system in non-equilibrium states. The present results offer much information about the configuration change and geometrical relaxation. Theoretical investigations of the electron-phonon and electron-electron interactions in various molecular systems are needed. In addition, the

present study opens a novel technique to investigate the real-time inter-mode exchange of the vibrational energy among various modes, which is closely related to photo- and thermo-chemical reactions.

The amounts of the modulated bond-length and bond-orders can be estimated from the frequency modulation. Lewis *et al.* introduced the following empirical relation [13]

$$r_{ij} = r_0 + \frac{B}{K_{ij}}, \quad (2)$$

where the stretching force constant  $K_{ij}$  between two atoms  $i$  and  $j$  is related to the bond-length  $r_{ij}$ . The parameters  $r_0 = 0.106$  nm and  $B = 1.65 \times 10^8$  N were evaluated in the case of PDA-PTS (2,4-hexadiyne-1,6-diol). Batchelder *et al.* estimated  $K_{ij}$ 's in the excited state as  $K_{C-C} = 474$  N/m and  $K_{C \equiv C} = 481$  N/m [14]. Because the modulation of  $C \equiv C$  stretching and two other stretching modes through bending modes are only weakly correlated, we only consider the coupling between the two stretching modes:

$$\begin{pmatrix} \Delta v_{C-C} \\ \Delta v_{C \equiv C} \end{pmatrix} = \begin{pmatrix} \frac{\partial v_{C-C}}{\partial K_{C-C}} & \frac{\partial v_{C-C}}{\partial K_{C \equiv C}} \\ \frac{\partial v_{C \equiv C}}{\partial K_{C-C}} & \frac{\partial v_{C \equiv C}}{\partial K_{C \equiv C}} \end{pmatrix} \begin{pmatrix} \Delta K_{C-C} \\ \Delta K_{C \equiv C} \end{pmatrix}. \quad (3)$$

The components of the matrix of differential coefficients  $\frac{\partial v_i}{\partial K_{ij}}$  are given in [15] for a PDA-PTS crystal in the ground state. There is no information about the excited state, which limits us to use these coefficients for the first calculation. The modulation depths  $\Delta v_{C-C} \cong \Delta v_{C \equiv C} \cong 16 \text{ cm}^{-1}$  yields the modulated bond-lengths of  $\Delta r_{C-C} = \pm 0.0026$  nm and  $\Delta r_{C \equiv C} = \mp 0.0025$  nm from Eqs. (1) and (2). Using  $r_{C-C} = r_{C \equiv C} = 0.14$  nm in the excited state [14], the relative modulations of  $r_{C-C}$  and  $r_{C \equiv C}$  are  $\pm 1.9\%$  and  $\mp 1.8\%$ , respectively.

The modulations of the  $\pi$ -bond-orders of single and double bonds are estimated by using the simple relationship between the mode frequency and bond-order  $\delta$  derived by Baughman *et al.* [16]. The modulation depth  $\Delta \delta$  is obtained as  $\pm 0.031$  from  $\Delta v_{C \equiv C}$  by applying Dewar's relationship  $\delta v_{C \equiv C} / d\delta = 512.4 \text{ cm}^{-1}$  to the  $2^1A_g$  state of a PDA-

4BCMU4A(8). If we set  $r_{C-C} = r_{C=C} = 0.14$  nm,  $\delta = 0.41$  [17] then the relative modulation is estimated as 7.6 %.

These estimations are based on the following several assumptions. First, the values of PDA-PTS investigated previously in detail [3-6] are used because there is no experiments of femtosecond spectroscopy of PDA-4BCMU4A(8). Second, in [14]  $K_{ij}$ 's and  $r_{ij}$ 's in the excited state were estimated by measuring resonance Raman excitation profiles, which only reflect the molecular structure in the  $1^1B_u$  state and includes no information about the  $2^1A_g$  state. Third, the values of  $\frac{\partial \nu_i}{\partial K_{ij}}$  in the ground state is used

with the assumption of Eq. (2). Finally, Dewar's relationship used in [16] is based on the assumption that in determining bond-lengths  $\pi$ -electron resonance is much less important than hybridization when only one classical structure of the molecule can be written [17]. The  $\pi$ -electron resonance is, however, to be non-negligible in a strongly electron-correlated system such as a PDA.

As mentioned before the geometrical relaxation is not complete and the structure of the backbone may be only "butatriene-like" even after geometrical relaxation. The  $C\equiv C$  bond is remained in the center of the butatriene-like unit with the reduced bond-order and also vibrating. However, because the bond is not connected with the  $C-C=C$  bending portion of a repeat unit, it may experience negligible effects by the bending motion and evolve almost independently. The amounts of modulations of the bond-lengths and bond-orders mentioned above may be overestimated because of the assumption of a completely delocalized structure ( $r_{C-C}=r_{C=C}$ ). In fact it is difficult to determine the amounts of the bond-orders in the  $2^1A_g$  state. Even though there is some ambiguities in the above estimated amounts of modulation depth, the present results are the first observation of coupling between normal modes via the vibration of other modes. These phenomena are expected to be widely observed in such a photoexcited non-equilibrium system in such a short time scale.

Here the sizes of amplitudes and frequencies are

compared with each other. The maximum fractional changes in the amplitude are as large as 25-30% as probed at 2.04 and 1.68 eV in Fig. 1. On the other hand, those in the frequency  $\delta(\Delta\omega/\omega)$  are less than about 2% at most. If the force constant change that induces frequency change as mentioned above is the only one origin of the amplitude modulation, then it is expected that these two fractions of modulation must be equal to each other. In real molecular systems time dependent configuration change induced by the bending motion leads to the change in the potential minimum coordinate and the zero-zero transition energy in the stretching configuration space.

In the case of PDA studied in the present paper, these effects are much larger than that due to force constant change. This phenomenon is also found in a dye molecular system of cresyl violet doped in poly(methylmetaacrylate) (PMMA), of which sample was prepared by casting on a substrate.

The present results will offer a valuable information about the geometrical relaxation and encourage the theoretical investigations of the electron-phonon and electron-electron interactions in non-degenerate conjugated polymers. The experimental technique of real-time spectroscopy with sub-5 fs pulses can reveal the structure of intermediates or transition states in the dynamical processes from the dynamic molecular vibrational spectra. It is invaluable to clarify the mechanism of chemical reactions, such as isomerization and tautomerization.

#### 4. Conclusion

Primary dynamics of polydiacetylenes has been studied with the highest time resolution. The vibrational non-equilibrium in the relaxed state is characterized by the modulations of instantaneous frequency and amplitude with 145-fs oscillation period. This phenomenon is explained by the coupling of the C=C and C-C stretching modes via an in-plane bending mode in the main chain. This is the first real-time observation of dynamic coupling between two modes.

#### Acknowledgement

The author thanks Dr. Shirakawa for collaboration and

Profs. Y. Toyozawa, H. Okamoto, M. Yoshizawa, K. Misawa, and Y. Takasu for valuable discussion. This work was partly supported by Research for the Future of Japan Society for the Promotion of Science (JSPS-RFTF-97P-00101). A. S. also acknowledges the support from Sumitomo Foundation.

### References

- [1] T. Kobayashi ed.: *Nonlinear Optics of Organics and Semiconductors*, Springer Proceeding Physics, Vol. **36** (Springer, Berlin, Heidelberg 1989).
- [2] T. Kobayashi ed., *Relaxation in Polymers* (World Scientific, Singapore, 1993).
- [3] E.g., T. Kobayashi, M. Yoshizawa, U. Stamm, M. Taiji, and M. Hasegawa, J. Opt. Soc. Am. B, **7**, 1558(1990).
- [4] M. Yoshizawa, A. Yasuda, and T. Kobayashi, Appl. Phys. **B53**, 296 (1991).
- [5] M. Yoshizawa, Y. Hattori, and T. Kobayashi, Phys. Rev. B **123**, 121(1994).
- [6] T. Kobayashi, M. Yasuda, S. Okada, H. Matsuda, H. Nakanishi, Chem. Phys. Lett. **267**, 472(1997).
- [7] A. Shirakawa, I. Sakane, and T. Kobayashi, Opt. Lett. **23**, 1292(1998); A. Shirakawa, I. Sakane, M. Takasaka, and T. Kobayashi, Opt. Lett., submitted.
- [8] H. Matsuzawa, S. Okada, H. Matsuda, and H. Nakanishi, Chem. Lett., 1105(1997).
- [9] M. J. J. Vrakking, D. M. Villeneuve, and A. Stolow, Phys. Rev. A **54**, 37(1996).
- [10] A. Vierheilg, T. Chen, P. Walther, W. Kiefer, A. Materny, A.H. Zeweil, Chem. Phys. Letters 312 (1999) 349.
- [11] R. Leonhardt, W. Holzapfel, W. Zinth, W. Kaiser, Chem. Phys. Letters 133(1987) 373.
- [12] A. Shirakawa, I. Sakane, T. Kobayashi, Opt. Lett. **23**, 1292 (1998);.
- [13] A. Shirakawa, I. Sakane, M. Takasaka, T. Kobayashi, Appl. Phys. Lett. **74**, 2268 (1999).
- [14] H. Matsuzawa, S. Okada, H. Matsuda, H. Nakanishi, Chem. Lett., 1105 (1997).
- [15] M. Yoshizawa, M. Taiji, and T. Kobayashi, IEEE J. Quantum Electron. **QE-25**, 2532 (1989).
- [16] A. Vierheilg, T. Chen, P. Walther, W. Kiefer, A. Materny, A.H. Zeweil, Chem. Phys. Letters 312 (1999) 349.
- [17] R. Leonhardt, W. Holzapfel, W. Zinth, W. Kaiser, Chem. Phys. Letters 133(1987) 373.
- [18] W. F. Lewis and D. N. Batchelder, Chem. Phys. Lett. **60**, 232 (1979).
- [19] D. N. Batchelder and D. Bloor, J. Phys. C **15**, 3005 (1982).
- [20] A. C. Cottle, W. F. Lewis, and D. N. Batchelder, J. Phys. C **11**, 605 (1978).
- [21] R. H. Baughman, J. D. Witt, and K. C. Yee, J. Chem. Phys. **60**, 4755 (1974).
- [22] M. J. S. Dewar, *Hyperconjugation* (Ronald Press, New York, 1962), p.48.



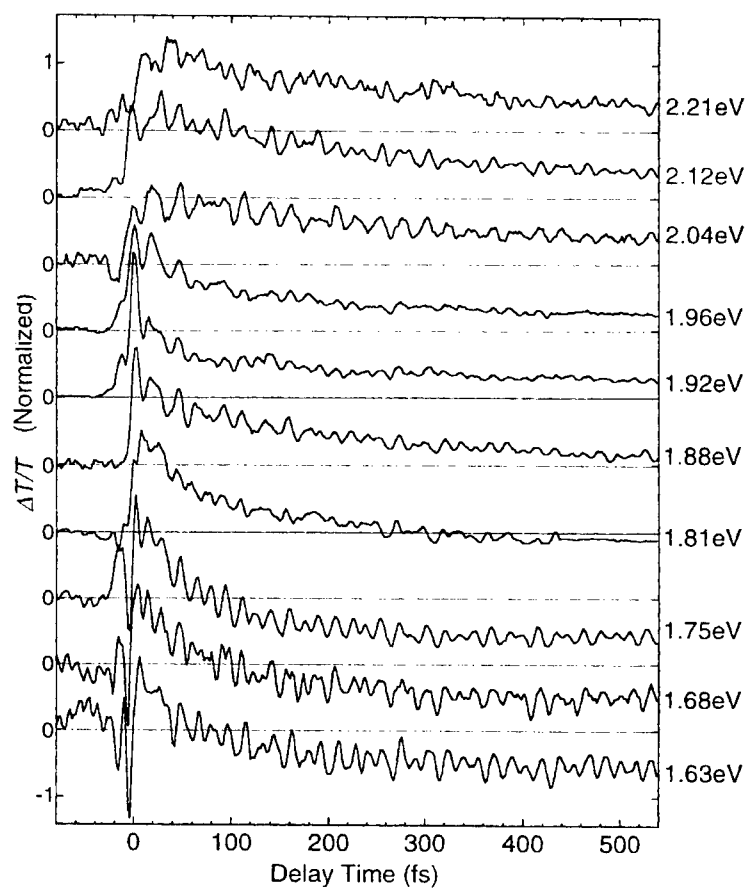


Fig.1. Coherent wavepacket motion in the transient differential transmittance. The probe photon energy is marked on the right. The probe-pulse spectrum after the sample was measured by a monochromator with a 5-nm resolution and a lock-in amplifier. The excitation photon density is about  $10^{15}$  photons/cm<sup>2</sup>.

## MOLECULAR ENGINEERING OF DAST FAMILY

SHUJI OKADA, KYOKO TSUJI, ANWAR, HACHIRO NAKANISHI,  
HIDETOSHI OIKAWA, AND HIRO MATSUDA\*  
Institute for Chemical Reaction Science, Tohoku University, Sendai 980-8577,  
Japan

\*National Institute of Materials and Chemical Research, 1-1 Higashi, Tsukuba 305-8565, Japan

**Abstract** Two categories of DAST derivatives were synthesized. For EO applications, the polyene analogues with increased double-bond number between two aromatic rings of DAST and fused-ring derivatives of DAST were prepared for larger  $\beta$  than DAST cation, and promising cations were found. For frequency conversion of diode lasers, substituted pyridiniums were investigated to obtain crystals better than inorganic compounds. By choosing proper counter anions, several SHG-active crystals without visible absorption have been found.

## INTRODUCTION

Organic ionic crystals have several advantages over conventional organic non-ionic crystals. For example, hyperpolarizability ( $\beta$ ) larger than that of non-ionic species, which originates from charged  $\pi$ -conjugated system,<sup>1</sup> can be realized. The orientation of ionic chromophores in crystals can be varied by substituting its counter anion.<sup>2</sup> Namely, if we could find an ionic species with large  $\beta$ , we could concentrate on searching proper counter ions to align the objective ionic species resulting in large nonlinear optical (NLO) coefficient  $d$  or electro-optic (EO) coefficient  $r$ . High melting points and hardness, which are important properties for fabrication process of the materials, are expected due to Coulombic attraction of the species in crystals. Among such compounds, 1-methyl-4-{2-[4-(dimethylamino)phenyl]ethenyl}pyridinium *p*-toluenesulfonate (DAST: **1f** in FIGURE 1) was first discovered by our group as an organic ionic NLO crystal<sup>3,4</sup> and was also investigated by Marder and colleagues.<sup>5,6</sup> It is now recognized as one of the best organic materials for second-order NLO applications.<sup>7-10</sup>

Research on the DAST family to improve the properties still continues, and our recent studies are conducted for the following two purposes. For EO telecommunication applications, input laser wavelengths around 1.3  $\mu\text{m}$  or 1.5  $\mu\text{m}$  can be used. Since the absorption cutoff wavelength ( $\lambda_c$ ) of DAST is around 700 nm and it can be shifted further to longer wavelengths for this purpose, ionic species with larger  $\beta$  than DAST cation can

be designed by its  $\pi$ -conjugation extension to enhance  $\beta$ . Thus, polyene analogues and fused-ring analogues of DAST cation were prepared. For frequency conversion of diode lasers, crystals without absorption in visible region are required. In order to shift  $\lambda_c$  to the UV region, substituted pyridinium derivatives with shorter  $\pi$ -conjugated systems than DAST cation were prepared for species with larger  $d$  constant than inorganic materials and hopefully for those with larger  $\beta$  than colored *p*-nitroaniline (*p*NA). This article reports preparation of DAST analogues mentioned above and their properties.

## EXPERIMENTAL

Chemical structures of the compounds investigated in this study and their synthetic procedures are shown in FIGURE 1. As precursors of polyene analogue of DAST cation,  $\pi$ -conjugated aldehydes having more than two double-bonds between a phenyl ring and the formyl group were obtained using a Wittig reaction<sup>11</sup> to increase the number of double bonds in a stepwise manner, starting from commercial 4-(dimethylamino)-cinnamaldehyde. DAST polyene analogues **2a-5a** with iodide as a counter anion were prepared by condensation reaction of 1,4-dimethylpyridinium iodide<sup>12</sup> and the corresponding aldehydes in methanol at room temperature using piperidine as a catalyst.<sup>13</sup> DAST analogues **1a'-5a'** that are soluble in chloroform were also synthesized in the similar manner using 4-methyl-1-octadecylpyridinium bromide instead of 1,4-dimethylpyridinium iodide.

For precursors of fused-ring analogues of DAST cation, 6-(dimethylamino)-2-naphthaldehyde and 2,6-dimethylisoquinolinium iodide were synthesized. A route to synthesize the former compound and naphthylene analogues of DAST (**6a** and **7a**) will be reported elsewhere.<sup>14</sup> The latter isoquinolinium compound was prepared by the reaction of 6-methylisoquinoline<sup>15,16</sup> and iodomethane in quantitative yield. The isoquinolinium analogues of DAST (**8a** and **9a**) were obtained by the reaction of 2,6-dimethylisoquinolinium iodide and the corresponding aldehydes in the presence of pyrrolidine<sup>17</sup> in ethanol under refluxed condition.

In order to prepare crystals with an optimal orientation of the chromophores resulting in crystals having large  $d$  values, the iodide anion was converted into substituted benzenesulfonate anions using silver salts of the corresponding anions for **1c-4c**, **1f-4f**, **1i-4i** and **1k-4k** or the sodium salt for **1l-4l**.

Substituted pyridinium iodides for colorless materials were synthesized by simple quaternization of the corresponding substituted pyridine by iodomethane. Pyridinium derivatives prepared were 4-methyl- (**10**), 4-ethyl- (**11**), 4-amino- (**12**), 4-dimethylamino- (**13**), 4-carbamoyl- (**14**), 4-methoxycarbonyl-, 4-cyano-, 3-carbamoyl-,

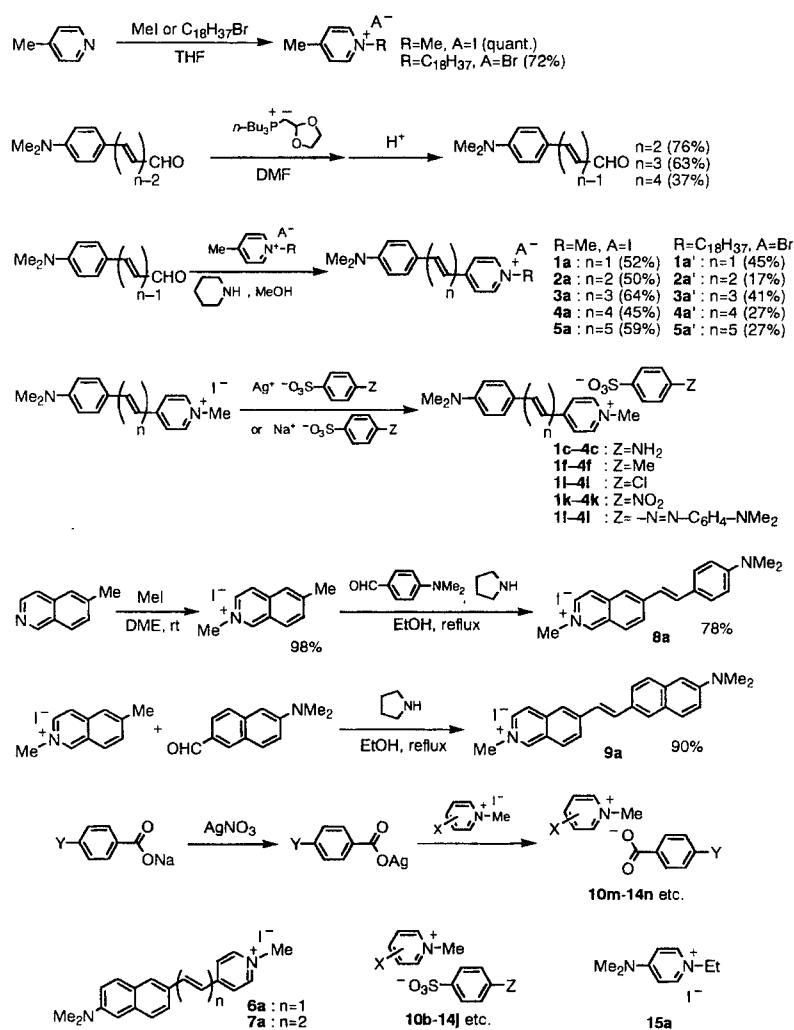


FIGURE 1 Synthetic procedures and chemical structures of compounds investigated.

3-methoxycarbonyl- and 3-chloro-1-methylpyridiniums in addition to 1-methylpyridinium. For the pyridinium salts with 4-substituted benzoate, anion exchange was performed for iodide salts using the corresponding silver benzoate. 4-Amino- (**m**), 4-hydroxy-, 4-methoxy-, 4-methyl-, 4-chloro-, 4-bromo- (**n**), 4-cyano- and unsubstituted-benzoates were used to prepare the salts. Pyridinium benzenesulfonate salts were directly obtained by quaternization reaction of the corresponding pyridine derivatives by methyl benzenesulfonate derivatives.<sup>18</sup> Benzenesulfonate derivatives used were 4-dimethylamino- (**b**), 4-amino- (**c**), 4-hydroxy- (**d**), 4-methoxy- (**e**), 4-methyl- (**f**), 4-acetyl-amino- (**g**), 4-chloro- (**i**), 4-bromo- (**j**) and unsubstituted- (**h**) benzenesulfonates. In addition, 1-ethyl-4-(dimethylamino)pyridinium iodide **15a** was also prepared from 4-(dimethylamino)-pyridine and iodoethane.

The structure and composition of these salts were confirmed by <sup>1</sup>H and <sup>13</sup>C NMR, IR, elemental analysis and differential scanning calorimetry. Optical properties of the salts were characterized by UV and visible absorption spectra in solution. The  $\beta$  values of the ionic species at zero frequency in vacuum were calculated using semiempirical MOPAC PM3 method, and these  $\beta$  values are expressed as  $\beta_{0,calc}$ . For compounds **1a**'-**5a**', experimental  $\beta$  values in chloroform at 1300 nm were evaluated by the modulated hyper-Rayleigh scattering (HRS) technique.<sup>19,20</sup> For the compounds without absorption at second-harmonic generation (SHG) wavelength of Nd:YAG laser, experimental  $\beta$  values in methanol at 1064 nm were evaluated by the conventional HRS method.<sup>21,22</sup> The obtained  $\beta$  values were corrected into  $\beta$  at zero frequency ( $\beta_{0,exp}$ ) according to the two-level model.<sup>23</sup> SHG activity of the salts synthesized was qualitatively investigated by the powder method<sup>24</sup> using 1079-nm input beam.

## RESULTS AND DISCUSSION

### Derivatives with extended $\pi$ -conjugation system

The absorption maximum wavelength ( $\lambda_{max}$ ) and  $\lambda_{co}$  in methanol of polyene analogues **1a**-**5a** are summarized together with their  $\beta_{0,calc}$  values in TABLE I. When the double-bond

TABLE I  $\lambda_{max}$ s and  $\lambda_{co}$ s in methanol and  $\beta_{0,calc}$ s of polyene analogues **1a**-**5a**

Compound	$\lambda_{max}$ / nm	$\lambda_{co}$ / nm	$\beta_{0,calc}$ / $\times 10^{-30}$ esu
<b>1a</b>	476	605	241
<b>2a</b>	495	670	419
<b>3a</b>	507	710	603
<b>4a</b>	518	755	870
<b>5a</b>	516	800	922

TABLE II  $\lambda_{\max}$ s,  $\lambda_{\text{co}}$ s and  $\beta_{0,\text{exp}}$ s of polyene analogues **1a'**–**5a'** in chloroform

Compound	$\lambda_{\max}$ / nm	$\lambda_{\text{co}}$ / nm	$\beta_{0,\text{exp}} / \times 10^{-30}$ esu
<b>1a'</b>	496	720	36
<b>2a'</b>	524	825	481
<b>3a'</b>	546	880	496
<b>4a'</b>	556	920	171
<b>5a'</b>	570	1040	224

number increases,  $\lambda_{\text{co}}$  gradually shifts to longer wavelength. However, the bathochromic shift of  $\lambda_{\max}$  is almost unchanged between **4a** to **5a**. Interestingly, the rate of increase in  $\beta_{0,\text{calc}}$  rises from **1a** to **4a** while it fairly drops from **4a** to **5a**. In chloroform solution of the similar compounds **1a'**–**5a'**,  $\lambda_{\max}$ ,  $\lambda_{\text{co}}$  and  $\beta_{0,\text{exp}}$ <sup>20</sup> values were evaluated as shown in TABLE II. The bathochromic shift of  $\lambda_{\max}$  becomes small in general from **1a'** to **5a'**, though the saturation tendency seems to be weak compared with the case of methanol solution of **1a**–**5a**. The bathochromic shift of  $\lambda_{\text{co}}$  from **4a'** to **5a'** becomes large due to broadening of the absorption band. The largest  $\beta_{0,\text{exp}}$  value was observed for **3a'** and similar value was also obtained for **2a'**. The reason for decrease in  $\beta_{0,\text{exp}}$  values of **4a'** and **5a'**, compared with those of **2a'** and **3a'**, may be due to contribution from single-*cis* conformers, which have smaller  $\beta$  values than the all-*trans* conformer, in solution.<sup>20</sup> Considering from these optical data and synthetic and crystal-growth easiness, cationic structures of **2a** and **3a** seemed to be the most interesting species among **1a**–**5a** to align them properly in crystals for large  $d$  and  $r$ .

Anion exchange from iodide to substituted benzenesulfonate was performed for **1a**–**4a**. From the powder SHG test, all 4-amino-, 4-methyl-, 4-chloro- and 4-nitro-benzenesulfonate salts except **3i** were found to be SHG active in their pure crystalline states. However, none of them shows SHG activity in their crystals with crystal water. On the other hand, 4'-(dimethylamino)azobenzene-4-sulfonate salts **1l**–**4l** are SHG inactive in their pure crystals. However, SHG activity was found in water containing crystals of **2l** and **3l**. For **2l**·H<sub>2</sub>O crystal, crystal structure analysis was completed and its crystal system and space group were found to be triclinic P1.<sup>13</sup> By applying the oriented gas model<sup>25</sup> to this crystal structure, its  $d$  value was estimated using  $\beta_{0,\text{calc}}$  values to be about 1.3 times as large as that of DAST, when the local field factors of **2l**·H<sub>2</sub>O crystal were set to be the same as those of DAST.

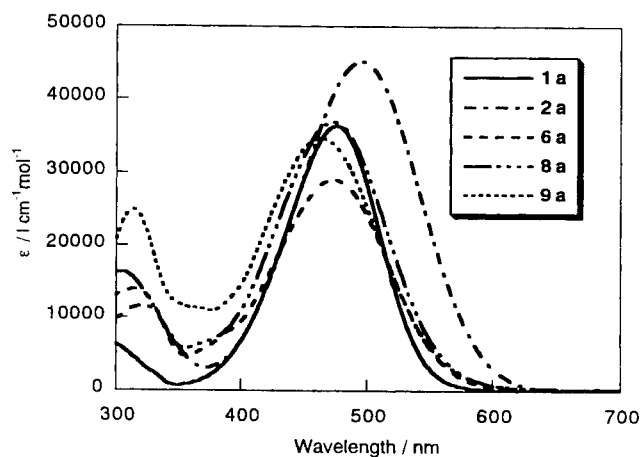
In the case of fused-ring systems,  $\beta_{0,\text{calc}}$  values became larger when compared with polyene analogues with calculated transition energy ( $E_{\text{eg,calc}}$ ) similar to that of the fused-ring derivative.<sup>26</sup> The  $\lambda_{\max}$  and  $\lambda_{\text{co}}$  in methanol and  $\beta_{0,\text{calc}}$  values of the fused-ring analogues of DAST synthesized are summarized in TABLE III. Actually,  $\lambda_{\max}$ s of **6a**, **8a** and **9a**

TABLE III  $\lambda_{\max}$ s and  $\lambda_{\text{on}}$ s in methanol and  $\beta_{0,\text{calc}}$ s of fused-ring analogues **6a–9a**

Compound	$\lambda_{\max}$ / nm	$\lambda_{\text{on}}$ / nm	$\beta_{0,\text{calc}} / \times 10^{-30}$ esu
<b>6a</b>	474	630	334
<b>7a</b>	482	690	509
<b>8a</b>	473	630	288
<b>9a</b>	463	640	340

were found to be shorter than those of **1a**, although these fused-ring compounds were calculated to have 1.2–1.4 times of  $\beta_{0,\text{calc}}$  of **1a**. The similar tendency was also found for the compounds with two double-bonds. Namely, the  $\lambda_{\max}$  of **7a** was also located at shorter wavelength than that of **2a**, although **2a** possesses only about 80% of  $\beta_{0,\text{calc}}$  of **7a**. However, absorption bands of fused-ring compounds tend to be broad as shown in FIGURE 2 resulting in  $\lambda_{\text{on}}$  extending to relatively longer region. Anion exchange to prepare SHG-active crystals are being studied for fused-ring systems.

The relationship between  $\beta_{0,\text{calc}}$  and absorption properties such as  $\lambda_{\max}$  and  $\lambda_{\text{on}}$  was investigated for the DAST analogues with extended  $\pi$ -conjugation. In FIGURE 3 (a) for  $\lambda_{\max}$  vs  $\beta_{0,\text{calc}}$ , the points for the fused-ring analogues are in the upper area than the line through the points for polyene analogues **1a–4a**. This implies that larger  $\beta$  is expected for the fused-ring analogues when compared with a polyene analogue having similar  $\lambda_{\max}$ .

FIGURE 2 Comparison of UV and visible absorption spectra among DAST analogues with extended  $\pi$ -conjugation.

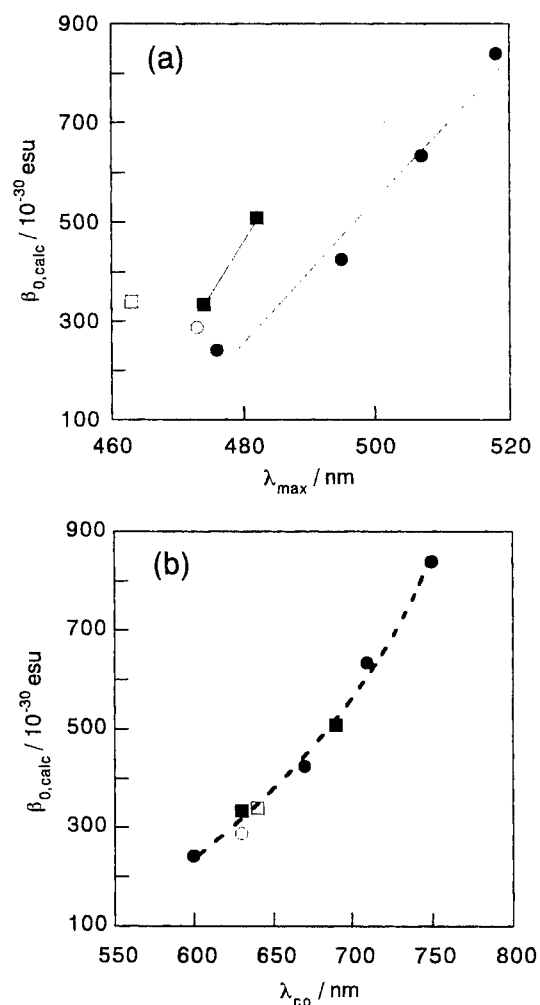


FIGURE 3 Relation between  $\beta_{0,calc}$  and absorption properties in methanol for some DAST analogues: (a)  $\lambda_{max}$  vs  $\beta_{0,calc}$  and (b)  $\lambda_{co}$  vs  $\beta_{0,calc}$ . Symbol ● is for a series of polyene analogues with pyridinium and phenylene rings (1a-4a). Symbol ■ is for a series of polyene analogues with pyridinium and naphthylene rings (6a and 7a). Symbols ○ and □ represent the compound with isoquinolium and phenylene rings (8a) and that with isoquinolium and naphthylene rings (9a), respectively. For (a), solid lines show the tendency among the same series of compounds. For (b), a dashed line indicates the tendency for all the compounds.



However, due to the broadening of the absorption band of the fused-ring analogues, all of the points for compounds investigated are on the same curve in FIGURE 3 (b) for  $\lambda_{co}$  vs  $\beta_{0,calc}$ . Thus, we can select an optimum NLO compound depending on input laser wavelength among these series of compounds.

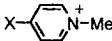
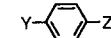
#### Derivatives with short $\pi$ -conjugation lengths

For frequency conversion of diode lasers, we have investigated pyridinium cations without absorption in the range longer than 400 nm. Their  $\beta$  values are comparatively large irrespective of their short  $\lambda_{co}$ s in UV region. For instance, the  $\beta_{0,exp}$  values of 4-(dimethylamino)-1-methylpyridinium with  $\lambda_{co}$  of about 390 nm was found to be about twice of that of colored pNA with  $\lambda_{co}$  of about 475 nm.<sup>27</sup> For counter anions of pyridinium derivatives, we have investigated mainly 4-substituted benzoates<sup>28</sup> and benzenesulfonates<sup>29</sup> because counter anions also should not have absorption in visible region. In spite of  $\lambda_{co}$  shorter than 400 nm, several anions were evaluated to have about equal to twice of the  $\beta_{0,exp}$  values of pNA.

SHG activity of these salts was qualitatively studied by the powder method. Among 99 pyridinium benzenesulfonate salts synthesized according to combinations between 11 pyridinium cations and 9 benzenesulfonate anions, SHG activity was observed for 16 crystals. For pyridinium benzoate derivatives, 73 salts could be crystallized from 88 combinations between 11 pyridinium cations and 8 benzoate anions, and only two SHG-active crystals were confirmed. The difference in probability of obtaining SHG-active crystals between benzenesulfonate and benzoate may be mainly due to molecular structure of anions; that is, though benzoate anion has a simple planer structure, benzenesulfonate anion is composed of a tetrahedral sulfonate group and a planer benzene ring.

Correlation between the substituents and SHG activity of those salts is tabulated in TABLE IV. This table includes all of SHG-active pyridinium salts found in this study. Among them, 4-amino-<sup>30</sup> and 4-carbamoyl-1-methylpyridinium<sup>31</sup> derivatives **12** and **14** showed relatively high probability to give noncentrosymmetric structures with strong SHG intensity in powder form. From the X-ray crystallographic analysis of these SHG-active salts, the hydrogen-bonding patterns were found to be an important factor to align the species in noncentrosymmetric structures. In the case of 4-aminopyridinium derivatives with SHG activity, hydrogen bonds are formed between a hydrogen atom in the amino group of a cation of an ion pair and an oxygen atom in the sulfonate group of the adjacent anion of the other ion pair. Two hydrogen atoms in an amino group are connected to two different sulfonate anions and two oxygen atoms in a sulfonate group are connected to two different pyridinium cations. Through this hydrogen-bonding

TABLE IV The powder SHG activities of prepared 1-methylpyridinium benzenesulfonate and benzoate salts

SUBSTITUTION PATTERNS AND SUBSTITUENTS												
												
	<b>b</b>	<b>c</b>	<b>d</b>	<b>e</b>	<b>f</b>	<b>g</b>	<b>h</b>	<b>i</b>	<b>j</b>	<b>m</b>	<b>n</b>	
	Y=SO <sub>3</sub> <sup>-</sup> Z=NMe <sub>2</sub>	SO <sub>3</sub> <sup>-</sup> NH <sub>2</sub>	SO <sub>3</sub> <sup>-</sup> OH	SO <sub>3</sub> <sup>-</sup> OMe	SO <sub>3</sub> <sup>-</sup> Me	SO <sub>3</sub> <sup>-</sup> NHCOMe	SO <sub>3</sub> <sup>-</sup> H	SO <sub>3</sub> <sup>-</sup> Cl	SO <sub>3</sub> <sup>-</sup> Br	CO <sub>2</sub> <sup>-</sup> NH <sub>2</sub>	CO <sub>2</sub> <sup>-</sup> Br	
<b>10:</b> X=Me	×	×	×	×	○	×	×	○	×	×	×	
<b>11:</b> X=Et	×	×	×	×	○	×	×	×	○	×	×	
<b>12:</b> X=NH <sub>2</sub>	○	×	⊙	⊙	⊙	×	×	⊙	⊙	×	×	
<b>13:</b> X=NMe <sub>2</sub>	×	○	×	×	×	×	○	×	×	○	○	
<b>14:</b> X=CONH <sub>2</sub>	×	×	○	⊙	×	○	×	×	⊙	×	×	

⊙=strongly active, ○=weakly active, ×=inactive

network, infinite ion-pair arrays with polar orientation are created in these crystals. For 4-carbamoylpyridinium derivatives, the SHG active crystals generally show the intermolecular hydrogen-bond formation between carbamoyl hydrogen atoms and sulfonate oxygen atoms or between carbamoyl hydrogen atoms of the adjacent ion-pairs, resulting in similar hydrogen-bond network, to give noncentrosymmetric structures. Beside these salts with aromatic anions, *N*-ethyl-substituted pyridinium iodide **15a** was curiously found to be SHG active though the ionic structures are relatively simple.

For SHG-active crystals, the SHG coefficients ( $d_s$ ) at 1064 nm were estimated by using the oriented gas model.<sup>25</sup> Based on the assumption of no intermolecular interactions, the diagonal and off-diagonal  $d$  components, i.e.  $d_{zzz}$  and  $d_{zxx}$ , respectively, and Z-axis corresponding to polar axis, were calculated according to the following equations:

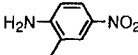
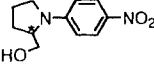
$$d_{zzz} = N f_z^{2\omega} (f_z^\omega)^2 \sum \beta_{zz} \cos^3 \theta \quad (1)$$

and

$$d_{zxx} = N f_z^{2\omega} (f_x^\omega)^2 \sum \beta_{zx} \cos \theta \sin^2 \theta, \quad (2)$$

where  $N$  is the number of chromophores in a unit volume,  $f_z^{2\omega}$ ,  $f_z^\omega$  and  $f_x^\omega$  are Lorentz's local field factors for the corresponding direction and frequency,  $\beta_{zz}$  denotes the  $\beta$  value along the molecular charge-transfer axis, and  $\theta$  represents angle between polar axis of the crystal and the molecular charge-transfer axis. Summation was performed over the cation and its counter anion in the crystals. In this estimation, the  $\beta_{0,calc}$  values for pyridinium cations and benzenesulfonate anions were employed. Local-field factors for present

TABLE V  $\lambda_{co}$ , space group, and calculated  $d$  values of several SHG-active crystals.

$X-\text{C}_6\text{H}_4\text{N}^+-R$ / $-\text{O}_3\text{S}-\text{C}_6\text{H}_4-\text{Z}$ or $\text{I}^-$	$\lambda_{co}$ / nm	Space group	$d_{zzz}^a$ / pmV <sup>-1</sup>	$d_{zxx}^a$ / pmV <sup>-1</sup>
<b>12d</b> : X=NH <sub>2</sub> , R=Me / Z=OH	340	P1	41	2
<b>12i</b> : X=NH <sub>2</sub> , R=Me / Z=Cl	340	Cc	37	3
<b>12j</b> : X=NH <sub>2</sub> , R=Me / Z=Br	340	Cc	38	3
<b>14e</b> : X=CONH <sub>2</sub> , R=Me / Z=OMe	370	Cc	6	11
<b>14j</b> : X=CONH <sub>2</sub> , R=Me / Z=Br	370	P2 <sub>1</sub>	5	12
<b>15a</b> : X=NMe <sub>2</sub> , R=Et / I <sup>-</sup>	390	P2 <sub>1</sub>	8	19
 (MNA)	475	Cc	86 <sup>b</sup>	10 <sup>b</sup>
 (NPP)	500	P2 <sub>1</sub>	9 <sup>c</sup>	25 <sup>c</sup>

<sup>a</sup>The  $d_{zzz}$  and  $d_{zxx}$  values were calculated using Eqs. (1) and (2), respectively.

<sup>b</sup>Experimental  $d$  values reported for MNA are 250 pmV<sup>-1</sup> for  $d_{11}$  and 38 pmV<sup>-1</sup> for  $d_{12}$ .<sup>33</sup>

<sup>c</sup>Experimental  $d$  values reported for NPP are 31 pmV<sup>-1</sup> for  $d_{22}$  and 83 pmV<sup>-1</sup> for  $d_{21}$ .<sup>34</sup>

crystals were referred to those of 3-methoxy-4-hydroxybenzaldehyde (MHBA) crystal,<sup>32</sup> whose space group and  $\lambda_{co}$  are monoclinic P2<sub>1</sub> and around 370 nm, respectively, and they were considered to be close to the crystals in this study. The  $d$  values of 2-methyl-4-nitroaniline (MNA)<sup>33</sup> and *N*-(4-nitrophenyl)-L-prolinol (NPP)<sup>34</sup> were also estimated for comparison. The calculated results are summarized in TABLE V. Among pyridinium derivatives, the largest diagonal  $d$  component was estimated for **12d** to be about half of that of MNA irrespective of its excellent transparency in visible region. This is mainly due to parallel orientation of the ionic chromophores for triclinic space group P1. On the other hand, the largest off-diagonal  $d$  component was obtained for **15a** which was estimated to be about three-fourths of that of NPP. The crystal of **15a** belongs to monoclinic space group P2<sub>1</sub>, and angle  $\theta$  was observed to be 56.8°, which is very close to optimal  $\theta$  of 54.7° needed to maximize  $d_{zxx}$  value. Since the present crystals are completely transparent in visible region, they have potential for frequency conversion of conventional diode lasers.

## CONCLUSION

For DAST derivatives with extended  $\pi$ -conjugation system, cationic structures of **2a** and

**3a** with larger  $\beta$  values compared with DAST cation are worth investigating for noncentrosymmetric alignment in crystals to achieve larger  $d$  and  $r$  values than those of DAST. Compounds to be used among series of polyene and fused-ring analogues of DAST may be selected for various absorption cutoff limits. However, if the using purpose of NLO crystals was limited to EO applications, DAST would be the best compound at present because of its large  $r$  value exceeding that of lithium niobate and its good crystal-growth ability. Thus, the studies concentrated on DAST, including growth of single crystals with high optical quality, waveguide fabrication without optical loss and so on, seems to be inevitable.

For molecules with short  $\pi$ -conjugation lengths, 4-substituted pyridinium salts were found to be promising for short cutoff materials for frequency conversion of diode lasers. Several of the SHG-active pyridinium salts provide good molecular arrangements in crystals to optimize diagonal or off-diagonal  $d$  component. Growth of their large crystals is in progress for measurement of  $d$  coefficients.

#### ACKNOWLEDGEMENTS

The authors wish to thank Dr. K. Clays (University of Leuven, Belgium) and his colleagues for modulated HRS measurement. We gratefully thank Dr. A. Watanabe (ICRS, Tohoku University, Japan) for help in measuring HRS. This research was partially supported by New Energy and Industrial Technology Development Organization (NEDO) as Regional Consortium Project.

#### REFERENCES

1. X.-M. Duan, H. Konami, S. Okada, H. Oikawa, H. Matsuda, and H. Nakanishi, *J. Phys. Chem.*, **100**, 17780 (1996).
2. G. R. Meredith, in *Nonlinear Optical Properties of Organic and Polymeric Materials*, ACS Symp. Ser., **233**, edited by D. J. Williams (American Chemical Society, Washington, D. C., 1983) pp. 27.
3. S. Okada, H. Matsuda, H. Nakanishi, M. Kato, and R. Muramatsu, Japanese Patent Application 61-192404 (1986); Japanese Patent 1716929 (1992).
4. H. Nakanishi, H. Matsuda, S. Okada, and M. Kato, in *Mater. Res. Soc. Int. Mtg. Adv. Mater.*, **1**, edited by M. Doyama, S. Somiya, and R. P. H. Chang (Materials Research Society, Pittsburgh, 1989) pp. 97.
5. S. R. Marder, J. W. Perry, and W. P. Schaefer, *Science*, **245**, 626 (1989).
6. S. R. Marder, J. W. Perry, and C. P. Yakymyshyn, *Chem. Mater.*, **6**, 1137 (1994).
7. G. Knöpfle, R. Schlessler, R. Ducret, and P. Günter, *Nonlinear Opt.*, **9**, 143 (1995).
8. F. Pan, M. S. Wong, Ch. Bosshard and P. Günter, *Adv. Mater.*, **8**, 592 (1996).
9. H. Adachi, Y. Takahashi, J. Yabuzaki, Y. Mori, and T. Sasaki, *J. Cryst. Growth*, **198/199**, 568 (1999).
10. S. Sohma, H. Takahashi, T. Taniuchi, and H. Ito, *Chem. Phys.*, **245**, 359 (1999).
11. C. W. Spangler and R. K. McCoy, *Synth. Commun.*, **18**, 51 (1988).

12. S. Okada, A. Masaki, H. Matsuda, H. Nakanishi, M. Kato, R. Muramatsu, and M. Otsuka, *Jpn. J. Appl. Phys.*, **29**, 1112 (1990).
13. K. Nogi, Anwar, K. Tsuji, X.-M. Duan, S. Okada, H. Oikawa, H. Matsuda, and H. Nakanishi, *Nonlinear Opt.* in press.
14. H. Umezawa, K. Tsuji, Anwar, X.-M. Duan, S. Okada, H. Oikawa, H. Matsuda, and H. Nakanishi, *Nonlinear Opt.* in press.
15. A. J. Birch, A. H. Jackson, and P. V. R. Shannon, *J. Chem. Soc., Perkin Trans. 1*, 2185 (1974).
16. W. J. Gensler, *Org. React.*, **6**, 191 (1951).
17. H. Nerenz, M. Meier, W. Grahn, A. Reisner, E. Schmälzlin, S. Stadler, K. Meerholz, C. Bräuchle, and P. G. Jones, *J. Chem. Soc., Perkin Trans. 2*, 437 (1998).
18. Anwar, X.-M. Duan, K. Komatsu, S. Okada, H. Oikawa, H. Matsuda, and H. Nakanishi, *Nonlinear Opt.*, **22**, 251 (1999).
19. G. Olbrechts, R. Strobbe, K. Clays, and A. Persoons, *Rev. Sci. Instrum.*, **67**, 1445 (1996).
20. K. Clays, K. Wostyn, G. Olbrechts, A. Persoons, A. Watanabe, K. Nogi, X.-M. Duan, S. Okada, H. Oikawa, H. Nakanishi, H. Vogel, D. Beljonne, and J.-L. Brédas, *J. Opt. Soc. Am. B*, **17**, 256 (2000).
21. K. Clays and A. Persoons, *Phys. Rev. Lett.*, **66**, 2980 (1991).
22. X.-M. Duan, S. Okada, H. Nakanishi, A. Watanabe, M. Matsuda, K. Clays, A. Persoons, and H. Matsuda, in *Organic, Metallo-Organic, and Polymeric Materials for Nonlinear Optical Applications Proc. SPIE*, **2143**, edited by S. R. Marder and J. W. Perry (SPIE, Bellingham, 1994) pp. 41.
23. J. L. Ouder and D. S. Chemla, *J. Chem. Phys.*, **66**, 2664 (1977).
24. S. K. Kurtz and T. T. Perry, *J. Appl. Phys.*, **39**, 3798 (1968).
25. J. Zyss and J. L. Ouder, *Phys. Rev. A*, **26**, 2028 (1982).
26. X.-M. Duan, N. Nishimura, H. Konami, S. Okada, H. Oikawa, H. Matsuda, and H. Nakanishi, *Nonlinear Opt.*, **20**, 105 (1999).
27. Anwar, X.-M. Duan, K. Komatsu, S. Okada, H. Oikawa, H. Matsuda, and H. Nakanishi, *Chem. Lett.*, 247 (1997).
28. Anwar, X.-M. Duan, S. Okada, H. Oikawa, H. Matsuda, and H. Nakanishi, *J. Chem. Soc. Perkin Trans. 2*, 2451 (1998).
29. X.-M. Duan, T. Kimura, S. Okada, H. Oikawa, H. Matsuda, M. Kato, and H. Nakanishi, *Mol. Cryst. Liq. Cryst.*, **280**, 1 (1996).
30. Anwar, S. Okada, H. Oikawa, and H. Nakanishi, *Chem. Mater.* in press.
31. Anwar, K. Komatsu, S. Okada, H. Oikawa, H. Matsuda, and H. Nakanishi, *Organic Nonlinear Optical Materials, Proc. SPIE*, **3796**, edited by M. Eich and M. G. Kuzyk (SPIE, Bellingham, 1999) pp. 219.
32. X. T. Tao, D. R. Yuan, N. Zhang, M. H. Jiang, and Z. S. Shao, *Appl. Phys. Lett.*, **60**, 1415 (1992).
33. B. F. Levine, C. G. Bethca, C. D. Thormond, R. T. Lynch, and J. L. Bernstein, *J. Appl. Phys.*, **50**, 2523 (1979).
34. I. Ledoux, D. Josse, P. Vidakovic, J. Zyss, J. F. Nicoud, and M. Coquillay, *Opt. Eng.*, **25**, 202 (1986).

## Photodegradation of Various Electro-Optic Polymer Families

G. I. STEGEMAN(a), A. GALVAN-GONZALES(a), M. CANVA(b),  
R. TWIEG(c), A. C. KOWALCZYK(d), X. Q. ZHANG(d), H. S.  
LACKRITZ(d), S. MARDER(e), S. THAYUMANAVAN(e), K. P.  
CHAN(f), A. K-Y. JEN(g), X. WU(g)

(a)School of Optics and CREOL, University of Central Florida,  
Orlando, FL 32826, USA; (b)Laboratoire Charles Fabry de l'Institut  
d'Optique, IOTA-Université d'Orsay-Paris XI, 91403 Orsay Cedex  
France; (c)Dept. of Chemistry & Liquid Crystal Institute, Kent State  
University, Kent, OH 44242, USA; (d) Gemfire Corporation, Palo  
Alto, CA 94303, USA; (e)Dept. of Chemistry, University of Arizona,  
Tucson, AZ 85721, USA; (f)Molecular OptoElectronics Corporation  
(MOEC), Watervliet, NY 12189-1903, USA; (g)Dept. of Materials  
Science, University of Washington, Seattle, WA 98195-2120, USA.

The photostability of different chromophore families has been studied as a function of probe wavelength in the spectral range 400 to 1320 nm. Multiple donor and acceptor groups have been attached to the main bridge structures containing stilbene, azobenzene, aniline, thiophene and aniline-thiophene substructures. The figure of merit  $B/\sigma$  was measured and the quantum efficiency  $B^{-1}$  was evaluated for over 40 dye containing polymers, including both side-chain and guest-host systems.

### Keywords

Photodegradation, Electro-optic Chromophores, Photo-oxidation,  
Trans-cis isomerization, Charge Transfer States, Polymer Photonics

## INTRODUCTION

Photonic devices based on polymers are promising for a number of applications, especially for very high bandwidth electro-optics, and their performance has improved steadily.[1,2] The temporal stability of the chromophore orientation necessary to retain the electro-optic activity has been investigated intensively and significant improvements have been accomplished.[3] However, it is also well-known from early pioneering work that electro-optic polymers under continuous illumination lose their nonlinearity with time due to a number of different mechanisms.[4,5] Therefore, the stability of these materials needs to be addressed as well. In response, we and other groups initiated programs to investigate the wavelength variation in photostability, the principal parameters on which it depends and the photostability for a number of families of electro-optic polymers.[6-12]. In this paper we compare the photodegradation of a number of polymer families that contain stilbene, azobenzene, aniline, thiophene and aniline-thiophene substructures. These structures of the dyes evaluated in this study are found in Table 1.

## MODEL AND MEASUREMENT OF THE PHOTODEGRADATION PROCESS

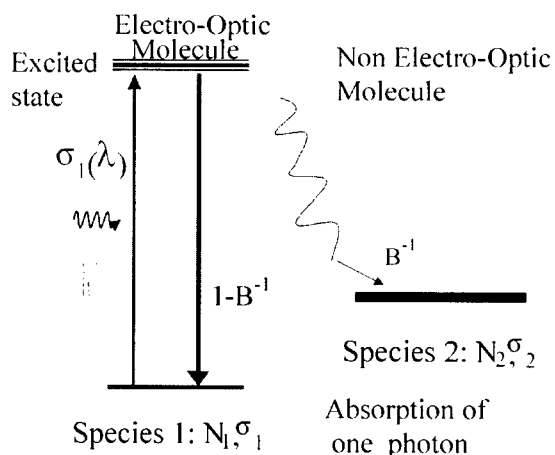


FIGURE 1 The mechanistic model used for the light activated photodegradation process.

The model we adopt for the photodegradation process is shown in Figure 1. Absorption of a photon into a charge transfer state initiates the process and the excited state can either decay back to the ground state, or a chemical reaction or isomerization can occur so that the molecule returns to a different ground state with a probability  $B^{-1}$ . This leads to

$$\partial N_2 / \partial t = B^{-1}(\lambda) \partial N_E / \partial t = [\sigma(\lambda) / B(\lambda)] N_1(t) n(t)$$

where  $N_E$  is the number of electro-optic chromophores in their excited state and  $N_1(t)$ ,  $n(t)$  and  $\sigma(\lambda)$  are respectively the local electro-optic active chromophore concentration, the photon flux, and the molecular absorptivity. If, as is frequently the case, there is more than one decay channel "i" out of the excited state then

$$1/B = \sum 1/B_i.$$

Essentially two experimental protocols were used to investigate photobleaching. It is assumed at the outset that the nonlinearity will be proportional to the concentration of the active species and that this concentration is reflected directly by the magnitude of the absorption associated with the charge transfer peak. For a selected number of materials, usually an example from each family of chromophores, the absorption spectrum was measured as a function of illumination time by a laser whose wavelength lies within the charge transfer absorption band. These experiments were performed on thin films prepared, maintained and measured in either air, nitrogen or oxygen in order to quantify the importance of oxygen in the photobleaching process. From the complex appearance of the absorption spectrum as a function of illumination time in different atmospheres it has proved possible to identify whether a single dominant or multiple competitive degradation channels were active in a given film.

The second experimental protocol used was to measure the transmission change in the long-wavelength tail of the absorption associated with the dominant charge transfer as the polymer film was illuminated with radiation of different wavelengths. As discussed previously, this leads directly to a measurement of  $B/\sigma$  versus photon energy or wavelength. This ratio in turns allows a direct prediction of the lifetime expected for the nonlinear activity of the material. Coupled with careful measurements of absorption spectrum, these experiments



yield the degradation probability  $B^{-1}$  as a function of wavelength. The wavelength dependence of  $B$ , if any, identifies the number of charge transfer states participating in the degradation process measured in these experiments.

### DEGRADATION MECHANISMS

In the course of our investigations we have observed three different kinds of behavior in terms of the number of degradation channels and participating charge transfer states. A typical example of changes in the absorption spectrum under different atmospheres is shown in Figure 2 for a Disperse Red 1 guest-host polymer film with 4% by weight loading of the chromophore in PMMA. In nitrogen there is a

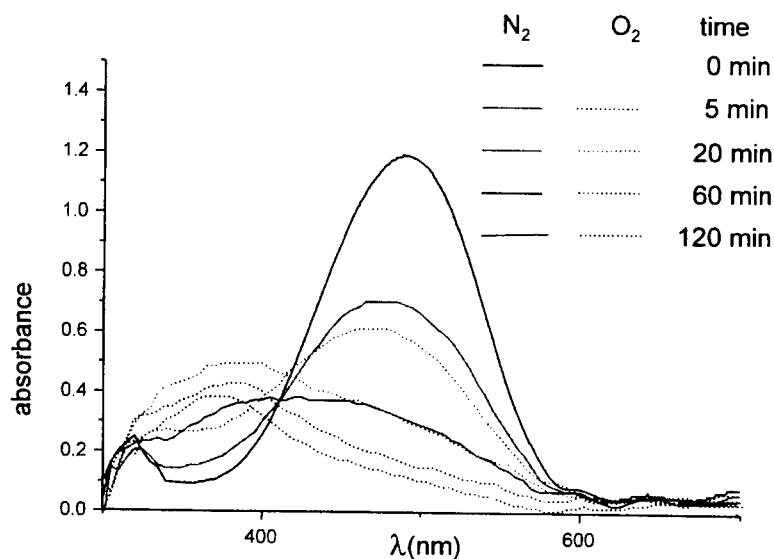


FIGURE 2 The absorption spectrum of Disperse Red 1 in a PMMA host when illuminated with 488 nm radiation for different periods of time in either an oxygen or a nitrogen.

single wavelength through which all of the absorption spectra pass (isobestic point). This indicates that there is only one dominant decay

channel from the excited state that we identify with trans-cis isomerization.[13] However, in an oxygen atmosphere, the degradation process occurs faster, produces no isobestic point and results in a different end product, as evidenced by the difference between the absorption spectra after two hours for the two cases. Clearly some new process, such as photo-oxidation occurs in the oxygen-containing environment. The results in air closely resemble those in pure oxygen, indicating that photo-oxidation is the dominant degradation process in ambient atmospheres.

We have previously shown that in stilbenes there are two charge transfer states that participate in the nonlinearity, and that they degrade via both photo-activated reactions and trans-cis isomerization.[7,10] For example, in DANS-SCP, the changes to the absorption spectrum are different in nitrogen versus oxygen atmospheres and in neither case is an isobestic point observed. In fact, in nitrogen, as well as in oxygen, there are two distinct absorption bands, centered at 300 nm and 430 nm, which are diminished with illumination time. Further evidence for the participation of two charge transfer states was obtained from a plot of  $B$  versus photon energy, as is shown in Figure 3. It is clear that there are two different values of  $B$  present in contrast to Disperse Red 1 for which  $B$  is independent of wavelength.

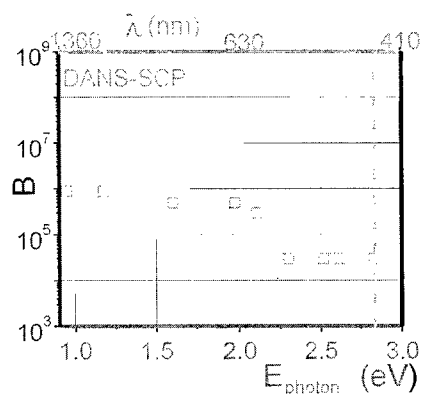


FIGURE 3 Variation in the parameter  $B$  as a function of photon energy and wavelength for DANS. The vertical dashed line identifies the location of the absorption maximum.

Of the approximately 10 materials that were studied using different atmospheres, the only clear case of a single degradation mechanism and a single participating charge transfer state was found in a cyano-thiophene chromophore. The change in the absorption spectrum with illumination time is shown in Figure 4.

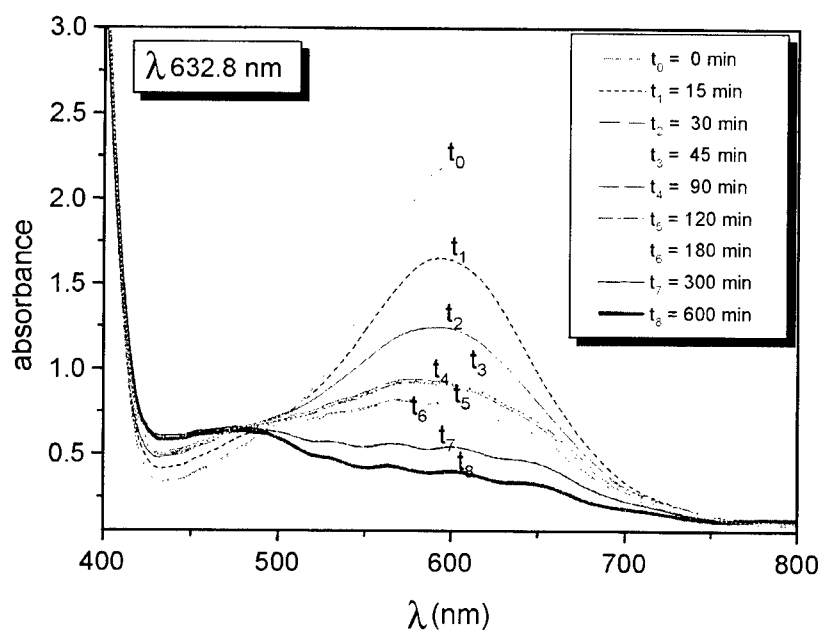


FIGURE 4 Variation in the absorption spectrum of 5[1,3(1,4 bis-dicyano 3-phenyl)butyl]diene] 2-N,N-di(4butyl)phenyl aniline-thiophene when illuminated for different periods of time with radiation of wavelength 633 nm.

#### WAVELENGTH VARIATION OF $B/\sigma$

The typical observed variation in  $B/\sigma$  with wavelength is shown in Figure 5 for a variety of chromophores that are listed in Table 1.

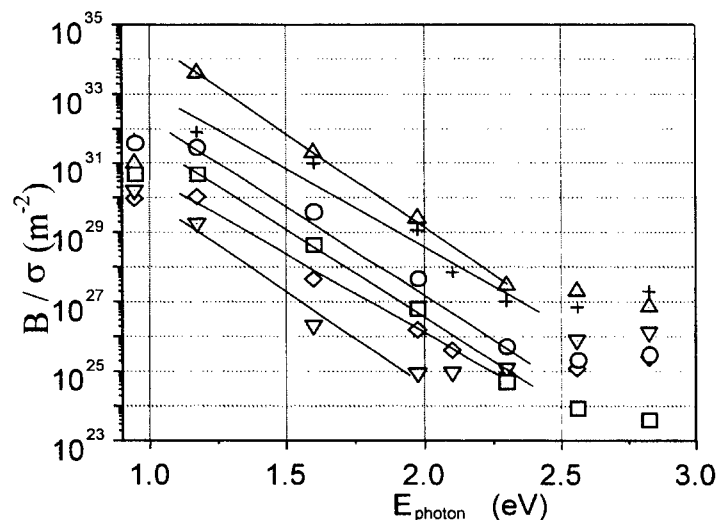


FIGURE 5 The variation with wavelength of the parameter  $B/\sigma$  measured for a variety of electro-optic polymers found in Table 1.

The wavelength variation shown is dominated by the wavelength dependence of the molecular absorptivity, i.e. the absorption spectrum. Comparison with the location of the peak of the absorption spectrum, i.e.  $\lambda_{\text{max}}$ , shows that the  $B/\sigma$  rises again on the high energy side of the absorption maximum. The straight line approximations in the Near-IR are typical of all 45 polymers investigated, and are again indicative of the wavelength dependence of the absorption. Noting that the time required for the concentration of electro-optic chromophores to drop to  $1/e$  of its original value, then the larger  $B/\sigma$  found, the longer is the lifetime. There is a clear variation of over five orders of magnitude in Figure 5. The decrease at 1320 nm has been noted previously and attributed to highly reactive singlet oxygen complexes.[4]

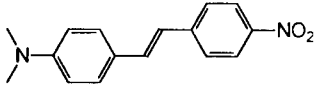
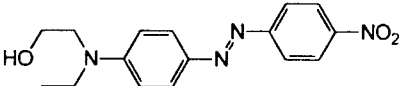
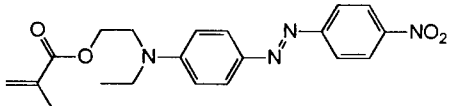
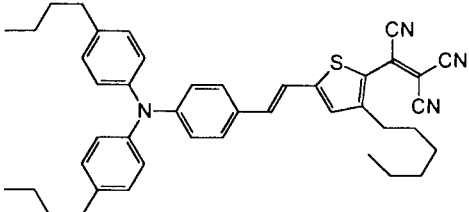
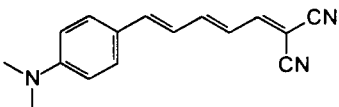
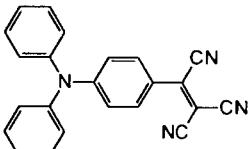
Symbol	Chromophore	$\lambda_{\max}$ (nm)
□		430
○		475
△		470
▽		640
◇		510
+		520

TABLE 1 Listing of the chemical structures for the chromophores whose measured  $B/\sigma$  were plotted in Figure 5 versus photon energy.

## PARAMETER B FOR VARIOUS CHROMOPHORE FAMILIES

The data for  $B/\sigma$  when coupled with measurements of the absorption spectrum, yields the quantum efficiency parameter B.

Family	B	$B/\sigma$ ( $\propto \tau$ ) 1064nm	# Decay Channels	# Active States
Stilbenes	$\rightarrow 5 \times 10^5$	$3 \times 10^{31}$	$\geq 2$	2
Azobenzenes	$\rightarrow 3 \times 10^8$	$5 \times 10^{33}$	2	1
Anilines	$\rightarrow 10^8$	$10^{32}$		
Thiophenes	$\rightarrow 8 \times 10^6$	$10^{31}$	1	1

Table 2 A summary of the photodegradation properties of various chromophore families listed by their characteristic bridge structure separating the donors and acceptors. Listed are the largest values for B and  $B/\sigma$  found in each family, and the number of strong charge transfer states and the number of decay channels for each state. The chromophore identified by  $\Delta$  includes an anti-oxidant which improves B and  $B/\sigma$  by a factor  $> 10$  over the next best azobenzene.

The stability of a material depends on both the value of B and  $B/\sigma$ . The larger B and the smaller  $\sigma$ , the more photostable the material is. The values at 1320 nm for  $B/\sigma$  are usually less than at 1064 nm and this is attributed to triplet oxygen. Values at 1550 nm are not known but are expected to be larger. By "how much?" the values are larger is the key question.

## ACKNOWLEDGEMENTS

This research was supported by the National Research Foundation, Air Force Office of Scientific Research and BMDO in the U.S.

## REFERENCES

- [1] for example, Y. Shi, W. Wang, J.H. Bechtel, A. Chen, S. Garner, S. Kalluri, W.H. Steier, D. Chen, H.R. Fetterman, L.R. Dalton and L. Yu, IEEE J. Selected Topics in Quant Electron. **2**, 289 (1996).
- [2] for example, A. Grunnet-Jepsen, C.L. Thompson, R.J. Twieg, W.E. Moerner, Appl. Phys. Lett. **70**, 1515 (1997).
- [3] for example D.H. Choi, J.H. Park, N. Kim, S.-D. Lee, Chem. Mater. **10**, 705 (1998); M. Stahelin, C.A. Walsh, D.M. Burland, R.D. Miller, R.J. Twieg, and W. Volksen J. Appl. Phys. **73**, 8471 (1993).
- [4] M. A. Mortazavi, H. N. Yoon, C. C. Teng, J. Appl. Phys. **74**, 4871 (1993); M. A. Mortazavi, H. N. Yoon, I. McCulloch, Polymer Preprints, **35**, 198 (1994); R. A. Norwood, D. R. Holcomb, F. F. So, J. Nonlin. Opt. **6**, 193 (1993).
- [5] M. Cha, W. E. Torruellas, G. I. Stegeman, W. H. G. Horsthuis, Appl. Phys. Lett. **65**, 2648 (1994).
- [6] Y. Shi, W. Wang, W. Lin, D. J. Olson, J. H. Bechtel, Appl. Phys. Lett. **70**, 1342 (1997).
- [7] Q. Zhang, M. Canva, G.I. Stegeman, Appl. Phys. Lett. **73**, 912 (1998).
- [8] Ph. Pretre, E. Sidlick, A. Knoesen, D. J. Dyer, R. J. Twieg, ACS Symposium Ser., **695**, 328 (1996).
- [9] T.C. Kowalczyk, R.J. Twieg, H.S. Lackritz, Extended Abstracts of 4<sup>th</sup> International Conference on Organic Nonlinear Optics (ICONO4 ), October 1998, 61.
- [10] A. Galvan-Gonzalez, M. Canva and G. I. Stegeman, Appl. Phys. Lett., **75**, 3306 (1999).
- [11] A. Galvan-Gonzalez, M. Canva, G. I. Stegeman, R. Twieg, A. C. Kowalczyk and H. S. Lackritz, Opt. Lett., **24**, 1741 (1999).
- [12] M. Bosch, C. Fischer, C. Cai, I. Liakatas, M. Jager, Ch. Bosshard and P. Gunter, Digest of 1999 Organic Thin Films for Photonics Applications (Optical Society of America, Washington, 1999), pp 73-5
- [13] A. Galvan-Gonzalez, M. Canva, G. I. Stegeman, S. Marder, S. Thayumanavan, R. Twieg, A. C. Kowalczyk, X. Q. Zhang, and H. S. Lackritz, Opt. Lett., in press
- [14] D. Riehl, F. Chaput, A. Roustamian, Y. Levy and J.-P. Boilot, Nonlin. Opt., **8**, 141, (1994).

## Nonlinear Optics and Photorefractivity of Polymer Composites

NAKJOONG KIM\*<sup>1</sup>, HYUNAE CHUN<sup>1</sup>, WOONG SANG JAHNG<sup>2</sup>,  
SANGYUP SONG<sup>2</sup>, DONG-HO SHIN<sup>2</sup>, and MINSOO JOO<sup>2</sup>

<sup>1</sup>Department of Chemistry, Hanyang University, Seoul 133-791, Korea;

<sup>2</sup>Center for Organic Photorefractive Materials, KIST, P.O. Box 131,  
Cheong-ryang, Seoul, 130-650, Korea

\*E-mail: kimnj@email.hanyang.ac.kr

**ABSTRACT** Photorefractive (PR) composites were prepared from polysiloxane with pendant carbazole as photoconducting host, a series of indole-derivatives as NLO chromophore, and 2,4,7-trinitro-9-fluorenone as photosensitizer. It was observed that two-beam coupling gain coefficient of composites were influenced by the rotational mobility of chromophore, providing the evidence that chromophore in low glass transition temperature ( $T_g$ ) matrix is realigned under the space-charge field. And the influence of chromophore on electro-optical property of composite was also discussed.

**KEYWORDS** photorefractive; electro-optic; chromophore; reorientation; mobility; indole.



## INTRODUCTION

Since the first discovery of photorefractive effect in polymer in 1991, polymeric materials have been intensively studied due to the potential optical applications [1]. Even though several photorefractive composites have been reported to have excellent steady-state performance, the understanding on photorefractive mechanism in polymeric system has been still limited. This work focuses on the influence of orientation of NLO chromophore on electro-optical (EO) and photorefractive (PR) performance of polymeric composite.

## EXPERIMENTAL

Carbazole-substituted polysiloxane (PSX) and NLO chromophores with indol-moiety were synthesized. 2,4,7-Trinitro-9-fluorenone (TNF, Kanto Chemical Co.) and butyl benzyl phthalate (BBP) were used as

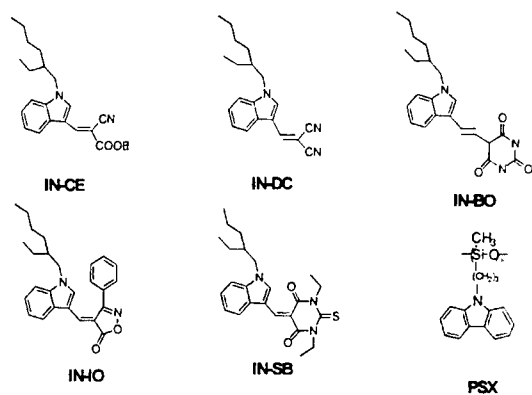


FIGURE 1 Chemical structures for NLO chromophores and carbazole-substituted polysiloxane

received. The chemical structures of molecules used in this work are given in Figure 1.

PR composite consisted of PSX (79 or 69 wt %), chromophore (20 or 30 wt %), and TNF (1 wt %). And this composite retained the phase stability over a year at room temperature.

The electro-optic property of composite was determined at the wavelength of 632.8 nm by transmission ellipsometric method. For EO measurement, the composite film with thickness of 100  $\mu\text{m}$  was used. Photoconductivity was measured at the wavelength of 632.8 nm ( $I = 1.58 \text{ mW}$ ) using a simple DC photocurrent technique. The current through the 10  $\mu\text{m}$  thick film was measured as a function of electric field before and during illumination. The PR material was characterized by the two-beam coupling (2BC) method. He-Ne laser with the intensity of 20  $\text{mW}/\text{cm}^2$  was used and the angle between the laser beams was  $30^\circ$ . The tilt angle with respect to sample normal was  $45^\circ$ .

## RESULTS AND DISCUSSION

A series of NLO chromophores containing indole ring were synthesized by varying the strength of electron acceptor. The optical parameters of chromophores are calculated using MOPAC method and the results are given in Table 1. In the case of low  $T_g$  polymer, the performance of chromophore is evaluated by the following equation ( $FOM$ ),

$$FOM = \left( \frac{2}{9kT} \right) \frac{\mu^2 \Delta\alpha}{M} + \frac{\mu\beta}{M}$$

where  $\mu$ ,  $\beta$ ,  $\Delta\alpha$ , and  $M$  are dipole moment, hyperpolarizability, polarizability anisotropy ( $\alpha_{||} - \alpha_{\perp}$ ) and molar mass, respectively [2].

TABLE 1 Molecular parameters of chromophores

NLO	$\mu^b$	$\Delta\alpha^b$	$\beta^c$	$F_{BR}^d$	$F_{Pockels}^e$
IN-CE	2.23	1.12	36.4	0.88	2.35
IN-DC	2.31	1.37	62.9	1.31	4.85
IN-BO	1.70	2.57	58.7	1.00	2.52
IN-IO	1.84	2.51	70.1	1.13	3.22
IN-SB	2.36	3.52	67.1	2.38	3.58

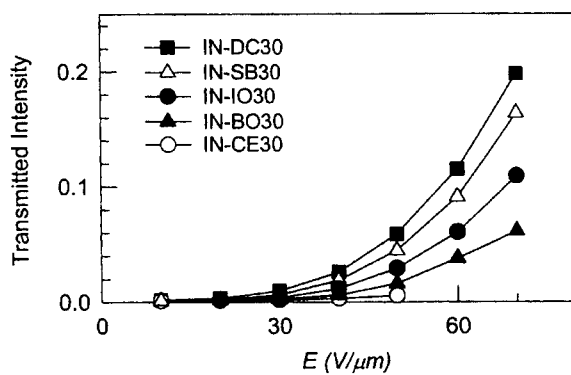
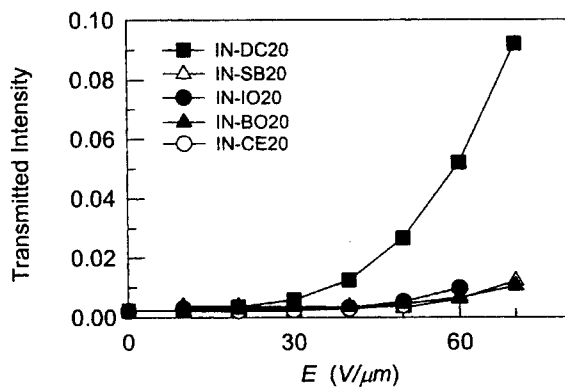
<sup>a</sup>  $10^{-29} \text{ C}\cdot\text{m}$ ; <sup>b</sup>  $10^{-28} \text{ m}^3$ ; <sup>c</sup>  $10^{-40} \text{ m}^4/\text{V}$ ; <sup>d</sup>  $F_{BR} = (2/9kT)(\mu^2\Delta\alpha/M)$ .

<sup>e</sup>  $10^{-65} \text{ C}\cdot\text{m}^5\text{mol}/\text{V}\cdot\text{kg}$ ; <sup>c</sup>  $F_{Pockels} = (\mu\beta/M)$ ,  $10^{-67} \text{ C}\cdot\text{m}^5\text{mol}/\text{V}\cdot\text{kg}$ .

According to this criterion, electro-optic (EO) property of indole-chromophore is expected to be in the order of IN-SB > IN-DC > IN-IO > IN-BO > IN-CE. The electro-optical property of PR composites composed of PSX/ TNF/ NLO = 69/ 1/ 30 wt % was determined by transmission ellipsometric measurement. As given in Figure 2, the transmitted intensity is in the order of IN-DC30 > IN-SB30 > IN-IO30 > IN-BO30 > IN-CE30, which is in fairly accord with calculated result. However, in the case of composites containing 20 wt % of chromophore, only IN-DC20 composite shows the appreciable electro-optic response, as given in Figure 3. All of the other composites show the low and similar values of transmission, irrespective of the kind of chromophore. It is speculated that the low EO activity of IN-SB20, IN-IO20 and IN-BO20 is related with the restricted rotational mobility of chromophore. As can be shown in Table 2,  $T_g$  for these composites are higher than room temperature and, consequently the orientation of chromophore must be limited by the high viscosity of medium at the room temperature. The observation that poling efficiency of IN-SB20 composite is significantly increased by the addition of plasticizer may prove the above suggestion. This result clearly demonstrates the significance of chromophore mobility, especially for *in-situ* poled material.

TABLE 2 Glass transition temperature ( $^{\circ}\text{C}$ ) of Composites

	IN-CE	IN-DC	IN-BO	IN-IO	IN-SB
20 wt%	25	25	38	38	42
30 wt%	17	15	34	34	36

FIGURE 2 Electro-optic properties of PR composites.  
[NLO] = 30 wt%FIGURE 3 Electro-optic properties of PR composites.  
[NLO] = 20 wt%.

The photorefractive properties of composites were characterized by the *2BC* measurement. In the case of composites containing 20 wt % of chromophores, IN-DC20 composite exhibits the higher gain coefficient than the other composites studied in this work. The IN-CE20 and IN-SB20 composites with the low EO properties show relatively low values of *2BC* coupling gain coefficient.

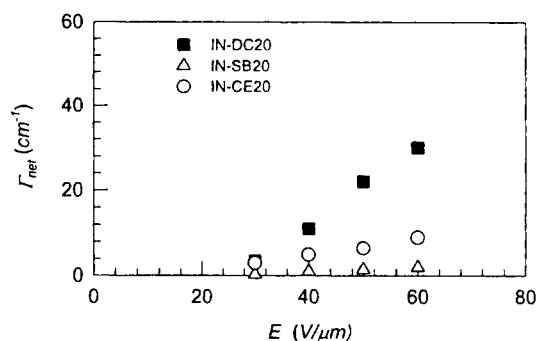


FIGURE 4 *2BC* gain coefficients ( $\Gamma$ ) of PR composites

In the case of IN-IO20 and IN-BO20 composites, virtually no gain coefficient in 2-beam coupling is observed up to 70 V/ $\mu$ m. Even at the higher chromophore concentration, the values of gain coefficient for both composites (IN-IO30 and IN-BO30) are *ca.* 3 cm $^{-1}$  at 70 V/ $\mu$ m, as shown in Figure 5. This is interesting observation since the EO activity of IN-IO30 and IN-BO30 composites is greater than that of IN-DC20 composite (see Figure 2 and Figure 3).

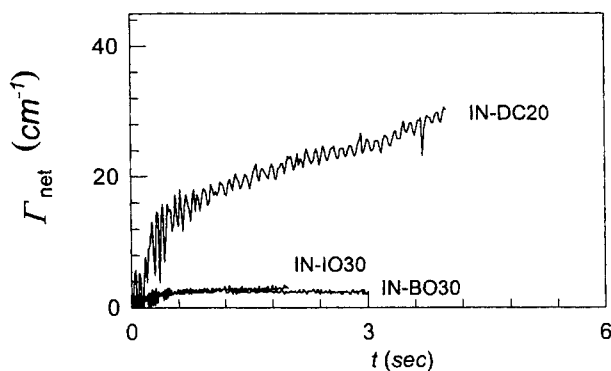


FIGURE 5 2BC gain coefficient ( $\Gamma$ ) of PR composites at  $70 V/\mu m$

It is well-accepted fact the birefringent chromophore in low  $T_g$  PR polymer is able to be re-aligned under the total electric field (= applied external field + space-charge field) and the modulation of refractive index is significantly enhanced by the reorientation of chromophore[3]. Thus, if the free reorientation of chromophore in composites is limited at measuring conditions, just as found in EO response (see Figure 3), it is probably difficult that PR composite exhibits the large photorefractive property.

In order to determine the chromophore mobility of composite used in this work, the transient ellipsometric measurement was carried out. The transmitted intensity of sample *as prepared* was measured as a function of time as soon as electric field turned on. The results in Figure 6 show that the build-up of EO response for IN-IO30 composite ( $T_g = 34^\circ C$ ) is much slower than that for IN-DC20 composite ( $T_g = 25^\circ C$ ). In the case of IN-IO30 composite, the reorientation of chromophore is not likely to occur at room temperature ( $25^\circ C$ ) during a short period of 2BC measurement. In order to improve the rotational

mobility, the small amount of plasticizer is added into IN-IO30 composite.  $T_g$  of IN-IO30 composites (p-IN-IO30) is lowered to be  $23^\circ\text{C}$ . As shown in Figure 6, the transient response of IN-IO30 composite becomes as fast as that of IN-DC20 composite. And 2BC

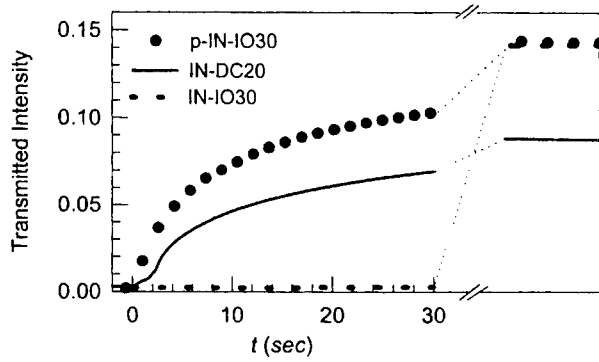


FIGURE 6 Transient EO response of composites as prepared at  $70\text{ V}/\mu\text{m}$

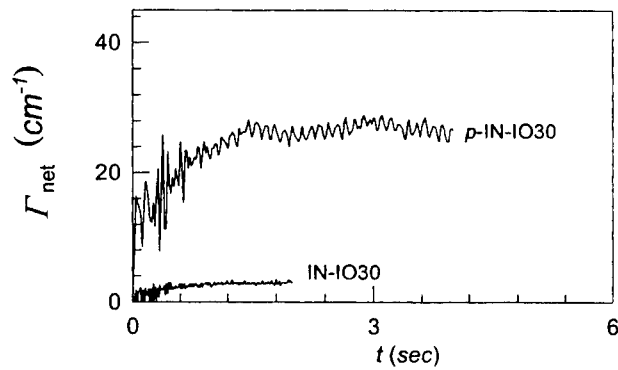


FIGURE 7 2BC gain coefficient ( $\Gamma$ ) of PR composites at  $70\text{ V}/\mu\text{m}$

gain of composite (p-IN-IO30) is also significantly increased, as given in Figure 7, being compared with the corresponding IN-IO30 composite. It is highly probable that the improvement of  $2BC$  gain results from the reorientation of chromophore, since the steady state value of transmission for IN-IO 30 composite ( $T = \text{ca. } 14 \%$ ) is not virtually varied by the addition of plasticizer. This observation provides the evidence on the significance of the reorientation of chromophore under the newly formed space-charge field ( $E_{sc}$ ).

#### ACKNOWLEDGEMENTS

The financial support by Creative Research Initiatives is gratefully acknowledged.

#### REFERENCES

1. W. E. Moerner and S. M. Silence, *Chem. Rev.*, **94**, 127 (1994).
2. R. Wortmann, C. Poga, R. J. Twieg, C. Geletneky, C. R. Moylan, P. M. Lundquist, R. G. DeVoe, P. M. Cotts, H. Horn, J. E. Rice and D. M. Burlnd, *J. Chem. Phys.*, **105**(23), 10637 (1996).
3. W. E. Moerner, S. M. Silence, F. Hache, and G. C. Bjorklund, *J. Opt. Soc. Am. B*, **11**, 320 (1994).



### **Periodically structured polymer films and applications.**

Licínio Rocha<sup>a</sup>, Vincent Dumarcher<sup>a</sup>, Christine Denis<sup>a</sup>, Paul Raimond<sup>a</sup>,  
Céline Fiorini<sup>a</sup>, Jean-Michel Nunzi<sup>a,b</sup>, Frank Sobel<sup>b</sup>, Denis Gindre<sup>b</sup>,  
Bouchta Sahraoui<sup>b</sup>

<sup>a</sup> *LETI (CEA - Technologies Avancées), DEIN/SPE, Groupe  
Composants Organiques, CEA Saclay, F-91191 Gif-sur-Yvette Cedex,  
France*

<sup>b</sup> *Laboratoire des Propriétés Optiques des Matériaux et Applications,  
Université d'Angers, 2 Boulevard Lavoisier, 49045 Angers Cedex,  
France*

Reversible holographic recording of surface-relief gratings in azo-dye polymers was recently evidenced using atomic force microscopy. Irradiation with an interference pattern between polarized laser beams was observed to lead to quantitative mass-transport. The origin of such efficient photo-driven mass transport comes from chromophore migration from the high to low intensity regions, in an inchworm like motion. In their motion, the chromophores work as molecular trucks, they track the whole polymer chain to which they are attached. As an application, we present a study of Distributed Feedback (DFB) laser emission in various polymer materials. The device permits to control the stimulated emission in dye doped polymer materials. Confinement and wave-guiding effects are evidenced.

#### Keywords

Organic devices; luminescent polymer; distributed feedback;  
molecular motors; surface relief gratings.

## INTRODUCTION

Patterning and micro-structuring of functional polymers are key technologies to fabricate organic devices. A recent achievement in this respect is the patterning of photoinduced surface-relief gratings using the interference pattern between optical beams.[1,2] This opens the route to molecular translation control using optical fields, in the same way as dual-frequency irradiation using appropriate combinations of circular beam polarizations have been demonstrated to enable a full control of the molecular polar order.[3-4] The well-known azo-dye aromatic polymers have been shown to be among the most efficient materials for such structuring processes using light matter interactions. A simple microscopic model accounting for the essential features of photoinduced surface-relief grating formation has been developed[5] and some of its peculiar features have been verified experimentally[6].

A challenging issue today is to pattern and micro-structure organic devices in order to control the emission properties of polymer thin films such as the one used for electroluminescent diodes. A control of the radiation modes of electroluminescent diodes has already been demonstrated using planar microcavities.[7-8] We propose here the use of a periodical excitation in a distributed feedback (DFB) scheme [9] to investigate the luminescence and lasing properties of dye-doped polymer thin films. The so-called organic lasers [10-11-12-13] have recently been revisited with an aim at building an organic semiconductor laser diode[14].

In 1971, Kogelnik and Shank first demonstrated DFB dye-laser operation using a dye doped gelatin film in which a grating had been previously printed optically.<sup>9</sup> They also showed that DFB laser action was possible by making a dynamic grating using the interference fringes from two pump beams inside a dye cell.[15] Narrow-band emission was tuned simply by changing the angle between the pump beams incident onto the dye cell. Efficient feedback is obtained from a spatial modulation of both gain and index of refraction of the polymer film. Modulation is photo-induced with the interference pattern produced by the two coherent laser beams.

Different interference schemes have already been proposed for DFB laser excitation : the so-call Lloyd's mirror which permits stable

operation in a compact set-up[16] and a more sophisticated interferometer which permits a better control of the pump beam characteristics[17]. We used both schemes to study DFB polymer dye laser characteristics. In particular, effects related to waveguiding of the laser emission into the polymer thin film were investigated. This appears as a very important feature in order to control stimulated emission using optically confined structures.

## EXPERIMENTS

The first results were obtained in polymer thin films of PMMA doped with rhodamine-6G (Rh6G), well known to be a highly emissive laser dye. The concentrations of Rh6G are taken in a range between 0.003 and 0.03 M. Such compositions have been widely studied for dye laser action[18]. The samples were deposited on glass substrates by the spin-coating method. The thickness of the films obtained was about 300 nm. In order to investigate the emission properties of such samples we made use of the experimental setup represented in figure 1. The films were pumped with the second harmonic ( $\lambda_p=532$  nm close to the Rh6G maximum absorption wavelength) of a Q-switched mode locked  $\text{Nd}^{3+}$ :YAG laser delivering 33 picosecond pulses at a 5 Hz repetition rate.

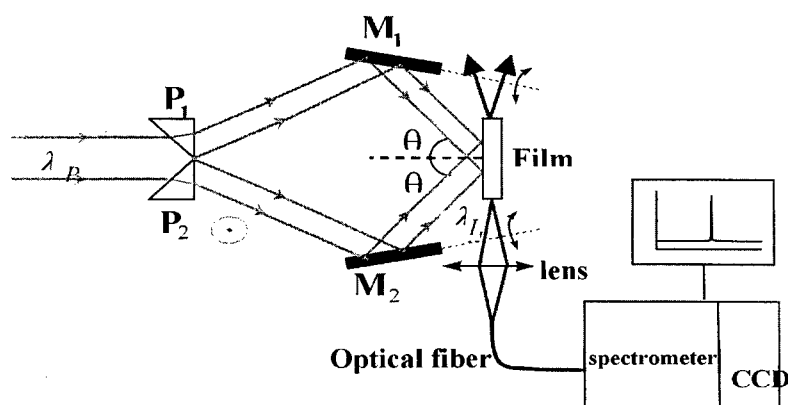


FIGURE 1 Set-up for DFB laser experiments

In this set-up, the pump beam is splitted by a system of two prisms ( $P_1$  and  $P_2$ ) and the two beams obtained interfere on the film after reflection on two co-rotating mirrors ( $M_1$  and  $M_2$ ). The interference pattern consists in an alternance of dark and white fringes, providing a sinusoidally periodical optical pumping of the medium.

We collect the emitted signal with help of a 5 cm focal length lens into an optical fiber coupled with a spectrometer. The light is then dispersed by a 12 cm focal length monochromator, using a 1200 lines/mm grating, and detected with a thermoelectrically cooled charged coupled device (CCD). Dispersion of the spectrometer is 0.15 nm per pixel.

DFB principle is the following : the periodical optical pumping generates a grating in the medium and with the presence of gain the device can then be seen as a superposition of laser microcavities with a length equal to the grating pitch, as represented in figure 2.

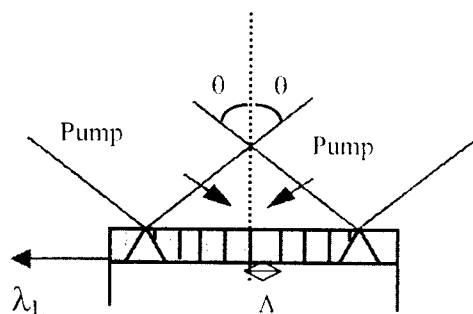


FIGURE 2 interference pattern between 2 pump beams in a luminescent polymer film. The device can be seen as a superposition of laser microcavities with a length equal to the interfringe spacing

The optical feedback, obtained by diffraction in the grating, and the gain are provided by the same absorption mechanism which makes this device be very compact

## RESULTS

The modes being able to propagate must verify the following equation :

$$\lambda_l = \frac{n\lambda_p}{m \sin \theta} \quad (1)$$

where  $\lambda_l$  is the emission wavelength,  $\lambda_p$  the pump wavelength,  $n$  the effective refraction index of the film,  $m$  the order of diffraction and  $\theta$  the incidence angle of the pump beams on the film.

This  $\theta$  dependence of the emission wavelength allows a tuneability of the laser emission simply by changing the inclination of the two co-rotating mirrors, i.e. changing the interfringes spacing.

Laser emission and tuneability was achieved in a PMMA doped Rh6G with angles  $\theta$  around  $40^\circ$  corresponding to the second order of diffraction ( $m=2$ ). Results are given in figure 3.

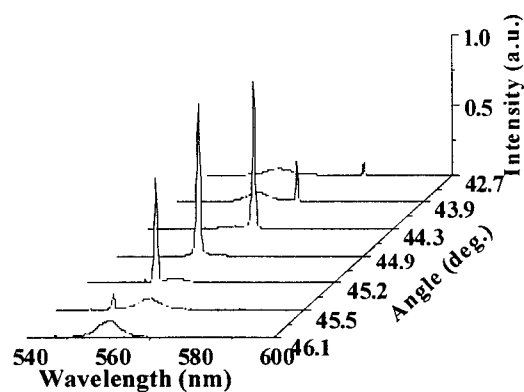


FIGURE 3 output spectrum as a function of the incidence angle  $\theta$  for DFB laser action of Rh6G in PMMA

We obtained a very narrow laser emission with a full width at half maximum equal to 2 nm. In figure 3 we have the spectral dependence of the laser emission in function of the incidence angle  $\theta$  of the pump beams onto the Rh6G film. The tuneability, limited by the spectral bandwidth of the stimulated emission spectrum, is equal to 25 nm.

## CONFINEMENT AND WAVEGUIDING

### Lateral confinement

In order to improve the lateral confinement we placed before the prisms a 30cm focal length cylindrical lens which effect is to reduce the pump beam interference surface along one direction. The pump energy is then concentrated in a narrow line of 20  $\mu\text{m}$  width, increasing then the directivity of the emission and reducing the threshold.

The effect of the pump surface onto the film is schematized in figure 4.

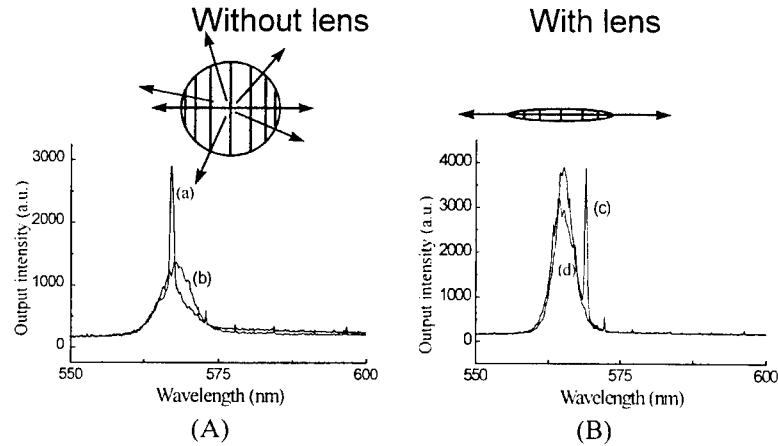


FIGURE 4 Influence of the pump beam surface on the laser threshold : (A) without lens. (B) with lens . The pump fluence are: (a) 3.8  $\mu\text{J}/\text{mm}^2$ , (b) 3.1  $\mu\text{J}/\text{mm}^2$ , (c) 1.1  $\mu\text{J}/\text{mm}^2$ , (d) 0.7  $\mu\text{J}/\text{mm}^2$

The confinement obtained is evidenced with the two spectra in figure 4 where we note the diminution of the threshold that is about  $1.1 \mu\text{J}/\text{mm}^2$  with the lens, against  $3.8 \mu\text{J}/\text{mm}^2$  without.

#### Wave guide effect

Vertical confinement in a direction perpendicular to the film plane was also studied with another laser dye : DCM.

For this purpose we consider the influence of the refractive index on the signal propagation. In this respect we have deposited two different films on glass substrates ( $n=1.5$ ) : a PVK doped DCM film ( $n=1.6$ ) and a PMMA film ( $n=1.5$ ) doped with the same dye. The PMMA index is closer to the glass index than PVK.

A similar experiment was done with two PMMA films deposited one on a glass substrate ( $n=1.5$ ) and the other one on a quartz substrate ( $n=1.45$ ).

In both cases the signal emitted is best guided in films with indices larger than the substrate index : we can see in figure 5 that laser emission is stronger by two orders of magnitudes in the PVK film on glass than in PMMA on glass, and in the same way in PMMA film on quartz than on glass.

With this experiment we find the well known result in wave guides that a good wave guide is a medium with a larger refraction index than the medium around it.

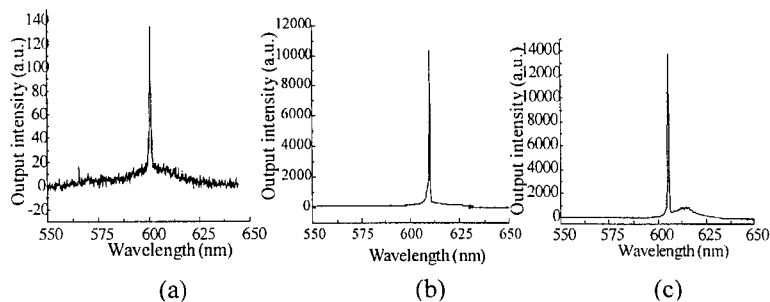


FIGURE 5 influence of the relative refractive index of film/substrate on the signal at fixed angle. (a) DCM/PMMA ( $n=1.5$ ) and (b) DCM/PVK ( $n=1.6$ ) on a glass substrate ( $n=1.5$ ), (c) DCM/PMMA on a quartz substrate ( $n=1.45$ )

The thickness effect was also evidenced in PVK doped DCM films deposited on glass substrates. We can see in figure 6 the number of laser modes increasing with the film thickness at a fixed angle from 1 at 215 nm to 3 at 1600 nm thickness.

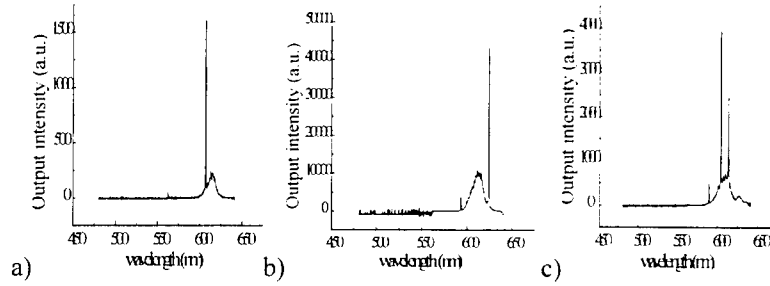


FIGURE 6 evolution of the laser emission with the film thickness  $e$ , at fixed angle.  
(a) :  $e=215$  nm. (b) :  $e=740$  nm. (c) :  $e=1600$  nm

Additionally the non periodical spectral spacing between the laser lines cannot be attributed to the free spectral range of a laser cavity. These modes correspond to modes of planar waveguides. Each mode can be tuned over a 40 nm range corresponding to the stimulated emission bandwidth of the DCM dye. This bandwidth also limits the number of modes that can be seen simultaneously.

#### PHOTONIC GAP

We have studied the signal emission dependence with the pump beam size using a Lloyd-mirror interferometer. This study was made in a



PMMA doped Rh6G film for 3 different lengths of the interference pattern onto the film (figure 7) : from 2.6 to 3.7 mm.

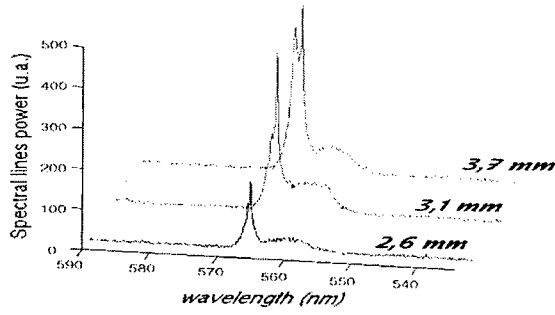


FIGURE 7 evolution (splitting) of a single laser line when grating length increases

We note the apparition of a splitting for a pump size equal to 3.7 mm. This splitting is predicted in the *coupled wave theory* and can be explain by the presence in the medium of an index grating due to a non linear effect of the third order, also called optical Kerr effect. This induces a modulation of the refractive index in the medium which can be written in the linear intensity regime (far from saturation) :

$$n = n_0 + \frac{3\chi^{(3)}}{4\varepsilon_0 n_0^2 c} I \quad (2)$$

where  $n_0$  is the mean refractive index of the film corresponding to the polymer index.

In the small gain limit the spacing between the two laser peaks, which is the width of the photonic gap, depends of the refractive index modulation :

$$\delta\lambda = \delta n \lambda_L$$

where  $\delta n$  is the amplitude of modulation of the index for second order diffraction.

We have here a good tool to determine the  $\chi^{(3)}$  induced in the film by calculating the  $\delta n$ . In this case the measured value of  $\delta\lambda$  is 2nm allowing a  $\delta n$  equal to  $4.10^{-3}$ .

The reason why this splitting isn't observed in this experiment for the two first spectra is that there is a competition between the two laser peaks, and when we increase the length of the interference pattern we also improve the coupling between the waves in the medium for a diminution of the threshold for lasing.

A similar result was obtained in PVK films doped with another well known dye, the Coumarine 515, (figure 8) deposited onto a glass substrate. Excitation was performed with 355 nm-wavelength. The film thickness was 430 nm and the incidence angle  $\theta$  was around  $33^\circ$  (diffraction in the second order).

We observe a splitting when the laser emission is near the edge of the stimulated emission band corresponding to a large enough index modulation. This effect is difficult to obtain at the gain maximum because the index modulation, real part of  $n$  in equation (2), vanishes (Kramers-Kronig relations).

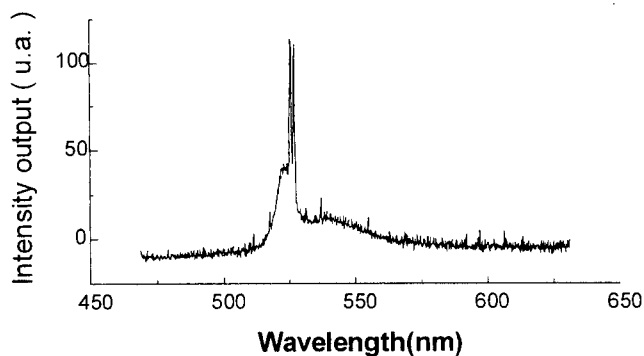


FIGURE 8 splitting of the laser peak of a PVK doped Coumarine 515 film

#### PERIODICAL PERMANENT STRUCTURES

The final step consists in the realization of permanent gratings. For this purpose we make use of an original technique of photoinduced patterning of surface relief gratings using laser controlled molecular motion. In this respect azo-dye aromatic polymers have been shown to offer interesting prospects for material engineering using light matter interaction.

Irradiation of films made of such materials leads to a migration from high to low intensity regions, following the interference pattern in the direction of the pump beam polarization. The chromophores migrate in an inchworm like motion as modelised below (figure 9). In their motion the chromophores track the whole polymer chain to which they are attached leading to modifications of the film surface.[5,6]

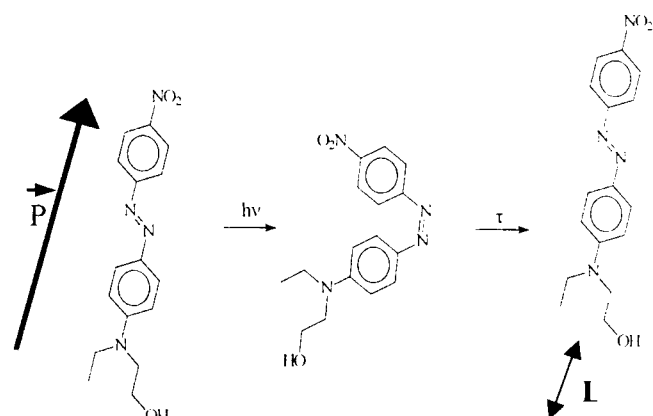


FIGURE 9 modelisation of an azo-dye molecule motion after irradiation

In typical experiments, the wavelength of the laser was chosen to be near the maximum absorption of the chromophores, typically  $\lambda = 488\text{nm}$  or  $514\text{nm}$  of an Argon laser, with intensities ranging from  $I = 50\text{-}1000\text{mW/cm}^2$ . In order to record surface-relief gratings, we made use of the now classical Lloyd mirror set-up (figure 10). The incident beam expanded from an Argon laser ( $\lambda=514\text{nm}$ ,  $I=100\text{mW/cm}^2$ ) is divided into two parts : first half is directly incident onto the sample and second half reflects onto a metallic mirror rigidly held at  $90^\circ$  to the sample. This permits to reduce side effects due to mechanical instabilities throughout the writing process (a few tens of minutes)

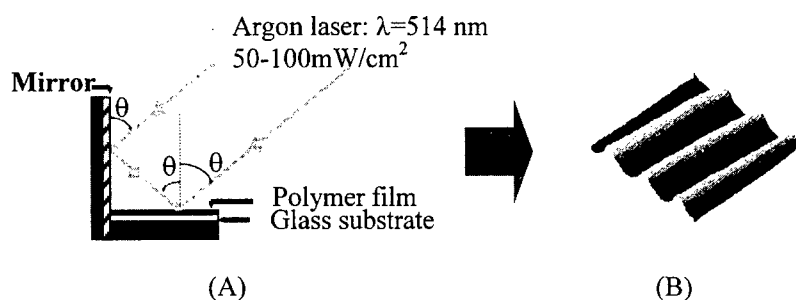


FIGURE 10 (A) Lloyd-mirror set-up used for modulation of the film. (B) picture of a surface relief grating recorded with an atomic force microscope (AFM)

Samples were spin-coated films of a yellow coloured azo-dye molecule analogous to Disperse Red 1 and attached to 35% of the monomers of a poly(methylmethacrylate) (PMMA) skeleton. Fig. 10 shows an example of a typical surface relief grating imaged with an AFM (atomic force microscope).

The grating pitch depends of the incidence angle of the pump beam onto the sample following the relation :

$$\Lambda = \frac{\lambda_{\text{laser}}}{2\sin\theta}$$

So we can choose the grating pitch with the appropriate incidence angle of the pump beams in the mirror-Lloyd setup.

The goal of the experiment was to study permanent DFB structures for transverse one-photon pumping as it is schematized in Fig. 11. In this respect, a layer of Rhodamine 6G in PMMA was deposited on top of the previously printed surface relief grating. The device was pumped with the same laser source as the one used for the above DFB

experiments. We obtained a very narrow laser peak with a full width at half maximum equal to 0.5 nm (figure 11). The tuneability was achieved with azo-dye aromatic polymer films insolated at different incidence angles, i.e. with different grating pitches.

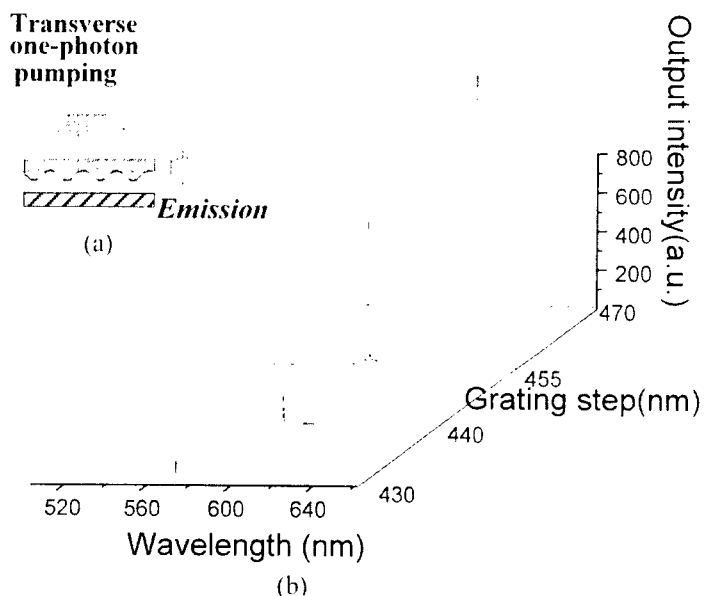


FIGURE 11 set-up for transverse one photon pumping (a), laser tuneability using different grating pitches (b)

## CONCLUSION

We have report here the development of a compact organic laser following a distributed feedback scheme. The first experiments where done with the help of well known laser dyes in order to implement and characterize the device in the case of dynamical gratings : waveguiding effects on the DFB laser emission have been studied in detail, gain and index grating features were identified.

The next step consisted in the realization of permanent gratings. Laser emission was obtained with a transverse one photon pumping scheme using a rhodamine doped film deposited onto the modulated surface of an azo-dye aromatic polymer film.

The goal of this study is the integration of such structures in opto electronic devices such as electroluminescent diodes in order to control their emission properties.

## ACKNOWLEDGMENTS

This work was partly funded by European Union ESPRIT project 28580 LUPO (A novel approach to solid state short wavelength laser generation using Luminescent Polymers).

- 
- [1] P. Rochon, E. Batalla, A. Natansohn, *Appl. Phys. Lett.*, **66**, 136 (1995).
  - [2] D.Y. Kim, L. Li, J. Kumar, S.K. Tripathy, *Appl. Phys. Lett.*, **66**, 1166 (1995).
  - [3] C. Fiorini, F. Charra, J.-M. Nunzi, P. Raimond, *J. Opt. Soc. Am. B*, **14**, 1984 (1997).
  - [4] A.-C. Etilé, C. Fiorini, F. Charra, J.-M. Nunzi, *Phys. Rev. A*, **56**, 3888 (1997).
  - [5] P. Lefin, C. Fiorini, J.-M. Nunzi, *Pure Appl. Opt.*, **7**, 71 (1997)
  - [6] C. Fiorini, N. Prudhomme, A.-C. Etilé, P. Lefin, P. Raimond, J.-M. Nunzi, *Macromol. Symposia*, **137**, 105 (1999) ; C. Fiorini, N. Prudhomme, G. de Veyrac, I. Maurin, P. Raimond, J.-M. Nunzi, to be published in *Synthetic Metals* (1999).
  - [7] N. Takada, T. Tsutsui, S. Saito, *Appl. Phys. Lett.*, **63**, 2032 (1993).

- [8] H.F. Wittmann, J. Gruner, R.H. Friend, G.W.C. Spencer, S.C. Moratti, A.B. Holmes, *Adv. Mater.*, **7**, 541 (1995).
- [9] H. Kogelnik, C.V. Shank, *Appl. Phys. Lett.*, **18**, 152 (1971).
- [10] M. Kuwata-Gonokami, R.H. Jordan, A. Dodabalapur, H.E. Katz, M.L. Schilling, R.E. Slusher, S. Ozawa, *Opt. Lett.*, **20**, 2093 (1995).
- [11] A. Schülzgen, Ch. Spiegelberg, M.M. Morell, S.B. Mendes, B. Kippelen, N. Peyghambarian, M.F. Nabor, E.A. Mash, P.M. Allemand, *Appl. Phys. Lett.*, **72**, 269 (1998).
- [12] V.G. Kozlov, G. Parthasarathy, P.E. Burrows, S.R. Forrest, Y. You, M.E. Thompson, *Appl. Phys. Lett.*, **72**, 144 (1998).
- [13] D. Fichou, S. Delysse, J.M. Nunzi, *Advanced Materials*, **9**, 1178 (1997).
- [14] D.G. Lidzey, D.D.C. Bradley, S. F. Alvarado, P. F. Seidler, *Nature*, **386**, 135 (1997).
- [15] C.V. Shank, J.E. Bjorkholm, H. Kogelnik, *Appl. Phys. Lett.*, **18**, 395 (1971).
- [16] M. Maeda, Y. Oki, K. Imamura, *IEEE J. Quant. Electr.*, **33**, 214 (1997).
- [17] G.M. Gale, P. Ranson, M. Denariez-Roberge, *Appl. Phys. B*, **44**, 221 (1987).
- [18] D.A. Gromov, K.M. Dyumaev, A.A. Manenkov, A.P. Maslyukov, G.A. Matyushin, V.S. Nechitailo, A.M. Prokhorov, *J. Opt. Soc. Am. B*, **2**, 1028 (1985).



## Waveguides of Conjugated Polymers with Large Cubic Nonlinearities

C. BUBECK<sup>\*</sup>, K. UEBERHOFEN,<sup>a</sup> J. ZIEGLER, F. FITRILAWATI,<sup>b</sup>  
U. BAIER,<sup>c</sup> H. EICHNER, C. FORMER, K. MÜLLEN, S. PFEIFFER<sup>d</sup>,  
H. TILLMANN<sup>d</sup>, and H.-H. HÖRHOLD<sup>d</sup>

*Max-Planck-Institute for Polymer Research, Ackermannweg 10, 55128  
Mainz, Germany*

<sup>a</sup>*Present address: Debis Systemhaus GEI, Goebelstr. 1-3, 64293  
Darmstadt, Germany*

<sup>b</sup>*Present address: Dept. of Physics, Institut Teknologi Bandung,  
Bandung 40132, Indonesia*

<sup>c</sup>*Present address: Nicolet Instrument, Senefelderstr. 162, 63069  
Offenbach, Germany*

<sup>d</sup>*Inst. for Organic and Macromolecular Chemistry, Friedrich-Schiller-  
Univ. Jena, 07743 Jena, Germany*

<sup>\*</sup> *Corresponding author*

**ABSTRACT.** Poly(p-phenylenevinylene) (PPV), its oligomers, several soluble derivatives and the polydiacetylene P4-BCMU were spin-cast on fused silica substrates. We obtained slab waveguides of substituted PPVs with attenuation losses < 1 dB/cm at 1064 nm. Third-harmonic generation spectroscopy was applied to measure  $\chi^{(3)}$ . The comparison of  $\chi^{(3)}$  of polymers with oligomers yields effective conjugation lengths of PPV derivatives. Intensity dependent prism coupling of waveguides is used to evaluate the dispersion of nonlinear refractive index  $n_2$  and nonlinear absorption coefficient  $\alpha_2$ . We observe onsets for two-photon absorptions in unsubstituted PPV at  $\lambda < 950$  nm and in P4-BCMU at  $\lambda < 1300$  nm. We conclude from their figures of merit that PPVs show better promise for all-optical switching than polydiacetylenes.

**Keywords:** PPV; P4-BCMU; waveguide; third-harmonic generation; prism coupling; two-photon absorption

## 1. INTRODUCTION

The delocalized one-dimensional  $\pi$ -electron system of conjugated polymers has raised much interest over many years. The technological application of conjugated polymers generally requires that they can be processed to thin films with high structural and optical quality. Aim of our investigations is to find materials that fulfill the application requirements for all-optical signal processing. Materials with sufficiently large cubic optical nonlinearities allow switching of light by light by means of the intensity dependence of refractive index  $n = n_0 + n_2 I$  or absorption coefficient  $\alpha = \alpha_0 + \alpha_2 I$ , respectively. The nonlinear optical coefficients  $n_2$  and  $\alpha_2$  are given by [1]

$$n_2(\omega) = \frac{3}{4} \frac{1}{n_0^2 c \epsilon_0} \text{Re}[\chi^{(3)}(-\omega; \omega, -\omega, \omega)], \quad (1)$$

$$\alpha_2(\omega) = \frac{3\omega}{2n_0^2 c^2 \epsilon_0} \text{Im}[\chi^{(3)}(-\omega; \omega, -\omega, \omega)]. \quad (2)$$

$\chi^{(3)}(-\omega; \omega, -\omega, \omega)$  denotes complex third-order susceptibility,  $\omega$  frequency,  $c$  velocity of light, and  $\epsilon_0$  permittivity of free space. Figures of merit have been introduced to judge the application potential of materials for all-optical signal processing [2,3]. Additional conditions are: The materials must be processible to planar waveguides to realize integrated optics configurations. Typical required numbers are: Waveguide losses  $\alpha_{\text{gw}} < 1 \text{ dB/cm}$ , damage threshold intensity  $I_{\text{dt}} > 100 \text{ MW/cm}^2$  and response times for the refractive index changes  $< 1 \text{ ps}$ .

The search for appropriate materials profits from a detailed study of the relations between chemical structure and third-order nonlinear optical properties [4-7]. In earlier investigations it has turned out that poly(p-phenylenevinylene) (PPV) and its derivatives are a particularly promising group of conjugated polymers as they possess good film forming properties and high third-order nonlinearity [5,8-16].

We shall describe linear optical properties of thin films, third-harmonic generation of PPV, its oligomers and several of its soluble derivatives. Cubic nonlinearities and figures of merit will be derived. We have shown recently how nonlinear prism coupling can be used to obtain the signs and magnitudes of  $n_2$  and  $\alpha_2$  of PPV [16]. We apply

this method for the investigation of the polydiacetylene P4-BCMU in order to determine its  $n_2$ - and  $\alpha_2$ -spectra in the near infrared.

## 2. FILM PREPARATION AND LINEAR OPTICAL CONSTANTS

The synthesis of the compounds shown in Fig. 1 has been referred to in earlier reports: PPV and OPV<sub>n</sub> [5], DPOP-PPV [14], MEH-PPV [17], DA-PPV [18], CNE-PPV [19] and P4-BCMU [20,21]. Thin films were prepared by spin-coating using different solvents, temperatures, concentrations and spinning speeds. Thickness  $d$  and surface roughness  $R_a$  were measured by surface profilometry and optimized by variation of the preparation parameters.

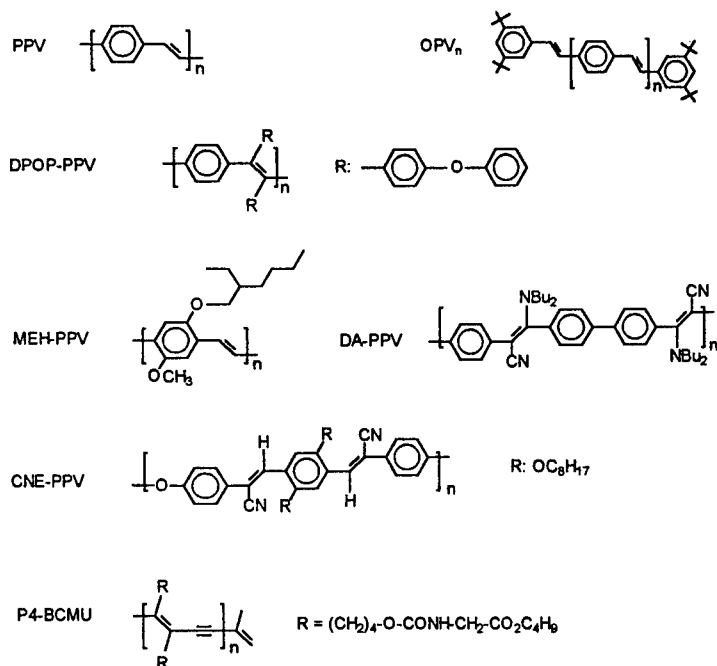


FIGURE 1 Chemical structures and abbreviated names of PPV, its derivatives and the polydiacetylene P4-BCMU.

The experimental setups for prism coupling and waveguide loss determination were described previously [16,22]. The laser beam enters the prism at an incidence angle  $\theta$ . It is totally reflected at the prism base. Its evanescent field can extend across the air gap between prism and film and is able to excite a waveguide mode which is possible at discrete coupling angles  $\theta_m$ , where  $m = 0, 1, 2, \dots$  describes the mode number. Consequently, the reflected intensity  $I_R$  has relative minima at  $\theta_m$  because of absorption and scattering losses in the film. The angles  $\theta_m$  can be used to evaluate  $n_0$  of the film following well-known procedures [23]. A half-cut prism is used to generate a free propagating waveguide mode. Its straylight is imaged onto a diode array to determine the attenuation loss of the waveguide  $\alpha_{gw}$  [22].

The waveguide losses  $\alpha_{gw}$  depend mainly on intrinsic absorption  $\alpha_0$  and additional scattering losses in the bulk and at the interfaces of the films. The surface scattering is related to the surface roughness  $R_s$ , which can be minimized by careful optimization of the preparation parameters [24]. Unsubstituted PPV has rather large losses in the order of 80 dB/cm at  $\lambda = 647$  nm because of its well-known polycrystalline morphology [16]. Appropriate synthesis of substituted PPVs can yield highly pure materials, e.g. MEH-PPV [17], that can be processed to waveguides with extremely low losses. We succeeded to prepare waveguides of MEH-PPV which had only  $\alpha_{gw} = 0.5$  dB/cm at  $\lambda = 1064$  nm [25]. The data of other polymers are shown in Chapter 4.

Transmission and reflection spectra of ultrathin films (typically  $d = 50$  nm) on fused silica substrates were measured with a spectrophotometer in the UV-VIS-NIR range. The reflection spectra at nearly perpendicular incidence and TE polarization were used to calculate the dispersion of  $n_0$  of the films by solving the Fresnel equations by an iteration procedure without any fit parameter as described earlier [5]. The dispersion of  $n_0$  agrees very well with the data from prism coupling [16]. The intrinsic absorption coefficient  $\alpha_0$  of the films is obtained from the transmission spectrum after subtraction of reflection losses at the film/air and film/substrate interfaces [5]. This procedure shows that apparent tails towards longer wavelengths of the main absorption bands of ultrathin films are caused by reflection losses.

The photostability of  $\pi$ -conjugated materials is always a matter of concern. Light in the wavelength range of the main absorption bands and sample handling at ambient air may cause photo-oxidation as indicated by carbonyl-bands in the IR-spectrum and by hypsochromic shifts and a decrease of the main absorption band [26]. Appropriate

sealing of the samples from UV-VIS light solves this problem. Nonlinear optics applications require large damage thresholds at NIR wavelengths. We have measured the damage threshold intensity  $I_{dt}$  of PPVs at 1064 nm (pulse duration 35 ps). PPV films at ambient air were exposed to series of 1000 pulses of subsequently increased peak intensities. The UV-VIS absorption spectra were measured before and after the laser irradiation. Up to  $I = I_{dt}$  no changes in the spectra were observed. At  $I > I_{dt}$ , however, the maximum of absorbance was reduced but the shape of the absorption spectrum did not change. Scanning the step profiler over the irradiated area clearly showed that the damage was caused by photoablation. We found  $I_{dt} = 5.8 \text{ GW/cm}^2$  for PPV [16] and  $I_{dt} > 12 \text{ GW/cm}^2$  for MEH-PPV [25]. These damage thresholds should be sufficient for device applications.

### 3. THG-SPECTROSCOPY

THG investigations of thin films on fused silica substrates were performed by using the Maker fringe technique and picosecond laser pulses with variable laser wavelengths  $\lambda_L$  from an optical parametric generator/amplifier configuration as described earlier [5]. Evaluations of  $\chi^{(3)}(-3\omega; \omega, \omega, \omega)$  of the polymer films were made relative to fused silica with a reference value  $\chi^{(3)}(-3\omega; \omega, \omega, \omega) = 3.11 \cdot 10^{-14} \text{ esu}$ . The comparison of materials is complicated by the three-photon resonance that occurs if laser wavelength  $\lambda_L = 3\lambda_{\text{max}}$  where  $\lambda_{\text{max}}$  denotes the wavelength of the absorption maximum.  $\chi^{(3)}(-3\omega; \omega, \omega, \omega)$  is imaginary at the three-photon resonance and the modulus of  $\chi^{(3)}(-3\omega; \omega, \omega, \omega)$  has its maximum value  $\chi^{(3)}_{\text{res}}$ . It is typically 3-5 times larger than the off-resonant data. It is rather difficult to obtain really non-resonant data with THG. Therefore we use the wavelength  $\lambda_0$  of the absorption edge that can be found by linear extrapolation of the absorption spectrum to the baseline. At  $\lambda_L = 3\lambda_0$  we obtain  $\chi^{(3)}_0$  and consider this also as a representative value for materials comparison.

Shorter oligomers  $\text{OPV}_n$  were dispersed in polystyrene (PS) using concentrations of 3-5 % by weight in order to obtain films with improved stability. The absorption coefficient  $\alpha_{\text{max}}$  at the maximum of the absorption band (at  $\lambda_{\text{max}}$ ) depends on the number of chromophores per unit volume. The data are shown in Tab. 1 and Fig. 2 to visualize structure-property relations.

TABLE 1 Linear and nonlinear optical data of thin films.

Compound	$\lambda_{\max}$ [nm]	$\alpha_{\max}$ [cm <sup>-1</sup> ]	$\chi_{\text{res}}^{(3)}(-3\omega;\omega,\omega,\omega)$ [esu]
OPV <sub>1</sub> in PS	361	$1.2 \cdot 10^4$	$(5.9 \pm 1.0) \cdot 10^{-13}$
OPV <sub>2</sub> in PS	386	$1.9 \cdot 10^4$	$(1.5 \pm 0.2) \cdot 10^{-12}$
OPV <sub>3</sub> in PS	403	$1.8 \cdot 10^4$	$(2.4 \pm 0.2) \cdot 10^{-12}$
OPV <sub>3</sub>	383	$2.0 \cdot 10^5$	$(1.6 \pm 0.3) \cdot 10^{-11}$
OPV <sub>4</sub> in PS	406	$1.6 \cdot 10^4$	$(2.0 \pm 0.4) \cdot 10^{-12}$
OPV <sub>4</sub>	394	$2.1 \cdot 10^5$	$(2.0 \pm 0.3) \cdot 10^{-11}$
OPV <sub>5</sub>	406	$2.4 \cdot 10^5$	$(4.0 \pm 0.5) \cdot 10^{-11}$
PPV	458	$3.4 \cdot 10^5$	$(1.6 \pm 0.2) \cdot 10^{-10}$
DPOP-PPV	359	$5.4 \cdot 10^4$	$(1.8 \pm 0.2) \cdot 10^{-12}$
DA-PPV	412	$6.2 \cdot 10^4$	$(3.1 \pm 0.1) \cdot 10^{-12}$
CNE-PPV	447	$1.1 \cdot 10^5$	$(6.2 \pm 0.2) \cdot 10^{-12}$
MEH-PPV	477	$1.5 \cdot 10^5$	$(2.1 \pm 0.2) \cdot 10^{-11}$

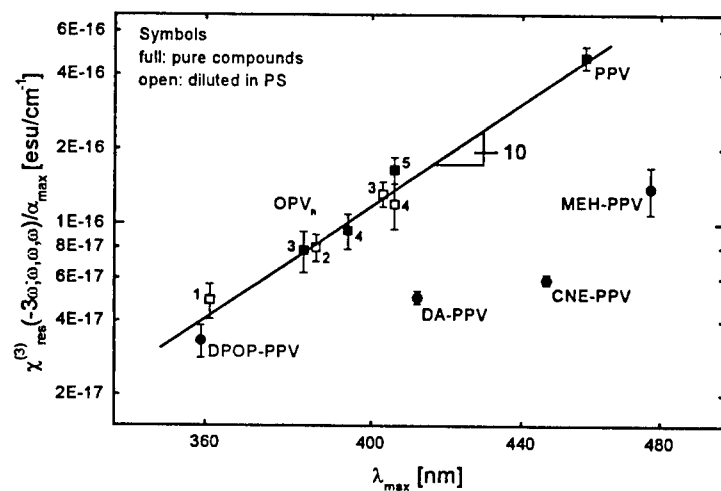


FIGURE 2 Masterplot of conjugated polymers and oligomers in a double logarithmic scale.

The data of OPV<sub>n</sub> and PPV are in good agreement with the scaling relationship [5]

$$\chi^{(3)}_{\text{res}}(-3\omega; \omega, \omega, \omega) / \alpha_{\text{max}} \sim (\lambda_{\text{max}})^{10}. \quad (3)$$

As we have pointed out already [5], relation (3) is valid only for oligomers and polymers with identical repeat units or systems that have a similar dependence of  $\lambda_{\text{max}}$  on the system size. Fig. 2 clearly shows that the substituted polymers DA-PPV, CNE-PPV and MEH-PPV deviate significantly from the scaling relation (3). This can be interpreted with the fact that substitutions with oxygen, alkoxy groups, or donor/acceptor groups lead to strong red-shifts of  $\lambda_{\text{max}}$ . This reduction of the HOMO-LUMO energy gap has been observed in similar polymers [27]. We conclude that the substitutions of DPOP-PPV, DA-PPV, CNE-PPV and MEH-PPV obviously do not lead to improvements of  $\chi^{(3)}(-3\omega; \omega, \omega, \omega)$ .

The  $\chi^{(3)}/\alpha_{\text{max}}$  data of DA-PPV and CNE-PPV are quite similar to the data of OPV<sub>1</sub>. This result indicates that the effective conjugation length (ECL) of DA-PPV and CNE-PPV is similar to the size of OPV<sub>1</sub>. For definition of ECL see Ref. [7]. Inspection of Fig. 1 shows that the repeat units of DA-PPV and CNE-PPV consist of 3 phenyl rings and 2 vinylene units. This is nearly the identical physical length as OPV<sub>1</sub>. We conclude that the  $\pi$ -electron delocalization is mainly limited by oxygen in the main chain of CNE-PPV and by steric constraints in the cases of DA-PPV and DPOP-PPV, which leads to nonplanar backbone conformations. By similar comparison with OPV<sub>n</sub> we conclude that ECL of MEH-PPV corresponds to approximately 4-5 repeat units.

These results indicate that THG-spectroscopy can be used to evaluate ECL of conjugated polymers by comparison with oligomers of precisely known size.

#### 4. FIGURE OF MERIT

The application potential of materials for all-optical waveguide switching can be estimated by figures of merit [2,3,28]. If the linear losses  $\alpha_0$  are much larger than the nonlinear losses (e.g. by two-photon absorption) the figure of merit  $W$  is used:

$$W = \frac{n_2 I}{2\alpha_0 \lambda}. \quad (4)$$

For the opposite case i.e. if  $\alpha_0 \ll \alpha_2 I$ , the figure of merit  $T$  applies:

$$T = \frac{2\alpha_2 \lambda}{n_2}. \quad (5)$$

Materials have to surpass the conditions  $W > 1$  and  $T < 1$  significantly in order to be good candidates for all-optical switching devices.

We use our data of  $\chi^{(3)}_0(-3\omega; \omega, \omega, \omega)$  and the measured total waveguide losses  $\alpha_{\text{gw}}$  to estimate  $W$ . We apply the conversion formula from esu- to SI-units [1]

$$n_2 [\text{cm}^2/\text{W}] = 0.039 n_0^{-2} \chi^{(3)}(-\omega; \omega, -\omega, \omega) [\text{esu}] \quad (6)$$

and the approximation  $\chi^{(3)}(-\omega; \omega, -\omega, \omega) \approx \chi^{(3)}_0(-3\omega; \omega, \omega, \omega)$ . The results are shown in Tab. 2. MEH-PPV has  $W = 10$  and appears to be one of the most promising conjugated polymers for all-optical waveguide switching. We will see below that the figure of merit  $T$  looks also more promising for PPVs as compared to polydiacetylenes.

The origin of  $\chi^{(3)}(-3\omega; \omega, \omega, \omega)$  is a pure electronic and not a thermal process. It would be still highly desirable to obtain  $n_2$ - and  $\alpha_2$ -data from intensity dependent refractive index measurements. But only few experimental investigations exist presently, see e.g. Refs. [12-16].

TABLE 2 Linear and nonlinear optical data of conjugated polymers used to estimate the figure of merit  $W$ . (a)  $\alpha_{\text{gw}}$  refers to total loss of  $\text{TE}_0$  mode at 1064 nm; (b) measured at  $\lambda_L = 3\lambda_0$  with THG; (c) evaluated for  $\lambda = 1064$  nm and  $I = 1$  GW/cm<sup>2</sup>; (d) estimate from 3 cm visible laser strike; (e) data from [29].

Polymer	$\lambda_0$ [nm]	$\alpha_{\text{gw}}^{(a)}$ [dB/cm]	$\chi^{(3)}_0(-3\omega)^{(b)}$ [esu]	$n_2$ [cm <sup>2</sup> /W]	$W^{(c)}$
PPV	521	40	$2.0 \cdot 10^{-11}$	$3.0 \cdot 10^{-13}$	0.15
DPOP-PPV	447	0.6	$1.5 \cdot 10^{-12}$	$2.1 \cdot 10^{-14}$	0.7
DA-PPV	502	6.3	$2.0 \cdot 10^{-12}$	$3.0 \cdot 10^{-14}$	0.1
CNE-PPV	514	0.4	$5.5 \cdot 10^{-12}$	$7.6 \cdot 10^{-14}$	4
MEH-PPV	570	0.5	$1.7 \cdot 10^{-11}$	$2.4 \cdot 10^{-13}$	10
P4-BCMU	585	$9^{(d)}$	$3 \cdot 10^{-11} \text{ (e)}$	$4.6 \cdot 10^{-13}$	1



### 5. NONLINEAR PRISM COUPLING

We have shown recently how intensity dependent prism coupling of thin film waveguides can be used to obtain the signs and absolute values of  $n_2$  and  $\alpha_2$  [16]. Our investigations of unsubstituted PPV reveal maxima of  $\alpha_2$  that fit perfectly to the two-photon fluorescence excitation spectrum of Baker et al [30]. We observe an onset for two-photon absorption (TPA) in PPV at  $\lambda_L < 950$  nm which is in good agreement with reports of TPA energy levels located well above the one-photon transitions [31,32].

We have also studied waveguides of P4-BCMU using picosecond laser pulses in the range  $700 \text{ nm} < \lambda_L < 1600 \text{ nm}$ . The evaluation procedure was simplified by the approximation of a constant air gap thickness of 50 nm between prism and film which represents the so-called overcoupled situation. Therefore, we can specify  $\alpha_2$  in arbitrary units only. The results are shown in Fig. 3.

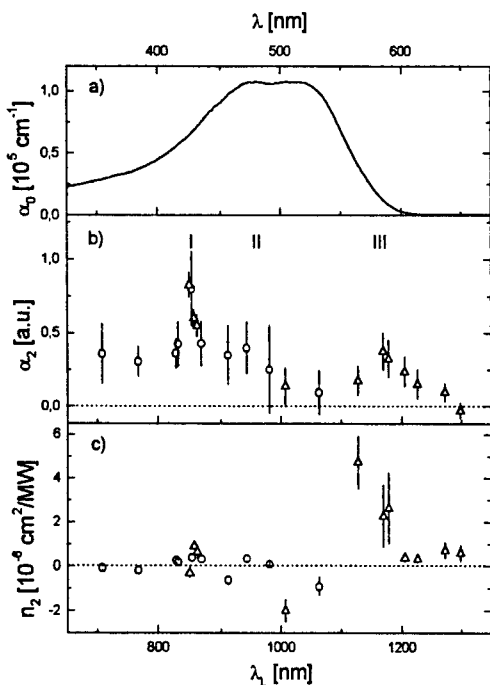


FIGURE 3 Linear and nonlinear spectra of P4-BCMU on fused silica ( $d = 950 \text{ nm}$ ). The  $\lambda$  scale of (a) is expanded by factor 2 as compared to (b) and (c) to visualize the spectral positions of TPA levels with respect to one-photon transitions.

The TPA spectrum (Fig. 3b) has two distinct maxima (I at  $\lambda_L = 850$  nm, III at  $\lambda_L = 1170$  nm) which are in good agreement with earlier results of Torruellas *et al* [33]. The less pronounced shoulder II at  $\lambda_L = 940$  nm was not observed before. The spectrum of  $n_2$  shows the typical dispersive behaviour at resonance I that we have described by model calculations recently [16]. Several changes of the sign of  $n_2$  exist in Fig. 3c. They indicate additional spectral features that have not been assigned yet. The onset for TPA in P4-BCMU occurs at  $\lambda_L < 1300$  nm which shows that TPA energy levels exist in P4-BCMU even below the one-photon transitions.

## 6. SUMMARY AND CONCLUSIONS

We have obtained waveguides of several soluble PPV-derivatives with losses  $< 1$  dB/cm. THG spectroscopy can be used to evaluate the effective conjugation lengths of conjugated polymers by comparison with oligomers. Our figures of merit  $W$  for several PPV derivatives and P4-BCMU and the observed onsets for TPA indicate that several PPVs show much better promise for all-optical waveguide switching than the polydiacetylene P4-BCMU.

## ACKNOWLEDGEMENTS

We thank Dr. K. Harre for the supply of P4-BCMU, Dr. K. Koynov for helpful discussions, A. Best, G. Herrmann, W. Scholdei and L. Horbach for technical support. Financial support was given in part by Volkswagen Foundation, by BMBF of Germany (grant 03N1021B7, OPTIMAS project), and by German Academic Exchange Service (DAAD) for a grant to F. F.

## REFERENCES

- [1] P. N. Butcher and D. Cotter, *The Elements of Nonlinear Optics* (Cambridge Univ. Press, Cambridge, 1990).
- [2] G.I. Stegeman and R.H. Stolen, *J. Opt. Soc. Am. B* **6**, 652 (1989).
- [3] J.L. Brédas, C. Adant, P. Tackx, A. Persoons, and B.M. Pierce, *Chem. Rev.* **94**, 243 (1994).
- [4] C. Bubeck, *Nonlinear Optics* **10**, 13 (1995).

- [5] A. Mathy, K. Ueberhofen, R. Schenk, H. Gregorius, R. Garay, K. Müllen, and C. Bubeck, *Phys. Rev. B* **53**, 4367 (1996).
- [6] C. Bubeck, in F. Kajzar and J.D. Swalen (Eds.): *Organic Thin Films for Waveguiding Nonlinear Optics*, *Advances in Nonlin. Opt.* Vol. 3, Gordon & Breach Sci. Publ., 1996, p. 137.
- [7] C. Bubeck, in G. Wegner, K. Müllen (Eds.): *Electronic Materials - The Oligomer Approach*, VCH Weinheim, 1998, p. 449.
- [8] T. Kaino, K.-I. Kubodera, S. Tomaru, and T. Kurihara, *Electron. Lett.* **23**, 1095 (1987).
- [9] B. P. Singh, P. N. Prasad, and F. E. Karasz, *Polymer* **29**, 1940 (1988).
- [10] C. Bubeck, A. Kaltbeitzel, R.W. Lenz, D. Neher J.D. Stenger-Smith, and G. Wegner, in J. Messier, F. Kajzar, P. Prasad, D. Ulrich (Eds.): *Nonlinear Optical Effects in Organic Polymers*, NATO ASI Series E **162**, Kluwer Acad. Publ., Dordrecht, 143 (1989).
- [11] D. D. C. Bradley and Y. Mori, *Jpn. J. Appl. Phys.* **28**, 174 (1989).
- [12] U. Bartuch, A. Bräuer, P. Dannberg, H.-H. Hörhold, and D. Raabe, *Int. J. Optoelectronics* **7**, 275 (1992).
- [13] A. Samoc, M. Samoc, M. Woodruff, and B. Luther-Davies, *Opt. Lett.* **20**, 1241 (1995).
- [14] T. Gabler, R. Waldhäusl, A. Bräuer, U. Bartuch, R. Stockmann, and H.-H. Hörhold, *Optics Commun.* **137**, 31 (1997).
- [15] T. Gabler, A. Bräuer, R. Waldhäusl, U. Bartuch, H.-H. Hörhold, and F. Michelotti, *Pure & Appl. Optics* **7**, 159 (1998).
- [16] K. Ueberhofen, A. Deutesfeld, K. Koynov, and C. Bubeck, *J. Opt. Soc. Am. B* **16**, 1921 (1999).
- [17] S. Pfeiffer and H.-H. Hörhold, *Macromol. Chem. Phys.* **200**, 1870 (1999).
- [18] G. Klärner, C. Former, K. Martin, J. Räder, and K. Müllen, *Macromol.* **31**, 3571 (1998).
- [19] H. Tillmann and H.-H. Hörhold, *Synth. Met.* **101**, 138 (1999).
- [20] K. Harre, Diploma Thesis, Mainz, 1993.
- [21] K. Ueberhofen, PhD Thesis, Mainz, 1996.
- [22] A. Mathy, H.U. Simmrock, and C. Bubeck, *J. Phys. D: Appl. Phys.* **24**, 1003 (1991).
- [23] R. Ulrich and R. Torge, *Appl. Opt.* **12**, 2901 (1973).
- [24] F. Fitrilawati, M.O. Tjia, J. Ziegler, and C. Bubeck, *Proc. SPIE* **3896**, 697 (1999).

- [25] F. Fitrilawati, H. Eichner, S. Pfeiffer, H.-H. Hörhold, and C. Bubeck, to be published.
- [26] L. J. Rothberg, M. Yan, F. Papadimitrakopoulos, M. E. Galvin, E.W. Kwock, and T. M. Miller, *Synth. Met.* **80**, 41 (1996).
- [27] H.A. Reisch and U. Scherf, *Macromol. Chem. Phys.* **200**, 552 (1999).
- [28] G.I. Stegeman, *SPIE* **1852**, 75 (1993).
- [29] M. Cha, W. Torruellas, G.I. Stegeman, H.X. Wang, A. Takahashi, and S. Mukamel, *Chem. Phys. Lett.* **228**, 73 (1994).
- [30] C. J. Baker, O. M. Gelsen, and D. D. C. Bradley, *Chem. Phys. Lett.* **201**, 127 (1993).
- [31] U. Lemmer, R. Fischer, J. Feldmann, R. F. Mahrt, J. Yang, A. Greiner, H. Bässler, E. O. Göbel, H. Heesel, and H. Kurz, *Chem. Phys. Lett.* **203**, 28-32 (1993).
- [32] Z. G. Soos, S. Etemad, D. S. Galvao, and S. Ramasesha, *Chem. Phys. Lett.* **194**, 341-346 (1992).
- [33] W.E. Torruellas, K.B. Rochford, R. Zanon, S. Aramaki, and G.I. Stegeman, *Opt. Commun.* **82**, 94 (1991).

## Molecular Chirality as a Tool for Second-order Nonlinear Optics

S. VAN ELSHOCHT<sup>a</sup>, T. VERBIEST<sup>a</sup>, T.J. KATZ<sup>b</sup>, C. NUCKOLLS<sup>c</sup>, B. BUSSON<sup>d</sup>, M. KAURANEN<sup>e</sup>, AND A. PERSOONS<sup>a</sup>

<sup>a</sup>University of Leuven, Laboratory of Chemical and Biological Dynamics, Celestijnenlaan 200 D, B-3001 Heverlee, Belgium ; <sup>b</sup>Department of Chemistry, Columbia University, New York, NY 10027, USA ; <sup>c</sup> The Skaggs Institute for Chemical Biology and the Department of Chemistry, The Scripps Research Institute, La Jolla, CA 92037 ; <sup>d</sup>Laboratoire LURE, Batiment 209 D, Centre Universitaire Paris-Sud, B.P. 34, 91898 Orsay Cedex, France ; <sup>e</sup>Tampere University of Technology, Institute of Physics, P.O. Box 692, FIN-33101 Tampere, Finland

We have analysed the second-order susceptibility tensor of Langmuir-Blodgett films of a chiral helicenebisquinone. The tensor components associated with chirality dominate the nonlinear response. We have also demonstrated quasi-phase-matched frequency conversion in a structure comprised of alternating stacks of the enantiomers

**Keywords** second-harmonic generation; Langmuir-Blodgett films

## INTRODUCTION

A necessary requirement for second-order nonlinear optical phenomena to occur is the strict absence of centrosymmetry on a molecular and

macroscopic level. On a molecular level, noncentrosymmetry is usually achieved by connecting strong electron donors and acceptors by a  $\pi$ -conjugated bridge, yielding strongly dipolar molecules. The macroscopic centrosymmetry, on the other hand, is usually artificially broken by techniques such as aligning molecular dipoles in an external electric field (poling) or by depositing Langmuir-Blodgett films or self-assembled films. All these techniques result in polar order, the net alignment of molecular dipoles along an axis, the polar axis of the material. Such materials are often unstable, and their nonlinear response therefore decreases with time [1].

However, polar order is not required for a material to be noncentrosymmetric. Chiral molecules and materials comprised of enantiomerically pure chiral molecules are inherently noncentrosymmetric. Accordingly, they give rise to second-order nonlinear optical effects even in the absence of polar order. In fact frequency mixing in isotropic solutions of chiral sugar molecules has been observed experimentally and it has been shown that the electro-optic effect could be allowed in isotropic chiral media [2,3]. Furthermore, the nonlinear optical coefficients associated with chirality can be quite large [4].

Not only noncentrosymmetry is important in the field of second-order nonlinear optics. For frequency conversion, the nonlinear interaction must be phase-matched, *i.e.* the nonlinear source polarization and the generated field must propagate through the medium in phase. Perfect phase-matching can be achieved in birefringent materials, relying

on the fact that their refractive indices depend on the polarizations of the interacting fields. However, several problems are associated with perfect phase-matching and one often uses an alternative known as quasi-phase-matching. Here, the signs of the nonlinearity are reversed after each coherence length which restores the phase relation between the source and the generated field, allowing the nonlinear signal to grow quasi continuously. In polar materials, quasi-phase-matching can be achieved by periodic poling which leads to a material in which the polar axis is reversed after each coherence length. Chiral molecules provide a very interesting alternative to periodic poling. The nonlinear coefficients related to chirality are opposite in sign for both enantiomers. Therefore, quasi-phase-matched frequency conversion is possible in structures composed of alternating stacks of enantiomers [5].

In this paper, we present a complete analysis of the second-order susceptibility tensor of Langmuir-Blodgett films of a chiral helicenebisquinone. We show that the chiral tensor components dominate the nonlinear response and use the material to demonstrate the concept of quasi-phase matching.

## EXPERIMENTS AND DISCUSSION

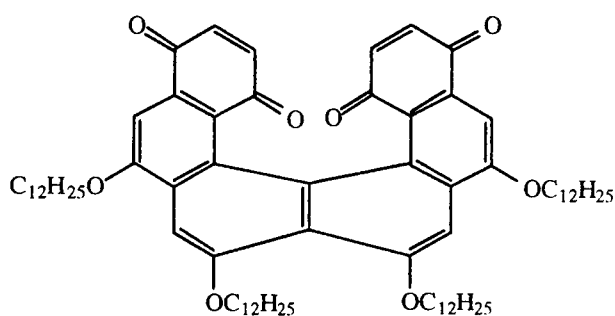


FIGURE 1 Chemical structure of the helicenebisquinone

In our experiments, we have investigated Langmuir-Blodgett films of the chiral helicenebisquinone shown in Fig. 1. Such films have unique second-order nonlinear optical properties. In the Langmuir-Blodgett films, the material forms supramolecular aggregates that enhance the nonlinear response of the enantiomerically pure material significantly compared to the racemic material [6]. Recently, the second-order susceptibility of a horizontally dipped Langmuir-Blodgett film of the nonracemic material has been completely characterized [7]. Here, we present a complete analysis of the susceptibility tensor of a vertically-dipped Langmuir-Blodgett film of the nonracemic material.

We constructed 30 layer thick LB-films by spreading a dilute chloroform solution of nonracemic helicenebisquinone onto the water



subphase of a Langmuir-Blodgett trough, followed by vertical deposition onto hydrophobic glass (treated with octadecyltrichlorosilane) slides. The deposition was Y-type and the deposition ratio was approximately 1 which is an indication of a good transfer of single monolayers from the water subphase onto the substrate.

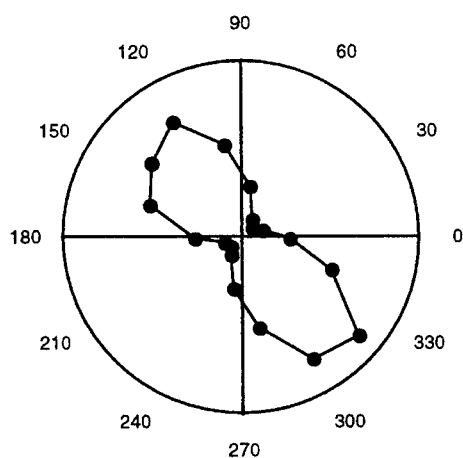


FIGURE 2 Second-harmonic generation intensity (in arb. units) as a function of the azimuthal rotation angle.

LB-films were studied with second harmonic generation (SHG). A Nd:YAG laser (1064 nm, 50 Hz, 8 ns) was used to irradiate the samples and the generated light at 532 nm was detected. First, the macroscopic symmetry of the LB-films was determined by detecting the

second harmonic signal while rotating the sample around the surface normal. The recorded pattern (Fig. 2) for a p-polarized fundamental and a s-polarized second-harmonic suggests a two-fold symmetry. Hence, our analysis of the second-order susceptibility tensor will be based on the assumption of a  $C_2$ -symmetry.

To determine the components of the susceptibility tensor, we used the polarization technique of [7]. For samples with a  $C_2$  symmetry it is convenient to define combinations of susceptibility components that are invariant under rotation around the two-fold axis. For a  $C_2$  symmetry, these combinations are  $\chi_{zzz}$ ,  $\chi_{xxz} + \chi_{zxy}$ ,  $\chi_{xxz} + \chi_{yyz}$  and  $\chi_{xyz} - \chi_{yxz}$ . Important is that the last combination is uniquely associated with chirality.

rotational invariant (represented by its Cartesian indices)	relative magnitude
xyz - yxz	1
xxz + yyz	0.05
zxx + zyy	0.03
zzz	0.05

TABLE 1 Relative magnitudes of the rotationally invariant combinations of susceptibility components of a 30-layer Y-type Langmuir-Blodgett film. All values were referenced to the xyz - yxz combination.

The values for these combinations are listed in Table 1. It is clear from Table 1 that the combination  $\chi_{xyz} - \chi_{yxz}$  is dominant and that the other susceptibility components can be considered negligible. This is not surprising since the Y-type structure of the Langmuir-Blodgett films is expected to cancel all achiral susceptibility components and only coefficients related to chirality are nonvanishing. Therefore, the actual symmetry of the sample will be close to  $D_2$ .

In chiral materials, the tensor components associated with chirality change sign between the enantiomers, whereas the achiral components maintain their sign. Therefore, structures consisting of alternating layers of the two enantiomers can provide a new approach to sign inversion requirements for quasi-phase-matching. To illustrate this effect, we prepared films whose units were four layers of a single enantiomer, either (P)-(+)- or the (M)-(-). The films were composed of maximum 32 layers comprised of eight identical (P/P/P...) or alternating (P/M/P...) units. Second-harmonic light emanating from the samples was detected in transmission. Since the coherence length in this case is much smaller than the thickness of the samples, the nonlinear response of each unit can be added. Because of the chirality of the helicene, the second-harmonic response of the P/P/P... samples should increase quadratically with the number of layers, while the P/M/P... structures should exhibit no SHG when the number of P units is equal to the number of M units. This was experimentally observed and is shown in Fig. 3.

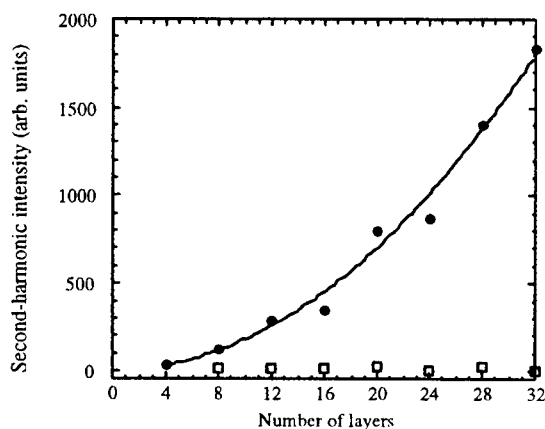


FIGURE 3 Second-harmonic intensity of the LB films as a function of the number of layers: P/M/P/... structures (open squares) and P/P/P/... (filled dots). The solid line is a quadratic fit of the data points for the P/P/P/... structures.

The first evidence of a quasi-phase matching effect was obtained by studying a set of samples consisting of different numbers of layers of one enantiomer on an equal number of the other. If this experiment had been conducted by detecting transmitted light, the number of layers would have been very large. To avoid having to deposit so many layers, we instead detected the second-harmonic light that was reflected, for the coherence length is then very short. The angle of incidence was  $42.6^\circ$ .

The SHG intensity as a function of the thickness was calculated assuming the quasi-phase-matching effect, taking into account the absorption of the second-harmonic beam by the sample [5]. The experimental data perfectly match the theoretical curve. In particular, the output intensity is observed to decrease when the stacks are thicker than the coherence length. The value for the coherence length deduced from the best fit corresponds to 48 molecular layers per stack.

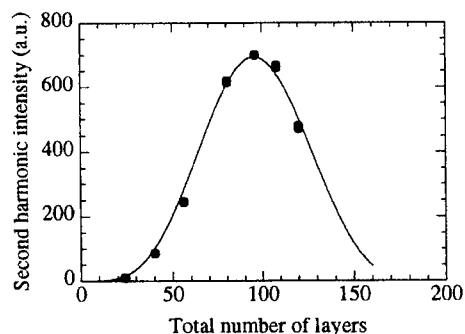


FIGURE 4 Phase-matching curve for the P/M structure. The solid line represents a theoretical fit to the experimental data points [5].

Finally, a new series of samples comprised of alternating stacks (each stack composed of 48 layers) of the two enantiomers were investigated. As shown in Fig. 5, the second-harmonic intensity grows continuously, demonstrating the quasi-phase-matching effect [5].

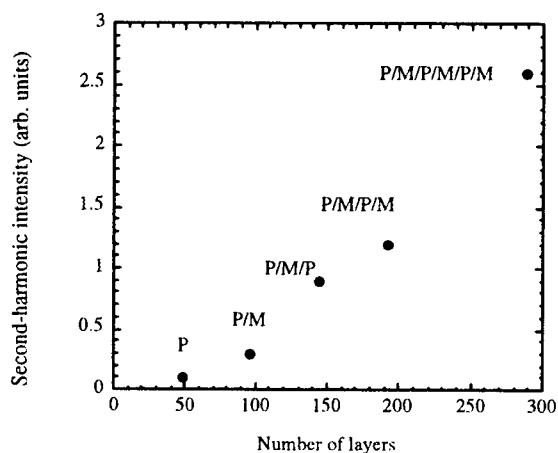


FIGURE 5 Second-harmonic intensities as functions of the total number of molecular layers of the quasi-phase-matched structures. The thickness of each stack is 48 molecular layers, calculated to be equal to one coherence length at the  $42.6^\circ$  angle of incidence [5].

#### ACKNOWLEDGEMENTS

We acknowledge the support of the Belgian Government (IUAP P4/11), the Fund for Scientific Research-Flanders (FWOV G.0338.98, 9.0407.98)

and the US National Science Foundation (CHE9802316). T.V. is a postdoctoral fellow of the Fund for Scientific Research-Flanders.

#### References

1. T. Verbiest, S. Houbrechts, M. Kauranen, K. Clays, A. Persoons, J. Mater. Chem., **7**, 2175 (1997)
2. P.M. Rentzepis, J.A. Giordmaine, K.W. Wecht, Phys. Rev. Lett., **16**, 792 (1966)
3. D. Beljonne, Z. Shuai, J.L. Brédas, M. Kauranen, T. Verbiest and A. Persoons, J. Chem. Phys., **108**, 1301 (1998)
4. T. Verbiest, S. Van Elshocht, M. Kauranen, L. Hellemans, J. Snauwaert, C. Nuckolls, T.J. Katz, A. Persoons, Science, **282**, 913 (1998)
5. B. Busson, M. Kauranen, C. Nuckolls, T.J. Katz, A. Persoons, Phys. Rev. Lett., **84**, 79 (2000)
6. C. Nuckolls, T.J. Katz, T. Verbiest, S. Van Elshocht, H.-G. Kuball, S. Kiesewalter, A.J. Lovinger, A. Persoons, J. Am. Chem. Soc., **120**, 8656 (1998)
7. M. Kauranen, S. Van Elshocht, T. Verbiest, A. Persoons, J. Chem. Phys., **112**, 1497 (2000)

## Synthesis and Mesogenic Properties of Liquid Crystals Containing a Methylene-1,4-Di-, Tetra- or Hexahydropyridine Core Unit

M. HE, R. J. TWIEG

Kent State University, Department of Chemistry and the Liquid  
Crystal Institute, Kent, OH 44242

A series of mesogens that contain derivatives of pyridine with 1,4 connectivity in the core have been prepared. The methodologies applied to the synthesis of these materials are outlined and preliminary characterization of their mesogenic properties is discussed comparing the behavior of homologues that differ in the extent of reduction of the pyridine core and in methylene substitution.

**Keywords:** pyridone, dihydropyridine, tetrahydropyridine, hexahydropyridine

## INTRODUCTION

Heterocycles are extremely important constituents of many organic molecules and their introduction influences numerous important physical properties and also dramatically opens up the available synthetic options. This is certainly the case in the area of liquid crystals where it is now commonplace to introduce heterocycles to modify a wide range of important physical properties. The introduction of pyridine (as a substitute for the benzene ring) into liquid crystals is illustrative. The literature contains well over 2900 examples of liquid crystals containing this ring in various forms: the parent pyridine ring usually substituted at either or both the 2 and 5 positions, condensed pyridines such as quinoline, salts and oxides of pyridine usually substituted at the 1 and 4 positions and intermolecular base-acid complexes such as with carboxylic acids. Additionally, also known but much less common, the use of fully reduced pyridine (piperidine or



hexahydropyridine) is also known and almost exclusively in a 1,4-substitution pattern. Other partially reduced pyridines and especially those with exocyclic conjugation are very uncommon or unknown and these latter systems are the type discussed here herein.[1]

We had previously described a simple synthesis and the mesogenic properties of some 1,4-methylenedihydropyridines.[2,3] We have now prepared a wide range of these systems that possess almost exclusively  $S_A$  phases and so we were curious to learn whether mesogenic activity is retained as the ring is next reduced to the 1,4-methylenetetrahydropyridine and again reduced further to the 1,4-methylenehexahydropyridine. In Figure 1 are found the general structures of the heterocycles of interest here.

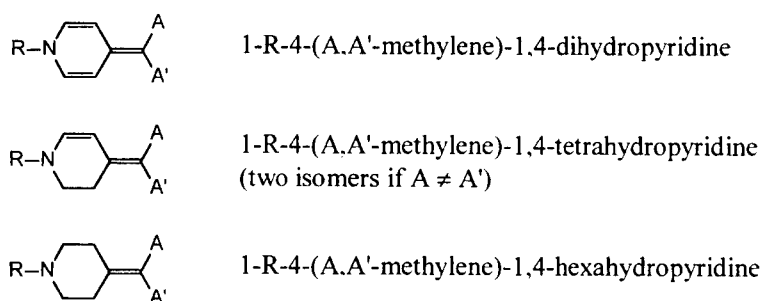
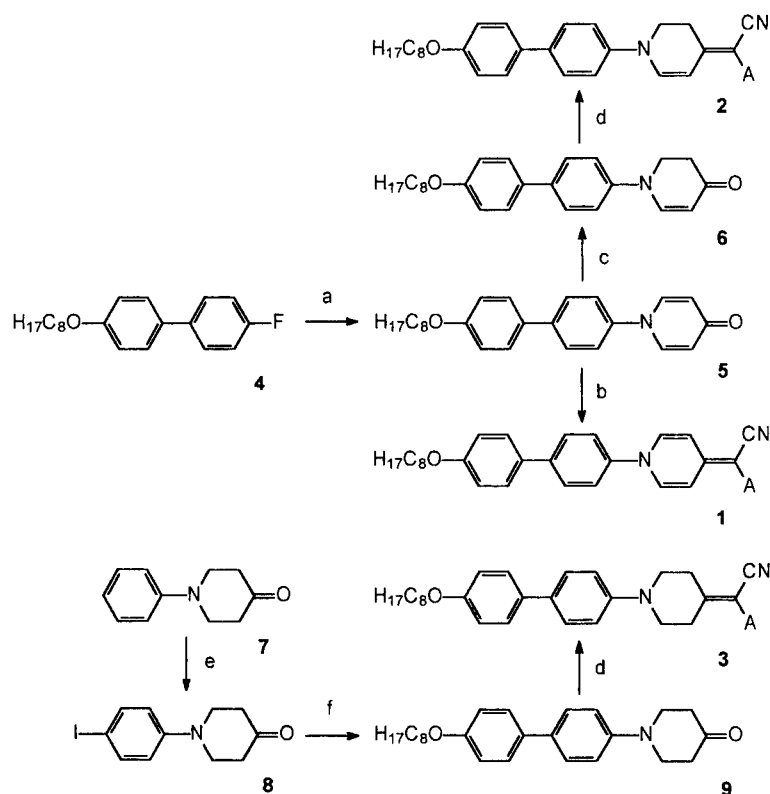


Figure 1. General Structures of the Heterocycles Under Investigation for Incorporation into Liquid Crystals.

The first and second entries in Figure 1 are clearly conjugated compounds capable of significant intramolecular charge transfer. Here the endocyclic nitrogen donor is coupled with an A / A' pair, either or both of which are acceptor groups, that terminate the exocyclic methylene group. These first two entries have resonance contribution which involve  $\delta^+$  charge on the N-donor and  $\delta^-$  charge on the carbon bearing A / A' acceptor group(s). In the third entry conjugation of the donor nitrogen with the acceptor unit is significantly diminished due to the absence of  $\pi$ -conjugation but is still possible (and evident) but by a through bond mechanism.[4]



Scheme 1. Synthesis of Liquid Crystals and Some Intermediates.

- a) 4-hydroxypyridine,  $\text{K}_2\text{CO}_3$ , NMP  
 b)  $\text{NCCH}_2\text{A, Ac}_2\text{O}$  ( $\text{A}=\text{CN}$  for **1a**,  $\text{A}=\text{COOMe}$  for **1b**)  
 c)  $[(\text{CH}_3\text{OCH}_2\text{CH}_2\text{O})_2\text{AlH}_2]\text{Na, THF/toluene}$   
 d)  $\text{NH}_4\text{OAc, HOAc, toluene}$  ( $\text{A}=\text{CN}$  for **2a,3a**,  $\text{A}=\text{COOMe}$  for **2b,3b**)  
 e)  $\text{I}_2, \text{NaHCO}_3, \text{CH}_2\text{Cl}_2, \text{H}_2\text{O}$   
 f)  $\text{H}_{17}\text{C}_8\text{OPhB(OH)}_2, \text{PdCl}_2(\text{dppf}), \text{K}_2\text{CO}_3, \text{DMF}$

The synthesis methods employed are outlined in Scheme 1. While the methylenedihydropyridines **1a,b** and methylenetetrahydropyridines **2a,b** are prepared via the common dihydropyridone **5** we have thus far failed to identify a way to prepare the hexahydropyridines **3a,b** involving this route. Instead, a separate route in which the 4-pyridone ring is introduced early in the sequence had to be devised. A number

of dead ends that were encountered in our synthetic plans will be discussed elsewhere along with the full experimental details of these successful approaches.

The coupled dihydro and tetrahydro series are discussed first. The 4-octyloxy-4'-fluorobiphenyl **4** is prepared from the known 4-fluoro-4'-biphenol [5] that itself was obtained by palladium mediated aryl coupling (in our case we employed the Suzuki coupling of fluorophenylboronic acid with 4-iodooctyloxybenzene or a protected 4-iodophenol with subsequent deprotection and alkylation). The 4-octyloxy-4'-fluorobiphenyl is then subjected to aromatic nucleophilic substitution with 4-hydroxypyridine. We have already demonstrated this method as very useful for preparation of a wide range of N-arylpyridones.[2,3,6] This pyridone **5** can be converted directly and in high yield to the methylene derivatives **1a** and **2a** by respective reaction in acetic anhydride with malononitrile or the methyl ester of cyanoacetic acid (other cyanoacetic acids have been used and give analogous cyanoesters as will be discussed elsewhere). One of the double bonds in pyridone **5** (a dienone) can be selectively reduced [7] to the monoenone **6** which is subsequently reacted with active methylene compound but here using ammonium acetate in acetic acid instead of acetic anhydride.

For the separate hexahydro series the known phenylpiperidone **7** [8] was iodinated to give **8** and then coupled to give the three ring piperidone **9** which is reacted next with an active methylene compound to give activated methylene derivatives **3a** and **3b**.

## RESULTS AND DISCUSSION

The physical properties of the final materials are provided in Table 1. For the methylene dihydropyridines **1a** and **1b** only the cyanoester **1b** showed mesogenic properties, a broad  $S_A$  phase, just as is usually the case with their smaller two ring homologues with simple alkyl or alkoxy tails.[3] In the case of the tetrahydropyridines both dicyano **2a** and cyanoester **2b** are mesogenic. The phase in **2a** that appears prior to clearing has not been assigned yet and in **2b** an additional small nematic range appears additionally prior to clearing. In the case of the hexahydro compounds **3a** and **3b** mesogenic activity is here found only in the case of the cyanoester **3b** that has a small  $S_A$  range. The

mesogenic activity of **3b** remarkable since these compounds appear to prefer an axial conformation of the N-substituent of the piperidine ring.[9] The wavelength and extinction coefficient of the charge transfer band for these molecules are also provided in Table 1. The methylenetetrahydropyridines have the longest wavelength absorption and the hexahydropyridines show the anticipated [4] charge transfer band as well, albeit with the shortest wavelength and weakest extinction coefficient in the series. It is of interest that ketone precursors **5** and **6** are mesogenic while **9** is not. The mesogenic activity of other pyridones like **5** has also been recently observed and studied in some detail.[10]

Compound	#, LC range $\lambda_{\max}$ ( $\epsilon$ , THF)
	<b>1a</b> K 220 I 383 (95800)
	<b>2a</b> K <sub>1</sub> 118 K <sub>2</sub> 157 S <sub>x</sub> 183 I 429 (34900)
	<b>3a</b> K 138 I 363 (6560)
	<b>1b</b> K 139 K 186 S <sub>A</sub> 277 I 391 (68368)
	<b>2b</b> K 155 S <sub>x</sub> 222 N 228 I 432 (37900)
	<b>3b</b> K 142 S <sub>A</sub> 150 I 360 (4516)

Table 1. Physical properties of a Contiguous Set of Three-ring Methylene Di-, Tetra- and Hexa-hydro Pyridines. The phase transitions were obtained by polarized optical microscopy.

In conclusion, a contiguous series of methylene dihydro, tetrahydro and hexahydro pyridine liquid crystals have been prepared and in the latter two cases this is the first demonstration of mesogenic activity in molecules containing these heterocycles. These molecules are of interest due to their multifunctionality; in this case the combination of mesogenic properties with optical or electronic properties potentially useful for photorefractivity or related applications.[11,12] Of special interest are those substances with through bond conjugation. The investigation of the electronic and optical properties of these and related materials are presently underway and the full experimental details and data will be forthcoming subsequently.

#### ACKNOWLEDGEMENTS

This study was supported by the NSF at KSU ALCOM (Center for Advanced Liquid Crystalline Optical Materials. DMR 89-29147).

#### REFERENCES

- [1] Data for LC structures and populations were obtained from the Liquid Crystal Database, Version 3.0, V. Vill. SciDex Database Tech.
- [2] D. J. Dyer, V. Y. Lee, R. J. Twieg, *Liq. Cryst.*, **24**, 271 (1998).
- [3] F. You, R. J. Twieg, D. Dyer, V. Lee, *Mol. Cryst. Liq. Cryst. Liq. Cryst. Sci. Tech. Sec. A - Mol. Cryst. Liq. Cryst.*, **332**, 2909 (1999).
- [4] T. Scherer, W. Hielkema, B. Krijnen, R. M. Hermant, C. Eijkelhoff, F. Kerkhof, A. K. F., Ng, R. Verleg, E. B van der Thol, A. M. Brouwer, J. W. Verhoven, *Recl. Trav. Chim. Pays-Bas*, **112**, 535 (1993).
- [5] H. Takatsu, K. Takeuchi, H. Sato, *Mol. Cryst. Liq. Cryst.*, **108**, 157 (1984).
- [6] F. You, R. Twieg, *Tet. Lett.*, **40**, 8759 (1999).
- [7] P. Guerry, R. Neier, *Synthesis*, 485 (1984).
- [8] J. J. L. Clair, *Angew. Chem. Int. Ed.*, **37**, 325 (1998).
- [9] B. Krijnen, H. B. Beverloo, J. W. Verhoeven, C. A. Reiss, K. Goubitz, D. Heijdenrijk, *J. Amer. Chem. Soc.*, **111**, 4433 (1989).
- [10] D. J. Dyer, V. Y. Lee, R. J. Twieg, *Liq. Cryst.*, **23**, 551 (1997).
- [11] P. M. Lundquist, R. Wortmann, C. Geletneky, R. J. Twieg, M. Jurich, V. Y. Lee, C. R. Moylan, D. M. Burland, *Science*, **274**, 1182 (1996).
- [12] A. Fort, J. Muller, L. Mager, *Chem. Phys.*, **243**, 115 (1999).

## Organic Crystal (DAST) for THz Wave Applications

PENGYU HAN,<sup>a</sup> MASAHIKO TANI,<sup>a,b</sup> FENG PAN,<sup>c</sup> XI-CHENG ZHANG<sup>a</sup>

<sup>a</sup>: Physics Department, Rensselaer Polytechnic Institute, Troy, NY 12180, USA;

<sup>b</sup>: Kansai Advanced Research Center, Iwaoka, Kobe, 651-2401 Japan;

<sup>c</sup>: Molecular Optoelectronics Corp. Watervliet, NY 12189, USA

Electro-optic (EO) crystals could be ideal materials for generating and detecting free-space ultra-broadband THz waves. We report recent results on the material selection of THz emitters and sensors for THz image applications. Organic DAST crystal is a promising candidate with high applicable frequency bandwidth up to 20 THz and large EO coefficients. We report the development of a novel scheme with DAST as an ultrafast THz wave sensor. The dielectric constant of DAST is obtained by transmission and reflection spectroscopy. Furthermore, 36 times enhancement of high-frequency THz radiation at 7 - 20 THz is obtained from optical rectification in a thin DAST, compared with our best ZnTe emitter.

**Keywords:** DAST; Terahertz (THz); Electro-optic; Sensor; Emitter; Birefringence.

### INTRODUCTION

Since the first invention of the organic ionic salt crystal 4-dimethylamino-*N*-methylstilbazolium tosylate (DAST), a lot of efforts have been made in its growth, characterization and applications

because of its attractively high nonlinear optical and electro-optical (EO) coefficients.[1-3] The second order nonlinear coefficient of DAST is 840 pm/V at 1542 nm. EO measurement at 820 nm resulted in a Pockels coefficient of 75 pm/V.[3] DAST has been used to generate broadband THz radiation by optical rectification [4,5] and narrowband THz by difference-frequency mixing using dual-wavelength laser [6]. Moreover, low dielectric constants of DAST allows high speed EO modulation and detection. An intensity modulation up to 18 GHz was observed from DAST waveguide.[7] DAST was also used to monitor mm wave field by interferometric methods.[8] With the recent development of free-space THz EO sampling technique,[9-11] it is of great interest to utilize the high Pockels coefficient of DAST as far infrared (IR) sensor, even as mid-IR sensor or emitter [12].

#### CHARACTERIZATION OF DAST AT FAR INFRARED

The dielectric constants of DAST has been characterized by THz transmission spectroscopy.[4,13] However, due to the strong absorption above 1 THz, it is difficult to get accurate data in that frequency region. Hence, THz reflection spectroscopy [14-17] is employed to obtain the complex dielectric constants of DAST. A *c*-cut DAST sample with a dimension of 4x6x1 mm<sup>3</sup> is used. Due to the strong birefringence, separate measurement is done with THz polarization parallel to *a* and *b* axis of DAST. A well-collimated THz beam is incident at DAST surface at 45°. THz beam is restricted to a diameter of 3 mm by an iris to fit the sample. Reflected THz beam is collected and focused by a paraboloidal mirror and detected by EO sampling setup.[17] As a reference, a silver mirror is used in place of DAST with over 99% reflectivity for THz beam. The complex reflectivity can be resolved in the whole spectrum from 0.2 to 3 THz. Fitting the data using an oscillator model yields a complete characterization of dielectric constants of DAST.

Fig. 1 shows the experimental reflectivity of DAST and the fitting curve using the oscillator model. At *a* axis, one phonon is observed and fitting yields the following parameters:

$$\epsilon = \epsilon_{\infty} + \frac{\epsilon_0 - \epsilon_{\infty}}{1 - \omega^2 / \omega_{LO}^2 - i\gamma\omega / \omega_{LO}^2} \quad (1)$$

where  $\epsilon_\infty=5.55$ ,  $\epsilon_0=6.39$ ,  $\omega_{TO}=1.11$  THz,  $\gamma=0.16$  THz. On the other hand, two phonons are observed in  $b$  axis:

$$\epsilon = \epsilon_\infty + \frac{\Delta\epsilon_1}{1 - \frac{\omega^2}{\omega_{TO1}^2} - \frac{i\gamma_1\omega}{\omega_{TO1}^2}} + \frac{\Delta\epsilon_2}{1 - \frac{\omega^2}{\omega_{TO2}^2} - \frac{i\gamma_2\omega}{\omega_{TO2}^2}} \quad (2)$$

where  $\epsilon_\infty=2.99$ ,  $\Delta\epsilon_1=0.21$ ,  $\Delta\epsilon_2=0.70$ ,  $\omega_{TO1}=1.12$  THz,  $\omega_{TO2}=1.53$  THz,  $\gamma_1=0.12$  THz,  $\gamma_2=0.31$  THz. We notice that the damping time constant obtained is short comparing with those of polar semiconductor crystal. The difference may be due to the different structural and crystal properties of the organic crystal.

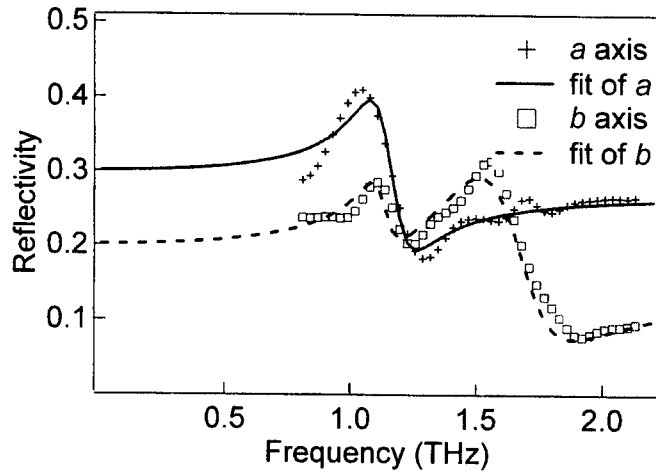


Fig. 1: Experimental reflectivity of DAST and the fitting curves using oscillator model along  $a$  and  $b$  axis.

#### THEORETICAL CALCULATION OF DAST AS TERAHERTZ EMITTER AND SENSOR



DAST crystal has a monoclinic structure with point group  $m$  and standard orientation. There are 10 independent nonzero second-order coefficients, and there are three, namely  $d_{11}$ ,  $d_{12}$ ,  $d_{26}$ , involved in the experiment with a (001) sample in normal incidence. The radiated THz field can be expressed as:

$$\begin{aligned} E_{THz,a} &= \frac{A}{4} [(d_{11} - d_{12} - 2d_{26})\cos 3\theta + (3d_{11} + d_{12} + 2d_{26})\cos \theta], \\ E_{THz,b} &= \frac{A}{4} [(d_{11} - d_{12} - 2d_{26})\sin 3\theta - (d_{11} + 3d_{12} - 2d_{26})\sin \theta]; \end{aligned} \quad (3)$$

Where  $E_{THz,a}$ ,  $E_{THz,b}$  are the THz components in  $a$  and  $b$  axis of DAST, and  $\theta$  is the angle between pump beam polarization and  $a$  axis.

When a  $c$ -cut DAST is used as EO sensor and  $E$  field is parallel to the crystal surface with an angle  $\phi$  with  $a$  axis, the ellipsoid difference of DAST at  $x$  and  $y$  axis can be derived as:

$$\begin{aligned} \frac{1}{n_z^2} - \frac{1}{n_y^2} &= \Delta \left( \frac{1}{n^2} \right) = \text{sqr}t \left[ \left( \frac{1}{n_x^2} - \frac{1}{n_y^2} + r_{11}E \cos \phi - r_{21}E \cos \phi - r_{62}E \sin \phi \right) \right. \\ &\quad \left. * \left( \frac{1}{n_x^2} - \frac{1}{n_y^2} + r_{11}E \cos \phi - r_{21}E \cos \phi + r_{62}E \sin \phi \right) \right] \\ &\cong \frac{1}{n_x^2} - \frac{1}{n_y^2} + r_{11}E \cos \phi - r_{21}E \cos \phi \end{aligned} \quad (4)$$

where  $r_{ij}$  are the corresponding components of the EO tensor and in the above equation, we make approximation by neglecting  $r_{62}$  since  $r_{62} \ll r_{11}, r_{21}$ . We can derive the following conclusions: 1). Maximum THz-induced change occurs when THz field is polarized in  $a$  axis; 2). Strong intrinsic birefringence exists in DAST and its compensation is necessary before used as EO sensor; 3). To probe the THz-induced refractive index change, optical probe beam should polarize at  $45^\circ$  with  $a$  and  $b$  axis of DAST.

## IMPLEMENTATION OF DAST AS THZ WAVE SENSOR

### Phase Matching of THz and Optical Pulses in DAST

Phase-matching between optical and THz pulses is a major factor determining the efficiency and bandwidth of a certain EO crystal,

hence the optimum thickness of a crystal for specific applications. Coherence length,[11] decided by phase matching condition, provides a very important reference for selecting EO crystals and their thickness:

$$l_c = \frac{\pi c}{\omega_{THz} |n_{opt} - \lambda_{opt} \frac{dn_{opt}}{d\lambda} - n_{THz}|} \quad (5)$$

where  $n_{opt}$ ,  $n_{THz}$  are the optical and THz refractive indexes, respectively. Based on the known refractive index at optical wavelength and the obtained dielectric constants at THz region, we calculate the coherence length of DAST at THz frequency, assuming an optical wavelength of 800 nm and both THz beam and optical beam have the same polarization in either  $a$  or  $b$  axis. The result is shown in Figure 2, indicating that DAST with thickness of a couple hundred microns is suitable for EO sampling up to a few THz.

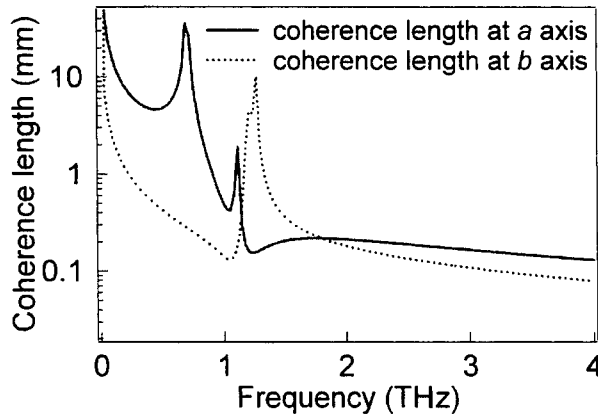


Fig. 2: Coherence length of DAST when both THz pulse and optical pulse have the same polarization at  $a$  and  $b$  axis.

#### Birefringence Compensation

DAST has a very strong birefringence with a group refractive index of  $n_{g,a}=2.70$  and  $n_{g,b}=1.89$  at a wavelength of 800 nm.[3] After transmitting a  $c$ -cut DAST with thickness of 0.7 mm, the field

components of optical pulse at  $a$  and  $b$  axis of DAST will have a phase difference of  $713 \times 2\pi$ , equivalent to 1.9 ps. Considering the pulse duration of 100 fs or less used in experiment, optical pulses along  $a$  and  $b$  axis will lose coherence after transmission of 0.7 mm DAST. The birefringence cannot be compensated by a compensator, which usually has a retardation range from 0 to  $\pi$ . Therefore, this is very different from isotropic crystal (such as ZnTe) or weakly anisotropic crystal (such as LiTaO<sub>3</sub>), of which the phase-delay of components along different optical axis is either negligible or can be compensated by a compensator. However, to monitor the small phase-shift between different optical axis of DAST induced by applied THz pulse, it is necessary to compensate the time shift between pulses at  $a$  and  $b$  axis.

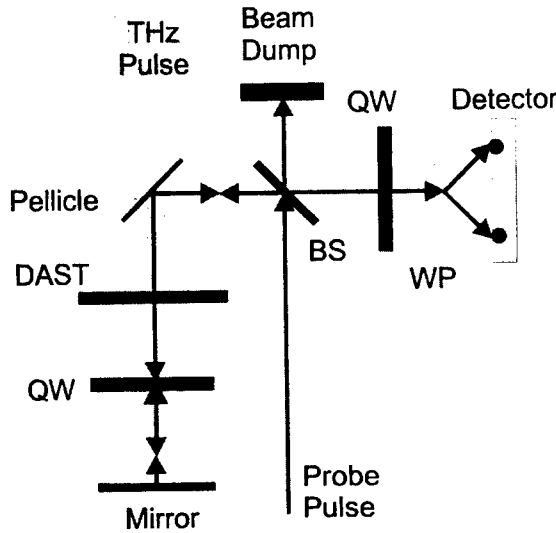


Fig. 3: Schematic experimental setup. QW: quarter waveplate; WP: Wollaston prism; BS: 50-50 optical beamsplitter.

Figure 3 shows the experimental setup used to compensate the birefringence. Optical probe beam goes through a quarter waveplate after transmitting a  $c$ -cut 0.7-mm-thick DAST crystal. The beam is then reflected back by a mirror and goes through the same quarter waveplate and DAST again. The quarter waveplate is orientated so

that s polarization (forward beam) becomes p polarization (backward beam) and vice versa. Because each component goes through the same DAST twice with two orthogonal polarization states, they have the same phase delay and birefringence is exactly cancelled. The temporal window between the forward and backward optical probe beam is longer than the THz pulse duration, so the returned optical probe pulse in the DAST crystal will not be further modulated by the THz pulse. A Ti:Sapphire laser oscillator with 100 fs pulse width and 1.5 W average power is used in this experiment. THz pulse generated by optical rectification in a 1-mm ZnTe is applied along *a* axis of DAST crystal and synchronized with the optical probe pulse when it passes the DAST. The probe beam is polarized at 45° from *a* axis. After the intrinsic birefringence is compensated, it is biased by another quarter waveplate to get linear response. Assuming good phase-matching, the balanced current is given by:

$$\Delta I / I_0 = \Delta \Gamma = \pi E_{THz} (n_d^3 r_{11} - n_b^3 r_{21}) L / \lambda \quad (6)$$

where  $r_{ij}$  are the corresponding components of the EO tensor, *L* is the effective crystal thickness and  $\lambda$  is optical wavelength.

#### Experimental Results and Discussions

Fig. 4 shows the THz waveform measured with the DAST sensor, along with result obtained using a 0.5-mm ZnTe sensor. The amplitudes, waveforms and spectra are all comparable. Since ZnTe has been known as an ideal THz sensor at less than 4 THz, we conclude that DAST is indeed a good EO sensor up to the frequency detected. From the known EO coefficients, the THz amplitude from DAST should be several times larger than that of ZnTe. We attribute the deviation from theory to the imperfection of optical quality of DAST, such as unflatness, inhomogeneity, misorientation and imperfect surface condition. These make it difficult to cancel the birefringence exactly. Hence, the bias point is not optimized. Moreover, intense laser beam can cause photorefractive effect, even melting of DAST. We also notice apparent difference from sample to sample. Nevertheless, this technique has some very attractive features. In addition to the total cancellation of intrinsic birefringence, local effects, such as thermal-induced birefringence in the crystal, can also be compensated. Furthermore, it can be applied to any other EO

crystal with intrinsic birefringence, such as LiNbO<sub>3</sub>, LiTaO<sub>3</sub>. Thus, it provides a simple method for the THz application of EO materials with high Pockels coefficients and intrinsic birefringence.

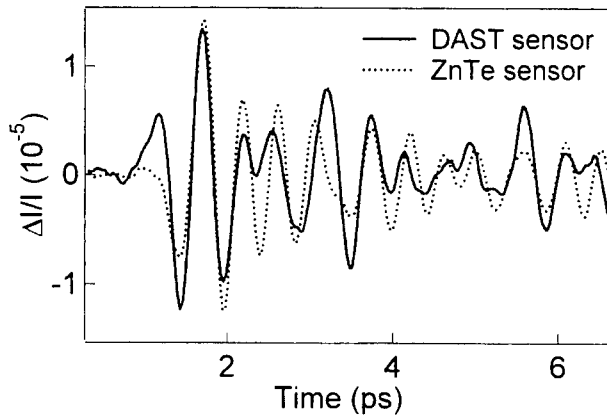


Fig. 4: THz waveforms obtained using DAST and ZnTe as EO sensors.

#### DAST AS HIGH-FREQUENCY THZ RADIATION SOURCE

With the development of THz spectroscopy, it is often desirable to perform it at higher frequency. For example, phonon dynamics is an interesting phenomenon and occurs at around 10 THz for some polar semiconductors.[17] DAST has been demonstrated as an excellent emitter at less than 3 THz.[4] Here, a Ti:Sapphire oscillator with 15-fs pulse is used to generate high frequency THz radiation, the setup is similar to that used in Ref. 12. Fig. 5 illustrates the THz pulse generated by optical rectification in a 100- $\mu\text{m}$  DAST crystal with observable bandwidth up to over 20 THz. It shows a dramatic six-fold increase of amplitude comparing with that of a 30- $\mu\text{m}$  ZnTe sample at the same condition, corresponding to 36 times enhancement of high-frequency THz power. Since the coherence length of ZnTe is less than 30  $\mu\text{m}$  for frequency region of 7-20 THz,[12] thicker ZnTe crystal will not increase the amplitude of the spectrum.

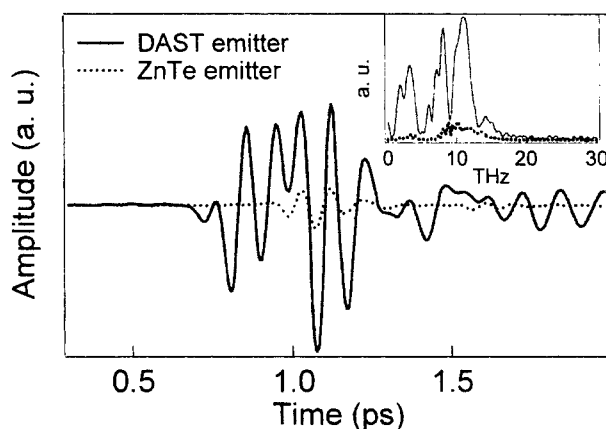


Fig. 5: Experimental THz pulse from a 100- $\mu\text{m}$  DAST emitter, showing a six-fold increase of amplitude comparing with that of a 30- $\mu\text{m}$  ZnTe sample. Inset: their spectra.

## CONCLUSIONS

In conclusion, we have resolved the resonant structures of DAST and fitted the complex dielectric constant by oscillator model at THz frequency. DAST as an ultrafast EO sensor at THz frequency has been demonstrated by employing a novel scheme for the first time. This extends the frequency response of DAST from GHz to THz and opens the door for its applications in high frequency EO waveguide modulator and other ultrafast EO devices at THz frequency region. Furthermore, this method can be applied to other EO crystals with intrinsic birefringence. At last, DAST has been shown to support bandwidth up to 20 THz as a THz emitter, demonstrates 36 times enhancement of radiation at 7-20 THz, comparing with our best ZnTe.

## ACKNOWLEDGEMENTS

This work was supported by the Army Research Office and the National Science Foundation of United States of America.

## REFERENCES

1. S. R. Marder, J. W. Perry, and W. P. Schaeffer, Science **245**, 626 (1989).
2. H. Nakanishi, H. Matsuda, S. Okada, M. Kato, Proc. MRS Int. Mtg. Adv. Mater. **1**, 97 (1989).
3. F. Pan, G. Knopfle, Ch. Bosshard, S. Follonier, R. Spreiter, M. S. Wong, and P. Gunter, Appl. Phys. Lett. **69**, 13 (1996).
4. X.-C. Zhang, X. F. Ma, Y. Jin, T.-M. Lu, E. P. Boden, P. D. Phelps, K. R. Stewart, C. P. Yakymyshyn, Appl. Phys. Lett. **61**, 3080 (1992).
5. T. J. Carrig, G. Rodriguez, T. Clement, A. J. Taylor, K. R. Stewart, Appl. Phys. Lett. **66**, 121 (1995).
6. K. Kawase, M. Mizuno, S. Sohma, H. Takahashi, T. Taniuchi, Y. Urata, S. Wada, H. Tashiro, H. Ito, Opt. Lett. **24**, 1065 (1999).
7. F. Pan, K. McCallion, and M. Chiapetta, Appl. Phys. Lett. **74**, 492 (1999).
8. S. Sohma, H. Takahashi, T. Taniuchi, H. Ito, Chem. Phys. **245**, 359 (1999).
9. Q. Wu and X.-C. Zhang, Appl. Phys. Lett. **67**, 3523 (1995).
10. P. U. Jepsen, C. Winnewisser, M. Schall, V. Schyja, S. R. Keiding and H. Helm, Phys. Rev. E **53**, R3052 (1996).
11. A. Nahata, A. S. Weling, T. F. Heinz, Appl. Phys. Lett. **69**, 2321 (1996).
12. P. Y. Han and X.-C. Zhang, Appl. Phys. Lett. **73**, 3049 (1998).
13. S. R. Keiding, in private communications.
14. T. Jeon and D. Grischkowsky, Appl. Phys. Lett. **72**, 3032 (1998).
15. C. Ronne, L. Thrane, P. Astrand, A. Wallqvist, K. Mikkelsen, S. R. Keiding, J. Chem. Phys. **107**, 5319 (1997).
16. D. M. Mittleman, S. Hunsche, L. Boivin, M. C. Nuss, Opt. Lett. **22**, 904 (1997).
17. P. Y. Han, G. C. Cho and X.-C. Zhang, J. Nonlinear Opt. Phys. & Mater. **8**, 89 (1999).

**SESSION A: NOVEL NONLINEAR OPTICAL  
PHENOMENA AND APPLICATIONS**



## Enhanced Two-Photon Absorption with Polyphenyl Oligomers

CHANTAL ANDRAUD,<sup>a</sup> AND PATRICE L. BALDECK<sup>b</sup>

<sup>a</sup> École Normale Supérieure de Lyon, Stéréochimie et Interactions  
moléculaires, UMR CNRS n° 5532, 69364 Lyon cedex 07, France;

<sup>b</sup> Spectrométrie Physique, Université Joseph Fourier, CNRS (UMR  
5588), B.P. 87, 38402 St Martin d'Hères, France

The theoretical study of two-photon absorption (TPA) properties of polyphenyls (with the number of benzene monomer units  $n = 1$  to 6) is related to cooperative effects between monomers. These effects lead to an increase of the TPA cross-section with  $n$  without saturation according to a power law.

**Keywords** Two-photon absorption; polyphenyls; CNDO/S calculations.

### INTRODUCTION

Two-photon absorption (TPA) properties of organic compounds are being involved in many applications [1]. New organic molecules are being optimized for these applications [2]. In general, the selected molecules result from a molecular engineering strategy that study the role of substituents and delocalized electron core on the two-photon absorption of substituted molecules [3-4]. Recently, the TPA properties of polyene oligomers have been investigated, and a strong correlation between their TPA and their lengths has been established [5].

The purpose of this work is to evaluate the interest of this oligomer approach as a new strategy to optimize molecules for TPA effects. Here, we report on TPA properties of polyphenyls, a model compound for applications at visible wavelengths. We use CNDO/S based calculations to investigate the changes of TPA properties with the oligomer length. All results are adequately rationalized using the three-level model.

### CALCULATIONS METHOD

The molecule geometry was optimized by using Sybyl, i.e. Tripos force field and AM1 from the MOPAC package [6] : the selected geometry corresponds to the lowest energy. For each molecule, the electronic state characteristics, i.e. singlet state energies, and dipole moments, were obtained by a configuration interaction (CI) procedure based on the CNDO/S method using the QCPE program #333. The CI calculations included 100 singly (SCI), and 100 doubly (DCI) excited configurations.

The TPA cross-section  $\sigma_{TPA}$  is proportional to the imaginary part of the average second hyperpolarizability:

$$\sigma_{TPA} = \frac{3}{10} \hbar \frac{\omega^2}{n^2 c^2 \epsilon_0} f^4 \text{Im} \langle \gamma(-\omega; \omega, -\omega, \omega) \rangle \quad (1)$$

$$\langle \gamma \rangle = \frac{1}{5} (\gamma_{xxxx} + \gamma_{yyyy} + \gamma_{zzzz} + \gamma_{xxyy} + \gamma_{yyxx} + \gamma_{yyzz} + \gamma_{zzyy} + \gamma_{xxzz} + \gamma_{zzxx}) \quad (2)$$

The tensor components  $\gamma_{ijkl}$  were computed using Orr and Ward's equation based on the time-dependent perturbation theory [7]. TPA spectra were evaluated by using the parameters of the 19 lowest excited states to obtain a good convergence of  $\sigma_{TPA}$  values [4]. The damping factors  $\Gamma$  were taken to be  $1000 \text{ cm}^{-1}$  for all states, and the refractive index was assumed to be 1.

Results were interpreted on the basis of the three-level model (Eq.(3)):

$$\gamma \propto \frac{\mu_{01}^2 \mu_{12}^2}{(E_{01} - \frac{E_{02}}{2})^2} \quad (3)$$

where  $\mu_{01}$ , and  $\mu_{12}$ , are the transition moment between the ground state  $S_0$  and the lowest charge transfer excited-state  $S_1$ , and the transition moment between  $S_1$  and the lowest two-photon excited state  $S_2$ , respectively.  $E_{01}$  and  $E_{02}$  are the energy of  $S_1$  and  $S_2$ , respectively. [3]

### RESULTS

The TPA cross-sections  $\sigma_{TPA}$  of polyphenyls ( $n = 1$  to 6, with  $n$  the number of benzene rings) are displayed on Table 1 with the positions of the TPA band. These calculations show a large increase of  $\sigma_{TPA}$  as a function of  $n$  according to a power law (Figure 1 and Eq. (4)) :

$$\sigma_{TPA} = 1.1 * 10^{-49} n^{3.0} \quad (4)$$

$n$	$\lambda_{TPA}$ (nm)	$\sigma_{TPA}$ ( $10^{-48}$ cm <sup>4</sup> s/photon)
2	436	0.8
3	469	3.3
4	469	6.1
5	487	12.6
6	492	20.9

TABLE 1 Theoretical two-photon resonances and cross-sections of polyphenyls as a function of the benzene ring number  $n$ .

No saturation effect was predicted up to  $n = 6$  in good agreement with experimental data on the tetra and the pentaphenyl [8]. This structure-nonlinearity relation is consistent with previous calculations on different hydrocarbon oligomers, such as polyenes for which a larger dependency of  $\sigma_{TPA}$  was found with  $L$  with  $\alpha \approx 5 - 6$  [5c].

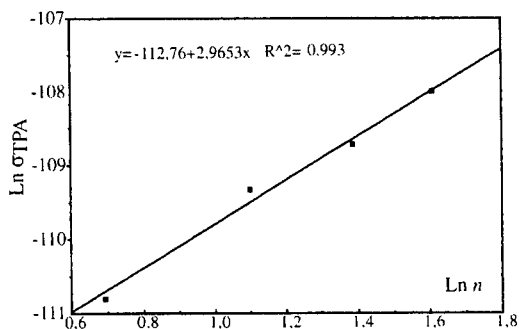


FIGURE 1 Theoretical two-photon cross-sections of polyphenyls as a function of the benzene ring number  $n$ .

The increase of  $\sigma_{TPA}$  values with  $n$  occurs with a red shift of the first absorption and of the  $\sigma_{TPA}$  bands (Table 1 and Figure 2b).

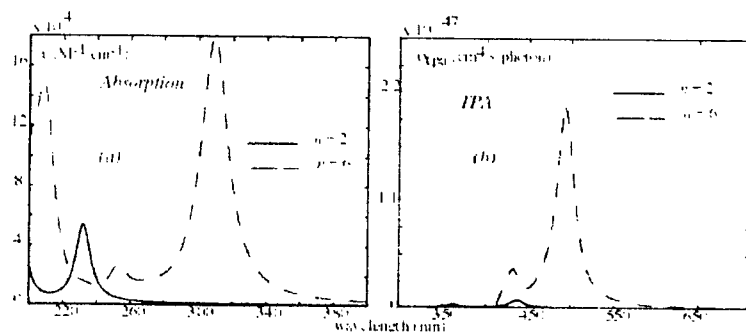


FIGURE 2 Absorption spectra of biphenyl and sexiphenyl :  
(a) linear absorption ; (b) two-photon absorption.

## DISCUSSION

As in the case of substituted molecules [3,4], all these results can be readily interpreted on the basis of the three-level model (Eq. (3)). Calculated excited state energies and transition dipole moments are displayed in Table 2. Due to conjugation, transition energies are red-shifted, and transition dipole moments increase with the monomer number  $n$ .

$n$	$\lambda_{01}$ (nm)	$\lambda_{02}$ (nm)	$\mu_{01}$ (D)	$\mu_{12}$ (D)
2	232	219	6.0	9.0
3	266	236	8.5	11.4
4	282	238	9.9	12.0
5	297	243	11.6	16.2
6	309	247	12.6	18.3

TABLE 2 Excited states parameters of polyphenyls.

The variations of each parameter  $P$  describing the two-photon absorption of polyphenyls in the three-level model can be described by a power law as in Eq. 4. The corresponding powers  $\alpha$  are displayed on Table 3.

$P$	$\mu_{01}$	$\mu_{02}$	$(E_{01} - \frac{E_{02}}{2})^{-1}$
$\alpha$	0.67	0.64	0.47

TABLE 3 Power dependency  $\alpha$  of parameters describing the two-photon absorption of polyphenyls in the three-level model (Eq. (3)).

Using these exponents in Eq. (3), one finds a  $\sigma_{\text{TPA}}$  power dependency  $\alpha = 3.5$  in good agreement with the power  $\alpha = 3.0$  obtained from the full calculation. Thus, on the basis of the three-level model, the enhancement of polyphenyls TPA can be rationalized by the simultaneous increase of ground-state transition dipole moment  $\mu_{01}$ , excited-state transition dipole moment  $\mu_{12}$ , and energy resonances with the number  $n$  of monomer units.

The power dependency of transition dipole moments, i.e.  $\alpha = 0.67$  and  $\alpha = 0.64$ , is comparable with the power  $\alpha = 0.5$  obtained in the exciton model for linear aggregates [9]. The difference in power laws could be due to the conjugation that occurs between monomers. A similar aggregate behavior has been previously involved to modelized the red-shift of optical transitions in polyphenyls [10]. Thus, the TPA enhancement with the oligomer size may be viewed as the result of cooperative effects in the optical response of monomers.

## CONCLUSION

This theoretical study shows that the two-photon absorption cross-section of polyphenyls increases with the number of monomer units. No saturation is predicted at least up to  $n=6$ . This TPA enhancement follows a power law that results from cooperative effects between monomers on excited state characteristics.

## References

- [1] B.A. Reihardt *Photonics Science News* **4**, 21 (1999).
- [2] (a) J.E. Ehrlich, X.L. Wu, I.-Y.S. Lee, Z.-Y. Hu, H. Röckel, S.R. Marder, J.W. Perry *Opt. Lett.* **22**, 1843 (1997); (b) J.W. Perry, S. Barlow, J.E. Ehrlich, A.A. Heikal, Z.-Y. Hu, I.-Y.S. Lee, K. Mansour, S.R. Marder, H. Röckel, M. Rumi, S. Thayumanavan, X.-L. Wu *Nonlinear Optics* **21**, 225 (1999); (c) S. Delysse, P. Filloux, V. Dumarcher, C. Fiorini, J.-M. Nunzi *Optical Materials* **9**, 347 (1998); (d)

- P.-A. Chollet, V. Dumarcher, J.-M. Nunzi, P. Feneyrou, P. Baldeck Nonlinear Optics **21**, 299 (1999); (e) C. Nguéfac, T. Zabulon, R. Anémian, C. Andraud, A. Collet, S. Topçu, P.L. Baldeck Nonlinear Optics **21**, 309 (1999).
- [3] M. Albota, D. Beljonne, J.L. Brédas, J.E. Ehrlich, J.-Y. Fu, A.A. Heikal, S.E. Hess, T. Kogej, M.D. Ievin, S.R. Marder, D. McCord-Maughon, J.W. Perry, H. Röckel, M. Rumi, G. Subramaniam, W.W. Webb, X.-L. Wu, C. Xu Science **281**, 1653 (1998).
- [4] C. Andraud, R. Anémian, A. Collet, J.-M. Nunzi, Y. Morel, P.L. Baldeck J. Opt. A: Pure Appl. Opt. (in press).
- [5] (a) A.A. Said, C. Wamsley, D.J. Hagan, E.W. Van Stryland, B.A. Reinhardt, P. Rodere, A. G. Dillard Chem. Phys. Lett. **228**, 646 (1994); (b) D. Beljonne, J.L. Brédas J. Opt. Soc. Am. B **11**, 1380 (1994); (c) P. Norman, Y. Luo, H. Agren Chem. Phys. Lett. **296**, 8 (1998); (d) P. Norman, Y. Luo, H. Agren J. Chem. Phys. **111**, 1 (1999).
- [6] SYBYL 6.5, from Tripos, 1699 S. Hanley Road, St. Louis, MO 63144-2913. (Tripos force field and AM1 calculation included in MOPAC package).
- [7] B.J. Orr, J.F. Ward Mol. Phys. **20**, 513 (1971).
- [8] Y. Morel, C. Andraud, P.L. Baldeck Nonlinear Optics (in press).
- [9] E.G. McRae, M. Kasha J. Chem. Phys. **28**, 721 (1958).
- [10] A.S. Davydov Zhur. Eksptl. i Teort. Fiz. **18**, 515 (1948).

## Tensorial Analysis of First-Order Hyperpolarizabilities of $C_{2v}$ Molecules

XUE-LIN YANG<sup>a,b</sup>, CHANTAL ANDRAUD<sup>a</sup>, JOSEPH ZYSS<sup>c</sup>

<sup>a</sup>Laboratoire de Stéréochimie et des Interactions Moléculaires, Ecole Normale Supérieure de Lyon, 46, Allée d'Italie, 69364 Lyon, Cedex 07, France;

<sup>b</sup>Institute of Optics and Photonics, Shanghai Jiao Tong University, 1954, Hua-Shan Road, Shanghai 200030, P.R.China;

<sup>c</sup>Laboratoire de Photonique Quantique et Moléculaire, Ecole Normale Supérieure de Cachan, 94235 Cachan Cedex, France

**Abstract** The first-order nonlinear optical (NLO) hyperpolarizabilities  $\beta^{2D}$  of two-dimensional(2D)  $C_{2v}$  multipolar molecules were analyzed theoretically using additive model, in which the  $\beta^{2D}$  tensor was dissected into an additive term  $\beta^A$  and an interaction term  $\beta^I$ . Within the irreducible representation, the influence of substituents on the magnitudes of  $\beta^{2D}$ ,  $\beta^A$  and  $\beta^I$  was calculated based on a CNDO/S program for various series of  $C_{2v}$  molecules. The results showed that, the magnitude of  $\beta^I$  is within the range of 8 to 72%, and that the interactions are relatively larger in molecules **III** and in polyeno-multipolar molecules **V<sub>n</sub>**.

**Keywords:** first-order hyperpolarizabilities, multipolar molecules, additive model, irreducible tensor

## INTRODUCTION

Organic molecular materials become prominent candidates for NLO applications due to the large NLO hyperpolarizabilities, ultra fast NLO responses, low dielectric constants, and great flexibility for design and for molecular engineering [1,2]. Until now, most of the organic molecules developed for first-order NLO applications were designed as dipolar molecules, in which the  $\pi$ -electron system substituted by electron donor and acceptor groups played an essential role. Using the well-known two-level model, the first-order NLO properties of the rod-like molecules can be well predicted. The  $\beta_{xxx}$  component was found to be dominant, and all other components almost vanished. However, this approach limited the full implementation of the tensorial nature of  $\beta$ , and led to strongly polarization dependent systems, which may not optimize the properties for some NLO applications. In order to overcome these problems, the multipole concept was recently introduced for the design of more isotropic NLO chromophores in which the tensorial nature of  $\beta$  could be fully expressed [3-6]. As the effects of the molecular symmetry, the contribution of the off-diagonal components of  $\beta$  may be larger than the diagonal  $\beta_{xxx}$ , providing a new design of NLO molecular engineering.

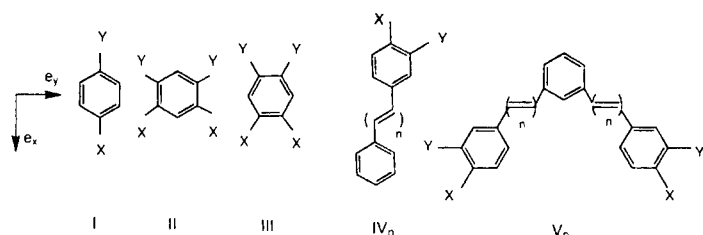


FIGURE 1 Structures of  $C_{2v}$  molecules and their parents. For molecules **II** and **III**,  $X$  is the acceptors  $\text{NO}_2$  or  $\text{CN}$ ,  $Y$  is the donors  $\text{NH}_2$ , or  $\text{N}(\text{Me})_2$ ; while for molecules  $\text{V}_n$ ,  $X$ ,  $Y$  are the donors  $\text{OMe}$  or  $\text{SMe}$ .

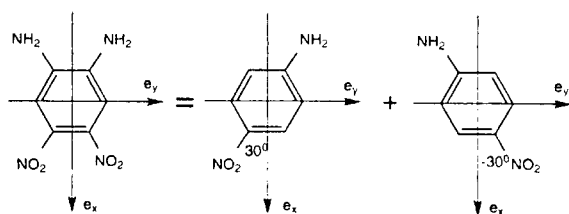


FIGURE 2 Decomposition of a  $C_{2v}$  molecule **III** into its parents, where the rotation angles  $\theta$  of the 1D units with respect to the  $x$  coordinate axis are  $\pm 30^\circ$ .

Conversely to the molecular engineering of dipolar systems, the prediction and understanding of NLO hyperpolarizabilities in multipolar system is more complex. In a recent paper, the additive model was introduced to explain the NLO properties of octupolar systems [7]. This model allows to evaluate the different contributions of hyperpolarizabilities to 2D molecules  $\beta^{2D}$  from the constituted 1D units, with the relationship  $\beta^{2D} = \beta^A + \beta^I$ , in which  $\beta^A$  is denoted as the additive term and  $\beta^I$  the interaction term. In this paper, we have extended this model to analyze more general multipolar  $C_{2v}$  molecules, as shown in Figure 1, where  $\beta_{J=1}$  is not vanished. Our purpose is to establish the relationship between the  $\beta^{2D}$  and  $\beta^{1D}$ , and to obtain the guidelines of predicting the relative first-order NLO properties for multipolar molecules from the NLO properties of 1D parents.

## Tensorial Analysis for $C_{2v}$ Molecules

According to the additive model, we can decompose a  $C_{2v}$  molecule into two 1D units, each of which has a rotation angle  $\pm 60^\circ$  (for **II** or  $\text{V}_n$ ),  $\pm 30^\circ$  (for **III**) with respect to the  $x$  coordinate axis, as shown in Figure 2. The tensorial rotation technique is employed to derive the expressions of  $\beta^A$  for  $C_{2v}$  molecules, the



additive term can be expressed as  $\beta_J^A = \sum_n \beta_J^{1D} \cos(J\theta)$ , where  $\theta$  is denoted as the rotation angle between  $x$  coordinate axis of 1D unit and that of the 2D molecule, and the summation takes over all 1D units [6]. For the case of nonresonant NLO interactions, we have  $\beta = \beta_{J=1} + \beta_{J=3}$ , thus:

$$\beta_{J=1}^A = \beta_{J=1}^{1D} [\cos \theta + \cos(-\theta)] = A \beta_{J=1}^{1D} \quad (1)$$

$$\beta_{J=3}^A = \beta_{J=3}^{1D} [\cos 3\theta + \cos(-3\theta)] = B \beta_{J=3}^{1D} \quad (2)$$

where  $A$ ,  $B$  are denoted as numeric coefficients. For the molecules **II** or **V<sub>n</sub>**,  $A = 1$ ,  $B = -2$ ; while for molecules **III**,  $A = \sqrt{3}$ ,  $B = 0$ . Introducing the expressions of  $\beta_{J=1}$  and  $\beta_{J=3}$  in the irreducible representation [6], we obtain:

$$\beta_{J=1}^A = \frac{3}{4} A \left[ (\beta_{xxx}^{1D} + \beta_{xyy}^{1D}) e_x + (\beta_{xxy}^{1D} + \beta_{yyx}^{1D}) e_y \right] (e_x \otimes e_x + e_y \otimes e_y) \quad (3)$$

$$\begin{aligned} \beta_{J=3}^A = & \frac{1}{4} B \left[ (\beta_{xxx}^{1D} - 3\beta_{xyy}^{1D}) e_x \otimes (e_x \otimes e_x - 3e_y \otimes e_y) \right. \\ & \left. + (\beta_{yyx}^{1D} - 3\beta_{xxy}^{1D}) e_y \otimes (e_y \otimes e_y - 3e_x \otimes e_x) \right] \end{aligned} \quad (4)$$

where  $e_x$  and  $e_y$  are the unit vectors of Cartesian coordinate axes. The  $x$  coordinate axis is set along the two-fold symmetric axis for all the  $C_{2v}$  molecules (**II**, **III** and **V<sub>n</sub>**) in the calculation of  $\beta_{ijk}$ , while it is set along the direction from donor to acceptor for the 1D parents (**I** and **IV<sub>n</sub>**). From the relationship of  $\|\beta^A\|^2 = \|\beta_{J=1}^A\|^2 + \|\beta_{J=3}^A\|^2$ , we obtain the norm of the additive term from Eqs. (3) and (4):

$$\begin{aligned} \|\beta^A\|^2 = & \frac{1}{4} \left[ 3A^2 (\beta_{xxx}^{1D} + \beta_{xyy}^{1D})^2 + 3A^2 (\beta_{xxy}^{1D} + \beta_{yyx}^{1D})^2 \right. \\ & \left. + B^2 (\beta_{xxx}^{1D} - 3\beta_{xyy}^{1D})^2 + B^2 (\beta_{yyx}^{1D} - 3\beta_{xxy}^{1D})^2 \right] \end{aligned} \quad (5)$$

The interaction term  $\|\beta^I\|$  is defined as  $\beta^I = \beta^{2D} - \beta^A$ , reflecting the interactions such as charge transfer or Coulombic between 1D units. It can be expressed as:

$$\begin{aligned} \beta_{J=1}^I = & \frac{3}{4} \left\{ [(\beta_{xxx}^{2D} + \beta_{xyy}^{2D}) - A(\beta_{xxx}^{1D} + \beta_{xyy}^{1D})] e_x \right. \\ & \left. + [(\beta_{xxy}^{2D} + \beta_{yyx}^{2D}) - A(\beta_{xxy}^{1D} + \beta_{yyx}^{1D})] e_y \right\} (e_x \otimes e_x + e_y \otimes e_y) \end{aligned} \quad (6)$$

$$\begin{aligned} \beta_{J=3}^I = & \frac{1}{4} \left\{ [(\beta_{xxx}^{2D} - 3\beta_{xyy}^{2D}) - B(\beta_{xxx}^{1D} - 3\beta_{xyy}^{1D})] e_x \otimes (e_x \otimes e_x - 3e_y \otimes e_y) \right. \\ & \left. + [(\beta_{yyx}^{2D} - 3\beta_{xxy}^{2D}) - B(\beta_{yyx}^{1D} - 3\beta_{xxy}^{1D})] e_y \otimes (e_y \otimes e_y - 3e_x \otimes e_x) \right\} \end{aligned} \quad (7)$$

Similarly, from the relationship  $\|\beta^I\|^2 = \|\beta_{J=1}^I\|^2 + \|\beta_{J=3}^I\|^2$ , we obtain the norm of the interaction term:

$$\begin{aligned} \|\beta^I\|^2 = & \frac{3}{4} \left\{ [(\beta_{xxx}^{2D} + \beta_{xyy}^{2D}) - A(\beta_{xxx}^{1D} + \beta_{xyy}^{1D})]^2 + [(\beta_{xxy}^{2D} + \beta_{yyx}^{2D}) \right. \\ & \left. - A(\beta_{xxy}^{1D} + \beta_{yyx}^{1D})]^2 \right\} + \frac{1}{4} \left\{ [(\beta_{xxx}^{2D} - 3\beta_{xyy}^{2D}) - B(\beta_{xxx}^{1D} - 3\beta_{xyy}^{1D})]^2 \right. \\ & \left. + [(\beta_{yyx}^{2D} - 3\beta_{xxy}^{2D}) - B(\beta_{yyx}^{1D} - 3\beta_{xxy}^{1D})]^2 \right\} \end{aligned} \quad (8)$$

The expressions of  $||\beta^A||$  and  $||\beta^I||$  given in Eqs. (5) and (8) are applicable for general 2D molecules other than  $C_{2v}$  symmetry by varying the coefficients  $A$  and  $B$ .

TABLE 1 The static first-order NLO hyperpolarizabilities  $\beta_{ijk}$  (unit:  $10^{-30}$  esu) for 1D molecules.

		$\beta_{xxx}^{1D}$	$\beta_{xyy}^{1D}$	$\beta_{yyy}^{1D}$	$\beta_{xyy}^{1D}$
X=NO <sub>2</sub> , Y=NH <sub>2</sub>	<b>I</b>	-9.8	0	0	1.8
X=NO <sub>2</sub> , Y=N(Me) <sub>2</sub>	<b>I</b>	-11.3	0	0	1.6
X=CN, Y=NH <sub>2</sub>	<b>I</b>	-4.8	0	0	0.6
X=CN, Y=N(Me) <sub>2</sub>	<b>I</b>	-10.3	0	0	0.8
X=OMe	<b>IV</b> <sub>1</sub>	-18.4	-0.8	-0.9	0.3
Y=OMe	<b>IV</b> <sub>2</sub>	-28.1	-3.6	-0.6	0.2
	<b>IV</b> <sub>3</sub>	-38.6	-6.9	-0.7	-0.6
	<b>IV</b> <sub>4</sub>	-48.7	-10.9	-1.1	-1.9
X=SMe	<b>IV</b> <sub>1</sub>	-29.7	-1.3	-1.2	-0.2
Y=OMe	<b>IV</b> <sub>2</sub>	-44.5	-4.5	-1.1	0.2
	<b>IV</b> <sub>3</sub>	-59.2	-8.6	-1.6	-0.7
	<b>IV</b> <sub>4</sub>	-70.9	-13.5	-1.3	-2.3
X=OMe	<b>IV</b> <sub>1</sub>	-16.0	-1.5	-2.2	-0.5
Y=SMe	<b>IV</b> <sub>2</sub>	-24.5	-3.9	-1.9	0.8
	<b>IV</b> <sub>3</sub>	-33.7	-6.8	-2.2	1.7
	<b>IV</b> <sub>4</sub>	-43.9	-10.6	-3.0	-3.6
X=SMe	<b>IV</b> <sub>1</sub>	-23.9	2.9	3.2	-1.9
Y=SMe	<b>IV</b> <sub>2</sub>	-35.0	6.2	3.3	-1.9
	<b>IV</b> <sub>3</sub>	-47.4	11.6	3.9	-3.6
	<b>IV</b> <sub>4</sub>	-78.2	15.3	4.3	-4.0

## RESULTS AND DISCUSSION

The method of molecular geometry optimization is based on the SYBYL software (from Tripos, USA), in which the MOPAC package and semi-empirical AM1/PM3 interface quantum calculation method are included [7]. All the first-order NLO hyperpolarizabilities  $\beta_{ijk}$  were calculated by a CNDO/S program as described in Ref. [8]. The values of static  $\beta_{ijk}$  for 1D and 2D molecules are collected in Table 1 and Table 2. From Eqs. (5) and (8), the corresponding magnitudes of the additive terms  $||\beta^A||$  and the interaction terms  $||\beta^I||$  were obtained for  $C_{2v}$  molecules **II**, **III** and **V<sub>n</sub>**, as shown in Table 2. In good agreement with the symmetry properties of various molecules, the off-diagonal components  $\beta_{yyy}^{1D}$ ,  $\beta_{xyy}^{1D}$  and  $\beta_{xyy}^{1D}$  are relatively much smaller than  $\beta_{xxx}^{1D}$  for 1D molecules **I** and **IV<sub>n</sub>**; while for the  $C_{2v}$  molecules, the  $\beta_{xyy}^{2D}$  components generally predominant with respect to  $\beta_{xxx}^{2D}$ . The structure **II** leads to higher magnitude of  $\beta^{2D}$  than that of structure **III** whatever the acceptor groups(NO<sub>2</sub> or CN).

From Table 2, we note that the  $||\beta^I||$  of molecules **III** are generally larger than the corresponding molecules **II**. Furthermore,  $||\beta^I||$  increases monotonically with the number of double bonds for each of the polyeno-multipolar series **V<sub>n</sub>**.

An example of the variations of the magnitude and direction of  $\beta^I$  in irreducible  $J = 1$  and  $J = 3$  space with the double bond  $n$  are illustrated in Figure 3. For all the molecules **II** and **III**, the value of  $||\beta^I||/||\beta^A||$  is within the range of 8-72%; while for molecules **V<sub>n</sub>** the range is within 16-52%. These percentages for the  $C_{2v}$  molecules are larger than that of the related octupolar  $C_{3h}$  molecules in Ref. [7], where the  $||\beta^I||/||\beta^A||$  is 20-30%.

TABLE 2 The static first-order NLO hyperpolarizabilities  $\beta_{ijk}$  (unit:  $10^{-30}$  esu) for 2D  $C_{2v}$  molecules, where  $||\beta^{2D}||$ ,  $||\beta^A||$  and  $||\beta^I||$  are the magnitudes of the 2D molecules, of the additive term and of the interaction term respectively,  $\Delta = ||\beta^I||/||\beta^A||$ .

		$\beta_{xxx}^{2D}$	$\beta_{xyy}^{2D}$	$  \beta^{2D}  $	$  \beta^A  $	$  \beta^I  $	$\Delta(\%)$
X=NO <sub>2</sub>	<b>II</b>	2.6	-9.0	15.8	16.7	1.4	8
Y=NH <sub>2</sub>	<b>III</b>	-6.7	1.0	6.2	12.0	8.6	72
X=NO <sub>2</sub>	<b>II</b>	-0.8	-9.8	17.0	18.2	2.0	11
Y=N(Me) <sub>2</sub>	<b>III</b>	-4.5	-4.3	8.6	14.5	8.1	56
X=CN	<b>II</b>	1.7	-6.7	11.7	7.5	4.4	59
Y=NH <sub>2</sub>	<b>III</b>	-4.3	-2.3	5.9	6.3	1.4	22
X=CN	<b>II</b>	0.8	-9.5	16.5	15.1	2.0	13
Y=N(Me) <sub>2</sub>	<b>III</b>	-7.5	-4.0	10.2	14.2	4.8	34
X=OMe	<b>V<sub>1</sub></b>	-1.3	-12.9	22.4	25.0	4.0	16
Y=OMe	<b>V<sub>2</sub></b>	-1.5	-19.2	33.3	39.0	12.5	32
	<b>V<sub>3</sub></b>	-1.3	-28.4	49.2	54.3	23.2	43
	<b>V<sub>4</sub></b>	-14.8	-34.6	61.7	69.8	33.3	48
X=SMe	<b>V<sub>1</sub></b>	-3.8	-25.0	43.5	39.1	7.4	19
Y=OMe	<b>V<sub>2</sub></b>	-5.9	-42.3	73.5	60.7	20.6	34
	<b>V<sub>3</sub></b>	-7.7	-53.5	93.0	81.3	32.2	40
	<b>V<sub>4</sub></b>	-9.3	-66.3	115.2	99.1	51.5	52
X=OMe	<b>V<sub>1</sub></b>	-2.7	-8.6	15.1	20.7	6.7	32
Y=SMe	<b>V<sub>2</sub></b>	-10.3	-14.7	27.5	35.6	14.9	42
	<b>V<sub>3</sub></b>	-14.8	-19.0	36.1	51.6	26.6	52
	<b>V<sub>4</sub></b>	-22.6	-24.6	48.2	61.3	32.0	52
X=SMe	<b>V<sub>1</sub></b>	-9.1	-13.3	24.8	29.8	8.6	29
Y=SMe	<b>V<sub>2</sub></b>	-17.0	-25.2	46.8	46.7	18.0	39
	<b>V<sub>3</sub></b>	-33.0	-36.6	71.5	66.5	37.4	56
	<b>V<sub>4</sub></b>	-53.0	-56.1	110.7	107.1	51.3	48

In summary, we provided a comprehensive analysis of the first-order NLO hyperpolarizabilities for multipolar  $C_{2v}$  molecules using an additive model based on CNDO/S calculations. We derived the expressions of  $||\beta^A||$  and  $||\beta^I||$  which is applicable to general 2D molecules. Different substituents were introduced to check the variations of  $||\beta^A||$  and  $||\beta^I||$ . It was found that,  $||\beta^I||/||\beta^A||$  is within the range of 8-72%, and that the interactions are relatively larger in molecules **III** and in polyeno-multipolar molecules **V<sub>n</sub>**.

*Acknowledgments.* One of the authors (X.Yang) is grateful for the financial supports from China Scholarship Council (CSC) and from Rhône-Alpes Region, France for his stay.

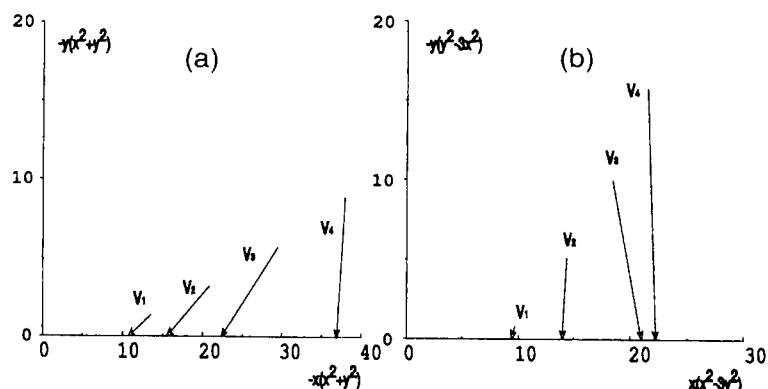


FIGURE 3 Variations of the magnitude and direction of the interaction term  $\beta^I$  (unit:  $10^{-30}$  esu) with the double bond  $n$  in irreducible representation, for the polyeno-multipolar molecules  $V_n$  with  $X = Y = \text{OMe}$ . (a)  $J = 1$  space; (b).  $J = 3$  space.

## References

- [1] J.Zyss, I.Ledoux, Molecular Nonlinear Optics: Materials, Physics and Devices, Academic Press, Boston, 1993.
- [2] D.S.Chelma, J.Zyss, Nonlinear Optical Properties of Organic Molecules and Crystals, Academic Press, New York, 1987.
- [3] J.Zyss, Nonlinear Optics 1 3 (1991).
- [4] J.Zyss, I.Ledoux, Chem. Rev. 94 77 (1994).
- [5] S.Brasselet, J.Zyss, J. Opt. Soc. Am. B 15 257 (1998).
- [6] J.Zyss, J. Chem. Phys. 98 6583 (1993).
- [7] C.Andraud, T.Zabulon, A.Collet, J.Zyss, Chem. Phys. 245 243 (1999).
- [8] C.Andraud, T.Brotin, C.Garcia, F.Pelle, P.Goldner, B.Bigot, A.Collet, J. Am. Chem. Soc. 116 2094 (1994).

## Molecular Engineering around Diaminobiphenyls for Optical Limiting at Visible Wavelengths

R. ANEMIAN<sup>a</sup>, C. ANDRAUD<sup>a</sup>, A. COLLET<sup>a</sup>, J.-M. NUNZI<sup>b</sup>,  
Y. MOREL<sup>c</sup>, P.L. BALDECK<sup>c</sup>

<sup>a</sup>Ecole Normale Supérieure de Lyon, Laboratoire de Stéréochimie et Interactions moléculaires, UMR 5532, 46, Allée d'Italie, 69364 Lyon Cedex 07, France; <sup>b</sup>CEA-LETI, DEIN-SPE, Groupe des Composants Organiques, 91191 Gif sur Yvette; <sup>c</sup>Laboratoire de Spectrométrie Physique, Université J. Fourier, UMR 5588, 38402 Saint Martin d'Hères, France

In this work, we have developed a molecular engineering strategy around the diaminobiphenyl **1** in order to design efficient nonlinear absorbers for optical limiting application in the visible range. Based on a photophysics engineering strategy, a significant improvement of efficiency is obtained by influencing the excited state dynamics. The role of the planarity of the conjugated system was also studied.

**Keywords** Optical limiting ; biphenyls

### INTRODUCTION

The development of high power tunable lasers couldn't be viewed without the performing of an efficient protection of vision sensors against damaged caused by an intense radiation. Optical devices limiting the laser

transmission fluence below the damage threshold at the sensor entrance permit to satisfy the above request [1]. Among the different phenomena which can be used, nonlinear absorption in organic materials initiated by a two-photon absorption step (TPA) followed by an excited state absorption step (ESA) appears as a promising limiting process [2-6]. In the case of a  $S_1$ - $S_n$  singlet transition and of an excited state relaxation faster than the laser pulse duration, the three photon absorption coefficient  $\alpha_3$  resulting from this two steps process can be described by the following equation [7] :

$$\alpha_3 = \frac{N}{V} f^6 \frac{\sigma_{TPA} \sigma_{1n} \tau_1}{2(\hbar\omega)^2} \quad (1)$$

where  $N/V$  is the concentration,  $\sigma_{TPA}$ , the two-photon absorption cross-section,  $\sigma_{1n}$ , the  $S_1$ - $S_n$  absorption cross-section,  $\tau_1$ , the lifetime of the state  $S_1$  and  $f$ , the local field factor. The optimization of  $\alpha_3$  requires the simultaneous optimization of all the parameters involved in Eq. (1).

From the tetraphenyl diamine (TPD) type dye **1**, which is already known for its promising properties for optical limiting in the visible range at the nanosecond regime [2], we developed a molecular engineering strategy based on both following directions : (i) influence of the conjugated system on the nonlinear absorption properties, (ii) role of the dynamics of the excited state on these properties. This was carried out respectively by the comparison of three-photon absorption (3-PA) properties of the molecule **1** with those of **4** and **5**, which bear the same donor group and differ by the charge transfer system (biphenyl vs fluorene or phenanthrene), and by the comparison of **1** with **2** and **3**, in which the roto-vibrational relaxation paths may be reduced (Figure 1).

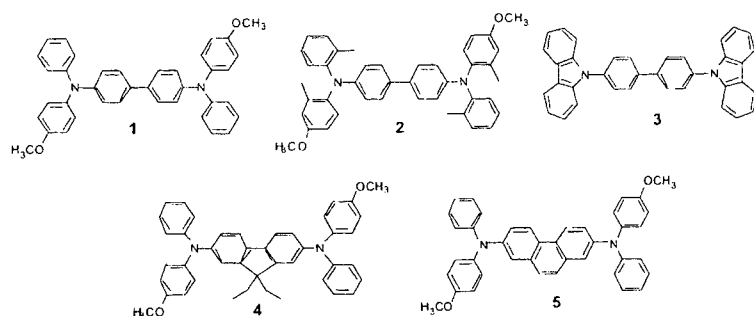


FIGURE 1 Molecular structures of studied systems

## EXPERIMENT

The three-photon absorption coefficient  $\alpha_3$  was measured from nonlinear transmission experiments using a collimated laser beam from a nanosecond optical parametric oscillator (OPO) pumped with the third harmonic of a Nd:YAG laser. The experimental setup was described elsewhere [8].

## RESULTS

### Linear absorption

The linear absorption spectra of compounds 1-5 show a strong UV transition satisfying our specification of linear transparency in the visible range ( $\lambda_{cut-off} \sim 420$  nm). A red shift is observed for molecules 4 and 5 with respect to 1 ( $\lambda_{max} = 374$  nm / 374 nm vs  $\lambda_{max} = 352$  nm respectively) (Table 1). This bathochromic effect is in good agreement with previous theoretical data [9]. As expected, the methyl substitution in 2 induces no perturbation on the conjugated system charge transfer with respect to 1, while the molecule 3 presents a linear absorption shifted towards the blue range with respect to 1.

Molecule	$\lambda_{0l}$ (nm)	$\lambda_{3-PA}$ (nm)	$\alpha_3^{max}$ (cm <sup>3</sup> GW <sup>-2</sup> )	$\alpha_3^{norm}$ (cm <sup>3</sup> GW <sup>-2</sup> )
<b>1</b>	352	535	4000 (265 g/l)	3000
<b>2</b>	350	535-585	9000-6000 (265 g/l)	7000-4500
<b>3</b>	320	490-600	1000-200 (30 g/l)	7000-1700
<b>4</b>	374	500 (s)	3000 (100g/l)	6000
<b>5</b>	365	475-615	1400-600 (100 g/l)	2800-1200

TABLE 1 Experimental data for **1-5** molecules : (a)  $\lambda_{0l}$  linear absorption wavelength; (b)  $\lambda_{3-PA}$  3-PA wavelength ; (c)  $\alpha_3^{max}$  3-PA coefficient at measurement concentration ; (d)  $\alpha_3^{norm}$  normalized 3-PA coefficient at 200 g/l.

#### Nonlinear absorption

All molecules **1-5** display similar broadband 3-PA spectra covering the visible range. Values of the 3-PA coefficient  $\alpha_3$  are summarized on Table 1 (maximum amplitudes reach 2000-7000 cm<sup>3</sup> GW<sup>-2</sup> for concentration of 200 g/l). The position and the magnitude of the resonance is sensitive to the nature of the molecule (Figure 2). Data must be discussed in regard to the structural modifications of each molecule with respect to **1**.

## DISCUSSION

#### Influence of the Excited State Properties

This effect can be seen from the properties comparison of **1** with those of **2** and **3**.

Molecules **1** and **2** present a similar linear absorption band centered around 350 nm, while that of **3** is shifted towards blue at 320 nm. A global enhancement of  $\alpha_3$  values is observed for **2** and **3** with a shift of the 3-PA spectrum of **3** towards blue range ; the other main difference in **2** and **3** 3-PA spectra is the narrowness of the bands. These effects were previously explained for **2** by a hindered rotation of peripheral rings due to the presence of the methyl groups [10] ; this interpretation was checked by S<sub>1</sub>-S<sub>N</sub> absorption spectroscopy and by the increase of the excited state lifetime



for **2**. The carbazole function in **3** induces a similar effect on 3-PA spectra than the methyl groups in **2**, with a shift of the bands due to a more efficient charge transfer phenomenon in **2** arising from the presence of the methoxy groups.

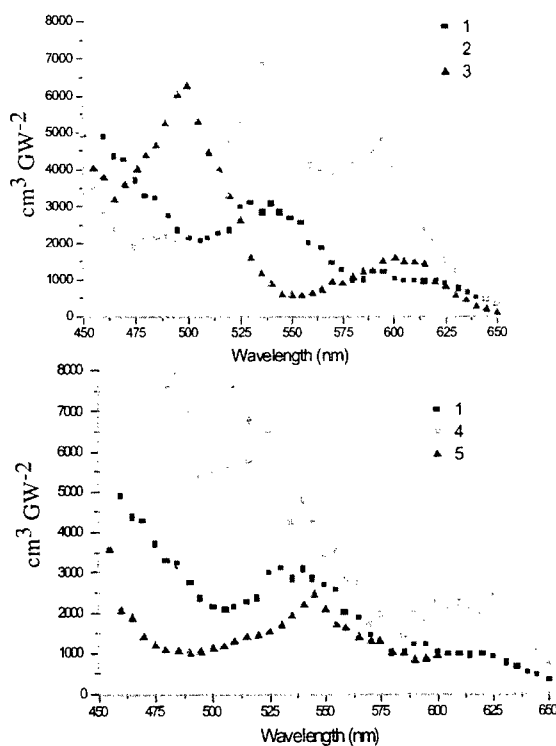


FIGURE 2 Normalized nonlinear absorption spectra of (a) **1-3** ; (b) **1, 4, 5**.

#### Influence of the Charge Transfer

This can be seen from the data comparison of **1** with those of **4** and **5**.

The quasi-planarity of molecules **4** and **5** induces an increase of the conjugation with respect to that of **1** [11] even though in **5** the conjugated system is very different from that of fluorene **4**, since electrons are delocalized over the three benzene rings ; this effect is reflected by the red shift of the linear absorption for these molecules with respect to **1**.

Unexpectedly, the effect of the planarity on the optical limiting properties leads to a shift of the 3-PA spectrum of **4** towards the blue range with an increase of the magnitude of  $\alpha_3$  ; in the case of the molecule **5**, no great difference is observed with respect to **1** for 3-PA properties, except sharper peaks.

Here, we have studied the 3-PA properties of compounds because of the immediate interest of nanoseconde time regime for optical limiting applications. For a better understanding these 3-PA spectra should be interpreted in the light of TPA and ESA spectra, since 3-PA spectra result from the product of the TPA and the ESA (Eq. (1)). These measurements are now in progress.

## CONCLUSION

In this paper, we developed a molecular engineering strategy to improve the optical limiting properties of **1**: (i) the optimization of the excited states dynamics by modifications of the peripheral benzene rings, (ii) the optimization of the conjugation by increasing the planarity of the molecule.

In the first case, the enhancement of the optical limiting properties could be readily interpreted in terms of an hindrance of the peripheral benzene ring rotation. In the second case, even though the  $\alpha_3$  coefficient seems to increase in the fluorene **4**, optical limiting properties were not improved, as expected, by a shift of the nonlinear absorption properties into the visible range.

## Acknowledgments

We are grateful to the Délégation Générale de l'Armement (DGA) for financial support. We also thank the Groupement de Recherche (GDR) "Matériaux et Fonctions de l'Optique Non Linéaire" for a fellowship for R.A.

## References

- [1] L.W. Tutt, T. F. Boggess, Prog. Quant Electr., **17**, 299 (1993)
- [2] J.E. Ehrlich, X.-L. Wu, I.-Y.S. Lee, Z.-Y. Hu, H. Röckel, S.R. Marder, J.W. Perry, Opt. Lett., **22**, 1843 (1997)
- [3] M. Albota; D. Beljonne; J.-L. Bredas; J.E. Ehrlich; J.-Y. Fu; A.A. Heikal, S.E. Hess; T. Kogej; M.D. Levin; S.R. Marder; D. McCord-Maughon; J.W. Perry, H. Röckel; M. Rumi; G. Subramaniam; W.W. Webb, X.-L. Wu; C. Xu, Science, **281**, 1653 (1998)
- [4] J.W. Perry, S. Barlow, J.E. Ehrlich, A.A. Heikal, Z.-Y. Hu, I.-Y.S. Lee, K. Mansour, S.R. Marder, H. Röckel, M. Rumi, S. Thayumanavan, X.-L. Wu, Nonlinear Optics, **21**, 225 (1999)
- [5] P.-A. Chollet, V. Dumarcher, J.-M. Nunzi, P. Feneyrou, P. Baldeck, Nonlinear Optics, **21**, 299 (1999)
- [6] C. Nguefack, T. Zabulon, R. Anémian, C. Andraud, A. Collet, S. Topçu, P.L. Baldeck, Nonlinear Optics, **21**, 309 (1999)
- [7] P.L. Baldeck, Y. Morel, C. Andraud, J.-F. Nicoud, A. Ibanez, Photonics Science News, **4**, 5 (1999)
- [8] P.-A. Chollet, V. Dumarcher, J.-M. Nunzi, P. Feneyrou, P. Baldeck, Nonlinear Optics, **21**, 299 (1999).
- [9] C. Andraud, R. Anémian, A. Collet, J.-M. Nunzi, Y. Morel, P. L. Baldeck, J. Opt. A : Pure and Applied Optics, **4** (July 2000, in press).
- [10] B. Paci, J.-M. Nunzi, R. Anémian, C. Andraud, A. Collet, Y. Morel, P. L. Baldeck, J. Opt. A : Pure and Applied Optics, **4** (July 2000, in press).
- [11] A torsional angle of 55° was calculated for **1**.

## **Theoretical investigation of the nonlinear circular dichroism in a liquid of chiral molecules**

F. Hache, M. C. Schanne-Klein, H. Mesnil  
Laboratoire d'Optique Quantique – CNRS/Ecole Polytechnique – 91128  
Palaiseau – France

Introducing nonlocal effects such as magnetic dipolar and electric quadrupolar ones in the time-dependent perturbation theory, we analyze the signature of optical activity in the nonlinear response of a liquid of chiral molecules. In particular, we show that such a liquid should display a nonlinear circular dichroism. Expressions for a three-level system are given.

**Keywords :** Chiral molecules; optical activity; nonlinear optics.

### **INTRODUCTION**

Liquids of chiral molecules have been investigated by optical methods for a long time, but only recently with techniques of nonlinear optics. Second-order processes (surface second harmonic generation) has been demonstrated [1,2], but third-order ones have not been studied yet. In this paper, we investigate such effects theoretically. In the next section, we extend the linear constitutive relations to the nonlinear regime and then apply the results to the special case of a two-level system. In the last section, we calculate the nonlinear circular dichroism (difference of absorption for a right and a left-circularly polarized light) that exists in liquids of chiral molecules described by a three-level system.

### **LINEAR AND NONLINEAR OPTICAL ACTIVITY**

Linear optical activity of an isotropic ensemble of chiral molecules is usually described in a phenomenological approach, by introducing

nonlocal contributions to the constitutive relations that connect the electric dipole  $\mu$  and the magnetic one  $m$  to the electric and magnetic fields [3]:

$$\mu = \alpha E - \beta \dot{B} \quad ; \quad m = \gamma \dot{E} \quad (1)$$

Another possibility is to introduce electric and magnetic susceptibilities in the frequency domain and to write the electric polarization and the magnetization as:

$$P = \chi^{ee} \cdot E + \chi^{em} \cdot B \quad ; \quad M = \chi^{me} \cdot E \quad (2)$$

The superscript *e* or *m* in the susceptibilities correspond to the occurrence of electric or magnetic fields in the processes. Connections of eqs (1) and (2) is straightforward by using the relation  $\dot{E} = -i\omega E$ . From the quantum expressions of  $\chi^{em}$  and  $\chi^{me}$  [4], it is easy to check the well-known relation  $\beta = \gamma$ . One should note that in eqs (1) and (2), no electric quadrupolar effect was taken into account. Such effects correspond to the same nonlocal approximation as magnetic terms, however, they are known to cancel out in an *isotropic* medium such as a liquid and don't contribute to the linear optical activity [4].

One can now wonder what happens when one considers the third-order nonlinear response (Kerr effect). In the local approximation, only the electric fields contribute and one has an extra nonlinear polarization that reads:

$$P^{NL} = \chi^{eeee} : EE^* E \quad (3)$$

When only one linearly-polarized light beam is present, one usually gathers  $EE^*$  in a term proportional to the light intensity *I* and replaces  $\alpha$  by  $\alpha_0 + \alpha_2 I$  in eq. (1)

What about the nonlocal contributions, responsible for the optical activity ? Considering those connected to the magnetic effects to the first order, one must introduce extra contributions to the nonlinear polarization:

$$P^{NL} = \chi^{eeem} : EE^* B + \chi^{eeme} : EB^* E + \chi^{emee} : BE^* E \quad (4)$$

and consider the existence of a nonlinear magnetization:

$$\mathbf{M}^{\text{NL}} = \chi^{\text{meec}} : \mathbf{E} \mathbf{E}^* \mathbf{E}. \quad (5)$$

In order to apprehend better the nonlinear response, let us consider a light beam propagating along the axis 3, linearly polarized along 1 ( $\mathbf{E} // 1$ ,  $\mathbf{B} // 2$  ( $= \mathbf{E}/c$ )). Utilizing the above expressions and the symmetry relations for isotropic third-rank tensors, one calculates the non-vanishing components of the extra nonlinear polarization and of the nonlinear magnetization:

$$\begin{aligned} P_2^{\text{NL}} &= \frac{1}{c} \{ \chi_{2112}^{\text{ceem}} + \chi_{2121}^{\text{cemc}} + \chi_{2211}^{\text{cmee}} \} |\mathbf{E}|^2 E \\ M_1^{\text{NL}} &= \chi_{1111}^{\text{meec}} |\mathbf{E}|^2 E \end{aligned} \quad (6)$$

According to these expressions, here again, the nonlinear effect can be described with intensity dependent parameters :  $\beta = \beta_0 + \beta_2 I$  and  $\gamma = \gamma_0 + \gamma_2 I$ , but in general, the nonlinear coefficients  $\beta_2$  and  $\gamma_2$  are not equal. This will be demonstrated in the next section.

Before going to a more precise calculation of the nonlinear susceptibilities, let us consider the contribution of the electric quadrupolar effects. One has to introduce the corresponding susceptibilities:

$$\begin{aligned} \mathbf{P}^{\text{NLQ}} &= \chi^{\text{eeqee}} : \mathbf{E} \mathbf{E}^* \nabla \mathbf{E} + \chi^{\text{eqeee}} : \mathbf{E} \nabla \mathbf{E}^* \mathbf{E} + \chi^{\text{eqeee}} : \nabla \mathbf{E} \mathbf{E}^* \mathbf{E} \\ \mathbf{Q}^{\text{NL}} &= \chi^{\text{qeeec}} : \mathbf{E} \mathbf{E}^* \mathbf{E} \end{aligned} \quad (7)$$

The quadrupolar susceptibilities introduced here are rank 5 tensors. They are symmetrical when interchanging the subscripts corresponding to the pair  $qe$  in the superscript as, by definition, the antisymmetric part can be cast in the magnetic response [5]. Furthermore, in an isotropic medium, only the components like  $\chi_{11123}$  (allowing permutation of the subscripts and interchanging of 1, 2, 3) are non vanishing. Owing to these properties, the only contribution to the nonlinear response for the previous beam propagating along the axis 3 is:

$$P_2^{\text{NLQ}} = \frac{i\omega}{c} \{ \chi_{21131}^{\text{eeqe}} - \chi_{21311}^{\text{eeqe}} + \chi_{23111}^{\text{eeqe}} \} |E|^2 E, \quad (8)$$

the nonlinear quadrupolarization, diagonal in an isotropic medium, being null in this configuration. The effect described by eq. 8 is formally non negligible, as electric quadrupolar and magnetic dipolar effects have generally the same order of magnitude. However, we will see in the next sections that in several pertinent cases, such contributions cancel out.

#### CALCULATION FOR A TWO-LEVEL SYSTEM

Let us consider now the particular case of a two-level system. If we suppose that the photon energy is close to the resonance, one can keep only the resonant terms in the quantum expression of the nonlinear susceptibilities. A complete calculation following that of ref. [6] shows that one has:

$$\chi_{1122}^{\text{meee}} = \chi_{1221}^{\text{meee}} = \chi_{1212}^{\text{meee}} = \frac{1}{3} \chi_{1111}^{\text{meee}} \quad (9)$$

Similar expressions can be obtained for the other nonlinear susceptibilities, and one gets the following relations:

$$\chi_{ijkl}^{\text{meee}} = -\chi_{lijk}^{\text{emec}} = \chi_{klij}^{\text{ecme}} = -\chi_{jkli}^{\text{ecem}}, \quad (10)$$

where  $ijkl = 1122, 1221$  or  $1212$ . The change of signs is connected to the occurrence of the magnetic interaction in an absorption or an emission process. As for quadrupolar effects, they can be shown to vanish identically in that particular case. According to these relations, one has:

$$\beta_2 \propto \frac{1}{3} \chi_{1111}^{\text{meee}} \text{ and } \gamma_2 \propto \chi_{1111}^{\text{meee}} \quad (11)$$

This gives a direct evidence that  $\beta_2$  is not equal to  $\gamma_2$  in the general case. This feature is due to the fact that by writing eqs 4 and 5,

one artificially separates the four magnetic contributions which have in reality equivalent effects.

### NONLINEAR CIRCULAR DICHROISM

It is possible to exploit the previous formalism by taking into account the four contributions as a whole. Utilizing the expressions of the nonlocal susceptibilities and calculating directly the energy transfer between the light and the molecules  $Im(\mathbf{E}^* \cdot \mathbf{P} + \mathbf{B}^* \cdot \mathbf{M})$  for right and left circularly polarized beams, one can check that the nonlinear absorptions are different. The expression of the corresponding nonlinear circular dichroism is [6]:

$$NLCD = \frac{64}{45\hbar^3} R_{01} |\mu_{01}|^2 E^3 B \frac{T_1 \Gamma^2}{[(\omega_{10} - \omega)^2 + \Gamma^2]^2} \quad (12)$$

where  $R_{01} = Im(\boldsymbol{\mu}_{01} \cdot \mathbf{m}_{10})$  is the rotational strength and E and B the electric and magnetic fields, the other symbols having their usual meaning. This corresponds to the signature of the Kerr effect in the circular dichroism.

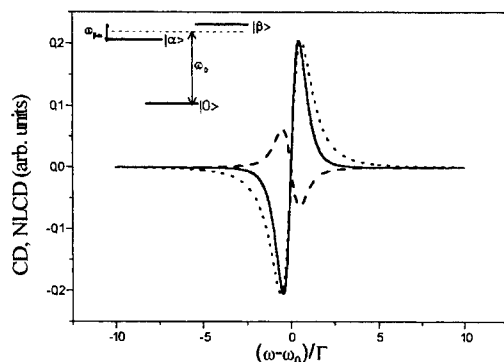


FIGURE 1 Linear (CD) and nonlinear (NLCD) circular dichroism for the three-level system depicted in the inset as a function of the frequency detuning (see text).

Description of a chiral molecule by a unique two-level system is however not adequate as it cannot satisfy the sum rule that states that



the total rotational strength must be equal to zero. We have therefore considered a three-level system as depicted in the inset of figure 1, supposing that the two transitions have opposite rotational strengths. The corresponding circular dichroism is displayed in fig. 1 (dotted line). Complete calculation of the nonlinear response [6] shows that this system behaves as the superposition of the two two-level systems  $|0\rangle \rightarrow |\alpha\rangle$  and  $|0\rangle \rightarrow |\beta\rangle$ , giving rise to a nonlinear circular dichroism (solid line in fig. 1). Beside this contribution, there exists another one connected to the mixing of the two transitions (dashed line). This latter is however much weaker by a factor  $1/\Gamma T_1$  and accessible only in experiments where several beams are present, as in a degenerate-four-wave-mixing one.

## CONCLUSION

In this paper, we have investigated the nonlinear optical activity of a liquid of chiral molecules. In particular, we have shown that there exist a nonlinear circular dichroism for molecules described by a three-level system. The expression of this NLCD (eq. 12) is very close of the usual expression of the absorption saturation for a two-level system. The major difference is the factor  $R_{01}|\mu_{01}|^2$  instead of the usual  $|\mu_{01}|^4$ . This remark allows to predict that the NLCD compared to the change in absorption due to saturation will be of the same order of magnitude as the CD compared to the absorption. Such effects should therefore be accessible in experiments such as pump-probe ones.

## References

- 1- M. Kauranen, T. Verbiest, J. J. Maki, and A. Persoons, *J. Chem. Phys.* **101**, 8193 (1994)
- 2- J. P. Byers, H. I. Yee, and J. M. Hicks, *J. Chem. Phys.* **101**, 6233 (1994)
- 3- W. Kauzmann, *Quantum Chemistry* (Academic Press, New-York, 1957)
- 4- G. H. Wagnière, *Linear and Nonlinear Optical Properties of Molecules* (VCH, Basel, 1993)
- 5- P. S. Pershan, *Phys. Rev.* **130**, 919 (1963)
- 6- F. Hache, H. Mesnil, and M. C. Schanne-Klein, *Phys. Rev.* **B60**, 6405 (1999)

## **New Properties of COANP and PNP Compounds: Optical Limiting Effect**

NATALIE V. KAMANINA\*, LEV N. KAPORSKII

Vavilov State Optical Institute, St.-Petersburg, 199034, Russia

\* E-mail: kamanin@ffm.ioffe.rssi.ru

Optical limiting effect in 2-cyclooctylamino-5-nitropyridine (COANP)-polyimide thin films doped with C<sub>70</sub> fullerene has been studied using second harmonic of pulsed Nd-laser. The optical limiting observed in these films has been caused by an additional interaction between electron subsystems of COANP and fullerene molecules. It has been established that the films investigated could be applied for limiting laser energy density of more than 5-6 J cm<sup>-2</sup>. The first optical limiting results for 2-(n-prolinol)-5-nitropyridine (PNP) structure doped with fullerene C<sub>60</sub> and C<sub>70</sub> has been presented for comparison.

**Keywords** fullerene, COANP, PNP, optical limiting

## **INTRODUCTION**

Due to a wide use of laser techniques in optoelectronics, the protection of sensors and eyes from laser beams is the burning problem. It has stimulated a search for highly nonlinear materials as media for optical power limiting. In the last decade it has been a common practice to carry out the optical limiting (OL) using the fullerenes as effective sensitizers for organic photosensitive systems [1-6].

Nonlinear properties of COANP and PNP films grown from supercooled melt are well known [7-10]. These systems show a large

second-order nonlinear optical response and are of highly delocalized  $\pi$ -electron states. Their unique properties can be modified by doping with dye, in particular, it was shown for COANP compound in the paper [11]. Recently we have first investigated COANP-toluene solution doped with fullerenes of  $C_{60}$  and  $C_{70}$  [12]. We have determined the OL level and shown these structures could be applied for limiting of high laser power in the visible spectral range.

In the present paper the optical limiting effect has been investigated in COANP-polyimide thin films doped with  $C_{70}$  fullerene. The first OL experiments for PNP structure doped with fullerenes of  $C_{60}$  and  $C_{70}$  have been presented for comparison. The potentialities of the systems studied for their applications in visible and IR spectral ranges have been discussed.

## EXPERIMENT

COANP and PNP thin films doped with fullerenes have been studied. 2.5% and 5% solutions of COANP and PNP in 1,1,2,2-tetrachloroethane were used. The  $C_{60}$  and  $C_{70}$  concentrations were varied from 0.1 wt.% to 5 wt.%. Non-photosensitive polyimide 81A was used as a film-forming base. 1-3  $\mu\text{m}$  thick COANP- and PNP-polyimide films were spun on glass substrates.

The second harmonic (532 nm) of a pulsed Nd-YAG laser was applied as a radiation source. The experimental setup was identical to that of paper [13]. A pulsewidth was 15 ns and a laser spot on the sample surface was 3-3.5 mm in diameter. Energies of the beams incident on the sample and s transmitted through it were measured. A set of light filters was used to vary the incident beam energy. OL experiments were carried out together with spectroscopic measurements using a Perkin-Elmer Lambda 9 instrument in the wavelength range 200-3000 nm.

## RESULTS and DISCUSSION

A dependence of the output energy ( $E_{\text{out}}$ ) on the input one ( $E_{\text{in}}$ ) is shown in Fig. 1 for fullerene-doped COANP samples.

The optical limiting effect is observed for all fullerene-doped samples at  $E_{\text{in}}$  more than 600-700 mJ, corresponding to the incident

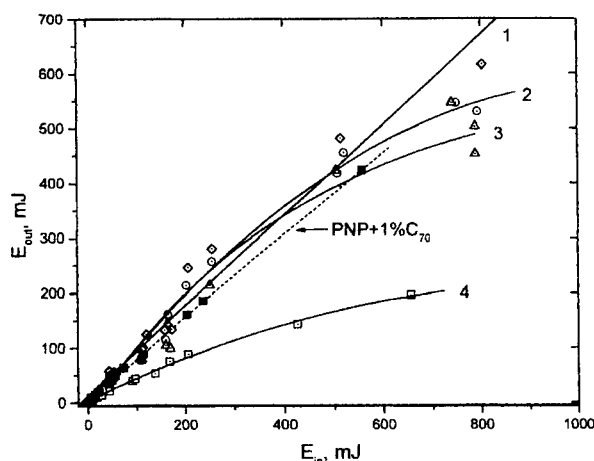


FIGURE 1 Dependence of  $E_{out}$  on  $E_{in}$  for the COANP-polyimide structure with the  $C_{70}$  concentration: 1 – 0; 2 – 0.5 wt.%; 3 and 4 – 5 wt.%. The relation between COANP and polyimide was 1:1 (curves 1-3) and 2:1 (curve 4). The dashed line indicates the dependence for the fullerene-doped PNP structure.

energy density of  $5\text{--}6\text{ J}\cdot\text{cm}^{-2}$ . A difference in transmission between samples 2 and 3 is determined by the fullerene concentration. However, the difference between samples 4 and 3 is twice as more at the same fullerene concentration. The result is caused not only by a more COANP concentration, but a complex formation between a donor fragment of the COANP molecule and fullerene as well.

The following evidences can be used. First, electron affinity of fullerene is 2.65 eV, that is more than the one for acceptor fragments of most organic molecules. Specifically, the acceptor fragment of the COANP molecule is a  $\text{NO}_2$  group, which is bound to the donor fragment by the benzene ring. For a separate  $\text{NO}_2$  molecule or radical, electron affinity is 2.3 eV, while the  $\text{NO}_2$  group bound to the benzene ring has electron affinity is only 0.54 eV [14], that is, it is smaller than the one of fullerene by a factor of 4. Therefore, fullerenes are more effective acceptors and hence they are likely to dominate over intramolecular acceptor fragment of COANP. Second, we have investigated absorption spectra, which show that the fullerene-containing samples are of very different spectral features from the

COANP-polyimide and polyimide-C<sub>70</sub> systems. There are two additional absorption peaks at 490 nm and 810-820 nm. As well known, the bathochromic shift testifies a change of molecule structure and that it is likely to determine the possibility of complex formation between fullerene and the donor fragment of COANP. Third, dark and photoconductivities of fullerene-doped samples are one order of magnitude more than those of fullerene-free sample. The conductivity was measured under bias voltage of 20-60 V. Fourth, mass-spectrometric experiments revealed two peaks of fullerene-COANP structure. Mass-spectrometric data for different thin fullerene-polymer systems allow the low- and high temperature stages to be attributed to a release of randomly dispersed fullerene molecules from the polymer matrix and to sublimation of fullerene molecules from small-crystalline phase, respectively [15]. The low temperature peak observed in the fullerene-COANP system supports the complex formation process in the organic system doped with fullerenes.

The dependence of the output energy ( $E_{out}$ ) on the input one ( $E_{in}$ ) is shown in Fig. 2 for fullerene-doped PNP samples. The OL effect is observed under larger optical power density than that for fullerene-doped COANP compounds. Perhaps, the more OL level in the PNP system testifies that the binding between fullerenes and the PNP is stronger in comparison with the COANP system.

Moreover, these results correlate with phase transition temperatures in the systems investigated. As shown by differential scanning calorimetry technique [16], the fullerene introduction influences these temperatures in the COANP compounds, decreasing, for example, the melting temperature. Recently we have found a similar effect of fullerenes on the phase transition temperatures in the PNP compounds. However, the temperature changes for PNP took place at higher temperatures than those for COANP [17]. This fact points to higher levels of thermal excitation in PNP. Therefore, the input beam energy applied in the present work is unlikely to be sufficient in order to reveal OL peculiarities in the fullerene-doped PNP compounds.

It should be remarked that future study of the fullerene-doped PNP structure is required to determine a nature of this binding. Here we have to say some words about spectral peculiarities of the system studied that we should take into account to the OL explanation. Our spectroscopic measurements showed that fullerene-doped PNP system has the absorption band extended from 2700 to 3200 nm. Therefore, the wavelength of laser excitation does not exactly coincide with the

absorption spectra of fullerene-doped PNP structure. This fact actuates the OL effect investigation in IR range.

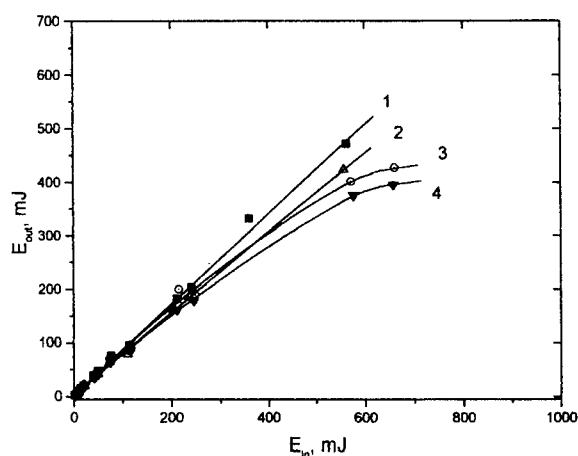


FIGURE 2 Dependence of  $E_{out}$  on  $E_{in}$  for the PNP-polyimide structure with the fullerene concentration: 1 – 0; 2 – 1 wt.%  $C_{70}$ ; 3 — 1 wt.%  $C_{60}$ ; and 4 — 1 wt.% ( $C_{60}+C_{70}$ ). The relation between PNP and polyimide was 1:1.

## CONCLUSION

In conclusion, the optical limiting effect and spectral peculiarities have been studied in the fullerene-doped COANP and PNP systems. The films obtained are of spectral features in visible and IR-region and can be applied as effective non-linear absorber of high laser power density more than  $5\text{-}10\text{ J cm}^{-2}$ .

## Acknowledgements

The authors wish to thank to Prof. B.V. Kotov, Dr. N.A. Vasilenko (Karpov Research Physical-Chemical Institute, Moscow, Russia), Drs. A.O. Pozdnyakov, O.F. Pozdnyakov and B.P. Redkov (Ioffe Physico-Technical Institute, St. Petersburg, Russia), Drs. A. Leyderman and A. Barrientos (University of Puerto-Rico, Mayagüez, PR, USA) for their help in this study. This work was partially supported by the Russian National Program "Optoelectronic and Laser Technologies".

### References

- [1] A.Kost, L.Tutt, M.B.Klein, T.K.Dougherty, W.E. Elias, Opt. Lett., **18**, 334 (1993).
- [2] M. Ouyang, K.Z. Wang, H.X. Zhang, Z.Q. Xue, C.H. Huang, D. Qiang, Appl. Phys. Lett. **68**, 2441 (1996).
- [3] K. Hosoda, K. Tada, M. Ishikawa, and K. Yoshino, Jpn. J. Appl. Phys. Part 2, **36**, L372 (1997).
- [4] V.P. Belousov, I.M. Belousova, V.G. Bespalov, V.P. Budtov, V.M. Volynkin, V.A. Grigor'ev, O.B. Danilov, A.P. Zhevlakov, A.G. Kalintsev, A.N. Ponomarev, S.A. Tul'skii, E.Yu. Yutanova, J. Opt. Technol., **64**, 870 (1997).
- [5] N.V. Kamanina, L.N. Kaporskii, B.V. Kotov, Opt. Commun. **152**, 280 (1998).
- [6] Z. Lu, S.H.Goh, S.Y.Lee, X.Sun, W.Ji, Polymer, **40**, 2863 (1999).
- [7] Ch. Bosshard, K. Sutter, P. Günter, G. Chapuis, J. Opt. Soc. Am. B, **6**, 721 (1989).
- [8] G. Lahajnar, I. Zupancic, R. Blinc, A. Zidansek, R. Kind, M. Ehrensperger, Z. Phys., **B95**, 243 (1994).
- [9] A. Leyderman, Y. Cui, Opt. Lett., **23**, 909 (1998).
- [10] Y.Cui, J.Wu, N.Kamanina, A.Pasaje, A.Leyderman, A.Barrientos, M.Vlasse and B.G.Penn, J. Phys. D: Appl. Phys., **32**, 3215 (1999).
- [11] K. Sutter, J. Hulliger, P. Gunter, Solid State Commun., **74**, 867 (1990).
- [12] N.V. Kamanina, L.N. Kaporskii, A. Barrientos, A. Leyderman, Proceed SPIE, **3939** (2000), to be published.
- [13] N.V. Kamanina, Opt. Commun. **162**, 228 (1999).
- [14] L.V. Gurvich, G.V. Karachevtsev, V.N. Kondrat'ev, Yu.A. Lebedev, V.A. Medvedev, V.K. Potapov, Yu.S. Khodeev, Energies of Chemical Bond Breaking, Ionization Potentials And Electron Affinity, Nauka, Moscow, 1974 [in Russian].
- [15] A.O. Pozdnyakov, O.F. Pozdnyakov, B.P. Redkov, V.N. Zgonnic, E.Yu. Malenevskaya, L.V. Vinogradova, B.M. Ginzburg, Tech.Phys.Lett., **22**, 759 (1996).
- [16] N. Kamanina, A. Barrientos, A. Leyderman, Y. Cui, V. Vikhnin, M. Vlasse. Mol. Mater. (2000) (to be published).
- [17] Y.Cui, J.Wu, N.Kamanina, A.Pasaje, A.Leyderman, A.Barrientos, M.Vlasse and B.G.Penn. J. Phys. D: Appl. Phys., **32**, 3215 (1999).

## Optical Limiting Effect in Polymer Organic Systems

NATALIE V. KAMANINA\*, LEV N. KAPORSKII

Vavilov State Optical Institute, St. Petersburg, 199034, Russia

\*E-mail: kamanin@ffm.ioffe.rssi.ru

Optical limiting effect in thin fullerene-doped polyimide films has been investigated under the second harmonic of a pulsed Nd-YAG laser. The malachite green and coumarin dyes have been applied as alternative polyimide matrix impurities. The optical limiting effect has been observed in all fullerene-doped and dye-doped systems, with the most optical limiting in polyimide simultaneously doped with fullerene and dye. The laser radiation has been attenuated at least by the factor 10-25. The Förster model has been used to interpret the experimental results. The optical limiting data for fullerene-doped polyimide-chloroform solutions have been mentioned for comparison.

**Keywords** polyimide; fullerene; optical limiting

## INTRODUCTION

Recent investigations of fullerene-doped toluene solutions performed by L. Tutt and A. Kost [1] have shown that solid films are desirable for many optical limiting applications. Since that time polymer systems doped with fullerenes have been wide investigated. The authors of paper [2] studied mechanisms of the optical limiting in polymethyl methacrylate doped with C<sub>60</sub>. They also determined the effect threshold and compared the results with the data obtained for the fullerene solution in toluene. In publication [3] a new complex based on thin



films of bicyanovinylpyridine- $C_{60}$  was synthesized. A bistability effect was observed in this system. Fullerenes were introduced into polysilanes [4], resulting in a photoconductivity change. The results on  $C_{60}$  and  $C_{70}$  introduction in polyvinyl carbazole were shown in paper [5]. The authors of paper [6] discussed a mechanism of the photoinduced charge transfer in polyvinyl carbazole doped with  $C_{60}$ . Optical limiting effect was found in thin films of  $C_{60}$ -polymethyl methacrylate and in  $C_{60}$ - $SiO_2$ -sol-gel matrix [7]. Holograms were also recorded in these media. The bathochromic shift in thin films of fullerene-doped photosensitive polyimides and first optical limiting experiments in them were presented in paper [8]. New benzylaminofullerene compound and copolymers based on it were synthesized [9]. An optical limiting behavior in the energy-dependent transmission of these systems were found. Therefore, the investigations have clearly demonstrated that fullerenes are a promising sensitizer for photosensitive polymer systems, which may be used as effective laser media for the sensor and eye protection.

In the present paper the optical limiting (OL) effect along with spectral properties has been studied in the fullerene-doped and fullerene-dye-doped polyimides films. Potentialities of the laser valves based on fullerene-doped and fullerene-dye-doped polyimides, which are capable of operating at a laser power density level of more than  $1.5 \text{ J cm}^{-2}$  over visible and near IR spectral ranges, have been discussed.

## EXPERIMENT

The thin polymer films based on 6.5 wt.% 6B polyimide solution in 1,1,2,2-tetrachloroethane (TCIE) were investigated. The general formula of the aromatic polyimide was described in paper [10]. The solution was doped with the fullerene mixture (in ratio  $C_{60}:C_{70} = 87:13$ ) or/and dyes. Malachite green and coumarin dyes were used as alternative impurities. The fullerene concentration was varied from 0.15 wt.% to 0.5 wt.%. It should be mentioned that fullerenes are of relatively high solubility (about  $5.3 \text{ mg mL}^{-1}$  for  $C_{60}$ ) in TCIE. The polyimide films were spun on the glass substrates coated with transparent indium-tin-oxide contacts. The sample thickness was about  $1.5 \text{ }\mu\text{m}$ . 0.5-1 wt.% polyimide solutions in chloroform with various fullerene concentration were prepared for comparative investigations.

The experimental setup for the optical limiting investigations was shown in paper [11]. The second harmonic (532 nm) of a pulsed Nd-YAG laser with a pulsewidth of 15 ns was applied as a radiation source. It should be noticed that the absorption spectrum of fullerene-polyimide system is overlapped with the fluorescence spectrum of malachite green and coumarin at the wavelength of the excitation radiation. The passive modulation was performed with a LiF crystal. Energies of the laser pulses incident on the sample and of the laser pulses transmitted through it were measured. A set of light filters was used to vary the incident beam energy. Spectroscopic measurements were carried out with a Perkin-Elmer Lambda 9 instrument in the wavelength range 200-3000 nm.

## RESULTS and DISCUSSION

Optical limiting was detected in all fullerene-doped structures with the effect level depending on the dopant concentration. The dependence of the output energy ( $E_{out}$ ) on the input energy ( $E_{in}$ ) is shown in Fig. 1 for fullerene-doped polyimide films.

As shown before, fullerenes sensitized the internal photoelectric effect in the molecular media with the donor-acceptor complexes efficiently [12]. The behavior observed is very neatly explained by following structural molecular characteristics. Low ionization potential of the donor fragment (triphenylamine) in the polyimide molecule and its spatial structure make possible an efficient charge transfer between triphenylamine and the fullerene molecule. The necessary condition for the transfer is to align the molecular planes in parallel, what provides the largest overlapping the electron densities of molecular orbitals. The shapes of  $C_{60}$  and  $C_{70}$  molecules are similar to soccer and rugby balls, respectively. On exciting, triphenylamine fragment of the polyimide molecule undergoes a conformational transformation from the neutral tetrahedral form to the ionized planar one. This effect, along with less dimensions of the triphenylamine fragment (0.5 nm) than those of the fullerene molecule (~0.65-0.8 nm), causes aligning their molecular planes in parallel. Therefore, OL effect in the fullerene-doped systems may be explained not only by the traditional conversion of the unexcited fullerene molecule to the excited state after absorption a quantum of light at  $\lambda=532$  nm [13], but by an additional interaction between fullerene and donor fragment of polyimide molecule or dye as

well. The absorption cross section for the new donor-acceptor complex of fullerene and triphenylamine was more than that for intramolecular polyimide complexes by the factor of 300 at  $\lambda = 530$  nm [12].

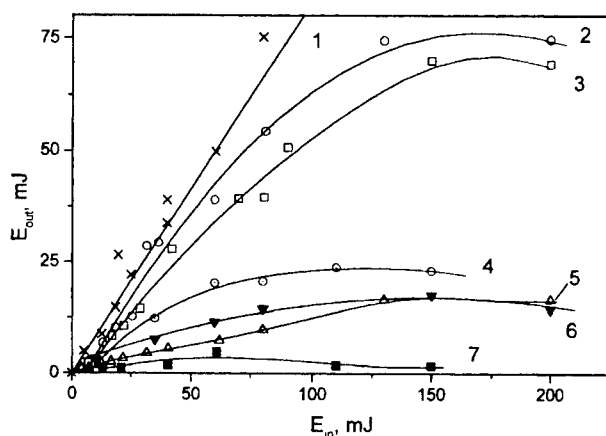


FIGURE 1 A dependence of the output energy ( $E_{out}$ ) on the input energy ( $E_{in}$ ) in films: (1) Pure polyimide (6.5 wt.% in TCIE); (2) polyimide with the 0.5 wt.% fullerene mixture; (3) polyimide with the 2 wt.% fullerene mixture; (4) polyimide with 0.5 wt.% malachite green; (5) polyimide film with 0.15 wt.% malachite green and the 0.5 wt.% fullerene mixture; (6) polyimide film with 0.2 wt.% coumarin; (7) polyimide with 0.2 wt.% coumarin and the 0.5 wt.% fullerene mixture.

The most OL was observed in the polyimide structure doped with fullerene and dyes simultaneously (Fig. 1, curves 5 and 7). Since the absorption spectrum of the fullerene-polyimide system is overlapped with the fluorescence spectrum of malachite green and coumarin at the excitation wavelength (532 nm), resonance conditions are fulfilled in the polyimide-dye-fullerene structure in accordance with the Förster mechanism [14]. The overlapping of the spectra points to the possibility to overlap the electron shells of the dye and fullerene molecules. Therefore, the free electron exchange between dye (as donor) and fullerene (as acceptor) provides the favorable conditions for the charge transfer complex formation. It should be noticed that electron affinity for the diimide fragment of the polyimide molecule is 1.12-1.46 eV, while it is 1.6-1.7 eV for malachite green and 2.65 eV for  $C_{60}$ .

Possibilities for the complex formation of fullerene with donor fragment of polyimide molecule have been discussed above. The dye introduction makes the process complicated. The optical limiting investigation allows multi-step interaction to be revealed in the multi-component system.

The fullerene-dye-polyimide systems have near-linear transmission till 50 mJ (Fig. 1, curve 7) and till 125 mJ (Fig. 1, curve 5). When the fullerenes and the complexes included them are activated the transmission decreases. The value of the input energy, at which optical limiting begins in the fullerene-dye-polyimide system, can be estimated. The saturation starts at  $E_{in} \geq 50$  mJ (Fig. 1, curve 7) and at  $E_{in} \geq 125$  mJ (Fig. 1, curve 5). Because the spot diameter of laser beam was 3-3.5 mm, the radiation energy density was 0.5 and 1.5 J·cm<sup>-2</sup>, respectively. Thus, the laser radiation was attenuated by the factor of 10 (Fig. 1, curve 5) and of ~25 (Fig. 1, curve 7). At the same time, the attenuation was 2-3 times and 4-8 times for the fullerene-polyimide structure and dye-polyimide, respectively.

It should be mentioned an additional complex formation evidence, namely, the appearance of peak in IR spectral range near 1405-1407 nm. This peak is associated with neither fullerene nor dye components. It is a manifestation of structural changes in the system investigated. The first OL experiments using the absorption in this spectral range was made by means of an iodine-laser at  $\lambda=1315$  nm with pulsewidth 30 ns. The results testify effective OL with the level of about 1.1 J·cm<sup>-2</sup> and the attenuation factor of 3.5.

It should be noticed somewhat less OL was observed in the fullerene-doped polyimide-chloroform solution. This result was determined by the cluster formation causing fluctuations of a solution density. The fluctuations resulted in irregular irradiation absorption across the beam diameter.

## CONCLUSION

In conclusion, OL effect has been investigated in the fullerene-doped polyimide systems. The largest OL was shown in the polyimide simultaneously doped with fullerene and dye. It was established the fullerene-dye-polyimide system could be applied for limiting power density of more than 1.5 J·cm<sup>-2</sup>. In this case the laser radiation was

attenuated at least by the factor of 10-20. The peculiarities observed may be explained in the Förster model framework.

### Acknowledgements

The authors wish to thank Prof. B.V. Kotov and Dr. N.A. Vasilenko (Karpov Research Physical-Chemical Institute, Moscow) for helpful discussions and Prof. I.M. Belousova and Dr. A.P. Zhevlakov (St.-Petersburg Institute for Laser Physics) for help in experiment at  $\lambda=1315$  nm. This work was partially supported by the Russian National Program "Optoelectronic and Laser Technologies".

### References

- [1] L.W.Tutt, A.Kost, Nature, **356**, 225 (1992).
- [2] A.Kost, L.Tutt, M.B.Klein, T.K.Dougherty, W.E. Elias, Opt. Lett., **18**, 334 (1993).
- [3] M.Ouyang, K.Z.Wang, H.X.Zhang, Z.Q.Xue, Appl. Phys. Lett., **68**, 2441 (1996).
- [4] K.Hosoda, K.Tada, M.Ishikawa, K.Yoshino, Jpn. J. Appl. Phys., **36**, L372 (1997).
- [5] Y.Wang N.Herron, J.Casper, Mater. Sci. Eng. B, **19**, 61 (1993).
- [6] A.Itaya, I.Suzuki, Y.Tsuboi, H.Miyasaka, J. Phys. Chem. B, **101**, 5118 (1997).
- [7] V.P.Belousov, I.M.Belousova, V.P.Budtov, V.V.Danilov, O.B.Danilov, A.G.Kalintsev, A.A.Mak, J. Opt. Technol., **64**, 1081 (1997).
- [8] N.V.Kamanina, L.N.Koporskii, B.V.Kotov, Opt. Commun., **152**, 280 (1998).
- [9] Z.Lu, S.H.Goh, S.Y.Lee, X.Sun, W.Ji, Polymer, **40**, 2863 (1999).
- [10] B.M.Rumyantsev, V.I.Berendyaev, N.A.Vasilenko, S.V.Malenko, B.V.Kotov, Polym. Sci. **A39**, 506 (1997).
- [11] N.V.Kamanina, Opt. Commun. **162**, 228 (1999).
- [12] Y.A.Cherkasov, N.V.Kamanina, E.L.Alexandrova, V.I.Berendyaev, N.A.Vasilenko, B.V.Kotov, Proceed. SPIE **3471**, 254 (1998).
- [13] S.Couris, E.Koudoumas, A.A.Ruth, S.Leach, J. Phys. B: At. Mol. Opt. Phys., **28**, 4537 (1995).
- [14] T. Förster, Disc. Farad. Soc., **27**, 7 (1959).

### ***In-situ* Observation of Thermochromic Behavior in Merocyanine J-aggregate Monolayers Using the Multipurpose Nonlinear Optical Microscope**

NORITAKA KATO\*, KENTARO SAITO\*, and YOSHIAKI UESU\*\*\*

\*Department of Physics,

\*\*Advanced Research Institute for Science and Engineering,  
Waseda University, 3-4-1 Okubo, Shinjuku-ku, Tokyo 169-8555, Japan.

We found the reversible thermochromic transition between different J-aggregate states of merocyanine dye (MD) monolayer on the subphase, which contains two kinds of counter-ions;  $\text{Cd}^{2+}$  and  $\text{Mg}^{2+}$ . This transition is induced by the mutual recombination of  $\text{Mg}^{2+}$  and  $\text{Cd}^{2+}$  to MD molecules, and the absorption band of the aggregate (J-band) at 620 nm in low temperature phase changes drastically to 595 nm in high temperature phase. From the in-situ observation using the multipurpose nonlinear optical microscope, it was revealed that this phenomenon can be exploited for controlling not only the J-band but also the size and the optical second harmonic activity of J-aggregate domain.

**Keywords** merocyanine dye, J-aggregate, monolayer at the air-water interface, thermochromism, multipurpose nonlinear optical microscope

### **INTRODUCTION**

The assembly of dye molecules often exhibits its absorption band different from that of monomer dye molecules as a result of the optical transition dipole moment interaction among the molecules. J-aggregate, which is one kind of the assembly, is characterized by Stokes-shift free fluorescence and sharp and red-shifted absorption band compared to

that of monomer dye molecules, and receiving much attention as a candidate of new nonlinear optical devices due to its large optical nonlinearity and fast decay of excited state [1]. The optical properties such as J-aggregate absorption band (J-band) are affected by the cohered structure; e.g. the arrangement manner of the dye molecules [1] and the degree of crystallinity [2,3]. Therefore, if the structure can be controlled by the external forces, the technique would be quite useful for fabricating high quality nonlinear optical devices or new structure-organized molecular devices [4-7]. In this report, we report the novel thermochromic transition between different J-aggregate states of amphiphilic merocyanine dye (MD) molecules (FIG. 1(a)) at the air-water interface. The phenomenon would provide potential application to various optical devices.

MD molecules form the two-dimensional J-aggregate crystallites (JC) on the aqueous subphase [8-10], and JC possesses the optical second harmonic (SH) activity as a result of the alignment of molecular dipole moment along the specific direction in JC [11]. The formation of JC depends on the ionic species contained in the subphase as a counter-ion for MD molecules [12]. On the subphase containing  $Mg^{2+}$ , J-band appears at 620 nm, and on the subphase containing  $Cd^{2+}$ , at 595 nm (FIG. 1(a)). When we use the binary counter-ion subphase which contains both  $Mg^{2+}$  and  $Cd^{2+}$ , the transition between the J-band at 620 and 595 nm occurs at definite temperature (FIG. 1(b)). In-situ observation using the multipurpose nonlinear optical microscope was performed to clarify changes in morphology and SH-activity.

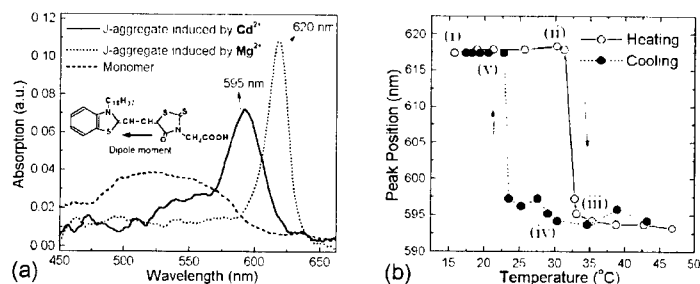


FIGURE 1 (a) indicates constitutional formula of MD molecule and absorption spectra of the monomer and JC states of MD molecules on the subphase containing  $Mg^{2+}$  or  $Cd^{2+}$ . The surface densities of molecules are not equal in these cases. (b) indicates the thermal hysteresis loop of the J-band position of the MD monolayer on the binary counter-ion subphase.

## EXPERIMENTAL

The binary counter-ion subphase is the aqueous solution of 0.5 mmol/l mixture of  $\text{MgCl}_2$  and  $\text{CdCl}_2$ , with 0.05 mmol/l  $\text{NaHCO}_3$  for stabilizing the pH at about 7. The molar fraction of  $\text{MgCl}_2$  to  $\text{CdCl}_2$  is 80 %. An experimental dish with  $\sim 3$  cm diameter is used as a trough.

The MD/arachidic acid (AA) mixed monolayer on the subphase was observed by M-NLOM [9,10]. AA was mixed for stabilizing the monolayer and the molar fraction of AA to MD was 60%. M-NLOM enables us to observe SH and fluorescence (FL) images as well as the FL, absorption and reflection (RF) spectra at the same part of the monolayer. Excitation wavelengths for SH and FL are 1064 and 532 nm, respectively. Fluences of each beams are less than 10 and 0.001  $\text{mJ/mm}^2$  per pulse, respectively. Though JA exhibits FL band, we preferentially used SH images to avoid the photo-bleaching of JA, because the SH signal can be excited by the beam far from the JA absorption. During the observation, RF spectra were measured to monitor the J-band. Details of the optical set-up are indicated in our previous papers [9,10].

## RESULTS AND DISCUSSIONS

From the measurement of the absorption spectrum change of MD monolayer on the binary counter-ion subphase as a function of subphase temperature, we obtained the thermal hysteresis loop of the J-band peak position (FIG. 1(b)). After spreading MD molecules on the binary counter-ion subphase at  $16^\circ\text{C}$ , the JC exhibits 620 nm band. During the increase of the subphase temperature, the 620 nm band remains with almost no shift of the peak wavelength up to  $32^\circ\text{C}$ , where it suddenly disappears and the 595 nm band raises. Up to  $48^\circ\text{C}$ , the 595 nm band keeps its profile unchanged. On cooling, the 595 band disappears and the 620 band is restored at  $23^\circ\text{C}$ . The isosbestic point was observed at about 605 nm. This phenomenon was observed to be reversible for several cycles. From the fact that the spectrum shape of the J-band of each phase corresponds exactly to that induced by  $\text{Mg}^{2+}$  or  $\text{Cd}^{2+}$  (FIG. 1(a)) and this transition did not occur on the subphase which containing single kind of counter-ion, this thermochromism originates in the mutual recombination of  $\text{Mg}^{2+}$  and  $\text{Cd}^{2+}$  with MD molecules. The change in the J-band is attributed to changes of aggregate structure and the number of cooperating molecules.



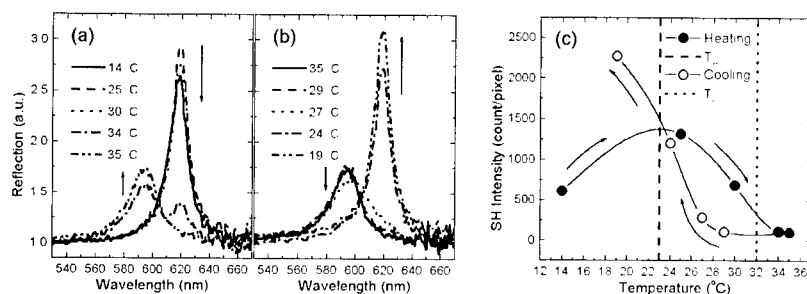
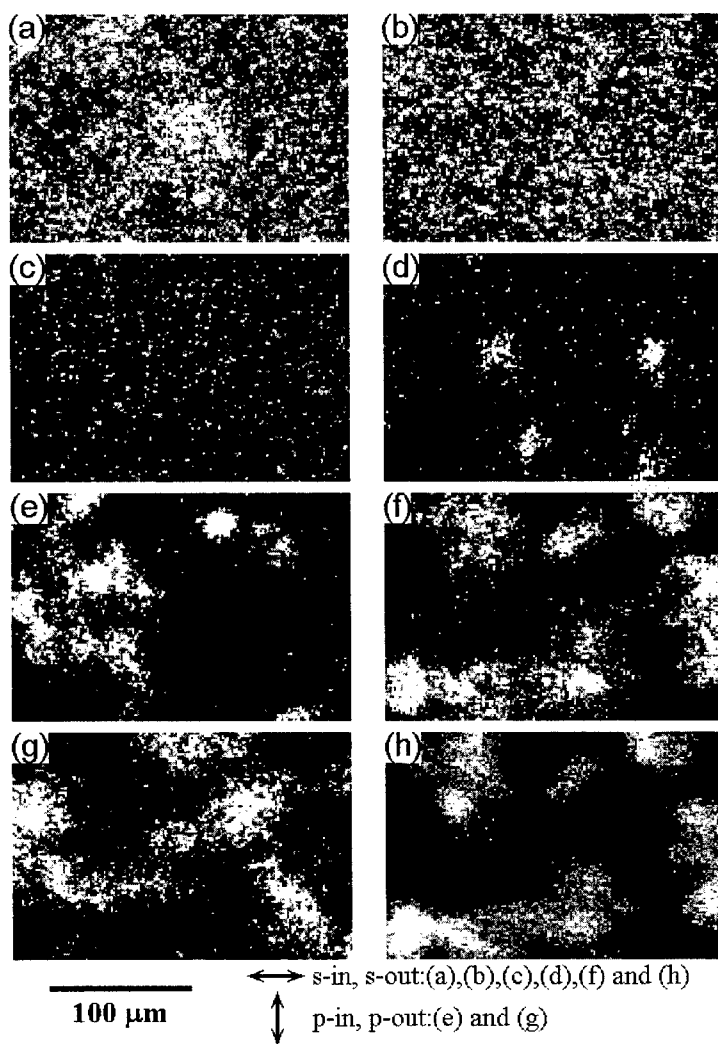


FIGURE 2 (a) and (b) indicate the change of RF spectra during the thermochromic transition on heating and cooling, respectively. (c) indicates the hysteresis of the averaged SH intensity during the transition. Dotted and dash lines indicate the transition points of heating and cooling processes determined by the hysteresis in FIG. 1(b).

RF spectra and SH images of the MD/AA mixed monolayer during the thermochromic transition are shown in FIG. 2(a) and (b), and FIG. 3, respectively. The observed temperatures are indicated in FIG. 1(b). FIG. 3(a) shows the SH image at 14°C (point (i) in FIG. 1(b)), where the bright region indicates the strong SH signal. The image shows no polarization dependence. Similar SH images were obtained up to 30°C (FIG. 3(b), and point (ii)). In this temperature range, JC are quite small ( $\sim 1 \mu\text{m}$ ) and distribute at random. Above the transition point (32°C) determined by the hysteresis in FIG. 1(a), almost no SH signal is observed. However, the RF spectrum at 34°C (FIG. 2 (a)) indicates the coexistence of low and high temperature phases. The SH image at 35°C (point (iii)) is shown in FIG. 3(c). The decrease of the SH signal is attributed to the smallness of JC ( $< 500 \text{ nm}$ ), which makes the macroscopic symmetry of the specimen centro-symmetric. Then the subphase is cooled. The small SH-active islands of about  $10 \mu\text{m}$  begin to appear from 29°C. The SH image at 27°C (point (iv)) is shown in FIG. 3(d) and (e). Islands in s-polarized image (d) are not observed in p-polarized one (e). This indicates that the each island is the uniform JC. Also, these images show the nucleation and growth process of highly SH-active regions in weak SH-active high temperature phase. This is the typical first-order phase transition. Finally, large SH-active domains ( $> 30 \mu\text{m}$ ) are observed at 19°C (point (v)) as shown in FIG. 3(f) and (g). The contrast of the image is reversed by alternating the polarization direction. This also means that each domain consists of one uniform JC. FIG. 3 (h) shows the FL image of JC taken under the same condition as



in (f). Coincidence between (h) and (f) confirms that the SH signals in (f) originates in JC. Note that the JA domain size in FIG. 3(f) and (g) becomes much larger than the initial state in FIG. 3(a). This is caused by the re-crystallization through the phase transition. FIG. 2(c) shows the change in SH intensity which is the intensity sum of the s- and p-polarized SH images with same size as shown in FIG. 3. After an increase of the intensity, it decreases before the transition point from 620 to 595 nm band on heating. This comes from the shrinking of highly SH-active JC in low temperature. On cooling, the intensity increases before the transition point due to the growth of highly SH-active islands in low temperature phase, and finally the intensity becomes much stronger than the initial state. This is due to the enlargement of the JC and the improvement of its crystallinity.

In the summary, we showed the structural phase transition of MD J-aggregate at the air-water interface, which is induced by the mutual recombination of different counter-ions with MD molecules. The phase transition is accompanied by the discrete change of absorption spectrum. Therefore, the phenomenon provides potential applicability to several kinds of optical device such as optical memory.

## References

- [1] J-Aggregates, T. Kobayashi (World Scientific, Singapore, 1996).
- [2] H. Fidder, J. Knoester & D. A. Wiersma, J. Chem. Phys., **95**, 7880 (1991).
- [3] E. O. Potma & D. A. Wiersma, J. Chem. Phys., **108**, 4894 (1998).
- [4] C. Ishimoto, H. Tomimura & J. Seto, Appl. Phys. Lett., **49**, 1677 (1986).
- [5] K. Minoshima, M. Taiji, A. Ueki, K. Miyano & T. Kobayashi, Nonlinear Optics, **14**, 39 (1995).
- [6] S. Özçelik, I. Özçelik & D. L. Akins, Appl. Phys. Lett., **73**, 1949 (1998).
- [7] E. I. Mal'tsev, D. A. Lypenko, B. I. Shapiro, M. A. Bruseatseva, V. I. Berendyaev, B. V. Kotov & A. V. Vannikov, Appl. Phys. Lett., **73**, 3641 (1998).
- [8] N. Kato, K. Saito & Y. Uesu, Thin Solid Films, **388** 5 (1999).
- [9] N. Kato, K. Saito, H. Aida & Y. Uesu, Chem. Phys. Lett., **312**, 115 (1999).
- [10] N. Kato, K. Saito & Y. Uesu, Ferroelectrics, inprint.
- [11] K. Kajikawa, H. Tekezoe & A. Fukuda, Chem. Phys. Lett., **205**, 225 (1993).
- [12] M. Yoneyama, T. Nagao & T. Murayama, Chem. Lett., 397 (1989).

## Semi-classical modeling of medium effects on NLO molecular properties

PETER MACAK<sup>a</sup>, YI LUO<sup>a</sup>, PATRICK NORMAN<sup>b</sup>, HANS ÅGREN<sup>a</sup>

<sup>a</sup>*Division of Theoretical Chemistry, Royal Institute of Technology, S-100 44 Stockholm, Sweden*

<sup>b</sup>*Department of Physics and Measurement Technology, Linköping University, S-581 83 Linköping, Sweden*

The solute nonlinear optical properties are shown to be quite ambiguous in definition. Connections between different conventions are presented. A general local field factor, differing from the commonly used Lorentz-Lorenz factor, is described. A simplified semi-classical approximation provides reliable results for systems as large as conjugated polymers and fullerenes.

**Keywords:** solvent effects, NLO, local field factors, conjugated polymers, fullerenes

### Introduction

The development of theoretical models simulating effects of a molecular environment on linear and nonlinear, optical, properties is well motivated by the fact that by far the most commonly available experiments are those conducted in the liquid or condensed phase. To accurately describe such effects in the liquid phase poses a theoretically intriguing problem and many models of today are simplified by employing a cavity, embedded in a dielectric continuum, in which one, or possibly a few, molecules are placed, so-called *reaction field* models [1]. These reaction field models have been incorporated into many electronic structure methods and studied for many years [1].

### Solute NLO properties

The molecular nonlinear optical properties are defined by the Taylor expansion of the total dipole moment in orders of the strength of a perturbing field  $\mathbf{F}$

$$\mu_i^{tot} = \mu_i + \alpha_{ij}F_j + \frac{1}{2}\beta_{ijk}F_jF_k + \frac{1}{6}\gamma_{ijkl}F_jF_kF_l + \dots \quad (1)$$

In the absence of the external field  $\mathbf{F}^E$  the solute dipole moment  $\mu^{sol}$  of the molecule gives rise, in the dipolar approximation, to the *initial*

reaction field  $\mathbf{F}^{\text{R}_0}$

$$F_i^{\text{R}_0} = f_{ij}^{\text{R}} \mu_j^{\text{sol}}, \quad (2)$$

$$\mu_j^{\text{sol}} = \mu_j + \alpha_{jk} F_k^{\text{R}_0} + \frac{1}{2} \beta_{jkl} F_k^{\text{R}_0} F_l^{\text{R}_0} + \dots, \quad (3)$$

where  $\mu, \alpha, \beta, \dots$  are the gas phase dipole moment, polarizabilities and hyperpolarizabilities of the molecule, and  $\mathbf{f}^{\text{R}}$  is the reaction field factor tensor.

In the presence of an external field  $\mathbf{F}^{\text{E}}$  the induced dipole moment can be expanded in terms of different fields which can easily lead to confusion in the definition of molecular properties in solution. In the literature, three different fields, namely the *external* Maxwell field  $\mathbf{F}^{\text{E}}$ , the *cavity* field  $\mathbf{F}^{\text{C}}$  and the *local induced* field  $\mathbf{F}^{\text{L}_1}$  have been used, which lead to *effective*, *cavity* and *local* field properties respectively [2]

$$F_i = \begin{cases} F_i^{\text{E}} & \rightarrow \text{effective properties} \\ F_i^{\text{C}} & \rightarrow \text{cavity field properties} \\ F_i^{\text{L}_1} & \rightarrow \text{local field properties} \end{cases}. \quad (4)$$

*Local field properties* (LFP) are the properties that can be expressed in terms of a perturbation expansion in the *initial reaction field*  $\mathbf{F}^{\text{R}_0}$

$$\begin{aligned} \alpha_{ij}^{\text{L}_1}(-\omega; \omega) &= \alpha_{ij}(-\omega; \omega) + \beta_{ija}(-\omega; \omega, 0) F_a^{\text{R}_0} \\ &+ \frac{1}{2} \gamma_{ijab}(-\omega; \omega, 0, 0) F_a^{\text{R}_0} F_b^{\text{R}_0} + \dots, \end{aligned} \quad (5)$$

$$\beta_{ijk}^{\text{L}_1}(-2\omega; \omega, \omega) = \beta_{ijk}(-2\omega; \omega, \omega) + \gamma_{ijka}(-2\omega; \omega, \omega, 0) F_a^{\text{R}_0} + \dots, \quad (6)$$

$$\gamma_{ijkl}^{\text{L}_1}(-3\omega; \omega, \omega, \omega) = \gamma_{ijkl}(-3\omega; \omega, \omega, \omega) + \delta_{ijkla}(-3\omega; \omega, \omega, \omega, 0) F_a^{\text{R}_0} + (7)$$

where  $\mathbf{F}^{\text{R}_0}$  is determined from Eqs. (2) and (3). It is these properties that experimentalists usually refer to as solute properties.

*Cavity field properties* (CFP) are on the other hand properties that usually come out of theoretical calculations. Self-consistent reaction field methods, which incorporate the induced reaction field in the unperturbed part of the Hamiltonian rather than as a perturbation, provide solute properties belonging to this category. Starting from the general expansion of the dipole moment, the following connection to the *local field properties* can be derived [2]

$$\alpha_{ij}^{\text{C}}(-\omega; \omega) = l_{ia}^{\omega} \alpha_{aj}^{\text{L}_1}(-\omega; \omega), \quad (8)$$

$$\begin{aligned}
\beta_{ijk}^C(-2\omega; \omega, \omega) &= l_{ic}^{2\omega} l_{ja}^\omega l_{kb}^\omega \beta_{cab}^{L_1}(-2\omega; \omega, \omega), \\
\gamma_{ijkl}^C(-3\omega; \omega, \omega, \omega) &= l_{id}^{3\omega} l_{ja}^\omega l_{kb}^\omega l_{lc}^\omega \gamma_{dabc}^{L_1}(-3\omega; \omega, \omega, \omega) \\
&\quad + \beta_{ija}^{L_1}(-3\omega; \omega, 2\omega) f_{ab}^{R\omega} \beta_{bkl}^C(-2\omega; \omega, \omega) \\
&\quad + \beta_{ika}^{L_1}(-3\omega; \omega, 2\omega) f_{ab}^{R\omega} \beta_{bjl}^C(-2\omega; \omega, \omega) \\
&\quad + \beta_{ila}^{L_1}(-3\omega; \omega, 2\omega) f_{ab}^{R\omega} \beta_{bjk}^C(-2\omega; \omega, \omega) \quad (10)
\end{aligned}$$

where  $l_{ij}^{n\omega} = \delta_{ij} + f_{ia}^{Rn\omega} \alpha_{aj}^C(-n\omega; n\omega)$ .

### Semiclassical model

Expressing *cavity field properties* in terms of *gas phase properties* from equations (5)-(7) and (8)-(10) would lead to rather complicated formulas. However, using the classical Onsager expression for the energy of the solvated molecule [1] one can under certain approximations derive a simplified set of expressions [3]

$$\mu_i^{\text{sol}} = \mu_i + \mu_m f_{mn}^R \alpha_{ni}, \quad (11)$$

$$\alpha_{ij}^C = \alpha_{ij} + \alpha_{im} f_{mn}^R \alpha_{nj} + \mu_m f_{mn}^R \beta_{nij}, \quad (12)$$

$$\beta_{ijk}^C = \beta_{ijk} + \alpha_{im} f_{mn}^R \beta_{njkl} + \alpha_{jm} f_{mn}^R \beta_{nik} + \alpha_{km} f_{mn}^R \beta_{nij} + \mu_m f_{mn}^R \gamma_{nij}, \quad (13)$$

$$\begin{aligned}
\gamma_{ijkl}^C &= \gamma_{ijkl} + \alpha_{im} f_{mn}^R \gamma_{njkl} + \alpha_{jm} f_{mn}^R \gamma_{nikl} + \alpha_{km} f_{mn}^R \gamma_{nijl} + \alpha_{lm} f_{mn}^R \gamma_{nijk} \\
&\quad + \beta_{ijm} f_{mn}^R \beta_{nkl} + \beta_{ikm} f_{mn}^R \beta_{njl} + \beta_{ilm} f_{mn}^R \beta_{njkl} + \mu_m f_{mn}^R \delta_{nijkl}^e. \quad (14)
\end{aligned}$$

The reliability of a semi-classical solvation model for optical properties of molecules in solutions have been examined for molecules with small, medium and large size[3].

Using these semiclassical relations for electronic properties similar relations for vibronic contributions to the properties can be derived [3]. Another possibility is to reformulate the above semiclassical equations in terms of total properties instead of pure electronic properties.

### Effective properties

A real experimental measurement is carried out with respect to the external field  $F^E$  which corresponds to the *effective properties*. Obviously, the connection to the *effective properties* is different for *local field properties* and *cavity field properties* which means that different *local field factors* have to be used. For *local field properties* we have [2]

$$\alpha_{ij}^E(-\omega; \omega) = l_{ia}^\omega f_{ab}^{C\omega} \alpha_{bj}^{L_1}(-\omega; \omega), \quad (15)$$

$$\beta_{ijk}^E(-2\omega; \omega, \omega) = l_{ia}^{2\omega} l_{jb}^{\omega} f_{bc}^{C\omega} l_{kd}^{\omega} f_{de}^{C\omega} \beta_{ace}^{L_1}(-2\omega; \omega, \omega), \quad (16)$$

$$\begin{aligned} \gamma_{ijkl}^E(-3\omega; \omega, \omega, \omega) &= l_{ia}^{3\omega} l_{jb}^{\omega} f_{bc}^{C\omega} l_{kd}^{\omega} f_{de}^{C\omega} l_{lf}^{\omega} f_{fg}^{C\omega} \gamma_{aceg}^{L_1}(-3\omega; \omega, \omega, \omega) \\ &+ [\beta_{ica}^{L_1}(-3\omega; \omega, 2\omega) \beta_{bde}^C(-2\omega; \omega, \omega) \\ &+ \beta_{ida}^{L_1}(-3\omega; \omega, 2\omega) \beta_{bce}^C(-2\omega; \omega, \omega) \\ &+ \beta_{iea}^{L_1}(-3\omega; \omega, 2\omega) \beta_{bcd}^C(-2\omega; \omega, \omega)] f_{ab}^{R2\omega} f_{cj}^{C\omega} f_{dk}^{C\omega} f_{el}^{C\omega}, \end{aligned} \quad (17)$$

which shows that part of the effects from the induced reaction field have to be incorporated into the *local field factors*. For the *cavity field properties* we have

$$\alpha_{ij}^E(-\omega; \omega) = f_{aj}^{C\omega} \alpha_{ia}^C(-\omega; \omega). \quad (18)$$

$$\beta_{ijk}^E(-2\omega; \omega, \omega) = f_{ja}^{C\omega} f_{kb}^{C\omega} \beta_{iab}^C(-2\omega; \omega, \omega), \quad (19)$$

$$\gamma_{ijkl}^E(-3\omega; \omega, \omega, \omega) = f_{ja}^{C\omega} f_{kb}^{C\omega} f_{lc}^{C\omega} \gamma_{inbr}^C(-3\omega; \omega, \omega, \omega). \quad (20)$$

which manifests that the whole effect of the total reaction field is accounted for in the properties rather than in the *local field factors*.

## Applications

### Conjugated polymers

*Ab initio* calculations of properties of isolated molecules together with the SC model for solvent effects enabled a treatment of oligomers with a sufficient number of repeat units to study the solvent effects on their static polarizabilities and hyperpolarizabilities in the polymer limit [3]. The solvent induced property changes were found to decrease rapidly with increasing chain length (see Fig.). The optical properties of very long oligomers in solution tend to approach the values in gas phase. The solvent effects have shortened the saturation lengths.

All advanced theoretical calculations for hyperpolarizabilities of polyenes have predicted much shorter saturation lengths than those obtained from experiment. Since for a perfectly ordered molecule the solvent effects can only enlarge the gap between theory and experiments, the most possible explanation for this difference is the conformational disorder of the molecules in the measurements, as already pointed out in previous studies.

### Fullerenes

From the point of view of medium effects, the amorphous thin fullerene films can be considered as randomly oriented molecular systems, similar

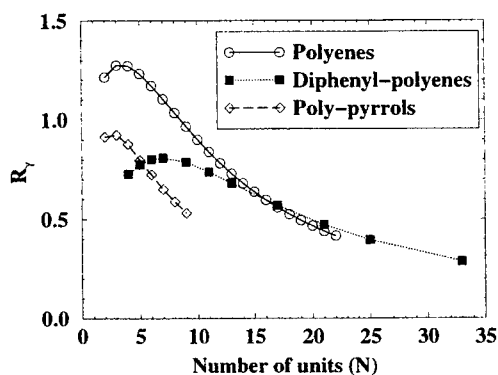


Figure 1. Length dependence of relative change of hyperpolarizability per unit,  $R_\gamma$ , for trans-polyenes, diphenyl-polyenes, and poly-pyrrols in strong polar solution,  $\epsilon=78$ .

to pure liquids. Consequently, the inter-molecular interaction effects on the nonlinear optical response can be simulated using the reaction field model.

For the case of the molecules that do not possess a permanent dipole moment, which is the case for fullerenes, the Onsager-Böttcher relation [1] can be utilized together with the help of expressions (8)-(10) to provide a general local field factor (without any reference to the cavity radius) for  $\chi^{(3)}(-3\omega; \omega, \omega, \omega)$  [4]

$$L_{\text{eff}}^{(3)}(\epsilon^\omega, \alpha(-\omega; \omega)) = \frac{(2\epsilon^{3\omega} + 1)(\epsilon^{3\omega} - 1)}{4\pi N \bar{\alpha}(-3\omega; 3\omega) 3\epsilon^{3\omega}} \left( \frac{\epsilon^\omega - 1}{4\pi N \bar{\alpha}(-\omega; \omega)} \right)^3. \quad (21)$$

where  $\alpha$  the polarizability in gas phase. Such a factor obviously differs from the frequently used Lorentz-Lorenz L-L local field factors

$$L_{\text{L-L}}^{(3)} = l_{\text{L-L}}^{\omega\omega} l_{\text{L-L}}^{\omega_1} l_{\text{L-L}}^{\omega_2} l_{\text{L-L}}^{\omega_3}, \quad l_{\text{L-L}}^{\omega_i} = \frac{\epsilon^{\omega_i} + 2}{3}. \quad (22)$$

For fullerene  $C_{60}$  the numerical evaluation revealed the traditional Lorentz-Lorenz factor to be  $L_{\text{L-L}}^{(3)} = 16$  compared to the general local field factor (21)  $L_{\text{eff}}^{(3)} = 21.2$ . That means that the Lorentz-Lorenz local field factor significantly underestimates the medium effect on the second hyperpolarizabilities in this case.

We can see good agreement [4] between the results for the electronic part of  $\chi^{(3)}(0; 0, 0, 0)$  based on theoretical values  $1.61 \times 10^{-12}$  esu of RPA,



$0.88 \times 10^{-12}$  esu of DFT/LDA and  $0.73 \times 10^{-12}$  esu of DFT/LB94 with the experimental value of  $0.9 \pm 0.3 \times 10^{-12}$ .

### Summary

The ambiguity in the definition of the solute nonlinear optical properties with respect to the different perturbing fields was examined and connections between different conventions were presented in this work. It was shown that special care must be taken when comparing theoretical and experimental solute properties.

The commonly used Lorentz-Lorenz local field was shown to lead to sizable systematic errors. A more general approach to the local field factors based on the Onsager-Böttcher relation was here suggested as a solution to this problem.

The reaction field model within the dipolar approximation was shown to provide reliable results for systems like conjugated polymers and fullerenes.

### Acknowledgements

We thank the National Supercomputer Center (NSC) in Linköping, Sweden, for grants in terms of CPU time on the T3E parallel computer. This work was supported by the Swedish Natural Science Research Council (NFR).

### References

- [1] (a) L. Onsager, *J. Am. Chem. Soc.*, 58:1486, 1936. (b) C.J.F. Böttcher., *Theory of electric polarization, Vol. I*. Elsevier, Amsterdam, 1973. (c) J. Tomasi and M. Persico. *Chem. Rev.*, 94:2027, 1994.
- [2] P. Macak, P. Norman, Y. Luo, and H. Ågren. *J. Chem. Phys.*, 112:1868, 2000.
- [3] (a) Y. Luo, P. Norman, and H. Ågren. *J. Chem. Phys.*, 109:3589, 1998. (b) P. Norman, P. Macak, Y. Luo, and H. Ågren. *J. Chem. Phys.*, 110:7960, 1999. (c) Y. Luo, P. Norman P. Macak, and H. Ågren. *J. Chem. Phys.*, 111:9853, 1999.
- [4] Y. Luo, P. Norman, P. Macak, and H. Ågren. *Phys. Rev. B*, 61:3060, 2000

## Simultaneous Second-Harmonic Generation And Two-Photon Excited Fluorescence Microscopy

L. MOREAUX<sup>a</sup>, O. SANDRE<sup>b</sup>, M. BLANCHARD-DESCE<sup>c</sup>,  
J. MERTZ<sup>a</sup>

<sup>a</sup>Laboratoire de Physiologie ESPCI INSERM EPI00-02, 10 rue  
Vauquelin 75005 Paris, France; <sup>b</sup>Laboratoire PCC Institut Curie, CNRS  
UMR168, 11 rue Pierre et Marie Curie, 75005 Paris, France; ENS  
Département de Chimie, CNRS UMR 8640, 24 rue Lhomond, 75005,  
France

We demonstrate that simultaneous second-harmonic generation (SHG) and two-photon excited fluorescence (TPEF) can be used to rapidly image membranes labeled with a lipophilic styryl dye. We have developed a model based on the theory of phased-array antennas which shows that the SHG radiation is highly structured and can be roughly of the same power as TPEF. This model provides a definition of a SHG cross-section which can be directly compared to the TPEF cross-section.

**Keywords:** nonlinear optics; optical second-harmonic generation; SHG; second-harmonic microscopy; two-photon microscopy

Second-harmonic generation (SHG) and two-photon excited fluorescence (TPEF) are nonlinear optical phenomena which scale with excitation intensity squared, and hence give rise to the same intrinsic three-dimensional resolution when used in microscopic imaging. Whereas TPEF microscopy is now widely used in biological imaging [1], SHG microscopy at high resolution has only recently been demonstrated as a tool for imaging of living cells [2,3]. Because SHG is

a coherent phenomenon involving radiative scattering whereas TPEF is an incoherent phenomenon involving radiative absorption and re-emission, the two provide intrinsically different contrasts. We show here the possibility of combining these contrasts in a single scanning microscope. By using a charge-transfer lipophilic styryl dye [4] and exciting near its absorption band, we benefit from a large SHG signal and also significant two-photon absorption, which allow simultaneous and rapid SHG and TPEF imaging of membranes.

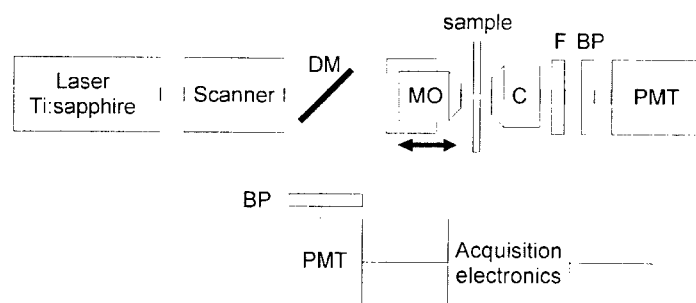


FIGURE 1 SHG and TPEF microscope: a Ti:sapphire laser beam is focussed into a sample with a microscope objective (MO). The transmitted SHG is collected with a condenser (C), bandpass filtered (BP), and detected with a photomultiplier tube (PMT). The transmitted laser light is blocked with a color glass filter (F). The TPEF from the sample is epi-collected, discriminated with a dichroic mirror (DM), bandpass filtered (BP) and detected with a PMT.

Our combined SHG and TPEF microscope is described in Figure 1 and consists of a homebuilt scanning microscope which includes transmitted light detection. The excitation source is a mode-locked Ti:sapphire laser (Spectra Physics) which delivers ~80 fs pulses at a 81 MHz repetition rate. The laser light is focussed into the sample and the resultant SHG is collected in the forward direction while the TPEF is collected in the backward direction. The sample consist of giant

unilamellar vesicles (GUVs) made of a phospholipid in water. The vesicles are labeled at 1-4 mol.% with the lipophilic styryl dye Di-6-ASPBS (N-(4-sulfobutyl)-4-(4-(dihexylamino) styryl)pyridinium); The preparation and labeling of GUV has been described in [5]. The dominating hyperpolarizability component of this molecule is along its charge-transfer axis (molecule-axis), and is denoted  $\beta$ .

When using a tightly focussed excitation beam in TPEF microscopy, the active volume from which fluorescence is generated is sharply confined near the focal center. Similarly, when imaging molecules in a membrane with SHG microscopy, only a small area about the focal center is active. Given the length scales involved, this area may be considered essentially flat and oriented parallel to the excitation propagation direction. The SHG efficacy is highly dependent on the geometry of excitation field near the focal center, and the use of a macroscopic surface susceptibility [6] to quantify SHG emission becomes inappropriate. Therefore, we have developed a model specifically tailored to a tight-focus geometry to characterize SHG in a membrane starting from the level of individual molecular hyperpolarizabilities (or nonlinear cross-sections). Our model is based on the theory of phased-array antennas, in which the dye molecules are regarded as elemental dipole radiators driven at the second-harmonic frequency of the excitation beam, in proportion to their hyperpolarizability. The SHG radiation pattern is derived by taking the excitation polarization to be along the molecular-axis and coherently summing the far-field amplitudes. The molecules are assumed to be perfectly aligned perpendicular to the surface of membrane. The SHG radiation is then found to be double-peaked in well-defined off-axis forward directions which correspond to the angles where the excitation and SHG fields are phase-matched, and critically depend on the phase anomaly of the focussed excitation beam [7]. By integrating the radiation pattern over all solid angles, the total SHG power can be expressed in the simple form:

$$P_{SHG} = \frac{1}{2} \Theta N^2 \sigma_{SHG} \overline{I^2} \quad (1)$$

where  $N$  is the effective number of molecules contributing to SHG,  $\overline{I^2}$  is the excitation mean square intensity,  $\Theta$  is a parameter dependent on the focus geometry, and  $\sigma_{SHG}$  is the SHG cross-section for a single molecule. The SHG cross-section is proportional to the molecule's hyperpolarizability squared, and may be expressed as

$$\sigma_{SHG} = \frac{4\hbar\omega^5}{3\pi m\epsilon_0^3 c^5} |\beta|^2 \quad [\text{m}^4/\text{photon s}^{-1}] \quad (2)$$

where  $n$  is the index of refraction. We recall that the fluorescence power emitted by  $N$  molecules undergoing two-photon excitation with a Gaussian focussed beam can be expressed similarly as

$$P_{TPEF} = \frac{1}{2} \frac{N}{\sqrt{8}} \sigma_{TPEF} \overline{I^2} \quad (3)$$

where  $\sigma_{TPEF}$  is the two-photon fluorescence (or "action") cross-section, defined by the two-photon absorption cross-section multiplied by the fluorescence quantum yield. The above equations lead to a simple expression for the ratio of total SHG to TPEF powers:

$$\frac{P_{SHG}}{P_{TPEF}} \approx \sqrt{8}\Theta \frac{N\sigma_{SHG}}{\sigma_{TPEF}}. \quad (4)$$

The donor-( $\pi$ -bridge)-acceptor structure of Di-6-ASPBS allows a large charge transfer along the molecular axis [8,9]. Though no direct experimental data on the hyperpolarizability of styryl dyes in membrane is available, based on two-state model [6,10] and experimental measurements [4] we can predict a large near-resonance hyperpolarizability for this molecule when inserted in a membrane and excited at 880 nm, leading to  $\sigma_{SHG} \approx 10^{-4}$  GM. In turn, the TPEF cross-section of Di-6-ASPBS in membrane at the same excitation wavelength is estimated to be  $\sigma_{TPEF} \approx 30$  GM. Although,  $\sigma_{SHG}$  is small compared to

$\sigma_{TPEF}$  for a single molecule, the ratio  $P_{SHG}/P_{TPEF}$  is significantly enhanced for a large number of molecules owing to the coherent summation of SHG field amplitudes. This ratio is even further enhanced if we consider that SHG power, because of its directional nature, can be more efficiently collected than TPEF power. In our experimental case the number of active molecule under excitation is about  $N \approx 2 \times 10^4$ , which leads to a power ratio approaching 0.3.

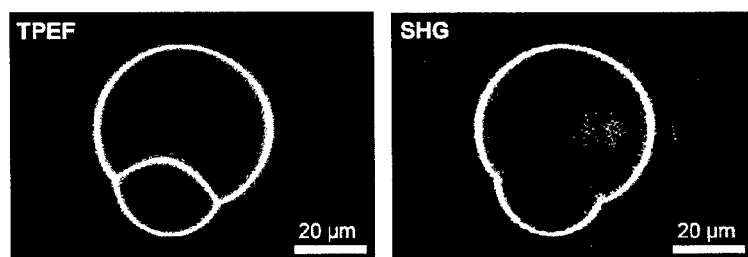


FIGURE 2 TPEF and SHG images of two adhering vesicles labeled with Di-6-ASPBS (equatorial slice), excited at 880 nm. The total acquisition time for the images was 1.5 s, for an excitation power at the sample  $<1$  mW. The adhesion area where the membranes are fused exhibits a centrosymmetric molecular distribution wherein TPEF is allowed but SHG is not.

SHG and TPEF images of Di-6-ASPBS molecules under the conditions described above are illustrated in Figure 2. The large hyperpolarizability of the molecule combined with the coherent summation of SHG resulted approximately equal measured powers in both images, allowing these to be acquired simultaneously. A feature of SHG is that it is a sensitive monitor of local molecular asymmetry. In particular, it is well known that SHG vanishes in the case of symmetric dipole distributions, as illustrated in Figure 2. This sensitivity to local asymmetry is inaccessible to TPEF and promises to be a powerful tool for the study of molecular organization in biological membranes.

### ACKNOWLEDGMENTS

The authors gratefully acknowledge financial support by the Institut Curie and by the Centre National de Recherche Scientifique (CNRS). L. Moreaux was supported by a Bourse Docteur Ingénieur (BDI).

### REFERENCES

1. W. Denk, J. H. Strickler, and W. W. Webb, *Science* **248**, 73 (1990).
2. G. Peleg, A. Lewis, M. Linial, and L. M. Loew, *Proc. Natl. Acad. Sci. USA* **96**, 6700-6704 (1999).
3. P. J. Campagnola, M. Wei, A. Lewis, and L. M. Loew, *Biophys. J.* **77**, 3341-3349. (1999).
4. L. M. Loew and L. L. Simpson, *Biophys. J.* **34**, 353 (1981).
5. Sandre, L. Moreaux, and F. Brochard, *Proc. Natl. Acad. Sci. USA* **96**, 10588-10596 (1999).
6. Y. R. Shen, *The Principles of Nonlinear Optics* (Wiley, New York, 1984).
7. L. Moreaux, O. Sandre, M. Blanchard-Desce, and J. Mertz, *Opt. Lett.* **25**, 320-322 (2000).
8. S. R. Marder, D. N. Beratan, and L.-T. Cheng, *Science* **252**, 103 (1991).
9. T. Kogej, D. Beljonne, F. Meyers, J. W. Perry, S. R. Marder, and J. L. Brédas, *Chem. Phys. Lett.* **298**, 1-6 (1998).
10. D. S. Chemla and J. Zyss, *Nonlinear Optical Properties of Organic Molecules and Crystals* (Academic Press, New York, 1984).

## **SESSION B: PHOTOREFRACTIVE EFFECTS**





## High Speed PVK-based Photorefractive Polymer Composites

<sup>a,b</sup>M.A. DÍAZ-GARCÍA, <sup>a</sup>D. WRIGHT, <sup>a</sup>J.D. CASPERSON,

<sup>a</sup>B. SMITH, <sup>a</sup>E. GLAZER, <sup>a,c</sup>W.E. MOERNER,

<sup>d</sup>L.I. SUKHOMLINOVA, <sup>d</sup>R.J. TWIEG

<sup>a</sup>Dept. of Chemistry, Univ. California San Diego, La Jolla, CA 92093-0340 (USA); <sup>b</sup>Dept. Física, Univ. Miguel Hernández, Elche-03202, Alicante (Spain); <sup>c</sup>Dept. of Chemistry, Stanford Univ., Stanford, CA 94305-5080 (USA); <sup>d</sup>Dept. of Chemistry, Kent State Univ., Kent, OH 44242 (USA)

The photorefractive properties of polymer composites based on poly(N-vinyl carbazole), doped with the sensitizer C<sub>60</sub>, the plasticizer butyl benzyl phthalate, and two series of styrene-based chromophores are presented. These materials exhibit very fast response times (beam-coupling growth times  $\tau_g$  as small as 60 ms at 50 V/ $\mu$ m applied field and 200 mW/cm<sup>2</sup> intensity and  $\tau_g$  as small as 5 ms at 100 V/ $\mu$ m and 1 W/cm<sup>2</sup>) of great interest for video-rate optical processing applications. The photorefractive properties are discussed in terms of the structure and oxidation potential of the chromophore.

**Keywords** photorefractive; polymer composites; high speed

### INTRODUCTION

The properties of photorefractive (PR) materials have been investigated during the last 30 years, mainly motivated by their potential applications in optical processing, phase conjugation, optical storage, etc..<sup>[1]</sup> Although most of the work has been focused on inorganic crystalline materials, such as LiNbO<sub>3</sub>, in 1991 photorefractivity was also demonstrated in polymers<sup>[2]</sup>. These materials have shown high

performance (net gain, overmodulated diffraction efficiencies  $\eta$ , sub-second response times  $\tau$  and gain coefficients  $\Gamma$  in the 100-200 cm<sup>-1</sup> range) in low-cost samples not requiring careful crystal growth. This high performance is mainly due to an orientational enhancement mechanism not present in inorganic materials.

Until now, most of the improvements in the performance of PR polymers have been focused on getting larger  $\Gamma$  and  $\eta$  values<sup>[3]</sup>. However, few advances have occurred in the speed of grating formation, with most materials showing grating growth times  $\tau$  in the range 0.1-100 s at the canonical 1 W/cm<sup>2</sup> writing intensity. Very recently, we reported several high-speed PR composites (e.g. PVK:AODCST:BBP:C<sub>60</sub>) with  $\tau$  < 10 ms at 1 W/cm<sup>2</sup>, while maintaining high net gain coefficients (> 100 cm<sup>-1</sup>), thus opening new possibilities for video-rate optical processing applications<sup>[4]</sup>.

In this work we investigate the PR properties of materials of the general composition PVK:Chromophore:BBP:C<sub>60</sub>, where only the chromophore structure changes<sup>[5]</sup>. Two series of chromophores have been studied: a series of dicyanostyrene (DCST) derivatives with varying amine donor (Table 1) and a series of cyanoesterstyrene (CEST) derivatives with varying amine donor (Table 2). We study the effect of the structure and oxidation potential of the chromophore on the PR properties, with particular emphasis on the speed of formation of two-beam-coupling gain.

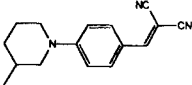
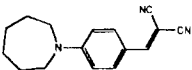
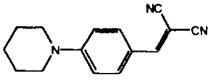
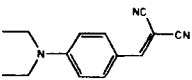
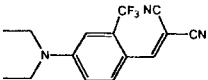
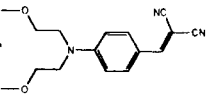
DCST	Chemical Structure	HOMO (meV)	DCST	Chemical Structure	HOMO (meV)
MPDCST		66	7-DCST		50
PDCST		66	DDCST		44
TDDCST		-	AODCST		5

TABLE 1.- HOMO position (relative to ECZ) for DCSTs

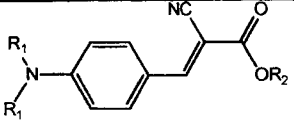
CEST			HOMO (meV)
	R <sub>1</sub>	R <sub>2</sub>	
1	C <sub>2</sub> H <sub>5</sub>	C <sub>3</sub> H <sub>7</sub>	118
2	C <sub>2</sub> H <sub>5</sub>	CH <sub>2</sub> CH <sub>2</sub> OCH <sub>3</sub>	114
3	C <sub>2</sub> H <sub>5</sub>	C <sub>8</sub> H <sub>17</sub>	122
4	C <sub>2</sub> H <sub>5</sub>	C <sub>4</sub> H <sub>9</sub>	122
5	C <sub>2</sub> H <sub>5</sub>	C(CH <sub>3</sub> ) <sub>3</sub>	138
6	C <sub>2</sub> H <sub>5</sub>	CH <sub>3</sub>	118
7	CH <sub>3</sub> OCH <sub>2</sub> CH <sub>2</sub>	CH <sub>2</sub> CH <sub>2</sub> OCH <sub>3</sub>	66
8	CH <sub>3</sub>	CH <sub>2</sub> CH <sub>2</sub> OCH <sub>3</sub>	106

TABLE 2.- HOMO position (relative to ECZ) for CESTs

### EXPERIMENTAL SECTION

Samples were prepared by following standard procedures<sup>[3]</sup>. The polymer composites consisted of the hole transporting polymer poly(n-vinyl carbazole) (PVK) (49.5 wt%), doped with a nonlinear chromophore (NLO) (35% wt%), the liquid plasticizer butyl benzyl phthalate (BBP) (15% wt) and the sensitizer C<sub>60</sub> (0.5 wt%). They were sandwiched between two indium-tin-oxide (ITO) coated glass plates, obtaining films with thickness ranging between 60 and 100  $\mu\text{m}$ .

The photoconductivity of the samples was measured by a simple DC technique. A voltage of 20 V/ $\mu\text{m}$  was applied to the sample in the dark and during illumination at 647 nm, with an intensity of 200 mW/cm<sup>2</sup>. The measurement of the current flowing through the sample in both cases permitted the determination of the dark conductivity ( $\sigma_d$ ) and the photoconductivity ( $\sigma_{ph}$ ).

The PR properties were investigated by standard two-wave-mixing (TWM) experiments in a tilted-geometry configuration at 647 nm. The applied electric field was 50 V/ $\mu\text{m}$  and the intensity of the incident

beam 200 mW/cm<sup>2</sup>. The gain coefficient ( $\Gamma$ ) was determined from the measurement of the multiplicative gain factor ( $\gamma_0$ ) at steady state. Finally, the time constant  $\tau_g$  was obtained by fitting the evolution of the growth of the gain with a single exponential function of the form

$$\gamma(t) = 1 + \gamma_0 \{1 - \exp[-(t/\tau_g)]\} \quad (1)$$

Cyclic voltammetry was performed in all the chromophores, in order to determine their first oxidation potential and the HOMO (highest occupied molecular orbital).

## RESULTS AND DISCUSSION

The photoconductivity  $\sigma_{ph}$  and the PR speed  $\tau_g^{-1}$  for composites (PVK/chromophore/BBP/C<sub>60</sub>) were determined as previously described. Although samples were prepared by adding a nominal 0.5 wt. % of C<sub>60</sub> to the sample mixture, the absorption coefficients ( $\alpha$ ) vary from one sample to another. Since both,  $\sigma_{ph}$  and  $\tau_g^{-1}$  are proportional to the rate of generation of mobile charges in the material, and therefore to  $\alpha$ , in order to compare the performance of the different chromophores,  $\sigma_{ph}$  and  $\tau_g^{-1}$  need to be normalized by dividing by  $\alpha$ . Such a comparison is illustrated in Figures 1(a) and 1(b) for DCST and CEST derivatives respectively, by plotting the normalized speed ( $\tau_g^{-1}/\alpha$ ) versus the normalized photoconductivity ( $\sigma_{ph}/\alpha$ ).

For the DCST derivatives (Fig. 1(a)) a clear trend of higher ( $\tau_g^{-1}/\alpha$ ) with larger ( $\sigma_{ph}/\alpha$ ) is observed. This suggests that the speed in this type of composites is determined by  $\sigma_{ph}$ , rather than by chromophore orientation. These results are in agreement with a previously reported study on AODCST<sup>[4]</sup>, where it was observed that both parameters ( $\tau_g^{-1}$  and  $\sigma_{ph}$ ) grew linearly with intensity without saturation. On the other hand, for the CEST derivatives (Fig. 1(b)) the correlation between ( $\tau_g^{-1}/\alpha$ ) and ( $\sigma_{ph}/\alpha$ ) is not so clear. Indeed, only small changes in speed are observed from one chromophore to another for almost all cases. To obtain further insight into the CEST materials, we performed intensity dependent studies of ( $\tau_g^{-1}/\alpha$ ) and ( $\sigma_{ph}/\alpha$ ). Also in this case a linear dependence is observed. However the slope of the speed line and the photoconductivity differ up to one order of magnitude for some of the systems (i.e. CEST-3). This suggests that

the speed is being affected by some other factor, which may be chromophore orientation or some other process.

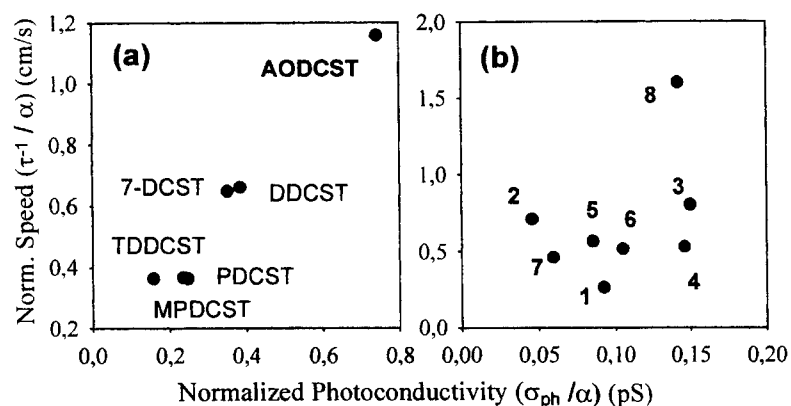


FIGURE 1 Normalized photorefractive speed ( $\tau_g^{-1}/\alpha$ ) versus photoconductivity ( $\sigma_{ph}/\alpha$ ) for composites of: (a) PVK/DCST/BBP/C<sub>60</sub> and (b) PVK/CEST/BBP/C<sub>60</sub>.

The deeper issue of the reason for the observed behaviour may be examined by utilizing the results from a previous study of trapping dynamics in C<sub>60</sub>-doped PR polymers<sup>[6]</sup>. That model proposed that the active trap is the C<sub>60</sub> anion, while the chromophores would act as compensators, trapping the holes produced by irradiation of the C<sub>60</sub>. This effect should affect then the charge mobility and hence  $\sigma_{ph}$ , with lower mobility/ $\sigma_{ph}$  for deeper hole traps. To test this idea, we performed cyclic voltammetry on all the chromophores, and used the first oxidation potentials to locate the relative energy of the HOMO of the chromophore relative to that for N-ethyl carbazole (ECZ). The results show (see Table 1) a very strong trend for the DCST derivatives: the higher ( $\sigma_{ph}/\alpha$ ) and ( $\tau_g^{-1}/\alpha$ ) values occur for the most shallow hole trap represented by the presence of the chromophore. On the other hand, for the CEST class (Table 2) no clear trend is observed, which is another hint that transport in CEST-based composites is more complex.

Overall, the most important result obtained is that these composites show very fast response times, as compared to other polymer composites previously reported, while keeping reasonable gain coefficients near  $100\text{ cm}^{-1}$ . Comparing DCST's to CEST's, with a few exceptions, both  $\sigma_{\text{ph}}$  and  $\tau_{\text{g}}^{-1}$  are higher in the DCST class. In addition, the steady-state  $\Gamma$  values are generally larger for the DCST's (ranging from 40 to  $80\text{ cm}^{-1}$ ) than for the CEST's (between 10 and  $45\text{ cm}^{-1}$ ). This difference is probably due to the enhanced ground state dipole moment of the DCST molecules relative to the CEST molecules.

Finally, in order to increase the speed even more we performed TWM experiments at higher electric fields and intensities (up to  $100\text{ V}/\mu\text{m}$  and  $1\text{ W}/\text{cm}^2$  respectively) for some of the compounds. Response times as small as 5 ms with gain coefficients around  $200\text{ cm}^{-1}$  were measured for AODCST<sup>[4]</sup>. However, the problem of the high fields used, is that sample breakdown eventually occurred, so further work is required in order to control this effect.

#### Acknowledgments

We thank Prof. Y. Tor for assistance with the CV measurements and M. DeClue for the synthesis of 7-DCST. The work at UCSD was partly supported by the U.S. AFOSR Grants F49620-96-1-0135 and F49620-97-1-0286. The work at KSU was supported in part by the NSF under an ALCOM grant DMR89-20147. Finally, some travel support was obtained from CICYT grant MAT1999-0622 and Consellería de Cultura, Educación y Ciencia grant GV99-158-1-15.

#### References

- [1] P. Günter, J-P. Huignard, Photorefractive Materials and Their Applications I and II; Springer Verlag: Berlin (1988).
- [2] S. Ducharme, J.C. Scott, R.J. Twieg, W.E. Moerner, Phys. Rev. Lett. **66**, 1846, (1991).
- [3] W.E. Moerner, A. Grunnet-Jepsen, C.L. Thompson, Ann. Rev. Mater. Sci. **27**, 585 (1997).
- [4] D. Wright, M.A. Díaz-García, J.D. Casperson, M. DeClue, W.E. Moerner, R. Twieg, Appl. Phys. Lett. **73**, 1490-1492 (1998).
- [5] M.A. Díaz-García, D. Wright, J.D. Casperson, B. Smith, E. Glazer, W.E. Moerner, L.I. Sukhomlinova, R. Twieg, Chem. Mater. **11**, 1784-1791 (1999).
- [6] A. Grunnet-Jepsen, D. Wright, B. Smith, M.S. Bratcher, M.S. DeClue, J.S. Siegel, W.E. Moerner, Chem. Phys. Lett. **291**, 553 (1998).

## Modelization of the Angular Redistribution in Optical Ordering Processes in Dye Containing Polymers.

Michel DUMONT

Laboratoire de Photonique Quantique et Moléculaire, ENS de Cachan, CNRS  
(UMR # 8537), 61 Avenue du Président Wilson, 94235 Cachan cedex, France

Photoinduced anisotropy (PIA) and all optical poling (AOP) imply an angularly selective resonant excitation of dye molecules followed by angular redistribution (AR). Most often, AR is due to photoisomerization. Optical pumping can induce dipolar or octupolar symmetries leading to a  $\chi^{(2)}$ . In amorphous materials (polymers), AR is isotropic and cannot produce order, but it is a necessary process for the durability of the order created by light. In this paper, the general tensorial formalism [1,2] is introduced in the model of optical pumping previously developed in axial symmetry for PIA[3-5]. As proved experimentally in the case of PIA, the efficiency of AR is the result of many successive photoisomerization cycles. They produce the mixing of tensorial orders, leading to complicated equations which can be solved numerically, but a very simple solution is given for the photostationary state.

**Keywords:** theory of optical ordering; all-optical poling; photoinduced anisotropy

Three different optical methods have been developed for ordering dye molecules in polymer films, for non-linear optics and telecommunication applications:

*Photoinduced anisotropy* (PIA) or Weigert effect: birefringence and dichroism are induced by a polarized resonant light excitation

*Photoassisted electrical poling* (PAEP): optical pumping increases the mobility of molecules, which can be oriented by a DC field, at room temperature [4-7].

*All-optical poling* (AOP) is the most recent method: The material is coherently pumped by the fundamental frequency and the second harmonic of a laser beam resonant at  $2\omega$  [8-10]. A  $\chi^{(2)}$  can be created with non polar molecules (octupolar molecules) and different macroscopic symmetries can be induced [1,2].

For PIA and PAEP a theoretical model has been built and has been successfully compared to the dynamical behavior of experiments [6]. The extension of this model to AOP has been proposed for cigar shape molecules pumped by linearly polarized beams [4,5]. The three optical ordering methods can be described by the combination of three mechanisms. Firstly, a *selective optical pumping, or angular hole burning* (AHB) depending on the polarization of pumping beam(s). Secondly, an *angular redistribution* (AR) occurring in the optical excitation process and/or during the lifetime of excited levels and/or in the relaxation process, back to the ground state. It leads to an accumulation of molecules in the less pumped orientation. AR is a partial thermalization of molecules orientation during the excitation process.



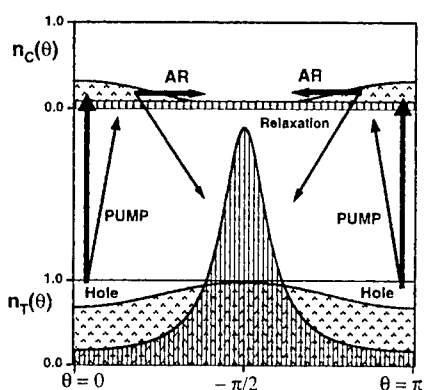


FIGURE 1. Illustration of angular hole burning and of angular redistribution, in the case of photoinduced anisotropy by a Z-polarized resonant light beam. The  $\cos^2\theta$  pumping burns holes near  $\theta = 0$  and  $\theta = \pi$ . Dotted areas represent the angular distributions  $n_T(\theta)$  and  $n_C(\theta)$ , in trans and in cis, at the beginning of pumping (first order of perturbation). The peak of  $n_T$  and the flat distribution of  $n_C$  (vertical hachures) represent the photostationary state, when AR (horizontal and oblique arrows) has accumulated trans molecules near  $\theta = \pi/2$ . This distribution is given by equation (12).

This angular redistribution is particularly efficient when a change of the geometrical structure of molecules occurs, *i.e.* when molecules perform photoisomerization. Azodyes are the most efficient molecules. In the following, we will refer to their reversible trans  $\rightarrow$  cis photoisomerization. Figure 1 schematizes AHB and AR. Finally, the *orientational diffusion* tends to restore the isotropy in the ground state. Of course, to build a permanent orientational order, this relaxation must be avoided.

Here the general tensorial formalism developed by S. Brasselet and J. Zyss [1,2] will be introduced in the model of the photoisomerization cycles, which describes more precisely the angular redistribution. Formally, the evolution of the angular distributions  $n_T(\Omega) \equiv n_T(\varphi, \theta, \psi)$  and  $n_C(\Omega)$ , in trans and cis, respectively, is given by:

$$\frac{dn_T(\Omega)}{dt} = -Pr(\Omega)n_T(\Omega) + \frac{1}{\tau_c} \int R_{CT}(\Omega' \rightarrow \Omega)n_C(\Omega')d\Omega' + \left( \frac{dn_T(\Omega)}{dt} \right)_{Diff} \quad (1)$$

$$\frac{dn_C(\Omega)}{dt} = \int R_{TC}(\Omega' \rightarrow \Omega)Pr_T(\Omega')n_T(\Omega')d\Omega' - \frac{1}{\tau_c}n_C(\Omega) + \left( \frac{dn_C(\Omega)}{dt} \right)_{Diff} \quad (2)$$

The population of electronically excited levels has been neglected because of their very short lifetime. For simplicity, we ignore the reverse optical pumping from cis to trans, in spite of its importance. It is easy to introduce it like in reference [5].  $R_{TC}$  and  $R_{CT}$  express the probability of angular redistribution from  $\Omega$  to  $\Omega'$ , in pumping and relaxation processes, respectively. The last term in (1) and (2) is the thermal orientational diffusion. In the case of AOP, the pumping probability is given by:

$$\begin{aligned}
\text{Pr}(\Omega) &\propto \alpha''_{\Omega}(-2\omega; 2\omega) \bullet \Re(E_{2\omega}^* \otimes E_{2\omega}) + 2\beta''_{\Omega}(-2\omega; \omega, \omega) \bullet \Re(E_{2\omega}^* \otimes E_{\omega} \otimes E_{\omega}) \\
&\quad + \gamma''_{\Omega}(-\omega; -\omega, \omega, \omega) \bullet \Re(E_{\omega}^* \otimes E_{\omega}^* \otimes E_{\omega} \otimes E_{\omega}) \\
&= \sum_{Kq} (-1)^q D_{q,q}^K(\Omega) \left[ \alpha''_{q,q}^{K(2)} E_{-q}^K + \beta''_{q,q}^{K(3)} E_{-q}^K + \gamma''_{q,q}^{K(4)} E_{-q}^K \right] \quad (3)
\end{aligned}$$

$E_{\omega}$  and  $E_{2\omega}$  are the complex amplitudes of fields and  $\alpha''_{\Omega}$ ,  $\beta''_{\Omega}$  and  $\gamma''_{\Omega}$  are the imaginary parts of molecular susceptibility tensors, in the laboratory frame, in Cartesian coordinates. In the second row, tensors have been written in the spherical irreducible representation and susceptibilities have been expressed in the molecular axes, with the help of the Wigner rotation operators  $D_{q,q}^K$ , according to references [1,2]. The factor 2, in front of  $\beta$ , comes from the existence of two equal contributions,  $\beta(-2\omega; \omega, \omega)$  and  $\beta(-\omega; -\omega, 2\omega)$  [5]. If the Kleinmann symmetry applies,  $K$  is 0 and 2 for  $\alpha$ , 1 and 3 for  $\beta$  and 0, 2 and 4 for  $\gamma$ , but because of the optical resonance other components may exist, such as  $\beta^{K=2}$ . Nevertheless, if the writing field tensors,  $^{(n)}E$ , are symmetrical (e.g. for parallel linear polarizations) the Kleinmann symmetry is restored.  $D_{q,q}^K(\Omega)$  functions appear to be the good basis to express angular distributions and to define generalized order parameters  $T_{Jm'm}$ :

$$n_T(\Omega) = \sum_{Jm'm} \frac{2J+1}{8\pi^2} T_{Jm'm} D_{m'm}^J(\Omega); \quad T_{Jm'm} = \int n_T(\Omega) D_{m'm}^{J*}(\Omega) d\Omega \quad (4)$$

Similarly,  $C_{Jm'm}$  will be the order parameters of cis. Equations (1) and (2) become:

$$\begin{aligned}
\frac{dT_{Jm'm}}{dt} &= - \int \sum_{L'n'n} \left( \frac{2L+1}{8\pi^2} T_{Ln'n} D_{n'n}^L(\Omega) \right) \left( {}^sA_{q,q}^K {}^sE_{-q}^K (-1)^q D_{q,q}^K(\Omega) \right) D_{m'm}^{J*}(\Omega) d\Omega \\
&\quad + \frac{1}{\tau_C} R_{CT}^J C_{Jm'm} - D_T^J T_{Jm'm} \\
&= - \sum_{Ln'n} P_{Jm'm}^{Ln'n} T_{Ln'n} + \frac{1}{\tau_C} R_{CT}^J C_{Jm'm} - D_T^J T_{Jm'm} \quad (5)
\end{aligned}$$

$$\frac{dC_{Jm'm}}{dt} = \sum_{Ln'n} R_{TC}^J P_{Jm'm}^{Ln'n} T_{Ln'n} - \left( \frac{1}{\tau_C} + D_C^J \right) C_{Jm'm} \quad (6)$$

The optical pumping coupling matrix contains all the terms  ${}^sA^K {}^sE^K$  of equation (3). The integration on  $\Omega$  of the three  $D$  functions gives  $3J$  coefficients which impose  $m = q+n$ ,  $m' = q'+n'$  and a triangular relation between  $J$ ,  $K$  and  $L$ :

$$P_{Jm'm}^{Ln'n} = \sum_{sKq'q} (2L+1) \begin{pmatrix} L & K & J \\ n' & q' & -m' \end{pmatrix} \begin{pmatrix} L & K & J \\ n & q & -m \end{pmatrix} {}^sA_{q,q}^K {}^sE_{-q}^K (-1)^{q+m'-m} \quad (7)$$

$D_T^J$ ,  $D_C^J$ ,  $R_{TC}^J$  and  $R_{CT}^J$  are damping factors, which depend only of  $J$ . Indeed, in amorphous materials, thermal diffusion in cis and in trans, as well as angular redistribution in isomerization processes, are isotropic.

Equations (5-6) are an infinite set of coupled differential equations. They can be solved, like in references [4,5], by assuming that order parameters are negligible above  $J = J_{\max}$  and by solving numerically the matricial equation:

$$\left[ \frac{dX(t)}{dt} \right] = [M][X(t)] + S \quad (8)$$

$[X]$  is a column matrix with  $1 + \sum_{J=1}^{J_{\max}} 2(2J+1)^2$  elements ( $T_{Jm'm}$  and  $C_{Jm'm}$  with  $J \leq J_{\max}$ ).  $S$  is coming from the condition  $T_{000} + C_{000} = N$ . The solution of (6) could be obtained numerically like in references [4-6], but the size of matrices is huge, in the general case (for  $J_{\max} = 6$ ,  $X$  has 909 elements!). For cigar molecules ( $q=0$ ) or for parallel linear polarizations ( $q=0$ ),  $D$  functions are reduced to spherical harmonics and the number of components is accessible to small computers (to be published soon).

The important feature of equations (5-6) is the coupling between the tensorial orders of angular distributions. In previous publications [1,2] the nonlinear properties of optically oriented materials were expressed at the first order in the pumping probability. This solution is obtained by replacing  $T_{Ln'n}$  by  ${}^{(0)}T_{000} = N$  in equations (5). For  $t = \infty$  one finds (assuming for simplicity that AR is complete in one cycle:  $R_{CT}^{1\pm 0} = 0$ ):

$${}^{(1)}T_{Jm'm} = -\frac{N}{D_T^1} P_{Jm'm}^{000} = \frac{-(-1)^m N}{(2J+1)D_T^1} [\alpha''_{m'} {}^{(2)}E_{-m}^J + \beta''_{m'} {}^{(3)}E_{-m}^J + \gamma''_{m'} {}^{(4)}E_{-m}^J] \quad (9)$$

With this first order one obtains the result of references [1,2]:

$$\chi_{m'}^{(2)J} = \sum_{m''} \beta_{m''}^J \int D_{Jm''m}^J(\Omega) n_T(\Omega) d\Omega = \frac{-N}{(2J+1)D_T^1} [\beta^J(2\omega_r) \bullet \beta''^J(2\omega_w)] {}^{(3)}E_{-m}^J \quad (10)$$

Where  $\omega_r$  and  $\omega_w$  are read and write frequencies, respectively. If  $\omega_r$  is out of resonance Kleinmann symmetry of  $\beta(2\omega_r)$  imposes  $J=1$  and 3 ( $J=3$  only for octupolar molecules or octupolar pumping fields *i.e.* counter-rotating circular polarizations [1,2]). As soon as at the second order, the coupling of tensorial orders appears:

$${}^{(2)}T_{Jm'm} \propto \sum_{\substack{Kq'qs \\ Ln'ns'}} \begin{pmatrix} L & K & J \\ n' & q' & -m' \end{pmatrix} \begin{pmatrix} L & K & J \\ n & q & -m \end{pmatrix} {}^s A_q^K {}^s E_{-q}^K {}^s A_n^L {}^s E_{-n}^L (-1)^m \quad (11)$$

It is the irreducible decomposition of tensorial products ( ${}^s A^K \otimes {}^s A^L$ ) and ( ${}^s E^K \otimes {}^s E^L$ ). For instance,  $\alpha^{K=2}$  and  $\beta^{L=3}$  produce in general  $1 \leq J \leq 5$ . The result is a modification of the ratio of components  $J=1$  and  $J=3$  in the expression (10) of  $\chi^{(2)}$ . Nevertheless, in the interesting case of counter-rotating circular polarizations,  $J=1$  never appears. Indeed, in that case, couples  $(K, q)$ , or  $(L, n)$  can be only  $(0, 0)$  or  $(2, 0)$  for  $E \otimes E$ ,  $(0, 0)$ ,  $(2, 0)$  or  $(4, 0)$  for  $E \otimes E \otimes E \otimes E$  and  $(3, \pm 3)$  for  $E \otimes E \otimes E$ . One gets  $m = \pm 3$  with  $J \geq 3$ , or  $m = 0$ : the  $3J$  cancel for  $J=1$ . At higher orders, this property is always valid. Nevertheless, in all cases, the estimation of the value of  $\chi^{(2)}$  necessitate a complete resolution of equations (5-6), since the perturbation development (9) is valid if  $P_{Jm'm}^{Ln'n} \ll D_T^1$ , *i.e.* if the angular diffusion in trans is fast. This condition is just what is to be avoided for obtaining a stable orientation of active molecules.

When the thermal diffusion in trans is negligible, there is a very simple stationary solution of equations (1-2), which is an isotropic distribution of molecules in cis ( $n_c(\Omega) = N_c/(8\pi^2)$ ). As AR and the diffusion in cis cannot modify this distribution ( $\int R_{CT}(\Omega' \rightarrow \Omega) d\Omega' = 1$ ), equation (1) becomes  $0 = \text{Pr}(\Omega) n_T(\Omega) - N_c/(8\pi^2 \tau_c)$ . The angular distribution in trans is proportional to the inverse of the probability of excitation and can be projected on the  $D_{Ln}^L$  functions:

$$n_T(\Omega) = \frac{N_C}{8\pi^2 \tau_c \text{Pr}(\Omega)} = N \left[ 8\pi^2 \text{Pr}(\Omega) \left( \tau_c + \int \frac{d\Omega}{8\pi^2 \text{Pr}(\Omega)} \right) \right]^{-1} \quad (12)$$

$$T_{Ln'n} = \frac{N_C}{8\pi^2 \tau_c} \int D_{n'n}^{L*}(\Omega) \left[ \sum_{sKq} D_{q'q}^K(\Omega)^s A_q^K s E_{-q}^K (-1)^q \right]^{-1} d\Omega \quad (13)$$

Using the properties of  $D_{n'n}^L$  functions, it is easy to show that this expression of  $T_{Ln'n}$  is the stationary solution of equation (5) (with  $C_{Jm'm} = N_C \delta_{J,0} \delta_{m,0} \delta_{n',0}$  and  $D_T^L = 0$ ).

In simple cases, it is easier to calculate directly  $n(\Omega)$  with the Cartesian components of the  $\beta$  tensor. Figure 1 shows  $n_T(\theta)$  and  $n_C(\theta)$  for cigar-like molecules pumped by a single Z-polarized resonant light beam (PIA). The probability of excitation is  $\text{Pr}(\theta) = a + b \cos^2 \theta$ . The first order solution ( $n_T(\theta) = 1 - n_C(\theta) = 1 - \epsilon \text{Pr}(\theta)$ , with  $\epsilon \ll 1$ ), is shown in this figure: it is the pure hole burning effect which can be observed at the beginning of pumping. The photostationary solution (12) is also represented. Let us notice that, in this model, the pumping probability must contain an isotropic part (a) for avoiding divergence for  $\theta = \pi/2$ . In practice, diffusion in trans and optical pumping from cis to trans reduce this accumulation of molecules.

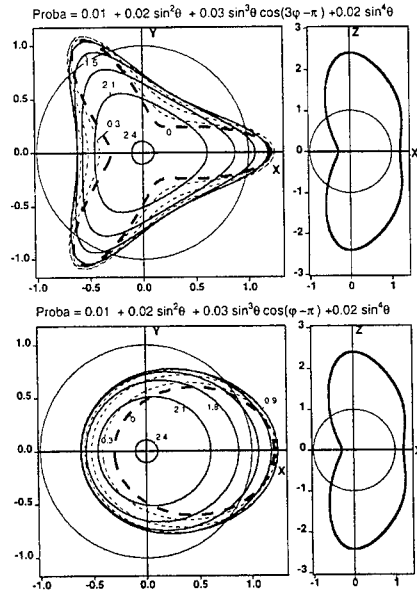


FIGURE 2. Photostationary angular distribution produced by all-optical poling of rod-like polar molecules, by circularly polarized beams at  $\omega$  and  $2\omega$ , as calculated from equation (12). The upper graph is obtained with counter-rotating waves and the lower graph with co-rotating waves. In right graphs, Z is the propagation axis of light beams. Left graphs show contour lines for different values of z. The thick dash curve is the contour in the x-y plane. The relative amplitude of the interference term has been exaggerated for the demonstration.

Figure 2 represents the all-optical poling of cigar-like molecules by two circularly polarized beams ( $\omega$  and  $2\omega$ ). Since molecules are uniaxial, one has  $q'=0$ , in (3) and the Wigner functions become spherical harmonics. The one photon and two photon pumping probabilities are proportional to  $\sin^2(\theta)$  and  $\sin^4(\theta)$ , respectively ( $K=0, 2, 4$  and  $q=0$ , as explained above). The interference term is proportional to

$$\sin^3\theta \cos(3\varphi - \Delta\Phi) \propto \Re\{Y_3^3(\theta, \varphi)e^{-i\Delta\Phi}\}, \quad (14)$$

for counter-rotating waves (upper graph in figure 2) and to

$$\sin^3\theta \cos(\varphi - \Delta\Phi) \propto \Re\{(\sqrt{14} Y_1^1(\theta, \varphi) - Y_3^3(\theta, \varphi))e^{-i\Delta\Phi}\}, \quad (15)$$

for co-rotating waves.  $\Delta\Phi$  is the phase difference between waves: it defines the orientation of the pattern in the x-y plane. Both patterns rotate along the propagation axis, because of the dephasing of waves. The first case is the pure octupolar pumping, with a three-fold symmetry, while the second case is a superposition of dipolar and octupolar pumping with a two-fold symmetry. S. Brasselet has shown these properties of  $\chi^{(2)}$  theoretically, at the first order, and experimentally [1,2].

### Conclusion

All optical ordering processes are strongly saturated, since it is an accumulation process. The first order calculation is insufficient for estimating the final result and particularly for determining the best relative intensity of the two beams, in AOP. Although not surprising, it is interesting to notice that the mixing of tensorial orders by saturation preserve the symmetry of the pumping process.

Here calculation methods have been proposed. The model is over simplified, but it is possible to improve it. Mathematically, it is easy to introduce the reverse optical pumping in equations (5-6) [5]. The difficulty is to know the value of molecular susceptibilities, particularly in excited states. In AOP experiments, the pumping beams are strong laser pulses: it should not be difficult to extend the model to pulses. The result should not be very different. The angular redistribution is exactly the same in AOP and in PIA. The only difference is the symmetry of light. PIA experiments [11] are of great interest to characterize the ability of molecules to be oriented by AOP.

### References

- [1] S. Brasselet, Thèse de doctorat, Université Paris-Sud, Orsay (1997)
- [2] S. Brasselet, J. Zyss, J. Opt. Soc. Am. **B 15**, 257-288 (1998) and J. Nonlinear Optical Phys. & Mat. **7**, 397-439 (1998)
- [3] Z. Sekkat And M. Dumont, Synthetic Metals **54**, 373-381 (1993).
- [4] M. Dumont, in : "Photoactive Organic Molecules", F. Kajzar, ed., Nato ASI Series Vol. **9**, 501-511, Kluwer Academic Publishers (1996).
- [5] M. Dumont and A El Osman, Chemical Physics, **245**, 437-462 (1999). In this reference, formula (A.4) is wrong, one must read  $(2\hbar)^{-1} \text{Im}[(\beta_z(2\omega) - \beta_z^*(\omega)) \dots]$
- [6] M. Dumont, G. Froc and S. Hosotte, Nonlinear Optics **9**, 327-338 (1995).
- [7] Z. Sekkat And M. Dumont, Appl. Phys. B **54**, 486-489 (1992) and, Mol. Cryst. liq. Cryst. Sci. Technol. secB: Nonlinear Optics, **2**, 359-362 (1992).
- [8] F. Charra, F. Kajzar, J.M. Nunzi, P. Raimond, E. Idiart, Optics Lett. **18**, 941 (1993)
- [9] C. Fiorini, F. Charra, J.M. Nunzi, P. Raimond, Nonlinear Optics **9**, 339 (1995).
- [10] J.M. Nunzi, F. Charra, C. Fiorini, J. Zyss, Chem. Phys. Lett. **219**, 349 (1994).
- [11] El Osman and M. Dumont, Proc. SPIE **417**, 36 (1998)

## Formation of an Anti-guide Structure in a Photorefractive Polymer by a Pump-light Beam

Takashi Fujihara<sup>a</sup>, Masahiro Tokuue<sup>a</sup>, Takafumi Sassa<sup>b</sup>, Kazutoshi Ozawa<sup>a</sup>,  
Shinsuke Umegaki<sup>a</sup>, Masaaki Yokoyama<sup>c</sup>, Tatsuo Wada<sup>b</sup>, and Hiroyuki Sasabe<sup>b,d</sup>

<sup>a</sup>Faculty of Science and Technology, Keio University, 3-14-1 Hiyoshi,  
Kohoku-ku, Yokohama, Kanagawa 223-8522, Japan

<sup>b</sup>The Institute of Physical and Chemical Research (RIKEN),  
2-1 Hirosawa, Wako, Saitama 351-0198, Japan

<sup>c</sup>Graduate School of Engineering, Osaka University,  
2-1 Yamada-oka, Suita, Osaka 565-0871, Japan

<sup>d</sup>Chitose Institute of Science and Technology,  
758-65 Bibi, Chitose, Hokkaido 066-8655, Japan

**Abstract** An anti-guide structure was formed by a pump-light beam in a photo-sensitive nonlinear-optical or photorefractive polymer. The formation was experimentally confirmed by the Maker-fringes method, using the polymer which was sensitive to the pump He-Ne laser but not to the fundamental Nd:YAG laser. Second-harmonic generation based on the confinement of the fundamental and its second-harmonic wave in the anti-guide was monitored by changing the temperature, the poling electric-field and the beam radii of the pump and the fundamental wave. The anti-guide formed in the photorefractive polymer might be applied to light-control by light.

### INTRODUCTION

Using the thin-film planar waveguide of a photorefractive (PR) polymer, the self-enhancement of the Cerenkov-radiation type second-harmonic (SH) power was observed. It was initially attributed to the gradually formed periodic structure, which satisfied the quasi-phase-matching [1, 2]. After that, however, it

was theoretically made clear that the relatively large enhancement experimentally obtained could be explained by the self-formed anti-guide structure[3].

In this paper, we report on the fabrication of an anti-guide structure by using a He-Ne laser as a pump wave. Moreover, it is confirmed by monitoring an SH wave of the fundamental Nd:YAG laser in the Maker fringes.

#### PREPARATION OF A PHOTOREFRACTIVE POLYMER

The PR polymer used in the Maker-fringes experiment was composed of 18.9 wt.% of the nonlinear-optical (NLO) chromophore 4-methoxy-4'-nitrostilbene, 0.1 wt.% of the photosensitizer 2,4,7-trinitro-fluorenone, and 40.4 wt.% of the plasticizer 1,3-Bis(*N*-carbazolyl) propane in a matrix poly(*N*-vinylcarbazole). The composite was sandwiched between two ITO glass substrates obtaining a film of thickness around 125  $\mu\text{m}$ .

This polymer was photo-sensitive to the wavelength 633 nm of the He-Ne laser but not to the wavelength of the Nd:YAG laser.

#### CONFINEMENT IN AN ANTI-GUIDE

The anti-guide structure has a core with a refractive index lower than that of its clad. Figure 1 schematically shows how such an anti-guide structure will be formed in a PR polymer. Here, the space charges generated in the pump beam and trapped outside of the beam shields and reduces the applied electric-field. The NLO molecules are reoriented to reduce the refractive index mainly due to

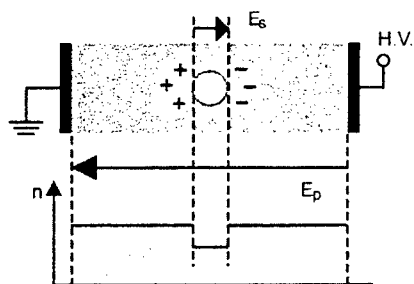


FIGURE 1 Formation of an anti-guide structure.  
 $E_p$ : poling electric-field,  $E_s$ : space-charge field.

the birefringence. The refractive index of the region irradiated by the pump beam or by the SH beam itself becomes lower than the surrounding poled PR polymer.

Using a 0.1 mW power-level He-Ne laser as a pump beam and rotating the sample, we obtained Maker fringes of the SH wave generated from a Nd:YAG laser. Figures 2(a) and (b) show the results in case of the poling voltage of 1.5 kV, for almost the same and the smaller pump-beam radius in comparison to the fundamental-beam radius, respectively. The comparison of the SH power with and without the pump shows that the enhancement was due to the confinement of the fundamental and its SH wave in the core of the anti-guide. Since the pump power was kept constant in order to make the pump-beam radius smaller in (b), the pump intensity and then, the number of photo-carriers increased. As a consequence, the refractive index of the pump-irradiated region in (b) was reduced more, inducing a larger confinement. Thus, the enhancement of the SH power in (b) is larger than that in (a).

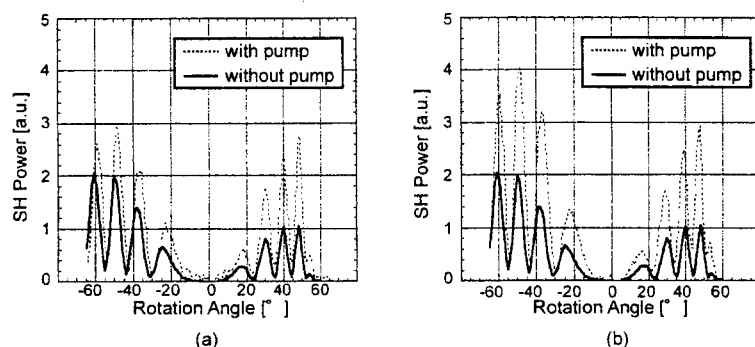


FIGURE 2 Maker fringes.  
The pump-beam radius (a) almost same as and (b) smaller than the fundamental-beam radius.

Figure 3 shows the results obtained by changing the pump power, with the pump-beam radius fixed and an applied voltage of 1.25 kV. It is observed that an increase of the pump power resulted in the increase of the SH power.

However, there is still the possibility that the anti-guide is formed by the reduction of the refractive index through the thermal effect or the thermo-optic (TO) effect.



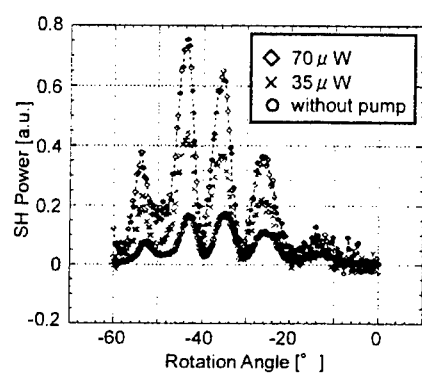


FIGURE 3 Maker fringes for two pump-power levels.

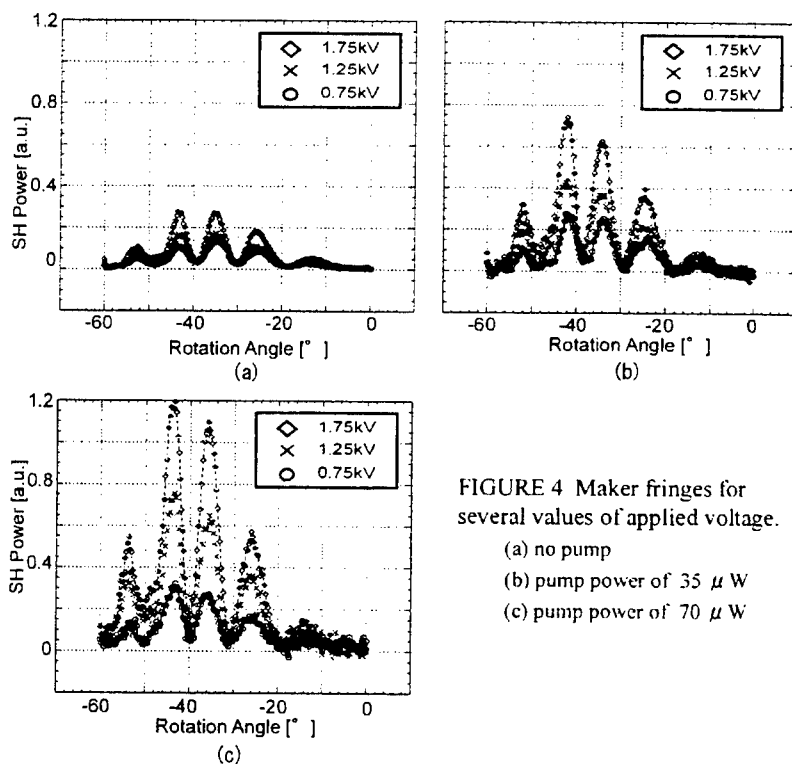


FIGURE 4 Maker fringes for several values of applied voltage.

- (a) no pump
- (b) pump power of  $35 \mu\text{W}$
- (c) pump power of  $70 \mu\text{W}$

### DEPENDENCE OF SH POWER ON APPLIED ELECTRIC-FIELD

In order to confirm the contribution of the space-charge field, we studied the dependence of the SH power on the externally-applied electric field. Figures 4(a), (b) and (c) show the Maker fringes for no pump, with a pump power of  $35 \mu\text{W}$  and of  $70 \mu\text{W}$ , respectively. Due to the poling, the SH power increased with an increase of the applied voltage in each figure. Ideally in (a), the slope should be 2 in the relation of  $\log(\text{SH power})$  for  $\log(\text{applied voltage})$ , where SH power was measured at one of the peaks in the Maker fringes. The slopes of (a), (b) and (c) were 1.84, 2.00 and 2.12, respectively. Although the slope of (a) was not equal to 2, the slopes of (b) and (c) were larger than that of (a). This suggests that the space-charge field or the screening field increased and the confinement was strengthened with an increase of the applied voltage based on the reduction of the refractive index. The poling electric-field or the drift field enhances the space-charge field and in organic PR materials, also increases quantum yield of photocharges, which induces the reduction due to the molecular reorientation.

The enhancement ratio of the SH power, that is, the ratio of the SH power with and without the pump more clearly gives the confinement based on the molecular reorientation by excluding the effect of poling. Here, it should be noted that this ratio is not dependent on the applied voltage in the case of the anti-guide thermally formed.

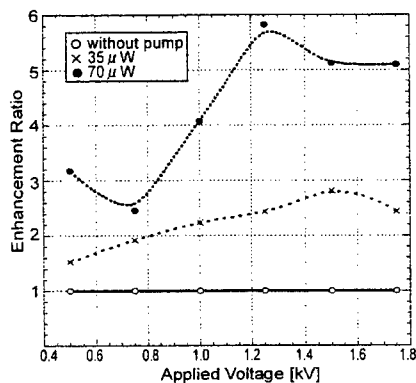


FIGURE 5 Enhancement ratio for applied voltage.

Figure 5 shows the ratio as a function of the applied voltage. In the case of the

pump power of 35  $\mu$ W, the ratio gradually increases with an increase of the reduction of the refractive index to form the anti-guide. However, the second-order nonlinearity is also reduced by molecular reorientation. Therefore, lastly, the reduction of the nonlinearity overcomes the confinement, which results in the decrease of the ratio. On the other hand, in the case of the higher pump power, the ratio initially decreases. This means that the heating of the pump-irradiated region increases the degree of the molecular orientation, and that results in a larger nonlinearity, as compared to the surrounding clad without enough space charges. When the space charges that screen the poling electric-field increase with the field, the degree of the orientation degrades resulting in the initial decrease of the ratio. Hence, the ratios in both cases are larger than unity in the lower externally-applied electric-field, due to thermal confinement.

#### DISCUSSIONS AND CONCLUSIONS

The anti-guide was formed by using the pump, which was monitored by the enhancement of the SH power. We could confirm that the formation was dominantly attributed to the molecular reorientation by the photo-generated space-charges and its screening field.

For quantitative evaluation of the enhancement in association with the optical confinement in the anti-guide, the sample with coplanar poling-electrodes will be required.

#### References

1. T. Sassa, W. Sakurai and S. Umegaki, CLEO'96, JTuE6 (1996).
2. T. Sassa and S. Umegaki, Opt. Lett., **22**, 856 (1997).
3. T. Sassa and S. Umegaki, J. Appl. Phys., **84**, 4071 (1998).

## LC SLM Based on Fullerene Doped Polyimide

NATALIE V. KAMANINA <sup>a)\*</sup>, NATALIE A. VASILENKO <sup>b)</sup>

<sup>a)</sup> Vavilov State Optical Institute, St.-Petersburg, 199034, Russia

\* E-mail: kamanin@ffm.ioffe.rssi.ru

<sup>b)</sup> Karpov Research Physical-Chemical Institute, Moscow, 103064, Russia

Liquid crystal spatial light modulator (LC SLM) based on a fullerene-doped polyimide photosensitive layer has been studied. LC SLM diffraction efficiency, sensitivity and temporal characteristics have been determined by the holographic technique. The significant improvement (from  $10^{-6}$  to  $5 \times 10^{-7} \text{ J} \cdot \text{cm}^{-2}$ ) in sensitivity has been found. This effect is attributed to a creation of additional donor-acceptor complexes in the system used.

**Keywords** modulator, polyimide, liquid crystal, fullerene,

## INTRODUCTION

A creation of new LC SLM has been stimulated by a development of complicated laser schemes and a design of optical memory devices [1-3]. Optically addressed LC SLM allows various physical problems to be solved. They are a control of laser directional pattern, a image selection, a phase aberration correction, etc. [4-7]. As the SLM photosensitive layer, soluble polyimides (PIs) hold the greatest promise, because their use allows a high resolution and a high sensitivity to be obtained. This effect is associated with the highly

delocalized  $\pi$ -electron states in polyimide, making possible control over its properties.

In the present work dynamic characteristics of LC SLM with the photosensitive layer based on fullerene doped polyimide have been investigated.

## EXPERIMENT

LC SLM had the typical structure [8,9]. For the purpose of sensitization, the polyimide solution in 1,1,2,2-tetrachloroethane (TCIE) was doped with fullerene  $C_{60}$  or the fullerene mixture of 87%  $C_{60}$  and 13%  $C_{70}$ . The fullerene concentration in polyimide was 0.25-0.5 wt.%. The compound was poured over a substrate and dried to remove the solvent. The thickness of photosensitive layer was 1-2  $\mu\text{m}$ . ZhK1289 and E7 (BDH) nematic LCs were used as an modulated layer of 5-10  $\mu\text{m}$  in thickness. Under the Raman-Nath diffraction conditions, a holographic grating was recorded with a pulsed Nd-laser at a wavelength of 532 nm and a pulsewidth of 15 ns (Fig. 1). It should be noticed that the laser wavelength fell within the overlap band of the fullerene-polyimide solution absorption spectrum with the polyimide fluorescence spectrum.

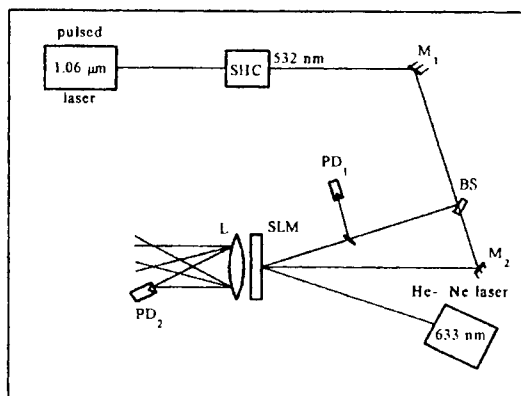


FIGURE 1 Experimental setup. SHC – second harmonic converter;  $M_1$  and  $M_2$  – rotating mirrors; BS – beam-splitting mirror;  $PD_1$  and  $PD_2$  – photodetectors; SLM – LC-SLM; and L – lens.

The readout was carried out by a CW He-Ne-laser ( $\lambda=633$  nm) with the power density of  $100 \mu\text{W}\cdot\text{cm}^{-2}$  in the collimated beam of diameter 5 mm. Both the grating vector and the vector of the readout beam field were aligned with the LC director during writing and readout.

Both pulsed and dc voltage was applied to supply LC-SLM. Rectangular pulses with amplitude of 60 V, width of 90 ms, and repetition frequency of 1 Hz were used as the pulsed supply voltage. A voltage of 60–90 V was applied as the dc supply voltage. LC-SLM operated in the transmission mode. The *S*-type electro-optical effect was used.

## RESULTS and DISCUSSION

Dependence of diffraction efficiency ( $\eta$ ) on the write energy density ( $W_{\text{wr}}$ ) is presented in Fig. 2 for LC SLM with fullerene-doped polyimide and dye-sensitized polyimide at spatial frequency of  $90 \text{ mm}^{-1}$ . *I-V* characteristics for fullerene-doped polyimide is shown in the inset.

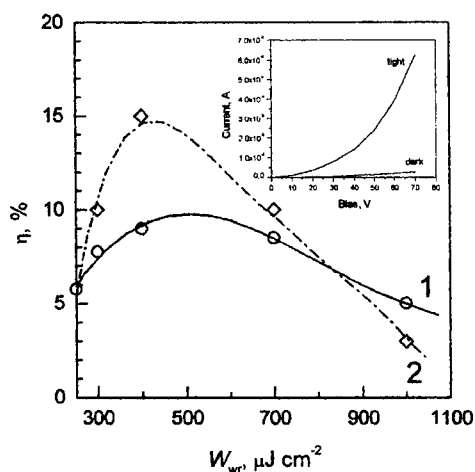


FIGURE 2 Dependence of diffraction efficiency  $\eta$  on a write energy density  $W_{\text{wr}}$  for (1) fullerene-doped PI LC SLM and (2) dye-sensitized PI LC-SLM; in the inset, *I-V* dark and light characteristics of fullerene-doped PI.

It should be noticed that the a similar decrease in  $\eta$  at high  $W_{wr}$  was observed for other SLM [10] and for individual LC composites [11]. The decrease in  $\eta$  at  $W_{wr} > 600\text{--}700\text{ }\mu\text{J cm}^{-2}$  was associated with two reasons [11,12]. The first one was both the breaking of side groups and the disruption of conjugation chains of the polyimide molecule under the intense laser irradiation. The second one was the dissociation of LC molecules also under the intense laser irradiation. In the latter case the concentration of traps increased limiting current through SLM. The trapped carriers formed local electric fields, which caused a disturbance of optimal write-read conditions, decreasing  $\eta$  and hence resolution of SLM. However, recent investigations on reverse saturable absorption in fullerene-doped PI [13,14] films have shown that the transmission of a polyimide film is linear up to energy density of  $0.77\text{--}0.85\text{ J cm}^{-2}$  at the fullerene concentration of 0.25–0.3 wt.%. At higher energy density the limiting of laser radiation transmission began. Therefore, the decrease in  $\eta$  of LC SLM at  $W_{wr} \geq 600\text{ }\mu\text{J cm}^{-2}$  is related to the LC molecule dissociation rather than the structural changes in polyimide.

In the present paper it has been found that the introduction of fullerenes into the polyimide photosensitive layer reduced  $\eta$  of LC SLM (Fig. 2, curve 1), but it improved the threshold sensitivity, which was defined as  $W_{wr}$  at  $\eta = 1\%$ . The basic characteristics of LC SLM, namely, diffraction efficiency ( $\eta$ ) at spatial frequency of  $90\text{--}100\text{ mm}^{-1}$ , sensitivity ( $S$ ), switch-on time ( $t_{on}$ ) and switch-off time ( $t_{off}$ ), with the fullerene-doped PI photosensitive layer are presented in the Table 1. The results for other PI LC SLMs are given for comparison.

TABLE 1 Basic characteristics of LC SLM.

Photosensitive layer of LC SLM	$\eta$ , %	$t_{on}$ , ms	$t_{off}$ , ms	$S$ , $\text{J}\cdot\text{cm}^{-2}$	Supply voltage	Write mode	Ref.
Non-sensitized PI	-	250	700	$10^{-5}$	dc	dc	[15]
Non-sensitized PI	18*	50	500	$5 \times 10^{-6}$	dc	pulsed	[16]
Dye-sensitized PI	10	10	120	$10^{-6}$	pulsed	pulsed	[9]
Fullerene-doped PI	7	5	80-100	$5 \times 10^{-7}$	dc	pulsed	this work

\* This experiment was carried out at spatial frequency of  $40\text{ mm}^{-1}$ .

As seen from this Table 1, the diffraction efficiency of LC SLM with fullerene-doped PI was less than that for LC SLM with fullerene-free PI. This effect is related to faster relaxation of the holographic grating at the fullerene-doped PI – liquid crystal interface. Really, the increase in photoconductivity of fullerene-doped PI film was found [14]. Because an energy of conductivity activation coincides with an energy of mobility activation in polyimides and the change in conductivity is determined by carrier mobility rather than carrier concentration over wide ranges of temperatures and electric fields [17], the increase in photoconductivity indicates convincingly that carrier mobility is higher in fullerene-doped PI. It should be noticed that, on the other hand, the fullerene introduction into the polyimide solution in TCIE caused bathochromic shift of the absorption spectra from 532 nm to 535 nm and 545 nm at the fullerene concentration of 0.25–0.3 wt.% and 0.5 wt.%, respectively [13]. This shift is evidence for an increase in the polyconjugation chain length and hence in carrier mobility. Therefore, higher carrier mobility in fullerene-doped PI results in faster relaxation of the holographic grating and hence in better temporal characteristics of LC SLM with fullerene-doped PI (Table 1).

The improvement in sensitivity of LC SLM with fullerene-doped PI is associated with a creation of charge-transfer complex between a donor (triphenylamine) fragment of the matrix PI molecule and fullerene, which has the electron affinity twice as large as that of acceptor PI fragment. The absorption cross section of new complex is several orders of magnitude more than the one of initial PI complex [18]. This peculiarity allows the device sensitivity to be improved significantly. The efficiency of fullerene sensitization for organic PIs was shown by us before [13,18].

## CONCLUSION

In conclusion, the basic characteristics of LC SLM based on fullerene-doped PI were studied using second harmonic of a pulse Nd-laser. The decrease in diffraction efficiency of fullerene-doped PI LC SLM was shown. This fact is caused by faster relaxation of the holographic grating in fullerene-doped PI LC SLM. The significant improvement (from  $10^{-6}$  to  $5 \times 10^{-7} \text{ J}\cdot\text{cm}^{-2}$ ) in sensitivity was found. This effect is explained by a creation of additional donor-acceptor complexes in the system investigated.



### Acknowledgements

The authors wish to acknowledge Dr. O.D. Lavrentovich (Kent State University), Prof. B.V. Kotov and Dr. V.I. Berendyaev (Karpov Research Physical-Chemical Institute, Moscow) for the help in this work. This work was partially supported by the Russian National Program "Optoelectronic and Laser Technologies".

### References

- [1] F. Pérennès and W.A. Crossland, Opt. Eng., **36**, 2294 (1997).
- [2] A.A. Vasil'ev, D. Casasent, I.N. Kompanets and A.V. Parfenov, Spatial Light Modulators, Radio i Svyaz', Moscow, 1987 [in Russian].
- [3] R.S. McEwen, J. Phys. B: Sci. Instrum., **20**, 364 (1987).
- [4] A.F. Kornev, V.P. Pokrovskii, Opt. Zh., **61**, 10 (1994) [in Russian].
- [5] F.I. Vladimirov, N.I. Pletneve, I.E. Morichev, and T.O. Reshetnikova, Sov. Phys. Tech. Phys., **36**, 950 (1991).
- [6] N.V. Kamanina, L.N. Soms, and A.A. Tarasov, Opt. Spectrosc., **68**, 691 (1990).
- [7] V.A. Berenberg, N.V. Kamanina, and L.N. Soms, Bull. Acad. Sci. USSR Phys. Ser., **55**, 41 (1991).
- [8] N.V. Kamanina and N.A. Vasilenko, Electron. Lett., **31**, 394 (1995).
- [9] N.V. Kamanina and N.A. Vasilenko, Opt. Quantum Electron., **29**, 1 (1997).
- [10] I.S. Zakharov, Spatial Light Modulators, Tomsk Univ., Tomsk, (1983) [in Russian].
- [11] O.V. Kuksenok, V.I. Sugakov, and S.V. Shiyanovskii, Ukr. Fiz. Zh., **37**, 589 (1992) [in Russian].
- [12] N.V. Kamanina and N.A. Vasilenko, Tech. Phys., **42**, 82 (1997).
- [13] N.V. Kamanina, L.N. Kaporskii, and B.V. Kotov, Opt. Commun., **152**, 280 (1998).
- [14] N.V. Kamanina, Opt. Commun., **162**, 228 (1999).
- [15] V.S. Myl'nikov, E.A. Morozova, N.A. Vasilenko, B.V. Kotov, and A.N. Pravednikov, Sov. Phys. Tech. Phys., **30**, 444, (1985).
- [16] M.A. Groznov, V.S. Myl'nikov, A.G. Sinikas, L.N. Soms, Trudy GOI, **60**, 69, (1986) [in Russian].
- [17] V.S. Mylnikov, Advances in Polymer Science, **115**, 3–88, Springer-Verlag, Berlin, Heidelberg, (1994).
- [18] Y.A. Cherkasov, N.V. Kamanina, E.L. Alexandrova, V.I. Berendyaev, N.A. Vasilenko, B.V. Kotov, Proceed. of SPIE, **3471**, 254, (1998).

## Optical Image Correlators Based on Nematic Liquid Crystals

A. MINIEWICZ<sup>a</sup>, P. SIKORSKI<sup>a</sup>, A. JANUSZKO<sup>a</sup>,  
S. BARTKIEWICZ<sup>a</sup>, J. PARKA<sup>b</sup>, F. KAJZAR<sup>c</sup>

<sup>a</sup>) Institute of Physical and Theoretical Chemistry, Wrocław University of Technology, 50-370 Wrocław, Poland; <sup>b</sup>) Institute of Technical Physics, Military University of Technology, 00-908 Warsaw, Poland;  
<sup>c</sup>) LETI (CEA - Technologies Avancées) DEIN - SPE, Groupe Composants Organiques, Saclay, F91191 Gif Sur Yvette, France

**Abstract.** We present an experimental realisation of optical correlation for a real-time pattern recognition by means of a joint-Fourier transform correlator. The correlator operates with a liquid-crystal active matrix spatial light modulator at the input data plane and, designed by us, optically addressed liquid crystalline spatial light modulators at the recording plane allowing both dynamic input and dynamic filtering. We test two different types of optimised liquid crystal cells acting as OA SLM's: (i) nematic liquid crystal doped with 0.4% w/w anthraquinone dye and (ii) hybrid- photoconducting polymer - nematic liquid crystal structure. We discuss performance characteristics of the correlator.

**Keywords:** liquid crystal; spatial light modulator; real-time holography; optical correlator, pattern recognition

### 1. INTRODUCTION

Real-time processing of optical information is nowadays possible because many materials have been developed which show capability of dynamic hologram recording. Among those materials liquid crystals devices such as electrically addressed spatial light modulators (EA LC

SLM's) and optically addressed ones (OA LC SLM's) play important roles. In this work we will focus our attention to the newly discovered liquid crystalline OA SLM's [1-5] which perform principal function in a Fourier plane of the optical correlator.

## 2. OPTICAL CORRELATOR

Pattern recognition is the main task of an optical correlator. This goal can be realised by architectures of different types. We assembled a joint-Fourier-transform (JFT) optical correlator [6] having the active matrix LC SLM for data input and optically addressed LC SLM for optical data processing. The optical diagram shown in Figure 1 illustrates the principle of correlator functioning. An expanded and collimated beam coming from the cw Nd:YAG laser doubled in frequency ( $\lambda = 532$  nm) illuminates an input mask containing objects to be recognised.

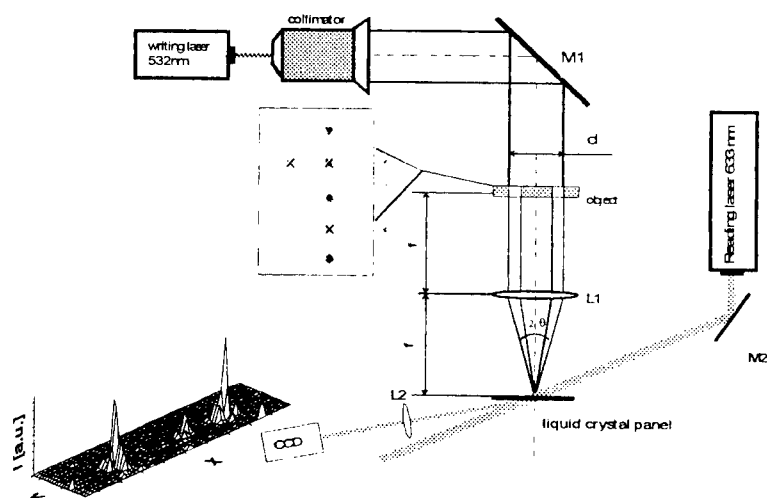


FIGURE 1. Scheme of a joint-Fourier-transform optical correlator having the LC SLM electrically addressed for input data and optically addressed LC SLM for optical data processing. Focal length  $f \approx 280$  mm, expanded beam diameter  $d = 20$  mm.

In a more advanced version an input mask was replaced by a transmissive active matrix spatial light modulator (VGA 640x480 pixels, KOPIN, USA) basing on twisted nematic structure. This EA SLM (15x11 mm in size) was steered by a computer and operated at a frame rate of 25 images per second. The patterns (images, textual data and binary data) could either be displayed in an amplitude mode (using a light polarizer at the rear face of the SLM) or in a phase mode without it. The Fourier lens ( $f = 300$  mm) performs a joint-Fourier transform of all input images and project them on the liquid crystalline OA SLM situated at the focal plane of this lens. Obviously identical objects give matching Fourier transforms. At light overlap regions of these transforms the diffraction phase gratings (holograms) are formed. Their periods and orientations (gratings wave vectors) are dependent on mutual position of the objects in the input plane ( $\Lambda = \lambda / (2 \sin \theta)$  where  $2\theta$  is an angle between the incidence directions of respective Fourier transforms. These holograms are then reconstructed by another laser beam (HeNe,  $\lambda = 632.8$  nm) illuminating the centre area of the Fourier plane. The first order diffracted waves contain the correlation signal of the input objects. The less similar are the objects the weaker gratings are formed in the liquid crystal panel and consequently the lesser amount of light from reading laser is diffracted. The correlation peaks are registered by a CCD camera, fed to the computer and analysed with an Image ProPlus programme. We noticed that the correlation peaks for objects displayed by active LC matrix were less visible when compared to that obtained when lithographically prepared masks were used. We link this with much lower contrast and resolution of images displayed by EA SLM than that provided by the masks.

### 3. LIQUID CRYSTALLINE OPTICALLY ADDRESSED SLM's

We prepared two types of LC panels. First one consisted of a planarly oriented multicomponent nematic mixture (low-angle rubbing, tilt  $2 - 3^\circ$ ) doped with an anthraquinone dye (1 % w/w) [1-3] which acted as a photoconducting dopant. Such LC panel is particularly suitable for optical correlation purposes as the holographic gratings can be written under normal light incidence.  $6.3 \mu\text{m}$  thick LC layer made that the system operated within the Raman-Nath light diffraction regime and the written holograms could be read at any incidence angle (no Bragg

angular selectivity). The diffraction efficiencies measured in the described panels were of the order of 1% making well visible correlation spots. Long-time operation required frequent voltage reversal ( $\pm 10$  V) in order to prevent possible memory effects and electrochemical reactions at electrode areas. The total light intensity entering the LC panel was kept well below  $300 \text{ mW/cm}^2$  in order to avoid damage of the system by an excessive heat at the focal point.

The second type panel was a hybrid structure containing a pure nematic liquid crystal (E-7 Merck) sandwiched between two polymeric photoconducting electrodes [4,5]. We employed poly(octylthiophene) as a dual function alignment inducing and photoconducting layer. Two principal effects occur under light illumination: (i) formation of spatially modulated space charge in a photoconducting polymeric layer and (ii) mapping of the space charge electric field into respective changes of an effective refractive index of nematic liquid crystal (via the process of molecular reorientations along the electric field lines). Contrary to the dye-doped liquid crystals, where charge carrier transport and index modulation occurs within the same medium, in the latter solution these functions are separated, thus electrode as well as photochemical side reactions are avoided improving the durability of the panel. The disadvantageous for optical correlator construction is the necessity of sample tilting for obtaining an efficient hologram recording.

#### 4. PERFORMANCE OF THE JFT CORRELATOR

Figure 2 shows the experimental results for pattern recognition by optical correlation. The cross has been identified among the simple symbols and localised among other symbols. In the centre of Figure 2 we show the correlation spots together with the 3D plots. The autocorrelation peaks between two crosses (cf. Fig. 2) are distinctly stronger (250 arbitrary units) than the correlations between the different symbols. Due to nonuniform illumination of the input scene and different carrier frequencies of the gratings for the individual objects the autocorrelation peaks differ in intensity.

Observation of a rise time of a correlation peak intensities after the laser beam opening allowed us to study the dynamics of the systems. Typically rise times amounted to 20 ms and the decay time of the diffracted signal measured after blocking one of the beams amounted to 30 ms. Then the entire recognition process in our system has been completed within 50 msec, and the system was ready for a new task.

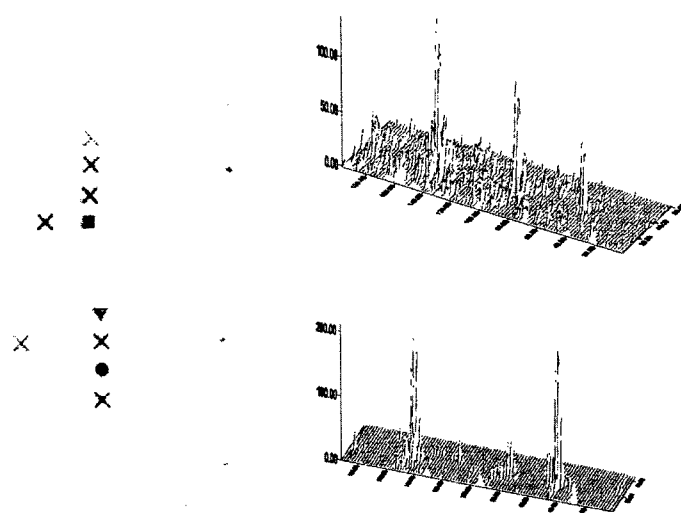


FIGURE 2 Experimental results of image recognition with the use of OA LC SLM's described in this paper. On the left are shown objects in the input scene, in the middle the correlation spots observed in the output plane and on the left their 3D plots.

The thickness of recording material  $d$  is related to the focal length  $f$  of Fourier transform lens by the formula [7]:

$$f > \sqrt{\frac{dhL_c}{n\lambda}}$$

In this formula  $h$  is the offset of the image ( $h = 8$  mm),  $L_c$  is the size of the correlation plane (here we take the diameter of a reading beam,  $L_c = 2$  mm),  $n$  is the refractive index of the liquid crystal ( $n = 1.6$ ). In our case minimal focal length should fulfil the relation  $f > 11$  mm. This result is encouraging because the considerable reduction of the total size of the optical system is possible.

For a long-time use the LC panel should be biased by a voltage changing its sign after each cycle of a hologram recording in order to avoid possible memory effects and electrochemical reactions at electrode areas. The light intensity level entering the LC panel should be kept well

below  $300 \text{ mW/cm}^2$  in order to avoid damage of the system by excessive heat at the focal point. The drawback of the presented system is a relatively low signal to noise ratio and a low resolution 50 lines/mm.

In conclusion we demonstrated a liquid crystal based optical correlator (where dye-doped and hybrid polymeric - nematic liquid crystal were used as optically addressed spatial light modulators). This in our opinion opens up possibility for constructing a reconfigurable (within 50 ms), small size, low intensity and low operating voltage devices.

#### Acknowledgements

This work has been supported by Wrocław University of Technology. Part of the research was supported within the programme of the Centre of Nanostructured Advanced Materials of Wrocław University of Technology in 1999.

#### References

1. S. Bartkiewicz, A. Miniewicz, A. Januszko and J. Parka, Pure Appl. Opt., **5**, 799-809 (1996).
2. A. Miniewicz, S. Bartkiewicz, W. Turalski, A. Januszko, in R.W. Munn, A. Miniewicz and B. Kuchta (eds.), Electrical and Related Properties of Organic Solids, NATO ASI Series, Vol. **3/24**, Kluwer Academic Publishers, Dordrecht, 1997, pp. 323-337.
3. A. Miniewicz, J. Parka, S. Bartkiewicz and A. Januszko, Pure Appl. Opt., **7**, 179-189 (1997).
4. S. Bartkiewicz, P. Sikorski and A. Miniewicz, Opt. Lett., **23 (22)**, 1769-1771 (1998).
5. F. Kajzar, S. Bartkiewicz and A. Miniewicz, Appl. Phys. Lett., **74 (20)**, 2924-2926 (1999).
6. C.S. Weaver and J.W. Goodman, Appl. Opt., **5**, 1248-1249 (1966).
7. K. Okada, K. Ito, T. Honda, J. Tsujiuchi, Optical Review, **1**, 166-169 (1994).

## Influence of the Chromophore Ionization Potential on the Magnitude of Photorefractive Effects in PVK-based Polymer Composites

DAVID VAN STEENWINCKEL<sup>(a)</sup>, ERIC HENDRICKX<sup>(a)</sup>, KURT VAN DEN BROECK<sup>(b)</sup>, CELEST SAMYN<sup>(b)</sup>, AND ANDRE PERSOONS<sup>(a)</sup>

<sup>(a)</sup>Laboratory for Chemical and Biological Dynamics, Center for Research on Molecular Electronics and Photonics, University of Leuven, Celestijnenlaan 200D, B-3001 Leuven, Belgium; <sup>(b)</sup>Laboratory of Macromolecular and Physical Organic Chemistry, University of Leuven, Celestijnenlaan 200F, B-3001 Leuven, Belgium

We report on the synthesis of three highly polar chromophores and their use as dopants in poly(N-vinylcarbazole) (PVK)-based photorefractive (PR) polymer composites sensitized with (2,4,7-trinitro-9-fluorenylidene)malononitrile (TNFDM). Small alterations in the amino donor group substituents were used to tune the dye's ionization potential ( $I_p$ ) by 0.2 eV. At 780 nm and an applied field of 59 V/ $\mu\text{m}$ , we observed complete internal diffraction and a gain coefficient of 167  $\text{cm}^{-1}$ . Diffraction efficiency and gain coefficient, as well as the PR phase shift, were found to correlate with the chromophore  $I_p$ .

**Keywords:** photorefractivity; ionization potential; chromophore.

### INTRODUCTION

The formation of a refractive index grating through the PR effect involves the creation of charges through the absorption of light, the diffusion, migration, and trapping of the free carriers, and the modulation of the refractive index by the space-charge field thus established [1]. The most efficient polymer composites developed so far were based on a photoconductive poly(N-vinylcarbazole) (PVK) / N-ethylcarbazole (ECZ) matrix, doped with a nonlinear optical chro-



mophore. When doped with the sensitizer (2,4,7-trinitro-9-fluorenylidene)malononitrile (TNFDM), these composite materials show very good PR performances at an excitation wavelength of 780 nm. The Figure-Of-Merit for chromophores in photorefractive applications is given by  $FOM = A\Delta\alpha\mu^2 + \mu\beta$ , where  $\Delta\alpha$  is the polarizability anisotropy,  $\mu$  the dipole moment,  $\beta$  the first hyperpolarizability, and  $A = 2/(9kT)$  is a scaling factor [2]. Optimization of this Figure of Merit, together with the lowering of the glass transition temperatures of the polymers [3], has lead to strong improvements in the photorefractive performances. Another issue that has attracted attention recently is the effect of the chromophore's ionization potential ( $I_p$ ). Theoretically, an increase in donor strength can increase the PR Figure-Of-Merit, and improve the diffraction efficiency of the PR polymer, but can also reduce the chromophore  $I_p$  and thus affect the transportation process of the charges. Since this transportation process is of paramount importance in the photorefractive grating formation, it can lead to changes in the photorefractive characteristics, such as buildup speed, refractive index modulation amplitude, and photorefractive phase shift.

## RESULTS AND DISCUSSION

### Section 1

The three D- $\pi$ -A-chromophores that were used as dopants in the photorefractive PVK-based composites are shown in Figure 1. We have determined the magnitude of the most important factor in the figure of merit ( $\Delta\alpha\mu^2$ ), by means of an ellipsometric technique [4]. This enables us to compare the relative efficiencies of the different chromophores in the photorefractive PVK composites. The results of the ellipsometric measurements are listed in Table 1.

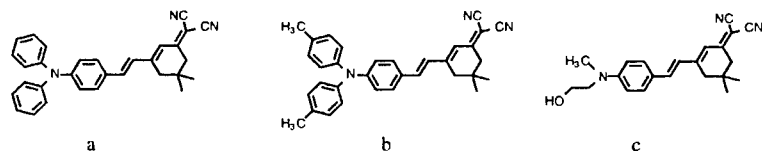


FIGURE 1 Structures of the chromophores used in the photorefractive polymer composites.

Apart from  $\Delta\alpha\mu^2$ , the  $\lambda_{max}$  and the ionization potentials  $I_p$  of the different chromophores were determined (see Table 1). The ionization potentials of the chromophores were calculated from cyclic voltammetry experiments using the ferrocene/ferrocenium-ion couple as an internal standard.

The photorefractive composite materials **A**, **B**, and **C** contained 28.5 wt. % of the chromophores **a**, **b**, and **c**, respectively, and the PVK/ECZ ratio was adjusted to equalize the glass transition temperatures and hence the contributions of birefringence to the total refractive index modulation. 1 wt. % of TNFDM was added as an external sensitizer.

Chromophore	$\Delta\alpha\mu^2$ ( $\cdot 10^{-57}$ esu)	$\lambda_{max}$ (nm)	Ip (eV)	$\vartheta$ (°) at 60 V/ $\mu$ m
<b>a</b>	$5.1 \pm 0.5$	496	5.59	37
<b>b</b>	$5.5 \pm 0.5$	516	5.46	29
<b>c</b>	$6.5 \pm 0.5$	499	5.40	25

TABLE 1 Values of  $\Delta\alpha\mu^2$ ,  $\lambda_{max}$ , and Ip for chromophores **a**, **b**, and **c**.  $\vartheta$  is the photorefractive phase shift in samples **A**, **B**, and **C**, at 60 V/ $\mu$ m. See Section 2.

In the standard model of photorefractivity for PVK-based polymers, the charges with the highest mobility are holes, that migrate by hopping from carbazole to carbazole. However, if the ionization potential of a dopant molecule in the PVK-matrix is smaller than that of carbazole (Ip of ECZ = 5.9 eV), as is the case for the chromophores used in this work, an electron can be transferred from the dopant molecule to the carbazole cation. We have verified this by measuring photoconductivity, that is a convolution of both photogeneration and mobility. Similar to what has been observed by Pai et al. in TPD-doped carbazole [5], we observed a large decrease in photoconductivity upon doping PVK with small amounts of chromophore **c**.

The injection of holes from the carbazole manifold into the chromophore manifold results in a stabilization of the positive charge since the chromophore has the smallest ionization potential. Due to the stabilization of the positive charges, a larger number density of charges accumulates in the film, including a larger number density of negatively charged species. Then, the chromophores act as compensators in the photoconducting matrix [6]. The time the charges spend on the compensator, depends on the ionization potential difference between the compensator chromophore and the carbazole host ( $\Delta$ Ip). Consequently, the total amount of free charges scales with the  $\Delta$ Ip between carbazole and the compensator.

In the model proposed by Grunnet-Jepsen *et al.*, the compensator is an inactive trap, and its only function is the buildup of a larger active trap density [6]. A factor that has not been taken into consideration, however, is the percolation of holes between the chromophores. In the photoconductive experiments, the

photoconductivity decreases as small amounts of chromophores are doped into PVK, but then increases as more chromophore is added. This is similar to what has been observed by Pai *et al.* [5], and suggests that the chromophore participates in the charge transport in the composites discussed in the present paper. The charge transporting abilities of the chromophores were further verified by assembling a sample containing chromophore **a**, doped in an inert polycarbonate (PC) matrix. Dioctyl phthalate (DOP) was added to lower the glass transition temperature ( $T_g$ ) of the sample. The sample had a composition of PC/chromophore **a**/DOP/TNFD: 53/27/19/1 wt. ratio. Apart from photoconductivity, the sample also showed good photorefractive performances, with a diffraction efficiency of 33% and a gain coefficient of  $52 \text{ cm}^{-1}$  at an applied field of  $60 \text{ V}/\mu\text{m}$ . Since no other charge transporting molecules were present, the charge transport in this sample clearly occurs in the chromophore manifold.

## Section 2

In this section we discuss the correlation between the ionization potentials of the chromophores, the steady state two-beam coupling gain coefficients, and degenerate four-wave mixing (DFWM) diffraction efficiencies. If the space-charge field is not completely saturated, the amplitude of the space-charge field and the refractive index modulation will scale with the charge density in the polymer film. As was explained in Section 1, the total amount of free charges in the photorefractive material scales with the difference in ionization potential between carbazole and the chromophore. A chromophore with a lower  $I_p$  has a stronger compensating role, and a larger charge density accumulates in the film. Consequently, both space-charge field and the refractive index modulation can be expected to enlarge. This was confirmed experimentally by measuring diffraction efficiencies and two-beam coupling gain coefficients.

The diffraction efficiencies of samples **A**, **B** and **C** are shown in Figure 2. Using Kogelnik's coupled wave theory for thick holograms [7], the amplitude of the refractive index modulation was calculated from the diffraction efficiency. Filling in all the geometry and absorption factors, we obtain the following relationship for the internal diffraction efficiency:

$$\eta = \sin^2(586 \cdot \Delta n) \quad (1)$$

We have determined the refractive index modulation of sample **C** to be 2.2 times larger than that of sample **B**. For samples **B** and **A** the ratio was 1.6. The measured ratios in  $\Delta\alpha\mu^2$  (1.2 and 1.06, respectively, see section 1) hence cannot explain the much larger difference in refractive index modulation, which leads to the conclusion that the refractive index modulation partly is determined by the amplitude of the space-

charge field, and by the difference in  $I_p$  between carbazole and the chromophore, as was anticipated.

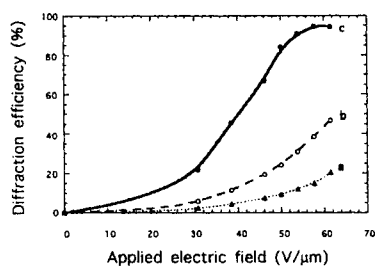


FIGURE 2 Diffraction efficiencies for samples A, B, and C.

As can be seen in Figure 3, the two-beam coupling gain coefficient  $\Gamma$  follows the same tendency as the diffraction efficiency.

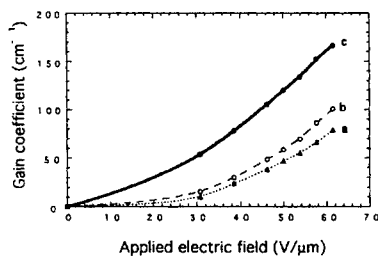


FIGURE 3 Gain coefficients for samples A, B, and C.

This was expected, since the gain coefficient is directly proportional to the product of the refractive index modulation amplitude and the sine of the phase shift between the space-charge field and the interference pattern:

$$\Gamma = \frac{4\pi}{\lambda} (\hat{e}_1 \cdot \hat{e}_2^*) \cdot \Delta n \cdot \sin \vartheta \quad (2)$$

$\lambda$  is the optical wavelength,  $\hat{e}_1$  and  $\hat{e}_2$  are the polarization vectors of the two writing beams,  $\Delta n$  is the refractive index modulation, and  $\vartheta$  is the phase shift between the space-charge field and the interference pattern generated by the interacting beams. Sample C shows a gain

coefficient of  $167\text{ cm}^{-1}$  at a field of  $59\text{ V}/\mu\text{m}$ , while complete internal diffraction also occurs at that field.

From the gain coefficient and the diffraction efficiency, the phase shift can be calculated, combining equations (1) and (2). The calculated phase shifts in samples **A**, **B**, and **C** at an applied field of  $60\text{ V}/\mu\text{m}$  are shown in Table 1. As the  $I_p$  of the chromophore decreases ( $\Delta I_p$  between chromophore and carbazole increases), smaller phase shifts are observed. This points out that more effective traps are present if  $\Delta I_p$  is large. The charges then have more difficulties migrating towards the darker parts in the illumination pattern. It agrees with the observations of reference 6, that chromophores with a smaller  $I_p$  have a stronger compensating role, and that a larger concentration of photoreduced sensitizer accumulates in the polymer. Since the latter acts as a photorefractive trap and hinders the hole transport in the polymer, a larger concentration of this trap produces a smaller phase shift.

In conclusion, we have tuned the ionization potential of three chromophores by small alterations in the amino donor group substituents. The steady-state amplitude of the index gratings and the photorefractive phase shifts in the PVK-based composites were found to correlate well with the chromophore  $I_p$ .

#### Acknowledgements

D. V. S. is a research assistant and E. H. is a research associate of the Fund for Scientific Research-Flanders (Belgium) (FWO). This research was supported by research grants from the FWO (G.0308.96), the University of Leuven (GOA/95/01), and the Belgian Government (IUAP P4/11).

#### References

- [1] P. Günter, and J.-P. Huignard, in Photorefractive Materials and their Applications; Springer: Berlin, Vols. I and II (1988).
- [2] B. Kippelen, F. Meyers, N. Peyghambarian, and S. R. Marder, *J. Am. Chem. Soc.* **119**, 4559 (1997).
- [3] W. E. Moerner, and S. M. Silence, *Chem. Rev.* **94**, 127 (1994).
- [4] Sandalphon, B. Kippelen, K. Meerholz, and N. Peyghambarian, *Appl. Opt.* **35**, 2346 (1996).
- [5] D. M. Pai, J. F. Yanus, and M. Stolka, *J. Phys. Chem.* **88**, 4714 (1984).
- [6] A. Grunnet-Jepsen, D. Wright, B. Smith, M. S. Bratcher, M. S. DeClue, J. S. Siegel, and W. E. Moerner, *Chem. Phys. Lett.* **291**, 553 (1998).
- [7] H. Kogelnik, *Bell. Syst. Techn. J.* **48**, 2909 (1969).

**SESSION C: POLED POLYMERS FOR SHG  
AND ELECTRO-OPTIC DEVICES**

## NUMERICAL ANALYSIS OF THE THREE DIMENSIONAL POLARIZATION DISTRIBUTION IN POLED NONLINEAR OPTICAL POLYMERS

ROBERT BLUM, KERSTEN PFEIFER, and MANFRED EICH  
Technische Universität Hamburg-Harburg, AB 4-09, D-21071 Hamburg, Germany

**Abstract** We present experimental and theoretical details on how to analyze the polarization distribution in poled second order nonlinear optical polymers in three dimensions. The polar order is analyzed in both the lateral and vertical directions by scanning second harmonic microscopy at various wavelengths along the absorption tail of the polymer.

**Keywords** scanning microscopy; second harmonic generation; polarization; depth profiling; homogeneity

### INTRODUCTION

The demand for high performance second order nonlinear optical (NLO) polymers is strongly increasing due to the recent need of high speed electro-optic (EO) components for telecommunication applications. Requirements for these polymers are low optical loss, large EO coefficient, and good stability (thermal and temporal as well as photostability). In general, electric field poling at temperatures close to the glass transition temperature of the polymer is used to orient the NLO chromophores and to achieve high EO coefficients. For good modulation properties and low loss waveguiding, most device concepts require that the polar order and, thus, the induced change in refractive index be adequately homogeneous across the waveguide dimensions. Poling induced scattering centers can lead to high optical losses and must therefore be avoided. It is therefore important to analyze how homogeneous the obtained nonlinearity is. In this paper, we will present the details of how to analyze the  $\chi^{(2)}$  profile in all three dimensions.

### THEORY

In the following, the equations describing the second harmonic (SH) generation in a poled polymer (with poling axis along the  $z$ -direction) will be derived. We allow for an inhomogeneous profile of the SH conversion tensor  $d$ , that is  $d$  can be a function of depth  $d(z)$ .<sup>1</sup> Furthermore, the absorption of the SH at  $2\omega$  is taken into account.

Let us assume the surface of the NLO polymer to be perpendicular to the  $z$ -direction and the plane of incidence to be in the  $x$ - $z$  plane. The fundamental beam with electric field  $E_\omega$  is incident at an angle  $\theta$  upon the polymer surface and propagates at an angle  $\theta_\omega$  inside the polymer. The nonlinear wave equation is given by:

$$\nabla^2 E_\omega - \frac{1}{c^2} \frac{\partial^2 E_\omega}{\partial t^2} = \mu_0 \frac{\partial^2 P_\omega^{(2)}}{\partial t^2} \quad (1)$$

For harmonic infinite plane wave propagation and this sample orientation,  $\hat{E}_\omega$  and  $\hat{E}_{2\omega}$  will only be a function of  $z$ .<sup>2</sup> With

$$kr = kz \cos \theta_\omega \quad (2)$$

and in slowly varying envelope approximation, equation (1) then reduces to

$$\frac{\partial \hat{E}_\omega}{\partial z} = -\frac{i\omega^2 \mu_0}{2k_\omega \cos \theta_\omega} \hat{P}_\omega^{(2)} \cdot e^{-ik_\omega z \cos \theta_\omega} \quad (3)$$

For second harmonic generation the nonlinear polarization is given by:

$$\hat{P}_{2\omega}^{(2)} = \frac{1}{2} \epsilon_0 \chi^{(2)}(-2\omega; \omega, \omega) \hat{E}_\omega \hat{E}_\omega e^{i2k_\omega z \cos \theta_\omega} = \epsilon_0 d_{eff} \hat{E}_\omega \hat{E}_\omega e^{i2k_\omega z \cos \theta_\omega} \quad (4)$$

Rewriting Eq. 3 for the second harmonic field (i.e.  $\omega \rightarrow 2\omega$ ), one obtains for  $E_{2\omega}$ :

$$\frac{\partial \hat{E}_{2\omega}}{\partial z} = -\frac{i\omega}{n_{2\omega} c \cos \theta_{2\omega}} d_{eff} \hat{E}_\omega^2 \cdot e^{i\Delta k z} \quad (5)$$

with

$$\Delta k = \frac{4\pi}{\lambda} (n_\omega \cos \theta_\omega - n_{2\omega} \cos \theta_{2\omega}) \quad (6)$$

For a weak nonlinear conversion efficiency (no pump depletion) and no absorption at  $\omega$ ,  $\hat{E}_\omega$  can be regarded as constant. It is then sufficient to examine only the following equation, which is Eq. 5 modified by a term that accounts for absorption at  $2\omega$ :

$$\frac{\partial \hat{E}_{2\omega}}{\partial z} = -\frac{i\omega}{n_{2\omega} c \cos \theta_{2\omega}} d_{eff} \hat{E}_\omega^2 \cdot e^{i\Delta k z} - \frac{\alpha}{2 \cos \theta_{2\omega}} \hat{E}_{2\omega} \quad (7)$$

For s-polarization and an inhomogeneous  $d$  profile we have in good approximation

$$d_{eff}(z) = d_{31}(z) \cdot \sin \theta_\omega \quad (8)$$

and one obtains<sup>3</sup> with  $I_{2\omega} = \frac{1}{2} n_{2\omega} \epsilon_0 c |\hat{E}_{2\omega}|^2$  for the second harmonic intensity:



$$I_{2\omega} = \exp[-\alpha L / \cos \theta_{2\omega}] \frac{2\omega^2}{\epsilon_0 c^3} I_{\omega}^2 \frac{T}{n_{2\omega} n_{\omega}^2} \frac{\sin^2 \theta_{\omega}}{\cos^2 \theta_{2\omega}} \left| \int_0^L d_{31}(z) \cdot \exp[(i\Delta k + \alpha/2 \cos \theta_{2\omega})z] dz \right|^2 \quad (9)$$

where  $T$  contains the transmission losses due to Fresnel reflections at the interfaces (quadratic for  $I_{\omega}$  and linear for  $I_{2\omega}$ ). Eq. 9 thus permits calculation of the SH intensity for arbitrary  $d(z)$  profiles. The absorption and the refractive index dispersion<sup>4</sup> are well known, the dispersion of  $d$  can be calculated or approximated using the two-level model.<sup>5</sup>

We can see that the influence of the  $\exp(\alpha z / \cos \theta_{2\omega})$  term under the integral is to weight the  $d_{31}(z)$  distribution. The  $d_{31}$  values close to the surface at  $z = L$  contribute more to the value of the integral than those values close to  $z = 0$ . The larger the absorption, the thinner the  $d_{31}(z)$  region that contributes significantly to  $I_{2\omega}$ . It is also evident, that, for asymmetric profiles, it matters which side of the film is facing the detector.

The idea of how to obtain a 3d profile of the  $\chi^{(2)}$  distribution is to generate the second harmonic in the NLO polymer for various wavelengths and film orientations. If these wavelengths are chosen such that the absorption coefficient for the SH wave varies sufficiently strong, it is possible to obtain a depth profile of  $\chi^{(2)}$ . Combined with a conventional 2d scan, this permits to obtain a 3d distribution.<sup>6</sup>

We will now calculate the SH intensity as a function of wavelength for various profiles of  $d_{31}(z)$  for a 5  $\mu\text{m}$  thick P(DRI-MMA) polymer with 10 mol% chromophore content on an ITO substrate (soda lime glass) at an angle of  $\theta = 30^\circ$  for two sample orientations (A and B as defined in Fig. 1). The polymer was poled in parallel plate configuration with a 150nm thick top gold electrode. The gold electrode was removed after poling.

In Fig. 1, the arrows indicate that various electric field distributions are possible in the polymer film. We keep in mind, that due to the fact that we apply a given voltage  $U$  between the electrodes, the integral over the electric field between any two points of the top and bottom electrode *must* equal  $U$ , or alternatively:

$$\int_0^L E(x_1, y_1, z) dz = U \quad (10)$$

for any  $x_1$  and  $y_1$ , where we have defined  $x$  and  $y$  to be in the plane of the ITO electrode. There is a direct consequence of this fact: At low absorption and for thin samples ( $L \ll l_c$ , where  $l_c$  is the coherence length), the SH signal is in good approximation proportional to the square of the integral over  $E$ . Therefore, a 2d scanning second harmonic plot at such a wavelength *must* be homogeneous - provided that  $d(z) \propto E(z)$  can be taken for granted. When we generate the second harmonic at high SH absorption, only light originating from a thin surface layer is detected. The 2d plot now can reveal strong variations in the polar order close to the surface.

In Fig.2, the SH intensity is compared for various profiles. Profile #1 has a constant  $d(z)$ . We recognize that the curves for both orientations (A and B) are identical except for a factor that arises from the different (wavelength dependent) Fresnel factors.

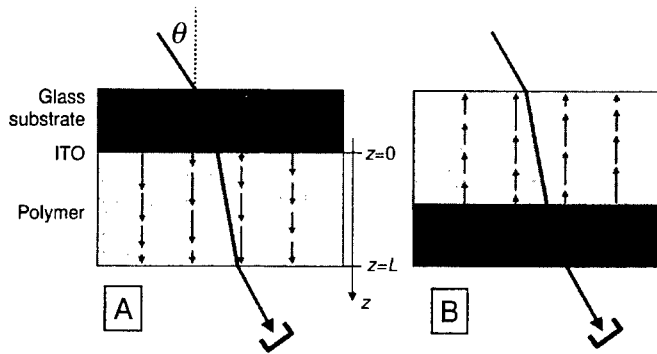


FIGURE 1 Schematic of sample geometry. A: Polymer oriented towards detector. B: polymer towards laser. The small arrows symbolize the different internal  $E$  field distributions that can result in the film.

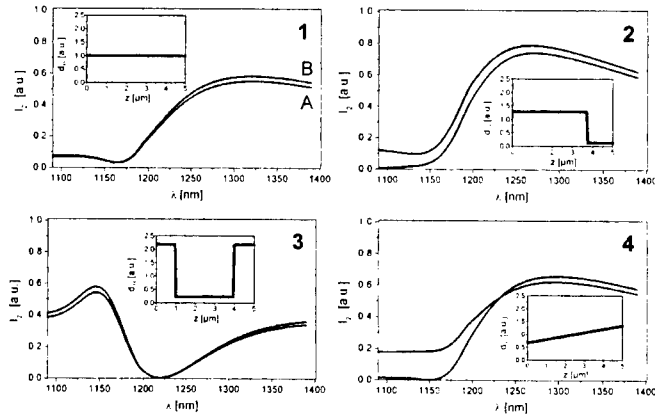


FIGURE 2 Calculated SH intensity vs wavelength for various profiles. The profiles are shown in the inset (from  $z=0$  to  $z=L$ ). The  $I_{2\omega}$  scale and the voltage drop across the sample are the same for all plots.

In Profile #2, we calculated the response for a step profile. Such an asymmetric profile could result after poling if *injected charges are trapped* close to the injecting electrode and the internal electric field is modified due to this charge layer (enhancement in the

sample orientations are no more parallel to each other. For smaller wavelengths there is a substantial difference between "front" and "rear" side of the film.

Profile #3 has an enhanced field at both electrodes. If the polymer has a high *ionic conductivity*, these ions can migrate from the bulk towards the electrodes and be trapped. Such a process will result in a lowering of the electric field inside the polymer and in an enhancement at one or both electrodes, depending on the mobility of the ions and the poling conditions. Finally, profile #4 models a (homogeneous) *space charge* distribution in the bulk. This would lead to a (linear) increase in the internal electric field. Please note the "crossover" at 1230nm, a wavelength below which the A orientation yields a higher signal than the B orientation, as expected from the profile.

We have limited our plots to a wavelength region, in which the dispersion of  $d$  is well described by the two level model. This permits the absolute values of the SH intensity to be plotted. The various profiles were all normalized, i.e. they can all result upon the application of the same voltage. For shorter fundamental wavelengths that are closer to the absorption maximum at  $\lambda/2 = 470\text{nm}$ , and for which the value of  $d$  might not be known precisely enough, one has to compare the different responses from the two sample orientations. For asymmetric profiles, this ratio can be substantially different from 1.

#### EXPERIMENTAL

Figure 3 shows the experimental setup used for the multi- $\lambda$  scanning second harmonic microscopy. As a tunable laser source we use a BBO optical parametric oscillator (OPO) from GWU that is pumped with a tripled Nd:YAG (Spectra Physics) at 355nm.

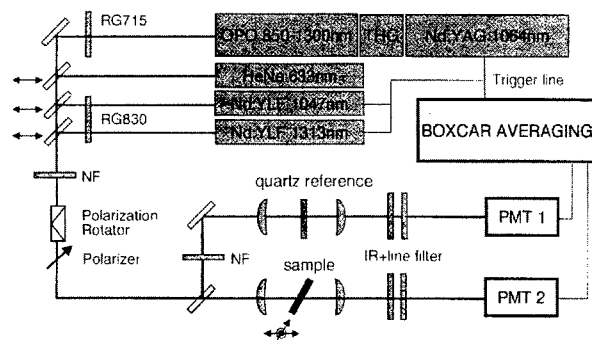


FIGURE 3 Multi-wavelength scanning second harmonic microscopy setup.

The overall tuning range of the OPO is from about 400nm to 2000nm (signal and idler wave). Other lasers used are two Nd:YLFs at 1047nm and at 1313nm and a HeNe for alignment purposes. Various Schott filters are used to either suppress unwanted pumping wavelengths before the sample or to block the fundamental wavelength after the sample.

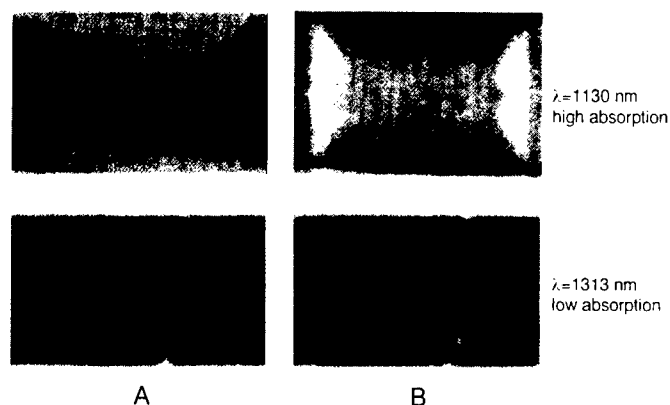


FIGURE 4 Scanning second harmonic microscopy images at 1130nm and at 1313nm (orientations A and B as defined in Fig. 1)

The poling homogeneity for a given polymer can depend on the choice of the substrate, the cladding and the electrode material, the drying and evaporation parameters as well as the poling conditions. Fig. 4 shows a measurement at  $\lambda=1313\text{nm}$  (low absorption) and at  $\lambda=1130\text{nm}$  (high absorption,  $1/e$  thickness =  $1\mu\text{m}$ ) for a  $5\mu\text{m}$  thick film that was poled at 450V (dimensions: width=7mm, height=2.4mm.). For a high absorption wavelength (top), those regions that have an enhanced signal for one sample orientation (e.g. the half moon shaped areas in A) have a lower value if the sample is turned around (B), as required by Eq. 10. For the measurements at low absorption, the field is homogeneous (with some variation due to the fact that the thickness is no longer negligibly small), as predicted by theory. The half moon shaped areas are precisely at the boundary between the ITO electrode and the soda lime glass, indicating that charge injection processes at the electrode edges lead to this field modification. These inhomogeneities at the edges of the bottom electrode are not observed if a less conductive substrate such as quartz is used.

#### REFERENCES

1. D. Pureur, A.C. Liu, M.J.F. Digonet, and G.S. Kino, *Optics Letters*, **23**, 588 (1998)
2. J. Jerphagnon and S. K. Kurtz, *J. Appl. Phys.*, **41**, 1667 (1970)
3. D. S. Chemla and J. Zyss, *Nonlinear Optical Properties of Organic Molecules and Crystals* (Academic Press, New York, 1987)
4. Ph. Prêtre, L.-M. Wu, A. Knoesen, and J.D. Swalen, *J. Opt. Soc. Am. B*, **15**, 359 (1998)
5. K. D. Singer, M. G. Kuzyk, and J. E. Sohn, *J. Opt. Soc. Am.*, **4**, 968 (1987)
6. R. Blum, M. Adameck, T. Elken, and M. Eich, *Nonlinear Optics*, **22**, 19 (1999)
7. R. Blum, M. Sprave, J. Sablotny, and M. Eich, *J. Opt. Soc. Am. B*, **15**, 318 (1998)

## Second Harmonic Generation in Photo-Bleached PU1-C4B Film Channel Waveguides

SUGURU HORINOUCHI<sup>1,2</sup>, MAKOTO FUKUDA<sup>2</sup>, KWANG-SUP LEE<sup>3</sup>, JE-HYUN LEE<sup>3</sup>, KEIICHI MITO<sup>2</sup> and KEISUKE SASAKI<sup>1,2</sup>

<sup>1</sup>TAO (Telecommunications Advancement Organization of Japan) Chitose Photonics Research Center, Chitose-Shimin-Gallery 4F, 5-7-1 Chiyoda-cho, Chitose-shi, Hokkaido 066-0062 JAPAN

<sup>2</sup>Chitose Institute of Science and Technology  
758-65 Bibi, Chitose-shi, Hokkaido 066-8655 JAPAN

<sup>3</sup>Department of Polymer Science & Engineering, Hannam University, Taejeon, KOREA

### Abstract

Polyurethane PU1-C4B film channel waveguides were fabricated by photo-bleaching process. After He-Cd laser operating at 442 nm with 9 kJ/cm<sup>2</sup> was irradiated, the refractive index change of 0.1 was observed in the polymer film. Phase matched second harmonic generation (SHG) at 415 nm was observed in PU1-C4B film waveguide.

### INTRODUCTION

Many interests have been paid to potential applications of organic materials for the future photonic devices such as frequency doubler, light modulator, optical switch, and optical amplification. Many kinds of materials (inorganic crystals, organic crystals, thin films fabricated by LB or self-assembly techniques, organic-inorganic hybrid materials, etc.) have been developed as nonlinear optical materials. Among them, poled polymers have advantages in regard to the ease of fabrication and structural modification.

In this study channel waveguides of the PU1-4CB film were fabricated via photo-bleaching process. There are several fabrication processes for developing channel waveguides such as UV lithography, laser ablation, reactive ion etching and so on. It

was shown that the photo-bleaching process had advantages of precise index control of nonlinear optical polymers, versatile applicability, simple and low cost process.

## RESULTS AND DISCUSSION

Organic materials have a lot of advantages; fast response, easy fabrication process, and low cost, but the long term stability of aligned dipoles and the insufficient nonlinearity in polymeric systems are the major handles. Polyurethane PU1-C4B polymer was developed to solve this problem. The molecular structure of the polymer is shown in Fig. 1. The molecule has a covalently attached stilbazolium salt chromophores in the side chain.

Polymer film was spin-coated on a Pyrex glass substrate as shown in Fig. 2(a), and He-Cd laser at 442 nm was irradiated on the spin-coated films. The width of the UV beam was controlled by changing the distance between the film sample and the lens shown in Fig. 2(b). This process lowered the refractive index of the PU1-C4B film. After He-Cd laser with 9 kJ/cm<sup>2</sup> was irradiated, the refractive index change of 0.1 was observed as shown in Fig. 3. The refractive index was measured by the m-line method. This characteristic reveals that channel waveguide of this film can be easily fabricated via this photo-bleaching

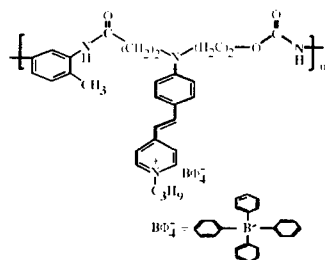
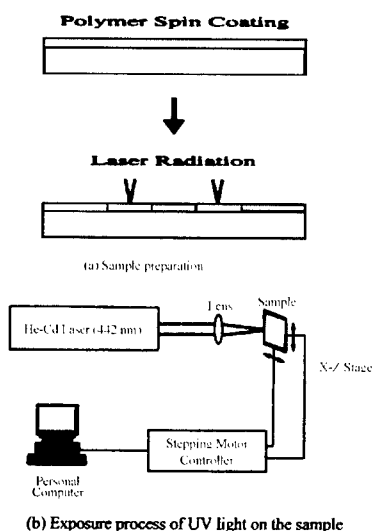


FIGURE 1 Molecular structure of PU1-C4B



(b) Exposure process of UV light on the sample

Figure 2 Experimental setup of (a) the PU1-C4B thin film preparation and channel waveguide, and (b) the exposure process of UV light on the sample.

process.

Corona discharge was utilized to induce second order nonlinearity in the polymer film samples. Electrical field of +10 kV was applied at 150°C to the tungsten wire for 15 minutes. The wire was located 10 mm above the polymer film sample.

Second order nonlinear coefficient of the PU1-C4B film was determined by the Maker-Fringe measurement. The initial value of  $d_{33}$  in corona-poled PU1-C4B film was 32.8 pm/V. Comparatively high nonlinearity is considered to be induced from the ionic effect of NLO chromophore and the high number density of chromophores. A notable feature of this polymer system is the extended temporal stability of poled dipoles. The initial value remained more the 1 month at room temperature after the corona-poling process. Moreover the sample retained almost 70% of the initial value after the sample was kept for 100 hours at 100°C. This result indicates that the stabilization effect of the hydrogen bonds among neighboring polyurethane chains prevented the relaxation of oriented molecular dipoles.

Cerenkov-type phase-matching condition of second harmonic at 415 nm was estimated using the refractive index as shown in Fig.3. Fig. 4 shows the calculated relation between the estimated conversion efficiency and the film thickness using the values of refractive index shown in Fig.3.

Three kinds of waveguides were fabricated on a spin-coated film sample as shown in Fig.5. Slab, channel(1)(50 $\mu$ m width) and

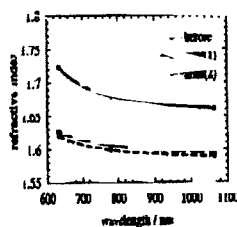


FIGURE 3 The relation between refractive index of the film and wavelength. Before, after(1) and after(2) indicate the film before the irradiation, irradiation of 15 minutes and irradiation of 30 minutes respectively.

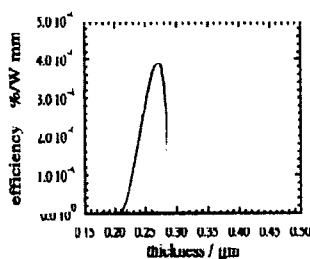


FIGURE 4 Calculated relation between the estimated conversion efficiency and the film thickness when Cerenkov phase-matching condition is satisfied

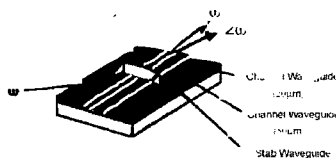


Fig.5 Prepared sample for the Cerenkov phase-matched SHG experiments

channel(2)(20 $\mu$ m width) waveguides were prepared. OPO pulse laser (pulse width  $\sim$  10ns) operating at 830 nm was utilized as a fundamental light source. The fundamental light was coupled into the waveguides by the prism and phase-matched second harmonic generation was observed in the waveguides. The relation between the input fundamental power (peak power) and the output SH power is shown in Fig.6. It can be seen in the result that better conversion

efficiency was achieved in the channel waveguide with narrower width.

In this study it was shown that this photo-bleaching process had advantages of precise index control of nonlinear optical polymers, versatile applicability, simple and low cost process. Further research will make this photo-bleaching process and this new material attractive in the field of future photonic devices.

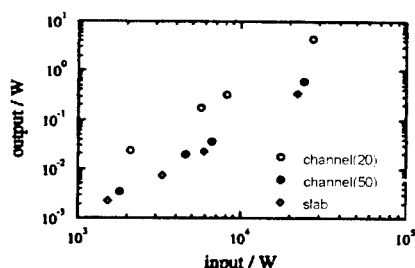


Fig.6 The relation between the input fundamental power and the output SH power.

## REFERENCES

- [1] A. E. Willner, M. N. Ruberto, D. J. Blumenthal, D. V. Podlesnik and R. M. Osgood, Jr., *Appl. Phys. Lett.* **54**, 1839 (1989).
- [2] A. Mukherjee, B. J. Eapen and S. K. Baral, *Appl. Phys. Lett.* **65**, 3179 (1994).
- [3] K. W. Beeson, K. A. Horn, M. McFarland and J. T. Yardley, *Appl. Phys. Lett.* **58** (18), 1955 (1991).
- [4] W. Feng, S. Lin, R. B. Hooker and A. R. Mickelson, *Appl. Opt.* **34**, 6885 (1995).
- [5] K. B. Rochford, R. Zanoni, Q. Gong and G. I. Stegeman, *Appl. Phys. Lett.* **55**, 1161 (1989).
- [6] M. B. J. Diemeer, F. M. M. Suyten, E. S. Trommel, A. McDonnell, J. M. Copeland, L. W. Jenneskens and W. H. G. Horsthuis, *Electron. Lett.* **26**, 379 (1990).
- [7] Y. Shi, W. H. Steier, L. Yu, M. Chen and L. R. Dalton, *Appl. Phys. Lett.* **58**, 1131 (1991).



## New Mesogenic 3,3'-Bipyridine Derivatives For Side-Chain Liquid Crystal Polymers - Second-Order NLO Properties.

NOELLA LEMAITRE<sup>a</sup>, ANDRE-JEAN ATTIAS<sup>a</sup>, ISABELLE LEDOUX<sup>b</sup>, JOSEPH ZYSS<sup>b</sup>

<sup>a</sup>ONERA-DMSC, 29 Av. de la Division Leclerc, B.P.72, F-92322 Châtillon Cedex; <sup>b</sup>ENS Cachan-LPQM, 61 Av. du Président Wilson, F-94230 Cachan.

**Abstract** A new class of push-pull mesogenic chromophores based on 3,3'-bipyridine derivatives are synthesized. The versatile chemistry employed allows easy modification of the  $\pi$ -conjugated core and of the acceptor/donor pair. We show how mesogenic (DSC, polarizing microscopy) and NLO (EFISH) properties can be tuned in this way. Furthermore, these chromophores, transparent at optical communication wavelengths (1.32 and 1.55  $\mu\text{m}$ ), can be grafted as side-chain on polyepichlorhydrin. Here also, they lead to liquid crystal or isotropic polymers depending on the chemical modification.

**Keywords** liquid crystals; 3,3'-bipyridine; push-pull molecules; second-order NLO; polymers

### 1. INTRODUCTION

Progress in telecommunications, optical information processing and data storage aroused the interest in optoelectronic organic materials <sup>[1,2]</sup>. Among them, side-chain liquid crystal polymers (SCLCPs) present several advantages for second-order nonlinear optics: they allow the preparation of thin films of good optical quality and good mechanical

properties. Indeed, the axial order brought by LC chromophores enhances field-induced polar ordering and stability of the films, therefore improving the efficiency of these materials <sup>[3,4]</sup>.

The present work reports on the synthesis and characterization of (i) new mesogenic chromophores (Scheme 1) efficient in second-order NLO, and (ii) corresponding side-chain polymers (Scheme 2).

Part 1 of the discussion shows how mesogenic and NLO properties of the chromophores can be tuned by varying the nature of attractive or donating groups (A/D pair) and/or the lateral substituent of the bipyridine core or phenyl ring ( $R_1$  and  $R_2$  respectively).

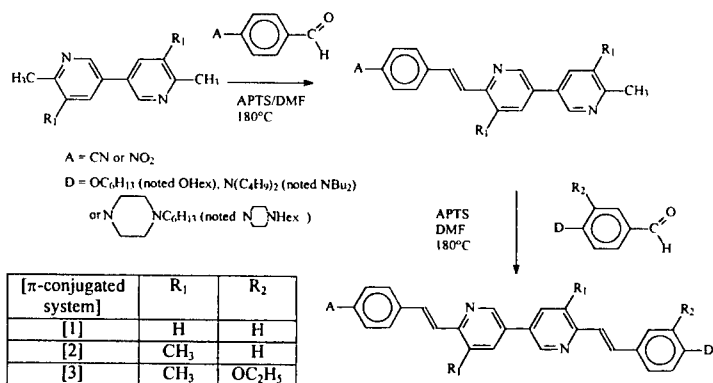
In the second part, the same tuning of mesogenic properties is reported for side-chain polymers.

## 2. EXPERIMENTAL PART

### 2.1. Syntheses

#### 2.1.1. Chromophores

All the compounds are obtained from 6,6'-dimethyl-3,3'-bipyridine and 5,5',6,6'-tetramethyl-3,3'-bipyridine according to Scheme 1, as described elsewhere <sup>[5-7]</sup>. The synthetic route is a two-steps Knoevenagel condensation under acidic conditions.



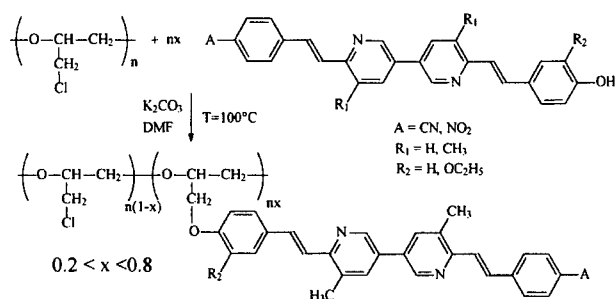
SCHEME 1 Synthetic route of the chromophores

According to their <sup>1</sup>H-NMR spectra, the chromophores, noted

A-[ $\pi$  conjugated system]-D, present two trans vinylene units, evidenced by a 16 Hz three bound coupling of trans carbon-carbon double bond.

### 2.1.2. Polymers

They are prepared by chemical modification of polyepichlorhydrin (PECH,  $\overline{M}_n = 1680$ ), according to Scheme 2, as described elsewhere [4]. Functionalized polymers are purified by precipitation into hot ethanol solution and dried in vacuo.



SCHEME 2 synthetic route of the side chain polymers

## 2.2 Characterizations

Chemical structures are substantiated by NMR and elemental analysis. The transition temperatures are measured using a differential thermal analyzer (Dupont 1090) operating at 20°C/min, under nitrogen. Phase assignments are based on polarizing microscopy (Nachet equipped with a Mettler Toledo hot stage). UV-visible absorbance spectra are recorded on a spectrometer (Perkin Elmer Lambda18). Second order molecular hyperpolarisabilities are measured in solution (chromophore concentrations of  $5.10^{-3}$  to  $10^{-2}$  mol.L<sup>-1</sup> in dichloromethane) by Electric Field Induced Second Harmonic generation<sup>[8]</sup> (EFISH) at 1320 nm.

## 3. RESULTS AND DISCUSSION

### 3.1. Chromophores

#### 3.1.1. Mesomorphic Behavior

Transition temperatures and texture observations are listed in Table 1.

Compound	Phase – T <sup>a)</sup> (°C) – [ΔH <sup>b)</sup> (J.g <sup>-1</sup> )	
CN-[1]-OHex	K - 120.7 [19.5] - S - 233.7 [6.9] - N - 302.5 [0.3] - I	
CN-[2]-OHex	K - 179.9 [124.6]	- N - 287.7 [3.2] - I
NO <sub>2</sub> -[2]-OHex	K - 92.4 [91]	- N - 281.3 [1.9] - I
NO <sub>2</sub> -[3]-OHex	K - 150.4 [66.7]	- I
CN-[1]-NBu <sub>2</sub>	K - 256.4 [48.6]	- I
CN-[2]-N $\square$ Hex	K - 202.9 [52.2]	- N - 327.3 [0.9] - I
NO <sub>2</sub> -[1]-NBu <sub>2</sub>	K - 244.8 [36.6]	- I
NO <sub>2</sub> -[2]-N $\square$ Hex	K - 193.3 [67.3]	- N - Td (>285) - I

a) T: transition temperature; b) ΔH: enthalpie change determined by DSC.

K: Crystal; S: smectic; N: nematic; I: isotropic liquid; Td: decomposition temperature

TABLE 1 phase transitions of the chromophores

Chromophores bearing the OHex donor group are studied with the three different  $\pi$ -conjugated cores. From the comparison of their mesogenic behavior, we can note that:

- introducing R<sub>1</sub> (change of [1] to [2]) destabilizes the LC character: smectic phases are suppressed and the apparition temperatures of nematic and isotropic phases are decreased,
- introducing R<sub>2</sub> (change of [2] to [3]) reinforces this tendency: the chromophore is isotropic whatever the temperature.

With NBu<sub>2</sub> as donor group, no LC phases are observed (as for Disperse Red 1). One way to force the LC nature is to constrain the amine in a cycle (N $\square$ Hex).

### 3.1.2. Linear and nonlinear optical properties

The absorption maximum ( $\lambda_{\max}$ ) and the values of  $\mu\beta$  and  $\mu\beta_0$  are reported in table 2.

All the chromophores present optical transparency ( $\lambda_{\max}$  ranges between 372 and 426 nm) at optical communication wavelengths (1320 and 1550 nm). The red shift observed when increasing the A/D strength (for instance, compare  $\lambda_{\max}$  of CN-[1]-OHex and NO<sub>2</sub>-[1]-NBu<sub>2</sub>) is an expected effect<sup>[1,2]</sup>: a better charge transfer stabilizes the first excited state.

For NLO results, as expected<sup>[1,2]</sup>, replacing a weak A/D pair (CN/OHex) by a stronger one (NO<sub>2</sub>/NBu<sub>2</sub>) enhances the  $\mu\beta_0$  values by a factor 8. On the other hand, R<sub>1</sub> and R<sub>2</sub> have no noticeable influence on NLO values.

Compounds	$\lambda_{\max}$ in nm	$\mu\beta \cdot 10^{-48}$ esu ( $\pm 10\%$ )	$\mu\beta_0 \cdot 10^{-48}$ esu ( $\pm 10\%$ )
CN-[1]-OHex	372	150	95
CN-[2]-OHex	373	130	80
NO <sub>2</sub> -[2]-OHex	391	325	195
NO <sub>2</sub> -[3]-OHex	392	300	185
CN-[1]-NBu <sub>2</sub>	418	1200	645
CN-[2]-N $\square$ NHex	398	510	295
NO <sub>2</sub> -[1]-NBu <sub>2</sub>	426	1480	775
NO <sub>2</sub> -[2]-N $\square$ NHex	406	765	430

$\mu$ : dipole moment;  $\beta$ : first hyperpolarisability;  $\beta_0$ : first hyperpolarisability extrapolated to infinite wavelengths

TABLE 2 results of absorption and EFISH measurements

The chromophores bearing NBu<sub>2</sub> donor group show better  $\mu\beta_0$  values than the commonly employed dye DR1 ( $\mu\beta_0 = 450 \cdot 10^{-48}$  esu<sup>[11]</sup>). But they are not LC. The best LC compound is therefore NO<sub>2</sub>-[2]-N $\square$ NHex which is about as efficient as DR1. Indeed, as far as we know from the literature<sup>[9]</sup>, it's one of the most efficient mesogenic chromophore for NLO.

### 3.2. Side-Chain Polymers

The same tuning of LC properties by chemical modification of the core is observed for polymers.

Polymers with core [1] are inadequate for NLO applications since they present 3 dimensional smectic phases, whatever the A/D and substitution rate. S<sub>3D</sub> are too viscous phases to enable the poling.

On the contrary, once R<sub>1</sub> is introduced, these S<sub>3D</sub> are suppressed (see for instance the thermogram in Figure 1.a. of a SCLCP with NO<sub>2</sub>-[2]-OH).

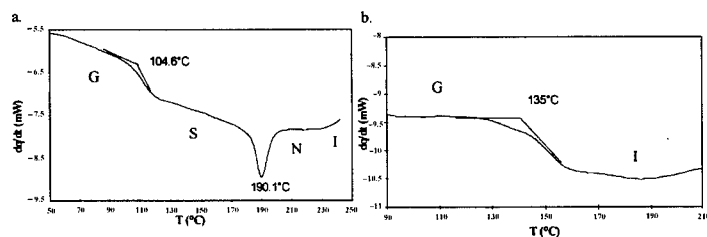


FIGURE 1 a. NO<sub>2</sub>-[2]-OH grafted at 80% on PECH  
b. NO<sub>2</sub>-[3]-OH grafted at 80% on PECH

The subsequent substitution with R<sub>2</sub> leads to an isotropic polymer (Figure 1.b).

### 3. CONCLUSION

The study of a series of new 3,3'-bipyridine chromophores shows that:

- both the substitution of the electronic core and the nature of A/D influence the mesomorphic behavior,
- the strenght of A/D pair affects NLO properties while substitution of the  $\pi$ -conjugated system doesn't.

The versatile chemistry used allows the preparation of SCPs, whose mesogenic properties can be tuned in the same way. We thus obtain a SCLCP and its non LC homologue (same A/D couple). The comparison of their poling and NLO properties should evidence the effect of LC character. These studies are under investigation.

### References

- [1] H. S. Nalwa, M. Seizo, Nonlinear Optics of Organic Molecules and Polymers, CRC Press : Boca Raton, FL (1994)
- [2] J. Zyss, Molecular Nonlinear Optics : Materials, Physics and Devices, Academic Press : New York (1994)
- [3] K. D. Singer, M. G. Kuzyk, J. E. Sohn, J. Opt. Soc. Am. B **4** (6), 320 (1987)
- [4] F. Kajzar, C. Noël, Adv. Mater. Opt. Electron. **8**, 247 (1998)
- [5] A.-J. Attias, C. Cavalli, B. Bloch, N. Guillou, C. Noël, Chem. Mater. **11**, 2057 (1999)
- [6] A.-J. Attias, P. Hapiot, V. Wintgens, P. Valat, Chem. Mater. **12**, 461 (2000)
- [7] N. Lemaître, A.-J. Attias, I. Ledoux, J. Zyss, manuscript in preparation
- [8] M. Barzoukas, D. Josse, P. Fremaux, J. Zyss, J. F. Nicoud, J. O. Morley, J. Opt. Soc. Am. **84**, 977 (1987)
- [9] J. Barbera, R. Gimenez, J. L. Serrano, R. Alcalá, B. Villacampa, J. Villalba, I. Ledoux, J. Zyss, Liquid Crystals **22** (3), 265 (1997)

## Photobleaching Mechanism Studies of Side-chain Polyimides

I. LIAKATAS, M. JÄGER, CH. BOSSHARD, P. GÜNTER,  
AND T. KAINO<sup>a</sup>

Nonlinear Optics Laboratory, Institute of Quantum Electronics,  
ETH-Hönggerberg, CH-8093, Zürich, Switzerland ;

<sup>a</sup>Institute for Chemical Reaction Science, Tohoku University,  
2-1-1 Katahira, Sendai, 980-8577 Japan

The effect of ultra-violet illumination on the absorption spectrum, the refractive index, and the scattering losses of a side-chain polyimide is investigated. The photobleaching mechanism is monitored through visible and infrared absorption spectra and the transition rates between the involved molecular states as well as other material parameters are derived using a simple model which considers four different molecular states.

**Keywords:** photobleaching, waveguides, polyimides

### INTRODUCTION

Ultraviolet photobleaching is one of the most commonly used methods for forming waveguide structures in polymer films [1]. In an attempt to understand the underlying mechanisms at the molecular level, several models have been proposed [2]. In this work, we study the effect of ultra-violet illumination on the azo-dye-attached side-chain polyimide A-95.11 (shown in Figure 1) used for electro-optic applications [3]. We determine qualitatively and quantitatively the different processes involved in photobleaching making use of the absorption spectrum of

the polymer at several illumination times and by considering a simple model where four molecular states are involved.

## MEASUREMENTS

### UV-Vis Absorption

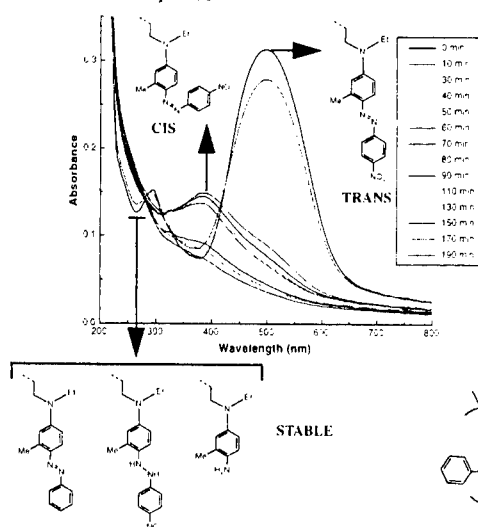


FIGURE 1 Absorption spectra of a 60 nm thin film of polyimide A-95.11 (structure shown below) at several illumination times with a mercury lamp ( $I=117 \text{ mW/cm}^2$ ). Possible molecular conformations contributing to the spectrum are depicted.

Most of the information about the photobleaching process are provided by the UV-VIS absorption spectrum of a film and its change during illumination. A 60 nm thin film of the polymer has been illuminated for 190 min with a mercury lamp and its spectrum was recorded at several time intervals as shown in Figure 1. The spectrum changes significantly; first mainly at the wavelength of maximum absorption (497 nm) where the peak completely disappears at long illumination times and second at a lower wavelength (377 nm) where a new peak appears and then again disappears. At even lower wavelengths (225-275 nm) there is also a moderate increase and decrease of the absorption. We define the *trans*-TE isomer of the molecules as the *trans* isomer oriented in the plane of



the film and *trans*-TM as the isomer oriented perpendicularly to the film surface. We attribute the peak at 497nm to the *trans*-TE isomer; a valid assumption because its absorption cross section is much larger than the one of the *trans*-TM isomer for our experimental geometry. The peak arising at 377nm is attributed to the *cis* isomer whereas the absorption at the deep UV wavelengths should come from shorter or non-conjugated species which are in a photostable state and which originate from the *cis* isomers after photobleaching.

#### FT-IR Spectra, Scattering Losses, and Refractive Indices

The FT-IR spectra of around 4.8  $\mu\text{m}$  thick films illuminated for 4.5 and 12 hours as well as of an unbleached one were measured and the absorbance of the N=N peak at  $1600\text{ cm}^{-1}$  and the  $\text{NO}_2$  peak at  $1336\text{ cm}^{-1}$  was determined using the two oxygens of the polyimide backbone as a reference. We observe that photobleaching has a larger influence on  $\text{NO}_2$  – 22% decrease after 12 hours – than on the N=N bond – 6% decrease after 12 hours. This result also gives an indication that the stable state of the molecules may be the one without the nitro group as shown in Figure 1.

Scattering loss measurements were performed using 4.5 to 5  $\mu\text{m}$  thick films on glass substrates and the prism coupling method at 1313 nm by imaging the light scattered from a planar waveguide. The scattering losses show an increase from 2 dB/cm to about 3.5 dB/cm after 12 hours illumination.

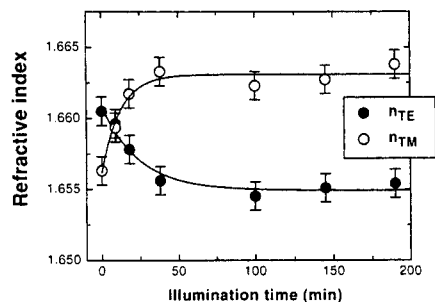


FIGURE 2 TE and TM refractive indices at  $1.55\text{ }\mu\text{m}$  of a  $2.84\text{ }\mu\text{m}$  thick film of polyimide A-95.11 after several illumination times with a mercury lamp ( $I=117\text{ mW/cm}^2$ ). The refractive indices were measured by grating coupling using a grating period of  $\Lambda=767\text{ nm}$  etched on fused silica.

The TE and TM refractive indices were measured at 1552nm *in-situ* during unpolarized UV illumination and using the grating coupling technique. A decrease of the TE refractive index of  $\Delta n \approx 7 \times 10^{-3}$  and an increase of the TM refractive index of  $\Delta n \approx 6 \times 10^{-3}$  after long illumination times was observed as shown in Figure 2. This is attributed to the *trans-cis-trans* isomerization which allows the molecules to orient in the more favourable direction perpendicular to the film surface (seen by the TM modes) than parallel to the film surface (seen by the TE modes).

#### THEORETICAL MODEL

We consider four possible states for the absorbing molecules: a *trans* state with  $N_{tE}$  molecules oriented in the plane of the film (*trans*-TE) at time  $t$ , a *trans* state with  $N_{tM}$  molecules oriented perpendicular to the plane of the film (*trans*-TM) at time  $t$ , a *cis* state with  $N_c$  molecules at time  $t$  and a *stable* state with  $N_s$  molecules at time  $t$ . We assume that at time  $t = 0$  all molecules are in the *trans* state ( $N_{tE}(t=0) = N_{tE}^0$ ,  $N_{tM}(t=0) = N_{tM}^0$ ,  $N_c(t=0) = N_s(t=0) = 0$ ). Under unpolarized illumination the *trans*-TE molecules undergo isomerization and move to the *cis* state with a transition rate  $g_{tc}$ . Part of the molecules in the *cis* state undergoes once again an isomerization and move to the energetically favourable *trans*-TM state with a transition rate  $g_{cm}$  and part of them experience structural changes with a transition rate  $g_{cs}$  and go to a *stable* state. The transition equations for the volumetric concentration of molecules at each state are  $dN_{tE}/dt = -g_{tc}N_{tE}$  (*trans*-TE),  $dN_c/dt = g_{tc}N_{tE} - (g_{cs} + g_{cm})N_c$  (*cis*),  $dN_s/dt = g_{cs}N_c$  (*stable*), and  $dN_{tM}/dt = g_{cm}N_c$  (*trans*-TM) where  $g_{tc} = \phi_{tc}\epsilon_t I$ ,  $g_{cs} = \phi_{cs}\epsilon_c I$ ,  $g_{cm} = \phi_{cm}\epsilon_c I$  are the *trans*-TE→*cis*, *cis*→*stable*, and *cis*→*trans*-TM transition rates, respectively, with  $\phi$  the quantum yield in  $\text{W}^{-1}\cdot\text{s}^{-1}$ ,  $\epsilon$  the absorption cross section in  $\text{m}^2$  and  $I$  the light intensity in  $\text{W}\cdot\text{m}^{-2}$ . The *trans*-TE→*cis* transition is in our case irreversible and therefore a *cis*→*trans*-TE transition is not considered. We also assume that no direct

transition from the *trans*-TE to the *stable* state is possible and that the light intensity is the same at 377nm and 497nm. Solving the above transition equations with the initial condition  $N_{tE} + N_c + N_s + N_{tM} = N_{tE}^0 + N_{tM}^0$  we obtain the solutions for all four states. We need, however, the transition equations for the absorbance as this is what we experimentally measure. The absorbance  $A_i$  ( $i = tE, c, s, tM$ ) of the molecules in every state  $i$  is given by  $A_i = \epsilon_i L N_i$  with  $L$  the film thickness and valid under the assumption that the thickness remains constant in time and that the light intensity is constant in the material, an assumption valid only for very thin films. If  $A_{tE, BG}$  and  $A_{c, BG}$  are the background absorbances of the polymer backbone at the wavelength of maximum absorption of the *trans*-TE and the *cis* state respectively, the measured total  $A_{tE}^m$  and  $A_c^m$  absorbances are:

$$A_{tE}^m = A_{tE}^0 e^{-g_{tc}t} + A_{t, BG} \quad \text{trans-TE state}$$

$$A_c^m = A_{tE}^0 \left( \frac{\epsilon_c}{\epsilon_{tE}} \right) \frac{g_{tc}}{g_{tc} - g_{cs} - g_{cm}} (e^{-(g_{cs} + g_{cm})t} - e^{-g_{tc}t}) + A_{c, BG} \quad \text{cis state}$$

TABLE 1 Parameters derived from our model.

absorption cross section ( <i>cis</i> state) /	$\epsilon_c / \epsilon_{tE}$	0.68±0.03
absorption cross section ( <i>trans</i> -TE state)		
<i>trans</i> -TE→ <i>cis</i> transition rate	$g_{tc}$	2.33±0.17·10 <sup>-2</sup> min <sup>-1</sup>
<i>cis</i> → <i>stable</i> + <i>cis</i> → <i>trans</i> -TM		
transition rate	$g_{cs} + g_{cm}$	1.56±0.18·10 <sup>-2</sup> min <sup>-1</sup>

Figure 3 shows the evolution of the *trans*-TE and *cis* absorption peaks as a function of illumination time (data obtained from the spectra of Figure 1) and the theoretical curves predicted by our model. The parameters of Table 1 could be determined in this way. We note that the absorption cross section of the *cis* state is considerably smaller (68%) than that of

the *trans*-TE one and that the transition rate bringing molecules to the *cis* state is 1.5 times larger than the one removing molecules from it.

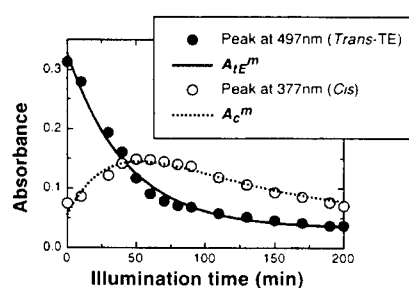


FIGURE 3 Absorbance of the 497nm (filled circles) and the 377nm (open circles) peaks of a 60nm thick film of the polymer at various illumination times as obtained from Figure 1. Lines represent best fits from our model to the data.

## CONCLUSION

We have shown that UV illumination of polyimide A-95.11 induces birefringence, an increase of the scattering losses as well as a *trans-cis* isomerization and photodegradation in a sequence that can be described by a simple theoretical model developed in this work. This model also allows the determination of the bleaching rate and other material parameters using only data from absorption measurements.

## Acknowledgments

We thank Dr. Tomaru and Mr. Shibata for their help with the measurements, and Mr. Bösch and Mrs. Fischer for helpful discussions. Financial support by the ETH research council, the Tohoku University and the Swiss-Asia Foundation is gratefully acknowledged.

## References

- [1] I. McCulloch, G. Boudoughian, and H.-T. Man, *Adv. Mater.*, **7**, 8, 715 (1995)
- [2] L. Palchetti, Q. Li, E. Giorgetti, D. Grando, and Stefano Sottini, *App. Opt.*, **36**, 6, 1204 (1997)
- [3] P. Prêtre, P. Kaatz, A. Bohren, P. Günter, B. Zysset, M. Ahlheim, M. Stähelin, F. Lehr, *Macromolecules*, **27**, 5476 (1994)

## Organized Organic Multilayer Structures for Frequency Doubling and Electro-Optics

C. FLUERARU<sup>a,c</sup>, S. SCHRADER<sup>a</sup>, B. DIETZEL<sup>b</sup>, V. ZAULS<sup>a</sup>, H. MOTSCHMANN<sup>c</sup>, B. SCHULZ<sup>b</sup>, G. DECHER<sup>d</sup>

<sup>a</sup> Universität Potsdam, Institut für Physik, Am Neuen Palais 10, D-14469 Potsdam, Germany; <sup>b</sup> IDM, Kantstr. 5, Teltow, Germany; <sup>c</sup> Max-Planck-Institut für Kolloid- und Grenzflächenforschung, Golm-Potsdam, Germany; <sup>d</sup> Institute Charles Sadron, CNRS - UPR 22, F-67083, Strasbourg, France

Organized organic films prepared from amphiphilic molecules in different supramolecular architecture were investigated with respect to second-order applications. The study included azochromophore containing maleic acid side chain polymer (AMS) and a low-molecular weight amphiphile, namely 2-docosylamino-5-nitropyridine (DCANP). The layers were prepared by Langmuir-Blodgett (LB) technique in order to control precisely the supramolecular architecture of the multilayers. For thicker layers nonlinear optical coefficients in the range of tens pm/V have been found. This indicates the potential of these materials for various applications in photonic devices.

**Keywords** Langmuir-Blodgett film; second harmonic generation; azochromophores; side chain polymers; DCANP

### INTRODUCTION

Organic materials have attracted great interest in the field of nonlinear optics, integrated optics and optical interconnects since they can be tailored by various synthetic methods. This implies architectural flexibility for molecular design and freedom in building up different supra-molecular structures. In principle, a huge variety of materials can be synthesised like main or side chain polymers suitable for spin-

coating, amphiphilic monomers or polymers for Langmuir-Blodgett (LB) deposition. The material requirements have been discussed in several review [1,2]. In this paper, we will report about our results obtained for materials having a big technological potential for frequency doubling and electro-optics.

#### EXPERIMENTAL METHODS

The applied linear optical techniques were single wavelength and spectroscopic ellipsometry and absorption spectroscopy. Samples were prepared on quartz glass substrates for transmission measurements or on silicon and gold substrates for measurements in reflection geometry. Second harmonic generation (SHG) measurements do not only provide  $\chi^{(2)}$  values but also information about chromophore orientation and about the internal structure of LB multilayers. The detailed description of experimental setup is given elsewhere [3,4]

#### MATERIALS

Using LB technique, monolayers can be deposited onto the substrate both on immersion and withdrawal resulting in a centrosymmetric arrangement of both layers (Y-type deposition) or just on immersion (X-type deposition) or on withdrawal (Z-type deposition) which provides noncentrosymmetric structures. For the present study three types of supramolecular architecture due to different types of deposition are investigated with respect to their potential for fabrication of passive and active waveguide structures.

##### X and Z type of deposition

A statistical co-polymer (AMS) was synthesized [4] which can be described by an average sum formula as given in figure 1 with  $m=0.3$  and  $n=0.7$ , respectively. Multilayer films of the polymers were obtained by depositing the LB monolayers at a target pressure of 25 mN/m, using the X and Z –type of deposition. Multilayers of 5, 10, 20, 30, 40, and 60 monolayers were prepared on these substrates. The value  $n=1.557$  of refractive index was found to be the same for these layers independent

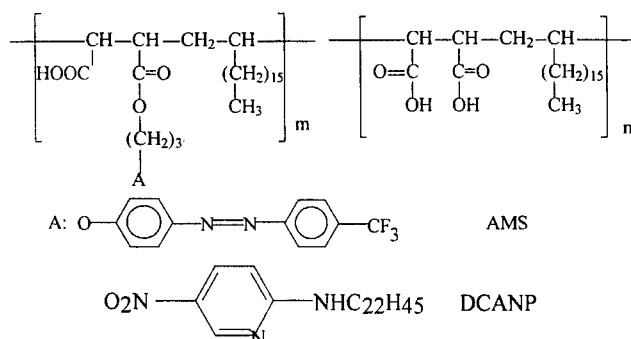


FIGURE 1 The molecular structure of AMS and DCANP

on the kind of substrate. For samples with more than 20 monolayers an ellipsometric model with two virtual layers has been used, because the slope of thickness versus number of monolayers is not constant. The first virtual layer is built up of 10 monolayers of polymer AMS, and the next layer covers the remaining number of monolayers deposited on the substrate. It was found that the thickness per monolayer for the upper virtual layer is about three times smaller than that for the lower virtual layer, but the film is still ordered. If the number of monolayers exceeds 40 the film starts to collapse, that means the next monolayers have a thickness below 0.2 nm. The investigation of molecular order by second harmonic generation led to the same result. The increase of the SHG signal follows the expected  $N^2$ -dependence only for the first 30 monolayers. Model calculations based on angular dependence of SHG intensity show that this intensity pattern resembles a situation where the chromophore is tilted towards the normal of the substrate plane by an angle of about  $30^\circ$  for the first monolayers, then the tilt angle is increasing with the number of monolayers. We found  $\chi_{zzz}^{(2)} = 20 \text{ pm/V}$  for our sample having 30 or less monolayers.

#### Y-type of deposition

Most Y type arrangements are centrosymmetric but, in a few cases the molecules adopt a herringbone structure. Bossard et al. [5] examined LB films of the amino nitropyridine derivatives  $\text{C}_n\text{H}_{2n+1}\text{-NH-C}_5\text{H}_3\text{N-NO}_2$  with alkyl chains of different length ranging from  $n=18$ -26.

They concluded that maximum SHG intensity is reached for 2-docosylamino-5-nitropyridine (DCANP). A systematic study of linear and nonlinear properties of DCANP was recently made [4]. The spectroellipsometric spectra for different number of monolayers are presented in figure 2 [4].

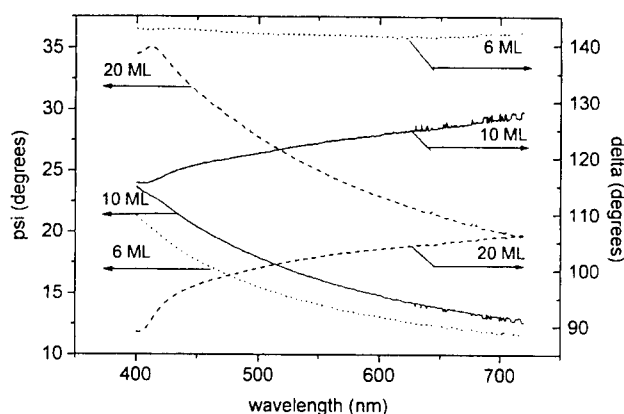


FIGURE 2 Ellipsometric angles psi and delta of DCANP on silicon in dependence on wavelength for three different numbers of monolayers (6, 10, 20 ML); incidence angle  $70^\circ$

The increasing of SHG intensity with number of bilayers is quadratically. The nonlinear susceptibility measured are  $\chi_{yyy} = 21.3 \text{ pm/V}$ ,  $\chi_{yxy} = 8.2 \text{ pm/V}$  and  $\chi_{yzx} = 3.97 \text{ pm/V}$  ( $\lambda = 1064 \text{ nm}$ ) [4]. Figure 3 shows the SHG intensities measured in a heterodyne experiment where the SHG signal generated by the DCANP layer is interfering with the SHG signal of a reference quartz crystal excited simultaneously by the same laser beam. A glass plate positioned in the SH beam of DCANP changes the phase of this signal with respect to the SH signal of the quartz crystal simply by its rotation. The rotation angle of this glass plate is plotted as abscissa of figure 3. In addition, an inset is plotted which shows the dependence of SHG signal of the DCANP multi-layer with respect to the azimuth angle towards the dipping direction of LB deposition. The maxima of the two signals detected for



$+15^\circ$  and  $-15^\circ$  are almost in anti-phase to each other, i.e. they attained a phase shift close to  $\pi$ . Since the small deviation from  $\pi$  is constant we assign it to misalignment of the reference (dipping direction) where from the angle is measured. This indicates that the DCANP molecules are well aligned creating a net dipole pointing along the dipping direction. Under the chosen azimuth angles of  $+15^\circ$ ;  $-15^\circ$  the probed projections of the dipole moment are consequently opposite to each other indicating the high order inside of the layers.

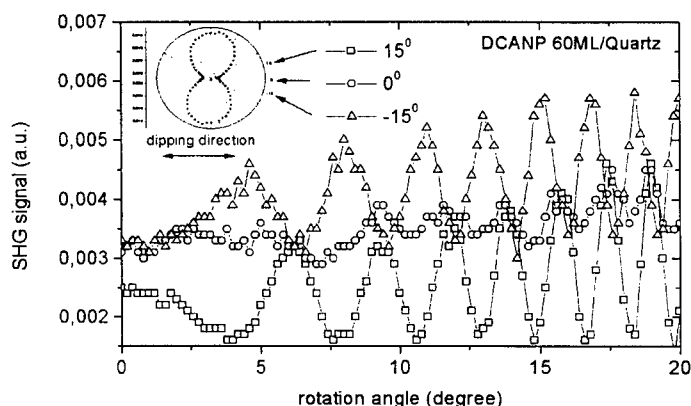


FIGURE 3 SHG intensities after interference of the signal of the DCANP layer and of the signal of a reference quartz crystal. The phase of the DCANP layer signal was shifted by rotation of a glass plate. The three different curves represent the superimposed signals for three different azimuth angles. The inset shows the dependence of SHG signal of the DCANP multilayer with respect to the azimuth angle. The three azimuth angles used for the phase measurements are also marked in the inset.

The Y-type of deposition of AMS shows a weak SHG signal originated from the first monolayer. The different alignment of molecular dipole in the same Y-type deposition of AMS and DCANP is associated with

difference between the pendant chromophore by the main polymeric backbone and the aliphatic chain, respectively. For DCANP, packing is induced by hydrogen bonding both within and between monolayers.

#### Alternate layer technique

In choosing a passive spacer to alternate with the optically nonlinear layer it is necessary to consider the compatibility and deposition characteristics of the components. We deposited successively active azopolymer monolayer and another maleic acid anhydride polymer without chromophore. Other sample was deposited using one monolayer of AMS followed by three monolayer of PMMA. This complex layer was repeated ten times. These two samples show no collapse until 40 monolayers, which seems that using this technique the collapse of film can be avoided. The drawback is that the nonlinear susceptibility is smaller than in case of X and Z type of deposition.

## CONCLUSIONS

The trade-off between the SHG efficiency and the stability of molecular architecture is investigated. The evaluation of molecular orientation and ordering of supramolecular arrangement for different LB deposition type is discussed.

#### Acknowledgments

Support of the DFG (Schr 462/3-1n./3-2) is gratefully acknowledged. We thank Dr. D. Fanter for ellipsometric measurements.

#### References

1. G. J. Ashwell, *J. Mater. Chem.* **9**, 1991 (1999)
2. H. S. Nalwa, S. Miyata, *Nonlinear Optics of Organic Molecules and Polymers*, CRC Press, 1996
3. S. Schrader, V. Zauls, B. Dietzel, C. Flueraru, D. Prescher, H. Motschmann, L. Brehmer, *Mat. Sci. Eng. C*, **8-9**, 527 (1999)
4. C. Flueraru, S. Schrader, V. Zauls, B. Dietzel, H. Motschmann, *Opt. Commun.*, submitted
5. Ch. Bossahard, M. Kupfer, M. Florsheimer, T. Borer, P. Gunter, Q. Tang, S. Zahir, *Thin Solid Films*, **210/211**, 198 (1992)

## Ultra-Efficient Electro-Optic Polymer Modulators for Short-Distance High-Speed Optical Interconnects

N. S. LAGALI<sup>a</sup>, D. J. W. KLUNDER<sup>a</sup>, G. J. GERRITSMA<sup>b</sup>, AND  
A. DRIESSEN<sup>a</sup>

<sup>a</sup>Lightwave Devices Group, <sup>b</sup>Low Temperature Division,  
MESA<sup>+</sup> Research Institute, University of Twente,  
P.O. Box 217, 7500 AE Enschede, The Netherlands

We investigate the possibility of realizing electro-optic polymer modulators with millivolt-regime driving voltages. Such efficient modulators are intended for applications in future short-distance, high bit-rate optical interconnects between networked data processors. By combining the benefits of polymeric optical waveguides with new optical modulator designs, ultra-low voltage modulation can be achieved.

**Keywords** Optical modulator; electro-optic polymer; superconductor; resonant electrode; ring resonator.

## INTRODUCTION

Modern semiconductor electronics is quickly approaching a barrier at which clock speeds of VLSI circuits saturate (at ~1 GHz), due mainly to issues of high power dissipation levels<sup>[1]</sup>. Superconductor-based electronic circuits, however, have the advantages of extremely low power dissipation and rapid response, thereby enabling processing speeds approaching THz clock frequencies<sup>[2]</sup>. As the development of superconductor-based technology continues, transporting these high-speed signals off-chip becomes important for parallel computing and networking applications.

The enormous bandwidth of optical fiber provides a means for transmitting THz bandwidth signals over short ( $< 100\text{m}$ ) distances. Interfacing the superconducting circuits with room-temperature optical transport, however, poses a number of challenges. For instance, a fundamental limitation of superconducting circuits is that the maximum AC voltage generated is typically below 10 mV. This must be sufficient to drive a high-speed electro-optic modulator with a modulation depth large enough to ensure error-free detection after a short propagation distance through an optical fiber. In practice a modulation depth as small as a few percent imposes an acceptable power penalty at the receiver<sup>[3]</sup>.

In this paper we investigate the use of superconducting modulation electrodes on electro-optic polymer waveguide components to achieve ultra-low voltage, high-speed optical modulators. Though direct modulation of THz signals has yet to be demonstrated, the designs presented here are suitable for integration in modulator arrays utilizing time- or wavelength-division multiplexing (TDM/WDM) techniques, resulting in aggregate bandwidths approaching the THz level.

## RESONANT SUPERCONDUCTING ELECTRODES

Polymer-based optical modulators have a number of advantages over conventional  $\text{LiNbO}_3$  modulator technology, such as velocity-matching over reasonable interaction lengths<sup>[4]</sup>, low dielectric constants (allowing denser device integration), and higher electro-optic coefficients ( $r_{33} = 83 \text{ pm/V}$  has recently been demonstrated)<sup>[5]</sup>. Also, the very low dielectric losses of certain polymers are especially attractive for achieving low electrode losses. Due to these advantages, we propose the use of electro-optic polymer modulators in combination with travelling-wave resonant superconducting electrodes to achieve ultra-low-voltage modulation.

To reduce the drive power of  $\text{LiNbO}_3$  modulators, in certain applications broadband operation has been traded off for band-limited modulation. The resonant electrode design was first proposed by Izutsu *et al.*<sup>[6]</sup> for achieving low-power, band-limited  $\text{LiNbO}_3$  modulators. A three-electrode coplanar waveguide design was used, consisting of a central feeder line, a short-circuited resonant line as the modulating electrode, and a stub to achieve impedance matching. This electrode design was successfully used to reduce the drive power in a  $\text{LiNbO}_3$  modulator by about a factor of ten, and a bandwidth of about 5 GHz at a (harmonic) resonant frequency of 35 GHz was measured<sup>[6]</sup>.

The design was subsequently improved by replacing the normal conducting electrodes by low- $T_c$  superconducting electrodes<sup>[7]</sup>. These electrodes have very low microwave propagation losses and dispersion, thereby enhancing the modulator efficiency<sup>[8]</sup>. The measured performance of a LiNbO<sub>3</sub> modulator with a low- $T_c$  electrode made from a Pb-In-Au alloy, however, is just marginally better than using normal conducting electrodes at the same temperature<sup>[7]</sup>.

In our application broadband modulation is not required, since various coding schemes can be used for data transmission at a fixed frequency. Furthermore, using polymeric materials allows longer resonant lines and hence a lower drive power. We choose a low- $T_c$  (4.2° K) niobium (Nb) electrode, since it has very low conductor losses and can be deposited at room temperature, thereby maintaining the electro-optic properties of the poled polymer, which degrade at elevated temperatures<sup>[9]</sup>.

To determine the reduction in driving voltage for a polymer:Nb modulator, we have followed the analysis of Yoshida *et al.*<sup>[7]</sup> to determine the modulator's frequency response. In a Mach-Zehnder interferometer, the optical intensity varies as  $I = I_0 \cos^2(\Delta\phi / 2)$ , where  $I_0$  is the maximum output intensity in the absence of an applied phase shift ( $\Delta\phi = 0$ ). The phase shift is a function of the modulation voltage  $V$  applied to one of the arms,

$$\Delta\phi = \pi \frac{V}{V_\pi} M(f) \quad (1)$$

where  $M(f)$  is the normalized modulation depth factor. For conventional electrodes  $M(f) = 1$  below the high-frequency roll-off, whereas for resonant electrodes, larger values of  $M$  (and therefore lower modulation voltages) can be achieved in narrow frequency bands.

The normalized modulation depth of the resonant electrode is<sup>[7]</sup>

$$M(f) = \left| \frac{2}{1 + y_0} \right| \cdot \left| \frac{\cosh(\gamma L) - \cos(\beta_0 L)}{(\gamma L)^2 + (\beta_0 L)^2} \right| \cdot \left| \frac{\gamma L}{\sinh(\gamma L)} \right| \quad (2)$$

where  $y_0$  is the normalized admittance,  $\gamma(f) = \alpha + j\beta$ ,  $\alpha(f)$  is the microwave attenuation constant,  $\beta$  is the microwave propagation constant, the resonator length is  $2L$ , and  $\beta_0$  is the optical propagation constant. The attenuation constant is given by<sup>[8]</sup>

$$\alpha_n(f) = \alpha_{cn} \sqrt{f} + \alpha_d f \quad (3)$$

$$\alpha_s(f) = \alpha_{cs} f^2 + \alpha_d f \quad (4)$$

where the subscripts  $n$  and  $s$  refer to normal and superconducting electrodes and  $\alpha_c$  and  $\alpha_d$  are the conductor and dielectric losses, respectively.

Our proposed modulator is a Mach-Zehnder interferometer with an electro-optic polymer core layer, polystyrene optical cladding layers, and Nb electrodes. The parameters for these materials are:  $\alpha_{cs} = 1.63 \times 10^{-5}$  dB/(cm·GHz<sup>2</sup>)<sup>[8]</sup>, and  $\alpha_d = 1.524 \times 10^{-4}$  dB/(cm·GHz) for polystyrene<sup>[10]</sup>. For purposes of comparison, we have also chosen a Pb-In-Au alloy on both polymer and LiNbO<sub>3</sub> substrates. The material parameters are:  $\alpha_{cn} = 0.43$  dB/(cm·GHz) for Au<sup>[8]</sup>,  $\alpha_{cs} = 3.93 \times 10^{-4}$  dB/(cm·GHz<sup>2</sup>) for Pb-In-Au<sup>[7]</sup>, and  $\alpha_d = 7.4 \times 10^{-3}$  dB/(cm·GHz) for LiNbO<sub>3</sub><sup>[8]</sup>. A resonator length of 5 cm is chosen, though this is optimistic for LiNbO<sub>3</sub> devices.

The modulation depth from (2) is used in (1) to determine the modulation voltage  $V$  shown in Figure 1, with  $V_\pi$  for LiNbO<sub>3</sub>:Au set at 4 V (a harmonic of the resonant peak is used). Switching to polymer-based devices results in modulation voltages an order of magnitude lower than in LiNbO<sub>3</sub>.

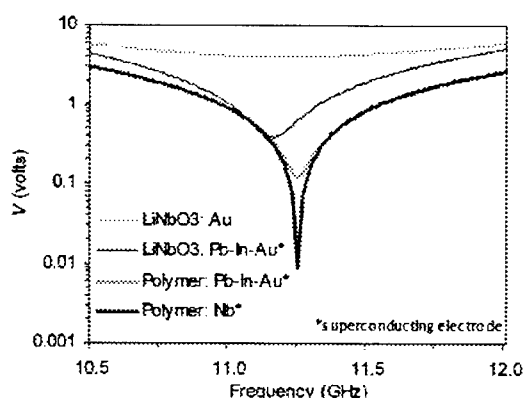


FIGURE 1 Calculated modulation voltage  $V$  for various modulators.

At the resonant frequency of 11.25 GHz, a modulation voltage of less than 10 mV and a 3 dB bandwidth of 10 MHz (frequency range at which  $V_\pi$  doubles) is predicted for the polymer:Nb device. Only a fraction of the modulation voltage (1 % or 100  $\mu$ V) still provides an optical modulation depth sufficient for short-distance optical fiber transmission.

Higher resonator harmonics can also be used; the modulation efficiency decreases at higher frequencies while the 3 dB bandwidth increases. For the polymer:Nb device, a  $V_\pi = 222$  mV is predicted at a

resonant frequency of 101.25 GHz, with a 3 dB bandwidth of 500 MHz. In this case, 1 % of the modulation voltage is 2.2 mV, which is well within the available voltage range of superconducting electronics.

A practical requirement of the above device is the reliability of the polymeric materials in a low-temperature environment. Much remains unknown about the low-temperature behaviour of optical polymers, but tests of polymeric optical switches in liquid nitrogen have been performed without any observed cracking<sup>[11]</sup>, and optical epoxies suitable for operation at 4 °K are commercially available<sup>[12]</sup>.

#### POLYMERIC RING RESONATOR MODULATOR

While the Mach-Zehnder modulator affords a long interaction length it still suffers from a low sensitivity of the optical output to an applied phase shift that is a fraction of  $V_\pi$ , and a total device size (including electrodes) that limits the achievable modulator array size.

As an alternative, we propose a ring resonator modulator with improved optical sensitivity and with dimensions suitable for integration of tens and possibly hundreds of modulators on a single substrate. A diagram of the proposed modulator is shown in Figure 2.

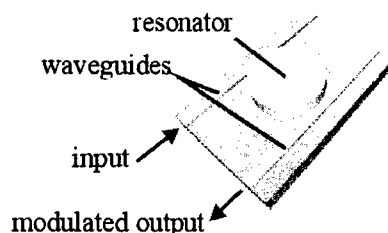


FIGURE 2 Diagram of the proposed ring resonator modulator.

The waveguide channels consist of an electro-optic polymeric core with a refractive index of 1.615 and a passive cladding polymer with a refractive index of 1.43. In the passive state, the input light propagates through the straight waveguide with minimal interaction with the ring. In the active state, an electrode over the ring tunes the effective modal index in the ring such that phase matching (resonance) occurs between the waveguide and ring modes, thereby coupling the light in the input waveguide through the ring into the output waveguide.

The optical response of this structure has been calculated for a ring with a 15  $\mu\text{m}$  diameter at a wavelength of  $\lambda = 850\text{ nm}$ . With a power coupling fraction of 5 % between the waveguides and the ring in the passive state, an extinction ratio of better than 20 dB can be achieved when the device is tuned through resonance. The finesse of the resonator is 150 and the switching voltage is 0.9 V, corresponding to an electro-optic coefficient of 30 pm/V and an effective index shift of  $6 \times 10^{-5}$ . The modulation voltage can be reduced to 1 %, or 9 mV while maintaining an extinction ratio adequate for short-distance transmission. Though the modulation speed of this device is limited to about 13 GHz due to the round-trip time in the ring resonator, the extremely small size allows the device to be fabricated in arrays with a high integration density.

## CONCLUSIONS

The feasibility of achieving millivolt-regime polymer-based electro-optic modulators has been investigated. Using a polymeric Mach-Zehnder modulator with resonant Nb electrodes, a reduction in the driving voltage to the millivolt level is predicted. An electro-optic polymer ring resonator provides a compact, sensitive alternative modulator design. Both designs are compatible with the millivolt signals and high speeds typical of superconducting electronics.

## References

- [1] See Web site <http://www.sematech.org/public/roadmap/doc>
- [2] W. Chen *et al.*, *IEEE Trans. Appl. Supercond.* **9**, 3212-3215 (1999).
- [3] E. E. Basch (ed.), *Optical-fiber transmission*, Howard W. Sams, Indianapolis, IN, 1987.
- [4] W. H. Steier *et al.*, *Chem. Phys.* **245**, 487-506 (1999).
- [5] A. Chen *et al.*, *Opt. Eng.* **38**(12), 2000-2008 (1999).
- [6] M. Izutsu and T. Sueta, *IOOC '89 Proceedings*, 19D4-1 (1989).
- [7] K. Yoshida, *et al.*, *IEEE Trans. Appl. Supercond.* **5**(2), 3183-3186 (1995).
- [8] K. Yoshida *et al.*, *IEEE Trans. MTT* **47**(7), 1201-1205 (1999).
- [9] R. M. de Ridder *et al.*, *Opt. Mater.* **12**, 205-214 (1999).
- [10] R. S. Eliot, *An introduction to guided waves and microwave circuits*, Prentice-Hall, Englewood Cliffs, NJ, 1993.
- [11] *FibreSystems magazine*, 24-25 (1997).
- [12] *MasterBond Inc.*, see Web site <http://www.masterbond.com>



## SHG at near resonance and chromophore orientational distribution function in p(DR1M) thin films oriented by corona poling

V. Rodriguez\* and C. Sourisseau

*Laboratoire de Physico-Chimie Moléculaire, UMR 5803 CNRS,  
Université Bordeaux I, 351 cours de la Libération  
Talence 33405, France.*

*\*email: vincent@morgane.lsmc.u-bordeaux.fr*

Polarized second harmonic generation transmission spectra at near the two photon absorption have been recorded on a p(DR1M) thin film oriented by corona poling, using a 1064 nm Nd/Yag laser pump. Experimental results were interpreted within a new multi-layered model including the two photon absorption contributions. The three  $\langle P_1 \rangle$ ,  $\langle P_2 \rangle$  and  $\langle P_3 \rangle$  Legendre polynomials or orientational order parameters were thus obtained. Then, a complete molecular orientational distribution function of the chromophores has been calculated using a phenomenological mean field potential approach including poling and external forces.

**Keywords** Polymer, corona poling, SHG, distribution function.

### INTRODUCTION

The interest in using polymers for second order nonlinear optics (NLO) is related to the production of inexpensive alternatives to inorganic crystals for frequency doubling, for optical data storage applications and electro-optic devices [1,2]. Polymeric films with large macroscopic second-order nonlinear properties can be obtained by orienting within a polymer matrix a molecular component with a large molecular hyperpolarizability; indeed, the guest dye molecules are easily oriented in the host polymer film by application of a static electric field. Many SHG studies have already been carried out on such devices but, as far as we know, only a few of them have determined the complete orientational distribution function,  $G(\theta)$ ; it relates the second-order NLO susceptibility of the bulk material to molecular properties. In this case, the uniaxial distribution function

has been partially characterized by the first four orientational order parameters,  $\langle P_1 \rangle$  to  $\langle P_4 \rangle$  [3, 4].

In the present study, we reinvestigate the NLO properties of a thin film of poly{4'-[[2-methacryloyloxy-ethyl] ethylamino] -4- nitroazobenzene} (namely, p(DR1M) or 100% functionalized DR1-covalently bonded polymer) oriented by corona poling. Visible spectra and polarized SHG transmission spectra at near resonance (using a 1064 nm Nd/YAG laser) were recorded in order to determine the orientational distribution function which describes the net polarization after the poling process. For this purpose an original SHG transmission setup using index matching hemi-cylindrical lenses has been designed improving the collection efficiency. Furthermore, the SHG Maker fringes were analyzed using a new general multi-layered uniaxial model including birefringence and anisotropic absorption contributions at the fundamental and harmonic frequencies [5]. As previously shown by Herman and Hayden any isotropic absorption at near the two photon energy may strongly perturb the Maker fringe profiles [6]. From our SHG multi-layered model, which considers anisotropic absorption at the harmonic frequency, it is now possible to calculate  $\langle P_1 \rangle$ ,  $\langle P_2 \rangle$  and  $\langle P_3 \rangle$  order parameters. Then, a complete orientational molecular distribution function,  $G(\theta)$ , is directly derived, assuming a phenomenological mean field potential including poling as well as external forces. It is thus shown that this approach leads to consistent results whether low field or high field poling conditions are taking place [3].

## EXPERIMENTAL PART

Thin films of p(DR1M) were spun coated onto standard microscope slides. The films (0.15 -0.20  $\mu\text{m}$  thickness) were corona poled with a wire held parallel to and above (5.0 mm) the film. The direction of the applied field will be referred hereafter as the Z axis.

A scheme of the experimental setup is shown in Figure 1. The source was a Q-switched Nd/YAG laser operating at the 1064 nm wavelength. The pulse width and repetition rate of output pulses were 200 ns and 100 Hz, respectively. The polarized source beam was split into two branches by a beam splitter: the first branch was used to control the fundamental intensity using a photomultiplier tube (PMT1); the second branch, which goes through a polarizer

## MOLECULAR ORIENTATION DISTRIBUTION FUNCTION UNDER HIGH FIELD CONDITIONS

From knowledge of the DR1 molecular hyperpolarizability and assuming that only the  $\beta_{zzz}$  component is non zero [8], a standard treatment of bulk susceptibilities  $\chi_{33}$  and  $\chi_{31}$  leads to the following order parameter values,  $\langle P_1 \rangle = \langle \cos\theta \rangle = 0.123$  and  $\langle P_3 \rangle = \langle 5\cos^3\theta - 3\cos\theta \rangle / 2 = 0.007$ . Here, another interesting point is that the even order parameter  $\langle P_2 \rangle = \langle 3\cos^2\theta - 1 \rangle / 2$  can also be calculated from the anisotropic absorption coefficients; we obtain  $\langle P_2 \rangle = (\alpha_{2w}^Z - \alpha_{2w}^\perp) / (\alpha_{2w}^Z + 2\alpha_{2w}^\perp) = 0.265$ , a result quite consistent with the above value extracted from the visible absorption spectra.

From this set of order parameters  $\langle P_1 \rangle$  to  $\langle P_3 \rangle$ , it is then possible to determine an orientational distribution function,

$$G(\theta) = \frac{\exp(-U_t/RT)}{2\pi \int_{-1}^{+1} \exp(-U_t/RT) d\cos\theta},$$

which is governed by a mean-field potential  $U_t = U_P + U_E$ , where  $U_P$  is the potential due to the poling field and  $U_E$  that accounting for external forces. Assuming an homogeneous spatial Landau-type "effective" potential for each value of  $\cos\theta$ , i. e. a constant density number of chromophores ( $N$ ),  $U_P$  and  $U_E$  are expressed as a function of the macroscopic homogeneous spontaneous polarization  $P(\cos\theta)$  :

$$\begin{aligned} U_P &= -P(\cos\theta) \cdot E_p, \\ U_E &= a \cdot P^2(\cos\theta) + b \cdot P^4(\cos\theta), \end{aligned}$$

where  $E_p$  is the applied electric field,  $P(\cos\theta) = N\mu^*\cos\theta$  and  $\mu^*$  is the mean molecular dipole moment corrected from local field effects.

Then, the numerically computed best values for the potential parameters are  $N\mu^*E_p/RT = 0.245$ ,  $a/RT = -9.36$  and  $b/RT = 7.79$ . Note that a truncated orientation function developed up to the fourth order leads to  $\langle P_4 \rangle = -0.144$  and to a much broader distribution (fig. 3) as already reported in the literature [3]. This demonstrates the advantage of the used general approach in calculating complete distribution functions; further investigations using such a potential are in progress and will be published in due course.

$A_{\perp} = 1.500$  after poling. This leads to a first estimate of the order parameter  $\langle P_2 \rangle = 1 - A_{\perp}/A_0 = 0.27$ .

Some typical polarized SHG results are shown on figure 2.

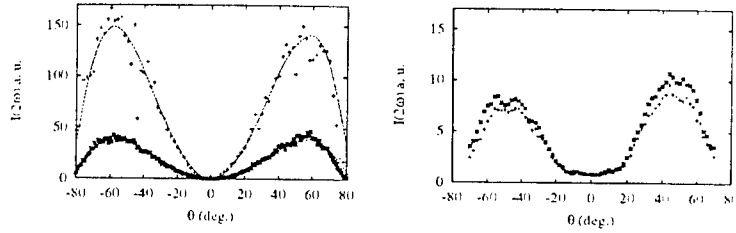


FIGURE 2. Dependence of SHG intensity on the polarization of fundamental and harmonic waves. Left: experimental p-p intensities with (+) and without (\*) hemi-cylindrical lenses, respectively; dotted lines represent best fit curves. Right: experimental s-p (+) and  $45^\circ - s$  (\*) intensities, respectively.

First, the increase in the p-p intensity using a quasi-matching sample setup is typical of a NL layer with a thickness far below the coherence length. As a consequence, the procedure to determine the sample thickness and the effective macroscopic susceptibility  $\chi^{(2)}$  may produce a 5% uncertainty. Also, it is evidenced on figure 2 that the  $s-p$  and  $45^\circ - s$  responses are quite comparable; one thus concludes that the Kleinman symmetry conditions hold in spite of the two photon absorption, so that within experimental errors  $d_{31} = d_{15}$ .

Finally, all the polarized SHG data are nicely fitted using a new multi-layered model, which includes an uniaxial anisotropic NL intermediate medium. Best fit values of the anisotropic two photon absorption coefficients at 532 nm and of the resonance enhanced macroscopic NLO coefficients  $d_{33}$ ,  $d_{31}$  are reported in Table 1. It is noteworthy that preliminary linear refraction index values at the fundamental and harmonic wave ( $1.62$  and  $1.70 \pm 10^{-2}$ , respectively) and the mean absorption coefficient ( $\overline{\alpha_{2\omega}} = (6 \pm 2) \mu m^{-1}$ ) were firstly determined on the unpoled sample from analyses of the p polarized reflected intensities ( $R_p$ ); all the results can be nicely compared.

film thickness (nm)	$n_w$	$\alpha_{2w}^o = \alpha_{2w}^1 (\mu m^{-1})$	$d_{33} (pm/V)$
$205 \pm 5$	$1.626 \pm 10^{-3}$	$5.3 \pm 0.2$	$39.8 \pm 0.2$
	$n_{2w}$	$\alpha_{2w}^e = \alpha_{2w}^2 (\mu m^{-1})$	$d_{33}/d_{31}$
	$1.696 \pm 10^{-3}$	$11.0 \pm 0.4$	$3.4 \pm 0.1$

TABLE 1. Results obtained from best fits of the SHG experimental data.

(P), was focussed on the sample with a spot diameter of  $100\ \mu\text{m}$ . The  $2\omega$  transmitted signal was detected by another photomultiplier tube (PMT2) and averaged over 10 to 25 pulses. The pulse energy at the sample was lower than  $5\ \mu\text{J}$  for the infrared beam. Absolute calibrations of the SHG intensities were obtained using a z-cut quartz plate assuming  $d_{11} = 0.3\text{ pm/V}$  [7]. This setup allowed also linear refractive index estimations at  $\omega$  or  $2\omega$ , using a third photomultiplier tube (PMT3), and collecting the  $2\theta$  reflected waves over the  $15 - 80^\circ$   $\theta$  range; a  $\text{LiNbO}_3$  crystal (F2) in phase matching condition was used as the  $532\ \text{nm}$  source to record the  $2\omega$  reflection signals.

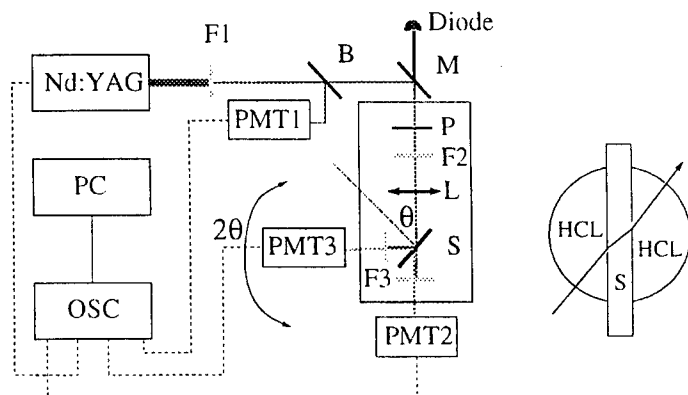


FIGURE 1. Left : Experimental setup. F1, density filter; B, beam splitter; M, mirror; P, polarizer; F2,  $532\ \text{nm}$  filter ( $1064\ \text{nm}$  source) or  $\text{LiNbO}_3$  crystal ( $532\ \text{nm}$  source); L,  $150\ \text{mm}$  focal lens; F3, selective set of filters and polarizers; OSC, oscilloscope; PC, personal computer. Right : Sample quasi index matching setup using  $10\ \text{mm}$  diameter hemi-cylindrical lenses (HCL, suprasil). The NLO optical path, which is now nearly twice longer, enhances the Maker fringe resolution.

## RESULTS

Absorption spectra ( $350\text{--}800\ \text{nm}$ ) of the films before and after poling were systematically compared and both polarized  $p$  and  $s$  spectra were recorded to check the uniaxiality ( $A_x = A_y = A_\perp$ ) of the poled films. Generally, one observes a broad absorption band ( $150\ \text{nm}$  FWHM) maximizing at about  $465\ \text{nm}$  with a mean isotropic absorbance  $A_0 = 2.055$  before poling and a weaker in-plane absorbance

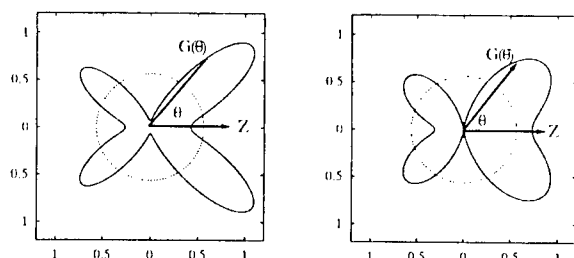


FIGURE 3. Polar plots of the distribution function,  $G(\theta)$  versus the polar angle  $\theta$ ; Left: complete distribution function, Right: function developed up to  $\langle P_4 \rangle$ ; curves are for the isotropic film (dashed curve) and the poled film (solid line).

### Acknowledgments.

Authors are thankful to A. Natansohn for providing the p(DRIM) sample and to F. Lagugné Labarthe for help in poling experiments.

### References

- [1] Molecular Nonlinear Optics, J. Zyss Ed., Academic Press Inc., London, England (1984).
- [2] Polymers for Second-Order Nonlinear Optics, G.A. Lindsay and K.D. Singer Ed., ACS Symposium series; 601, USA (1995).
- [3] M.G. Kuzyk, K.D. Singer, H.E. Zahn and L.A. King, J. Opt. Soc. Am. B, **6**, 742 (1989).
- [4] K.D. Singer, M.G. Kuzyk and J.E. Sohn, J. Opt. Soc. Am. B, **4**, 968 (1987).
- [5] V. Rodriguez and C. Sourisseau, (to be published).
- [6] W.N. Herman and L.M. Hayden, J. Opt. Soc. Am. B, **12**, 416 (1995).
- [7] P. Kaatz and D.P. Shelton, J. Chem. Phys., **105**, 3918 (1996).
- [8] D.R. Martinez, K. Koch, F.K. Ratsavong and G. O. Carlisle, J. Appl. Phys., **75**, 4273 (1994).

**SESSION D: NONLINEAR OPTICAL ORGANIC  
CRYSTALS**

## Rationalising the SHG Response in DCNP through Anomalous Atomic Thermal Motion

Jacqueline M. Cole<sup>a</sup>, Chick C. Wilson<sup>b</sup>, Judith A. K. Howard<sup>c</sup>

<sup>a</sup>Department of Chemistry, University of Cambridge, Lensfield Road, Cambridge, CB2 1EW, UK; <sup>b</sup>ISIS Facility, Rutherford Appleton Laboratory, Chilton, Didcot, Oxon, OX11 0QX, UK. <sup>c</sup>Department of Chemistry, University of Durham, South Road, Durham, DH1 3LE, UK

### Abstract

An analysis of the atomic thermal motion in the organic non-linear-optical material, DCNP, is presented. The phenyl group in this compound librates within the molecular plane. This motion induces a quinoidal electronic configuration of the ring which enhances molecular charge transfer. This in turn aids the large second-harmonic-generation output that is observed in the material.

**Keywords:** diffraction; second-harmonic-generation; libration.

### INTRODUCTION

There exists an inherent relationship between crystal structure and non-linear-optical (NLO) properties such that property determining features can be probed by diffraction techniques. On a molecular scale, the extent of charge-transfer (CT) across the NLO chromophore determines the level of SHG output [1,2]: the greater the CT, the larger the SHG output. The present study illustrates the effects of atomic thermal motion on CT effects and thus on SHG activity.



The case study, 3-(1,1-dicyanoethenyl)-1-phenyl-4,5-dihydro-1H-pyrazole (hereafter DCNP) exhibits excellent SHG activity: approximately 100 times that of urea when using a fundamental wavelength of 1.9  $\mu\text{m}$  [3,4]. Theoretical investigations have shown that the nature of the pyrazole group is in part responsible for this [5]. However, this study shows that the phenyl group also, in part, dictates the SHG properties due to the consequences of its atypical atomic thermal motion. This motion was characterised by a structural investigation that comprised single-crystal neutron and X-ray diffraction measurements.

## EXPERIMENTAL

The neutron diffraction study of monoclinic DCNP [ $\text{C}_{13}\text{H}_{10}\text{N}_4$ ,  $M_r = 220.0$ , space group, Cc,  $a = 11.571(2)\text{\AA}$ ,  $b = 12.258(3)\text{\AA}$ ,  $c = 7.868(2)\text{\AA}$ ,  $\beta = 90.11(3)^\circ$ ,  $Z = 4$ ] was performed on the single-crystal diffractometer, SXD, at the ISIS facility, Chilton, U.K., at 100(1)K. The single-crystal variable-temperature X-ray diffraction studies were all carried out using the Bruker SMART-CCD diffractometer at the temperatures 90(2)K, 100(2)K, 200(2)K and 290(2)K. This instrument is ideal for a variable temperature study since, by nature of its large area detector, data can be recorded at several different temperatures in just a few days.

## RESULTS AND DISCUSSION

Figure 1 shows the 100K neutron derived structure of DCNP. The centre of the ellipsoids on each atom represent the time-averaged static atomic positions whilst the topology of each ellipsoid depicts the volume around this point where there is a 50% probability that the atom may lie at any one instance. The greater the level of atomic vibration, the further away from its time-averaged static position an atom may be found: i.e. the larger the ellipsoid. The topology of each ellipsoid will be spherical if atomic motion is due purely to vibration within a three-dimensionally isotropic potential. However, an atom will usually vibrate within an anisotropic potential, leading to a non-spherical

ellipsoid. In addition, atoms can undergo rotations about bond vector(s) and the level to which the ellipsoid reflects this motion can be measured to yield the extent (and sense) of this rotational component. An atom that has a non-zero rotational component (all atoms must have a non-zero vibrational component) is said to librate.

It is evident from the elongation of the ellipsoids in Figure 1 that the phenyl group is involved in a significant level of libration about the cross-vector of the C(8)-N(4) bond.

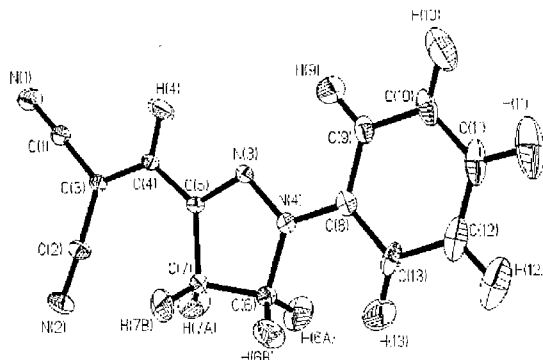


FIGURE 1: The 100K neutron structure of DCNP.

Analogous X-ray diffraction measurements made at 100K also illustrate this thermal behaviour (although this can only be observed in the carbon atoms since the hydrogen atoms are much less well defined in the X-ray diffraction study). Further X-ray diffraction measurements on DCNP at temperatures of 90K, 200K and 290K yielded ellipsoids with the same topology, their size being linearly proportional to temperature, as is characteristic of libration. The diagonal tensorial component of each ellipsoid in the direction closest to the normal of the molecular axis within the molecular plane are plotted against temperature in Figure 2 which illustrates this linear dependence for each atom.

For a system undergoing purely vibrational atomic motion, the gradient of each line depicted in Figure 2 will be the same for each atom. The presence of a non-zero rotational component associated with a given atom augments this gradient, the larger this component being,

the greater this augmentation. It is thus evident from Figure 2 that the atoms associated with the phenyl group are involved in a significant level of libration in the molecular plane, in the direction approximately normal to the molecular axis.

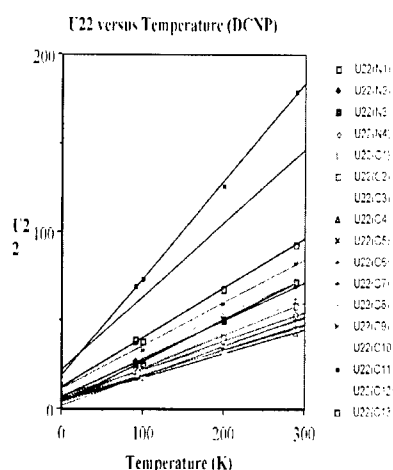


FIGURE 2: The extent of atomic motion in the crystallographic U22 principal direction (near-normal to the molecular axis within the molecular plane) for each atom as a function of temperature for DCNP.

The presence of libration makes difficult the location of the true interatomic distances between atoms that undergo this type of motion, using conventional single-crystal structural refinement techniques. However, libration can be modelled and thus parameterised by the thermal motion analysis method of Trueblood and co-workers [6]. Once parameterised, the results can be used to correct the bond geometries calculated from the conventional structural refinement technique to give more precise bond parameters.

Whilst libration of small terminal groups (e.g. H, -CH<sub>3</sub>, -CF<sub>3</sub> groups) in molecules is quite common, libration in a terminal phenyl group is not common, especially to this extent. Therefore, it was deemed pertinent to undertake this thermal motion analysis with a view

to understanding its origin. This work utilised the THMA11 program [7]. Full details of these calculations and results are given elsewhere [8] but the salient conclusions are reported here.

The corrected interatomic distances for the phenyl group [C(8)-C(9): 1.393Å, C(9)-C(10): 1.389Å; C(10)-C(11): 1.397Å; C(11)-C(12): 1.397Å; C(12)-C(13): 1.388Å; C(8)-C(13): 1.406Å] are more representative of a quinoidal electronic configuration than an aromatic one, the preponderance of the latter configuration being originally supposed in view of the resonance stabilisation energy associated with an aromatic system.

We believe that the librational motion in the phenyl group provides the energy necessary to overcome this aromatic stabilisation energy barrier such that a system with conjugation extending across the whole molecule results (Figure 3). In turn, bond parameters show that the resulting neutral conjugated system exhibits a good level of resonance with its charge-separated state which is important for minimising bond-length-alternation and enhancing molecular CT and thus  $\beta_{ijk}$ . Whilst libration is present primarily in this ring, the nitrile groups also librate, albeit to a lesser extent. This results in a greater susceptibility of the triple-bonds to vary in bond-order with time. A reduction in triple-bond character yields a lower bond-length alternation value which further enhances SHG activity. The analysis of libration thus clearly helps to more fully rationalise the structural origins of the favourable SHG properties in DCNP.

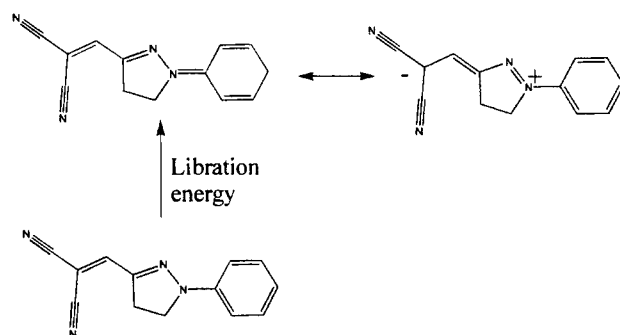


FIGURE 3: Overcoming the aromatic stabilisation energy and resulting resonance structures of DCNP.

## CONCLUDING REMARKS

The study on libration in DCNP hitherto described illustrates the potential importance of libration on SHG activity in organic compounds. In this example, its role appears to significantly enhance the molecular CT and thus  $\beta_{ijk}$  by alleviating the energy barrier from the aromatic to quinoidal electronic configuration.

## ACKNOWLEDGEMENTS

The authors would like to thank the ISIS facility, Chilton, Oxon, UK, for access to neutron beam-time. J. N. Sherwood and E. E. A. Shepherd (Department of Pure and Applied Chemistry, University of Strathclyde, UK) for supplying the relevant crystals. The Institut Laue Langevin is also thanked for a PhD studentship (JMC).

## REFERENCES

- [1] J. L. Oudar, J. Zyss, *Phys. Rev. A* **26** 2028 (1982).
- [2] S. J. Lalama, A. F. Garito, *Phys. Rev. A* **20**, 1179 (1979).
- [3] S. Allen, T. D. McLean, P. F. Gordon, B. D. Bothwell, M. B. Hursthouse, S. A. Karaulov, *J. Appl. Phys.* **64** 2583 (1988).
- [4] S. N. Black, R. J. Davey, P. R. Morley, P. Halfpenny, E. E. A. Shepherd, J. N. Sherwood, *J. Mater. Chem.* **3**, 129 (1993).
- [5] V. J. Docherty, D. Pugh, J. O. Morley, *J. Chem. Soc., Faraday Trans. 2*, **81**, 1179 (1985).
- [6] K.N. Trueblood, J.D. Dunitz, *Acta Crystallogr.*, **B39**, 120 (1983).
- [7] K. N. Trueblood, E. Huber-Buser, THMA11. Program for Thermal Motion Analysis, University of California, Los Angeles, USA, 1987.
- [8] J. M. Cole, C. C. Wilson, J. A. K. Howard, F. R. Cruickshank, *Acta Crystallogr. B* (accepted for publication, 2000).

## Preparing Polydiacetylene Single Crystal Thin Films

A. FELDNER, TH. FEHN, TH. VOGTMANN AND  
M. SCHWOERER

Physikalisches Institut and Bayreuther Institut für  
Makromolekülforschung (BIMF), Universität Bayreuth, D-95440  
Bayreuth, Germany  
e-mail: andreas.feldner@uni-bayreuth.de

Polydiacetylene (PDA) single crystals show extremely high and anisotropic values of the third order susceptibility. Here we describe a method to prepare polydiacetylene single crystal thin films of about a micrometer thickness and several square millimeters surface area. It is shown how to grow single crystals of the monomer and how to avoid crystal cleaving or other damages during the polymerization process that usually occur due to a slight contraction of the crystal. Being a one-pass crystallization process, the resulting optical quality is very good, and the films are well suited as wave guides. No difference of (linear) optical properties were found in these thin film single crystals when compared to macroscopic PDA crystals.

**Keywords:** polydiacetylene; organic crystal; wave-guide; non-linear optics

## INTRODUCTION

All-optical switching may be a key technology to handle the drastic increase of data transmission than can be expected within the next 10 years. Although much research has been done in this area, no suitable solution has yet appeared. For a long time, the main approach was to

search for materials with a significantly higher nonlinear optical susceptibility  $\chi^{(3)}$ , but switching times still in the sub-picosecond regime. In recent years, optimized device geometries were proposed instead, to make use of linear dispersion as well as of the nonlinearity. The linear dispersion of a waveguide can be tailored by periodic modulation of the guide index, to add to the effect of the nonlinearity [1].

A key to an all-optical switch therefore is a good waveguide. Ideally, the nonlinear medium itself is used for guiding the wave, to use its full intensity for triggering nonlinear effects. Therefore, the material should provide low losses on a length scale needed to build a working switch with the material's nonlinearity. PDA single crystals show one of the largest nonresonant nonlinear susceptibilities ( $\chi^{(3)} \sim 10^{-10}$  esu). For these crystals and the gap soliton switch geometry, simulations yielded a typical length of 0.3mm to observe a switching effect [2]. For a monomode waveguide, the thickness must be of the order of wavelength.

The main problems in polymers are not usually absorptive losses, but scattering due to microcrystallinity, inhomogenities and impurities. An elegant way to avoid these sources of scattering, is to use thin single crystals in the correct geometry.

Polydiacetylenes show a unique feature in that it's possible for many of its derivatives to polymerize in a crystal, resulting in alignment of all the polymer backbones [3]. The polymerization process can be triggered by gamma ray treatment or even, with some derivatives, by modest heating. The polymerization reaction causes a contraction in the chain direction. This results in a strain in the monomer crystal, once a certain amount of polymers have been induced. The crystal strain drives the polymerization reaction of the remaining monomer [4]. The contraction in the direction of the reaction is especially high for the thermally polymerizable polydiacetylenes, e.g. 5% for TS-6.

## PROBLEMS WITH CURRENT METHODS TO PREPARE PDA CRYSTALS

Preparing crystals of polydiacetylene involves a two-step process. First, a crystal of diacetylene monomer is grown, then this monomer crystal is turned into a polymer crystal by gamma ray treatment or heating.

The first step has been widely discussed in the past, and some methods were published that are very suitable to generate monomer waveguides. To prepare the monomer crystals, we use a growth method similar as published and patented by Thakur and Meyler [5, 6]:

A liquid layer of dissolved monomer is packed between two substrates. While applying pressure to the substrates, the solvent is slowly evaporated. The pressure can be used to control the resulting film thickness. If you do this at reduced temperatures and choose a slowly evaporating solvent, you may delay the process to a period of about a month. Then, monomer crystals of typically 2 mm lateral size and 1  $\mu\text{m}$  thickness form without further interaction. These crystals have a good optical quality and smooth surfaces; as such they are suited as waveguides, but they don't have any extraordinary optical properties; huge optical nonlinearities only appear after polymerization.

However, this second step, the polymerization, involves a major problem, as there is a slight contraction of the crystal in the direction of the forming polymer chains. This causes two types of cracks in the crystals: as expected, wide cracks perpendicular to the polymer chains, typically separated by about a millimeter, but, much worse, due to lateral contraction and the low mechanical stability of the crystals against stress perpendicular to the polymer chains, very fine regular cracks parallel to the chains, separated by some 10  $\mu\text{m}$ . These latter cracks inhibit any use as nonlinear-optical waveguides, because the electrical field vector must be parallel to the chains and therefore the wave must propagate in a direction perpendicular to the cracks.

### NEW PREPARATION STEP TO AVOID CRACKING

To address this problem, the monomer crystals should be removed from the substrate before polymerization. Although it is possible to remove them partially, simply by putting the substrates in a bath of water, with detergent to reduce surface tension, only smaller crystals, or small parts of the larger ones, will detach from the substrate surfaces. Also, leaving them in the bath for long time destroys the crystal surfaces.

The general idea that allowed us to successfully circumvent this problem is, instead to remove the crystals from the substrate, to dissolve the substrate itself.

The choices of buffer layer material, solvent for monomer solution, and solvent for buffer layer obviously must fulfil the condition that the solvent for the monomer solution may not react with the buffer layer and the solvent for the buffer layer may not dissolve the monomer crystals. We use a mixture of Acetone and Cyclohexanone as solvent for the monomer solution, while the formed crystals do not dissolve in water. An ideal candidate for the buffer layer material was therefore found in the water dissolvable Polyvinylalcohol (PVOH).



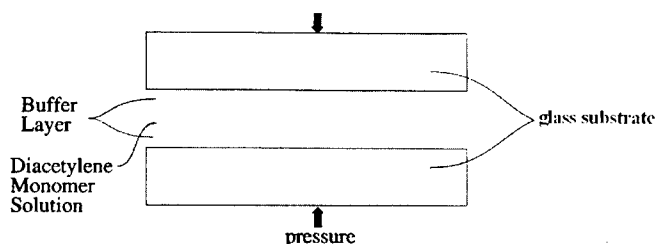


FIGURE 1 Scheme of the layered setup to grow monomer crystals. By slow evaporation of the solvent, diacetylene monomer crystals form in the central layer. These crystals can be detached from the substrates without mechanical stress by dissolving the buffer layer in a water bath.

The practical realization is only slightly more complicated: a five layer structure, where on each glass substrate is coated an additional thin dissolvable buffer layer, just thick enough (about  $1\ \mu\text{m}$ ) to keep the forming crystals from direct contact to the glass substrate (figure 1). Dissolving the buffer layer is much faster than dissolving a whole substrate, and we avoid mechanical stress to the crystals that could be expected by soaking thick layers of PVOH.

Using this setup, the formed monomer crystals can be removed from the substrates without any mechanical damage. The free floating crystals can then be polymerized in the water bath by heating and finally be brought to any (water resist) target substrate.

As a test for the crystal surface, and especially its homogeneity, we put the crystals between crossed polarizers. Because of the large birefringence, the crystal destroys the linear polarization from the polarizer if the polymer axes are not exactly parallel or perpendicular. Therefore, if the crystal is aligned, but contains misaligned or even polycrystalline domains, these domains will be visible as bright areas. With our preparation method, nearly all crystals show uniform orientation of the polymer backbones over the whole crystal, i.e. they are monocrystalline. If the crystal is turned out of alignment, it appears bright. In this view, inhomogeneities of thickness, cracks and other defects can be seen very clearly (figure 2). As expected, the crystals show only a few singular defects, probably caused by dust particles, and few cracks at the crystal's ends.

No difference of linear optical properties were found in these crystals when compared to other PDA crystals [7].



FIGURE 2 p-TS-6 crystal between two crossed polarizers. The crystal axes are turned  $45^\circ$  against the polarizer direction.

#### ATTACHING THE CRYSTALS TO THE TARGET SUBSTRATE

As shown in AFM measurements (figure 3), there are net-like structures on the surface of the crystals, with a height of typically 50 nm and a mesh size of  $\sim 1 \mu\text{m}$ . We assume that these structures result from deposits from the drying water. Therefore, it is important that the bubble, in which the crystal is transferred to the final substrate, consists of a clean solvent.

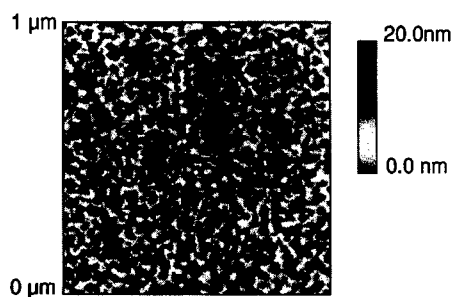


FIGURE 3 Net-like structures on a crystal surface, as seen by atomic force microscopy.

To achieve this, after polymerizing we put the crystal directly, without letting it dry, through a series of solvent baths, water, acetone, and hexane. Indeed, the resulting surface did only show a different, much smaller structure (figure 4). Its origin is yet unknown, but the structure

is too small to have any influence on the optical properties.

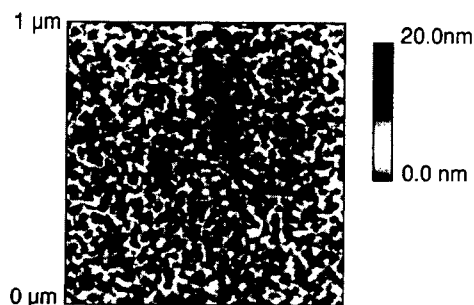


FIGURE 4 Surface of a crystal that was put through the described series of baths of increasing purity. Note the different scales in comparison to figure 3.

#### Acknowledgements

The authors want to thank Irene Bauer for preparation, Jürgen Gmeiner for many useful suggestions, and George I. Stegeman and Lars Friedrich for using our crystals in some of their experiments. Their feedback was very valuable.

This work was funded by the German Bundesministerium für Bildung, Wissenschaft, Forschung und Technologie (BMBF) (project 03N1021D2).

#### References

- [1] C.M. de Sterke and J.E. Sipe, *J. Opt. Soc. Am. B* **6**, 1722 (1989)
- [2] H.M. Keller, S. Pereira, J.E. Sipe, *Opt. Comm.* **170**, 35 (1999)
- [3] G. Wegner and W. Schermann, *Z. Naturforschung* **24b**, 824 (1969)
- [4] R.H. Baughman, *J. Chem. Phys.* **68**, 3110 (1978)
- [5] M. Thakur and S. Meyler, *Macromolecules* **18**, 2341 (1985)
- [6] US Pat.-Nr. 04684434, 04793893, 04698121
- [7] L. Friedrich, T. Pliska, M. Liu, G.I. Stegeman, S. Park, A. Feldner, Th. Vogtmann, and M. Schwoerer: *Linear Optical Properties of P-toluene Sulfonate PTS*, to be published.

## SHG-active p-nitroaniline thin films grown by dip-coating

HIROYUKI KOBAYASHI, HIROYUKI OKUYAMA AND  
MASAHIRO KOTANI

Faculty of Science, Gakushuin University,  
Mejiro, Tokyo 171-8588, Japan

Thin films that are strongly second-harmonic active are grown when p-nitroaniline is dip-coated on a glass plate. The intensity of the second harmonics is comparable to that from a film of 2-methyl-4-nitroaniline. The SHG-active phase is metastable and undergoes a transition into a SHG-inactive phase, the transition rate being dependent on the temperature and the solvent used.

**Keywords** p-nitroaniline; second harmonic generation; thin film

## INTRODUCTION

p-Nitroaniline (p-NA) is a compound which has a large second-order polarizability. However, it crystallizes in a centrosymmetric structure and the crystal is considered to be inactive in SHG. Effort has been made to realize a SHG-active system by arranging p-NA moiety in a favourable way, e.g., by electrical poling [1], co-crystallization [2], epitaxy [3]. We have reported an observation that an intense second-harmonic is generated at etch pits developed on a single crystal surface. It is supposed that a microcrystal having an acentrosymmetric structure grows at the etch pits [4]. Here we report another example in which a SHG-active arrangement of p-NA molecules is realized. Thin films prepared by dip-coating exhibit intense SHG, comparable to thin films of 2-methyl-4-nitroaniline (MNA). Interestingly, the SHG activities of films prepared with different organic solvents differ in durability, as well as its magnitude. The SHG-active phase seems to be metastable and changes into an inactive phase, with a half life which depends both on the temperature and the solvent used.

## EXPERIMENTAL

p-NA was purchased from Tokyo Kasei Co. and was purified by zone-melting. Glass plates were cleaned by sonicating in an ethanol solution and were used as substrates. Thin films were formed by dipping the substrate into a solution or by spin-coating. The coverage was determined by measuring the absorbance of a solution, prepared by dissolving a film in ethanol.

A SHG image of a film was taken with an arrangement shown in Fig. 1. A film was illuminated with a pulse from a Q-switched Nd:YAG laser (New Wave Research, MiniLase 2). The image of the illuminated area was magnified by an objective lens, the  $1.06 \mu\text{m}$  component being removed with a combination of a dichroic mirror and a filter (HOYA, CM500), and focused on a CCD (MK-0321E). For taking a conventional microscope image the Nd:YAG laser was replaced by a tungsten lamp.

X-ray diffraction was measured with a diffractometer (Rigaku, RINT2000) with an X-ray tube with a chromium target ( $\lambda = 2.2896 \text{ \AA}$ ). A  $\theta$ - $2\theta$  scan was made which gives a conventional powder pattern when the sample was in a powder form. When applied to a film grown on a plane surface, this procedure probes the periodicity along the surface normal.

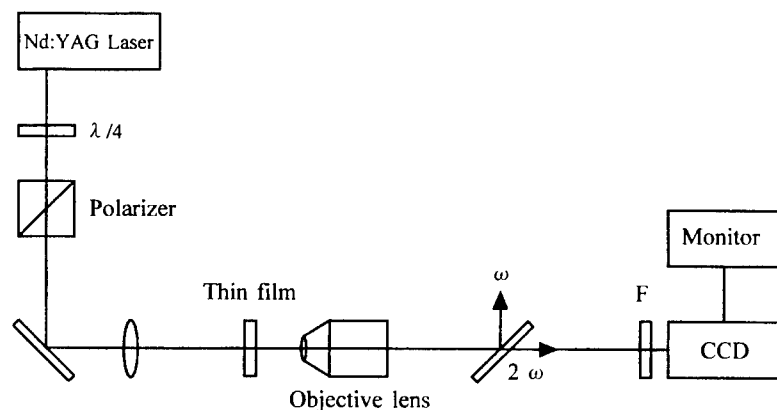


FIGURE 1 Experimental arrangement for SH-detected microscopy.

## RESULTS AND DISCUSSION

The intensity of the second-harmonics from a thin film depends on

the solvent used. While SHG-active films grow from ether or benzene solution, films grown from ethanol or acetone are mostly inactive in SHG. A film grown from a benzene solution exhibits SHG that is comparable in intensity to those of MNA.

Another factor which influences the film growth is the speed of the solvent evaporation. A slow evaporation of benzene solution leads to a SHG-inactive film, while spin-coating or dip-coating, where solvents evaporate rapidly, results in films that are SHG-active.

Figure 2 shows microscopic images of a p-NA thin film, spin-coated with a benzene solution. The image (a), taken with tungsten lamp illumination, shows that the film is composed of needle, or fibrous, crystals, several microns thick and tens of microns long. The SH image (b) has been taken with illumination with circularly polarized light. It is clearly seen that needle (or fibrous) crystals are responsible for the SHG-activity.

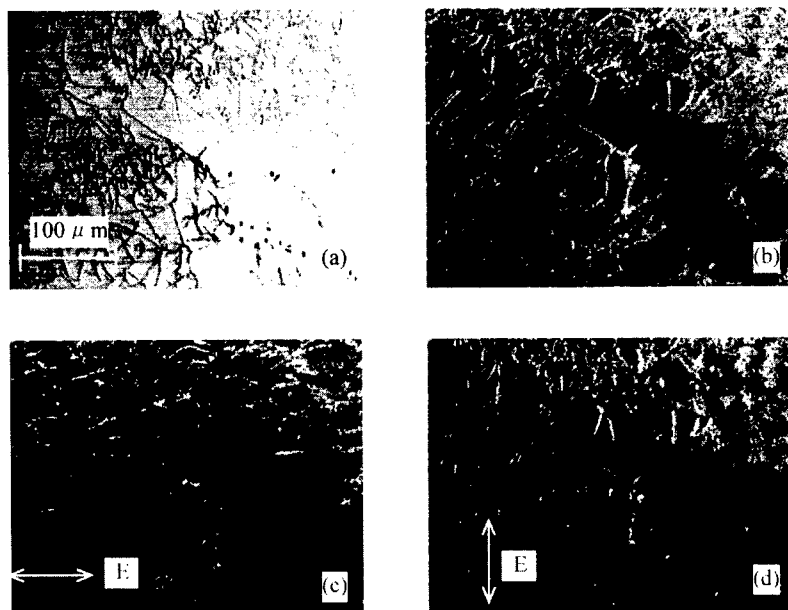


FIGURE 2 Microscopic images of a p-nitroaniline thin film spin-coated with a benzene solution (a) with conventional lighting, (b) (c) (d) the same field taken with SH detection. The image (b) has been taken with circularly polarized excitation. In (c) and (d) the arrows show the orientation of the polarizer for the fundamental. Second-harmonic is generated when the laser light is polarized parallel to the needle axes.

Images (c) and (d) are also SH images and have been taken with illumination with linearly polarized light. The arrows indicate the direction of the electric field of the illuminating light ( $1.06 \mu\text{m}$ ). It may be seen that in Fig. 2(c) horizontal lines are accentuated, while in Fig. 2(d) vertical lines are prominent. By comparing these observations with Fig. 2(b) one can conclude that second-harmonic is generated when the polarization of the laser is parallel to the needle axes of the crystals. This in turn suggests a crystal structure which is asymmetric along the needle (or fiber) axis of the crystal. The films prepared with benzene or ether solution do not relax into SHG-inactive form at room temperature. Their SHG activity does show deterioration when the films are stored at an elevated temperature, but this decline seems to be due to the evaporation of the material, rather than a solid-to-solid phase transition.

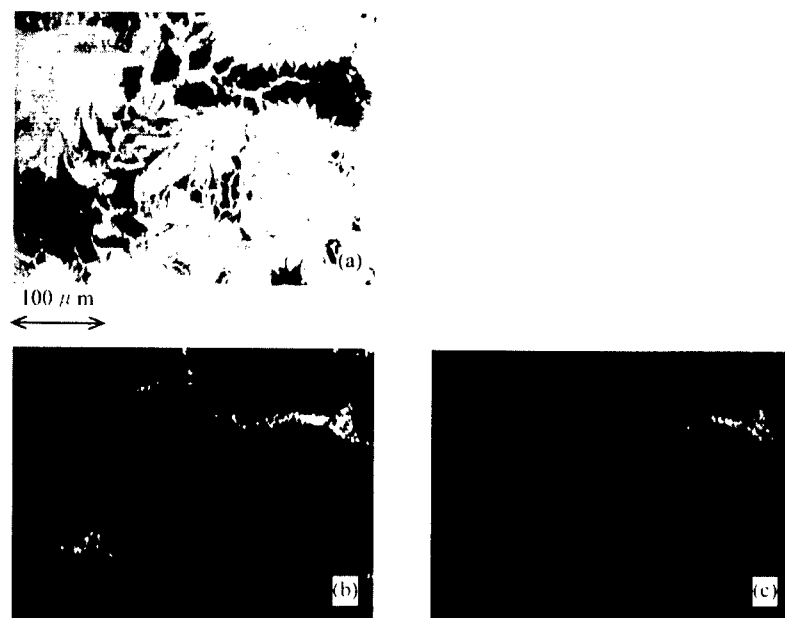


FIGURE 3 Microscopic images of a p-nitroaniline thin film prepared by spin-coating from an ethanol solution. (a) With conventional illumination with a tungsten lamp. (b) A SH image of the same field, 2 min after preparation. The illumination was made at  $1064 \text{ nm}$  and the image was detected at  $532 \text{ nm}$ . Note that most crystals are inactive in this case. Only crystals grown in the last phase of the drying seem to be active in SHG. (c) The same as in (b), but after 7 min.

Figure 3 shows microscopic images of a film prepared by spin-coating of an ethanol solution. Figure 3(a) shows an image taken with conventional illumination. It is seen that the crystals have a habit quite different from crystals grown from a benzene solution (Fig. 2(a)). The crystals are largely leaflets, rather than needles. Figure 3(b) shows the second-harmonic image taken with circularly polarized light. It may be seen that most of the crystals are inactive in SHG. Only a small fraction of the crystals are active. Those crystals which are SHG-active are localized along lines which form the boundaries between the domains and might have been formed at the last phase of the drying process. This observation suggests possible role of an impurity, or water, in the nucleation process. Figure 3(c) shows SHG-image of the same field, but 7 minutes after preparation. It clearly shows that the SHG activity of the film decreases rapidly with time.

Crystal structure analysis of the SHG-active phase has not been made. We have made preliminary measurements of X-ray diffraction with the film. Figure 4(a) shows a powder diffraction pattern taken with ordinary p-NA powder which is inactive in SHG. The peak at  $38^\circ$  is the reflection from (202) plane and corresponds to the thickness ( $3.5 \text{ \AA}$ ) of a layer in which p-NA molecules are lying flat [5]. Figure 4(b) shows the diffraction from powder of SHG-active crystals. The sample has been collected by scratching off the SHG-active films by razor blades. We have found that the SHG-activity goes lost on grinding the powder. Accordingly, the collected powder was only filtered with a stainless steel mesh (100 mesh) and pressed against a quartz plate for diffraction measurements. The results in Fig. 4(b) indicate that the SHG-active phase has a structure different from an ordinary crystal. The (202) peak, which is strong in the ordinary crystal, is much

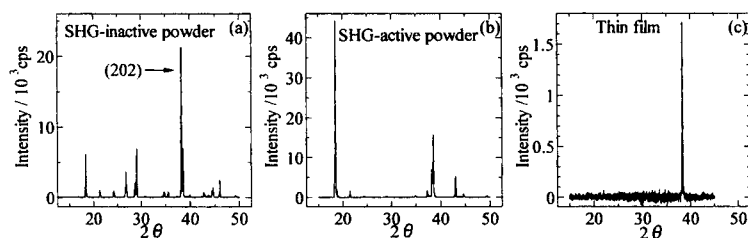


FIGURE 4 X-ray diffraction patterns of (a) SHG-inactive powder, (b) SHG-active powder and (c) a thin film, dip-coated with benzene solution.



weaker in the SHG-active powder, and gains intensity as the SHG-activity deteriorates. Figure 4(c) shows the diffraction pattern obtained from an SHG-active film. Only a single peak is seen which corresponds to the (202) reflection of the ordinary phase. This suggests that molecules are lying flat on the surface of the substrate and form a layer-like stack, as in the ordinary phase. The most prominent feature of the structure is its polarity (lack of centrosymmetry) that is responsible for its SHG-activity.

#### ACKNOWLEDGEMENTS

The authors are indebted to Dr. A. Kubo, Dr. T. Suzuki and Prof. M. Akaogi for their very willing help and advice in X-ray diffraction measurements.

#### REFERENCES

- [1] T. Watanabe, K. Yoshinaga, D. Fichou and S. Miyata, J. Chem. Soc. Chem. Commun. 250 (1988).
- [2] T. Miyazaki, T. Watanabe and S. Miyata, Jpn. J. Appl. Phys., **27**, L1724 (1988).
- [3] H. Kobayashi, T. Ehara and M. Kotani, J. Chem. Soc. Faraday Trans., **90**, 3685 (1994).
- [4] H. Kobayashi and M. Kotani, Mol. Cryst. Liq. Cryst. **278**, 125-130 (1996).
- [5] K. N. Trueblood, E. Goldish, and J. Donohue, Acta Cryst. **14**, 1009 (1961).

## Observation of Second-Harmonic Generation in Sol-Gel Glass Doped with N-4-nitrophenyl-(L)-prolinol Nanocrystals

IRENE WANG<sup>a</sup>, NATHALIE SANZ<sup>b</sup>, ALAIN IBANEZ<sup>b</sup>, PATRICE L. BALDECK<sup>a</sup>,

<sup>a</sup> Laboratoire de Spectrométrie Physique, Université J. Fourier, CNRS (UMR 5588) - BP 87, 38402 Saint Martin d'Hères cedex, France;

<sup>b</sup> Laboratoire de Cristallographie, CNRS, BP 166, 38042 Grenoble cedex 09, France.

We have observed second harmonic generation (SHG) in N-4-nitrophenyl-(L)-prolinol (NPP) nanocrystals embedded in sol-gel glass. The harmonic signal was produced in localised areas. A 16 T magnetic field was applied to some samples during the crystallisation process. In these samples, the frequency of occurrence of the SHG signal is increased. To better understand these observations, samples containing a non-polar SHG active molecule: 3-methyl-4-nitropyridine-1-oxide (POM) were also elaborated. POM nanocrystals did not generate second harmonic signal whether they were prepared under magnetic field or not. Therefore, dipolar interactions between NPP nanocrystals may lead to the formation of oriented domains in the sol-gel media.

**Keywords** sol-gel glass; organic nanocrystals; second-harmonic generation

Organic nanocrystals in sol-gel glasses [1] are a promising new type of material for optical applications. Solid transparent optical grade samples in bulk or thin film can be obtained with high concentration in active organic molecules (>30% in weight). Organic crystals received much attention because of their large quadratic nonlinear response in the visible and near infrared spectral range. Here we want to study the

second-order nonlinear properties of organic nanocrystals which may become a suitable alternative to large single crystals due to their easy processing and better stability. We present preliminary tests on nanocrystals of N-4-nitrophenyl-(L)-prolinol (NPP), which has already been extensively studied for applications in quadratic nonlinear optics [2-7], and 3-methyl-4-nitropyridine-1-oxide (POM) [8].

Bulk sol-gel samples containing NPP and POM nanocrystals were prepared. We could identify by transmission electron microscopy organic crystals with sizes ranging from 12 to 24 nm that are randomly dispersed in the gel glass, the average inter-particle distance being approximately 100 nm. Magnetic-field oriented samples were prepared using a superconducting coil to apply a 16 T magnetic-field during the nucleation and growth of nanocrystals. The detailed elaboration process will be reported separately.

The NPP nanocrystals structure is still unknown. In this paper, we assume in a first approximation that it is close to the bulk crystal structure given in Ref. 2.

### INFLUENCE OF THE MAGNETIC FIELD

Like most organic material, NPP and POM molecules show diamagnetic anisotropy. In their case it is dominated by the anisotropy of the aromatic ring. The induced magnetic moment is orthogonal to the plane of the benzene ring. As a result, under the magnetic field, the molecules tend to lay in the plane perpendicular to its direction as indicated on fig.1. On this figure, only one molecule was represented for simplicity, but efficient orientation will occur only for aggregates big enough so that magnetic interaction energy becomes comparable to thermal agitation. For bulk NPP crystals, the molecular packing shows that all molecular mean planes are parallel, thus forming a cleavage plane [2]. Therefore, it can be inferred that magnetic field favours the formation of nanocrystals with the same crystalline structure as in the bulk and preferential orientation of the cleavage plane orthogonal to the magnetic field direction.

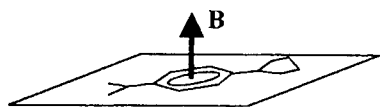


FIGURE 1 Preferential orientation in presence of magnetic field

Birefringence observations carried on NPP doped samples confirms the magnetic field-induced anisotropy. In a first evaluation, the resulting birefringence is estimated to be  $\Delta n=0.004$ .

## SECOND HARMONIC MEASUREMENTS

All samples have been tested for SHG using a Nd-YAG laser with 2.6 ns pulse duration and 300 mJ maximum pulse energy. The beam incident on the sample has an 2.5mm radius. On NPP samples prepared without magnetic field, second harmonic generation could be observed at some areas. Those samples which had undergone magnetic field exhibited more numerous areas showing harmonic response. On POM samples however, no harmonic signal could be detected whatever the preparation manner.

In order to determine the structure of the SHG active areas in NPP, measurements were performed using variable polarisation at normal incidence. Samples with all four faces polished were elaborated for this purpose so that both parallel and perpendicular propagation directions with respect to the magnetic field could be investigated. The fundamental wave at  $\lambda=1.14\mu\text{m}$  had nanosecond pulse duration and 10 $\mu\text{J}$  average energy. It was focused in the sample into a 200 $\mu\text{m}$  diameter waist. The linear polarisation of the incident beam was made to rotate. Either the total SHG output intensity was recorded or an analyser was used to select one polarisation of the harmonic signal.

The data obtained proved to be often difficult to interpret due to the superposition of signals originating from adjacent areas with different orientations. Fig.2 displays a typical curve when the sample is probed with the laser beam perpendicular to the magnetic field to which it has been submitted.

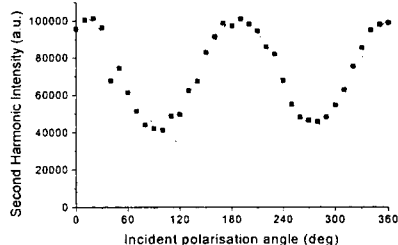


FIGURE 2 Polarisation analysis of SHG for propagation direction orthogonal to magnetic field (no analyser).

The intensity maxima occur when the incident polarisation is parallel to the preferential orientation of the molecular charge transfer plane that we have predicted. This confirms the magnetic field induced orientation.

When probing with the beam at normal incidence on the preferential plane for molecular orientation, the data shown on fig.3 have been obtained for one particular area. As the SHG signal almost reaches zero for some incident polarisation, we can assume that it is emitted by one domain where all particles are approximately oriented in the same direction. The polarisation dependencies recorded for other SHG active areas can be interpreted as the superposition of two or more of such responses that are not in phase.

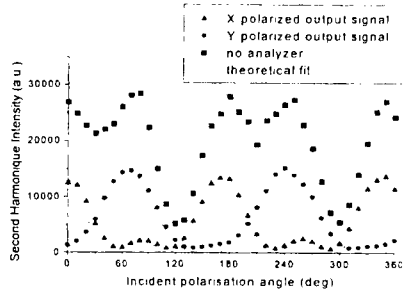


FIGURE 3 Polarisation analysis of SHG for propagation direction parallel to magnetic field.

The following equations were used to fit the data on fig.3:

$$I_{int} \propto \left( \frac{\alpha_{21}}{\alpha_{22}} \cos^2(\theta - \theta_0) + \sin^2(\theta - \theta_0) \right)^2 + \left( 2 \frac{\alpha_{21}}{\alpha_{22}} \cos(\theta - \theta_0) \sin(\theta - \theta_0) \right)^2$$

$$I_X \propto \left[ 2 \frac{\alpha_{21}}{\alpha_{22}} \cos(\theta_0) \cos(\theta - \theta_0) \sin(\theta - \theta_0) - \sin(\theta_0) \left( \frac{\alpha_{21}}{\alpha_{22}} \cos^2(\theta - \theta_0) + \sin^2(\theta - \theta_0) \right) \right]^2$$

$$I_Y \propto \left[ 2 \frac{\alpha_{21}}{\alpha_{22}} \sin(\theta_0) \cos(\theta - \theta_0) \sin(\theta - \theta_0) + \cos(\theta_0) \left( \frac{\alpha_{21}}{\alpha_{22}} \cos^2(\theta - \theta_0) + \sin^2(\theta - \theta_0) \right) \right]^2$$

The overall corresponding symmetry is shown on fig.4:

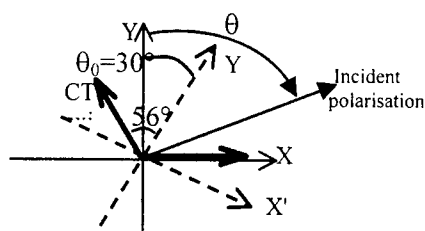


FIGURE 4 Dielectric framework deduced from the data on fig.3

$\alpha_{21}$  and  $\alpha_{22}$  are the coefficients of the nonlinear susceptibility  $\chi^{(2)}$  in the  $X'Y'$  axes. The ratio  $\alpha_{21}/\alpha_{22}$  provides an evaluation of the charge transfer direction, as microscopic 1 D model for the quadratic hyperpolarizability  $\beta$  was shown to be valid for NPP [5]. The angle between the two-fold axis  $X'$  and the charge transfer axis was found to be  $56^\circ$ , a value very close to that of bulk NPP crystals ( $58.6^\circ$ ).

It was not possible to determine the size of this coherent area, as our resolution is limited by the waist of the laser beam (approx.  $200\mu\text{m}$ ). Estimation of the conversion efficiency leads to a total volume of emitting crystals of  $1.5\mu\text{m}^3$ . Taking into account the sol-gel media, the active volume should be approximately  $50\mu\text{m}^3$ .

## DISCUSSION

The observation of SHG on NPP samples demands further understanding. Providing the particles were in a totally disordered state, the media will appear homogenous and centrosymmetric to the incident light, because the size and inter-particle distance of the NPP nanocrystals are very small compared to the probing wavelength. In this case no harmonic wave should be generated. The centrosymmetry should not be broken when a magnetic field is applied to the nanocrystals, for it let them freely rotate in a plane orthogonal to its direction.

These assertions seem to explain why POM nanocrystals were found to be SHG inactive. The main difference between POM and NPP nanocrystals is that the permanent dipole moment of NPP is about 7 D whereas POM has almost no molecular dipole moment. Therefore, the detection of a harmonic wave may be attributed to the formation of locally non-centrosymmetric domains in the assembly of NPP

nanocrystals, because of their strong dipolar interactions. Application of a magnetic field helps to reduce the orientation disorder of the crystals by creating a plane of preferential orientation. This can result in more numerous well-defined domains. The response shown on fig.3. may come from one domain of oriented nanocrystals. The mechanism of this self-orientation as well as the possibility to obtain further experimental evidence are still to be investigated.

## CONCLUSION

Sol-gel glasses containing NPP nanocrystals were shown to exhibit second harmonic generation in localised areas. This tendency is enhanced when a magnetic field is applied during crystallisation causing the media to become birefringent. Comparison between two different nonlinear molecules, NPP and POM, leads us to form the hypothesis that SHG signal originate from non-centrosymmetric local self-oriented areas which are made up by the strong dipolar interaction between nanocrystals.

## ACKNOWLEDGEMENT

We are grateful to DGA (Direction Générale de l'Armement) for supporting I.Wang's PhD thesis.

## REFERENCES

- [1] A. Ibanez, S. Maximov, A. Guiu, C. Chaillout and P.L. Baldeck, Advanced Materials, **18**,1540 (1998)
- [2] J. Zyss, J.F. Nicoud, M. Coquillay, J. Chem. Phys., **81**(9), 4160 (1984)
- [3] I. Ledoux, D. Josse, P. Vidakovic, J.Zyss, Opt. Eng., **25**(2), 202 (1986)
- [4] I. Ledoux, J. Zyss, A. Migus, J. Etchepare, G. Grillon, A. Antonelli, Appl. Phys. Lett., **48**(23), 1564(1986)
- [5] I. Ledoux, C. Lepers, A. Périgaud, J. Badan, J. Zyss, Optics Communications, **80**(2), 149 (1990)
- [6] Jianjun Xu, Ligui Zhou, M. Thakur, Appl. Phys. Lett., **69**(9), 1197(1996)
- [7] Zuo Wang, D.J. Hagan, E.W. VanStryland, J.Zyss, P. Vidakovic, W. E. Torruellas, J. Opt. Soc. Am. B, **14**(1), 76(1997)
- [8] J. Zyss, D.S. Chemla, J.F. Nicoud, J. Chem. Phys., **74**(9), 4800(1981)

## Phase-matching properties of the organic crystal (S)-3-Methyl-5-nitro-N-(1-phenylethyl)-2-pyridinamine

M. RINI <sup>a</sup>, G.P. BANFI <sup>a</sup>, V. DEGIORGIO <sup>a</sup>, J.N. SHERWOOD <sup>b</sup>

<sup>a</sup> Istituto Nazionale per la Fisica della Materia and Dipartimento di Elettronica, Università di Pavia, via Ferrata 1, 27100 Pavia, Italy;

<sup>b</sup> Department of Pure and Applied Chemistry, University of Strathclyde, Glasgow, G1 1XL, Scotland, UK

From refractive index measurements performed by the minimum deviation method we derive a set of Sellmeier coefficients for (S)-3-Methyl-5-nitro-N-(1-phenylethyl)-2-pyridinamine (S3MeMBANP). By using our Sellmeier set, whose accuracy has been confirmed by a second harmonic generation experiment, we calculate the phase matching properties of S3MeMBANP for all the principal planes.

**Keywords** Nonlinear optics; Phase-matching; Second-harmonic generation; Organic crystals

Organic nonlinear optical materials are promising candidates for playing a key role in the field of optical wave manipulation [1], because they may present a large and fast nonlinear response. By exploiting the unlimited variety of available molecules that can be developed through a molecular engineering approach several organic crystals were proposed and tested for nonlinear optical studies. The crystal MBANP, (S)-5-nitro-N-(1-phenylethyl)-2-pyridinamine, developed since the early 1980's [2], possesses significant second order optical nonlinearities in the near infrared, but the disposition of the dielectric axes and refractive indices is not particularly favourable to the production of large phase-matched



second harmonic signals [3]. In the past few years, a number of derivatives of MBANP have been synthesised in order to investigate if they may crystallise in more advantageous ways [3].

Among those derivatives, an interesting one is S3MeMBANP, (S)-3-Methyl-5-nitro-N-(1-phenylethyl)-2-pyridinamine, a methyl-substituted derivative of MBANP, identified as having significant second-order susceptibilities [3]. The structural formula of S3MeMBANP is given in Figure 1.

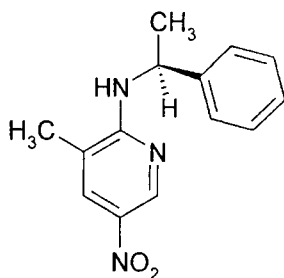


FIGURE 1 Structural formula of S3MeMBANP.

The S3MeMBANP crystal is orthorhombic, of space group  $P2_12_12_1$  and point group 222. A detailed description of this crystal can be found in [4]. Ease of crystal growth is an attractive feature of S3MeMBANP and, in general, of this family of derivatives of MBANP, possibly associated with the L-shaped structure of the molecules and the propensity to form strong hydrogen bonded chains in certain directions. Large, high quality, single crystals of S3MeMBANP of size up to  $40 \times 40 \times 15 \text{ mm}^3$  can be grown either from solution by the temperature lowering technique or by the Bridgman technique [4], allowing a complete optical characterization. A sketch of the orientation of the crystals used in our experiments is given in Figure 2.

A set of Sellmeier expressions for the principal refractive indices  $n_x$ ,  $n_y$  and  $n_z$  has already been given in [4], but its validity is limited to wavelengths below  $1.1 \mu\text{m}$ . We performed a linear characterization of this crystal at longer wavelengths, measuring all the principal refractive index dispersion curves, by mean of two prisms of S3MeMBANP with a different cut (Figure 2b). From our data we derive a new set of Sellmeier coefficients whose validity extends up to  $1600 \text{ nm}$ . We checked the

accuracy of our Sellmeier set by a second harmonic generation (SHG) experiment, performed on two different samples of S3MeMBANP (see Figure 2a), whose orientation is rather similar except for a different tilt angle  $\delta$  between the surface normal and the x axis. The tunable source used in our experiments is a  $\beta$ -barium borate (BBO) type-I optical parametric oscillator (OPO) synchronously pumped by a frequency doubled, 30 ps active/passive mode-locked, 10 Hz, Nd:YAG laser. The OPO bandwidth is reduced to approximately 0.3 nm by means of a reflection grating and a beam expander in the cavity. In the SHG experiment the beam of the fundamental signal at the input of the crystal has a spot size of 1.5 mm and its divergence is kept well below the acceptance angle of the crystal for SHG.

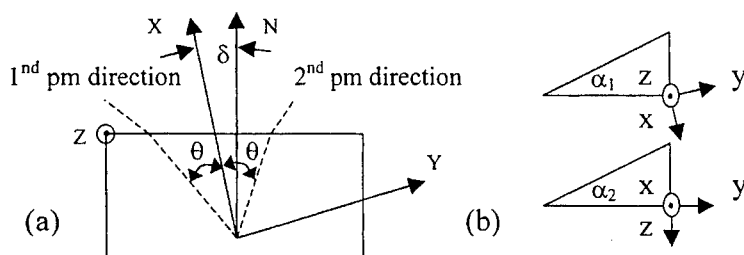


FIGURE 2 (a) Sketch of the orientation of the two samples used in the SHG experiment:  $\delta = 17.5^\circ$  for the first sample,  $3^\circ$  for the second. (b) Orientation of the two prisms employed in the refractive indices measurements:  $\alpha_1 = 16.700 \pm 0.008$  deg,  $\alpha_2 = 13.467 \pm 0.008$  deg.

By using the two prisms of S3MeMBANP we measured the refractive indices by the minimum deviation method [5], which yields an accuracy of typically  $\pm 0.005$ . By using a polarization parallel to the prism axis, it was possible to evaluate  $n_z$  in the first prism and  $n_x$  in the second. With a polarization in the incidence plane the values of  $n_y$  can be determined in both prisms by solving pairs of equations in  $n_x$  e  $n_y$  (in the first prism) and  $n_z$  and  $n_y$  (in the second). The values of the refractive indices in the y direction obtained from the two types of prism agreed with each other within the experimental uncertainty. The data are shown in Figure 3. The values of  $n_x$ ,  $n_y$  and  $n_z$  were fitted to the four-parameter,

one-pole Sellmeier equation:

$$n^2 = A + \frac{B\lambda^2}{\lambda^2 - C} - D\lambda^2$$

The values of the coefficients we obtained by a least-square fitting are reported in Table 1.

	A	B	C ( $\mu\text{m}^2$ )	D ( $\mu\text{m}^{-2}$ )
$n_x$	2.48696	0.15890	0.16193	0.01138
$n_y$	2.33345	0.60733	0.15030	0.01342
$n_z$	2.54969	0.20019	0.15513	0.02693

TABLE 1 Coefficients of the Sellmeier Equations.

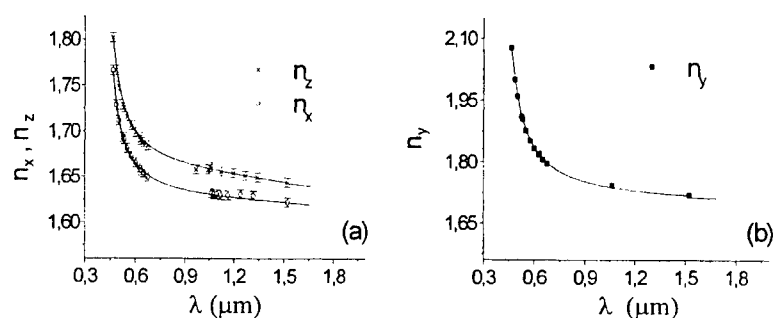


FIGURE 3 Data, error bars and four-parameter Sellmeier fit (full lines) for  $n_x$ ,  $n_z$  (a) and  $n_y$  (b).

We measured the type-I SHG phase-matching (PM) angle in the  $xy$  principal plane of the crystals as a function of the wavelength  $\lambda_1$  of the fundamental beam. The cut and the surface quality of the two samples didn't allow to obtain SHG in other planes. In the  $xy$  plane the interaction is of the "eeo" (extraordinary-extraordinary-ordinary) type, so that the PM relation is:  $n_1^{xy}(\theta) = n_2^z$ , where  $\theta$  is the angle between the wave vector of the incident beam and the  $x$  axis,  $n_1$  and  $n_2$  are the indices of

refraction at the fundamental and second harmonic wavelength. The crystal is mounted on a goniometer, with the  $z$  axis along the vertical direction. The fundamental beam is horizontally polarized, whereas the second harmonic field generated is polarized along the  $z$  axis. The phase matching angle  $\theta$ , measured as function of  $\lambda_1$  for the two samples of S3MeMBANP is plotted in Figure 4.

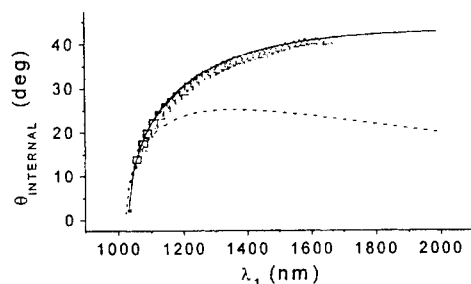


FIGURE 4 Phase matching internal angle versus the incident wavelength  $\lambda_1$  for SHG in the  $xy$  plane. The triangles and the squares are the experimental data taken from the first and the second sample respectively. The solid curve is calculated from our Sellmeier formula. The dashed curve is predicted by the Sellmeier set of Ref [4].

Note that all the angles quoted here are internal to the crystal. To convert the external angles to internal, we have used our Sellmeier expressions. The wide aperture of the crystals allowed us to take data up to large angles, measuring the SHG PM angles for almost the entire transmission range of the crystal. In both samples, the phase-matching situation is found to occur, at a given wavelength, at two angles that are not symmetric with respect to the face normal, as shown in Fig 2. From this asymmetry we deduced the tilt angle  $\delta$  between the face normal and the  $x$  axis: from our data we derive  $\delta=17.5^\circ$  and  $\delta=3^\circ$ , respectively for the first and the second sample. The agreement between the data taken from the two samples is very good, as can be seen in Figure 4. The larger tilt angle of the first sample allowed SHG PM for wavelengths up to 1650 nm, since for this sample the same internal PM angle  $\theta$ , relative to the  $x$  axis, corresponded to smaller angles relative to the surface normal. In the same figure we reported in solid line the PM curve predicted by using the

Sellmeier set given above. This shows a good fitting of the data and confirms our refractive-index measurements. For sake of comparison, the curve calculated from the Sellmeier set found in [4] is also shown in Figure 4. The improvement of the fitting given by our new Sellmeier set is quite evident.

By using our Sellmeier set, we are now able to calculate a complete phase-matching criticality curve: such a curve shows the dependence of the PM wavelength on angle for all the principal planes of the crystal. In Figure 5 we report the criticality curve predicted by our Sellmeier set. Note that, due to the symmetry of point group 222, in S3MeMBANP the only nonzero coefficients of the d-matrix are those where all three coordinate indices are different,  $d_{14}$ ,  $d_{25}$ ,  $d_{36}$ . As a consequence, the effective d coefficient for SHG ( $d_{\text{eff}}$ ) vanishes under angle-noncritical phase-matching conditions.  $d_{\text{eff}}$  vanishes also in the principal plane xz, since in this plane type-I PM is of the "ooe" (ordinary-ordinary-extraordinary) type.

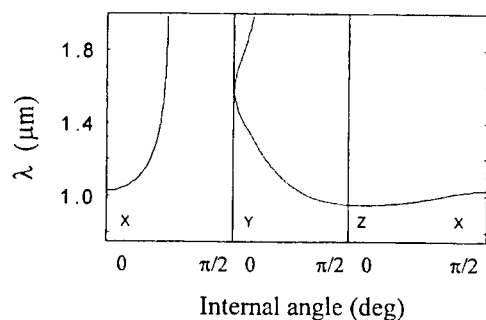


FIGURE 5 Phase matching criticality curves, as predicted by our Sellmeier set. The PM is "eo" on the xy and yz plane, "ooe" on the xz plane.

As a conclusion, we measured the refractive indices of the organic crystal S3MeMBANP for a wide range of wavelengths, covering the near-infrared region. From the measured data we derive a set of Sellmeier coefficients, whose validity extends up to 1600 nm. The accuracy of the set has been confirmed by a SHG experiment on the xy principal plane of the crystal. By using our Sellmeier set, we are able to draw a complete phase-matching criticality curve, showing the phase-matching properties

of S3MeMBANP for propagation on all the principal planes of the crystal.

#### Acknowledgements

We are grateful to E.E.A. Shepherd for the crystal preparation.

#### References

- [1] G.P. Banfi, P.K. Datta, V. Degiorgio, D. Fortusini, E.E.A. Shepherd, J.N. Sherwood, Chem. Phys. **245**, 345-357 (1999).
- [2] R.J. Twieg, K. Jain, Y.Y. Cheng, J.S. Crowley, A. Azema, Polym. Rep. **23**, 147 (1982).
- [3] R.T. Bailey, F.R. Cruickshank, S. Lochran, D. Pugh, J.N. Sherwood, P.J. Langley, J.D. Wallis, Bull. Mat. Sci. **22**, 421-430 (1999).
- [4] S. Lochran, R.T. Bailey, F.R. Cruickshank, D. Pugh, J.N. Sherwood, G.S. Simpson, J.D. Wallis, P.J. Langley, J Phys. Chem. A **102**, 8520-8525 (1998).
- [5] M.C Simon, P.A. Larocca, Appl. Opt. **34**, 709-715 (1995).

---

## **SESSION E: FUNDAMENTAL STUDIES**

## Modeling and Characterisation of Nonlinear Materials for Optical Limiting. Mononuclear and Binuclear Platinum Ethynyls

ANDERS ERIKSSON<sup>a</sup>, CESAR LOPES<sup>b</sup>, MIKAEL LINDGREN<sup>a,b</sup>,  
SÖREN SVENSSON<sup>b</sup>, TIM McKAY<sup>c</sup>, JULIANNE DAVY<sup>c</sup>

<sup>a</sup> Department of Physics and Measurement Technology, Linköping  
University, S-581 83 Linköping, Sweden;

<sup>b</sup> Defence Research Establishment, Department of Sensor Technology  
PO Box 1165, S-581 11 Linköping, Sweden

<sup>c</sup> Electronic Warfare Division, Defence Science and Technology  
Organisation, PO Box 1500 Salisbury South Australia 5108, Australia

Platinum ethynyls for optical limiting applications were synthesised and optically characterised. Both mononuclear and binuclear compounds were investigated. Optical limiting measurements have been performed in an f#5 system. A previously reported modeling tool relying on a Gaussian decomposition of the laser beam was used to model the experiments. This numerical tool, which allows for non-Gaussian laser beams and thick samples exhibiting both nonlinear refraction and absorption, was found to fit well with some of the optical limiting experiments.

**Keywords** Optical limiting, Platinum ethynyl

### INTRODUCTION

Three different platinum ethynyls were investigated for optical limiting purposes. Mononuclear platinum ethynyls have previously been shown to possess some interesting features, which include; acting over a large



range of pulse lengths, and showing evidence of being broadband optical limiters [1]. Both mononuclear and binuclear compounds with different ligands were synthesised in order to investigate the nonlinear effect, stability and solubility. The bis(diphenylphosphino)methane (dppm) complexes were prepared from  $[\text{PtCl}_2(\text{dppm})]$  and lithium ethynyls with THF / toluene as solvent [2].

Organophosphine ligands are rather labile and can easily be lost in contact with solvent. This can lead to decomposition of the compound, and, seems to occur for the platinum(II) ethynyl ( **I** ) in figure 1. In order to improve the stability, bis(diphenylphosphino)methane (dppm) was introduced ( **II** and **III** ).

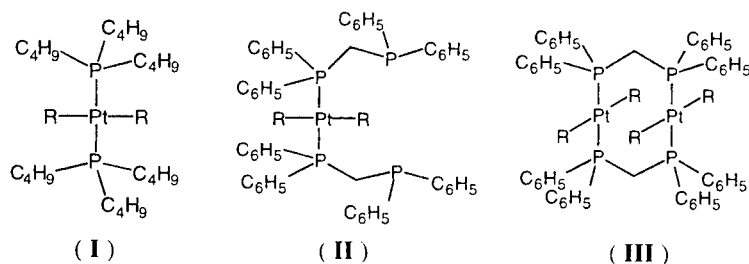


FIGURE 1. Mononuclear and binuclear platinum(II) ethynyls.

The two different ligands ( R ) shown in figure 2 were used.

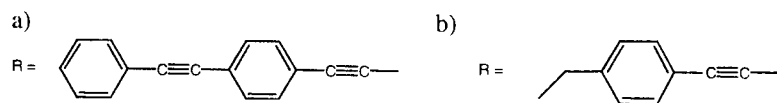


FIGURE 2. Ligands used in the platinum(II) ethynyls. a) was used in compound ( **I** ) and ( **II** ) while b) was used in ( **III** )

## EXPERIMENTS

The capability for protecting an optical sensor was investigated in test-beds with a top-hat laser beam in an f#5 geometry. The focus was centred to the middle of a 2 mm cell containing the nonlinear material. The sample was several Rayleigh lengths, and thus the irradiance much lower at the surface than at the focus. A frequency-doubled YAG operating at a wavelength of 532 nm giving a pulselength of 5 ns was used. The laser energy was varied from below  $\mu\text{J}$  to some 150-200  $\mu\text{J}$ . Transmission spectra of the 2 mm cells with the nonlinear materials were collected.

## RESULTS

Transmission spectra of the samples including the 2 mm cell are shown in figure 3. The linear transmission for the THF solutions of platinum(II) ethynyls were between 70 and 90 % at 532 nm. The results of the optical limiting experiments are shown in figure 4 and 5.

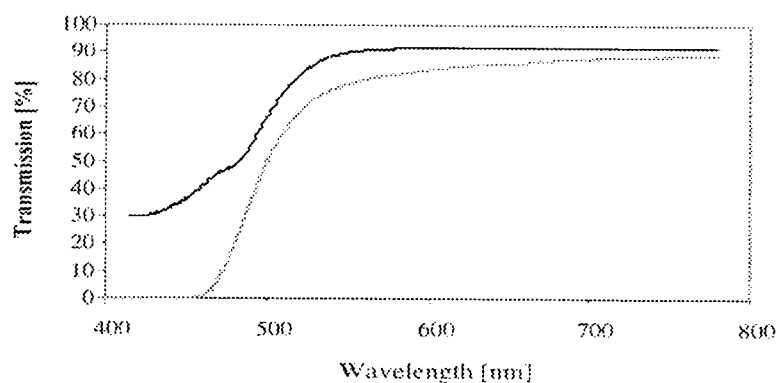


FIGURE 3. Transmission spectra of a 100 mM solution platinum(II) ethynyl (I) in THF (black), and of a 100 mM solution platinum(II) ethynyl (II) in THF (grey).

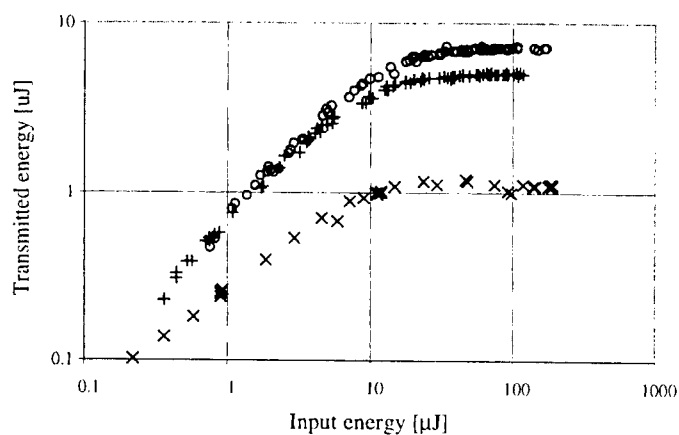


FIGURE 4. Optical limiting with THF solutions of platinum(II) ethynyl (I). The photopic transmission including the cells were 90%, corresponding to 0.05 M (o), and 87 %, corresponding to 0.1 M (+). A measurement on a sample with 70 % linear transmissions at 532 nm was also performed (x).

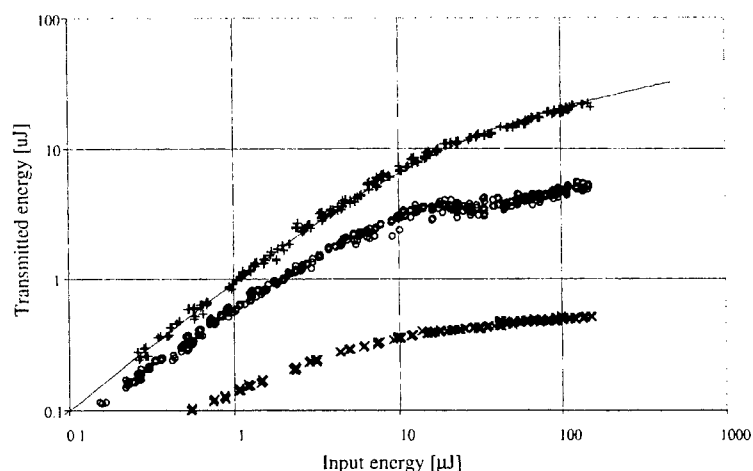


FIGURE 5. Optical limiting with a 0.1 M solution of platinum(II) ethynyl (**II**) in THF giving 73.5 % transmission at 532 nm (+), and 5 mM platinum(II) ethynyl (**III**) in THF giving 87 % transmission (o). The linear transmission for the sample with Silicon-Naphthalocyanine (SiNC) (x) was 40 % at 532 nm. The modeling tool gave values in good agreement with experimental values for compound (**III**)

A previously reported numerical modeling tool [3], for Z-scans with thick samples and nonlinear absorptive and refractive optical properties, was used to model the optical limiting measurements. Assuming a pure TPA (two-photon absorption) process with a two-photon crosssection  $\sigma = 208 \text{ cm}^4/\text{GW}$ , it is possible to get good agreement between the model and measurements on compound (**III**). However, the model does not fit well with data from compounds (**I**) and (**II**). This is probably due to a combination of different nonlinear processes occurring in the samples, such as two-photon absorption and reverse saturable absorption.

The capability of optical limiting was shown for several compounds. The platinum ethynyls gave promising results although they did not reach the same clamping level as SiNC. Compound (**I**) was found to

limit the energy more efficiently than a pure two-photon absorber. A great advantage of these compounds are that they are very transparent in the visible.

#### References

- [1] J. Staromlynska, T. J. McKay, J. A. Bolger and J. R. Davy, "Evidence for broadband optical limiting in a Pt:ethynyl compound," J. Opt. Soc. Am. **B15**, 1731-1736 (1998)
- [2] C. R. Langrick, D. M. McEvan, P. G. Pringle and B. L. Shaw, J. Chem. Soc., Dalton Trans. 2487 (1998)
- [3] A. Eriksson, M. Lindgren, S. Svensson, T. Bubner, T. McKay and J. Staromlynska "Numerical modeling of z-scans of thick nonlinear absorbers," SPIE **3472**, 144-150 (1998)

## Improved Photogeneration Efficiency of Charge-Transfer Complexes Between $C_{60}$ and Low Ionization Potential Arylamines

E. HENDRICKX, B. KIPPELEN, S. THAYUMANAVAN,<sup>a</sup> S. R. MARDER,<sup>a</sup> A. P. PERSOONS,<sup>b</sup> and N. PEYGHAMBARIAN  
Optical Sciences Center, The University of Arizona, Tucson, AZ  
85721, kippelen@u.arizona.edu

<sup>a</sup> Department of Chemistry, The University of Arizona, Tucson, AZ  
85721, smarder@u.arizona.edu

<sup>b</sup> Laboratory of Chemical and Biological Dynamics, University of  
Leuven, Celestijnenlaan 200 D, B-3001 Heverlee, Belgium.

Photogeneration of charge carriers was measured at 633 nm in a series of polymer composites based on polystyrene, doped with a triphenyldiamine derivative as hole transport molecule and  $C_{60}$  as sensitizer. Light absorption and generation of mobile carriers was achieved through the charge-transfer (CT) complex formed between the hole transport molecule and the sensitizer. We discuss the influence of the ionization potential of the hole-transport molecule on the photogeneration efficiency of the CT complex it forms with the sensitizer  $C_{60}$ . In one composite we have found a photogeneration efficiency of unity at an applied electric field of 55 V/ $\mu\text{m}$ .

**Keywords** Photogeneration efficiency;  $C_{60}$ ; photoconductivity; organic photoconductors

## INTRODUCTION

Photoconductive materials find applications in a variety of technologies, such as photodetectors and xerography.<sup>[1]</sup> The photogeneration efficiency  $\eta$ , that is the number of free carriers produced divided by the number of absorbed photons, is a basic parameter in the evaluation of photoconductor performance. We have prepared and tested new organic photoconductors based on the hole-transporting biarylamine derivatives shown in Figure 1. As a sensitizer, a small amount of  $C_{60}$  was added. The host polymer was polystyrene. The new polymers had photogeneration quantum efficiencies of 100 % at applied electric fields as low as 55 V/ $\mu\text{m}$ . We have also found a correlation between the ionization potential  $I_p$  of the donor molecule and the photogeneration quantum efficiency of the polymer.

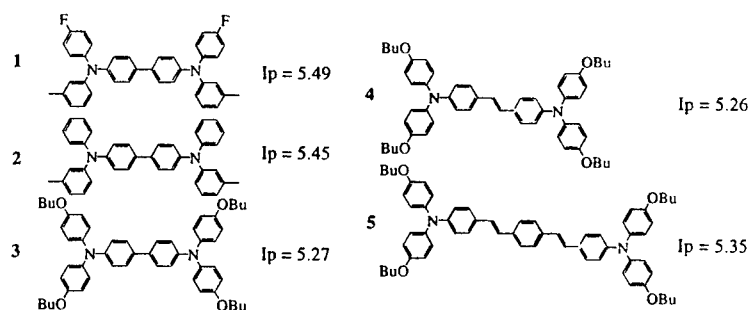


FIGURE 1 Structure and numbering schemes of the arylamines.

## EXPERIMENTAL

The compositions of the polymers, the ionization potential  $I_p$  of the arylamine and the extinction coefficient at 633 nm are shown in Table 1. The arylamine  $I_p$  was calculated from the redox potential as  $I_p$  (eV) =  $E^0 + 4.50$ .  $E^0$  was measured by cyclic voltammetry in  $\text{CH}_2\text{Cl}_2$  solution. As can be seen in Table 1, the arylamine  $I_p$  was varied over 0.25 eV by substitution with the electron withdrawing fluorine atoms and electron donating methoxy groups. The setup shown in Figure 2 was used for the measurement of the photoconductivity. From the voltage  $V_{ph}$  change measured over a resistor  $R$  upon illumination (633

nm, intensity  $I = 0.60 \text{ W/cm}^2$ ) of a biased sample (field  $E$ ) in series with the resistor, the photogeneration efficiency was calculated as:<sup>[2]</sup>

$$\eta(E) = \frac{V_{ph}}{eR} \frac{2\hbar\omega}{I\alpha Sd} \quad (1)$$

where  $S$  is the illuminated area,  $d$  the sample thickness ( $\cong 100 \text{ }\mu\text{m}$ ),  $e$  the elementary charge,  $\alpha$  the extinction coefficient, and  $\hbar\omega$  the photon energy.

Table 1: Sample identification scheme and composition, extinction coefficient at 633 nm, and ionization potential of the arylamine derivative or carbazole electron donor, respectively. For the numbering of the molecules 1-5 see Fig. 1. PS: Polystyrene. \* Average value of  $I_p$  as measured from cyclic voltammetry in solution and solid state ultraviolet photo-emission spectroscopy.

Sample	Composition (wt. %)	$\alpha_{633}$ ( $\text{cm}^{-1}$ )	donor $I_p$ (eV)
A	PS:1:C <sub>60</sub> (69:30:1)	30	5.49*
B1	PS:2:C <sub>60</sub> (87:12:1)	13	5.45*
B2	PS:2:C <sub>60</sub> (77:22:1)	17	5.45*
B3	PS:2:C <sub>60</sub> (69:30:1)	25	5.45*
B4	PS:2:C <sub>60</sub> (59:40:1)	36	5.45*
C	PS:3:C <sub>60</sub> (69:30:1)	20	5.27
D	PS:4:C <sub>60</sub> (69:30:1)	20	5.26
E	PS:5:C <sub>60</sub> (69:30:1)	32	5.35
F	PVK:ECZ:C <sub>60</sub> (59:40:1)	37	5.9

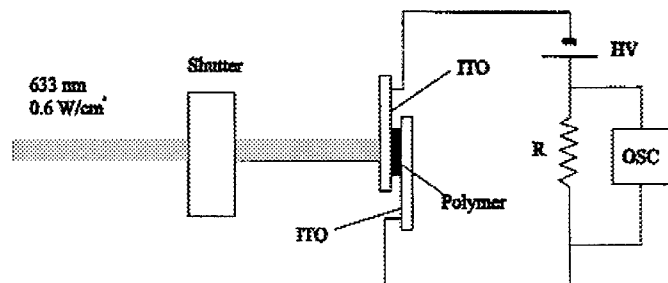


Figure 2: Setup for photoconductivity experiments, OSC = oscilloscope, HV = High Voltage Power Supply



## RESULTS AND DISCUSSION

A first observation is that all the arylamines in Figure 1 form charge-transfer (CT) complexes with the sensitizer  $C_{60}$ . The absorption spectra of samples A, B4, C, and a reference polystyrene/ $C_{60}$  1 wt. % (REF) polymer are shown in Figure 3. The increased absorptivity in the range from 500-900 nm is assigned to the complexation between  $C_{60}$  and the arylamine. As has been found in many studies on CT complexes,<sup>[3]</sup> a linear relationship between the arylamine donor  $I_p$  and the photon energy of the CT transition exists. The complexation bands of the complexes of  $C_{60}$  with arylamines 1, 2, 3, 4, and 5 peak at 610 nm, 630 nm, 790 nm, 790 nm and 730 nm, respectively.

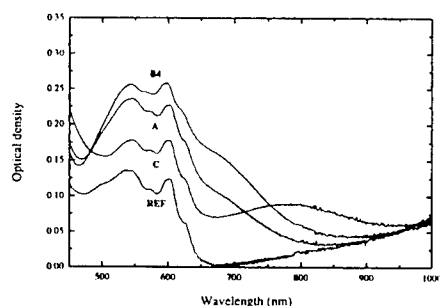


Figure 3: Absorption spectra of polymers A, B4, C and a reference polystyrene/ $C_{60}$  1 wt. % polymer.

The evolution of the photogeneration efficiency  $\eta$  as a function of applied field for polymers E, B3, A, and F are summarized in Figure 4. For the polymers with donors having a high  $I_p$ ,  $\eta$  keeps increasing with electric field up to 90 V/ $\mu\text{m}$ . For sample E it reaches a maximum value of unity at a field of 55 V/ $\mu\text{m}$ . For sample D  $\eta$  reached 61 % at an applied field of 70 V/ $\mu\text{m}$ . Figure 5 shows  $\eta$  of samples A, B3, C, D, E, F at a field of 55 V/ $\mu\text{m}$  as a function of the biarylamine  $I_p$ . These are among the highest efficiencies reported for organic polymers at 633 nm. We have also found an exponential increase of the photogeneration efficiency with arylamine number density in series B1-4.

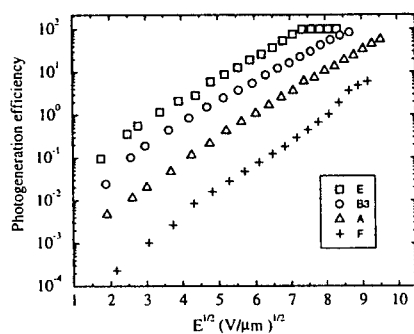


Figure 4: Photogeneration efficiency as a function of electric field

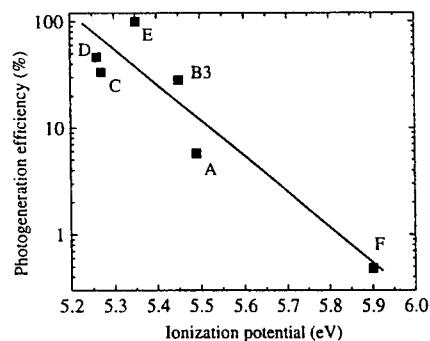


Figure 5: Photogeneration efficiency as a function of arylamine ionization potential.

These results can be rationalized in the framework of the geminate recombination model for photogeneration in organic polymers that is summarized in Figure 6. A larger photogeneration efficiency after optical excitation (step 1) can follow from a faster electron transfer from the donor molecule to the excited CT complex (step 2) or from a faster dissociation (step 3).

A lower donor  $I_p$  corresponds to a stronger electron donor, and hence to a larger enthalpy of complexation  $\Delta H_c$ . Following Marcus

theory for the rate of electron transfer,<sup>14</sup> a larger  $\Delta H_c$  will increase the rate of step 2. Thus a reduction of the donor  $I_p$  should lead to a higher photogeneration efficiency. Evidence that the mobility (step 3) is important is found in the electric-field dependence of the photogeneration efficiency. This parameter follows the typical Poole-Frenkel field dependence of the mobility  $\mu = \mu_0 \exp(a\sqrt{E})$ . The fact that samples **B**, **C**, **D**, and **E** all reach a photogeneration efficiency close to 100 % at high field, suggests that the limitation of the photogeneration efficiency at low fields is due to the mobility.<sup>15</sup>

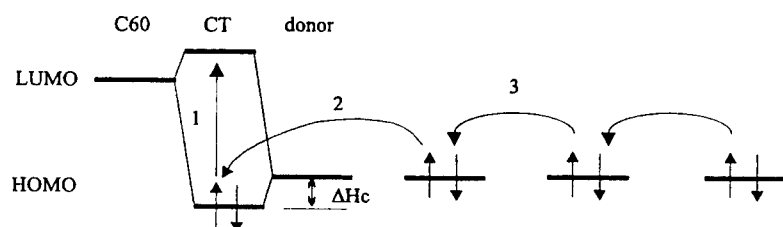


Figure 6: Steps leading to photogeneration of charges.

#### Acknowledgements

This work was supported by the Office of Naval Research (ONR) through the MURI Center (CAMP), by the Air Force Office of Scientific Research (AFOSR) and by the National Science Foundation (NSF). E. H. is a postdoctoral fellow of the Fund for Scientific Research-Flanders (Belgium).

#### References

- [1] P. M. Borsenberger and D. S. Weiss in Organic Photoreceptors for Xerography (Marcel Dekker, Inc. New York, 1993).
- [2] B. Kippelen, K. Meerholz, and N. Peyghambarian in Nonlinear Optics of Organic Molecules and Polymers, H. S. Nalwa and S. Miyata, Eds. (CRC, Boca Raton, 1997).
- [3] R. Foster in Organic Charge-Transfer Complexes (Academic Press, London and New York, 1969).
- [4] R. A. Marcus Annu. Rev. Phys. Chem. **15**, 155 (1964).
- [5] M. Umeda, T. Shimada, T. Aruga, T. Niimi, and M. Sasaki J. Phys. Chem. **97**, 8531 (1993).

## Control of the First Hyperpolarizability of Functionalized Mesosstructures through Cation Binding

STEPHAN HOUBRECHTS\*, TATSUO WADA, HIROYUKI  
SASABE

*Frontier Research Program, The Institute of Physical and Chemical  
Research (RIKEN), 2-1 Hirosawa, Wako, Saitama 351-01, Japan*

*\* Laboratory of Chemical and Biological Dynamics, Catholic University  
of Leuven, Belgium*

YUJI KUBO

*Department of Applied Chemistry, Faculty of Engineering, Saitama  
University, 255 Shimo-ohkubo, Urawa, Saitama 338-8570, Japan*

The effect of cation complexation on the nonlinear optical properties of functionalized ionophores has been studied by means of hyper-Rayleigh scattering. Cation complexation is shown an excellent route to tune the molecular hyperpolarizability.

**Keywords** Charge transfer, ionophores, donor-acceptor systems, nonlinear optics

## INTRODUCTION

For years, the photophysics and photochemistry of fluorophores and chromophores linked to cyclic structures as crown ethers or calixarenes have been an area of growing interest. Particularly those compounds where insertion of a cation into the ligand cavity substantially alters the optical properties have been the subject of profound investigations.[1, 2] Herein, one can distinguish two main groups (Figure 1): compounds of type (I) that interact with the ion through the acceptor site of the chromophore and structures of type (II) that interact through the donor

site. For the first group, complexation will enhance the internal charge transfer (ICT) and thus induces a bathochromic shift. Type (II) interactions on the other hand reduce the ICT, which results in a hypsochromic shift of the charge transfer band.

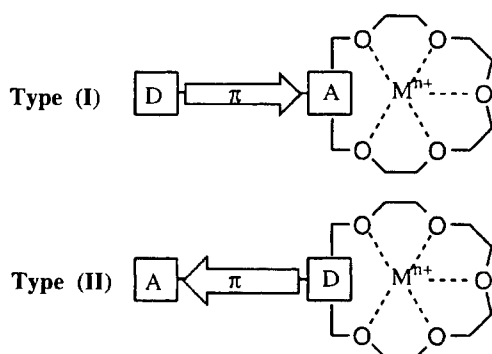


FIGURE 1 Types of complexation between chromoionophores and cations.

In like manner, elaborate studies have been performed on the relationship between the molecular structure and the nonlinear optical (NLO) response for organic and organometallic compounds.[3] Moreover, the molecular hyperpolarizability has been shown to depend on the CT transition between donor and acceptor for dipolar structures.[4] As such, cation complexation with donor or acceptor is expected to alter the molecular hyperpolarizability.

In this regard, we have studied the second-order nonlinear optical properties of NLO-functionalized mesostructures (Figure 2) and determined the changes in the first hyperpolarizability upon binding of alkaline and alkaline-earth ions. The results reveal that cation complexation is an excellent tool to modify the NLO response “after synthesis”, and a potential alternative to photochemical and electrochemical tuning.[5-7]

## RESULTS AND DISCUSSION

The experimental results are collected in Table 1. Both structures show an intense absorption in the visible, which is attributed to a donor (D)

to acceptor (A) ICT. However, interaction with the potassium cation  $K^+$  has distinct consequences. Compound (**a**) displays a clear red shift (40 nm) of its ICT accompanied with an increase in oscillator strength, whereas for compound (**b**) an antiauxochromic (hypsochromic and hypochromic) shift is found. These observations are in accordance with a type I (**a**) and a type II (**b**) interaction respectively.

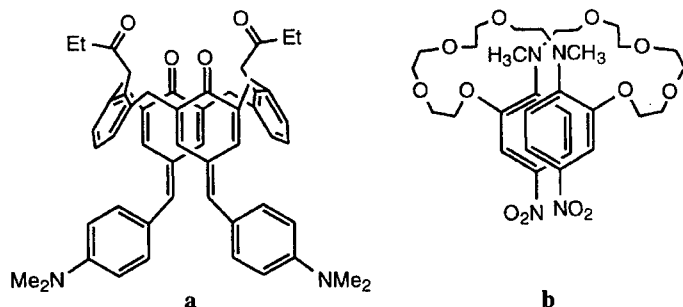


FIGURE 2: NLO functionalized ionophores of type I (**a**) and type II (**b**).

In contrast to the calixarene (**a**), the crown ether (**b**) displays a well-defined isosbestic point upon a gradual addition of cation, suggesting a 1:1 stoichiometry for the crown-ion complex formed. This will allow a straightforward assessment of the stability constant.

The molecular hyperpolarizability of ionophores and complexes are determined by hyper-Rayleigh scattering (HRS).<sup>[8]</sup> As expected for a type I interaction, the hyperpolarizability of the calixarene (**a**) shows an increase of 70% in the presence of an excess amount of  $K^+$ . This enhancement of the nonlinear response is also apparent in the evolution of the HRS-signal as a function of the cation concentration (Figure 3).

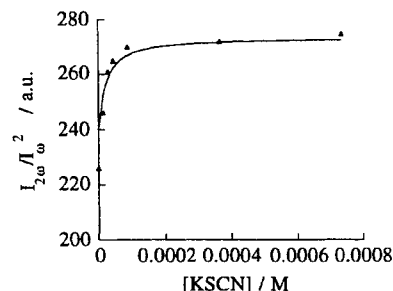


FIGURE 3: HRS signal of (**a**) vs. the cation concentration. The solid line represents the best fit with equation 1.

TABLE I. Experimental results for the crown ether.

	$\Delta\lambda^a$ (nm)	$\log K_A^b$	$\log K_{HRS}$	$\beta_{\text{excess}}^c$ ( $10^{-30}$ esu)	$\beta_{\text{titr}}^d$ ( $10^{-30}$ esu)
Calixarene (a)				170	
+ $K^+$	40	/	/	309	
Crown (b)				38	
+ $Na^+$	-12	$1.20 \pm 0.02$	$1.6 \pm 0.1$	32	28
+ $K^+$	-14	$2.23 \pm 0.02$	$2.5 \pm 0.1$	27	28
+ $Ba^{2+}$	-13	$6 \pm 3^e$	$3 \pm 2^e$	24	26

<sup>a</sup>  $\lambda_{\text{max}}$  of (a) is 602 nm, and of (b) 406 nm. <sup>b</sup> Stability constant K obtained by absorption (A) measurements. <sup>c</sup> Hyperpolarizability obtained using an excess of cation. <sup>d</sup> Hyperpolarizability obtained by titration. <sup>e</sup> Relative error on  $\beta$ : 5%, except for  $Ba^{2+}$ : 10%. <sup>f</sup> A slight increase of the signal at high concentrations prohibits a more accurate determination of K. This increment most likely originates from a weak type (I) interaction.

However, the absence of a 1:1 stoichiometry prohibited a reliable determination of the stability constant K.

In contrast, the 1:1 stoichiometry of the crown-ion complex formed (Figure 4) allows for a straightforward determination of the stability constant K; and this in combination with the hyperpolarizability (equation 1.). The stability constants obtained by HRS and absorption spectrometry respectively are in excellent agreement. Furthermore both, addition of an excess amount of cation and the titration experiment (HRS response in function of the added amount of cation), reveal a reduction of 25% (Figure 5). As the electron donor strength of the amine and/or ether function is diminished by direct interaction of the cation with the corresponding lone pairs, the lower nonlinear response

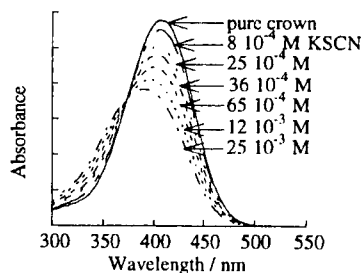


FIGURE 4: Absorption spectra of (b) before and after addition of KSCN.

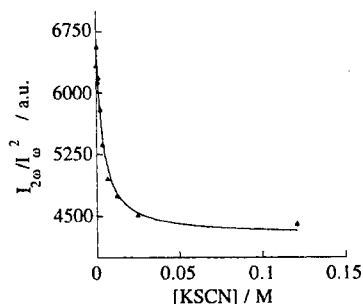


FIGURE 5: HRS signal of (b) vs. the cation concentration. The solid line represents the best fit with equation 1.

was expected for this type II system.

Similar results were obtained for the sodium ( $\text{Na}^+$ ) and barium ( $\text{Ba}^{2+}$ ) complexes of (b). Moreover, the interaction with  $\text{Ba}^{2+}$  leads to the largest reduction of the hyperpolarizability. As the bivalent ion is more efficient in attenuating the electron donor character of the crown nitrogen, this result is not unexpected. However, notwithstanding that both diameter and charge of alkaline(earth) ions are known to act upon complexation with ionophores, the hyperpolarizability here seems to be influenced by their charge only. In contrast, the stability constant clearly depends on both charge and diameter of the cation, indicating that the match between ligand topology and cation characteristics determines the ion affinity.

In conclusion, we have demonstrated that the NLO response of functionalized ionophores can be tuned by cation complexation, an event that also can be used to study the interaction between metal ions and ligands. In this regard, HRS is shown to be an additional technique to determine the stability constants.

## EXPERIMENTAL

The quadratic hyperpolarizabilities are determined by HRS using *p*-nitroaniline as an external reference.[9] Details on the experimental procedure have been discussed previously.[8]

For complexes with a 1:1 symmetry, both the concentration of free ionophore and complex can be written as a function of the initial



concentration of cation. Analogous to the relations used in spectrometric studies of ionophores,<sup>[10]</sup> the HRS equation then becomes:

$$\left( \frac{I_{2\omega}}{I_{\omega}^2} \right) = g[S]\beta_S^2 + g[C]_0\beta_C^2 + g(\beta_{MC}^2 - \beta_C^2) \frac{a - \sqrt{a^2 - 4[C]_0[M]_0}}{2} \quad (1)$$

With

$$a = [C]_0 + [M]_0 + 1/K \quad (2)$$

#### ACKNOWLEDGEMENTS

This work was supported by the Frontier Research Program. SH is a postdoctoral researcher of the F.W.O.-Flanders.

#### REFERENCES

- 1 H. G. Löhr and F. Vögtle, *Acc. Chem. Res.* **18**, 65 (1985).
- 2 T. Hayashita and M. Takagi, in *Molecular Recognition: Receptors for Cationic Guests*, edited by J. L. Atwood, J. E. D. Davies, D. D. MacNicol, F. Vögtle and G. W. Gokel ( Elsevier Science Ltd., Oxford, 1996)
- 3 T. Verbiest, S. Houbrechts, M. Kauranen, K. Clays and A. Persoons, *J. Mater. Chem.* **7**, 2175 (1997).
- 4 J. L. Oudar and D. S. Chemla, *J. Chem. Phys.* **66**, 2664 (1977).
- 5 H. Sakaguchi, T. Nagamura and T. Matsuo, *Jpn. J. Appl. Phys.* **30**, L377 (1991).
- 6 K. Alagesan, P. C. Ray, P. K. Das and A. G. Samuelson, *Current Science* **70**, 69 (1996).
- 7 B. J. Coe, S. Houbrechts, I. Asselberghs and A. Persoons, *Angew. Chem.* **38**, 366 (1999).
- 8 S. Houbrechts, K. Clays, A. Persoons, V. Cadierno, M. Pilar Gamasa, J. Gimeno, I. R. Whittall and M. G. Humphrey, *Proc. SPIE-Int. Soc. Opt. Eng.* **2852**, 98 (1996).
- 9 M. Stähelin, D. M. Burland and J. E. Rice, *Chem. Phys. Lett.* **191**, 245 (1992).
- 10 J. Bourson, J. Pouget and B. Valeur, *J. Phys. Chem.* **97**, 4552 (1993).

## **Ellipsometric Polarization Contour Measurement for Anisotropy in Organic Materials**

MINSOO JOO<sup>1</sup>, HYUNAE CHUN<sup>2</sup>, and NAKJOONG KIM\*<sup>2</sup>

<sup>1</sup> Center for Organic Photorefractive Materials, KIST,  
P.O. Box 131, Cheong-ryang, Seoul, 130-650, South Korea;

<sup>2</sup> Department of Chemistry, Hanyang University, Seoul 133-791, Korea

\*E-mail: kimnj@email.hanyang.ac.kr

**ABSTRACT** Ellipsometric Polarization Contour Measurement (EPCM), which consists of conventional ellipsometric measurement system with rotational mode of an analyzer, was applied to study about the anisotropic properties of organic materials. EPCM technique was first tested by optical components such as wave plates and then applied to the organic photorefractive materials, PDCST20 and PDCST30, to study about the poling process with applied electric field. Comparing to the conventional ellipsometric measurement, EPCM makes the anisotropic properties of the materials more directly characterized and gives additional information about the optic axis of the materials.

**KEYWORDS** photorefractive; anisotropy; polarization; electro-optic.

## INTRODUCTION

Orientation in polymers is of great technical and theoretical importance and therefore, the measurement of orientation in polymers provides valuable information to understand the structures and properties of polymers. The information about molecular orientation in polymeric samples is to be reflected on the polarization state of light that travels through the samples. Ellipsometric technique is widely used for the measurement of polarization state and the anisotropic properties of materials are analyzed in terms of optical birefringence. Ellipsometric Polarization Contour Measurement (EPCM), which consists of conventional ellipsometric measurement system with rotational mode of an analyzer, can directly measure the polarization characteristics of light passing through samples. EPCM gives not only the information about the polarization state of light but other useful information such as the optic axis of the samples [1].

## THEORY AND EXPERIMENTAL

By adopting rotational mode of an analyzer in conventional ellipsometric measurement system, the anisotropic properties of materials can be directly characterized. As the light propagates through materials, the polarization ellipse of the light changes and the change of the polarization state can be described by the Jones matrix as Eq.(1) [2]:

$$E_{out} = M_A M_S E_{in} \quad (1)$$

where  $E_{in}$ ,  $M_S$ , and  $M_A$  are the Jones vector for the input beam, the Jones matrices for a sample, and for a rotating analyzer, respectively. If input beam is right circularly polarized (RCP), then output beam intensity can be described by Eq.(2).

$$I_{RCP} = \frac{I_o}{2} \{1 + \sin \Delta\phi \sin 2(\theta - 2\alpha)\} \quad (2)$$

where  $I_o$ ,  $\theta$ , and  $\alpha$  are the input beam intensity, the rotation angle of an analyzer, and the tilt angle of the sample around the ray, respectively.  $\Delta\phi$  is the phase difference between two polarization components after the transmitted intensity passes through the sample. Therefore, if light passing through a sample is scanned by a rotating analyzer, then the polarization state of light can be determined and the information about the optical state of a sample can be obtained from Eq.(2).

The intensities of light passing through a sample at various rotating angles of an analyzer are detected and the data collected as a function of analyzer angles were fitted by Eq.(2) according to the input beam polarization state. EPCM with LHP input beam was first tested by optical components such as tilted wave plates and then applied to the organic photorefractive materials, PDCST20 and PDCST30, with RCP input beam. PDCST20 consists of 20 wt% of 4-piperidino-benzylidene-malononitrile (PDCST), 79 wt% of polysiloxane with pendant carbazole, and 1 wt% of TNF. PDCST30 consists of 30 wt% of PDCST, 69 wt% of carbazole-substituted polysiloxane, and 1wt% of TNF.

## RESULTS AND DISCUSSION

The validity of Eq.(2) was confirmed by the experiment with a tilted half-wave plate. The polarization contour diagram calculated from simulation with Eq.(2) is given in Fig.1. The lines with symbols in Fig.1 are for the cases of no tilt with various phase differences and the solid line is for the case of 45° tilt with 45° phase difference. The tilt

effect is obvious in the EPCM diagram. The experimental data for PDCST30 obtained from EPCM are shown in Fig.2

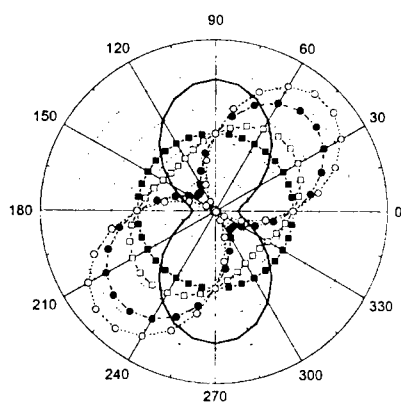


FIGURE 1 EPCM diagram for the simulation results from Eq.(2). Filled-squares are for  $0^\circ$ , open-squares for  $15^\circ$ , filled-circles for  $45^\circ$ , and open-circles for  $90^\circ$  and the solid line is for the case of  $45^\circ$  tilt with  $45^\circ$  phase difference.

The fitting results for PDCST30 with Eq.(2) are shown in Fig.3 by lines; solid line for  $0 \text{ V}/\mu\text{m}$ , dash for  $10 \text{ V}/\mu\text{m}$ , dash-dot for  $20 \text{ V}/\mu\text{m}$ , dash-dot-dot for  $30 \text{ V}/\mu\text{m}$ , and short-dash for  $40 \text{ V}/\mu\text{m}$ . No tilting of the optic axis is observed in both PDCST20 and PDCST30, as applied voltage increases. Phase differences of light passing through the organic samples, PDCST20 and PDCST30, due to the electric field are given in Fig.4 as a function of applied electric field.

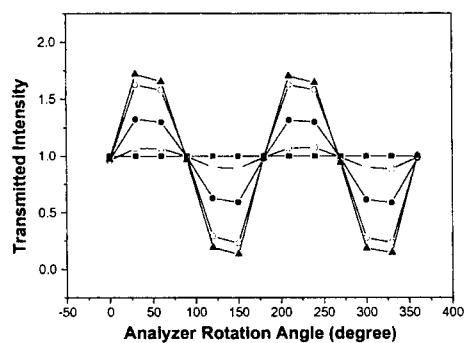


FIGURE 2 EPCM experimental data for PDCST30. Filled-squares are for  $0\text{V}/\mu\text{m}$ , open-squares for  $10\text{V}/\mu\text{m}$ , filled-circles for  $20\text{V}/\mu\text{m}$ , open-circles for  $30\text{V}/\mu\text{m}$ , and filled-triangles for  $40\text{V}/\mu\text{m}$ .

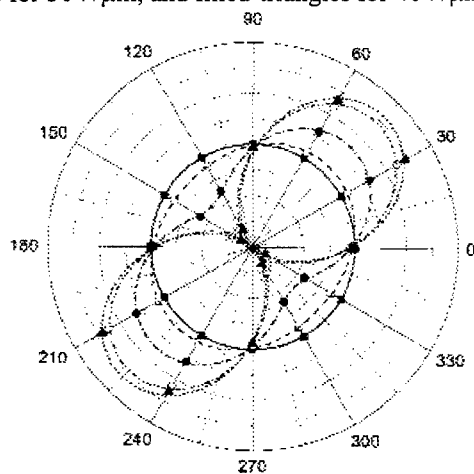


FIGURE 3 Experimental data for PDCST30 obtained from EPCM and fitting results. Filled-squares are for  $0\text{V}/\mu\text{m}$ , open-squares for  $10\text{V}/\mu\text{m}$ , filled-circles for  $20\text{V}/\mu\text{m}$ , open-circles for  $30\text{V}/\mu\text{m}$ , and filled-triangles for  $40\text{V}/\mu\text{m}$ . Solid line is for  $0\text{ V}/\mu\text{m}$ , dash for  $10\text{V}/\mu\text{m}$ , dash-dot for  $20\text{V}/\mu\text{m}$ , dash-dot-dot for  $30\text{V}/\mu\text{m}$ , and short-dash for  $40\text{V}/\mu\text{m}$ .

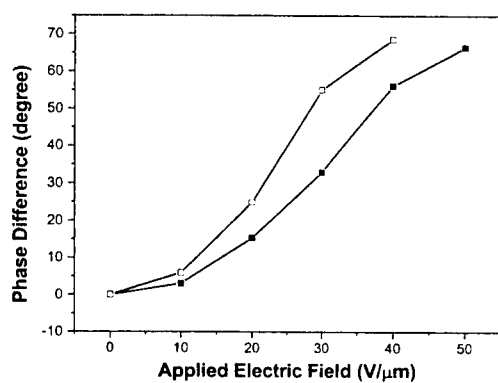


FIGURE 4 Phase differences for PDCST20 (filled squares) and for PDCST30 (open squares) obtained from EPCM.

#### ACKNOWLEDGEMENTS

This work is support by Creative Research Initiatives.

#### REFERENCES

1. M. Joo and N. Kim, submitted to Appl. Phys. Lett.
2. D. Clarke and J. F. Grainger, Polarized Light and Optical measurement, Pergamon Press (1971)

## Second Order Nonlinear Optical Response at the Two-Photon Resonance in a Two-Dimensional NLO Molecule

GUILIA MESHULAM<sup>a</sup>, PNINA SHAIER<sup>a</sup>, GARRY BERKOVIC<sup>a</sup>,  
AMOS BEN-ASULY<sup>b</sup>, ROYI MAZOR<sup>b</sup>, LEV SHAPIRO<sup>b</sup>,  
VLADIMIR KHODORKOVSKY<sup>b</sup> and ZVI KOTLER<sup>a</sup>

<sup>a</sup>Photonic Materials Group, Soreq NRC, Yavne 81800, Israel

<sup>b</sup>Department of Chemistry, Ben-Gurion University of the Negev,  
Beer-Sheva 84105, Israel

Rod-shaped organic nonlinear optical molecules are generally described as one-dimensional molecules with a single  $\beta$  component. However, analogous molecules having a carbazole group as the electron donor, exhibit special two-dimensional second harmonic behavior due to the presence of two  $\beta$  components, a positive  $\beta_{zzz}$  and a negative  $\beta_{zxz}$ . Those components arise from different transitions within the molecule. The effective  $\beta$  of these molecules, measured using either EFISH or the thin film technique in the off-resonance regime, is very small since the two components cancel each other. However, the same measurement in the two-photon resonance regime yields a very strong amplitude enhancement of  $\beta$  which is fitted well by a simplified three-level model.

**Keywords** organic NLO molecule; two-photon resonance

### INTRODUCTION

Nonlinear optical (NLO) properties of rod shaped “one-dimensional”  $\pi$ -conjugated organic charge-transfer molecules have attracted considerable interest since their study gives insight into the inter- and intra- molecular origins of nonlinear phenomena, and assists in the



development of new materials and devices. The second-order nonlinearity of these molecules is dominated by a single  $\beta_{zzz}$  tensor component which can be described satisfactorily by the 2-level model<sup>[1]</sup>.

We have shown in previous work that different nonlinear behavior can be induced when the donor in a one-dimensional charge transfer molecule is changed from an amine to a carbazole group<sup>[2,3]</sup>. We have studied a large number of typical one-dimensional push-pull molecules, having indandione as the acceptor group and amines as the donor group and compared them with similar molecules having carbazole in the donor site. From quantum chemical (QC) calculations, electric field induced second harmonic (EFISH) and Hyper-Rayleigh scattering (HRS), we showed that two  $\beta$  components are developed in the carbazole containing molecules, which are therefore "two-dimensional" NLO molecules. One component, which is along the long axis of the molecule produces a positive  $\beta_{zzz}$ , while the carbazole group induces an additional off-diagonal negative  $\beta_{zxx}$  contribution. Those two  $\beta$  components develop as a result of two closely lying, overlapping excited states, which contribute to  $\beta$  with opposite signs. In the off-resonance regime, at low frequency, the EFISH signal is negligible, since the two  $\beta$  contributions with opposite signs add<sup>[4]</sup>, and largely cancel each other.

In this study we report the  $\beta$  behavior of a two-dimensional molecule in the two-photon resonance regime, where  $2\omega$  coincides with the molecular absorption. In a previous study, we have described the measurement and analysis of the hyperpolarizability in the two-photon resonance regime<sup>[5]</sup> for a one-dimensional molecule with an amine donor. The frequency dependence of  $\beta$  was analyzed according to the two-level model, which is suitable for a one-dimensional molecule. The dispersion formula for  $\beta$  (relative to its zero frequency value  $\beta_0$ ) is derived from the sum over states, perturbation theory approach to hyperpolarizability given by Orr and Ward<sup>[6]</sup> which is simplified for the 2-level model to a single term given by equation (1).

$$\beta = \frac{\beta_0 \omega_0^2 (\omega_0 - i\gamma)^2}{[(\omega_0 - i\gamma)^2 - \omega^2] \cdot [(\omega_0 - i\gamma)^2 - 4\omega^2]} \quad (1)$$

Equation (1) assumes homogeneous broadening ( $\gamma$ ) of the two-level molecular absorption peak ( $\omega_0$ ), but is easily extended to

include inhomogeneous broadening of the absorption peak by integration of a Gaussian distribution of homogeneous peaks<sup>[5,7]</sup>.

For the two-dimensional carbazole-containing molecules with two  $\beta$  components<sup>[2]</sup> and two important (overlapping) excited states we must therefore use a 3-level Orr and Ward<sup>[6]</sup> formula. Second harmonic generation (SHG) by a 2-D molecule in an aligned medium, such as poled polymer, depends on the vector component of  $\beta$  along the dipole axis, given by summation of the two components in equation (2a)<sup>[4,8]</sup>. We calculate this using a simplified 3-level Orr and Ward formula, which can be characterized as a "double two-level" model, given by equation (2b)

$$\beta_z = \beta_{zzz} + \beta_{zxx} \quad (2a)$$

$$\beta_z = \frac{\beta_{10} \omega_{10}^2 (\omega_{10} - i\gamma)^2}{[(\omega_{10} - i\gamma)^2 - \omega^2][(\omega_{10} - i\gamma)^2 - 4\omega^2]} + \frac{\beta_{20} \omega_{20}^2 (\omega_{20} - i\gamma)^2}{[(\omega_{20} - i\gamma)^2 - \omega^2][(\omega_{20} - i\gamma)^2 - 4\omega^2]} \quad (2b)$$

where  $\beta_{10}$  and  $\beta_{20}$  are the zero frequency first hyperpolarizabilities of the two components and  $\omega_{10}$  and  $\omega_{20}$  are the frequencies of the two excited states. As before, inhomogeneous broadening of the peaks can be included by Gaussian convolution.

## MATERIALS AND METHODS

### Material

The molecule investigated, denoted IDS-Cab, is illustrated in Figure 1. A thin (600 Å) film of this molecule in PMMA was formed by spin coating, and then corona poled. The SHG measurements were performed immediately after the completion of the poling.

### Experimental setup

The laser system is based on a commercial (Continuum Surelite-II) Q-switched Nd:YAG laser ( $\lambda=1.064\mu\text{m}$ , 10Hz, 7nsec, 550mJ), frequency doubling, and a BBO crystal as an OPO tunable light source. The doubled Nd:YAG beam (200mJ energy, 3.5mm diameter) pumps the OPO, and by changing the angle between the laser beam and the crystal surface the output wavelength is continuously tunable from 850nm to 960nm. An additional source is provided by a Raman cell

(CH<sub>4</sub> at 40 atm.) used to shift the Nd:YAG fundamental beam to 1.54  $\mu\text{m}$ .

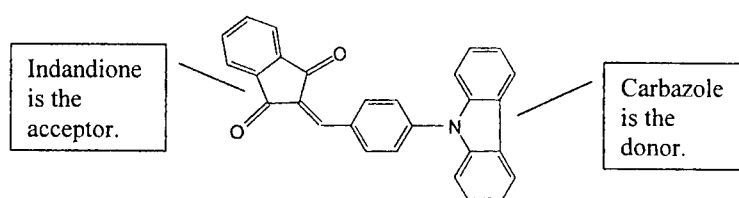


FIGURE 1 Two-dimensional molecule, IDS-Cab, incorporating the electron-accepting indandione group, and carbazole as the donor.

The thin poled polymer film is placed at 60° to the laser beam and the SHG signal is measured, after spectral filtering, by a photomultiplier. Since the experiment is performed in the two-photon resonance regime, an absorption correction is made for the attenuation of the poled polymer signal at each specific wavelength<sup>[9]</sup>. A quartz plate was used as a reference, placed at the same location and scanned by a rotation stage. An identically poled thin film of pure PMMA was also measured and its susceptibility was negligible compared to the poled IDS-Cab containing film, except for the 1.54  $\mu\text{m}$  measurement. In this case the polymer susceptibility was subtracted from that measured for the film. Comparison of the SHG signals of the thin film and the quartz, taking into account the frequency dispersion of the coherence length, and  $\chi^{(2)}$  of the quartz according to Miller's rule<sup>[10]</sup>, yields the relative  $\beta_z$  values of the IDS-Cab molecule at the various wavelengths.

## RESULTS AND DISCUSSION

The second harmonic signal of the poled polymer containing the two-dimensional molecule IDS-Cab was measured in the two-photon resonance regime (850–960 nm) and off-resonance (1.064 and 1.54  $\mu\text{m}$ ) and relative molecular  $\beta_z$  values extracted. Results are plotted in Figure 2 relative to  $\beta_0$ , which is taken to be 1.7 times smaller than the value measured at the lowest experimental energy (1.54  $\mu\text{m}$ ) in accordance with equation (2b).

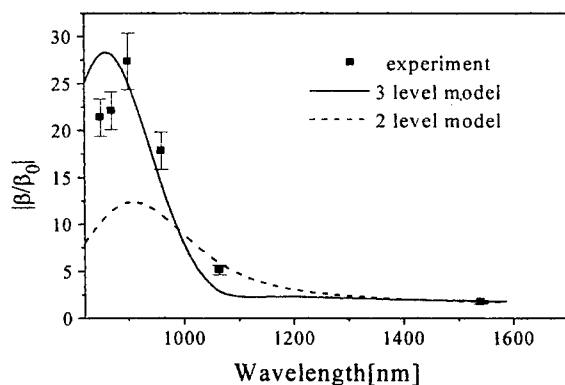


FIGURE 2 Frequency dependence of  $|\beta_z|$  for the two-dimensional molecule IDS-Cab in the two-photon resonance regime, measured in a poled PMMA film. Results are compared to predictions of the 2-level and the simplified 3-level models of equations (1) and (2b) with inhomogeneous broadening.

Figure 2 also shows that a good fit to all the experimental results is achieved by using our 3-level model, equation (2b). The parameters used to produce this fit were:  $\beta_{10} = 48$ ,  $\beta_{20} = -80$  (in units of  $10^{-30}$  esu),  $\omega_{10} = 21830 \text{ cm}^{-1}$ ,  $\omega_{20} = 23255 \text{ cm}^{-1}$ , and a Gaussian half width of  $1600 \text{ cm}^{-1}$ . All these parameters are taken<sup>[2]</sup> from the absorption spectrum of the molecule and the low frequency EFISH and HRS measurements. Thus there are no free parameters in the calculation, and the only fitting done was to adjust the parameters within their experimental uncertainty.

This 3-level model (double 2-level model) gives a stronger resonance enhancement for the amplitude of  $\beta$  than is possible from the normal 2-level model. As given by equation (1), the 2-level model predicts a maximum enhancement of only 12, while our 3-level model predicts an enhancement factor of 28. The 3-level model prediction shows very good agreement with the experimental result of approximately 27.

Another interesting consequence of the 3-level model given by equation (2b) is that at the two-photon resonance regime the second order susceptibility can become real since the imaginary parts from the

two terms cancel each other. EFISH results that show this behavior will be published elsewhere.

## SUMMARY

We have shown that the two-dimensional IDS-Cab molecule, having carbazole in its donor site, has a unique resonance behavior of  $\beta$ . The  $\beta$  amplitude shows a strong resonance enhancement that is reproduced very well by the predictions of our simple 3-level model created by a "double two level" model.

## ACKNOWLEDGMENTS

The authors thank A. Englander and I. Paiss for assistance in setting up the OPO, and the Israeli Ministry of Science for support of this research.

## REFERENCES

- [1] J.L. Oudar, *J. Chem. Phys.* **67**, 2664 (1977).
- [2] G. Meshulam, G. Berkovic, Z. Kotler, A. Ben-Asuly, R. Mazor, L. Shapiro and V. Khodorkovsky, *Proc. SPIE* **3796**, 279 (1999).
- [3] G. Meshulam, G. Berkovic, Z. Kotler, A. Ben-Asuly, R. Mazor, L. Shapiro and V. Khodorkovsky, *Synthetic Metals* in press.
- [4] C. Boutton, K. Clays, A. Persoons, T. Wada, H. Sasabe, *Chem. Phys. Lett.* **289**, 101, (1998).
- [5] G. Berkovic, G. Meshulam and Z. Kotler, *J. Chem. Phys.* **112**, 3997 (2000).
- [6] B.J. Orr and J. F. Ward, *J. Mol. Phys.* **20**, 513 (1971).
- [7] A. Otomo, G.I. Stegeman, M.C. Flipse, M.B.J. Diemeer, W.H.G. Horsthuis and G.R. Möhlmann, *J. Opt. Soc. Am. B.* **15**, 759 (1998).
- [8] H. S. Nalwa and S. Miyata, editors, *Nonlinear Optics of Organic Molecules and Polymers* (CRC Press, Boca Raton, 1997) Chap. 3.
- [9] M.A. Mortazavi, A. Knoesen, S.T. Kowel, B.G. Higgins and A. Dienes, *J. Opt. Soc. Amer. B* **6**, 733 (1989).
- [10] R.C. Miller, *Appl. Phys. Lett.* **5**, 17 (1964).

## Large Two-Photon Absorption In Tetra and Penta Phenyl Compounds

YANNICK MOREL <sup>a</sup>, CHANTAL ANDRAUD <sup>b</sup>, PATRICE L.  
BALDECK <sup>a</sup>

<sup>a</sup> Laboratoire de Spectrométrie Physique, Université Joseph Fourier,  
CNRS (UMR 5588), B.P. 87, 38402 St Martin d'Hères, France; <sup>b</sup> Ecole  
Normale Supérieure de Lyon, Stéréochimie et Interactions  
Moléculaires, UMR CNRS n° 117, 69364 Lyon cedex 07, France

We have studied the two-photon absorption (TPA) spectra of two polyphenyl compounds. At resonance, the TPA amplitude is enhanced when increasing the number of phenyl rings. This improvement is in agreement with semi-empirical quantum chemistry calculations that predict enhancement of TPA when changing the oligomer size.

**Keywords** two-photon absorption ; nonlinear optics ; organic materials.

### INTRODUCTION

Organic materials with large two-photon absorption present considerable interest in optoelectronics. Applications such as optical limiters, two-photon microscopy, 3D data storage are demanding for materials with strong two-photon cross-sections<sup>[1]</sup>.

Concerning the optimization of TPA in organic molecules, strategies based on the influence of the charge transfer conjugation system and of the substituents have been developed<sup>[2-4]</sup>. In this work, we have studied the spectral dependence of the two-photon cross-section ( $\sigma_{\text{TPA}}$ ) of a tetraphenyl and a pentaphenyl derivative. The results are analyzed with

a three level model and compared with a theoretical one based on quantum chemistry calculations.

## EXPERIMENTAL

Figure 1 shows the molecular structure of the compounds studied experimentally. The tetraphenyl (BiBuQ) and pentaphenyl (QUI) derivatives are commercial laser dyes and were purchased from LambdaPhysik. The substituents allow a good solubility of the dyes at room temperature. Both compounds were dissolved in chloroform at concentrations of  $4.4 \cdot 10^{-2}$  M for BiBuQ and  $4.9 \cdot 10^{-2}$  M for QUI.

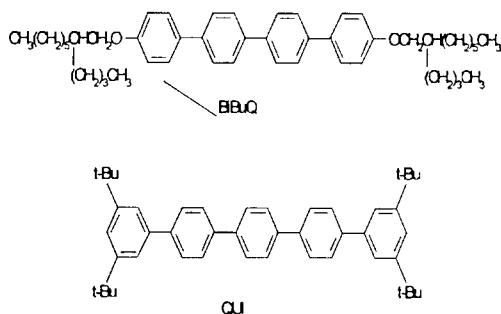


FIGURE 1 Structures of the compounds studied in this work

The two-photon cross-section spectra have been determined by two-photon excited fluorescence measurements. The laser was a frequency tripled Nd:YAG which pumped an optical parametric oscillator (OPO). The OPO delivered 2.6 nanosecond (ns) pulses in the range 450-650nm. The beam was collimated over the 5mm path length of the sample. The fluorescence emission was collected at 90° from the exciting beam by a lens and injected in an optical fiber connected to a spectrometer. Calibrations of  $\sigma_{\text{TPA}}$  were performed using a reference standard : p-Bis(o-methylstyryl)-benzene<sup>[5]</sup>.

## RESULTS

In figure 2, we show the intensity squared dependence of the fluorescence for both compounds.

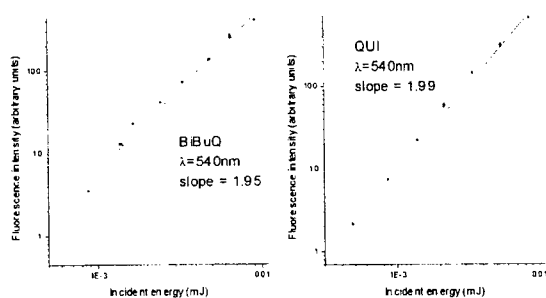


FIGURE 2 Dependence of the two-photon fluorescence with intensity

As it can be seen, the fluorescence emission obeys the intensity squared law as long as the incident energy is below 0.01mJ. Deviations were observed at higher energies mostly due to excited-state absorption. Figure 3 shows the  $\sigma_{\text{TPA}}$  spectra derived from the two-photon excited fluorescence measurements.

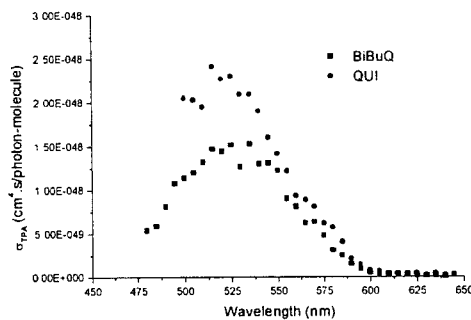


FIGURE 3 Two-photon cross-section spectra of the polyphenyl

For BiBuQ and QUI, the TPA spectra extend from 600nm to 475nm and the TPA resonance points near 530nm with peak values of  $1.5 \times 10^{-48}$  and  $2.5 \times 10^{-48} \text{ cm}^4/\text{s/photon-molecule}$  respectively.



## THREE LEVEL MODEL

The two-photon cross section is related to the imaginary part of the third order polarisability  $\gamma(-\omega;\omega,\omega,-\omega)$ . Using 1 dimensional, centrosymmetric molecules, and making the assumption that the linear response of the material is dominated by a single excited state  $|1\rangle$ , TPA can be described by a three level model. In this model, the two-photon transition occurs between the ground state  $|0\rangle$  and an upper excited state  $|2\rangle$  which is strongly coupled to  $|1\rangle$  (see figure4).

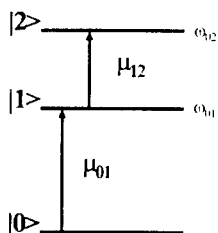


FIGURE 4 Three level model of the TPA

A simplified form of the two-photon cross-section  $\sigma_{TPA}$  at resonance for the transition  $|0\rangle \rightarrow |2\rangle$  is :

$$\sigma_{TPA} \propto \frac{\mu_{01}^2 \mu_{12}^2}{\left(E_{01} - \frac{E_{02}}{2}\right)^2} \quad (1)$$

where  $E_{ij}$  is the transition energy between the  $|i\rangle$  and  $|j\rangle$  states,  $\mu_{ij}$  is the transition dipole moment between  $|i\rangle$  and  $|j\rangle$ .

Analyse of the linear absorption spectrum of BiBuQ and QUI allows to derive the position of the first excited state  $|1\rangle$  and the transition dipole moment  $\mu_{01}$ . Using equation (1) and the  $\sigma_{TPA}$  spectrum, energy of the state  $|2\rangle$  and  $\mu_{12}$  can be estimated. Figures 5 presents the three level model obtained for the two compounds.

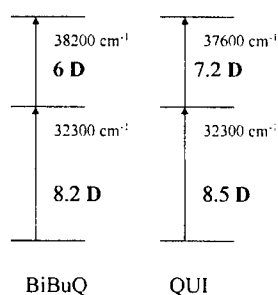


FIGURE 5 Experimental three level model for the two polyphenyl molecules

#### THEORETICAL MODEL

We used a semi empirical approach to perform calculations of the two-photon cross section. The geometry of the molecules was optimized by using the MOPAC package and the electronic states energies and dipole moments were obtained by a configuration interaction based on the CNDO method. The electronic states and transition dipole moment of a tetraphenyl and a pentaphenyl molecules have been calculated. The results of the calculations are shown figure 6.

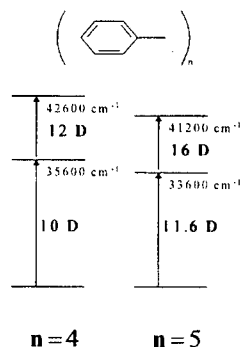


FIGURE 6 Comparisons of the theoretical electronic state features of tetraphenyl and pentaphenyl molecules

## DISCUSSION

The comparisons between experimental and theoretical results show that increasing the number of phenyl rings gives an enhancement of the transition dipole moments and therefore an enhancement of  $\sigma_{\text{TPA}}$ . Experimentally, improvement by a factor of 1.6 is observed going from four to five phenyl rings. Theoretically, we found that the pentaphenyl has a cross-section at resonance enhanced by a factor of 2.9 with respect to the tetraphenyl. The main reason is the improvement of the transition dipole moment contribution  $\mu_{01}^2 \mu_{12}^2$  by a factor of 2.4 and also a decrease in the transition detuning term  $(E_{01} - E_{12}/2)$  from 14300 to 13000  $\text{cm}^{-1}$ . In the case of a coherent coupling between the monomers (the phenyl ring), one would have expected a factor of 1.6. The difference resides in the fact that the pentaphenyl has a conjugation length longer than the tetraphenyl. This also explains the red-shift of the one and two-photon transitions in the calculations.

## CONCLUSION

We have shown experimentally that polyphenyl molecules exhibit large two-photon cross-sections and that the TPA increases with the number of phenyl rings. This result is also demonstrated theoretically. Other studies are in progress to determine the optimum size of molecules for efficient TPA.

## REFERENCES

- [1] B.A. Reinhardt, *Photonics Science News*, **4** (1998).
- [2] M. Albota; D. Beljonne; J.-L. Bredas; J.E. Ehrlich; J.-Y. Fu; A.A. Heikal, S.E. Hess; T. Kogej; M.D. Levin; S.R. Marder; D. McCord-Maughon; J.W. Perry, H. Röckel; M. Rumi; G. Subramaniam; W.W. Webb, X.-L. Wu; C. Xu, *Science*, **281** (1998).
- [3] J.E. Ehrlich, X.-L. Wu, I.-Y.S. Lee, Z.-Y. Hu, H. Röckel, S.R. Marder, and J.W. Perry, *Opt. Lett.*, **22**, (1997).
- [4] C. Nguefack, T. Zabulon, R. Anemian, C. Andraud, A. Collet, S. Topcu, and P.L. Baldeck, *Nonlinear optics* **21** (1999).
- [5] S.M. Kennedy and F.E. Lytle, *Anal. Chem.*, **58**, (1986).

## Polarization Recording and Reconstruction in a Photoinduced Anisotropic Medium

YOSHIKO OKADA-SHUDO

Department of Electronic Engineering, The University of Electro-  
Communications, Chofu, Tokyo 182-8585, Japan

We have derived the polarization state of the wave that is diffracted at two types of polarization gratings; one is recorded with two orthogonal linearly polarized waves, the other with two orthogonal circularly polarized waves. The corresponding experiments using bacteriorhodopsin films are interpreted in terms of this simplified model.

**Keywords** polarization holography; photoinduced anisotropy; polarization grating; bacteriorhodopsin

### INTRODUCTION

Traditional holography uses the interference phenomenon to record the amplitude and phase of light. Complete optical recording, including the storage of information about the amplitude, phase, and polarization state of light, requires the use of a general elliptically polarized wave. The photosensitivity of photoinduced anisotropic materials are utilized for recording polarization holograms[1-3]. Spatially variable anisotropic transparencies such as polarization gratings are of potential use in optical information processing[4,5]. The aim in this paper is to determine the selectivity dependence on the diffracted wave polarization by the polarization thin gratings.

### THEORETICAL BACKGROUND

#### Polarization Gratings Recorded with Two Orthogonally Polarized Waves

We consider two types of polarization interference pattern formed by two plane waves  $R$  and  $S$  with equal intensity.  $R$  and  $S$  are lying in

the  $xz$ -plane and subtending an angle  $2\theta_w$  (Figure 1). The grating **a** is recorded by orthogonal linear ( $R$  : horizontal,  $S$  : vertical) and **b** by circular ( $R$  : left-hand,  $S$  : right-hand) polarized waves on the  $xy$ -plane. The resulting light field are described respectively for the case **a** and **b** by

$$E_a = \begin{pmatrix} E \\ E \exp(2\delta i) \end{pmatrix}, E_b = \begin{pmatrix} E \cos \delta \\ E \sin \delta \end{pmatrix},$$

where  $\delta = 2\pi x \sin \theta_w / \lambda_w$ ,  $2\delta$  is the phase shift between  $R$  and  $S$  whose wavelength is denoted by  $\lambda_w$ . The period of these gratings  $d = \lambda_w / 2 \sin \theta_w$ . The shape of the modulations are shown in Figure 1.

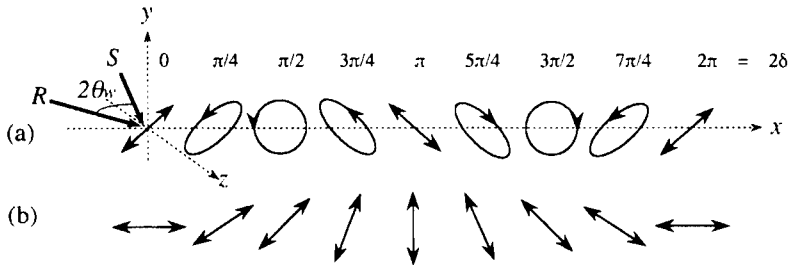


FIGURE 1 Arrangement for recording and polarization modulation on the  $xy$ -plane. (a) is recorded by orthogonal linear ( $R$  : horizontal,  $S$  : vertical) and (b) by circular ( $R$  : left-hand,  $S$  : right-hand) polarized waves.

We assume that only linear anisotropy (dichroism and birefringence) is induced in the material. The Jones matrices for the gratings are

$$JM_a = \begin{pmatrix} \frac{t_o + t_e}{2} & \frac{t_o - t_e}{2} \cos 2\delta \\ \frac{t_o - t_e}{2} \cos 2\delta & \frac{t_o + t_e}{2} \end{pmatrix}, \quad (1)$$

$$JM_b = \begin{pmatrix} t_o \cos^2 \delta + t_e \sin^2 \delta & (t_o - t_e) \sin \delta \cos \delta \\ (t_o - t_e) \sin \delta \cos \delta & t_o \sin^2 \delta + t_e \cos^2 \delta \end{pmatrix}, \quad (2)$$

where  $t_o$  and  $t_e$  are the amplitude transmissions of the ordinary and extraordinary wave, respectively. The Jones vector for the incident wave (a general elliptic) can be written as

$$P = \frac{a}{\sqrt{a^2 + b^2}} \begin{pmatrix} 1 \\ i \end{pmatrix} + \frac{be^{i\varphi}}{\sqrt{a^2 + b^2}} \begin{pmatrix} 1 \\ -i \end{pmatrix}, \quad (3)$$

where  $a$  and  $b$  are the lengths of the principal axes.

The amplitude distribution on  $z_1$  plane in case **a** is obtained by multiplying Eqs.(1) and (3);

$$U_{a1}(x_1) = \frac{t_o + t_e}{2} \left\{ \frac{a}{\sqrt{a^2 + b^2}} \begin{pmatrix} 1 \\ i \end{pmatrix} + \frac{be^{i\varphi}}{\sqrt{a^2 + b^2}} \begin{pmatrix} 1 \\ -i \end{pmatrix} \right\} \\ + \frac{t_o - t_e}{4} (e^{\frac{2\pi i}{d}x_1} + e^{-\frac{2\pi i}{d}x_1})i \left\{ \frac{a}{\sqrt{a^2 + b^2}} \begin{pmatrix} 1 \\ -i \end{pmatrix} - \frac{be^{i\varphi}}{\sqrt{a^2 + b^2}} \begin{pmatrix} 1 \\ i \end{pmatrix} \right\} \quad (4)$$

In case **b**, it is obtained by multiplying Eqs.(2) and (3);

$$U_{b1}(x_1) = \frac{t_o + t_e}{2} \left\{ \frac{a}{\sqrt{a^2 + b^2}} \begin{pmatrix} 1 \\ i \end{pmatrix} + \frac{be^{i\varphi}}{\sqrt{a^2 + b^2}} \begin{pmatrix} 1 \\ -i \end{pmatrix} \right\} \\ + \frac{t_o - t_e}{2} \left\{ e^{\frac{2i\pi}{d}x_1} \frac{a}{\sqrt{a^2 + b^2}} \begin{pmatrix} 1 \\ -i \end{pmatrix} + e^{-\frac{2i\pi}{d}x_1} \frac{be^{i\varphi}}{\sqrt{a^2 + b^2}} \begin{pmatrix} 1 \\ i \end{pmatrix} \right\}. \quad (5)$$

#### Polarization Property of Diffracted Wave

The amplitude distributions on  $z_1$  plane as shown in Eqs.(4) and (5) are regarded as the pupil functions. After some manipulations the basic integral for Fraunhofer diffraction on  $z_2$  plane,  $U_{a2}(x_2)$  and  $U_{b2}(x_2)$ , turn out to take the forms (we omit here a constant factor) as,

$$U_{a2}(X) = \pi(t_o + t_e) \left\{ \frac{a}{\sqrt{a^2 + b^2}} \begin{pmatrix} 1 \\ i \end{pmatrix} + \frac{be^{i\varphi}}{\sqrt{a^2 + b^2}} \begin{pmatrix} 1 \\ -i \end{pmatrix} \right\} \delta(X) \\ + \frac{\pi(t_o - t_e)i}{2} \left\{ \frac{a}{\sqrt{a^2 + b^2}} \begin{pmatrix} 1 \\ -i \end{pmatrix} - \frac{be^{i\varphi}}{\sqrt{a^2 + b^2}} \begin{pmatrix} 1 \\ i \end{pmatrix} \right\} \delta(X + \frac{2\pi}{d}) \\ + \frac{\pi(t_o - t_e)i}{2} \left\{ \frac{a}{\sqrt{a^2 + b^2}} \begin{pmatrix} 1 \\ -i \end{pmatrix} - \frac{be^{i\varphi}}{\sqrt{a^2 + b^2}} \begin{pmatrix} 1 \\ i \end{pmatrix} \right\} \delta(X - \frac{2\pi}{d}), \quad (6)$$

$$U_{b2}(X) = \pi(t_o + t_e) \left\{ \frac{a}{\sqrt{a^2 + b^2}} \begin{pmatrix} 1 \\ i \end{pmatrix} + \frac{be^{i\varphi}}{\sqrt{a^2 + b^2}} \begin{pmatrix} 1 \\ -i \end{pmatrix} \right\} \delta(X) \\ + \pi(t_o - t_e) \frac{a}{\sqrt{a^2 + b^2}} \begin{pmatrix} 1 \\ -i \end{pmatrix} \delta(X + \frac{2\pi}{d}) \\ + \pi(t_o - t_e) \frac{be^{i\varphi}}{\sqrt{a^2 + b^2}} \begin{pmatrix} 1 \\ i \end{pmatrix} \delta(X - \frac{2\pi}{d}). \quad (7)$$

where  $X \equiv 2\pi x_2/\lambda_i l$ . Here  $l$  denotes the distance between  $z_1$  and  $z_2$ , and  $\lambda_i$  the incident wavelength.

Equation (6) shows that diffracted waves at the polarization grating **a** is split into three plane waves, the direction of which are  $\lambda_i/d$ ,  $-\lambda_i/d$ , 0, respectively. 0-th order wave has the same polarized state as the incident wave  $P$ , and  $\pm 1$  order diffracted waves are polarized orthogonal to the incident wave. From Eq.(7), it is noticed the diffracted waves at the grating **b** are split into the same direction as the case **a**. The state of polarization of the order +1 is left-circular and that of the order -1 is right-circular, no matter what the polarization state of the incident wave.

## EXPERIMENTAL PROCEDURE

To verify the relationships derived above, we carried out experiments using the natural biologic photochromes, bacteriorhodopsin (bR), for various combinations of the polarization states of the recording and incident waves. The size of bR film is  $\phi 20 \text{ mm} \times 30 \mu\text{m}$ . The experimental arrangement is shown schematically in Figure 2. The bR film is irradiated by two recording waves  $R$  and  $S$  emanating from an Ar-ion laser (515 nm). They cross at an angle of  $8^\circ$ . A He-Ne laser is used to probe the grating at a different wavelength (633 nm). All three waves are adjusted to linear polarization, and expanded to a diameter of 2 cm on the sample. The intensities of each of the recording waves are equal to  $2 \text{ mW/cm}^2$ , while that of the probe beam is  $0.6 \text{ mW/cm}^2$ . Half-wave or quarter-wave plates  $R$  are inserted into these waves to change their polarization. The polarization state of

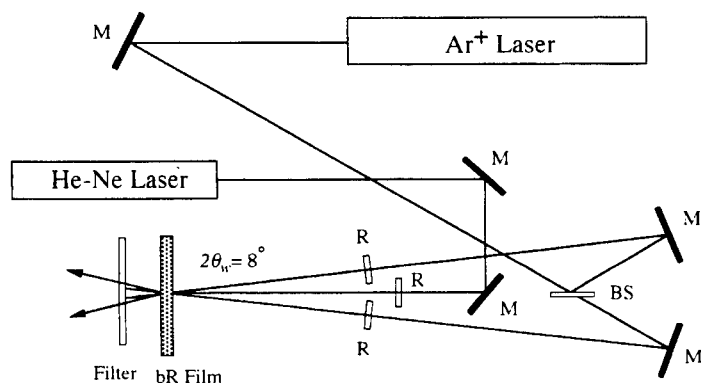


FIGURE 2 Experimental setup for investigating polarization effect of the diffracted wave at polarization gratings.

(a)

$R$	$S$	$I$	$D_{+1}$	$D_{-1}$	$DE_{+1}$	$DE_{-1}$
$\updownarrow$	$\updownarrow$	$\updownarrow$	$\updownarrow$	$\updownarrow$	1.0	1.0
		$\longleftrightarrow$	$\longleftrightarrow$	$\longleftrightarrow$	0.28	0.28
		$\odot$	$\odot$	$\odot$	0.79	0.78
		$\ominus$	$\ominus$	$\ominus$	0.93	0.92
$\longleftrightarrow$	$\updownarrow$	$\updownarrow$	$\longleftrightarrow$	$\longleftrightarrow$	0.25	0.25
		$\longleftrightarrow$	$\updownarrow$	$\updownarrow$	0.25	0.25
		$\odot$	$\ominus$	$\ominus$	0.23	0.23
		$\ominus$	$\odot$	$\odot$	0.21	0.22

FIGURE 3 Experimental results for recording waves of linear polarization.

(b)

$R$	$S$	$I$	$D_{+1}$	$D_{-1}$	$DE_{+1}$	$DE_{-1}$
$\odot$	$\odot$	$\updownarrow$	$\updownarrow$	$\updownarrow$	0.88	0.88
		$\longleftrightarrow$	$\longleftrightarrow$	$\longleftrightarrow$	0.77	0.76
		$\odot$	$\odot$	$\odot$	0.84	0.83
		$\ominus$	$\ominus$	$\ominus$	0.87	0.85
$\ominus$	$\odot$	$\updownarrow$	$\ominus$	$\odot$	0.44	0.43
		$\longleftrightarrow$	$\ominus$	$\odot$	0.42	0.42
		$\odot$	$\ominus$	$\times$	0.93	0
		$\ominus$	$\times$	$\odot$	0	0.91
$\odot$	$\ominus$	$\updownarrow$	$\odot$	$\ominus$	0.46	0.45
		$\longleftrightarrow$	$\odot$	$\ominus$	0.41	0.40
		$\odot$	$\times$	$\ominus$	0	0.88
		$\ominus$	$\odot$	$\times$	0.93	0

FIGURE 4 Experimental results for recording waves of circular polarization.

diffracted wave  $D$  is determined by using a retarder and an analyzer. Figures 3 and 4 show the experimental results of the diffracted wave for various combinations. The sixth and seventh columns show the experimental values of the relative diffraction efficiency. They are normalized with respect to the value of ordinary hologram equal to



0.005 in the first row of Figure 3. Hence the diffraction efficiency for the ordinary and the polarization hologram is of the same order of magnitude.

All the results for the polarization states agree well with the theoretical prediction. The polarization state of diffracted wave at the grating *a*, as shown in Figure 3, is orthogonal to that of the incident wave. The bR film causes a phase retardation of  $\pi$  in the diffraction; it plays the role of a half-wave plate. From Figure 4, we find that the amplitudes of first order waves depend on the polarization state of the incident field. When the polarization of incident wave changes over left- to right-circular frequently, using a Pockels cell, the grating *b* acts as a very fast optical switching device.

## CONCLUSION

In conclusion, theoretical and experimental studies have been presented for the polarization characteristics of the diffracted wave at the polarization gratings recorded in a material showing photoinduced anisotropy. We have demonstrated reconstruction of the polarized wave using bacteriorhodopsin (bR) films and observed generally good agreement with the theoretical prediction. The results of our investigations have clarified the following points. The polarization grating plays the role of a perfect polarization phase conjugator or a retarder of  $\pi$ , depending on the polarization states of recording waves. These devices might be useful for both image recording by polarization multiplexing and new optical logic processors using polarization encoding.

## ACKNOWLEDGEMENT

The author gratefully acknowledges a collaboration with Dr. J. M. Jonathan from Institut d'Optique Théorique et Appliquée. This work was supported partially by the KONICA Imaging Science Foundation.

## REFERENCES

1. Sh. Kakishashvili, *Opt. Spectrosc.* **33**, 90 (1972).
2. J. M. Jonathan and M. May, *Opt. Commun.* **29**, 7 (1979).
3. L. Nikolova and N. Todorov, *Opt. Acta* **31**, 579 (1984).
4. P. Rochon, V. Drnoyan, and A. Natansohn, *Proc. of SPIE* **3491**, 306 (1998).
5. F. Gori: *Opt. Lett.* **24**, 584 (1999).

## **Second Harmonic Spectroscopy and SHG Microscopic Observation of J-aggregate Domains in Merocyanine at the Air-Water Interface**

YOSHIAKI UESU\*\*\*, NORITAKA KATO\* and KENTARO SAITO\*

\*Department of Physics,

\*\*Advanced Research Institute for Science and Engineering,

Waseda University, 3-4-1, Okubo, Shinjuku-ku, Tokyo 169-8555, Japan.

Second harmonic(SH) spectra of merocyanine dye(MD) at the air-water interface were investigated in the SH energy region from 1.95 to 4.13eV. Distinct two peaks were observed at 2 and 4eV, which are the resonant J-band of the SH wave and the fundamental wave, respectively. In addition to these peaks, a small peak appeared at 3.95eV, the origin of which is not clearly but probably related to the bound state of two Frenkel excitons. Two dimensional SH images were taken by using SHG microscope at several photon energies. Careful comparison among the SH images revealed that the SH spectra originate in the J-aggregate state of MD.

**Keywords** second harmonic spectrum, J-aggregate, merocyanine dye, second harmonic images

## **INTRODUCTION**

Certain kinds of dye molecule are known to form the J-aggregate, which is characterized by a red-shifted sharp absorption band and Stokes-shift-free fluorescence[1]. Among these dye molecules, merocyanine(MD) is unique in the sense that it exhibits second-harmonic(SH) activity as a result of molecular asymmetry. Thus the second harmonic generation(SHG) provides a powerful tool for investigating the J-aggregate state of MD as well as fluorescence(FL)

and absorption measurements. Our recent investigations using the SHG/FL microscope clarified the morphological structure of MD/arachidic acid (AA) mixed monolayer at the air-water interface and MD was found to form mesoscopic J-aggregate domains which are SH-active[2]. Purpose of the present study is to clarify the energy state of MD which is related to the J-aggregation, using the SH spectroscopy. Besides we aimed at finding active sites which produce the characteristic nonlinear optical properties of the MD/AA monolayer system. With this motivation, we measured first the SH spectra in the wide energy range including the resonant spectra, then took the SH images at several photon energies and examined carefully the distribution of SH-active sites in these images.

## EXPERIMENTAL

MD/AA monolayers with molar ratio MD/AA of 2:3 were used in the present study. AA was mixed to stabilize the MD monolayer. The mixture compound was solved in chloroform (1mmol/l) and the solution was gradually spread on the subphase of aqueous ammonia (<0.03 wt.%, >pH10). Surface pressure was less than 14.7mN/m.

The incident photon energy was varied from 0.97 to 2.07eV by using the optical parametric oscillator (OPO). The average power of out-put wave from OPO is 1.3~30mW and the repetition frequency is 20Hz. SH spectrum was detected by a polychromator equipped with semiconductor detector array. Absorption spectrum was also detected by the polychromator. SH images were taken by an integrated charge coupled device (ICCD) with gating image intensifier synchronized with the laser oscillation. The exposure time is 20~30 seconds.

## RESULTS AND DISCUSSIONS

The formation of the J-aggregate of each sample was examined by observing characteristic J-band absorption and fluorescence spectra at 2eV. Obtained SH spectra from 1.95 to 3.35eV are shown in Fig.1 together with the absorption spectrum. A sharp peak was observed in the SH spectrum at 2eV, which is the resonant spectrum of the J-band for the SH wave. Fig.2 shows the SH spectra in high energy region from 3.76 to 4.13eV. Other two peaks were observed at 4 and 3.95eV. The former is easily discriminated as the resonant J-band for the

fundamental wave, while the origin of the latter is not clear at present. It is probably related to the resonance with excitonic 2-strings, which is the bound state of two Frenkel excitons [3], but precise examination is necessary.

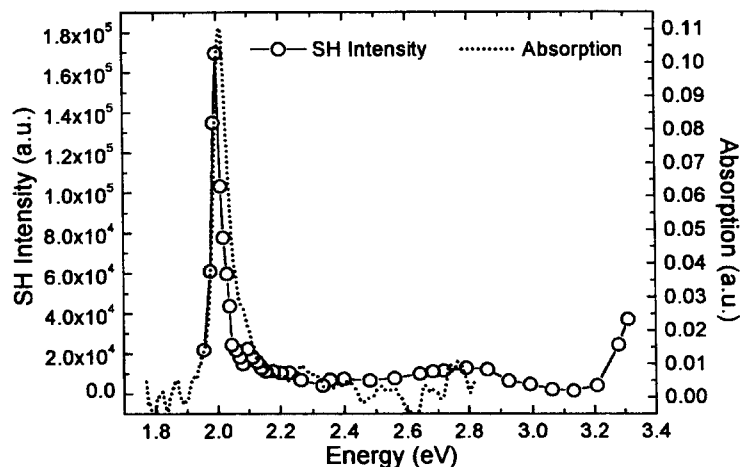


FIGURE 1 SH and absorption spectra of MD/AA mixed monolayer at the air-water interface in the energy range from 1.95 to 3.35eV.

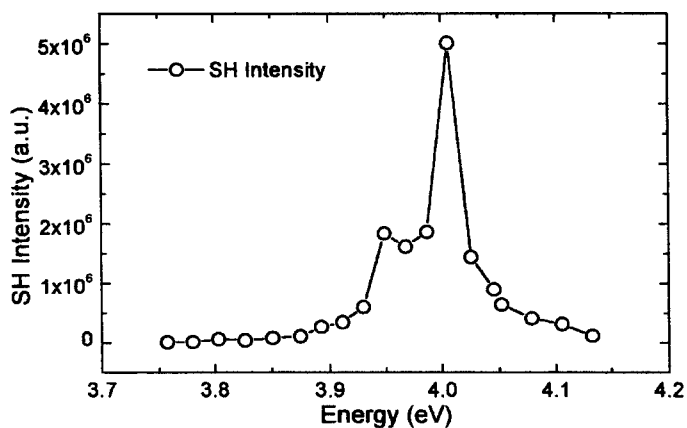


FIGURE 2 SH spectra of MD/AA mixed monolayer at the air-water interface in the energy range from 3.76 to 4.13eV.

SH intensity was found to decay near resonance regions. In particular, the decay near 4eV is remarkable as shown in Fig.3. The temporal change of the SH intensity  $I^{(2\omega)}$  is well fitted by double exponential form as

$$I^{(2\omega)} = A \exp(-t/\tau_1) + B \exp(-t/\tau_2) \quad (1)$$

with  $\tau_1 = 0.99\text{s}$  and  $\tau_2 = 9.54\text{s}$  at 4eV, for example. Dependences of  $\tau_1$  and  $\tau_2$  on the photon energy are indicated in Fig.4. SH intensities shown in Fig.2 were calculated by taking the decay effect into consideration.

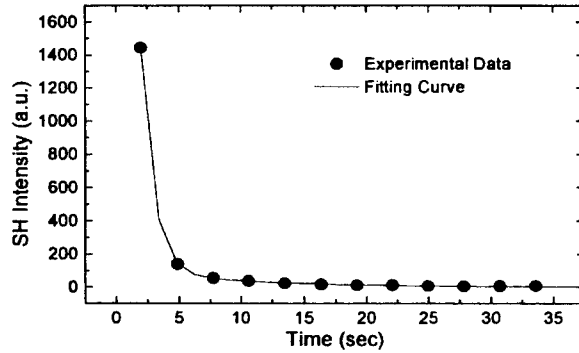


FIGURE 3 The decay of SH intensity near the resonance region.

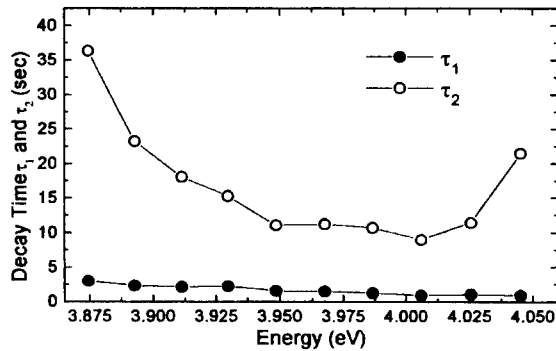


FIGURE 4 Photon energy dependence of the decay time  $\tau_1$  and  $\tau_2$ .

SH images of the MD/AA system were taken at several photon energies. During the observation, the optical geometry of OPO should have been rearranged when the incident photon energy was larger than 1.43eV and it necessitated the preparation of new samples. Thus we choose the SH image taken at 1.43eV as the reference image and compared the images for all spectrum range. The results for the low energy ( $\leq 2.86$ eV) and high energy ( $\geq 2.86$ eV) sides are shown in Fig.5 and 6, respectively. In these images, the parts enclosed by white dotted lines are one of J-aggregate domains, as they coincide with FL image. It is clearly shown that no significant differences in size and figure are observed in examined photon energy region. Thus we can safely conclude that whole SH spectra in Fig.1 is generated from the J-aggregate domains in MD/AA mixed monolayer system. The spatial resolution of our SHG microscope is about several ten  $\mu\text{m}$  at the air-water interface and further improvement is now developing.

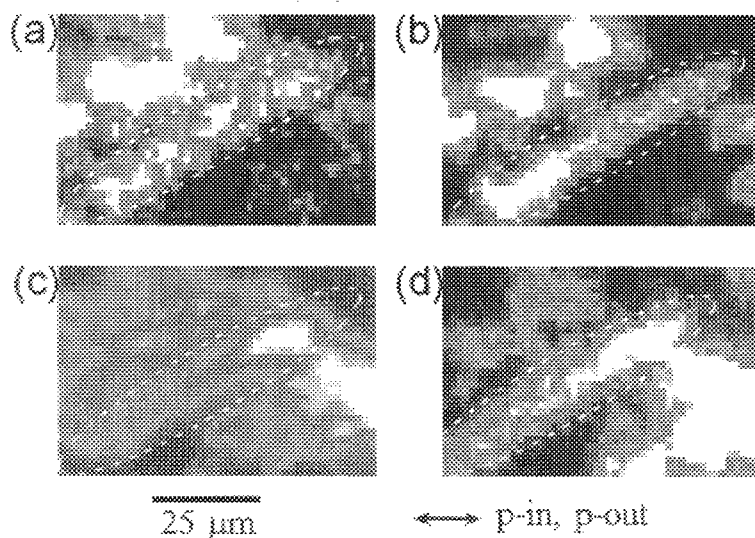


FIGURE 5 SH images of MD/AA mixed monolayer system taken at 1.98eV(a), 2.0(b), 2.32(c) and 2.86(d) of the SH photon energy. The polarization direction of the incident and SH beams are indicated in the arrow.

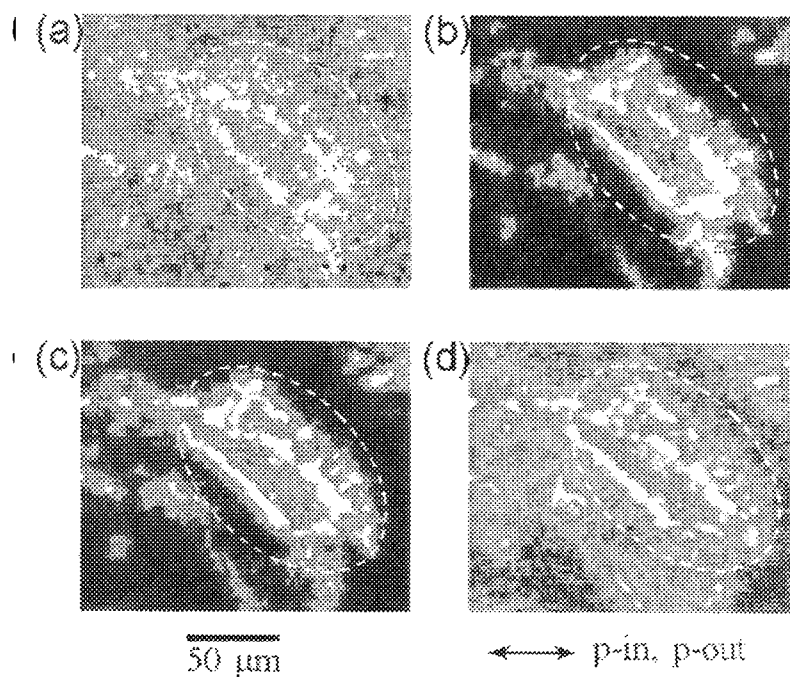


FIGURE 6 SH images of MD/AA mixed monolayer system taken at 2.86eV(a), 3(b), 3.18(c) and 3.23(d) of the SH photon energy. The polarization direction of the incident and SH beams are indicated in the arrow.

### References

- [1] T. Kobayashi, J-aggregates, (World Scientific, Singapore, 1996).
- [2] N. Kato, K. Saito, and Y. Uesu, Chem. Phys. Lett. **312**, 115(1999).
- [3] Tokihiro, M. Kuwata-Gonokami, R. Shimano, K. Ema, E. Hanamura, B. Fluegel, K. Meissner, S. Mazumdar, N. Peyghambarian, Solid State Commun., **88**, 211 (1993).

## Orientation and non linear optical properties of DAN crystals on PTFE substrates

RENAUD VALLEE<sup>a</sup>, PASCAL DAMMAN<sup>a</sup>, MARCEL DOSIERE<sup>a</sup>, ERIC  
TOUSSAERE<sup>b</sup>, JOSEPH ZYSS<sup>b</sup>.

<sup>a</sup>Université de Mons-Hainaut, 20, place du Parc, 7000 Mons, Belgium; <sup>b</sup>Ecole  
Normale Supérieure de Cachan, 61, Avenue du président Wilson, 94235 Cachan  
Cedex, France.

\*Pascal Damman is a Research Associate of the Belgian National Funds for  
Scientific Research.

The growth of DAN crystals on nano-structured PTFE substrate has been investigated by means of X-ray, FTIR and NLO ellipsometry. Two types of structural arrangements were detected, depending on the growth conditions. In both cases, the (001)<sub>DAN</sub> plane contacts the (100)<sub>PTFE</sub> substrate plane. The major difference between both types of samples lies in the presence of azimuthal orientation at the interface. The comparison between the various techniques used in this study to characterize the obtained thin films showed a remarkable agreement. With respect to this, the Second Harmonic Generation revealed once again as a powerful technique for the study of orientation effects in crystalline layers of NLO organic materials.

Keywords: crystal; growth; interface; organic; orientation; SHG.

### INTRODUCTION

Realization of oriented films of organic molecules is of practical importance for fabricating organic devices.<sup>1</sup> In order to obtain a complete characterization about crystal orientation, X-ray diffraction experiments provide a very powerful technique of investigation, both in so-called  $\theta/2\theta$  and grazing incidence (GIXD) geometries. Furthermore, when combined to the very sensitive optical second harmonic generation (SHG) tool,<sup>2</sup> the nonlinear optical (NLO) coefficients and the crystalline orientational distribution functions (COFDs) at surfaces and interfaces can be obtained.<sup>3</sup> In this paper, we show how it is possible to get such informations for thin films of DAN crystals deposited on a nanostructured poly(tetrafluoroethylene) (PTFE) substrate.

### SAMPLES PREPARATION AND X-RAY DIFFRACTION

Highly oriented PTFE substrates were prepared according to the method described in previous publications.<sup>4</sup> Crystals of DAN were directly grown on PTFE substrates by sublimation under vacuum (0.05 Torr). In some cases, these layers were further annealed at a temperature close to the melting point (164.5°C).

The X-ray diffraction measurements were performed on a Rigaku Denki RU300 rotating anode (18kW). The planar orientation was determined from  $\theta/2\theta$  scans: with this geometry the lattice plane parallel to the substrate plane can be probed. The azimuthal orientation can only be obtained with a grazing incidence geometry, thus allowing for the determination of the lattice planes perpendicular to the substrate. In terms of the transfer momentum



vector  $\mathbf{q}$ , the  $\theta/2\theta$  and the grazing incidence geometry correspond to  $\mathbf{q}$  vectors respectively perpendicular and parallel to the substrate plane.

The DAN molecule is a donor-acceptor (D-A) trisubstituted benzene derivative exhibiting a high molecular nonlinearity, with a charge transfer interaction between the dimethylamino and nitro groups in para positions (Figure 1).

The molecular engineering of these molecules favours the growth of non centrosymmetric crystals with a  $P2_1$  monoclinic structure. The unit cell parameters are  $a = 0.4786\text{nm}$ ,  $b = 1.3053\text{nm}$ ,  $c = 0.8736\text{nm}$  and  $\beta = 94.43^\circ$  (Figure 2).

Depending upon crystallization time, two types of samples have been obtained from sublimation, at a substrate temperature kept at  $30^\circ\text{C}$  and a powder temperature of  $150^\circ\text{C}$ . For short crystallization time, we get a typically lower than  $0.3\text{ }\mu\text{m}$  thickness sample, and its diffraction curve presents two peaks when investigated by  $\theta/2\theta$  geometry (Figure 3a).

Those peaks, observed at  $q_{\text{perp}} = 7.25\text{nm}^{-1}$  and  $q_{\text{perp}} = 14.43\text{nm}^{-1}$ , correspond respectively to (001) and (002) reflections. A (001)<sub>DAN</sub>/(100)<sub>PTFE</sub> is thus grown, the azimuthal orientation of which having to be studied with the GIXD tool.

Figure 3b shows the reflections observed in the  $\chi$ -GIXD scans for such a thin sample, and table 1 summarizes the information obtained by such a technique. The indexation of the observed reflections, with their  $q_{\text{par}}$  momentum transfert and associated angular positions  $\phi^*$  with respect to the PTFE chain axis are given.

TABLE 1

Numéro	(hkl)	$\chi(^{\circ})$	$q_{\text{par}}(\text{nm}^{-1})$	$\phi^*$
1	020	6.75	9.5	90
2	100	9.25	13.8	0

The a and b crystallographic axes of the DAN crystals are respectively parallel and perpendicular to the PTFE chain axis. The average orientation at the interface can therefore be summarized by the following orientational relationships:

$$\begin{array}{ll} (001)_{\text{DAN}} & \parallel (100)_{\text{PTFE}} \\ [100]_{\text{DAN}} & \parallel [001]_{\text{PTFE}} \\ [010]_{\text{DAN}} & \parallel [100]_{\text{PTFE}} \end{array} \quad (1)$$

On the basis of these relations, a very large lattices mismatch can be calculated at the interface:

$$\Delta = \frac{d_{010}^{\text{DAN}} - 2d_{010}^{\text{PTFE}}}{2d_{010}^{\text{PTFE}}} = 15.3\%. \quad (2)$$

Furthermore, the  $\phi$ -GIXD scan curves exhibit peaks with a FWHM close to  $20^\circ$ .

Both results indicate a lack of azimuthal orientation and it is in fact hazardous to speak about epitaxy.<sup>3</sup>

The molecular view representing the proposed (001)<sub>DAN</sub>/(100)<sub>PTFE</sub> interface is presented on figure 4.

The second type of samples are obtained when the growth is pursued over longer crystallization times and consist of samples thicker than  $1\text{ }\mu\text{m}$ . In this case, the (001)<sub>DAN</sub>

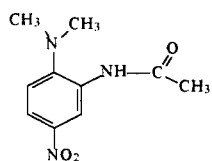


Figure 1: Schematic of the DAN molecule.

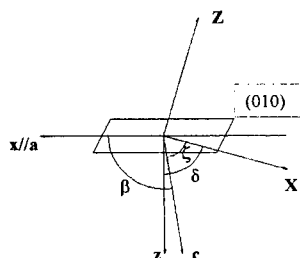


Figure 2: Relations between crystallographic and dielectric reference frames.

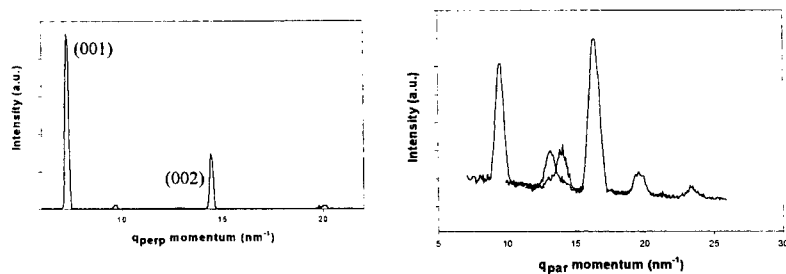


Figure 3:  $\theta/2\theta$  X-ray diffraction experiment and GIXD experiment

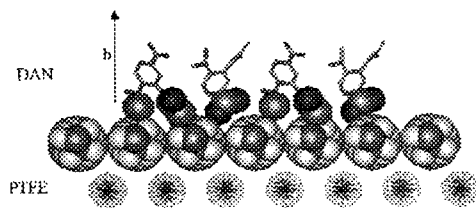


Figure 4: Representation of the  $(001)_{\text{DAN}} / (100)_{\text{PTFE}}$  interface

Figure 4: Representation of the  $(001)_{\text{DAN}} / (100)_{\text{PTFE}}$  interface

planar orientation is conserved while the azimuthal orientation is completely lost (uniaxial orientation).

#### NLO EXPERIMENTAL RESULTS AND DISCUSSION

The nonlinear optical (NLO) properties of DAN crystalline layers were determined from second harmonic generation (SHG) experiments. A Q-switched Nd:YAG laser generating 10 nanosecond pulses at a 10 Hz repetition rate, at a wavelength of 1340 nm was used. The samples were mounted on a rotating and translatable stage with the PTFE sliding direction set either parallel or perpendicular to the polarization direction of the incident laser beam. The orientation dependence (ellipsometry configuration)<sup>3</sup> of the SHG signal was measured by rotating the polarisation ( $\theta$ ) of the incident beam from 0° to 360°, the analyser remaining fixed either parallel (p) or perpendicular (s) to the PTFE sliding direction.

DAN crystals are monoclinic and biaxial, with point group  $C_2$ , one principal axis of the dielectric tensor being constrained by symmetry to be parallel to the twofold axis  $b$  of the unit cell, the other principal axes lie in the (010) crystallographic plane as a result of subtle packing and dielectric considerations. Their orientation has already been determined experimentally.<sup>5,6</sup>

For crystal belonging to point group 2 (class of MAP),<sup>7</sup> the second harmonic polarization  $P$  is expressed by the tensorial relation:

$$\begin{pmatrix} P_x \\ P_y \\ P_z \end{pmatrix} = \begin{pmatrix} 0 & 0 & 0 & d_{14} & 0 & d_{16} \\ d_{21} & d_{22} & d_{23} & 0 & d_{25} & 0 \\ 0 & 0 & 0 & d_{34} & 0 & d_{36} \end{pmatrix} \begin{pmatrix} E_x^2 \\ E_y^2 \\ E_z^2 \\ 2E_y E_z \\ 2E_z E_x \\ 2E_x E_y \end{pmatrix} \quad (3)$$

Assuming validity of the Kleinman's symmetry relations in agreement with the off-resonance conditions of our experiment, only four coefficients remain independent, namely:

$$d_{21} = d_{16}, d_{22}, d_{23} = d_{34}, d_{25} = d_{14} = d_{36}. \quad (4)$$

Since the crystallographic axes are not orthogonal, we will use an arbitrary orthogonal sample system, defined with the following convention:  $x$  and  $y$  are respectively along the  $a$  and  $b$  axis, and the perpendicular  $z$  axis is along the  $c^*$  axis. An angle of 4.43° between  $z$  and  $c$  is shown on figure 2.

The experimental set-up for the SHG-measurement is as follows: the samples are mounted on a stage so that the fundamental wavevector is oriented normal to the (001) plane, i.e. along the  $z$  axis. We then let the polarization vector of the fundamental electric field vary uniformly in this plane from a  $\theta = 0$  angle chosen to be in the direction of the  $y$  axis all the way to 360°. Finally, the second harmonic signal was recorded after polarization analysis along the  $y$  or  $x$  direction, in the so-called q-p and q-s configurations. The measured SHG signal is then expressed as:

$$I_{2\omega} \propto |d_{eff}|^2 I_{\omega}^2 \quad (5)$$

where the effective nonlinear susceptibility is given by:

$$d_{eff} = \{e(2\omega) \cdot [d] : e(\omega)e(\omega)\} \quad (6)$$

$e(\Omega)$  refer to unit vectors along the polarization of fields at  $\Omega = \omega$  or  $2\omega$ .

The pulse width and area of the laser spot are not crucial to this analysis provided that the latter is large enough relative to the size of the crystals. We also neglect here local-field and transmission factors. These approximations allow observations of differences in SH signals produced by the samples presented above to be determined.

For thin samples, experiments show a q-s curve (figure 5) which presents a maximum of SHG intensity for an approximately s incoming direction of polarisation, while the q-p curve is essentially isotropic.

To explain these observations, let us first express the relationships between the (xyz) sample frame and the (XYZ) dielectric reference frame. As shown on figure 2, the angle  $\delta$  between the z axis and the X dielectric axis is equal to  $54.98^\circ$ , y being parallel to Y.

Due to the sublimation procedure on PTFE substrate, our samples are made-up of numerous tiny crystallites. X-ray diffraction results indicate that for both types of films (thin and thick), the contact plane corresponds to the  $(001)_{DAN}$  plane while the azimuthal orientation drastically differs. The thin samples are characterised by a single-crystal-like orientation with a broad distribution, the a parameter being parallel to the PTFE sliding direction. In order to take into account the broad distribution of orientation observed in GIXD for the DAN crystals, we consider the following box model: each tiny crystal of the layer is represented by its own (XYZ) dielectric frame with the attached X axis (parallel to the a crystallographic axis) making a random angle  $\phi$  with respect to the PTFE chain axis in the  $(001)_{DAN}$  plane. For all the crystals of the layer, the  $\phi$  angles are then allowed to vary uniformly in a box-like orientational distribution of aperture range  $[-a_0, a_0]$ . The transformation matrix, which permits to connect the (xyz) external sample frame in which measurements are being performed onto the (XYZ) internal dielectric reference frame, is given by:

$$L : \begin{pmatrix} x \\ y \\ z \end{pmatrix} \rightarrow \begin{pmatrix} X \\ Y \\ Z \end{pmatrix} = \begin{pmatrix} -\sin \delta \cos \phi & -\sin \delta \sin \phi & \cos \delta \\ -\sin \phi & \cos \phi & 0 \\ -\cos \delta \cos \phi & -\cos \delta \sin \phi & -\sin \delta \end{pmatrix} \quad (7)$$

As the laser beam propagates along the z-axis, conservation of the x and y tangential components of the electric field in the (xyz) sample frame permits to determine the following expressions for the field components in the dielectric frame:

$$\begin{aligned} E_X(t, \phi) &= A \sin(t + \phi) \\ E_Y(t, \phi) &= \cos(t + \phi) \\ E_Z(t, \phi) &= B \sin(t + \phi) \end{aligned} \quad (8)$$

where A and B are only functions of the  $\delta$  angle defined here above and of the permittivities at optical frequencies  $\epsilon_X = 1.5172$  and  $\epsilon_Z = 1.8432$  as determined previously.<sup>6</sup>

$$\begin{aligned} A &= -\frac{\sin \delta}{\epsilon_X} \frac{1}{\sin^2 \delta + \cos^2 \delta} \\ B &= -\frac{\cos \delta}{\epsilon_Z} \frac{1}{\sin^2 \delta + \cos^2 \delta} \end{aligned} \quad (9)$$

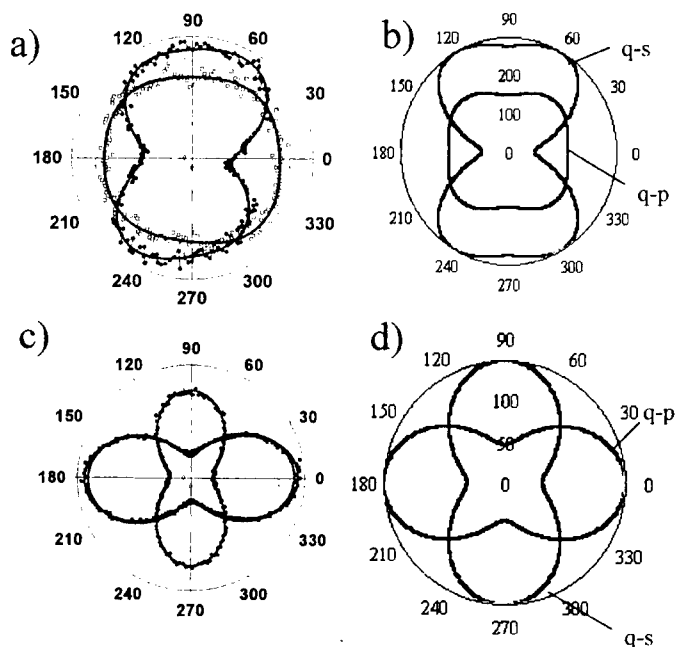


Figure 5: Experimental (a) and simulated (b) curves obtained by the nonlinear ellipsometry technique for thin samples. Experimental (c) and simulated (d) curves obtained by the nonlinear ellipsometry technique for thick samples.

The second order polarizations  $P_X, P_Y, P_Z$  in the dielectric frame are then determined by means of equations (3), taking into account Kleinman relations (4) and lead to the following polarizations expressed in the (xyz) sample frame:

$$\begin{aligned} P_x(t, \phi) &= -\sin \delta \cos \phi I'_X(t, \phi) - \sin \phi I'_Y(t, \phi) - \cos \delta \cos \phi P_Z(t, \phi) \\ P_y(t, \phi) &= -\sin \delta \sin \phi P_X(t, \phi) - \cos \phi P_Y(t, \phi) - \cos \delta \sin \phi P_Z(t, \phi) \end{aligned} \quad (10)$$

Reported values of the nonlinear coefficients are  $d_{21} = 1.5 \text{ pm/V}$ ,  $d_{22} = 5.2 \text{ pm/V}$ ,  $d_{23} = 50 \text{ pm/V}$  and  $d_{25} = 1.5 \text{ pm/V}$ .

Considering that the numerous DAN crystals of the layers are characterised by a broad distribution of orientation spreading over a  $[-34^\circ, 34^\circ]$  interval, the x and y polarized intensities are obtained by averaging according to:

$$\begin{aligned} I_x(t) &= \frac{1}{68} \int_{-34}^{34} (P_x(t, \phi))^2 d\phi \\ I_y(t) &= \frac{1}{68} \int_{-34}^{34} (P_y(t, \phi))^2 d\phi \end{aligned} \quad (11)$$

respectively for the q-s and q-p polarization configurations. Figure 5b shows the simulated curves in this case.

NLO experimental data thus account for a uniform distribution of the crystals in the layer with their a axis distributed over a  $[-34^\circ, 34^\circ]$  distribution around the PTFE sliding direction.

For yellow samples on the other hand, q-p and q-s curves are given in figure 5c.

The observation of two maxima of intensity at right angles to each other is clearly the signature of a unoriented powder-like sample. NLO experimental data are then well reproduced by averaging over a full angular spread for random in-plane crystal orientation in the overlayer. Figure 5d shows the simulated results.

## CONCLUSION

The measurements effectuated by means of X-ray diffraction and, subsequently, by the surface SHG nonlinear ellipsometry technique, have led us to fully characterize the interface DAN/PTFE, with the determination of the structural relations between the lattices. Furthermore, the analysis of the CODFs has allowed us to confirm ratios of NLO dominant coefficients of DAN crystals, already reported in the literature.

<sup>1</sup>Y.R. Shen, Nature, 333, 542 (1988).

<sup>2</sup>B. Jerome and Y.R. Shen, Phys.Rev., E48, 4556 (1993).

<sup>3</sup>Submitted to J.A.C.S.

<sup>4</sup>J. C. Wittmann and P. Smith, Nature, 352, 414 (1991).

<sup>5</sup>J.-C. Baumert, R.J. Twieg, G.C. Bjorklund, J.A. Logan, and C.W. Dirk, Appl. Phys. Lett. 51(19), 1484 (1987).

<sup>6</sup>P. Kerkoc, M. Zgonik, K. Sutter, Ch. Bosshard, and P. Günter, Appl. Phys. Lett. 54(21), 2062 (1989).

<sup>7</sup>J.L. Oudar, J. Zyss, Phys.Rev. A 26(4), 2016 (1982).

## Influence of Conjugation Length on the First Hyperpolarizability of Fluorescent Hemicyanine (DAST) Homologues

KURT WOSTYN (a), GEERT OLBRECHTS (a), KOEN CLAYS (a),  
ANDRE PERSOONS (a, b), AKIRA WATANABE (c), KYOKO NOGI  
(c), XUAN-MING DUAN (c), SHUJI OKADA (c), HIDETOSHI  
OIKAWA (c), HACHIRO NAKANISHI (c), HENRYK VOGEL (d),  
DAVID BELJONNE (d), JEAN-LUC BREDAS (d, e)

(a) Laboratory of Chemical and Biological Dynamics, Center for  
Research on Molecular Electronics and Photonics, University of Leuven,  
Celestijnenlaan 200 D, B-3001 Leuven, Belgium; (b) Optical Science  
Center, University of Arizona, Tucson, AZ 85721; (c) Institute for  
Chemical Reaction Science, Tohoku University, Katahira, Aoba-ku,  
Sendai 980-8577, Japan; (d) Laboratory for Chemistry of Novel  
Materials, Center for Research on Molecular Electronics and Photonics,  
University of Mons-Hainaut, place du Parc 20, B-7000 Mons, Belgium;  
(e) Department of Chemistry, The University of Arizona, Tucson,  
Arizona 85721-0041

**Abstract** The influence of the conjugation length on the first hyperpolarizability of a series of five fluorescent hemicyanine homologues is studied by femtosecond hyper-Rayleigh scattering. A frequency-resolved detection scheme has been used to suppress the multi-photon fluorescence contributions to the HRS signal. The obtained fluorescence-free first hyperpolarizabilities are compared with theoretical values.

**Keywords** : first hyperpolarizability; DAST homologues; HRS

## INTRODUCTION

Ionic chromophores have since long been envisaged as promising precursors for non-linear optical (NLO) materials. The introduction of the hyper-Rayleigh scattering (HRS) technique made it possible to measure the first hyperpolarizability  $\beta$  of ionic chromophores [1, 2]. Multi-photon fluorescence (MPF), however, can contribute to the incoherent HRS signal leading to an overestimated  $\beta$ -value. Recently, a frequency-resolved femtosecond HRS setup has been devised to differentiate between immediate scattering and the time-delayed fluorescence in the frequency domain [3].

## TECHNIQUE

The frequency-resolved femtosecond HRS technique relies on the time-delayed fluorescence response of the chromophore in the time-domain leading to a demodulation of the fluorescence signal in the frequency domain. Therefore, at high amplitude-modulation (AM) frequencies of the fundamental light beam, the observed demodulation tends to zero at high AM frequencies. On the contrary, no such demodulation will be observed for the immediate scattering resulting in an observed constant scattering intensity, irrespective of the AM frequency. Whereas the generic laser type for HRS experiments is a  $\text{Nd}^{3+}$ :YAG laser (1064 nm), a femtosecond  $\text{Ti}^{3+}$ :sapphire laser (800 nm) has to be used for the frequency-resolved HRS measurements. A femtosecond optical parametric oscillator (OPO) has been inserted as well to shift the fundamental wavelength towards the infrared (1300 nm) resulting in a second-harmonic wavelength of 650 nm.

Measuring at a very high modulation frequency (several GHz) would enable us to demodulate the fluorescence completely. Only HRS would be observed, leading to a  $\beta$ -value not overestimated by fluorescence. Unfortunately, measuring at this very high modulation frequency cannot be attained experimentally. We have resolved this problem by measuring the demodulation of the fluorescence as a function of the modulation frequency. As a result, multiple HRS experiments at various modulation frequencies have to be performed. A fit of the obtained demodulation curve (apparent  $\beta$ -value versus modulation frequency) then reveals the



intrinsic fluorescence-free  $\beta$ -value in the high-frequency limit. The fitting equation includes the fluorescence decay parameters, i.e., the fluorescence lifetime(s) with their respective amplitudes as well as the intrinsic  $\beta$ .

### EXPERIMENTAL RESULTS

The technique was used to measure the influence of the conjugation length on the first hyperpolarizability of five fluorescent ionic hemicyanine homologues (DAST) of increasing conjugation length (see Figure 1). In earlier studies on non-ionic and non-fluorescent chromophores, a large influence of the conjugation length on  $\beta$  has been observed initially followed by a levelling-off behaviour afterwards [4, 5, 6, 7]. This observation is in good agreement with theoretical predictions on these chromophores. Moreover, theoretical calculations on the  $\beta$  of ionic and fluorescent DAST chromophores predict a similar behaviour.

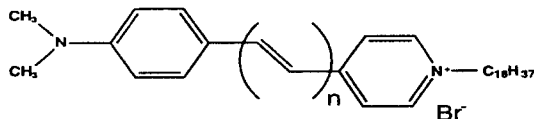


FIGURE 1. Structure of the hemicyanine homologues. The conjugation length of the studied chromophores varies from  $n = 1$  to  $n = 5$ .

However, the experimentally obtained  $\beta$ -values of the DAST chromophores show a somewhat different dependence upon the conjugation length. The experimental first hyperpolarizabilities ( $\beta_{\text{exp}}$ ) are shown in Table 1. The static first hyperpolarizabilities ( $\beta_{0,\text{exp}}$ ), calculated using the two-level model, as well as the theoretical values ( $\beta_{0,\text{theo}}$ ) together with the wavelength of maximum absorption ( $\lambda_{\text{max}}$ ) are summarised in Table 1.

Figure 2 shows the influence of the conjugation length on the experimentally determined values and on the theoretically predicted values of the first hyperpolarizability. The static first hyperpolarizabilities retrieved using the standard femtosecond HRS technique [8] are also shown for comparison. The  $\beta_{\text{exp}}$  values are obtained from the analysis of

the demodulation curve [9]. The huge discrepancy between the apparant  $\beta_0$ -values, obtained from standard femtosecond HRS, and the fluorescence-free  $\beta_0$ -values is indicative of the strong fluorescence contribution present for these stilbazolium chromophores. On the contrary, the agreement found between the  $\beta_{0,\text{exp}}$  and  $\beta_{0,\text{theo}}$  for  $n = 1, 2$  and 3 illustrates the ability of the frequency-resolved femtosecond HRS technique to retrieve the fluorescence-free  $\beta$ -values. The different trend in  $\beta_{0,\text{exp}}$  versus  $\beta_{0,\text{theo}}$  upon enlarging the conjugation length can be explained considering excited-state isomerization. If an isomerization takes place in the excited state, then the all-trans configuration is lost and a less conjugated cis-isomer is generated, leading to a reduced  $\beta$ -value. For the longer conjugation lengths, a partial cis-configuration becomes more probable leading an even lower  $\beta$ -value. This explains the maximum behaviour of the first hyperpolarizability for the DAST homologues.

n	1	2	3	4	5
$\lambda_{\text{max}}$	496	524	546	556	570
$\beta_{\text{exp}}$	100	1640	2045	780	1200
$\beta_{0,\text{exp}}$	36	481	496	171	224
$\beta_{0,\text{theo}}$	222	399	632	855	1087

TABLE 1. The wavelengths of maximum absorption ( $\lambda_{\text{max}}$ ) are in nm. The theoretically and experimentally obtained values of the first hyperpolarizability  $\beta$  are in  $10^{-30}$  esu.  $n$  is the conjugation length as defined in Figure 1.

The theoretical calculation on the other hand considers only the all-trans isomers of the chromophores. As, however, isomerization takes place, the calculation should incorporate several cis-isomers as well.

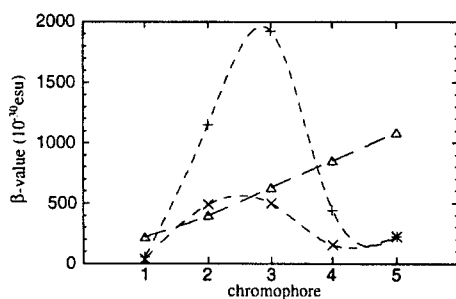


FIGURE 2. Influence of conjugation length on the experimentally ( $\beta_{0,exp}$ , X) and theoretically ( $\beta_{0,theo}$ ,  $\Delta$ ) determined static first hyperpolarizability. Also the uncorrected static first hyperpolarizabilities (apparent  $\beta_{0,exp}$ , +), as obtained from the standard femtosecond HRS technique, are shown. The lines are only intended to guide the eye and do not represent a model.

A previous study on an inclusion complex of a stilbazolium chromophore in an amylose helix [10] supports this assumption as a doubling of the first hyperpolarizability was observed, as compared to the stilbazolium chromophore free in solution.

## CONCLUSION

Five fluorescent hemicyanine homologues of increasing conjugation length were studied. Theoretical predictions suggest the same behaviour as predicted by previous studies on non-ionic, non-fluorescent chromophores. The experimental results, however, show a different behaviour that can be explained by excited-state isomerization. This explanation is supported by previous studies on amylose inclusion complexes.

### ACKNOWLEDGEMENTS

K. W. and G. O. are Research Assistants and K. C. is a Senior Research Associate of the Fund for Scientific Research - Flanders (FWO-V). D. B. is a Research Fellow ("Chercheur Qualifié") of the Belgian National Fund for Scientific Research (FNRS). This research was supported by research grants from the FWO-V (G.0338.98 and G.0407.98), from the University of Leuven (GOA/95/01), and from the FNRS. The Leuven-Mons collaboration is supported by the Belgian Federal Government (IUAP IV/11, "Supramolecular Chemistry and Supramolecular Catalysis").

### REFERENCES

1. K. Clays, A. Persoons, *Phys. Rev. Lett.*, **66**, 2980-2983, (1991)
2. K. Clays, A. Persoons, *Rev. Sci. Instrum.*, **63**, 3285-3289 (1992)
3. G. Olbrechts, R. Strobbe, K. Clays, A. Persoons, *Rev. Sci. Instrum.*, **69**, 2233-2241 (1998)
4. R. A. Huijts, G. L. J. Hesselink, *Chem. Phys. Lett.*, **126**, 209-212 (1989)
5. J. L. Oudar, H. L. Person, *Opt. Comm.*, **15**, 258-262 (1975)
6. J. L. Oudar, *J. Chem. Phys.*, **67**, 446-457 (1977)
7. A. Dulcic, C. Flytzanis, C. L. Tang, D. Pépin, M. Fétizon, Y. Hoppilliard, *J. Chem. Phys.*, **74**, 1559-1563 (1981)
8. K. Clays, A. Persoons, *Rev. Sci. Instrum.*, **65**, 2190-2194 (1994)
9. K. Clays, K. Wostyn, G. Olbrechts, A. Persoons, A. Watanabe, K. Nogi, X.-M. Duan, S. Okada, H. Oikawa, H. Nakanishi, *J. Opt. Soc. Am. B*, **17**, 256-265 (2000)
10. K. Clays, G. Olbrechts, T. Munters, A. Persoons, O.-K. Kim, L.-S. Choi, *Chem. Phys. Lett.*, **293**, 337-342 (1998)

## **Preparation of the Anisotropic Thin Film of a One-dimensional Material on an ITO Electrode**

TAKANORI TANO, TAKEHITO KODZASA, HIROBUMI USHIJIMA,  
TOSHIHIDE KAMATA\*  
National Institute of Materials and Chemical Research, 1-1 Higashi, Tsukuba,  
Ibaraki 305-8565, Japan

For the development of the light up-conversion device utilizing organic electroluminescence, we have tried to introduce a highly oriented columnar structure into a photo conductor layers.  $d^8$  transition metal complex with dionedioxime has been examined as a columnar structure molecule. We have attempted a fabrication of the film with its metal chain orienting perpendicular to the surface of an indium-doped tin oxide (ITO) electrode. It was shown for the first time that control of deposition conditions permits the fabrication of the film with perpendicular orientation of the metal chains on the ITO substrate.

**Keywords:** bis(diphenylglyoximate)platinum(II); ITO electrode;  
one-dimensional metal complex; organometallic complex;  
photoconductivity; organic electroluminescence device

## **INTRODUCTION**

Recently, there has been increasing interest in the application of OEL diodes to new types of devices [1,2]. A light amplification device based on hybridization of OEL diodes has been reported, which have ability of light up-conversion from red to green. In such a device, metal-phthalocyanine molecules with a columnar structure are generally used as a photo conductor layer. However, these compounds are only able to respond to the restricted wavelength of the irradiation light. Therefore, other compounds which absorb wide wavelength range of the light from UV-vis to near infrared region have been requested.

On the other hand, it has been shown that wavelength of absorption band of  $d^8$  transition metal complexes with dionedioxime could be easily changed from UV-

vis to near infrared region by selecting ligands [3,4]. Therefore, these complexes are considered to become a good candidate for consisting a photo conductor layer. It has been known that these complexes in the evaporated thin film have a square planar configuration and stacks face-to-face, forming a one-dimensional metal chain (Figure 1) [3,5]. Because of its columnar structure, it is expected to show anisotropic photoconductivity. Thus, the orientation control of the column is important to fabricate a high quality photo conductor layer.

Previously, we have found that the column of the dioxime complexes with  $d^8$  transition metals in an evaporated film orients perpendicularly to an alkali halide surface by epitaxial growth under the lattice match condition [6]. In this study, we have examined the molecular structure in the film prepared on an ITO electrode, of which surface has large roughness and does not appear a strict lattice, by UV-vis spectroscopy and AFM measurements.

## EXPERIMENTAL

Thin films were prepared by the vacuum evaporation technique onto a quartz or an ITO substrate. The sample chamber was evacuated at ca.  $10^{-5}$  Pa. Substrate temperatures were varied between 25 and  $-175$  °C, and deposition rates were changed from 10 to 0.1 nm/min. The film thickness, measured with a Tencor Alpha-step 300 surface profilometer, was from 100 to 150 nm. Absorption spectra were recorded on a Shimadzu UV-3100 spectrophotometer in a wavelength range 300-1000 nm. A *p*-polarized ultraviolet or visible beam through a Glan-Thompson prism was incident upon the film at an angle of  $70^\circ$ . AFM images were taken using noncontact mode on either a Seiko SPA with an SPI 3800 probe station or a JEOL JSPM-4200.

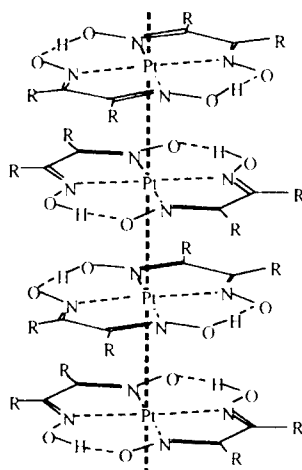


FIGURE 1 Molecular structure of platinum dioxime complex and the stacking arrangement of the molecular column in the solid state.

## RESULTS AND DISCUSSION

Figure 2 shows absorption spectra of bis(diphenylglyoximate)platinum(II);  $\text{Pt}(\text{dpg})_2$  film prepared on a quartz substrate at (A) 25 °C and (B) -175 °C. In the absorption spectra, we have aimed at the band observed at ca. 550 nm, assigned to the  $5d_z^2-6p_z$  transition of platinum. Since this transition originates in the  $d$ -orbital overlap between adjacent platinum ions in the linear metal chain [3,7], the transition moment of the band is parallel to the metal chain. Therefore, one could estimate the orientation of the linear metal chain by estimating dichroic ratio of the band [4]. In case of the film prepared at 25 °C, no obvious dichroism was observed. This indicates that the film has random orientation. Figure 3A shows a

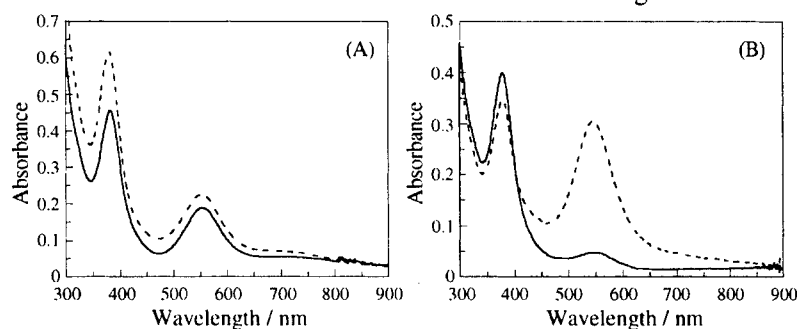


FIGURE 2 Absorption spectra of  $\text{Pt}(\text{dpg})_2$  film on a quartz substrate prepared at (A) 25 °C and (B) -175 °C. The solid line is the spectrum of normal incidence; the dotted line is that of 70° incidence from surface normal.

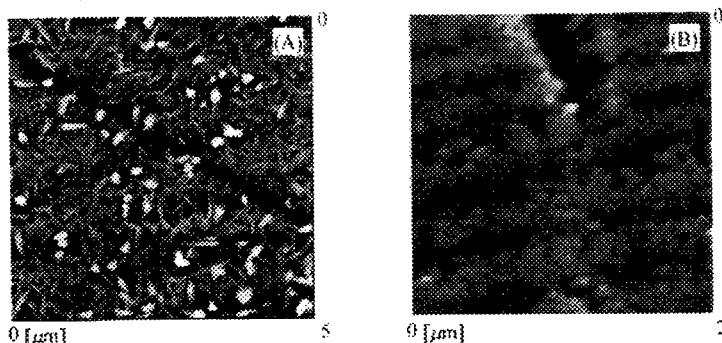


FIGURE 3 AFM images of  $\text{Pt}(\text{dpg})_2$  film on a quartz substrate prepared at (A) 25 °C and (B) -175 °C after annealing at 100 °C for ten minutes.

topographic image of the film. AFM image shows that the film is composed of worm-like or needle-like crystals without any regular orientation supporting the spectral results.

On the other hand, a large dichroism was observed in the absorption spectrum of the film prepared at  $-175^{\circ}\text{C}$ , (Figure 2B). It is indicating that the molecular columnar axis is orienting almost perpendicular to the substrate surface. Figure 3B displays a topographic image of  $\text{Pt}(\text{dpg})_2$  film prepared at  $-175^{\circ}\text{C}$  after annealing at  $100^{\circ}\text{C}$ . The image is not identical with that shown in Figure 3A at all. The film is composed of rod-like crystal of which orientation is almost perpendicular to the film surface and the respective rod-like crystals seem to have almost same length in this film thickness. This film structure would give a high advantages to form a carrier transport layer of the device. From further detailed study, it was shown that such a film structure can be obtained in a film prepared on a quartz surface at least below  $-100^{\circ}\text{C}$ .

Moreover, we examined to form perpendicular orientation using bis(dimethylglyoximate)platinum(II),  $\text{Pt}(\text{dmg})_2$ , where phenyl group of  $\text{Pt}(\text{dpg})_2$  is substituted by methyl group. It was revealed that the film has random orientation independent of the substrate temperature. This result means that the orientation of the column is also dependent on the molecule structure. The crystal of both compounds has the same space group as orthorhombic. Therefore, main difference between  $\text{Pt}(\text{dpg})_2$  and  $\text{Pt}(\text{dmg})_2$  molecules is the substituent. Since phenyl group is electron-rich, the interaction energy between a  $\text{Pt}(\text{dpg})_2$  molecule and a quartz substrate considered to be much larger than the case of  $\text{Pt}(\text{dmg})_2$ . Namely, weak interaction between  $\text{Pt}(\text{dmg})_2$  and a quartz substrate appears to cause such a random orientation.

Since we have examined a fabrication condition in case of a quartz substrate, we applied this strategy to an ITO electrode. Figure 4A shows an absorption spectrum of  $\text{Pt}(\text{dpg})_2$  film prepared at  $25^{\circ}\text{C}$ . No dichroism was clearly observed in the band intensity at 550 nm. Spectrum figure is very similar to that of  $\text{Pt}(\text{dpg})_2$  film on a quartz substrate prepared at the same temperature (Figure 2A). These results indicate that molecular orientation in the film is not very much different from that in the film shown in Figure 3A.

When the  $\text{Pt}(\text{dpg})_2$  film on an ITO substrate were prepared at  $-110^{\circ}\text{C}$ , drastic change was occurred in the absorption spectrum (Figure 4B). At normal



incidence, almost no absorption was present at around 550 nm. As for oblique incidence, a strong broad band could be observed. This shows that the  $\text{Pt}(\text{dpg})_2$  molecules are stacked as its axis is almost perpendicular to the substrate surface.

In the film prepared at  $-175^\circ\text{C}$ , a spectrum with extremely small band intensity was obtained and the dichroic ratio was no longer observed (Figure 4C). This indicates that the columnar structure of the  $\text{Pt}(\text{dpg})_2$  molecule is hardly present in the film. In the absorption spectrum of the chloroform solution dissolving  $\text{Pt}(\text{dpg})_2$ , the band at 550 nm was not observed. Therefore,  $\text{Pt}(\text{dpg})_2$  molecules seem to be randomly dispersed in the film. Since the ITO electrode has generally surface roughness with several nm size [8], it is likely that the surface roughness and low substrate temperature are probable reasons. Namely, when molecules are deposited on the rough surface, they are trapped in trough and not able to re-orient or move around because of low substrate temperature.

From above results, it was revealed that substrate temperature at around  $-100^\circ\text{C}$  leads to a unique orientation of molecules even in case of an ITO electrode. However, the optimum condition was strongly dependent on the type of substrates.

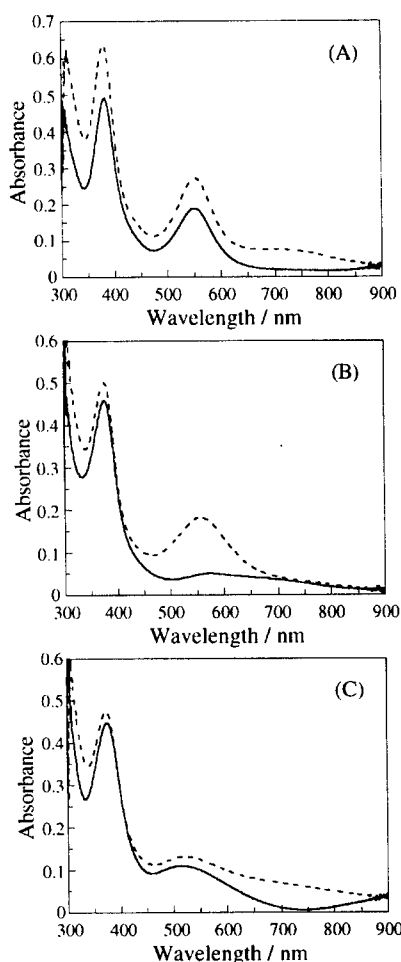


FIGURE 4 Absorption spectra of  $\text{Pt}(\text{dpg})_2$  film prepared on an ITO electrode at (A)  $25^\circ\text{C}$ , (B)  $-110^\circ\text{C}$  and (C)  $-175^\circ\text{C}$ .

## CONCLUSION

For the development of the light up-conversion device utilizing OEL phenomena, we have tried the introduction of a columnar structure into a transport layer. We have found out the optimum conditions for fabricating the film with the column orienting perpendicular to the substrate surface. In spite of surface roughness of the ITO electrode, Pt(dpg)<sub>2</sub> film prepared at -110 °C was composed of highly oriented columnar structure. Therefore, the film is applicable to a photo conductor layer in the OEL device.

## REFERENCES

- [1] T. Katsume, M. Hiramoto, and M. Yokoyama, Appl. Phys. Lett., **66**, 2992 (1995).
- [2] K. Yase, T. Hanada, N. Takada, Y. Ichino, Y. Kagawa, Y. Okada, K. Abe, Y. Yoshida, and N. Tanigaki, Mol. Cryst. Liq. Cryst., in press.
- [3] T. Kamata, T. Fukaya, H. Matsuda, F. Mizukami, M. Tachiya, R. Ishikawa, and T. Uchida, J. Phys. Chem., **99**, 13239 (1995).
- [4] T. Tano, T. Kodzasa, H. Ushijima, and T. Kamata, Mol. Cryst. Liq. Cryst., in press.
- [5] S. Isoda, M. Tsujimoto, K. Yoshida, T. Kobayashi, and T. Kamata, Mol. Cryst. Liq. Cryst., **316**, 15 (1998).
- [6] K. Yamamoto, T. Kamata, Y. Yoshida, K. Yase, F. Mizukami, and T. Ohta, Adv. Mater., **10**, 1018 (1998).
- [7] Y. Ohashi, I. Hanazaki, and S. Nagakura, Inorg. Chem., **9**, 2551 (1970).
- [8] T. Hanada, H. Takiguchi, Y. Okada, Y. Yoshida, N. Tanigaki, and K. Yase, J. Cryst. Growth, **204**, 307 (1999).

**SESSION F: ULTRAFAST NONLINEAR OPTICS  
IN ORGANICS**

## Optical and nonlinear optical properties of low-dimensional aggregates of amphiphilic cyanine dyes

R.V.Markov<sup>a</sup>, P.A.Chubakov<sup>a</sup>, A.I.Plekhanov<sup>a</sup>, Z.M.Ivanova<sup>b</sup>,  
N.A.Orlova<sup>b</sup>, T.N.Gerasimova<sup>b</sup>, V.V.Shelkovnikov<sup>b</sup>, and J.Knoester<sup>c</sup>

<sup>a</sup>Institute of Automation and Electrometry SB of RAS, 1 Acad. Koptug Ave., 630090 Novosibirsk, Russia; <sup>b</sup>Novosibirsk Institute of Organic Chemistry, 9 Acad. Koptug Ave., 630090 Novosibirsk, Russia; <sup>c</sup>Institute for Theoretical Physics and Material Science Center, University of Groningen, Nijenborgh 4, 9747 AG Groningen, The Netherlands

Thin solid films of low-dimensional J-aggregates of amphiphilic cyanine dyes with various lengths of the N-alkyl substituents were obtained. It has been found that the length of the alkyl substituent influences the structure of the aggregates, which allows for the control of their optical properties. These films possess an optical cubic susceptibility ( $10^{-5}$  esu). The dispersion of  $\text{Im}\chi^{(3)}$  within the exciton absorption band was measured by the Z-scan technique. The indexes of refraction and absorption coefficients of the films were measured by spectral ellipsometry.

### Keywords

J-aggregates; Thin films; N-alkylsubstituted pseudoisocyanines; Optical spectra; Cubic susceptibility; Refractive index

## INTRODUCTION

The low-dimensional molecular aggregates of cyanine dyes, so called J-aggregates, attract the attention of researchers due to their interesting optical properties. J-aggregates of cyanine dyes are characterized by a narrow band of exciton absorption (J-peak) which is red shifted compared to the absorption of the monomer form of the dye. The J-peak appearance is a collective phenomenon and is connected with the dipole-dipole interactions between the excited dye molecules that are contained in the aggregate. It leads to the formation of de-localized excitonic states with high oscillator strength of the optical transition. Recent theoretical [1-3] and experimental [4-10] works have shown that molecular J-aggregates pos-

sess high cubic optical susceptibility ( $10^{-7}$  -  $10^{-6}$  esu) [4-7] and fast switching times ( $\sim 10^{-12}$  s) at the J-peak resonance condition.

At present, methods are known to form J-aggregates in water solutions, in frozen glasses, and in polymer matrices [11]. It was shown that the length of alkyl substituents may influence the structure and optical properties of aggregates formed in a water solution of amphiphilic cyanine dyes [12]. It is also important to have knowledge about the linear and nonlinear optical properties of thin solid films of the cyanine J-aggregates, keeping in mind the possible practical applications.

The purpose of the present work is to study the optical and nonlinear optical properties of thin films of J-aggregates of cyanine dyes with various lengths of the N-alkyl group.

## EXPERIMENTAL

### Dyes and Methods of preparation of thin films

In this work we have used 1,1'-diethyl-2,2'-cyanine iodide (PIC) with a series of N-alkyl substituents with symmetric position **1a** - **e**: **Alk** - **Alk** = **a** -  $C_2H_5 - C_2H_5$ , **b** -  $C_6H_{13} - C_6H_{13}$ , **c** -  $C_{10}H_{21} - C_{10}H_{21}$ , **d** -  $C_{15}H_{31} - C_{10}H_{31}$ , **e** -  $C_{18}H_{37} - C_{18}H_{37}$ ; and nonsymmetrical position **2a** - **d**: **Alk** - **Alk'** = **a** -  $C_2H_5 - C_6H_{13}$ , **b** -  $C_2H_5 - C_{10}H_{21}$ , **c** -  $C_2H_5 - C_{15}H_{31}$ , **d** -  $C_2H_5 - C_{18}H_{37}$  [13]. The absorption spectra of the organic solutions of PIC **1a** - **e** and **2a** - **d** at concentrations smaller than  $10^{-3}$  M show no differences, which indicates that the optical properties of the monomers do not depend on the length of the substituents.

Dye films were prepared by spin-coating (at 2000 - 3000 rpm) on a glass substrate, from dye solutions (acetonitrile or ethylene dichloride) at concentrations  $\sim 10^{-2}$  M.

### Optical properties and structure of thin films of J-aggregates

From the optical spectra of the thin solid films one can conclude that the J-aggregated form of the dye is present for the samples with nonsymmetrical PIC (**2a-d**), while dyes with symmetrical position of the substituents give H-aggregates. H-aggregates are characterized by an exciton absorption band that is blue-shifted compared to the monomer absorption. The tendency to increase the spontaneous conversion of the dye monomer to J-aggregates during film formation when increasing the length of the alkyl substituents was observed for PIC **2b-d**. This is clearly seen from Figure 1, which gives the film spectra at low dye concentration. PIC **2b** dye practically has not given the J-aggregate form, while the PIC **2c** and PIC **2d** give such form, and the J-peak for PIC **2d** dye is more noticeable.

The typical widths (HWHM) of J-peaks were  $200\text{--}230\text{ cm}^{-1}$  and practically did not depend on the length of the substituent.

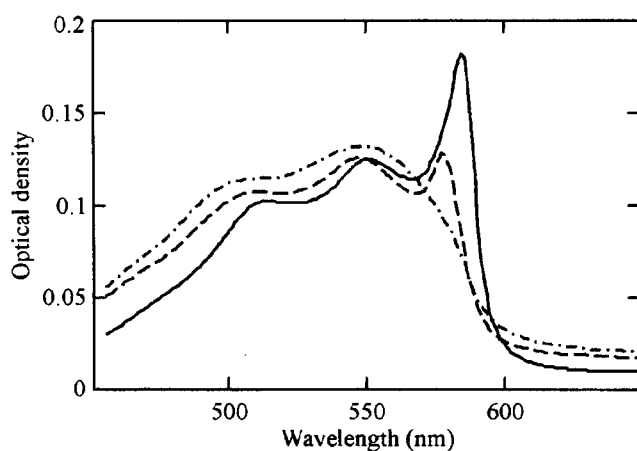


FIGURE 1. Linear absorption spectrum of J-aggregate films, dot-dash line - for PIC 2b, dotted line - for PIC 2c, solid line - for PIC 2d. The films are prepared from dye solution of acetonitrile at concentration  $10^{-3}$  M. Spinning velocity is 3000 rpm.

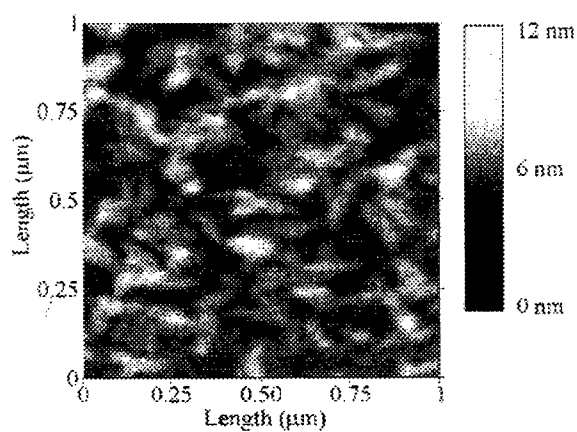


FIGURE 2. AFM image of PIC 2d J-aggregates film, for which the optical spectrum shows the sharp J-peak.

The films of PIC **2b-d** J-aggregates are stable at room temperature for more than one month, while the stability of PIC **1a** J-aggregates is higher than 1-2 days. With increasing the humidity of the air the J-peak of these films grows. This may be explained by enhancement of the hydrophobic properties of the amphiphilic dye with growing length of the N-alkyl substituents.

The thin film with the J-aggregate peak of the **2d** dye was investigated by means of atomic force microscopy (AFM) to obtain the image of the dye film surface on the glass plate (Figure 2). Here the aggregated dye molecules represent a view of chaotically located cigar-like structures. Their average size is 80-110 nm in length, 40-60 nm in width and about 6-12 nm in height. This structure differs from the thread-like aggregates, which have been observed by near field microscopy [14]. The cigar-like structure may result from the adhesion of thread-like micelles leading to multilayer ribbon micelles. Such process is known for paired cationic N-alkyl surfactant [15].

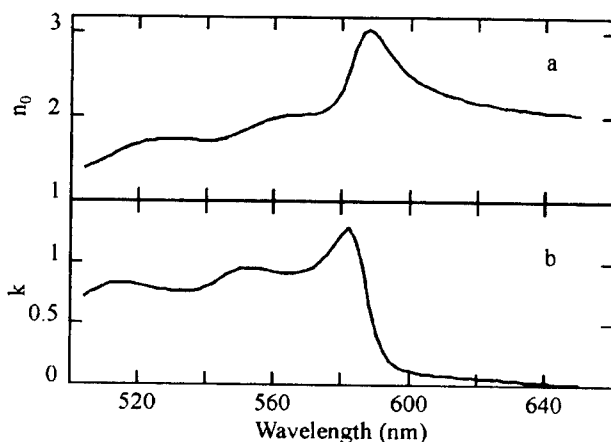


FIGURE 3. Refractive index  $n_o$  and absorption coefficient  $k$  of the film of PIC **2d** J-aggregates on silica substrate. The film thickness is 16 nm.

The film thickness and the frequency dispersions of the refractive index ( $n_o$ ) and the absorption coefficient ( $k$ ) were determined by spectral ellipsometry [16] for the J-aggregated films of PIC **2b-d**. The optical constants of the thin films were measured with an accuracy  $\pm 0.01$  for  $n_o$  and  $k$  and  $\pm 0.5$  nm for the thickness.

Figure 3a,b shows the dispersion curves of the refractive index and the absorption coefficient of the PIC **2d** J-aggregated film. Similar behaviours were observed for the films with other substituent lengths. One

observes the normal dispersion of  $n_o$  within the long wave spectral region of film transparency, and the anomalous dispersion of  $n_o$  within the region of dye absorption (500-570 nm), with  $n_o$  value 2.7 at the maximum of the J-peak. The absorption coefficient  $k$  at 585 nm, corresponding to the J-peak maximum, has value  $\alpha_o = 4\pi k/\lambda \approx 2.4 \cdot 10^5 \text{ cm}^{-1}$ .

#### Dispersion of the nonlinear susceptibility of J-aggregates in thin films

The nonlinear absorption spectrum of PIC **2b-d** J-aggregate films was measured by the Z-scan technique [10,17]. The measurements were carried out with a pulsed dye laser ( $\tau \approx 5 \text{ ns}$ ) at room temperature and humidity (approximately 60%).

Figure 4 (diamonds) shows the typical experimental dispersion curve of the nonlinear susceptibility  $\text{Im}\chi^{(3)}(\lambda)$ . There is dynamical bleaching and the maximal value of  $\text{Im}\chi^{(3)} = -1.3 \cdot 10^{-5} \text{ esu}$  is coinciding with the J-peak position with 1 nm accuracy. Nonlinear spectrum is asymmetrical and apart from the bleaching band also shows a darkening peak that is red-shifted by 4-5 nm from the J-peak. The wavelength of the bleaching maximum was found to move to the blue side by 2.0 nm when the intensity increases from 0.6 to 3 MW/cm<sup>2</sup>. At the same time, nonlinear darkening grows by 30 – 40 %.

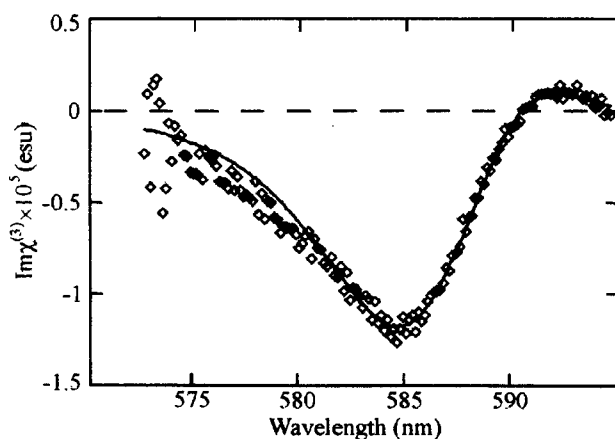


FIGURE 4. Dispersion of the imaginary part of the third-order susceptibility for the film of PIC **2d** J-aggregates. Diamonds are the experimental data. The solid line is the fit based on the four-level model.

The standard free exciton model of aggregates without exciton-exciton interaction cannot explain the observed nonlinear spectrum features, such as the red-shifted nonlinear darkening. We have chosen to



analyze the nonlinear absorption by using the effective four-level model of exciton transitions proposed in Ref. [10]. The nonlinear bleaching is caused by the absorption saturation of the transition from the ground to the one-exciton state. The population relaxes either to the ground state or to a lower-lying excitonic state. Now, nonlinear induced absorption results from the transition of the lower lying state to a higher (fourth) one. Evidence for the existence of a lower lying excitonic state was deduced from the observation of a red emission near 630 nm upon excitation of the films by yellow or green light. As was shown in Ref. [18], PIC monomers do not phosphoresce, but the luminescence at 640-660 nm is due to phosphorescence of aggregates at 4.2 K.

Based on the four-level model and solution of equations for density matrix in steady-state condition we obtain the expressions for  $\text{Im}\chi^{(3)}$  and  $\text{Re}\chi^{(3)}$  [10]. The fitting curve of  $\text{Im}\chi^{(3)}(\lambda)$  corresponding to this model (Figure 4, solid line) shows good agreement with the experimental data. According to the fitting results, the width of the nonlinear bleaching line for J-aggregates of PIC with substituents **2c,d** turns out to be narrower by 10 - 15% than predicted by the model of saturation of a transition with homogeneous broadening. This fitting has allowed to determine the features of  $\chi^{(3)}(\lambda)$ , i.e. its maxima position and widths. The nature of nonlinear darkening remains open. Free excitons in J aggregates give rise to a blue-shifted induced absorption [19]. A red-shifted induced absorption in J aggregates may in principle result from exciton-exciton interactions, provided they are rather strong [20]. In that sense the exciton-exciton interactions are one of the probable explanations of the observed phenomenon.

## CONCLUSION

The current research shows the possibility to obtain spin-coated stable thin solid films of J-aggregates of pseudo-isocyanine dyes with long alkyl substituents (PIC **2b-d**), with film thickness 15-30 nm. Dispersions of the refractive index and absorption coefficient for these films were measured. The  $n_0$  value at the J-peak maximum is 2.7. The magnitude and dispersion of the imaginary part of the optical cubic susceptibility were measured. The maximal value of  $\text{Im}\chi^{(3)}$  is about  $-10^{-5}$  esu. The observed dispersion curve is in agreement with a four-level model of exciton transitions in the aggregate.

## Acknowledgments

Authors are very grateful to Prof. S.G.Rautian, Prof. S. Daehne and Dr. L.Daehne for fruitful discussions and to S. Leporatti for carrying out the AFM measurements. This work was supported by INTAS 97-10434 and Minnauka «Laser Physics» 6.35 grants.

## REFERENCES

1. F. C. Spano and S. Mukamel, Phys. Rev. A, **40**, 5783 (1989).
2. J. Knoester, Phys. Rev. A, **47**, 2083 (1993).
3. J. Knoester, Chem. Phys. Lett. **203**, 371 (1993).
4. Y. Wang, J. Opt. Soc. Am. B, **8**, 981 (1991).
5. V. A. Bogdanov., E. N. Viktorova, S. V. Kulay, et al. JETF Lett. **53**, 100 (1992).
6. F. A. Zhuravlev, N. A. Orlova, V. V. Shelkovnikov, et al. JETF Lett. **56**, 260 (1992).
7. R. Gadonas, K-H. Feller, A. Pugzlys. Opt. Commun. **112**, 157 (1994).
8. K. Minoshima, M. Taiji, K. Misawa, et al. Chem. Phys. Lett. **218**, 67 (1994).
9. S. Kobayashi, F. Sasaki. J. Lumin. **58**, 113 (1994).
10. R. V. Markov, A. I. Plekhanov, S. G. Rautian, et al. Optics and Spectroscopy. **85**, 588 (1998).
11. J. Kobayashi, J-aggregates (Word Scientific Publishig Co. Pte. Ltd., Singapore, 1996).
12. U. De Rossi, J. Moll, M. Spieles et. al. J. Prakt. Chem. **337**, 203 (1995).
13. N. A. Orlova, E. F. Kolchina, F. A. Zhuravlev, et al. Journal of Heterocyclic Compounds, will be published.
14. D.A. Higgins and P. F. Barbara, J. Phys. Chem. **99**, 3 (1995).
15. R. Oda, I. Huc, J-C. Homo, et al. Langmuir. **15**, 2384 (1999).
16. V. A. Shvets and S. V. Rykhlitsky. Optoelectr., Instrum. Data Proces. **1**, 5 (1997).
17. M. Sheik-Bahae, A. A. Said, and E. W. Van Stryland. Opt. Lett. **14**, 955 (1989).
18. G. Gradl, J. Fredrick, E. Daltrozzo. J. Chem. Phys. **94**, 2301 (1990).
19. H. Fidler, J. Knoester, D.A. Wiersma, J. Chem.Phys. **98**, 6564 (1993).
20. F. C. Spano, Chem. Phys.Lett. **234**, 29 (1995).

## Picosecond Optical Limiting Action through a Thin MMA-Octupole Copolymer Layer near the Total Reflection State

R. MOUNTASSER,<sup>a\*</sup> H. MAILLOTTE,<sup>b†</sup> F. CHÉRIOUX<sup>c</sup> and M. AYADI<sup>a</sup>

<sup>a</sup>Département de Physique, Faculté des Sciences, Université Hassan II, BP 146, Mohammedia, Morocco; <sup>b</sup>Laboratoire d'Optique P.M. Duffieux, UMR CNRS/Université de Franche-Comté n°6603, Institut des Microtechniques de Franche-Comté, 25030 Besançon cedex, France; <sup>c</sup>Laboratoire de Chimie et Electrochimie Moléculaire, Université de Franche-Comté, 25030 Besançon cedex, France

Non-resonant optical transmission near the critical angle of incidence, through a thin nonlinear copolymer layer surrounded by two linear glass slabs, is studied experimentally in the picosecond range. The thin spin-coated film is made up from MMA polymer reticulated by a new octupolar molecule displaying off-resonant third order susceptibility. The transmittance of the layer is switched by more than 40% with microjoule pulses, from a high transmission state to a weak transmission state when increasing the input intensity. The switching behavior is completely reversible and exhibits long-term stability.

**Keywords:** thin Kerr film; octupole; polymer; picosecond switching; critical incidence

### INTRODUCTION

Intensity-dependent transmission near the total reflection state, through a thin nonlinear Kerr film surrounded by two linear slabs, has been introduced as a tool for ultrafast switching and optical limitation. As shown in the relevant theoretical studies<sup>[1-3]</sup>, the main advantages of this nonlinear sandwich, when compared to the single nonlinear interface case<sup>[4]</sup>, are the lower switching energy and the transverse stability of the transmitted beam. The previous experimental works<sup>[1,5,6]</sup> dealt with nonlinear refraction induced by absorption and thermal effects in the sandwich, *i.e.* in a rather slow diffusive regime. The present study focuses on non-resonant transmission in the picosecond range through a thin film made up from a new MMA-octupole copolymer.

\* Work conducted during the author's stay at Laboratoire d'Optique P.M. Duffieux  
† Corresponding author – e-mail address: herve.maillotte@univ-fcomte.fr

removed under reduced pressure. The obtained crude orange solid was dissolved in 50 ml of  $\text{CH}_2\text{Cl}_2$  and washed three times with 50 ml of water. The organic layer was dried on anhydrous  $\text{Na}_2\text{SO}_4$  and solvent was removed under reduced pressure. The resulting solid was washed quickly with 100ml of anhydrous ether and two times with 100ml of anhydrous acetone to give 2.2g of the pure copolymer (Yield : 90%).  $^1\text{H}$  and  $^{13}\text{C}$  NMR data are in perfect agreement with the chemical structure proposed in Figure 2.

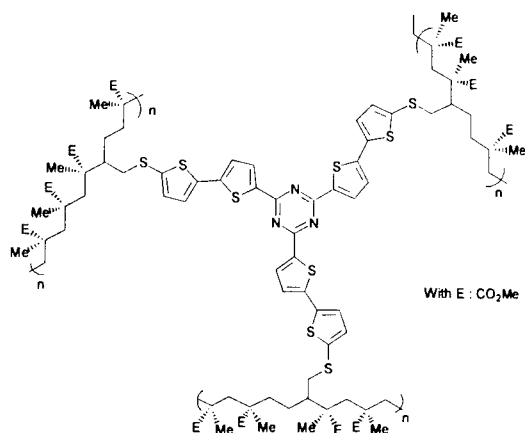


FIGURE 2 Structure of the copolymer(MMA-octupole)

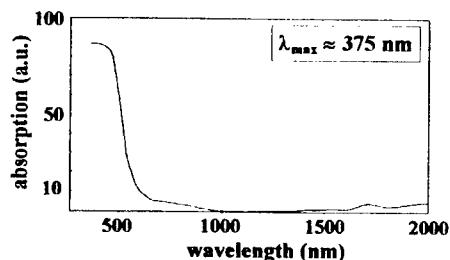


FIGURE 3 Absorption spectrum of the thin film

A  $\text{CH}_2\text{Cl}_2$  solution of the copolymer was used to make a spin-coated layer of 5  $\mu\text{m}$  thickness on the first optical glass slab (refractive index  $n' = 1.501$ ). The layer was then heated at  $80^\circ\text{C}$  for about two hours. After cooling, the second glass slab was carefully squeezed on the free face of the copolymer layer using a Teflon screw to eliminate the air gap.

## PRINCIPLE

We consider an optical thin film whose thickness is about a few wavelengths, sandwiched between two identical linear glass slabs. The refractive index of the film varies according to the optical Kerr law  $n = n_0 + n_2 I$ , with  $n_0$  the linear index,  $n_2$  the Kerr coefficient and  $I$  the intensity. The linear slabs have a refractive index  $n'$  slightly higher than  $n_0$ .

Figure 1 illustrates the principle of the experiment. At low intensity, the incident beam is adjusted either slightly higher than the critical angle of incidence  $\theta_c$  (positive  $n_2$  case, total internal reflection occurs but there is low transmission due to optical tunneling effect) or slightly lower than  $\theta_c$  (negative  $n_2$  case, high transmission). By increasing the incident intensity  $I$ , the value of  $\theta_c = \sin^{-1}[(n_0 + n_2 I) / n']$  changes. If  $n_2$  is positive,  $\theta_c$  can be increased beyond the incident angle. Therefore, from a threshold intensity, the layer switches from a weak transmission state (0) to a high state (1). On the contrary, if  $n_2$  is negative, the transmittance of the layer decreases gradually from a relatively high state (1) to a low state (0) as  $\theta_c$  shifts towards the total internal reflection state.

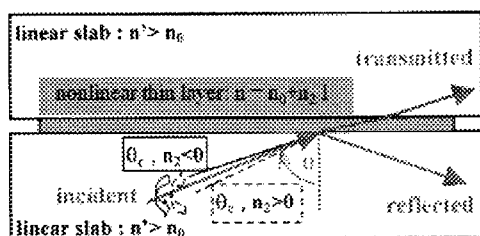


FIGURE 1 Non-resonant optical transmission through a nonlinear Kerr sandwich near the critical angle of incidence.

## EXPERIMENTS AND RESULTS

### Synthesis of the Copolymer(MMA-Octupole)

The octupolar monomer 2,4,6-tris(5'-thioallyl-2,2'-dithienyl)-1,3,5-triazine was synthesized via a triple aromatic nucleophilic substitution of dithienyl derivatives on cyanuric chloride<sup>[7]</sup>. Then, the new MMA-octupole copolymer was synthesized with quantitative yield by copolymerization of the allyl monomer with methyl methacrylate: 1g, 1.3mmol of the monomer was dissolved in 100 ml of toluene. Methyl methacrylate (1.5g, 15mmol) was added to it once. This mixture was heated at 100°C during five hours with catalytic amount of AIBN as radical initiator. After cooling at room temperature, the solvent was

The linear refractive index of the copolymer, measured by an optical refractometer, is  $n_0 = 1.477$  at  $\lambda_0 = 1064$  nm.

Figure 3 shows the absorption spectrum of the film. A single linear absorption band centered near 375 nm is displayed. We noticed that there was negligible shift of the absorption peak wavelength  $\lambda_{\text{max}}$  of the allyl octupolar monomer<sup>[7]</sup> after its copolymerization with MMA.

### Experimental Set-up

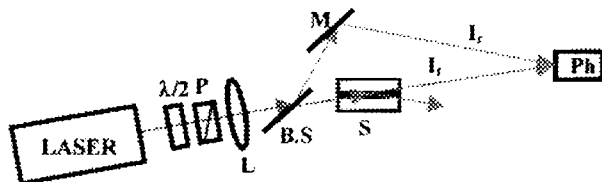


FIGURE 4 Experimental setup. Laser: pulsed Nd:YAG;  $\lambda/2$ : half-wave plate; P: polarizer; L: converging lens; B.S: beam splitter; M: mirror; S: nonlinear Kerr sandwich; Ph: photodiode;  $I_r$ : reference intensity;  $I_t$ : transmitted intensity.

The experimental set-up is shown in Figure 4. The experiments were performed with a Q-switched mode-locked Nd:YAG laser, operating at  $\lambda_0 = 1064$  nm with a repetition rate of 10 Hz. An electro-optic shutter ensured selection of a single nearly Gaussian pulse of 50 ps duration from the mode-locked pulse train. The  $\text{TEM}_{00}$  beam was linearly polarized and its energy was adjusted by means of a half-wave plate and a Glan polarizer. Then the beam was focused onto the nonlinear thin film by lens L (focal distance 400 mm). The measured waist radius was about 40  $\mu\text{m}$  and the incidence angle was adjusted at  $79.6^\circ$ , slightly lower than the measured critical angle of incidence at low intensity  $\theta_c = 79.74^\circ$ . Before the nonlinear sandwich, a reference pulse ( $I_r$ ) was taken from the incident pulse with a beam splitter. Both the reference and the pulse ( $I_t$ ) transmitted through the nonlinear sandwich impinged a fast photodiode connected to a 350 MHz analog oscilloscope. The time delay between the transmitted and reference pulses was adjusted so that both signals were clearly separated and appeared simultaneously on the screen of the oscilloscope. The reference intensity was adjusted so that  $I_r < I_t$  at low incident intensity.

### Results

Starting from the linear regime, the incident intensity was gradually increased and the relative peak values of the transmitted and the reference pulses were recorded.

Figure 5 shows the optical limiting behavior of the nonlinear sandwich, yielding a large diminution of the ratio  $I_t/I_r$  when incident intensity increased. Either one-shot or cumulative measurements were carried out to check the reversibility and the stability of the results against successive increases and decreases of the incident intensity. No hysteresis cycle was observed and we found that the optical limiting behavior exhibited complete reversibility and long-term stability, without parasitic slow effects due to pulse accumulation, such as thermal effects, photo-isomerization or photobleaching.



FIGURE 5 Evolution of  $I_t$  and  $I_r$  when increasing the incident intensity (10 ns/div).

Figure 6 presents the normalized transmittance of the sandwich versus the incident intensity. The experimental data (+) represent the intensity ratio of the transmitted pulse to the incident one on a single laser shot. When increasing the input intensity by nearly  $1 \text{ GW/cm}^2$ , the transmittance of the layer is decreased by more than 40%. The corresponding incident pulse energy increases from  $4 \mu\text{J}$  to  $6.5 \mu\text{J}$ .

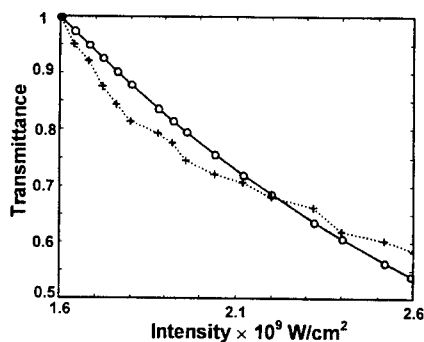


FIGURE 6 Normalized transmittance of the nonlinear sandwich versus the incident intensity. Crosses (+): experimental data. Open circles (o): theoretical values obtained from a plane-wave model by fitting the measurements with  $n_2 = -7.8 \cdot 10^{-17} \text{ m}^2/\text{W}$  and the other parameters listed in the text.

Starting from a plane-wave model, we fitted the experimental data using the experimental parameters listed above and the usual Fresnel relations giving the optical transmittance of a thin film<sup>[8]</sup>.

Though a focused Gaussian beam was used in the experiments, the plane-wave model has been shown to satisfactorily describe the behavior of a nonlinear Kerr sandwich in the case of negative  $n_2$ 's when incident Gaussian beam diameters higher than several wavelength are considered<sup>[2]</sup>.

The Kerr coefficient  $n_2$  of the thin film was thus determined by minimizing the difference between the measured and the theoretical transmittance curves using a least-square method. The negative value of  $n_2$  was found to be about  $-7.5 \cdot 10^{-17} \text{ m}^2/\text{W}$ , i.e. -20 times that of  $\text{CS}_2$ . This estimation is in rough agreement with extrapolated values deduced from additional picosecond Z-scan measurements that we realized on the MMA-octupole copolymer in toluene solutions.

## CONCLUSION

We have experimentally studied the non-resonant nonlinear transmittance near the critical angle of incidence of a thin film, made up from a new MMA-octupole copolymer, and surrounded by two linear glass slabs. In the single-shot picosecond regime, the experiments show that the transmittance decreases by more than 40% when increasing the incident intensity by nearly  $1 \text{ GW}/\text{cm}^2$ . This all-optical limiting action was found to be completely reversible and to exhibit long-term stability. The behavior of the nonlinear sandwich was in good agreement with a classical plane-wave model, from which a strong off-resonant negative  $n_2$  value of the MMA-octupole copolymer was found. We believe that this new stable polymer can be promising for nonlinear optical applications.

## ACKNOWLEDGMENTS

We thank the European Community for financial support and B. Carquille (Laboratoire d'Optique P.M. Duffieux) for providing the absorption spectrum.

## REFERENCES

- [1] T. Peschel, P. Dannberg, U. Langhein and F. Lederer, *J. Opt. Soc. Am.* B5, 29 (1988).
- [2] E. Lantz, D. Métin, H. Cornet and A. Lacourt, *J. Opt. Soc. Am.* B11, 347 (1994).
- [3] H. Mitchinel, *Opt. and Quantum Electron.* 30, 79 (1998).
- [4] a) A.E. Kaplan, *JETP Lett.* 24, 114 (1976). b) W.J. Tomlinson, J.P. Gordon, P.W. Smith and A.E. Kaplan, *Appl. Opt.* 21, 2041 (1982). c) H.W. Li, G. Martinelli, C. Froehly and A. Lacourt, *Opt. Commun.* 75, 321 (1990). d) R. Mountasser and A. Lacourt, *Ann. Phys.* 20, 93 (1995).
- [5] I.C. Khoo and P. Zhou, *Opt. Lett.* 17, 1325 (1992).
- [6] K. Strobl and I. Golub, *IEEE J. Quantum Electron.* QE-28, 1435 (1992).
- [7] F. Chérion, H. Maillotte, P. Audebert and J. Zyss, *Chem. Commun.*, 2083 (1999).
- [8] M. Born and E. Wolf, *Principles of Optics* 6<sup>th</sup> Edition, Pergamon Press, 61 (1980).



## Resonant Nonlinearities In An Organic Material: Irradiance Dependence.

R. RANGEL-ROJO<sup>a</sup>, H. MATSUDA<sup>b</sup>, H. KASAI<sup>c</sup>, AND H. NAKANISHI<sup>c</sup>

<sup>a</sup>Optics Department, Centro de Investigación Científica y Educación Superior de Ensenada, Apdo. Postal 2732. Ensenada B.C. 22860, México, e-mail: rrangel@cicese.mx; <sup>b</sup>Molecular Photonics Group, National Institute of Materials and Chemical Research, 1-1 Higashi, Tsukuba 305-8565, Japan; <sup>c</sup>Institute for Chemical Reaction Science Tohoku University, Sendai 980-77, Japan

We present experimental data for the irradiance dependence of the optical nonlinearity of a suspension of vanadyl-phthalocyanine nano-crystals in cyclohexane at different wavelengths across resonance. The refractive and absorptive contributions to the nonlinearity were resolved using the z-scan technique with a tunable picosecond laser source. A three-level model is used to describe the observed dependence of the nonlinearity with irradiance, which is considered as arising solely from excited-state absorption. A fit to the experimental data is made, allowing the extraction of molecular parameters which are of interest for a full characterisation of the nonlinearity.

**Keywords:** Excited-state absorption, nano-crystals, saturation

### INTRODUCTION

The optical nonlinearities of organic materials have been studied extensively, due to, among other things, their potential use in optical information processing devices. The manipulation of molecular structure and aggregation state in an almost infinite fashion, gives scope to the optimization of the nonlinear response for the intended

applications. The desired characteristics are: a reasonably large nonlinearity, small linear and nonlinear absorption, an ultrafast response, along with others such as processability, durability, etc. Recently, a systematic study of the spectral dependence of nonlinear refraction and nonlinear absorption has been carried out on different materials in nano-crystalline form in the on- and near-resonance regime [1] using the z-scan technique. By using materials in nano-crystalline form, some of the issues of material processability and control of aggregation state were addressed. These studies allowed the identification of spectral ranges where the nonlinearity is dominantly refractive, and therefore free of nonlinear absorption effects which are in general deleterious for the proposed applications.

Independently of the experimental technique employed, resonant interactions usually show a nonlinear response that is not purely of third-order, and the contribution of higher order terms, or some non-perturbative nonlinearity, needs to be considered. In either case, a study of the irradiance dependence of the nonlinear response becomes imperative to determine the proper figures of merit. A particularly important effect is the saturation of refractive index change, which can hinder attaining a sufficiently large phase change needed to perform switching operations [3].

In this paper we present experimental results for the nonlinear response of a vanadyl-phthalocyanine nano-crystal aqueous suspension at different wavelengths across resonance using the z-scan technique with a tunable picosecond laser source. The z-scan technique allowed the simultaneous determination of the refractive and absorptive contributions to the nonlinearity. We also present a study of the

irradiance dependence of the z-scan results at two different wavelengths where saturable and reverse saturable absorption are observed. A three-level model for the nonlinear response of the nano-crystals is used to explain the observed irradiance dependence of the nonlinear signals, which is explained in terms of excited state absorption.

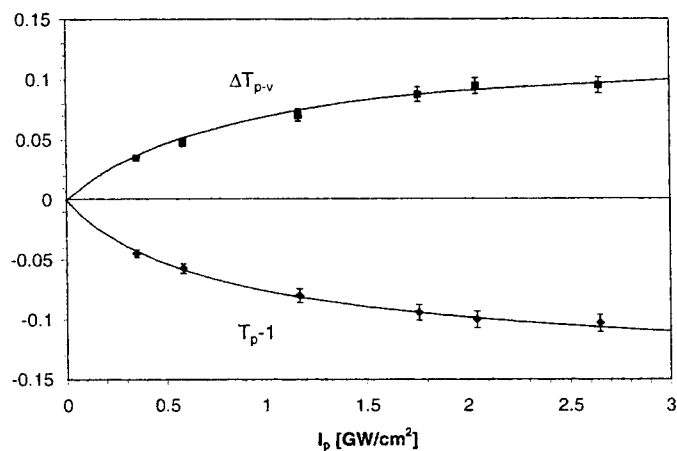


Figure 1. Irradiance dependence of z-scan results at 580 nm. The points are the experimental data, and the full lines the best fits obtained using the three-level model for the nonlinearity.

#### EXPERIMENTAL Z-SCAN RESULTS.

The sample studied was a cyclohexane suspension of tetrakis(thiohexyl) vanadyl-phthalocyanine  $\text{VOPc}(\text{C}_6\text{S})_4$  nano-crystals, which have on average a 40 nm diameter at a 0.2 mM concentration. The technique used to produce these nano-crystals has been described elsewhere [4]. The z-scan experiments were carried using 10 ps pulses from a tunable laser source based on an optical parametric generator pumped by the third harmonic of a mode-locked Nd:YAG laser. Figure 1 shows the

experimental z-scan results obtained for the VOPc nano-crystals as a function of irradiance for  $\lambda=580$  nm. For the open aperture z-scan, the measured  $T_p-I$  value, which is the difference between the peak transmittance  $T_p$  found at the focal plane and the linear transmittance measured far away from focus (normalized to 1), is shown. For the closed aperture z-scan we plot  $\Delta T_{p-v}$ , the difference between the normalized peak and valley transmittance:  $T_p-T_v$ . At this wavelength,  $T_p-I < 0$ , indicating that induced absorption is present. Figure 2 shows the results at 633 nm, where saturable absorption is now present. For both wavelengths the nonlinear refraction contribution remains positive [2]. From the figures is clear that a saturation effect is present, *i.e.* the transmittance changes do not grow linearly with irradiance, as it would be expected for a purely third-order nonlinearity [5].

### THREE-LEVEL MODEL.

In order to explain the observed irradiance dependence, a microscopic model for the response of the material is needed. A three-level model has been successfully used to describe the spectral dependence of the nonlinearity of polydiacetylene nano-crystals [1], and since this model results in a non-perturbative expression for the susceptibility, it can be used to describe the irradiance dependence of the response. According to this model, the real and imaginary components of the effective susceptibility  $\chi_{eff}$  are given by:

$$\text{Im } \chi_{eff} = \frac{n_0 c}{\omega} \alpha_0 \left\{ \frac{p[\sigma_{23}(W_{21} + W_{32}) + \sigma_{12}W_{32}] + W_{21}W_{32}}{3p^2\sigma_{12}\sigma_{23} + p[W_{21}\sigma_{23} + 2W_{32}\sigma_{12}] + W_{21}W_{32}} \right\}, \quad (1)$$

and,

$$\text{Re } \chi_{\text{eff}} = \frac{n_0 c}{\omega} \alpha_0 \times \left\{ \frac{p[(\sigma_{12} W_{32} + \sigma_{23} W_{21}) \Delta_{21} T_2 + \sigma_{23} W_{32} \Delta_{23} T_3] + W_{21} W_{32} \Delta_{21} T_3}{3p^2 \sigma_{12} \sigma_{23} + p[W_{21} \sigma_{23} + 2W_{32} \sigma_{12}] + W_{21} W_{32}} \right\}, \quad (2)$$

where  $p = I/\hbar\omega$  is the photon flux,  $W_{ji} = 1/\tau_{ij}$  are the transition rates,  $\Delta_{ji} = \omega - \omega_{ji}$ , the detuning factors, and  $\sigma_{ij}$  the absorption cross-sections for the  $j \rightarrow i$  transitions,  $N_0$  is the number density, and  $\alpha_0 = N_0 \sigma_{12}$ . This complex susceptibility can be used to calculate the irradiance-dependent absorption coefficient  $\alpha(I)$ , and the nonlinear refractive index change  $\Delta n(I)$ , which are then used to calculate the z-scan traces [6].

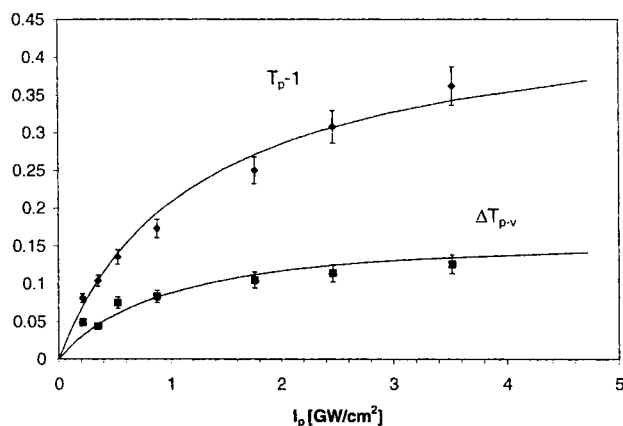


Figure 2. Irradiance dependence of z-scan results at 633 nm. The points are the experimental data, and the full lines the best fits obtained using the three-level model for the nonlinearity.

Figures 1 and 2 show the fits to the experimental data obtained using this model. As it can be seen from the figures, the model worked well for the different wavelengths studied. Some of the parameters,

namely  $\Delta_{21}$ ,  $\Delta_{23}$ ,  $T_2$ ,  $T_3$ , and  $\alpha_0$ , are extracted from the linear absorption spectrum. The fits to the irradiance dependence of the z-scan data yields the values of the ratios  $\sigma_{12}/\sigma_{32}$ ,  $\tau_{21}/\tau_{32}$ , and the saturation irradiance  $I_s$  at the two wavelengths studied, which are given in table I.

$\lambda[nm]$	$\Delta_{12} \times 10^{15}$ [Hz]	$\Delta_{23}/\Delta_{12}$	$I_s[GW/cm^2]$	$\sigma_{32}/\sigma_{21}$	$\tau_{32}/\tau_{21}$
580	0.39	4.48	0.75	$2.0 \pm 0.1$	$< 0.002$
633	0.12	12.5	0.59	$0.35 \pm 0.05$	$< 0.002$

Table I. Parameters extracted from the fits to experimental data using the three-level model described in the text.

The parameters thus extracted, will allow the evaluation of the different figures of merit that assess the performance of the material in all-optical switching devices.

## REFERENCES

- 1.- R. Rangel-Rojo, S. Yamada, H. Matsuda, H. Kasai, H. Nakanishi, A.K. Kar, B.S. Wherrett, *J. Opt. Soc. Am. B* **15**, 2937 (1998).
- 2.- R. Rangel-Rojo, S. Yamada, H. Matsuda, H. Kasai, Y. Komai, S. Okada, H. Oikawa, and H. Nakanishi, *Jpn. J. Appl. Phys. Part 1* **38**, 69 (1999).
- 3.- G.I. Stegeman, R.H. Stolen, *J. Opt. Soc. Am. B* **6**, 652 (1989).
- 4.- H. Kasai, H.S. Nalwa, H. Oikawa, S. Okada, N. Minami, A. Kakuta, K. Ono, A. Mukoh, and H. Nakanishi, *Jpn. J. Appl. Phys.* **31**, L1132 (1992).
- 5.- M. Sheik-Bahae, A.A. Said, E.W. Van Stryland, *Opt. Lett.* **14**, 955 (1989).
- 6.- R. Rangel-Rojo, H. Matsuda, H. Kasai, H. Nakanishi, submitted to *J. Opt. Soc. Am. B*.

## Thin Films of a Novel Polydiacetylene for Applications to All-Optical Signal Processing

S. SOTTINI, G. MARGHERI, E. GIORGETTI, F. GELLI,  
*Istituto di Ricerca sulle Onde Elettromagnetiche - CNR, Via  
Panciatichi 64, 50127, Firenze, Italy.*

A. CRAVINO, D. COMORETTO, C. CUNIBERTI, C.  
DELL'ERBA, I. MOGGIO and G. DELLEPIANE  
*INFM, INSTM, Dipartimento di Chimica e Chimica Industriale,  
Università di Genova, Via Dodecaneso 31, 16146 Genova, Italy.*

The measure of the third order nonlinear susceptibility of the novel polycarbazolydiacetylene polyDCHD-HS is described. The experiments were performed at  $\lambda = 1064$  nm and in the ps time regime, by using Surface Plasmon Spectroscopy. They gave a value of  $\chi^{(3)} = -4.4 \times 10^{-17} \text{ (m/V)}^2$  for the real part, while the imaginary part was below  $10^{-18} \text{ (m/V)}^2$ .

**Keywords:** Polymer Films, Surface Plasmon Spectroscopy

### I. INTRODUCTION

Polydiacetylenes (PDAs) exhibit one of the largest available off-resonance values of  $\chi^{(3)}$ . These polymers can be synthesized from monomers with special substituents. In particular, the synthesis of

novel carbazolyldiacetylene monomers has opened a way to the preparation of soluble PDAs that, in powder form, arrange in two-dimensional highly ordered supramolecular assemblies. Such organization was detected by powder X-ray diffraction for at least one of these polymers, the polyDCHD-HS (which is a polycarbazolyldiacetylene having long alkyl groups on the carbazoyl substituents to the backbone), and found to consist of polydiacetylenic columns in a hexagonal array [1]. Moreover, the absorption spectra of solutions of polyDCHD-HS in benzene show an excitonic peak around 540 nm which has an intensity and a sharpness never observed before in solutions of PDAs and typical of PDA single crystals. These results suggest a certain degree of order also in spun films and a consequently large  $\chi^{(3)}$ , thus stimulating our research on the linear and nonlinear properties in polyDCHD-HS spun films.

## II. NONLINEAR TESTS ON ULTRATHIN PDCHD-HS FILMS

The synthesis of the monomer DCHD-HS is reported in ref. 1.

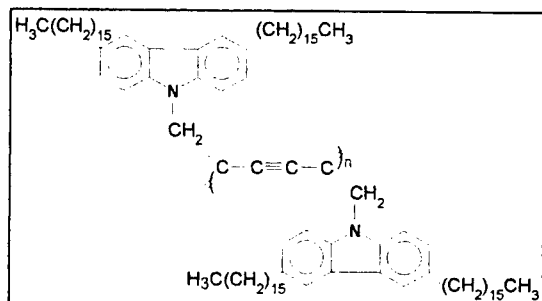


FIGURE 1 Chemical structure of polyDCHD-HS.



Its thermal solid state polymerization was performed at 85° C (m.p. 95° C ) and the chemical structure of polyDCHD-HS is reported in Fig. 1. Several films of polyDCHD-HS with thickness ranging between 9 nm and 3.6  $\mu$ m were spun on soda lime microscope slides. Their characterization as optical waveguides and preliminary photobleaching tests to obtain film patterning are described elsewhere [2, 3]. The Kerr nonlinearity of thinner films was investigated by Surface Plasmon Spectroscopy (SPS). It is well known that the excitation of a surface electromagnetic wave at the interface between a metal and a dielectric is an angular-dependent phenomenon, that exhibits a sharp minimum of the reflected light (resolution  $\approx 0.01^\circ$  or even better), so that even a weak variation of the optical properties of the media forming the interface can be detected with extreme sensitivity. For this reason, SPS has been extensively used to measure the thickness and the complex dielectric constant of ultrathin layers. On the contrary, to our knowledge, only few SPS tests have been performed to monitor Kerr nonlinearities, that produce intensity dependent refractive index changes in thin films [4]. The need of TM polarized light and the fact that the film under investigation must be deposited on a metal layer, typically silver, represent non negligible limitations of the technique. However, these drawbacks are largely balanced by the insensitivity to film inhomogeneities and propagation losses and by the possibility of monitoring the nonlinearity of ultrathin layers of material, thus helping to get an insight into the film structure and the origin of its nonlinearity.

The nonlinear SPS experiments were performed on a set of very thin (9÷50 nm) films of polyDCHD-HS which were deposited on a

silver layer by spinning from dilute toluene solutions ( $4\div 8$  g/l). The silver films ( $30\div 60$  nm-thick) were obtained by electron gun assisted evaporation on glass microscope slides. The resulting glass/metal/polymer samples were coupled to the hypotenuse of a  $45^\circ$  total internal reflection BK7 prism, thus achieving a Kretschmann configuration [5]. The Kretschmann prism including the sample was mounted on a remotely controlled high precision rotating stage. The *p*-polarized light from a Nd-YAG mode locked laser ( $\lambda = 1064$  nm, 27 ps FWHM pulses with 10 Hz repetition rate) was focussed on the prism hypotenuse by a converging lens and the incident energy was varied by acting directly on the amplification factor of the laser.

Before the spin coating of the polymer film, the thickness and complex dielectric constant of the silver layer were measured by SPS at low and high intensities: these parameters are successively required by the best fit procedure to extract the linear and nonlinear parameters of the polymer film. At the same time, these measurements allowed to check the behaviour of silver within the irradiation regime used in the experiments. In fact, though a significant thermal absorption of the polymer film can be avoided by using few short laser pulses and low repetition rates, a fast absorption of the laser light inside the silver layer with consequent increase of the temperature at the metal/polymer interface cannot be excluded and deserves a careful investigation. Indeed, we observed some evidence of the heating of the silver films. This effect was measured and taken into account in the best fit procedures by introducing an intensity dependent dielectric constant of silver. As a matter of fact, the temperature increase at the silver/polymer

interface was considered also in ref. 4 with encouraging conclusions: no evidence of a significant thermal contribution to the polymer nonlinearity was detected. Also in our tests, though an exhaustive analysis is still in progress, the silver heating seemed quite uncorrelated to the behaviour of the polymer non linear index.

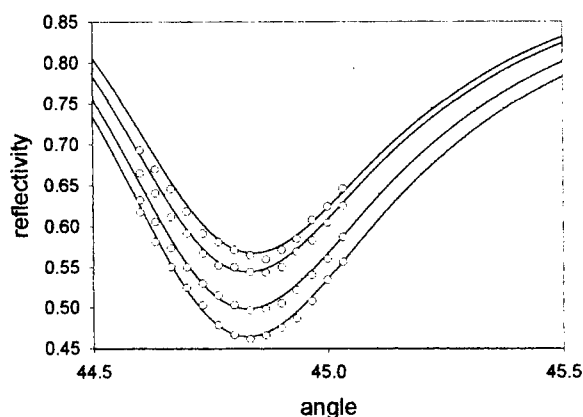


FIGURE 2 Reflectivity versus coupling angle for a 46.7 nm-thick PDCHD-HS film deposited on a 30.8 nm-thick silver layer at surface plasmon intensities of 0.086, 0.13, 0.32 and 0.55  $\text{GW}/\text{cm}^2$  (increasing in downward direction). Dots and continuous lines represent experimental points and best fit curves, respectively.

After the polymer film deposition, SPS measurements were performed with different pulse energies and the reflectivity was registered for several angles of incidence around its minimum. Fig.2 shows a typical result: the theoretical curves which are characterized by a decreasing minimum as the pulse energy increases, fit very well the reflectivity measurements. From the best fit parameters, in particular from the angular shift of the reflectivity dips, the refractive

component of the material  $\chi^{(3)}$  could be evaluated by assuming a Kerr behaviour. In the case of Fig.2, a real and negative  $\chi^{(3)} = -1.2 \times 10^{-17} \text{ m}^2/\text{V}^2$  was found. Concerning its imaginary part, we could only give the upper limit of  $10^{-18} \text{ m}^2/\text{V}^2$ .

Similar results were obtained in the same intensity regime with other samples, having thickness between 9 and 15 nm. For each sample, the corresponding  $\chi^{(3)}$  values were measured in different film areas and varied between  $-4.7$  and  $-1 \times 10^{-17} \text{ m}^2/\text{V}^2$  with a 30% experimental error. It was also verified that the sample behaviour was perfectly reversible within the adopted intensity range: on this basis, any material damage during the experiments could be excluded.

### III. CONCLUSIONS

The third order nonlinearity of polyDCHD-HS films was measured at  $\lambda = 1064 \text{ nm}$  and gave a very large value: its real part was significantly larger than that of PTS at the same wavelength, though our tests are not yet conclusive, particularly for what concerns possible thermal contributions and the presence of higher order nonlinear terms. In case further investigations of polyDCHD-HS films at 1300 and 1550 nm confirm these results, such films could be promising candidates for applications to all optical signal processing devices

### ACKNOWLEDGMENTS

This research was partially supported by the Italian Progetto Finalizzato MST-II of the National Research Council.

## REFERENCES

1. B. Gallot, A. Cravino, I. Moggio, D. Comoretto, C. Cuniberti, G. Dellepiane, *Liquid Crystals*, 1437-1444, **26**, 10 (1999).
2. A. Cravino, I. Moggio, C. Dell' Erba, D. Comoretto, C. Cuniberti, G. Dellepiane, E. Giorgetti, D. Grando, S. Sottini, *Synthetic Metals*, 943-944, **102:1-3** (1999).
3. E. Giorgetti, G. Margheri, F. Gelli, S. Sottini, D. Comoretto, A. Cravino, C. Cuniberti, C. Dell'Erba and G. Dellepiane, Proceedings of the International Conference on Lasers '99, Quebec City (Canada), Dec. 1999 (in press).
4. R.J. Cook, N.P.K. Cotter, J.R. Sambles, R. Rangel-Rojo, G. Spruce, B.S. Wherret, *Optics. Comm.*, 344-352, **113** (1994).
5. Y.R. Shen, *The Principles of nonlinear optics*, Chapter 25, New York (1984).

## **SESSION G: FIBERS AND WAVEGUIDES**

## Drift correction of polymer based Mach-Zehnder modulators

P. LABBÉ<sup>a,b</sup>, A. CLOUQUEUR<sup>b</sup>, R. HIERLE<sup>b</sup>, E. TOUSSAERE<sup>b</sup>,  
J. ZYSS<sup>b</sup>

<sup>a</sup> *Centre de Recherche Motorola - Paris, Espace technologique de  
Saint Aubin, 91193 Gif-su-Yvette, France*

<sup>b</sup> *ENS-Cachan, LPQM, 61, avenue Président Wilson, 94235 Cachan,  
France.*

The maturing of electrooptic polymer based Mach-Zehnder intensity modulators qualifies them as serious contenders for telecom applications. Their manufacturing is now at the quality control level and several outstanding demonstrations of their capacities have been reported (high modulation up to 110GHz [1], quenching voltages lower than 2V [2], polarization insensitivity [3] and long term stability [4]). Nevertheless, a slow drift of their characteristics has been observed.

In order to solve this problem, we report an electronic system that is able to follow the evolutions of the modulator characteristics so as to correct the slow variations of the operating point. This approach will further enhance the reliability of this type of devices.

Keywords Drift correction; Intensity modulator; Polymer

### INTRODUCTION

Different factors may modify the stability of electro-optic polymer modulators. Factors which may induce short term variations of the

modulation amplitude include space charge fluctuations upon application of DC electric field or thermo-optic effects due to temperature variations in asymmetric devices. Long term effects may be due to the relaxation of chromophore orientation, cracks due to mechanical aging or long term photo-degradation. In this study we address the problem of cancelling fluctuations of the modulation efficiency in polymer Mach Zehnder modulators through the application of an adequate bias correction electric field.

Since the modulators were characterized on an optical bench without any temperature stabilization, drift of their modulation characteristics could be observed as a shift of the operating point and can be expressed by the addition of a static phase  $\varphi^s$  (ideally null) in the modulated intensity:

$$I_s = \frac{I_c}{2} \left\{ 1 + \sin \left[ \varphi^d \sin (\Omega t) + \varphi^s \right] \right\} \quad (1)$$

$\varphi^d$  is the dynamic phase amplitude which can be determined by the measurement of the extinction tension  $V_\pi$ ;  $I_c$  and  $I_s$  are the input and the output light signal intensities (defined figure 1). As soon as the drift occurs,  $\varphi^s$  is slowly varying compared to the modulating rate and can be compensated for by the application of a constant voltage. Expressing the output signal as a sum of Fourier harmonics, we obtain:

$$\begin{aligned} I_s = & \frac{I_c}{2} \left\{ 1 + \sin (\varphi^s) J_0 (\varphi^d) \right. \\ & + 2 \cos (\varphi^s) \sum_{k=0}^{+\infty} J_{2k+1} (\varphi^d) \sin [(2k+1) \Omega t] \\ & \left. + 2 \sin (\varphi^s) \sum_{k=1}^{+\infty} J_{2k} (\varphi^d) \cos [2k \Omega t] \right\} \end{aligned} \quad (2)$$

where  $J_n$  are the first kind  $n$ -th order Bessel functions. A signed correction of the drift phenomenon can be obtained measuring the second harmonic of the optical modulation frequency in the output intensity (corresponding to  $k=1$  in the last term of equation 2).

We therefore designed and tested a system able to generate a signal at low frequency to modulate the optical signal and detect the corresponding second harmonic of the response (explain in §1). In §2, we will show that this system can be made independent from any



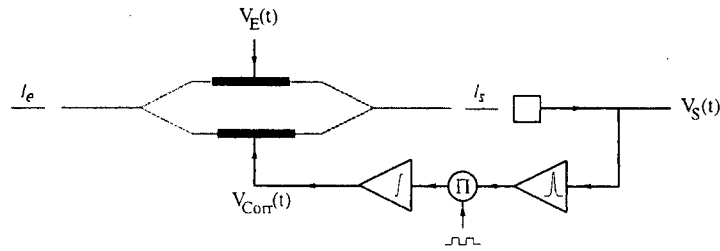


FIGURE 1: Global scheme of the system.  $I_e$  and  $I_s$  are the input and output light intensities respectively.  $V_E(t)$  is the command voltage and  $V_S(t)$  the output voltage.  $V_{Corr}(t)$  is the bias voltage.

kind of information coded at higher frequencies and fed simultaneously to the modulator electrodes. The global scheme of the setup is presented in figure 1.

## 1. EXPERIMENTAL SETUP

We used a linearly polarized laser diode at  $\lambda = 1.3\mu m$  without any temperature nor current regulation as optical source. Electrooptic polymer modulators were made by spin coating different polymer layers on an oxidized silicon wafer with photolithographically patterned gold electrodes [6]. Measured dynamic and static halfwave voltages were 15V and 5V respectively. The device was butt coupled with  $\times 20$  microscope objectives and alignment stability was ensured by piezo-electric micro-positioners. The optical signal was detected with an InGaAs based photodiode (model G3476-03 from Hamamatsu) reversly biased under 15V and was subsequently amplified ( $\times 50$ ). To avoid any evolution of the source characteristics, we normalized the output signal of the photodiode by the continuous part of the signal (proportional to the total power of the laser source). The global system presents a 1.8MHz bandpass limited by photodiode electronics.

The first experiment consisted in adding a triangular signal at low frequency (arbitrarily centered at 520Hz) to the bias voltage. The

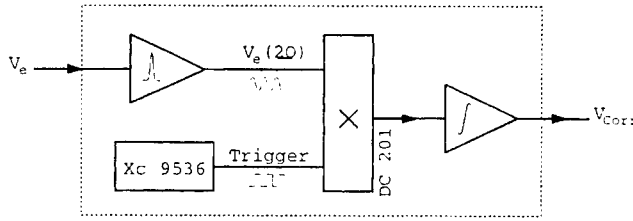


FIGURE 2: The input voltage  $V_e$  is first filtered by a selective amplifier centered a twice the modulation frequency multiplexed by a DC 201 with a trigger signal produced by a FPGA (Xilinx 9536) and then integrated in order to build the correcting signal  $V_{corr}$ .

operating point is obtained when the amplitude of the second order term of the optical signal is minimum. A lock-in detection is therefore used at twice the modulation frequency to yield the amplitude of the second harmonic distortion which is then amplified and mixed back with the driving voltage as a correcting bias signal (electrical feedback represented on figure 2).

All amplification stages are experimentally determined in order to minimize the number of iterations and the time constant of the global correction. Moreover, the bias voltage amplitude is wide enough to follow a shift of twice the extinction voltage. Taking into account the speed of the drift phenomenon, a correction time constant of a millisecond is sufficient.

In order to characterize the performances of the system, we measured the amplitude of a high frequency pure harmonic introduced in the system as data signal and the bias voltage produced to correct the drift. Drift evolution is evidenced in figure 3, in first minutes of application of a bias field, where the DC correction has to be adjusted in order to stabilize a 290kHz modulation signal amplitude.

The system also shows its robustness to a quicker disruption such as an illumination which usually shifts the operating point within a few seconds.

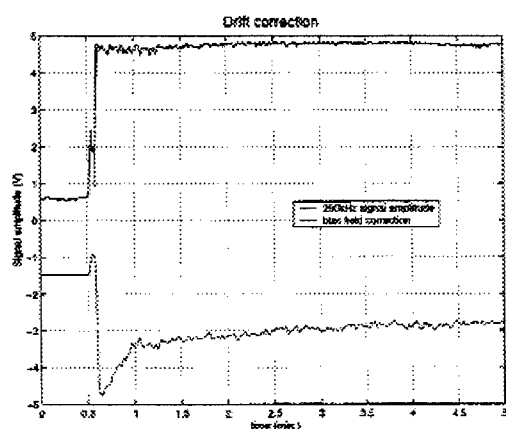


FIGURE 3: Temporal response of the system when the feedback loop is turned on at  $t=30s$ .

## 2. GLOBAL SYSTEM EXPERIMENTATION

To demonstrate the capabilities of our system, we introduce a real data signal, issued from a CD player. The data signal approximately 20kHz large was coded on a 290kHz frequency carrier. At the end of the system, the signal was amplified by a selective amplifier centered at 290kHz, demodulated by an integrated phase lock loop (Motorola CD4046) and fed to a speaker. This first level demonstration was build with a low frequency carrier because of the simplicity of the electronic devices used to build the modulation/demodulation chain.

We didn't notice any perturbations on the functioning of the feedback loop : the drift correction has been checked during more than 12 hours without any problem.

## CONCLUSION

We have built-up a compact electronic system composed of simple and low-cost electronic devices allowing for analogue processing of the output signal of a Mach-Zehnder intensity modulator. The op-

erating point of a polymeric intensity modulator could be stabilized efficiently.

Further work will focus on increasing the frequency of the data carrier up to 800MHz and the bandwidth of the data signal in order to be compliant to the GSM standard.

### References

- [1] D. Chen, H. R. Fetterman, A. Chen, W. H. Steier, L. R. Dalton, W. Wang, Y. Shi, Applied Physics Letters, **70**(25), 3335-3337 (1997).
- [2] A. Chen, V. Chuyanov, S. Garner, H. Zhang, W. H. Steier, Optics Letters, **23**(6), 478-480 (1998).
- [3] A. Donval, E. Toussaere, R. Hierle, J. Zyss, Journal of Applied Physics, (to be published).
- [4] H.T. Man, H.N. Yoon, Applied Physics Letters, **72**(5), 540-541 (1998).
- [5] Y. Shi, W. Wang, W. Lin, D.J. Olson, J.H. Bechtel, Applied Physics Letters, **71**(16), 2236-2238 (1997).
- [6] R. Levenson, J. Liang, C. Rossier, R. Hierle, E. Toussaere, J. Zyss, *ACS Symposium (Series 601, Polymers for Second-Order Nonlinear Optics*, G.A. Lindsay, K.D. Singer Eds, 1995), pp.436-455.

## Gaussian Profile Bragg Gratings in Polydiacetylene Waveguides: Characterization and Application in Integrated Optics

MARK ANDREAS BADER AND GERD MAROWSKY

Laser-Laboratorium Göttingen e.V., Hans-Adolf-Krebs-Weg 1,  
D-37077 Göttingen, Germany

Optical nonlinear devices are required to control the processing of fast optical signals. Polymeric materials with high optical nonlinearities are particularly suited to realize novel all-optical switching concepts. To open up the wide field of device applications in integrated optics based on periodically structured planar polymer waveguides, we studied nonuniform Bragg gratings in polydiacetylene channel waveguides. The fabrication using an optimized photobleaching setup and optical characterization of shallow Gaussian profile gratings in the poly(4-BCMU) polydiacetylene is reported. The suitability of the system to nonlinear switching processes based on Bragg soliton generation is discussed.

**Keywords** polymer waveguides; Bragg gratings; poly(4-BCMU); integrated optics

## INTRODUCTION

Novel all-optical switching concepts based on Bragg grating structures in planar waveguides are of increasing interest for integrated optics [1]. A high third-order nonlinearity of the material causes a detuning of the photonic band gap of the periodic structure which, as a result, changes from its reflective to a completely transmissive state as intensity in the device is increased and so-called gap solitons that stabilize the switching process are created [2].

Nonlinear propagation effects resulting in all-optical switching or nonlinear optical pulse narrowing have been predicted and observed in both planar and fiber waveguide devices [3-6]. Organic materials such as the conjugated polymer polydiacetylene are known to be among the most promising candidates for high-speed photonic switching and signal processing concepts, due to their high third-order susceptibilities and fast response times [7].

We present the fabrication and characterization of high quality nonuniform Bragg gratings in planar poly(4-BCMU) waveguides and show the suitability of our system for all-optical switching phenomena.

## GRATING FABRICATION AND CHARACTERIZATION

Bragg gratings in planar poly(4-BCMU) waveguides of about 1.25  $\mu\text{m}$  thickness were fabricated by UV-photobleaching using the third harmonic of a picosecond Nd:YAG laser ( $\lambda_{\text{THG}} = 355 \text{ nm}$ ). A change in the refractive index  $n$  is induced in the material when irradiated by UV-light. The refractive index decrease  $\delta n/n$  per laser pulse was deduced from the bleaching behavior of the material, which we investigated by evaluating reflection and absorption spectra during irradiation. A linear bleaching rate with respect to the fluence on the polymer was found.

Our goal concerning the shape of the Bragg grating in the polymer film was to generate a periodic refractive index modulation that shows a Gaussian shaped envelope of the modulation amplitude. The idea was to use a Gaussian shaped UV laser beam to generate the desired index modulation. To provide this beam the third harmonic of the picosecond Nd:YAG laser with a diameter of 5.5 mm was focussed on a circular diamond pinhole with a diameter of 150  $\mu\text{m}$  using an optical lens with a focal length of 1 meter. The pinhole served as a spatial filter providing a Gaussian beam shape which was confirmed when monitored by a CCD camera. The  $1/e$ -width of the generated Gaussian beam was measured to be 4 mm at the position of the polymer film. Assuming a waist spot size  $w_0$  of 150  $\mu\text{m}$  the Rayleigh length is calculated to be  $z_R = 20 \text{ cm}$ .

This beam was used to illuminate a periodic phase mask which was optimized to diffract 355 nm light equally into the two first diffraction orders suppressing the zero and higher diffraction orders. By interference of these two first order diffraction beams on the polymer surface a periodic refractive index modulation was generated in the polymer film. An optimized setup, as shown in Figure 1, was used to

determine and control the grating period. The diffracted beams were led onto variable steering mirrors, the grating period was determined by the angle of incidence of the beams. With a phase mask of a center period of 720 nm, the angle of incidence onto the steering mirrors was set to a deviation of  $+3^\circ$  from a right angle with respect to the phase mask plane to get the grating period of  $g = 455$  nm as needed in our experiments. In addition, the remaining zero order noise of the phase mask, which amounts to about 2-3% of the incident intensity, can be completely suppressed. Good quality nearly Gaussian profile Bragg gratings were thus fabricated by applying this method, a clear improvement compared to gratings fabricated earlier by UV-photoablation [8] could be achieved. For the Bragg grating characterized in this work, we applied an energy density of about  $1.5 \text{ mJ/cm}^2$ , the polymer film was irradiated for about 20 minutes.

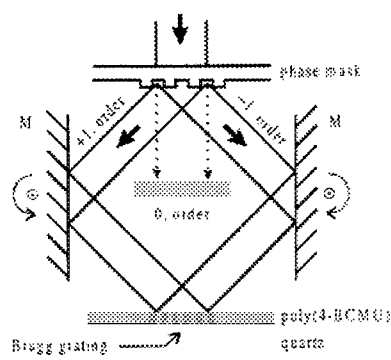


**FIGURE 1** Fabrication of Bragg gratings in planar poly(4-BCMU) waveguides by UV photobleaching. The  $\pm 1$ . diffraction orders of the phase mask interfere on the film surface.

For the linear optical characterization of the device, a 355 nm Nd:YAG-pumped continuously tunable optical parametric generator (OPG) was scanned across the photonic band gap of the Gaussian profile grating. The infrared idler beam with a pulse length of 40 ps and linewidth of  $3 \text{ cm}^{-1}$  was coupled into and out of the waveguide by two identical glass prisms. The transmission spectrum of the device was recorded at different incident intensities to allow the detection of intensity-dependent nonlinear effects.

According to the theory of planar dielectric waveguides [9], the effective index of refraction for the TE-mode in the waveguiding film is  $n_{\text{eff}} = 1.525$  assuming a film thickness of  $d = 1.25 \mu\text{m}$ , a refractive index of poly(4-BCMU)  $n_f = 1.572$ , and a refractive index of the quartz substrate  $n_s = 1.449$ , at a wavelength of 1400 nm.

The linear transmission of a Gaussian profile Bragg grating in a poly(4-BCMU) 200  $\mu\text{m}$  channel waveguide is shown in Figure 2. A grating period of  $g = 455 \text{ nm}$  was determined experimentally. The OPG was scanned across the photonic band gap centered at around 1370 nm. The transmitted signal completely vanishes in the stop gap of the grating whose full width at half maximum amounts to  $\Delta\lambda = 20.5 \text{ nm}$ . The steepness of the stop gap edges are given by 3.5 and 16.0  $\text{cm}^{-1}$  for the 25% threshold. This indicates a strong asymmetry in the transmission spectrum as expected for a Gaussian profile grating and the corresponding shape of its photonic band structure [10]. The calculated modulation strength of the refractive index for a Gaussian grating with these parameters is  $(\delta n/n)_{\text{max}} = (\Delta\lambda/\lambda)_{\text{max}} = 1.4 \times 10^{-2}$ .

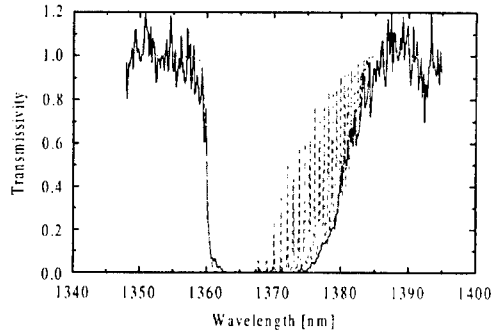


**FIGURE 2** Linear transmission of a Gaussian profile Bragg grating in a poly(4-BCMU) channel waveguide: comparison between experimental data (solid line) and theoretical fit (dashed line).

For uniform Bragg gratings, we earlier found transmission band edges of a considerably flatter shape. They are considered to be related to an interference pattern induced by the reflected light from both ends of the grating, which is smeared out mainly by the limited linewidth of our laser system. Nonuniform gratings and Gaussian profile gratings in



particular, however, show a smooth transition from the grating region to the unbleached waveguide and therefore favor steeper band edges in the transmission spectrum [10]. Thus, an intensity dependent shift of the band edge has a greater impact on the transmitted light and therefore the device can be more easily used in all-optical switching applications.

## DISCUSSION – APPLICATION IN INTEGRATED OPTICS

Fabry-Perot like resonances in the flat edge of the transmission spectrum, as expected for a Gaussian shaped grating [10], are clearly visible in the theoretical fit in Figure 2 (dashed line) which was carried out by solving the linear coupled mode equations [11]. The sharp peaks, however, are not resolved in the experimental data because of the finite laser linewidth of  $3 \text{ cm}^{-1}$ . Nevertheless, at some points of the experimental curve, one can guess the beginning of the resonance peaks. The parameters to describe the grating were obtained as a result of the theoretical fit. A good understanding of the shape of the transmission spectrum and the grating under investigation itself could be achieved. For the theoretical fit shown in Figure 2, we assumed a calculated effective index of refraction  $n_{\text{eff}} = 1.525$ , an experimentally determined linear absorption coefficient  $\alpha = 5 \text{ dB/cm}$ , and a device length  $l = 0.5 \text{ cm}$ . The grating fit parameters and their values are the design wavelength  $\lambda_B = 1384.1 \text{ nm}$ , the refractive index modulation  $\delta n/n = -0.0053$ , a DC over AC ratio for the grating structure  $r = 5.7$  (the ratio for a Gaussian grating usually is  $r_{\text{Gauss}} = 2$ ), and a full width at half maximum of the grating structure  $\Delta_{\text{fwhm}} = 0.072 \text{ cm}$ . Especially the large deviation of the DC to AC ratio from the usual Gaussian grating indicates an unexpected index modulation function. Apart from higher order Gaussian contributions in the laser beam shape, which we think can be neglected concluding from our beam shape investigation results, an incomplete overlap of the two diffracted beams could be a reason for that deviation from the expected Gaussian shape.

Considering all-optical switching applications of poly(4-BCMU) waveguides for integrated optics, we looked at the nonlinear behavior of the device. According to our numerical simulations, a shift of the transmission spectrum band edge of  $10 \text{ cm}^{-1}$  is expected, given the nonlinear refractive index of poly(4-BCMU)  $n_2 \approx 10^{-13} \text{ cm}^2/\text{W}$  ( $\chi^{(3)} \approx 10^{-11} \text{ esu}$ ) [12] and a power density in the waveguide of  $F \approx 10 \text{ GW/cm}^2$ , which is what we should be able to achieve in our experiments. This

shift should be easily demonstrated under the given conditions. However, any clearly detectable shift has not been observed in our experiments so far, which we believe is due to a weak coupling efficiency of the prism couplers and a possibly high scattering loss in the waveguide. We measured an extremely low coupling efficiency of 0.02%, the power loss in the waveguide is described by a measured absorption coefficient of  $\alpha = 5$  dB/cm. Two-photon-absorption as a reason for a strong power loss can be neglected in the investigated wavelength range. To observe all-optical switching in poly(4-BCMU) waveguides, and especially to realize the so-called gap-soliton switch, future experiments will be slightly modified. It is our goal to improve the coupling efficiency by using grating couplers as well as reduce the scattering losses in the polymer by extracting more thoroughly possible remaining monomer crystals from the  $\gamma$ -polymerized material. The existence of such crystals could lead to scattering losses that are sufficiently high to prevent nonlinear behavior in the waveguide.

In conclusion, we have characterized Bragg gratings in poly(4-BCMU) channel waveguides as a step towards device applications in integrated optics. We obtained waveguides and nonuniform gratings of high quality which, we believe, can be employed to demonstrate nonlinear optical switching at telecommunication wavelengths in the near future.

### Acknowledgments

We thank Irene Bauer of Universität Bayreuth, Lehrstuhl für Experimentalphysik II, Prof. Dr. M. Schwoerer, for her assistance in preparing the poly(4-BCMU) waveguides.

This work has been supported by the German Federal Department of Education and Research (BMBF), MaTech program, project 03N1021A4, and under the German-Canadian Science and Technology Agreement, project KAN MPT 28 "Gap Soliton Switches".

### References

- [1] G. I. Stegeman, A. Miller in *Photonics in Switching*, edited by J. E. Midwinter, Vol. 1, 81-145 (Academic Press, San Diego, 1993)
- [2] C. M. de Sterke, J. E. Sipe in *Progress in Optics*, E. Wolf, editor, Vol. XXXIII, 203-260 (Elsevier Science, Amsterdam, 1994)
- [3] P. D. Townsend, J. L. Jackel, G. L. Baker, J. A. Shelburne, S. Etemad, *Appl. Phys. Lett.* **55**, 1829 (1989); K. Sasaki, S. Sasaki, O. Furukawa, *Mat. Res. Soc. Symp. Proc.* **247**, 141 (1992)

- [4] N. D. Sankey, D. F. Prelewitz, T. G. Brown, *Appl. Phys. Lett.* **60**, 1427 (1992)
- [5] B. J. Eggleton, R. E. Slusher, C. M. de Sterke, P. E. Krug, J. E. Sipe, *Phys. Rev. Lett.* **76**, 1627 (1996)
- [6] D. Taverner, N. G. R. Broderick, D. J. Richardson, R. I. Laming, M. Ibsen, *Opt. Lett.* **23**, 328 (1998)
- [7] G. I. Stegeman in *Nonlinear Optics of Organic Molecules and Polymers*, edited by H. S. Nalwa, S. Miyata, 799-812 (CRC Press, Boca Raton, 1997)
- [8] M. A. Bader, H.-M. Keller, G. Marowsky, *Opt. Mat.* **9**, 334 (1998)
- [9] H. Kogelnik in *Topics in Applied Physics*, 2nd ed., edited by T. Tamir Vol. **7**, 13-81 (Springer-Verlag, Berlin, 1982)
- [10] J. E. Sipe, L. Poladian, C. M. de Sterke, *J. Opt. Soc. Am. A*, **11**, 1307 (1994)
- [11] C. M. de Sterke, J. E. Sipe, *Phys. Rev. A*, **42**, 2858 (1990)
- [12] C. C. Hsu, Y. Kawabe, Z. Z. Ho, N. Peyghambarian, J. N. Polky, W. Krug, E. Miao, *J. Appl. Phys.* **67**, 7199 (1990)

## Compression of Self-trapped Pulses in Kerr-type Planar Waveguides

Monika E. Pietrzyk <sup>a</sup>

Institut für Festkörpertheorie und Theoretische Optik,  
Friedrich-Schiller Universität Jena,  
Max-Wien Platz 1, Jena 07-743, Germany <sup>b</sup>

### Abstract

The compressors of optical pulses based on a Kerr-type planar waveguide enable one to obtain large compression, assuming that dispersion of the pulse is anomalous. However, the compression is localized in the waveguide (i.e. the distance of propagation on which the width of the pulse is nearly constant and equal to the minimal width, which can be obtained during the propagation of the pulse down the waveguide, is very small). We demonstrate how this can be avoided by introducing a subsidiary pulse, whose dispersion is normal. Based on the numerical solutions of two coupled (2+1)- and (1+1)-dimensional nonlinear Schrödinger equations (NSEs), which model the proposed configuration, we show that the best parameters of compression can be achieved in the case of vanishing dispersion of the subsidiary pulse, when the self-trapped solutions arise.

**Keywords:** planar Kerr waveguides, pulse compression.

Currently, there is a large demand for generation of short optical pulses which are useful for a variety of applications such as the measurement of ultrafast physical processes, optoelectronics sampling, generation of ultrafast X-ray radiation and ultrahigh-order harmonics. They can also be used to design spectroscopic and imaging devices for investigations of atomic or molecular systems, including diagnostic and therapeutic tools for microbiology and medicine. Moreover, generation of short optical pulses is of great interest for laser satellite communication, ultrahigh-bit-rate and long distance optical communication, ultrafast optical storage and data process-

<sup>a</sup>On leave from: Faculty of Physics, Warsaw University of Technology, Poland.

<sup>b</sup>*Monika.Pietrzyk@rz.uni-jena.de*

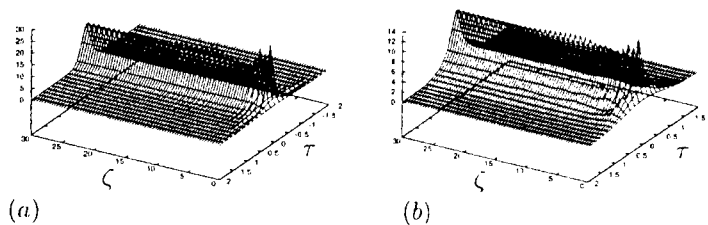


Figure 1: The evolution of the temporal cross-section of the signal pulse (a) co-propagating with the auxiliary pulse (b) (the evolution of the spatial cross-section is very similar),  $\kappa_1 = 1.0, \sigma = -1, \kappa_2 = 2.0$ .

ing. In the future, short pulses may play a crucial role in a development of all-optical computers. In addition, in some applications, e.g. for nanostructuring, it is essential that pulses are localized not only in time, but also in space. A compressor meeting this requirement can be based, for example, on a Kerr-type bulk medium [1] or a planar waveguide [2, 3] in which a dispersive pulse, with anomalous or normal dispersion, propagates.

This paper is devoted to the study of the compression mechanism of the pulse with anomalous dispersion, propagating together with a subsidiary pulse whose dispersion is neglected due to its large duration. Although, in the configuration under discussion, a simultaneous spatio-temporal compression of pulses can occur, we will consider only the temporal aspect of the compression.

The temporal compression can be characterized by three parameters. The first one, the maximal compression factor, is defined as follows:

$$c_{max} := \frac{w_\tau(0)}{w_{\tau min}(\zeta_{min})}, \quad \delta \ll 1,$$

where  $w_\tau(0)$  is the initial temporal width of the pulse, and  $w_{\tau min}$  is the minimal temporal width, which can be achieved during the propagation of the pulse down the waveguide. From the above definition it follows that the minimal temporal width of the pulse takes place at a propagation distance  $\zeta_{min}$ , which is referred to as the optimal length of the compression. Finally, we define the compression length

as the interval of the propagation distance,

$$\Delta\zeta := \{\zeta : w_\tau(\zeta) - \delta w_{rmin} < w_{rmin}\},$$

within which the evolution of the pulse does not change significantly, i.e. its temporal width is approximately constant and equals to the minimal width.

The compressor based on a planar waveguide with Kerr-type nonlinearity and a single pulse has been studied in the literature [3, 2]. It was shown that anomalous dispersion of the pulse results in a large compression factor,  $c_{max}$ ; moreover, spatio-temporal splitting of the pulse, which can occur in the case of normal dispersion, is eliminated. In order to optimize such a compressor (i.e. to obtain  $c_{max}$  and  $\Delta\zeta$  as large as possible) the values of the parameters describing the system should be just below the threshold of catastrophic self-focusing [4]. When this condition is satisfied the compression length can be quite large,  $\Delta\zeta \approx 1$ , which allow for a trivial adjustment of the compressor length. However, in this configuration, the maximal compression factor is rather small,  $c_{max} \approx 1.5$ . Besides, meeting the optimization condition would be, as a matter of fact, quite difficult in practice. This can be explained as follows: for a given medium which constitutes the basic element of the compressor (with a fixed value of the group velocity dispersion and the nonlinear refraction index), and for a fixed wavelength of the pulse, the only free parameter of the system is the energy of the pulse. It means that such a compressor cannot be considered as a universal device, for its operation is limited to pulses with energy belonging to a narrow interval of values (i.e. just below the threshold of catastrophic self-focusing).

In order to improve the operation of the above described compressor we consider that a subsidiary pulse is introduced to the system. Such a configuration was studied in [4], where it was assumed that the subsidiary pulse propagates in normal dispersion regime. It was shown that the optimization of the compressor can be achieved either when (i) the values of the parameters describing the configuration are just below the threshold of catastrophic self-focusing or when (ii) the dispersion of the auxiliary pulse vanishes. In the case (i) the maximal compression factor and the compression length can be, respectively,  $2.5 \div 3$  times larger and  $1.5 \div 5$  times smaller than the corresponding values in the configuration with a single pulse. However, the compression length in this case is rather large. We will

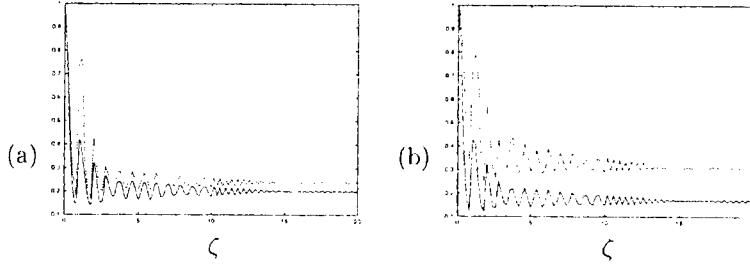


Figure 2: The dependence of the temporal,  $w_\tau$ , (the dotted lines) and spatial,  $w_\zeta$ , (the continuous lines) widths of the signal pulse, (a) co-propagating with the auxiliary pulse, (b),  $\kappa_1 = 1.0$ ,  $\sigma = -1$ ,  $\kappa_2 = 2.0$ .

try to answer to the question whether or not it is possible to remove the latter disadvantage. We will concentrate basically on the case (ii), i.e. vanishing dispersion of the subsidiary pulse.

The configuration with a subsidiary pulse, as described above, can be modeled by a system of two coupled (2+1)- and the (1+1)-dimensional NSEs:

$$i \frac{\partial}{\partial \zeta} \Psi_1 + \frac{1}{2} \frac{\partial^2}{\partial \xi^2} \Psi_1 + \frac{1}{2} \sigma_1 \frac{\partial^2}{\partial \tau^2} \Psi_1 + (|\Psi_1|^2 + 2|\Psi_2|^2) \Psi_1 = 0, \quad (1a)$$

$$i \frac{\partial}{\partial \zeta} \Psi_2 + \frac{1}{2} \frac{\partial^2}{\partial \xi^2} \Psi_2 + (|\Psi_2|^2 + 2|\Psi_1|^2) \Psi_2 = 0, \quad (1b)$$

where  $\zeta, \tau, \xi$  denote, respectively, the longitudinal coordinate, the local time, and the transverse spatial coordinate. The subscript  $j = 1$  ( $j = 2$ ) corresponds to the pulse referred to as the signal (subsidiary) pulse. The second terms in equations (1)a,b are associated with diffraction, which causes spreading of the pulse in space. The third term in equation (1)a is due to first-order group velocity dispersion, which leads to temporal broadening of the signal pulse; the dispersion-to-diffraction ratio,  $\sigma$ , is positive, since it is assumed that the signal pulse propagates in anomalous dispersion regime. The forth term in (1)a and the third one in (1)b describes self-phase modulation, while the last terms in (1)a,b describe cross-phase modulation - a nonlinear effect through which the phase of one pulse is affected by another pulse and, as a result, leads to a redistribution of energy between pulses. The terms describing four-wave mixing

are neglected, i.e. energy transfer between pulses is not taken into account. The terms proportional to the difference in group velocities of the pulses are also omitted.

Based on the numerical simulations of the set of equations (1)a,b we found that when the parameters of the system are properly chosen, i.e. the energy of the signal pulse is below the threshold of catastrophic self-focusing and energy of the auxiliary pulse is above the threshold of soliton generation, there can exist self-trapped solutions to (1)a,b, which propagate down the waveguide with constant shapes, amplitudes and widths. As an example let us examine the following parameters:  $\kappa_1 = 1.0, \sigma = -1, \kappa_2 = 2.0$ . From Figure 1, where the temporal cross sections of the pulses have been displayed (the evolution of the spatial cross sections are very similar), it is evident that both pulses undergo periodic oscillations. The amplitudes of these oscillations decrease with the propagation distance,  $\zeta$ . For sufficiently large propagation distance,  $\zeta > 15$ , the oscillations' amplitudes practically vanish, giving rise to the self-trapped solution. The formation of the self-trapped solution can be explained as follows: the pulse with negligible dispersion, since its dynamics can be modeled by integrable (1+1)-dimensional NSE, creates a waveguide in the medium in which it propagates and the other pulse gets trapped into this waveguide [5]. From Figure 2, which displays the evolution of the temporal and spatial widths of the pulses, it is evident that both widths of the pulses, which constitute such a self-trapped solution, are few times smaller than the initial widths. It means that the formation of the self-trapped solution is accompanied by a spatio-temporal compression. The parameters of the compressor operating in the proposed configuration would be as follows: large maximal compression factor,  $c_{max} \approx 5$ , large optimal length,  $\zeta_{min} \approx 15$ , and also large compression length,  $\Delta\zeta \gg 1$  (the maximal compression factor is more than 3 times larger, and the optimal length of the compressor is at least 10 times bigger than the corresponding values for a compressor with a single anomalous pulse). Note that the optimal length of the compressor is equivalent to the distance of propagation necessary for the formation of self-trapped solutions. The compression length, which is associated with the distance of propagation on which self-trapped solutions maintain their shapes, should be infinitely large, assuming that self-trapped solutions are stable against small perturbations (we hope to analyze this



question in a forthcoming publication). Moreover, in such a configuration much smaller energies of signal pulses can be used to obtain the same compression as in the single-pulse case. Besides, the compressor operating in the configuration under discussion, as opposite to the compressor with a single pulse, can be viewed as a universal device. Its operation only slightly depends on initial parameters of the signal pulse: since the compression length is relatively large, it is always possible to choose the length of compressor in such a way that optimally compressed pulses are obtained in the output, irrespective of their initial shapes, amplitudes and widths. To our knowledge, there is only one circumstance which can be considered as a disadvantage of the proposed two-pulse configuration: namely the large optimal length of the compressor, which requires long waveguides and implies technical problems with preparing them. However, we believe that the proposed configuration has potential to be realized in practice. For this purpose AlGaAs structures, which have high nonlinear refraction index and large damage threshold, could be used. In this paper we investigated only the temporal aspect of the compression; however, in the configuration under discussion one obtains pulses which are confined not only in time but also in space. Such pulses, compressed both temporally and spatially, can be beneficial, e.g., for nanostructuring. Note also that the two-pulse configuration proposed in this paper could be used also in optical steering or switching devices.

## References

- [1] Y. Silberberg, Opt. Lett. **15**, 1282 (1990).
- [2] A. T. Ryan, G. P. Agrawal, J. Opt. Soc. Am. B. **12**, 2382 (1995).
- [3] M. Pietrzyk, Opt. Q.E. **29**, 579 (1997).
- [4] M. E. Pietrzyk, to appear in J. Mod. Opt. (2000)
- [5] M. E. Pietrzyk, to appear in Rep. Math. Phys. (2000)

## Channel Waveguide Fabrication of Organic Nonlinear Optical Crystal, DAST, by Using Oxygen RIE

KAZUYA TAKAYAMA, MUNEO YOSHIDA, HUI-HUA DENG,  
KYOUJI KOMATSU, TOSHIKUNI KAINO

Institute for Chemical Reaction Science, Tohoku University  
2-1-1 Katahira, Aoba-ku, Sendai 980-8577 JAPAN

An organic salt, 4-*N,N*-dimethylamino-4'-*N'*-methyl-stilbazolium tosylate, DAST, has large second-order optical nonlinearities. A ridge waveguide of the DAST crystal was fabricated, for the first time to our knowledge, by using photolithography and oxygen reactive ion etching (RIE). The DAST ridge waveguide,  $34 \times 20 \mu\text{m}$  and  $6 \times 6 \mu\text{m}$  channels with 2mm in length were successfully fabricated by this process.

**Keywords** DAST; channel waveguide; organic crystal; RIE; photolithography

### INTRODUCTION

Organic nonlinear optical(NLO) crystals are promising material for practical photonic applications because of their large nonlinearities, fast response time, low dielectric constant, and high optical damage threshold. DAST crystal is of particular noteworthy among those materials because its largest NLO coefficient  $d_{11}$  is  $540 \pm 110 \text{ pm/V}$  ( $\lambda = 1.54 \mu\text{m}$ ).<sup>[1]</sup> This value

is almost 20 times larger than that of  $\text{LiNbO}_3$  crystal  $d_{33}$ .<sup>[2]</sup> DAST crystal is relatively easy to handle among organic NLO materials because it is an ionic salt with excellent hardness, harder than those of standard molecular crystal. This is an important feature of NLO crystals for micro processing of them to fabricate channel waveguide applied to practical photonic devices. Figure 1 shows molecular structure of DAST.

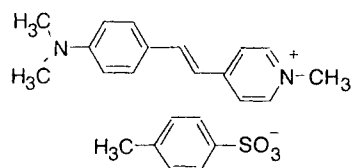


FIGURE 1 Molecular structure of DAST.

X-ray structure determination of the DAST single crystals revealed that the charge-transfer axes of the stilbazolium moiety makes angle of  $+20^\circ$  and  $-20^\circ$  with respect to the  $a$ -axis of the crystal.<sup>[2]</sup> Therefore, the DAST crystal has a large electro-optic (EO) coefficient along the  $a$ -axis. The waveguide core ridge was fabricated parallel to the  $b$ -axis in the  $ab$  plane to make the use of NLO coefficient,  $d_{11}$ , of it effectively.<sup>[3][4]</sup> Figure 2 shows schematic illustration of the DAST crystal habit and its waveguide structure.

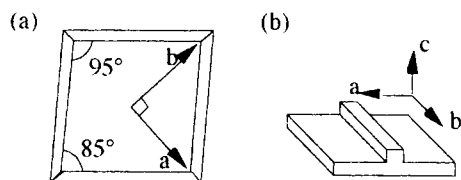


FIGURE 2 Schematic illustration of (a) DAST crystal habit and (b) DAST waveguide structure.

As far as organic crystal waveguide fabrication concerns, only two materials, MNBA<sup>[5][6]</sup> [4-methoxy-3-acetamido(4'-nitrobenzylidenyl)aniline] and MBANP<sup>[7][8]</sup> [( $-$ )-2-( $\alpha$ -methylbenzylamino)-5-nitropyridine], had been reported. These materials are molecular crystal which are usually insoluble

in water. As MNBA is hard to dissolve in organic solvents, standard photolithography process could not be applied. On the other hand, MBANP can be dissolved in standard organic solvents, a special aqueous photoresist was applied to fabricate a ridge waveguide of it. As the DAST is an organic salt, it is easily dissolved in organic solvents of photoresist and in an aqueous solvent. These features of organic ionic crystal is a major problem for fabricating a waveguide of them.

In this paper, a ridge waveguide of the DAST crystal was fabricated by using a special buffer layer which protect the crystal from organic solvents of photoresist and its developer in a photolithography process and reactive ion etching(RIE) process. To our knowledge, it is for the first time that the DAST crystal ridge was fabricated.

## EXPERIMENTS

The bulk crystals of the DAST to fabricate a ridge waveguide were grown from a methanol solution by a temperature lowering technique. The grown crystal was  $4 \times 4 \times 0.3 \text{ mm}^3$  in size with a large *ab* plane. At first, we examined the solubility of DAST to typical organic solvents. As shown in Table I, only four solvents among them do not dissolve the DAST crystal. We selected toluene and poly(methyl methacrylate)(PMMA) as a solvent

TABLE I Solubilities of DAST for typical organic solvents

Solvent	Solubility (g/dm <sup>3</sup> , at 24°C)	Solvent	Solubility
Methanol	15.20	Cyclohexanone	$8.66 \times 10^{-2}$
Formic acid	14.08	Dichloromethane	$7.07 \times 10^{-2}$
Ethanol	4.79	Acetone	$3.75 \times 10^{-2}$
1-Propanol	1.79	1,4-Dioxane	$4.28 \times 10^{-3}$
2-Propanol	1.52	Chlorobenzene	$2.87 \times 10^{-3}$
Dimethylsulfoxide	0.80	Tetrahydrofuran	$1.96 \times 10^{-4}$
Dimethylformamide	0.52	Diethyl ether	0.00
Deionized water	0.23	n-Hexane	0.00
Chloroform	0.15	Ethyl acetate	0.00
Acetic acid	0.11	Toluene	0.00
2-Butanone	$9.54 \times 10^{-2}$		

and a polymer as a buffer layer for protecting it from organic solvents of resists.

Schematic diagram of the fabrication process of the DAST waveguide is shown in Figure 3. At first, the DAST single crystal was molded by a resin without covering the *ab* plane that is a top surface, then the molded crystal was fixed on Silicon substrate. Then PMMA was spun on the DAST crystal surface as a buffer layer to protect it from a photoresist solution and its developer. An etching mask was patterned from a photoresist by photolithographic technique. A core ridge was then fabricated by  $O_2$  RIE. Finally, the residual etching mask was removed by dissolving the PMMA layer in toluene at  $40^\circ\text{C}$ . The PMMA acted as a lift-off layer.

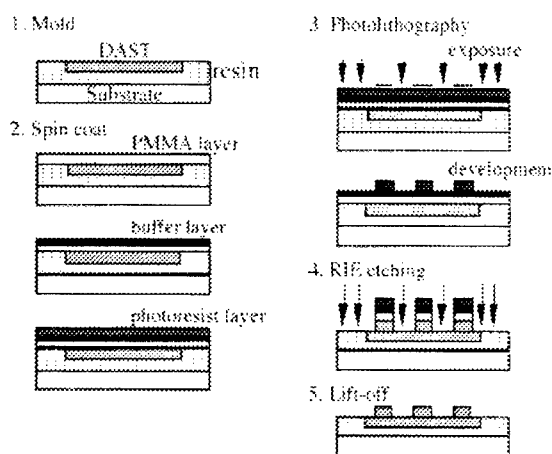


FIGURE 3 Schematic diagram of the fabrication process of DAST waveguide.

## RESULTS AND DISCUSSION

The core ridge of the DAST crystal waveguide was successfully fabricated by using  $O_2$  RIE. When a  $40\mu\text{m}$  wide etching mask with 5 hours etching time were taken, the core ridge was  $34\mu\text{m}$  in width and  $20\mu\text{m}$  in height. When a  $8\mu\text{m}$  wide etching mask with 1.5 hours etching time were taken, it was  $6\mu\text{m}$  in width and  $6\mu\text{m}$  in height. So, the etching rate of the

DAST crystal by  $O_2$  RIE with an optimal condition was  $4.0\mu\text{m}/\text{h}$ . As shown in Figure 4, the side wall of the DAST ridge was almost perpendicular to the etched crystal surface because it has no anisotropic etching by  $O_2$  RIE.

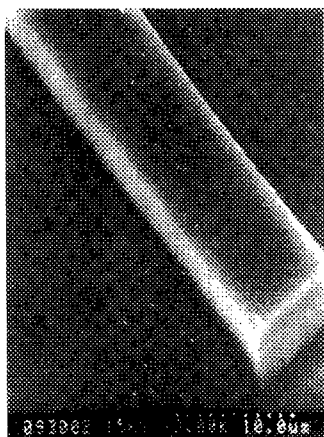


FIGURE 4. Typical SEM image of a core ridge of DAST waveguide.

The optical propagation loss of the DAST ridge waveguide without a cladding layer with the core ridge of  $20\mu\text{m}$  in height and  $34\mu\text{m}$  in width were examined by a cutback method. A  $1.3\mu\text{m}$  laser light was launched into the waveguide through a multi-mode fiber without using a refractive index matching oil. The result is shown in Figure 5. From the slope, we

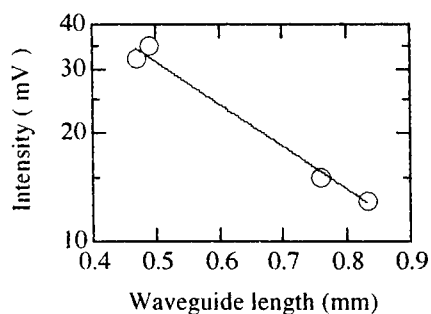


FIGURE 5. Optical loss dependence on waveguide length. Solid line is calculated by the least square method.

calculated the propagation loss of the waveguide to be 11.8 dB/cm. We are sure that this propagation loss could be reduced by using a cladding layer with appropriate refractive index and by treating the endface of the waveguide using a dicing saw and polishing them.

### CONCLUSIONS

A ridge waveguide structure of the DAST parallel to the *b*-axis of the crystal was successfully fabricated on an *ab* plane of the DAST crystal by using O<sub>2</sub> RIE and a PMMA buffer layer. This will be the first report of the DAST crystal waveguide fabrication. The sidewall of the DAST ridge was almost perpendicular to the etched crystal surface. The optical loss of the ridge waveguide was measured to be 11.8dB/cm.

### ACKNOWLEDGMENT

This work was supported by NEDO, a regional program.

### REFERENCES

- [1] G. Knöpfle, R. Schlessler, R. Ducret, and P. Günter, Nonlinear Optics, **9**, 143-149 (1995).
- [2] S. R. Marder, J. W. Perry, and C. P. Yakymyshyn, Chem. Mater., **6**, 1137-1147 (1994).
- [3] F. Pan, G. Knöpfle, Ch. Bosshard, S. Follonier, R. Spreiter, M. S. Wong, and P. Günter, Appl. Phys. Lett., **69**, 13-15 (1996).
- [4] F. Pan, K. McCallion, and M. Chiappetta, Appl. Phys. Lett., **74**, 492-494 (1999).
- [5] T. Dietrich, R. Schlessler, B. Erler, A. Kündig, Z. Sitar, and P. Günter, J. Crystal Growth, **172**, 473-477 (1997).
- [6] G. Knöpfle, Ch. Bosshard, R. Schlessler, and P. Günter, IEEE J. Quantum Electron., **30**, 1303-1312 (1994).
- [7] K. Tsuda, T. Kondo, F. Saito, T. Kudo, and R. Ito, Jpn. J. Appl. Phys., **31**, L134-L135 (1992).
- [8] T. Kondo, R. Morita, N. Ogasawara, S. Umegaki, and R. Ito, Jpn. J. Appl. Phys., **28**, 1622-1628 (1989).

**SESSION H: NOVEL MOLECULAR DESIGN  
AND SYNTHESIS**



## New Octupolar Star-shaped Molecules with Non-resonant Quadratic Optical Nonlinearities

FREDERIC CHERIOUX,<sup>a,\*</sup> SOPHIE BRASSELET,<sup>b</sup> PIERRE AUDEBERT<sup>c</sup> and JOSEPH ZYSS<sup>b</sup>

*a) Laboratoire de Chimie et Electrochimie Moléculaire, Université de Franche-Comté, La Bouloie, 16 route de Gray, F-25030, Besançon cedex; b) LPQM, Ecole Normale Supérieure de Cachan, 61 avenue du Président Wilson, F-94235 Cachan cedex; c) PPSM, Ecole Normale Supérieure de Cachan, 61 avenue du Président Wilson, F-94235 Cachan cedex.*

### Abstract

Two new classes of octupolar nonlinear chromophores, deriving from 1,3,5-triazines and oligothiénylic crystal violet analogues, have been synthesized, and their nonlinear properties investigated using the Harmonic Light scattering experiment. The easy preparation of these molecules qualify them attractive candidates for further applications. Off-resonant measurements evidence high nonlinearities together with a broad range transparency, which designate these compounds for the emerging schemes of nonlinear optical applications whereby the multipolar character of the chromophores is of a major new asset.

**Keywords** Octupoles, multipoles, quadratic, non-resonant, nonlinear susceptibility

### 1. INTRODUCTION

Octupolar molecules have recently generated increasing interest in the field of quadratic nonlinear optics. At the microscopic level, strategies have been developed during the past decade in order to circumvent the eventual drawbacks of unidimensional and so-called dipolar molecules, for which a strong nonlinearity is often antagonized by a strong absorption at the visible harmonic wavelength. In particular, the large class of octupolar molecules belonging to the  $T_d$ ,  $D_{3h}$  or  $C_{3v}$  symmetry groups, has attracted the attention of both physicists and chemists since the early demonstrations that significant second order nonlinear efficiency could be achieved from non-dipolar molecules [1,2]. Octupolar molecular systems, due to their strictly cancelled

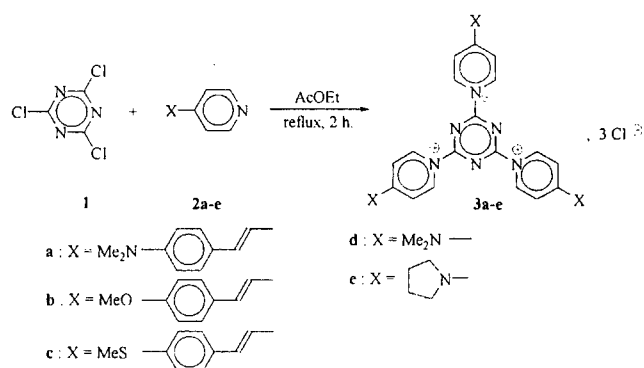
ground state dipole moment, belong to a particular class of chromophores that are not amenable to traditional molecular nonlinear optics measurements that require electric field-induced orientation of the molecules in order to retrieve their hyperpolarizability coefficient  $\beta$ . The revival of the earlier harmonic light scattering experiment introduced by Maker *et al.* [3], performed in isotropic solutions and therefore adapted to such molecular systems [4], has helped point out the particular interest of octupolar systems in terms of their favorably displaced nonlinearity-transparency trade-off, opening therefrom new schemes in the field of molecular engineering for nonlinear optics [5-8]. This field has furthermore significantly gained in interest since the first demonstration of the possibility to induce permanent macroscopic noncentrosymmetric order using octupolar molecules [9]. The possibility to design new symmetry schemes at the macroscopic level [10] has further triggered the design of non-dipolar molecules, and in particular of octupolar compounds such as those reported in this work.

We have recently reported the preparation and electrochemical properties of families of octupolar conjugated molecules [11]. In this work, we explore and confirm the nonlinear optical properties of these compounds. Nonlinear optical measurements were performed using the HLS experiment in off-resonance conditions, avoiding subsequently any eventual two photon fluorescence background which frequently arises when working at the vicinity of the two-photon absorption band of the molecules [12,13]. After briefly recalling the synthetic procedure and structural semi-empirical computations, we report off-resonant second harmonic generation measurements from two series, 1,3,5-triazines and oligothiénylic crystal violet analogues, respectively.

## 2. RESULTS AND DISCUSSION

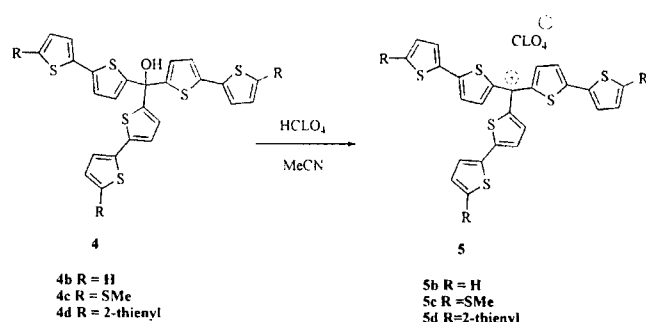
### Synthesis of the molecules

The trisubstituted 1,3,5-triazines are readily obtained from aromatic nucleophilic substitution on cyanuric chloride **1** with the appropriate 4-styrylpyridines **2a-e** (see Scheme 1) [11a]. The substitution took smoothly place within two hours upon gentle warming with cyanuric chloride in ethyl acetate, to give the tri-substituted adduct **3a-e** as sole product (see Scheme 1) [11a].



**Scheme 1** : Synthesis of 2,4,6-tri-[1-Pyridinium]-1,3,5-triazine trichloride **3**

The tris(2-thienyl)methanol and tris(2-thienyl)methylation **5a** were synthesized by the method described in literature [14]. The precursor carbinols **4b-d** are usually prepared by reaction of the corresponding 2-thienyllithium or 5-(2,2'-dithienyl)lithium with ethylchloroformate with a 3/1 stoichiometry. All the tris[5-(oligothienyl)]methyl cations **5b-d** were produced by adding a stoichiometric amount of perchloric acid to a solution of the carbinols **4b-d** in dry acetonitrile (see Scheme 2) [11b].



**Scheme 2** : Synthesis of tris[5-(oligothienyl)]methylcations **5b-d**

The perchlorate salt of the cation precipitates instantaneously as an intense deep blue or violet colored powder in a quantitative yield. In the case of tris(2-thienyl)methylation, the color of the salt is bright orange.

#### Semi-empirical molecular computations.

The 3D geometry of each compounds **3** and **5** has been optimized by semi-empirical computations with the PM3 method. Molecules **3** belong to the  $D_{3h}$  symmetry group and appear to be fully planar. This geometry was determined also by *ab-initio* computations. In the case of compounds **5**, semi-empirical computations designate the  $C_3$  symmetry group.

#### Nonlinear optics measurements.

The Harmonic Light Scattering (HLS) experiment has been used to determine the quadratic non-linear optical properties of all compounds. The fundamental IR laser source at 1.34  $\mu\text{m}$ , is a transverse and longitudinal single-mode flash pumped Nd:Yag laser emitting pulses of 10 MW peak power and 10 ns duration at a 10 Hz repetition rate. The incident intensity  $I^0$  is monitored by a half-wave plate and a Glan polarizer. A fraction of the incident beam is removed by a glass plate at a small reflection angle and sent onto a reference NPP frequency doubling calibrated powder followed by a first photomultiplier. The fundamental beam is focused in a cell, which contains the adequately filtered solutions. The scattered harmonic signal is then collected at right angle on a second photomultiplier after spectral selection through an interference filter with 10 nm spectral resolution. A reference  $\text{CCl}_4$  solution with  $\langle\beta^2\rangle^{1/2}=0.26\times10^{-30}$  esu [3a] is used to calibrate the experiment. An initial series of measurements addresses the pure solvent, namely dimethylsulfoxide (DMSO) with subsequent results further introduced in the analysis of the solution data. Measurement of the solvent nonlinearity results in a nonlinear coefficient value of  $\langle\beta^2\rangle^{1/2}=0.23\times10^{-30}$  esu [15]. Typical concentration values are around  $10^{-4}$  mol/L.

The nonlinear  $\langle\beta^2\rangle^{1/2}$  coefficients of the 1,3,5-triazine trichloride compounds **3a-e** and tris[5-(oligothienyl)]methylcations **5a-d** are given in Table I together with their  $\lambda_{\text{max}}$  absorption wavelength. The corresponding  $\langle\beta^2(0)\rangle^{1/2}$  static values were derived from a degenerate two-level dispersion model [2]. In the case of compound **3a**, detection of the HLS signal at several distinct wavelengths around 670 nm performed by use of different interference filters evidenced that the harmonic wavelength signal was buried within a broad two-photon emission peak around 650 nm. Compounds **3b-e** were studied using the same precautions, and did not present any two-photon fluorescence background. The nonlinearity of compounds **3b**, **3d** and **3e** are slightly higher than the classical *paranitroaniline* molecule,

with  $\langle\beta^2\rangle^{1/2}=5\times 10^{-30}$  esu as measured in chloroform in similar experimental conditions. The highest value was obtained for compound **3c**, which can be readily accounted for by a more favorable charge transfer ensured by the stronger donor end group.

Compound	$\lambda_{\text{max}}$ (nm)	$\langle\beta^2\rangle^{1/2}$ ( $10^{-30}$ esu)	$\langle\beta^2(0)\rangle^{1/2}$ ( $10^{-30}$ esu)
<b>3a</b>	547	fluorescence	
<b>3b</b>	440	18.5	9.4
<b>3c</b>	470	45.6	20.3
<b>3d</b>	432	14.5	7.6
<b>3e</b>	310	11	8.2
<b>5a</b>	360	17.4	11.8
<b>5b</b>	350	20.5	14.3
<b>5c</b>	370	22.7	15
<b>5d</b>	360	45	29.7

**Table 1.** Experimental values of the  $\langle\beta^2\rangle^{1/2}$  nonlinear coefficient of compounds **3a-e** and **5a-d** as obtained by the HLS measurement performed at  $\lambda=1.34\mu\text{m}$  in DMSO, and corresponding  $\langle\beta^2(0)\rangle^{1/2}$  static values.

Comparison between the **5a**, **5b** and **5d** values exemplifies the strong enhancement of the charge transfer efficiency provided by the extension of the oligothiénylic chains. The relatively higher efficiency obtained for compound **5d**, while maintaining a broad transparency range in the visible domain, appears of particular relevance in terms of nonlinear-transparency trade-off. In spite of the poor donor strength of the end group of the three branches of this octupolar compound, the nonlinear efficiency of molecule **5d** is significant and might be further improved by adequate grafting of donor groups.

The nonlinear values of the different compounds of this work are lower than those obtained for the well-known crystal violet carbocation for which  $\langle\beta^2(0)\rangle^{1/2}=168\times 10^{-30}$  esu [16]. This compound has however a higher absorption wavelength, a situation potentially leading to contamination of the HLS signal by two-photon fluorescence [16]. A high absorption in the visible range is moreover detrimental for applications related to the second harmonic generation and parametric emission.

Molecules **3a-c** are furthermore good candidates for molecular engineering of macroscopic orientation of octupoles via the all-optical poling experiment. While presenting promising nonlinear efficiencies, octupolar compounds studied in this work offer the additional advantage of a weaker absorption in the visible range, thus permitting to decrease the attenuation of interactive waves in the material.

### 3. CONCLUSION

The molecular engineering of 1,3,5-triazines and oligothiénylic crystal violet analogues has been presented as a promising implementation of octupolar schemes for nonlinear optics. High off-resonant second order nonlinear coefficients have been reported in the case of oligothiénylic compounds, while the chemical structure of both families of molecules may be of particular interest for future applications related to optical orientation in polymer matrices. These results, calling for further optimization of the molecular structure and in particular of the donor and acceptor groups, already confirm the relevance of these new octupolar compounds in the field of nonlinear optics.

### REFERENCES

- \* corresponding author, e-mail : frederic.cherieux@univ-fcomte.fr
- [1] M. Joffre, D. Yaron, R. Silbey, J. Zyss, *J. Chem. Phys.*, **97**, 5607 (1992).
  - [2] a) J. Zyss, *Nonlinear Optics*, **1**, 3 (1991). b) J. Zyss, *J. Chem. Phys.*, **98**, 6583 (1993). c) J. Zyss, I. Ledoux, *Chem. Rev.*, **94**, 77 (1994).
  - [3] a) R.W. Terhune, P.D. Maker, C.M. Savage, *Phys. Rev. Lett.*, **14**, 681 (1965). b) D. Maker, *Phys. Rev. A*, **1**, 923 (1970).
  - [4] a) K. Clays, A. Persoons, *Phys. Rev. Lett.*, **66**, 2980 (1991).
  - [5] M.A. Pauley, H.W. Guan, C.H. Wang, A.K.Y. Jen, *J. Chem. Phys.*, **104**, 7821 (1996).
  - [6] J. Zyss, T. Chauvan, C. Dhenaut, I. Ledoux, *Chem. Phys.*, **177**, 281 (1995).
  - [7] C. Dhenaut, I. Ledoux, I.D.W. Samuel, J. Zyss, M. Bourgault, H. Le Bozec, *Lett. to Nature*, **374**, 339 (1995).
  - [8] C. Fiorini, F. Charra, J.M. Nunzi, I.D.W. Samuel, J. Zyss, *Optics Lett.*, **24**, 2469 (1995).
  - [9] a) T. Verbiest, K. Clays, A. Persoons, F. Meyers, J.L. Bredas, *Opt. Lett.*, **7**, 525 (1993). b) S. Stadler, F. Feiner, C. Brauchle, S. Brandl, R. Gompper, *Chem. Phys. Lett.*, **2-3**, 292 (1995).
  - [10] a) S. Brasselet, J. Zyss, *J. Opt. Soc. Am. B*, **1**, 257 (1998). b) S. Brasselet, J. Zyss, *Opt. Lett.*, **22**, 1464 (1997).
  - [11] a) F. Cherieux, P. Audebert, P. Hapiot, *Chem. Mater.*, **7**, 1984 (1998). b) F. Cherieux, L. Guyard, P. Audebert, *Adv. Mater.*, **13**, 1013 (1998).
  - [12] I.D. Morrison, R.G. Denning, W.M. Laidlaw, M. A. Stammers, *Rev. Sci. Instrum.*, **4**, 1445 (1996).
  - [13] P. Kaatz, D. P. Sheldon, *Rev. Sci. Instrum.*, **4**, 1439 (1996).
  - [14] B. Abarca, G. Asensio, R. Ballesteros, T. Varea, *J. Org. Chem.*, **56**, 3224 (1991).
  - [15] M. Blanchard-Desce, J. B. Baudin, O. Ruel, L. Jullien, S. Brasselet, J. Zyss, *Optical materials*, **9**, 276 (1998).
  - [16] T. W. Chui, K. Y. Wong, *Chem. Phys. Lett.*, **4**, 1439 (1996).

## Nonlinear Optical Properties of the Langmuir-Blodgett Films of an Intermolecular Charge Transfer Complex

JUN KAWAMATA, TOMOYUKI AKUTAGAWA, TATSUO  
HASEGAWA, KUON INOUE, TAKAYOSHI NAKAMURA  
*Research Institute for Electronic Science, Hokkaido University  
N12W6, Kita-ku, Sapporo 060-0812, JAPAN*

Langmuir-Blodgett (LB) films of a charge transfer (CT) complex, OMTTF (bis(tetramethylene)tetrathiafulvalene)-C<sub>10</sub>TCNQ (decyltetracyanoquinodimethane) were fabricated and the optical properties were examined. The UV-visible-NIR as well as IR spectra showed a neutral CT state of the complex. The nonlinear optical parameters were evaluated by the electroabsorption and second harmonic generation measurements. The  $\chi^{(2)}$  value of 10 pm/V was obtained by the latter method.

**Keywords:** Langmuir-Blodgett films; IR spectroscopy; UV-Visible-NIR spectroscopy; Electrooptical spectroscopy; Charge transfer complex; Second harmonic generation

### INTRODUCTION

Langmuir-Blodgett (LB) films of charge transfer (CT) complexes have potentials for technological application in the field of molecular electronics and photonics.<sup>[1,2]</sup> From the viewpoints of electrical conduction, highly conducting LB films with metallic transport properties have been already reported.<sup>[3-5]</sup>

The degree of CT ( $\delta$ ) from donor ( $\mathcal{D}$ ) to acceptor ( $\mathcal{A}$ ) molecules is one of the fundamental parameters determining the physical properties

of CT complex. For example, metallic state of the complexes requires a partial CT state with segregated columnar structure, whereas an integer valence ( $\mathcal{D}^{+1}\mathcal{A}^{-1}$ ) leads to an insulating behavior due to the large electron correlation.<sup>[6]</sup> In insulating mixed stack CT complexes, the neutral-ionic phase transition, where the electronic structure of ground ( $g$ -) state changes from neutral ( $\mathcal{D}^{+\delta}\mathcal{A}^{-\delta}$ ;  $\delta < 0.5$ ) to ionic ( $\mathcal{D}^{1-\delta}\mathcal{A}^{\delta-1}$ ) state, takes place by lowering temperature or by applying of pressure.<sup>[7]</sup> Intermolecular CT interactions within mixed stack complexes are also promising for constructing photonics devices. The CT transition between  $g$ - and excited ( $e$ -) states of the complex will cause large 2nd order nonlinear optical (NLO) effects.<sup>[8]</sup>

The molecular orientations and configurations of  $\mathcal{D}$  and  $\mathcal{A}$  molecules can be controlled by LB technique.  $X$ -,  $Z$ -type, and alternate LB films have non-centrosymmetrical molecular arrangements with permanent dipole moments, which fulfill one of the requirements for 2nd order NLO effects.<sup>[9]</sup>

In this paper, we will describe linear and 2nd order nonlinear optical properties of the LB films of the CT complex, OMTTF (bis(tetramethylene)tetrathiafulvalene) and C<sub>10</sub>TCNQ. The donor molecule, which does not have any hydrophobic alkyl moieties, is combined with C<sub>10</sub>TCNQ to form an amphiphilic charge transfer complex.

## EXPERIMENTAL

The solid CT complex of OMTTF-C<sub>10</sub>TCNQ was obtained as powder by combining hot solution of each molecule. The composition was confirmed as the donor:acceptor ratio of 1:1 by the elemental analysis. The powder complex was dissolved in benzene-acetonitrile 1:1 mixed solution which was spread onto pure water surface to form monolayers. Arachidic acid (AA) was added as a matrix molecule (OMTTF-C<sub>10</sub>TCNQ/AA = 1/1) to increase the quality of LB films. The concentration of CT complexes in the spreading solution was fixed at  $1 \times 10^{-3}$  M.  $X$ -type LB films were fabricated by the horizontal lifting method.

CaF<sub>2</sub> or quartz substrates, coated with five layers of cadmium arachidate, were used for linear and nonlinear optical measurements. The sample arrangement for electro-absorption (EA) spectra measurements is as follows; quartz / ITO (indium tin oxide) / cadmium



arachidate (5-layers) / CT complexes (40-layers) / cadmium arachidate (6-layers) / aluminum.

## RESULTS AND DISCUSSION

### Redox Potentials

The difference between the first oxidation potential of the donor ( $E^1_{1/2}(\mathcal{D})$ ) and the first reduction potential of the acceptor ( $E^1_{1/2}(\mathcal{A})$ ),  $\Delta E (=E^1_{1/2}(\mathcal{D}) - E^1_{1/2}(\mathcal{A}))$ , is one of the useful complex-formation parameters to evaluate the CT interaction. Partial CT states are observed in the region  $0.02 < \Delta E < 0.34$  V.<sup>[10]</sup> Since the value of  $\Delta E$  of OMTTF-C<sub>10</sub>TCNQ is 0.1 V,<sup>[11]</sup> the electronic states of the complex is located within the range of partial CT state. In spite of the mixed-valence nature of the complex, which is also revealed by optical measurements (see below), the conductivity of the film was found to be low. Therefore, the film should consist of mixed stack of the donor and acceptor as observed in OMTTF-(2,4-dimethylTCNQ).<sup>[12]</sup>

### Linear Optical Properties and Electronic State of the Film

Figure 1 shows the electronic absorption spectra of the LB film. The spectra were taken at an angle of 45° between the substrate plane and the incident beam with *s*- or *p*-polarization. Two sample arrangements are referred to as 45*p* and 45*s*. The B-band ( $5.1 \times 10^3$  cm<sup>-1</sup>) is assigned to the CT transition. The C and D-bands are the intramolecular transitions of  $\mathcal{D}$  or  $\mathcal{A}$  molecule. The intensities of the absorption bands in 45*s* are larger than those in 45*p* in the whole measuring range, indicating that the directions of all the transition moments are rather within the substrate plane. No in-plane anisotropy in molecular arrangement was observed in the polarized spectra measured separately at normal incidence with the polarized direction orthogonal to each other (data not shown).

The neutral CT state of the complex was confirmed by the CN stretching band of C<sub>10</sub>TCNQ appeared at 2214 cm<sup>-1</sup>. The corresponding peaks for neutral and fully charge transferred C<sub>10</sub>TCNQ species appear at 2222 and 2179 cm<sup>-1</sup>, respectively. Assuming a linear relationship between charge transfer ratio and shift in CN stretching band, the charge on C<sub>10</sub>TCNQ is estimated to be 0.2.<sup>[13]</sup> Therefore, high 2nd order NLO effects are expected through the intermolecular CT interactions in the mixed CT complex.<sup>[11]</sup>

We note that the neutral complexes with a mixed stack structure may show a neutral to ionic phase transition if they are located near the neutral-ionic boundary which is determined by  $\Delta E$  and  $h\nu_{CT}$  (energy of CT transition).<sup>[8]</sup> The  $\Delta E$  of 0.1 V and the  $h\nu_{CT}$  of 0.65 eV suggest that this complex is close to the boundary, indicating this system is a promising candidate for realizing a neutral to ionic phase transition in the LB films. To examine this, we measured the temperature dependence of the CN stretching band. A slight blue-shift of the band by lowering temperature down to 10 K was observed. No evidence, however, of the neutral-ionic transition in the LB film was detected.

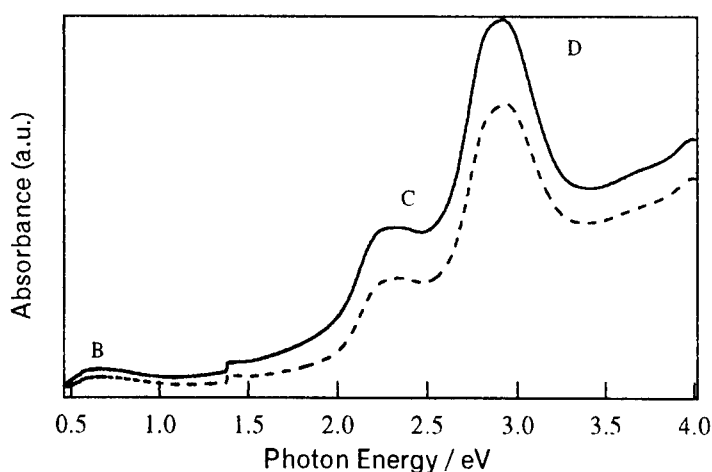


FIGURE 1. Electronic spectra of the LB films taken with 45° incidence of *p*- (dotted line) and *s*-polarized light (solid line). See text for the assignment of the peaks.

#### Nonlinear Optical Properties

The NLO parameters were evaluated from EA spectra<sup>[14]</sup> and by the second harmonic generation (SHG) measurements. The electroabsorption spectra over photon energy range from 1.5 to 4.0 eV were measured for 20-layer LB film. The modulated absorption spectra,  $\Delta\alpha = -\Delta T/T$  at electric field  $E$  were converted to the imaginary part of the second order electric susceptibility,  $\text{Im}[\chi^{(2)}(-\omega; \omega, 0)]$ . The  $\text{Im}[\chi^{(2)}(-\omega; \omega, 0)]$  reached 0.3 pm/V at 2.2 eV.

The result of the SHG measurements is shown in Fig. 2. The measurement was carried out on a one-layer LB film. Fundamental light (1.2 eV, 1064 nm) of Nd-YAG laser (20 mJ, 8 ns) was polarized parallel to the incident plane. The interference fringe pattern was analyzed in a similar way as in the case of an LB monolayer of a phenylhydrazone dye.<sup>[15]</sup> The second order NLO coefficient,  $d_{33}$  was 10 pm/V when quartz crystal was used as a reference.

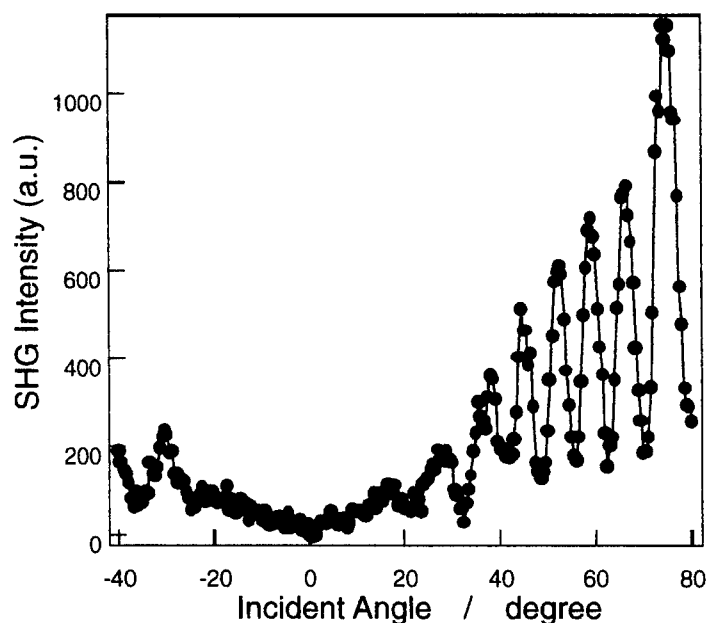


FIGURE 2. Fringe pattern of a one-layer LB film of OMTTF-C<sub>10</sub>TCNQ

#### Acknowledgments

This work was partly supported by a Grant-in-Aid for Science Research from Ministry of Education, Science, Sports, and Culture of Japan. We are grateful to Dr. T. Matsunaga, National Institute of Materials and Chemical research for the assistance of low-temperature IR measurements.

## References

- [1] M. R. Bryce and M. C. Petty, *Nature*, **374**, 771 (1995).
- [2] T. Nakamura, in *Handbook of Organic Conductive Molecules and Polymers vol. 1*, H. S. Nalwa (ed.), John Wiley & Sons, Chichester (1997) pp.727-780.
- [3] T. Nakamura, G. Yunome, R. Azumi, M. Tanaka, H. Tachibana, M. Matsumoto, S. Horiuchi, H. Yamochi and G. Saito, *J. Phys. Chem.*, **98**, 1882 (1994).
- [4] H. Isotalo, J. Paloheimo, Y. F. Miura, R. Azumi, M. Matsumoto and T. Nakamura, *Phys. Rev. B*, **51**, 1809 (1995).
- [5] H. Ohnuki, T. Noda, M. Izumi, T. Imakubo and R. Kato, *Phys. Rev. B*, **55**, 10225 (1997).
- [6] T. Ishiguro, K. Yamaji and G. Saito, *Organic Superconductors 2<sup>nd</sup> ed.*, Springer-Verlag, Heidelberg (1998)
- [7] (a) J. B. Torrance, J. E. Vazquez, J. J. Mayerle, and V. Y. Lee., *Phys. Rev. Lett.*, **46**, 253 (1981). b) J. B. Torrance, A. Girlando, J. J. Mayerle, J. I. Crowley, V. Y. Lee, P. Batail and S. J. Laplaca, *Phys. Rev. Lett.*, **47**, 1747 (1982).
- [8] Y. Tokura, in *Organic Nonlinear Optical Materials*, M. Kotani and T. Shimidzu (eds), Gakkai Shuppan Center, Tokyo (1992) pp191-203
- [9] M. C. Petty, *Langmuir-Blodgett films. An introduction*, Cambridge University Press (1996).
- [10] (a) G. Saito and J. P. Ferraris, *Bull. Chem. Soc. Jpn.*, **53**, 2141 (1980). (b) D. O. Cowan, *New Aspects of Organic Chemistry*, eds. Z. Yoshida, T. Shiba and Y. Oshiro, Kodansha Ltd., Tokyo (1989)
- [11] T. Konuma, T. Akutagawa, T. Yumoto, T. Nakamura, J. Kawamata, K. Inoue, T. Nakamura, H. Tachibana, M. Matsumoto, H. Ikegami, S. Horiuchi, H. Yamochi and G. Saito; *Thin Solid Films*, **327-329**, 348 (1998).
- [12] P. D. Chasseau and F. Leroy, *Acta. Cryst.*, **B37**, 454 (1981).
- [13] T. Nakamura, T. Yumoto, T. Suzuki, T. Akutagawa, T. Hasegawa, H. Tachibana, M. Matsumoto, S. Horiuchi, H. Ikegami, H. Yamochi and G. Saito, *Mol. Cryst. Liq. Cryst.*, **327**, 83 (1999).
- [14] T. Hasegawa, T. Akutagawa, T. Konuma, T. Nakamura, J. Kawamata and K. Inoue, *Nonlinear Optics*, **22**, 143 (1999).
- [15] D. Lupo, W. Prass, U. Scheunemann, A. Laschewsky, H. Ringsdorf and I. Ledoux; *J. Opt. Soc. Am. B*, **5**, 300 (1988).

## Structural Analyses of Clay-Metal Complex Hybrid Films by Observation of Optical Second Harmonic Generation

JUN KAWAMATA<sup>a</sup>, YUICHIROU OGATA<sup>b</sup>, AKIHIKO YAMAGISHI<sup>b</sup> and KUON INOUE<sup>a</sup>

<sup>a</sup> Research Institute for Electronic Science, Hokkaido University, Sapporo, 060-0812, Japan; <sup>b</sup> Division of Biological Science, Graduate School of Science, Hokkaido University, Sapporo, 060-0810, Japan

We observed the optical second harmonic generation (SHG) from clay-metal complex hybrid films. The Langmuir-Blodgett films, having non-centrosymmetric molecular alignment, were prepared by forming a monolayer of tris(4,7-diphenyl-1,10-phenanthroline)ruthenium(II)-perchlorate onto an aqueous dispersion of a clay. The dependence of the SHG signal intensity on the condition of the sample preparation was examined. Based on the results, we have analyzed the characteristics of the molecular alignment in those films.

**Keywords** Nonlinear Optics; Second-Harmonic Generation; SHG; Hybrid-Film; Clay; Metal Complex

## INTRODUCTION

Organometallic compounds have been considered to possess a large nonlinear optical coefficient owing to a metal-to-ligand and ligand-to-metal charge transfer (MLCT and LMCT) transition<sup>[1]</sup>. Therefore, the study of organometallic compounds for a nonlinear-optical (NLO) material is currently of great technological and scientific interest<sup>[2]</sup>.

Organic and organometallic compounds have a tendency to crystallize in a centrosymmetric array in most cases. Therefore, a means of imposing a noncentrosymmetric structure on those

compounds is needed. The Langmuir Blodgett (LB) technique is one of the various methods that can implement a noncentrosymmetric structure. However, for LB films, a few problems, which include poor thermal and mechanical stability, and poor optical quality, are often encountered<sup>[3]</sup>.

We made a "stable" LB film by hybridizing a clay and a metal complex<sup>[4]</sup>. Here a clay was chosen as a component to reinforce the film structure because it consists of two-dimensional ultra-thin layers (1 nm thick). Since the clay layer is charged negatively, a molecule which has a positively charged moiety is considered to be aligned on the clay monolayer by electrostatic force. In this study, we have attempted to fabricate hybrid LB films of different clays and tris(4,7-diphenyl-1,10-phenanthroline)ruthenium(II)perchlorate ( $\text{Ru(dpp)}_3$ ; Figure 1), which is not equipped with any alkyl chain. A fundamental study on the SHG properties was performed. As a result, we have confirmed that their SHG properties are almost the same as those of conventional LB films.

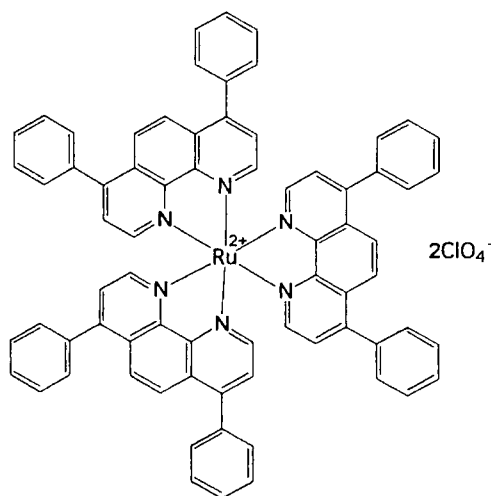


FIGURE 1. Chemical Formula of tris(4,7-diphenyl-1,10-phenanthroline)ruthenium(II)perchlorate ( $\text{Ru(dpp)}_3$ )

### SAMPLE PREPARATION

A monolayer of  $\Delta\text{-Ru(dpp)}_3$  was formed onto an aqueous suspension of a clay. Though the  $\Delta\text{-Ru(dpp)}_3$  molecule was not equipped with an aliphatic chain, a single clay layer that was charged negatively was thought to attach to the positively charged monolayer of  $\Delta\text{-Ru(dpp)}_3$  to form a clay-metal complex hybrid film (Figure 2.). We fabricated four types of hybrid films by replacing the varieties of clays. As the clay, lithium-hectorite, sodium montmorillonite, natural saponite and synthetic saponite were employed. The Z-Type hybrid-films were prepared by the horizontal lifting method. On the other hand, the Y-Type hybrid films were prepared by the vertical dipping method. The deposition of the hybrid film on a fused silica substrate was achieved at a surface pressure of 15 mN/m.

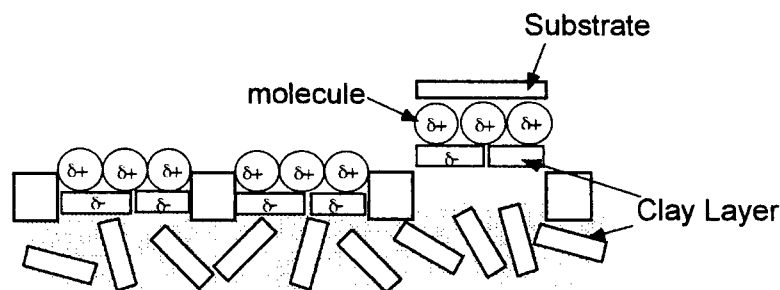


FIGURE 2. Schematic representation of the deposition of the hybrid-film of a clay and metal-complex by the horizontal lifting method.

### OPTICAL EXPERIMENTS

The spectrum of UV-Vis-NIR on the substrate was measured by a JASCO Ubest-30 spectrophotometer. SHG measurements were made by using a pulsed beam from a Q-switched Nd-YAG laser (Quanta-Ray, Model DCR-2; 20Hz), operating at a wavelength of  $1.064\ \mu\text{m}$  with a pulse duration of 8 nsec, and an energy of 2 mJ was used for excitation.

## RESULTS AND DISCUSSION

### Linear Optical Property of the Films

As already reported<sup>[4]</sup>, the wavelength of the second-harmonic wave (532 nm) is located at the tail of the charge-transfer absorption band. Consequently, weak resonant enhancement of the signal intensity of the second-harmonic generation (SHG) should be expected.

The absorption spectrums taken from the hybrid films were almost the same with that from a film fabricated without any clay. Therefore, it is natural to consider that the electronic state of the  $\text{Ru(dpp)}_3$  is not affected by the hybridization with those clays.

### Dependence of the SHG Intensities on the Characteristics of the Clay

The interference patterns for the Y-Type hybrid-film of the four kinds of clay and  $\Delta\text{-Ru(dpp)}_3$  are shown in Figure 3. The signal intensities observed for those films show the dependence on the kinds of the clay.

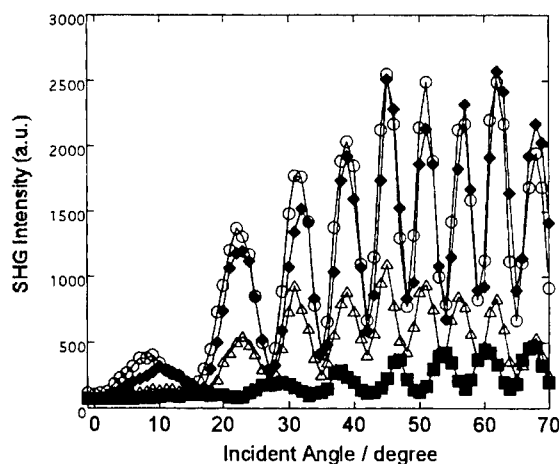


FIGURE 3. Angular dependence of SH signals from a  $[\text{Ru(dpp)}_3]^{2+}$ /four types of clay hybrid film deposited at 15 mN/m. ■, lithium-hectorite; ◆, montmorillonite; △, natural saponite; ○, synthetic saponite. Solid lines are guide to eyes.



The clay minerals used have diverse physical and chemical properties. The average particle size changes as  $1\sim 10\text{ }\mu\text{m}$  (lithium hectorite),  $0.1\sim 1\text{ }\mu\text{m}$  (sodium montmorillonite and natural saponite) and  $0.05\sim 0.1\text{ }\mu\text{m}$  (synthetic saponite). The cation exchange capacity (meq/g) changes as 1.4 (lithium hectorite), 1.15 (sodium montmorillonite) and 0.80 (natural and synthetic saponites)<sup>[5]</sup>. The negative charge is located in the inner octahedral sheet for sodium montmorillonite and in the outer tetrahedral sheet for other clays<sup>[5]</sup>. When the observed SHG intensity in Figure 3 is compared with those properties, it seems difficult to correlate the SHG intensity with any one of the properties of the clays. At present, it is suffice to say that the SHG intensity is influenced by the slight change of film structure and/or clay properties.

Furthermore, we have fabricated montmorillonite /  $\text{Ru(dpp)}_3$  hybrid films under the different concentrations of the clay suspension (0.01, 0.02 and 0.05 g/l). As for those samples, the observed SHG signal intensities were almost identical. Therefore, it is considered that the concentration of the clay suspension is not crucial for the molecular alignment.

#### Other Features of the Hybrid Films

The SHG intensities were measured for four combinations of polarization of the fundamental and second harmonic waves (data not shown). The p-polarized fundamental wave gave a substantially larger p-polarized SHG response than the s-polarized one. The SHG intensities generated by the s-polarized fundamental wave were negligibly small for both polarizations of the SHG waves. Similar tendencies were found for films consisting of other clays. This behavior is often seen in the case of a conventional LB film<sup>[6]</sup>. This fact indicates that the molecular alignment of the present hybrid film is almost the same as that of the conventional LB film.

Finally, here are the results of a preliminary experiment studying the dependence of the SHG signal intensity on the number of layers making up montmorillonite /  $\text{Ru(dpp)}_3$  hybrid film. For up to 3 layers, the SHG signal intensity has been found to be in proportion to the square of the number of layers. This fact indicates that the present hybrid film can maintain a head-to-tail stacking even with multi-layer structure. Therefore, it is concluded that the use of the present type hybrid film is promising for the study of NLO properties for a number of metal complexes which have a positively charged moiety.

## CONCLUDING REMARKS

We have demonstrated the SHG measurement of hybrid films incorporated with  $\Delta$ -Ru(dpp)<sub>3</sub>, a typical example of organometallic compounds, which does not have any aliphatic chain. Clear SHG responses thus far have been observed. This fact indicates that the present hybrid LB films have a molecular alignment almost identical to that of the conventional LB film which is composed of a amphiphilic chromophore. Therefore, it should be concluded that a molecule that has a positively charged moiety can be aligned on the clay layer even though the molecule is not equipped with any aliphatic chain. The use of the hybrid film has a great deal of potential for development of a novel matter of molecular alignment. Further experiments making use of a twitter molecule are now in progress.

## Acknowledgement

The present study was financially supported by a Grant-in-Aid for Scientific Research on Priority Areas (A) from the Japanese Ministry of Education, Science, Sports and Culture.

## References

1. D. S. Chemla and J. Zyss, ed. Nonlinear Optical Properties of Organic Molecules and Crystals, Academic Press, New York, (1987).
2. S. R. Marder, D. N. Beratan, B. G. Tiemann, L. Cheng and W. Tam, in Organic Materials for Nonlinear Optics II, ed. R. A. Hann and D. Bloor, Cambridge, 165 (1991).
3. S. Allen, T. G. Ryan, D. P. Devonald, M. G. Hutchings, A. N. Burgess, E. S. Froggatt, A. Eaglesham, G. J. Ashwell and M. Malhotra, in Organic Materials for Nonlinear Optics II, ed. R. A. Hann and D. Bloor, Cambridge, 51 (1991).
4. J. Kawamata, Y. Ogata, M. Taniguchi, A. Yamagishi and K. Inoue, Mol. Cryst. Liq. Cryst., in press.
5. Y. Nakamura, A. Yamagishi, T. Iwamoto and M. Koga, Clay and Clay Minerals, 36, 530 (1988).
6. S. Yamada, T. Nakano and T. Matsuo, This Solid Films, 245, 196 (1994).

## MO Calculations of Dyes for the Solid State Absorption Spectra

YOSHIKI SAKURAI, HISAYOSHI SHIOZAKI, SATORU NAKAO,  
and MASAKI KIMOTO

Technology Research Institute of Osaka Prefecture, 2-7-1 Ayumino,  
Izumi, Osaka 594-1157, Japan

Absorption spectral shift of dyes, which have large  $\chi^{(3)}$  values in spite of the small  $\pi$ -conjugation system, was studied. These dyes have both characteristics of large bathochromic shift of  $\lambda_{\max}$  from the solution to solid state, and strong  $\pi$ - $\pi$  interactions between the molecular layers. CNDO/S and *ab initio* methods were used to calculate this spectral shift. To reproduce the spectral shift, the CNDO/S program was modified by amplifying the intermolecular resonance integral term.

**Keywords:** solid-state spectra; bathochromic shift; modified CNDO/S; nonlinear optics; MO calculation; resonance integral

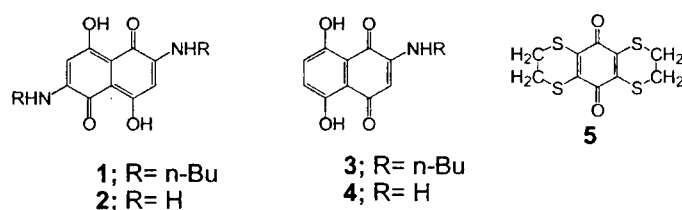
## INTRODUCTION

In general, the properties of the dyes as coloring agent for fiber or cloth are dependent on the characteristics of a single molecule. However, the dyes for organic photonic materials, such as nonlinear optical (NLO) materials, are used as single crystal or solid state. Accordingly, the property on solid or crystal state should be important for such purpose. Recently, Matsuoka and co-workers identified a series of dyes, which have large third order NLO susceptibility,  $\chi^{(3)}$ , values in spite of their small  $\pi$ -conjugation systems as shown in Table I<sup>[1,2]</sup>. These dyes have both characteristics of a large bathochromic shift of  $\lambda_{\max}$  from the solution to solid state, and strong  $\pi$ - $\pi$  interactions between the molecular layers. From these results, we proposed that the large

bathochromic shift could be an indication of obtaining a higher  $\chi^{(3)}$  value, and that the estimating the shift was useful for the molecular design of NLO materials<sup>[3]</sup>. In this paper, we tried to evaluate the shifts accurately by MO calculations.

## RESULTS AND DISCUSSION

In the single crystal, the molecules of dye **1** align in the same plane and are parallel to each other with an interlayer distance of 3.3 Å. To study the bathochromic shift in absorption spectra of dye **1**, we used dye **2** as the model compound for dye **1**. We have already reported the spectra of the monomer and the dimers of dye **2** calculated by both normal CNDO/S program and the single excitation configuration interaction (SE-CI) calculations with the 6-31G(d) basis set, implemented in the Gaussian 94 program<sup>[3,4,5]</sup>. The three dimers, shown in Figure 1, for calculations were constructed by extracting the nearest pairs from the crystallographic data of dye **1** and replacing the butylamino groups with amino groups. The calculated results were shown in Table 2<sup>[3]</sup>.



Scheme 1

TABLE 1 Absorption spectra and  $\chi^{(3)}$  values of quinone dyes in solution and solid state

Dye	in CHCl <sub>3</sub>	Thin film		$\chi^{(3)}/\text{esu}^a$
	$\lambda_{\text{max}}/\text{nm}$	$\lambda_{\text{max}}/\text{nm}$	$\Delta\lambda/\text{nm}$	
<b>1</b>	541	641	100	$4.8 \times 10^{-11}$
<b>3</b>	534	534	0	$\sim 10^{-13}$
<b>5</b>	429	538	109	$1.7 \times 10^{-11}$

<sup>a)</sup> measured by the third harmonic generation method in vapor deposited thin film.

The SE-CI calculation for the CONH dimer showed a bathochromic shift of 0.101 eV, which corresponds to about 30% of the observed shift (0.358 eV) for dye 1. The calculated absorption spectra by CNDO/S were also shown in Table 2. The shifts calculated by CNDO/S were smaller in eV scale than that by *ab initio* calculations. We estimated that this defect of CNDO/S was derived from the inadequacy in the

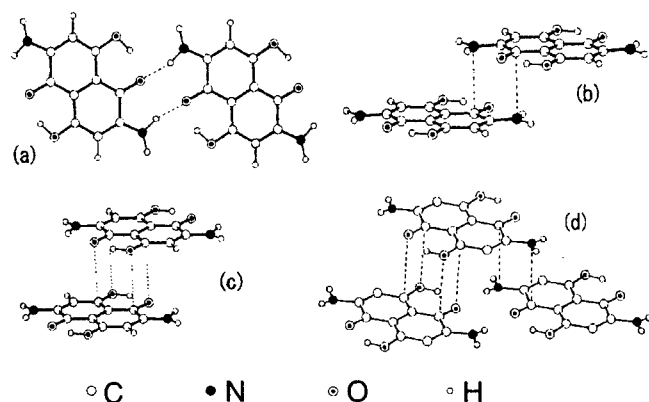


FIGURE 1 Structures of dye 2 for the spectral calculations: (a) H-bond dimer; (b) CONH dimer; (c) parallel dimer; (d) trimer.

TABLE 2 Calculated  $\lambda_{\max}$  of the monomer, dimers and tetramer of dye 2 by Gaussian 94 and CNDO/S

	SE-CI/6-31G(d)	CNDO/S <sup>a)</sup>	modified CNDO/S <sup>a)</sup>
	$\frac{\lambda_{\max}[\lambda_{\max}(\Delta\lambda)]}{\text{nm eV}}$	$\frac{\lambda_{\max}[\lambda_{\max}(\Delta\lambda)]}{\text{nm eV}}$	$\frac{\lambda_{\max}[\lambda_{\max}(\Delta\lambda)]}{\text{nm eV}}$
Monomer	365[3.394]	473[2.620]	473[2.620]
Dimer			
H-bond	374[3.314(-0.08)]	488[2.543(-0.08)]	489[2.534(-0.09)]
CONH	377[3.293(-0.10)]	485[2.557(-0.06)]	495[2.503(-0.12)]
Parallel	351[3.531(0.14)]	452[2.741(0.12)]	454[2.734(0.11)]
Trimer	-	486[2.553(-0.07)]	497[2.497(-0.12)]

<sup>a)</sup> Configuration interactions were made with 100, 400 and 900 configurations for monomer, dimers and trimer, respectively.

evaluation of the intermolecular interaction. To correct this defect, the resonance integral term of the CNDO/S program was modified. In the original CNDO/S approximation, the core matrix element  $H_{\mu\nu}$  between orbitals  $\mu$  and  $\nu$  on atoms  $r$  and  $s$  respectively, is obtained by

$$H_{\mu\nu} = (1/2)(\beta_r^0 + \beta_s^0)(S_{\mu\nu}^\sigma + \kappa S_{\mu\nu}^\pi) \quad (1)$$

where  $S_{\mu\nu}^\sigma$  and  $S_{\mu\nu}^\pi$  are the  $\sigma$  component and  $\pi$  component of overlap integrals, respectively, and  $\kappa$  is a constant of 0.585. To amplify the intermolecular interaction, we used the equation (2) to calculate the  $H_{\mu\nu}$ , only when the atoms  $r$  and  $s$  belong to different molecules to each other.

$$H_{\mu\nu} = 1.25(\beta_r^0 + \beta_s^0)(S_{\mu\nu}^\sigma + \kappa S_{\mu\nu}^\pi) \quad (2)$$

In other words, the equation (1) was used for the intra-molecular resonance integral, and the equation (2) was used for the inter-molecular resonance integral. The factor 1.25 in equation (2) was decided to give the most consistent spectroscopic data in the present series of compounds. The calculated results for the monomer, dimers and trimer by the modified CNDO/S program were also shown in Table 2. Since the trimer includes the three types of intermolecular interactions of the three dimers shown in Figure 1, the calculated spectral shift for the trimer should be more important in comparison with the observed spectral shift than that for the dimers. The modified CNDO/S gave a bathochromic shift of 23 nm (0.123 eV) to the trimer. On the other hand, the shift for the trimer calculated by normal CNDO/S was 12 nm. These results indicate that the modification with equation (2) corrected the above-mentioned defect of the normal CNDO/S program. The shifts calculated by the modified CNDO/S were larger than that by SE-CI/6-31G(d), and the calculated spectra were closer to the observed absorption spectra than that by the SE-CI/6-31G(d).

We calculated the spectra of dyes **4**, which was used as a model structure of dye **3**, and **5** too. In the single crystal, the molecules of dye **3** don't align in the same plane, and have a zigzag or twisted structure. Four dimers were also constructed by extracting four nearest pairs from the crystallographic data of dye **3** and replacing the butylamino groups with amino groups. No dimer of dye **4** showed a significant spectral shift. The calculated spectra of the monomer and the one of the four dimers were shown in Figure 2.

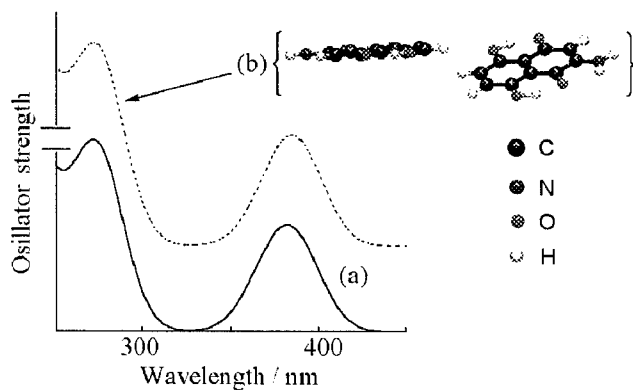


FIGURE 2 Calculated absorption spectra of dye 4; (a) monomer; (b) one of the nearest pairs. The spectral curves were drawn with the Gaussian distribution function.

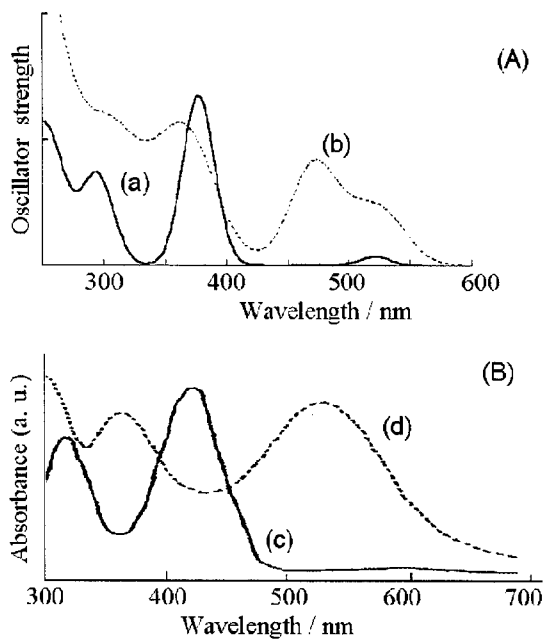


FIGURE 3 Absorption spectra of dye 5: (A) calculated spectra of the monomer (a) and the tetramer (b); (B) observed spectra in chloroform (c) and of the thin film (d). The spectral curves of (A) were drawn with the Gaussian distribution function.

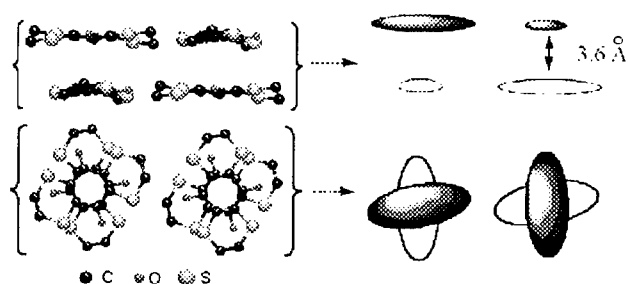


FIGURE 4 Structure and schematic description of the tetramer of dye 5. Description of protons are omitted.

For the dye 5, the tetramer includes the three types intermolecular interactions generated from the nearest pairs of dye 5. The spectral shift calculated by the modified CNDO/S program for the tetramer was about 100 nm, and the spectral curves drawn in Figure 3 were in good agreement with the observed spectral curves. The structure of the tetramer of dye 5 was shown in Figure 4.

It is most important for a semi-empirical method to fit the experimental phenomena. The modification by the equation (2) with the factor of 1.25 gave a good consistent spectroscopic data for the dyes 1 - 5. In the subsequent paper, we will calculate the spectra for many other compounds, and will report a more sophisticated value of the factor in equation (2) to give the good consistent spectroscopic data for many compounds.

#### Acknowledgments

The authors would like to thank Professor M. Matsuoka of Kyoto Women's University for his helpful suggestion.

#### References

- [1] M. Matsuoka, A. Oshida, A. Mizoguchi, Y. Hattori, and A. Nishimura, *Nonlinear Optics*, **10**, 109 (1995).
- [2] K. Takagi, A. Mizuno, A. Iwamoto, M. Furusyo, and M. Matsuoka, *Dyes and Pigments*, **36**, 35 (1998).
- [3] H. Shiozaki and M. Matsuoka, *J. Mol. Struct. (Theochem)*, **427**, 253 (1998).
- [4] Y. Ono, JCPE program No. 83.
- [5] Gaussian 94, Revision D.4, M. J. Frisch, *et al.*, Gaussian, Inc., Pittsburgh PA, 1995.



## Novel N-aryl carbazole derivatives for two-photon absorption applications

MARK SIGALOV, AMOS BEN-ASULY, LEV SHAPIRO AND  
VLADIMIR KHODORKOVSKY\*

Department of Chemistry, Ben-Gurion University of the Negev, Beer-Sheva, 84105 Israel

The absorption and emission spectra as well as their solvatochromism in a series of novel highly conjugated carbazole derivatives are discussed. It was found that incorporation of the carbazole moiety into the stilbene and distyrylbenzene cores results in strongly fluorescent compounds.

**Keywords:** unsaturated carbazole derivatives, fluorescence

### INTRODUCTION

Recently, much effort is being focused on designing fluorescent organic molecules with large two-photon absorption cross-section, for various future technologies [1]. For practical applications, these molecules have to be photostable, with large two-photon absorption cross section and high fluorescence quantum yield [2].

The stilbene derivatives play a very important role as main components of effective materials for many photochemical and photophysical applications [1,3]. It has been found [1] that symmetrical stilbene derivatives with electron releasing or electron withdrawing end groups, possess a large cross-section of two-photon absorption.

Recently, we have found that stilbene and distyrylbenzene analogs involving the carbazole electron donating group (Scheme 1) are photostable, possess strong fluorescence and according to the preliminary measurements exhibit two-photon absorption cross section values in the range of 200–1200 GM, some of them exceed the best known values to date [4].

Here we report in detail on the absorption and fluorescence properties of these derivatives.

## RESULTS AND DISCUSSION

Scheme 1. The compounds investigated

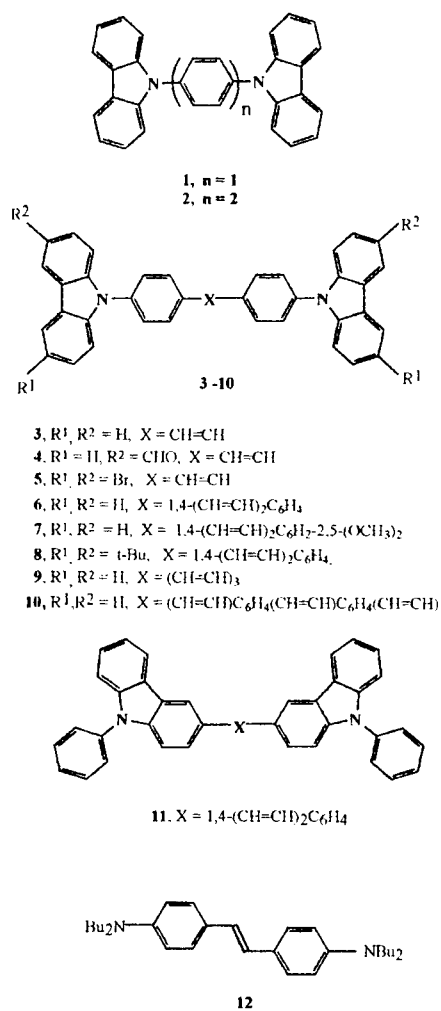


Table 1. Absorption, fluorescence and quantum yields of derivatives 1-12

Entry	Solvent	$\lambda_{\text{abs}}$ ( nm )	$\lambda_{\text{em}}$ ( nm )	Quantum yield
1	Toluene	326, 341	349, 363	0.46
2	Toluene	329, 342	363	0.67
	Dichloromethane	318, 340	377	0.60
3	Toluene	348	397, 418	0.67
4	Toluene	332, 343	395, 415	0.20
5	Dichloromethane	344, 358	402, 420	0.14
6	Toluene	378	426, 448	0.70
7	Toluene	406	458, 485	0.77
8	Toluene	387	433, 459	0.87
	Dichloromethane	384	463	*
	Acetonitrile	378	474	*
9	Toluene	388	434, 459	0.68
	Dichloromethane	384	440, 462	0.51
10	Dichloromethane	395	444, 469	0.89
11	Toluene	392	431, 457	0.92
12	Toluene	376	411, 435	0.78

\* Not measured

The general features of spectral behavior of these compounds (Table 1 and Figure 1) are:

- all derivatives absorb at wavelengths lower than 400 nm and are transparent in the visible spectral region;
- the extension of conjugation brings about a substantial long-wave shift of both absorption and fluorescence bands as well as an increase in quantum yield;
- donating substituents on the carbazole moiety and at the central aromatic ring increase the quantum yields (compounds 6-8), whereas an accepting substituent (4) and heavy atoms (5) drastically diminish the quantum yields. Planarity of the conjugated fragments in 9-phenyl-3-carbazolyl moiety (entries 6 and 11) also increase the quantum yields.

The solvatochromic shifts of absorption and emission bands (Table, entries 2 and 8, Figure 1a) have opposite signs. For compound 8 the solvatochromic behaviour was studied in more detail. The experimental data analysis of absorption and emission was done in

terms of non-empirical theory [5] based on Onsager's model [6]. According to this theory in the absence of specific solute-solvent interactions the energy of phototransition (absorption, emission) of solute molecule can be expressed as

$$E = E_{\text{vac}} - \Delta E_{\text{D}} - \Delta E_{\text{R}} \quad (1)$$

where  $E_{\text{vac}}$  is the vacuum phototransition energy,  
 $\Delta E_{\text{D}}$  – difference between energies of dispersion (Van der-Waals) solute-solvent interaction in excited (e) and ground (g) states:

$$\Delta E_{\text{D}} = D \cdot f(n^2) \quad (2)$$

here  $D = 1/a^3(D_e - D_g)$  is constant;  $n$  – solvent refractive index;  $f(x) = (x-1)/(x+2)$ ,  $a$  – Onsager's cavity radius.

$\Delta E_{\text{R}}$  is the difference of energies of electro-dipole interaction of solute molecule in excited and ground states (the interaction of dipole moments  $\mu_e$  and  $\mu_g$  with reactive electric fields  $R$  in the Onsager's cavity:

$$\Delta E_{\text{R}} = A \cdot f(n^2) + B \cdot [f(\epsilon) - f(n^2)] \quad (3)$$

where  $\epsilon$  is a solvent dielectric constant,  $A$  and  $B$  are constants, the value and sign of which depend on  $\mu_e$  and  $\mu_g$ :

$$\begin{aligned} A &= 1/a^3(\mu_e^2 - \mu_g^2) \\ B &= 2/a^3\mu_g(\mu_e - \mu_g) \quad \text{- for absorption} \\ B &= 2/a^3\mu_e(\mu_e - \mu_g) \quad \text{- for emission} \end{aligned} \quad (4)$$

Molecule **8** in *trans*-configuration has a center of symmetry. In this case  $\mu_e, \mu_g = 0$  and hence  $A, B = 0$ . This configuration of the molecule is indeed observed for ground state in all studied solvents, as proven by NMR spectroscopy, and therefore the contribution of  $\Delta E_{\text{R}}$  to equation (1) is zero, and the solvatochromism of absorption should be described by

$$E = E_{\text{vac}} - D \cdot f(n^2) \quad (5)$$

Indeed, the experimental data on the absorption of **8** are excellently described by equation (5) with correlation coefficient  $r = 0.996$ , as shown on Figure 1b. It confirms that the main conformation for

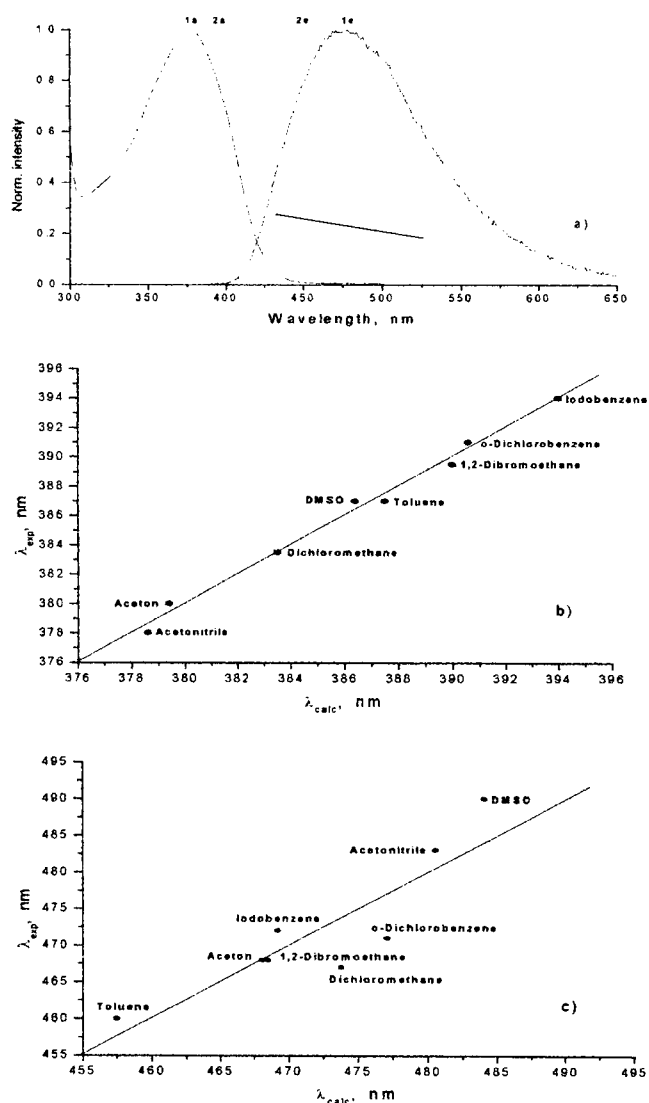


FIGURE 1.

Absorption and emission solvatochromism of **8**. a – experimental spectra: 1a, 1e – in acetonitrile, 2a, 2e – in iodobenzene; b – solvatochromism of absorption according to Eq. (5); c – solvatochromism of emission according to Eq. (6).

ground and vibrationally non-relaxed excited states is a *trans*-configuration.

However, no such correlation ( $r = 0.2$ ) was observed for emission spectra. Therefore, either there is a considerable contribution of specific solute-solvent interactions in the vibrationally relaxed excited state, or the configurations with  $\mu_e \neq 0$  are essentially populated. Since the satisfactory description of the emission data (Fig. 1c,  $r = 0.889$ ) is achieved by equation (1) in its full form:

$$E = E_{\text{vac}} - (D+A)*f(n^2) - B*[f(\epsilon) - f(n^2)] \quad (6)$$

we can conclude that the contribution of the second factor into observed solvatofluorochromism is predominant.

## CONCLUSION

Spectroscopic properties, solvatochromism and fluorosolvatochromism of a new series of conjugated N-arylcarbazole derivatives was investigated. The fluorescent quantum yields within the series are highly dependent on substituents. High reactivity of the carbazole moieties allows easy modification of the chromophore structure and fine tuning their spectroscopic behavior.

## REFERENCES

- [1]. M. Albota, D. Beljonne, J.-L. Bredas, J. E. Ehrlich, J.-Y. Fu, A.A. Heikal, S.E. Hess, T. Kogej, M.D. Levin, S. Marder, D. McCord-Maughton, J.W. Perry, H. Rockel, M. Rumi, G. Subramanian, W.W. Webb, X.-L. Wu and C. Xu, *Science*, **281**, 1653(1998).
- [2]. J.A. Ridsdale and W.W. Webb, *Biophys. J.*, **64**, A109(1993).
- [3]. T. Kogej, D. Beljonne, F. Meyers, J.W. Perry, S.R. Marder, J.L. Bredas, *Chem.Phys.Lett.*, **298**, 1(1998).
- [4]. J. Segal, Z. Kotler, M. Sigalov, A. Ben-Asuly and V. Khodorkovsky, *Proc. SPIE*, **3796**, 153(1999).
- [5]. A.T. Amos and B.L. Burrows, *Adv. Quant. Chem.*, **7**, 289-313(1973).
- [6]. L. Onsager, *J. Am. Chem. Soc.*, **58**, 1486(1936).

## Organic / Inorganic Quantum Confinement Structures Based on Lead Halide Perovskites

YUKO TABUCHI<sup>a, b</sup>, KEISUKE ASAI<sup>a, b</sup>, MASAHIRO  
RIKUKAWA<sup>b, c</sup>, KOHEI SANUI<sup>b, c</sup>, and KENKICHI ISHIGURE<sup>a</sup>

<sup>a</sup>University of Tokyo, 7-3-1, Hongo, Bunkyo-ku, Tokyo 1130033, Japan, <sup>b</sup>CREST, Japan Science and Technology Corporation, <sup>c</sup>Sophia University, 7-1, Kioi-cho, Chiyoda-ku, Tokyo 1028554, Japan

Thin films of two-dimensional layered perovskite compounds  $(\text{RNH}_3)_2(\text{CH}_3\text{NH}_3)_{m-1}\text{Pb}_m\text{X}_{3m+1}$  ( $\text{X} = \text{Cl}, \text{Br}$  and  $\text{I}$ ;  $m = 1 - 3$ ), which have multilayer quantum wells, were systematically prepared. X-ray diffraction patterns demonstrated that the control of the inorganic layer thickness was achieved in all the halogen systems. These layered perovskite films showed a strong, clear exciton absorption peak. The exciton peak shifted to lower energy as the halogen in the structure was changed from  $\text{Cl}$ ,  $\text{Br}$  to  $\text{I}$ . This is due to the difference in the band gap energy. Moreover, with the increasing numbers of inorganic layers, a red shift in the exciton peak was observed.

**Keywords:** quantum wells; perovskite-type compounds

## INTRODUCTION

Organic / inorganic perovskite-type materials  $(\text{RNH}_3)_2\text{PbX}_4$  ( $\text{R} : \text{C}_n\text{H}_{2n+1}$ ,  $\text{X} : \text{halogen}$ ) have been known to form quantum-well structures. In these compounds, the inorganic semiconductor layers of  $[\text{PbX}_6]^{4-}$  and

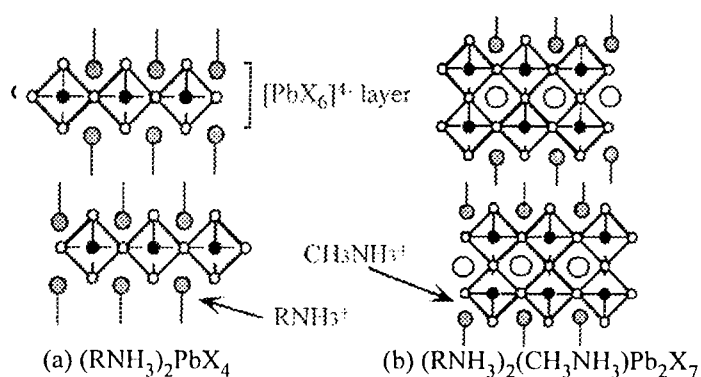


FIGURE 1 Schematic structures of layered perovskite-type materials  $(\text{RNH}_3)_2\text{PbX}_4$  and  $(\text{RNH}_3)_2(\text{CH}_3\text{NH}_3)\text{Pb}_2\text{X}_7$ .

the organic layers of  $[\text{RNH}_3]^+$  are alternately stacked as shown in Figure 1(a). Due to the low-dimensionality of these semiconductor sheets, the exciton of  $(\text{RNH}_3)_2\text{PbX}_4$  has a large binding energy, which enables strong photoluminescence along with a high optical nonlinearity sufficient to offer potential applications in optical devices<sup>1) - 3)</sup>. In addition to the single-layer compounds, multilayer compounds with variable well thicknesses,  $(\text{RNH}_3)_2(\text{CH}_3\text{NH}_3)_{m-1}\text{Pb}_m\text{X}_{3m+1}$ , have been recently prepared<sup>4)</sup>. In these compounds, the multilayer  $\text{CH}_3\text{NH}_3\text{PbX}_3$  are sandwiched between the  $[\text{RNH}_3]^+$  layers. Among these compounds, the optical properties of  $(\text{RNH}_3)_2(\text{CH}_3\text{NH}_3)_{m-1}\text{Pb}_m\text{I}_{3m+1}$  compounds<sup>5), 6)</sup> have been reported widely, however, there are few reports on the  $(\text{RNH}_3)_2(\text{CH}_3\text{NH}_3)_{m-1}\text{Pb}_m\text{X}_{3m+1}$  ( $\text{X} = \text{Cl}$  and  $\text{Br}$ ). In this study, we tried to fabricate the layered perovskites,  $(\text{RNH}_3)_2(\text{CH}_3\text{NH}_3)_{m-1}\text{Pb}_m\text{X}_{3m+1}$  based on  $\text{PbCl}$ ,  $\text{PbBr}$  and  $\text{PbI}$ .

## EXPERIMENTAL

The two-dimensional perovskites  $(\text{C}_6\text{H}_{13}\text{NH}_3)_2(\text{CH}_3\text{NH}_3)_{m-1}\text{Pb}_m\text{X}_{3m+1}$  ( $\text{C}_6\text{H}_{13}\text{Pb}_m\text{X}_{3m+1}$ ,  $\text{X} = \text{Cl}$ ,  $\text{Br}$  and  $\text{I}$ ) were prepared by reacting  $\text{C}_6\text{H}_{13}\text{NH}_3\text{X}$  and  $\text{CH}_3\text{NH}_3\text{X}$  with  $\text{PbX}_2$  in  $\text{N}$ ,  $\text{N}$ -dimethylformamide. Control over the number of inorganic layers is achieved by controlling the relative



concentrations of the two amines. The  $C_6PbX_4$  ( $m = 1$ ) and  $C_6Pb_2X_7$  ( $m = 2$ ) compounds were obtained by a stoichiometric reaction. The  $C_nPb_3X_{10}$  ( $m = 3$ ) perovskite was obtained by adding excess  $CH_3NH_3X$  to the stoichiometry. Thin films were fabricated by the spin-coating method. Optical absorption spectra of the films were taken using a Hitachi U-3500. X-ray diffraction measurements were performed using a Rigaku RAD-IIA with a copper  $K\alpha$  target.

## RESULTS AND DISCUSSION

### X-ray diffraction

The two-dimensional perovskite-type compounds were structurally characterized by X-ray diffraction. Figure 2 shows the X-ray diffraction profiles for a series of spin-coated films of  $C_6PbX_4$  with (A)  $X = Cl$ , (B)  $X = Br$  and (C)  $X = I$ . A series of (00l) diffractions corresponding to the interlayer spacing is clearly observed for the each sample. This reveals that these films were highly oriented with c-axis normal to the substrate. From the diffraction peaks, the long cell dimension along the c-axis was calculated to be (A) 18.4, (B) 18.0 and (C) 16.4 Å, respectively. Considering the molecular size of the lead halide,  $C_6PbI_4$  is thought to show the longest d-spacing. However, as

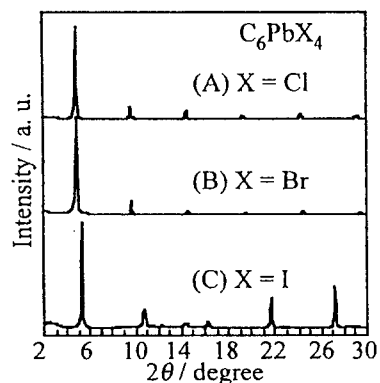


FIGURE 2 X-ray diffraction profiles of  $C_6PbX_4$  spin-coated films with (A)  $X = Cl$ , (B)  $X = Br$  and (C)  $X = I$ .

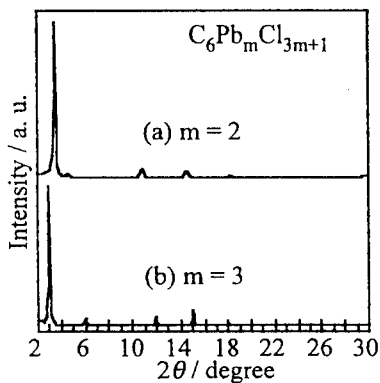


FIGURE 3 X-ray diffraction patterns of  $C_6Pb_mCl_{3m+1}$  films with (a)  $m = 2$  and (b)  $m = 3$ .

the halogen becomes bigger, the interlayer spacing decreases. This trend can be explained by the fact that  $C_nPbX_4$  with long alkyl chains have more space to tilt or interdigitate due to the in-plane spacing with the larger halogen size.

X-ray diffraction patterns for a series of  $C_6Pb_2Cl_7$  ( $m = 2$ ) and  $C_6Pb_3Cl_{10}$  ( $m = 3$ ) spin-coated films are displayed in Figures 3(a) and (b), respectively. A series of (00l) diffractions is clearly observed in each profile similar to the monolayer compounds,  $C_6PbCl_4$ . No evidence for the monolayer compounds could be detected. The interlayer d-spacing values of  $C_6Pb_2Cl_7$  and  $C_6Pb_3Cl_{10}$  calculated from the X-ray diffraction patterns are 24.5 and 29.4 Å, respectively. An increase in the layer spacing was observed in each system compared to the  $m = 1$  compounds. The increase from the  $m = 1$  to the  $m = 2$  and  $m = 3$  structure is 6.1 Å and 11.0 Å, respectively. The thickness of one  $[PbCl_6]^{4-}$  octahedra layer was calculated to be 5.68 Å from the lattice constant of the cubic perovskite  $CH_3NH_3PbCl_3$ <sup>31</sup>. Therefore, the increase observed in  $C_6Pb_2Cl_7$  ( $m = 2$ ) and  $C_6Pb_3Cl_{10}$  ( $m = 3$ ) is the result of inserting one or two more  $CH_3NH_3PbX_3$  perovskite layers per unit cell.

$C_6Pb_2X_7$  and  $C_6Pb_3X_{10}$  for the bromo and iodide compounds were obtained. The structure determinations confirm the “bi” and “trilayer” assignments, respectively.

#### Optical absorption spectra

Figure 4 displays the optical absorption spectra of the  $C_6Pb_mX_{3m+1}$  ( $m = 1 - 3$ ) films measured at room temperature. Each compound exhibits a strong absorption peak due to the lowest exciton states which are formed due to the confinement in the semiconductor wells by the electronic potential and the dielectric confinement effect.

As shown in Figure 4(a),  $C_6Pb_mCl_{3m+1}$  shows a red shift as the inorganic layer width increases. This is due to the decrease in bandgap energy. Similar results were obtained for the  $PbBr$ (b) and  $PbI$ (c) systems. The excitonic bands in the bromides occur at a smaller energy than those of the corresponding chlorides and those of the iodides at a much lower energy than those of the bromides. This is due to the decrease in the

band gap as the halogen changes from Cl→Br→I. Moreover, the exciton peaks of the chlorides are sharper than those of the bromides and much sharper than the iodides. This indicates that the exciton in the PbCl systems has the largest binding energy. The exciton absorption peaks are listed in Table 1.

TABLE 1 Exciton absorption peaks of  $C_6Pb_mX_{3m+1}$  films

X	Exciton absorption peaks / nm (eV)		
	$C_6PbX_4$	$C_6Pb_2X_7$	$C_6Pb_3X_{10}$
Cl	330 (3.76)	349 (3.56)	356 (3.48)
Br	395 (3.14)	431 (2.88)	450 (2.76)
I	512 (2.42)	569 (2.18)	604 (2.05)

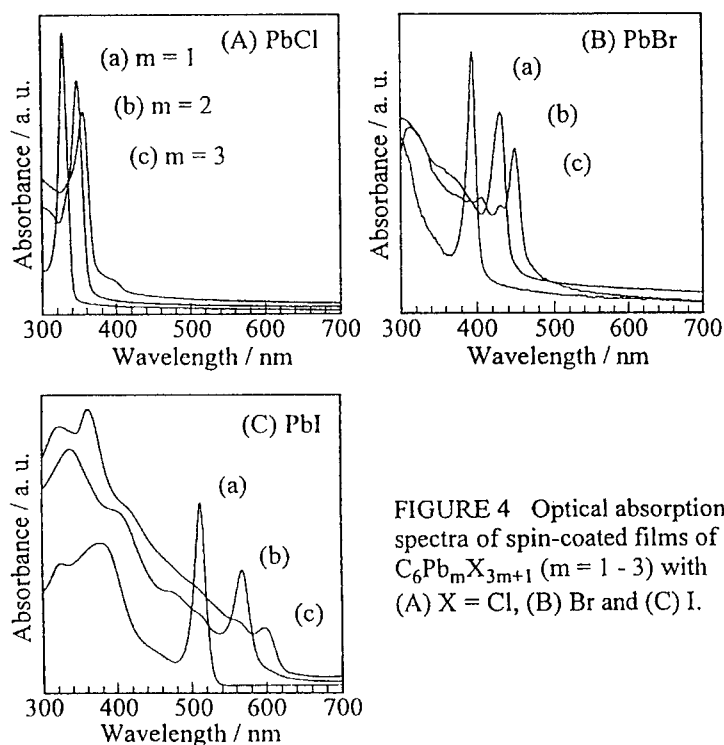


FIGURE 4 Optical absorption spectra of spin-coated films of  $C_6Pb_mX_{3m+1}$  ( $m = 1 - 3$ ) with (A)  $X = Cl$ , (B)  $Br$  and (C)  $I$ .

The thin films of  $\text{C}_6\text{PbX}_4$  ( $m = 1$ ) exhibit a strong photoluminescence even at room temperature. A strong and sharp PL peak was observed at 332, 407 and 523 nm. As the halogen changes from Cl to Br and I, a red shift in the PL peaks was observed similar to exciton absorption. The Stokes shifts from the exciton absorption are calculated to be 17.7, 92.5 and 50.9 meV, respectively. The fact that the exciton was observed even at room temperature demonstrates the stability of the exciton states.

## CONCLUSION

Two-dimensional layered perovskite compounds  $(\text{RNH}_3)_2(\text{CH}_3\text{NH}_3)_{m-1}\text{Pb}_m\text{X}_{3m+1}$  ( $\text{X} = \text{Cl, Br and I; } m = 1 - 3$ ) were systematically prepared. The layered perovskite films showed a strong, clear exciton absorption peak at room temperature due to their large exciton binding energy. The exciton state was found to be controllable by changing the halogen and the number of inorganic layers.

## Acknowledgements

This work was supported by the Core Research for Evolutional Science and Technology (CREST) of the Japan Science and Technology Corporation.

## References

- [1] T. Ishihara, *Optical properties of low-dimensional materials*, 289, World Scientific (1995).
- [2] M. Era, S. Morimoto, T. Tsutsui and S. Saito, *Appl. Phys. Lett.*, **65**, 676 (1994).
- [3] D. B. Mitzi, *Progress in Inorg. Chem.*, **48**, 89 (1999).
- [4] J. Calabrese, N. L. Jones, R. L. Harlow, N. Herron, D. L. Thorn and Y. Wang, *J. Am. Chem. Soc.*, **113**, 2328 (1991).
- [5] G. C. Papavassiliou and I. B. Koutselas, *Synthetic Metals*, **71**, 1713 (1995).
- [6] T. Kataoka, T. Kondo, R. Ito, S. Sasaki, K. Uchida and N. Miura, *Physica B*, **201**, 423 (1994).

## **SESSION I: ORGANIC LIGHT EMITTING MATERIALS**

## Quinoxaline films for hetero-layer light emitting devices

PAOLO IMPERIA<sup>a</sup>, SIGURD SCHRADER<sup>a</sup>, MARIA BENEDETTA CASU<sup>a</sup>, MARKUS JANDKE<sup>b</sup>, PETER STROHRIEGL<sup>b</sup>

<sup>a</sup>Universität Potsdam, Institut für Physik LS PKM, Germany;

<sup>b</sup>Universität Bayreuth, Makromolekulare Chemie I, Germany;

Hetero-layer devices were realised by combination of hole transporting materials like poly(paraphenylenevinylene) (PPV) with new electron transporting heterocyclic polymers and oligomers: poly(phenylquinoxalines) (PPQs) and tris(phenylquinoxalines) (TPQs), respectively. The PPQ and TPQ, suitable as electron-transporting/hole-blocking layers in OLED devices, were studied by combined investigations of ultraviolet photoelectron spectroscopy (UPS), near edge X-ray absorption fine structure, thermally stimulated discharge currents and dielectric relaxation spectroscopy. Furthermore, we used semi-empirical quantum-chemical calculations to understand the valence electronic structure of isolated molecules and to interpret the measured UPS spectra.

**Keywords** Organic light emitting devices; heterocyclic model compounds; ultraviolet photoelectron spectroscopy; quantum chemical calculation; thermally stimulated discharge current.

## INTRODUCTION

The combination of hole transporting and electron transporting materials in hetero-layer structures is a fruitful approach to improve the performances of Organic Light Emitting Devices (OLEDs). Heterocyclic compounds are very interesting as hole blocking/electron transporting materials. The heterocyclic rings are responsible for a high

ionization potential and high electron affinity, in comparison to typical hole transporting materials like polyparaphenylenevinylene (PPV).

## EXPERIMENTAL

We investigated different types of heterocycles i.e. two types of phenylquinoxalines, (PPQ IA and PPQ IIB) and one type of starburst trisphenylquinoxalines (TPQ), (figure 1). We applied the following techniques: ultraviolet photoelectron spectroscopy (UPS), near edge X-ray absorption fine structure (NEXAFS), thermally stimulated discharge current (TSDC), dielectric relaxation spectroscopy (DES) and current-voltage-luminance characteristics.

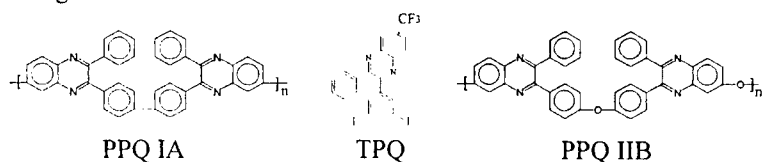


FIGURE 1 Chemical structures of investigated substances.

Both UPS and NEXAFS measurements were performed at BESSY I in Berlin. UPS measurements were carried out at the beam line TGM-2, using an ADES 400 angle resolving spectrometer system, in the incident photon energy range between 35 and 65 eV, at room temperature. The base pressure during the experiments was  $2 \times 10^{-10}$  mbar. Films of TPQ were prepared in-situ by evaporation from pinhole-sources on a Si substrate. The samples were directly transferred to the main chamber, without braking the vacuum, under UHV conditions. The polymer layers were prepared ex-situ by spin coating. NEXAFS measurements were carried out on the same samples, at the CL-RCM beam line, characterised by a constant length Rowland circle soft x-ray monochromator, in total yield detection, with a typical retarding voltage for carbon (-200 V). All the recorded spectra were normalised by a reference grid monitor current. TSDC measurements were performed on polymer films, cast onto fresh aluminium surface from a chloroform solution, subsequently a second aluminium electrode was evaporated under UHV conditions. Details of devices preparation

and of the experiments are given elsewhere [1].

## RESULTS AND DISCUSSION

Figure 2a shows the UPS spectra of TPQ and their theoretical simulation. As expected, for the amorphous nature of the layers, the energy series doesn't show any dispersion of the peaks in dependence on the incident photon energy. This also indicates that no observable charging effects occurred. We directly determined the ionisation potential, 6.0 eV, from the HOMO-onset (highest occupied molecular orbital) by a linear extrapolation and the secondary-electron cutoff, and the work function, 4.2 eV, measured with the sample negatively biased. The theoretical results were obtained using a semi-empirical quantum-chemical calculation method (AM1).

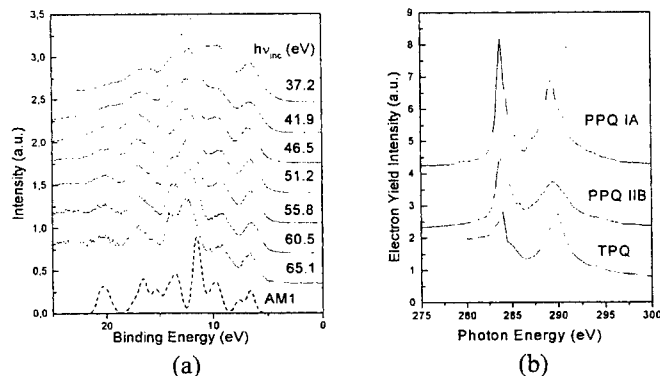


FIGURE 2 (a) Valence electronic spectra of TPQ (full lines) and simulated spectrum (AM1, dash line). They were measured with an angle of incidence of  $45^\circ$  and an emission angle of  $90^\circ$ . The incident photon energy is also indicated. The valence band is given with respect to the vacuum level set at zero; (b) C 1s NEXAFS spectra of PPQ IA, PPQ IIB and TPQ. Vertical offsets are used for clarity.

The effect due to Auger electrons was not considered for the simulation. The calculation was performed taking into account only one molecule.



Since the molecules interact only by van der Waals interaction, and the electronic structure of an organic solid largely preserves that of a molecule or a single chain, we obtained a good agreement with the measured UPS spectra. This allowed to assign the different peaks to the molecular orbitals. While the peak at lowest binding energy is essentially related to the HOMO orbital, the second peak is already due to electron states modified by the molecular interaction, it means a mixture of  $\pi$ - and  $\sigma$ -states. Figure 2b presents C 1s NEXAFS spectra for PPQ IA, PPQ IIB and TPQ. From a qualitative viewpoint we can assume that the spectra of all the species are dominated respectively by the strong  $C\ 1s \rightarrow \pi^*_{C=C}$  and  $C\ 1s \rightarrow \pi^*_{C=N}$  features around 284 and 289 eV [2]. In the PPQ IIB the peaks are broader than in PPQ IA due to the presence of the oxygen bridges while the TPQ has a intensity ratio  $\pi^*_{C=C}/\pi^*_{C=N}$  of about 1 because of the bigger number of heterocyclic rings that favours the  $C\ 1s \rightarrow \pi^*_{C=N}$  signal in comparison to PPQ spectra.

The oxygen bridges also influence TSDC curves as it can be seen in figure 3a. The TSDC spectra show several peaks and in principle they can be of dipolar origin or resulting from charge transport processes. To prove their dipolar nature, we carried out DES measurements on both types of PPQ. Assuming a single elementary relaxation process and described by an Arrhenius law for the relaxation frequency:

$$\alpha(T) = \alpha_r \exp\left(-\frac{A}{kT}\right) \quad (1)$$

with  $A$  activation energy,  $T$  absolute temperature,  $k$  Boltzmann's constant and  $\alpha_r$  natural frequency, we analysed each peak [1] obtaining the values for  $A$  and  $\alpha_r$ . TSD current density is linked in the simplest case to relaxation frequency through the following equation [3]:

$$j(T) = \varepsilon_a \Delta\varepsilon \frac{V}{L} \alpha(T) \exp\left(-s \int_{T_0}^T \alpha(T') dT'\right) \quad (2)$$

$\varepsilon_a$  is the dielectric constant of free space,  $V$  the applied charging voltage,  $L$  the sample thickness,  $s$  the reciprocal heating rate,  $T$  the actual temperature,  $T_0$  the starting temperature and  $\Delta\varepsilon = (\varepsilon_0 - \varepsilon_\infty)$  the relaxation strength, where  $\varepsilon_0$  is the dielectric constant at low

frequencies (static limit),  $\epsilon_\infty$  is the dielectric constant at high frequencies (optical limit). On the other hand the complex component of the dielectric constant is described by the Debye equation [4]. Finding the maximum of this function with respect to the measurement frequency, the condition  $\omega/\alpha = 1$  has to be satisfied. Substituting the following we obtain

$$T_m = -\frac{A}{k \ln \frac{\alpha}{\alpha_r}} \quad (3)$$

Equation 3 allows to determine a temperature range around the  $T_m$  value to be analysed in order to verify whether the peaks in TSDC spectra have a dipolar nature. Exemplifying, for peak I in PPQ IA, a  $T_m$  value between 245 K and 280 K was expected, figure 3b shows the DES analysis linked to this peak: the dielectric relaxation processes exactly occurs in this range and it is softly quenched with the temperature reaching 285 K.

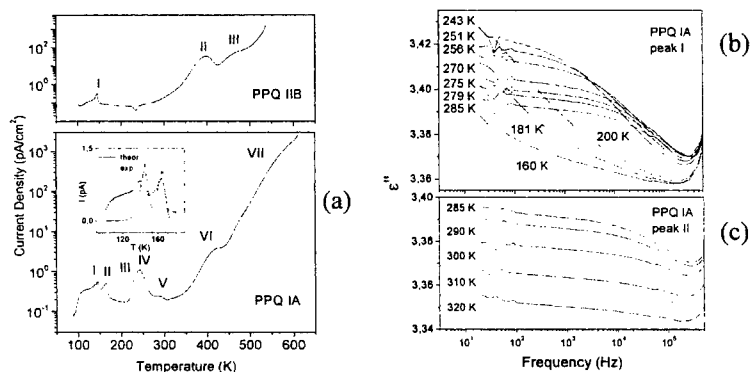


Figure 3 (a) TSDC spectra, the inset shows the simulation of the peaks I and II for PPQ IA; DES spectra peak I (b) and peak II (c).

In figure 3c the same analysis performed for the peak II is shown, the expected  $T_m$  range was between 283 and 320 K, the DES curves do not show any dipolar relaxation. We found that the peaks I and II, even

if they are so close in temperature, figure 3a, have different nature as we have demonstrated with DES measurements. The full spectroscopic and electrical characterisation of the materials forms the background for understanding their behaviour in hetero-layer devices. The use of PPQ and TPQ for preparation of bi-layer devices in combination with PPV leads to an increase of efficiency in comparison to PPV single layer device at least by two orders of magnitude. The on-set voltage of the double layer PPV/PPQ (100 nm/20 nm) device is between 2.2 and 3 V, depending on preparation conditions. At bias of 7 V a brightness of about 250 cd/m<sup>2</sup> was achieved. The double layered PPV/TPQ (70 nm/20 nm) device is also characterised by improved performances with respect to the single layer device: the on-set decreases from 6.5 V to 4.1 V and the luminance increases by 30 %.

## CONCLUSIONS

The UPS measurements provide, in combination with the other spectroscopic techniques, all information about valence electronic structure of the investigated heterocyclic materials. Their high ionization potential favours the hole blocking properties and their high electron affinity favours electron injection from the cathode. The efficiency increases in comparison to single layer devices and this confirms that PPQ and TPQ are promising materials for OLEDs.

## Acknowledgement

Financial support of the European Commission under contract number FMRX-CT97-0106 (TMR-*EUROLED*) is gratefully acknowledged.

## References

- [1] S. Schrader, P. Imperia, N. Koch, G. Leising and B. Falk, Proceeding of SPIE **3797**, 209 (1999)
- [2] J. Stöhr, NEXAFS Spectroscopy, Springer-Verlag Berlin (1996)
- [3] J. Van Turnhout, Electrets, Topics in Applied Physics **33** Springer-Verlag Berlin (1980)
- [4] J. Vanderschueren and J. Gasiot, Thermally Stimulated Relaxation in Solids, Topics in Applied Physics **37** Springer-Verlag Berlin (1979)

## Photoelectron Spectroscopy on a running Organic Light Emitting Diode

M. KIY\*, I. BIAGGIO, and P. GÜNTHER

*Nonlinear Optics Laboratory  
Swiss Federal Institute of Technology  
CH-8093 Zurich, Switzerland, <http://nlo-serv.ethz.ch>*

The Mg cathode surface of a simple ITO / NPB / Alq<sub>3</sub> / Mg Organic Light Emitting Device (OLED) was observed by Ultraviolet Photoelectron Spectroscopy (UPS) during operation of the device in ultra-high-vacuum (UHV). We found that even with a 35 nm thin Mg-cathode, the underlying organic layer never appeared at the surface also after hours of operation in the ultra-pure conditions typical of UHV. The only signs of deterioration at the cathode are a slow oxidation of the Mg-surface. We could show that OLEDs with semitransparent cathodes are stable if they are operated under ultra-high-vacuum conditions.

**Keywords:** Organic; electroluminescence; OLED; UPS; UHV

### 1. INTRODUCTION

The stability of the metal-organic interface at the cathode of an Organic Light Emitting Device (OLED) is an important parameter that can impose a limit on the lifetime of the device. In order to allow an optimization of the devices towards such applications as wide area displays, it is important to better characterize and understand the intrinsic degradation mechanisms that can take place at the cathode interface even in encapsulated devices. In this work we examined the cathode surface of a running, “encapsulated” OLED, by operating it in Ultra-High-Vacuum (UHV) and using Ultraviolet Photoelectron Spectroscopy (UPS). UPS is a very sensitive tool to detect surface changes. Since the device was fabricated and

\*Corresponding author: [kiy@iqe.phys.ethz.ch](mailto:kiy@iqe.phys.ethz.ch)

operated in UHV, we can exclude the effects of impurities, and the isolation of the device from the environment is better than any encapsulation technique.

Any intrinsic deterioration mechanism that affects the Mg-cathode would be visible as a change of the electronic states at the surface of thin Mg cathodes. As an example, one might expect that the Mg further diffuses inside the organic material underneath during operation of the device, and that after a while the electronic states belonging to the organic material start being detected at the surface by UPS.

In order to be able to use a thin Mg cathode, and in order to be able to perform this kind of surface-sensitive measurements, a Ultra-High-Vacuum (UHV) is required.

## 2. EXPERIMENTAL

We produced very simple bilayer device structures on a glass substrate coated with an Indium Tin Oxide (ITO) anode ( $\sim 30$  nm thick), the hole transport layer NPB (N,N'-bis-(1-naphthyl)-N,N'-diphenyl-1,1'-biphenyl-4,4'-diamine,  $\sim 65$  nm thick) and Alq<sub>3</sub> (tris (8-hydroxyquinoline aluminium),  $\sim 80$  nm thick) as an electroluminescent layer, and with Mg ( $\sim 35$  nm) as cathode material. The thicknesses were measured using a calibrated quartz microbalance. Exact thickness measurements of the organic and Mg layer by Rutherford Backscattering Spectroscopy (RBS) were used to calibrate the quartz microbalance (RBS measurements on organic layers are discussed, *e.g.*, in Ref. [1]).

The devices were fabricated in an UHV deposition chamber (base pressure  $3 \cdot 10^{-10}$  mbar) using masks for the device structure. After fabrication the sample was moved without breaking the UHV to a special surface analysis chamber equipped with a He discharge lamp, and a hemispherical electron analyzer (base pressure  $5 \cdot 10^{-10}$  mbar).

An existing electrical connection for applying a bias voltage to the sample during UPS measurements was used to contact the cathode of the device. The OLED anode can be contacted with the walls of the vacuum chamber, which are grounded. Using these two contacts we can apply a voltage to the OLED, and inject a current to induce the electroluminescence, while at the same time measuring the UPS energy distribution curve (EDC). By moving the sample holder slightly, one can remove the

electrical connection of the device anode to the ground, which allows an UPS measurement of the cathode of the inactive device, without electroluminescence.

### 3. ULTRAVIOLET PHOTOELECTRON SPECTROSCOPY

For the UPS measurement we used the He I line (photon energy 21.2 eV) to measure the photoelectron spectrum of the Mg cathode on top of the device. We confirmed that Ultraviolet Photoelectron Spectroscopy (UPS) does not induce any change in the brightness of the electroluminescence. This means that the 21.2 eV photons we use do not lead to rapid photodegradation of the organic layers in our OLEDs. The diameter of the UV spot on the cathode was about 2 mm, while the device size was 4×4 mm. Since the electroluminescence was visible through our thin Mg cathode, we could check the position of the beam while the OLED was running, confirming that the electroluminescence was always visible under the UV beam spot. The small surface area illuminated by the UV light in the middle of the cathode guarantees that all collected photoelectrons come from the cathode of the device. The electron analyzer position is perpendicular to the sample surface.

In the case where the anode has no contact to the chamber the arrangement does not differ from a standard UPS measurement: the surface of the cathode (the material to be analyzed by UPS) is negatively charged, relative to the electron analyzer, by the applied bias voltage. This is the usual technique used to avoid slow electrons which otherwise can not be well detected. For the UPS measurement alone, no change is expected if the anode of the OLED is grounded, because the charge on the cathode is the same. The only difference is that, with the electrical connection between anode and ground in place, a current flows inside the OLED, inducing the electroluminescence.

### 4. RESULTS AND DISCUSSION

Figure 1 shows a UPS measurement on the cathode surface of an OLED before it was operated for the first time (solid curve). After application of a 8 Volts bias voltage to the device, bright green light was visible on the

whole cathode area. After 22 minutes we measured again the UPS signal, and this time obtained the dashed line in Figure 1. The current which was flowing through the  $18 \text{ mm}^2$  area of the device at this time was 3.9 mA. We made several measurements later. The curve after 74 min is shown as a dotted curve in Figure 1. The intensity of the UPS signal is increasing with time. The inset in Figure 1 shows the photoelectron intensity of the peak at 6.1 eV binding energy versus time. The line connecting the points corresponds to a linear relation.

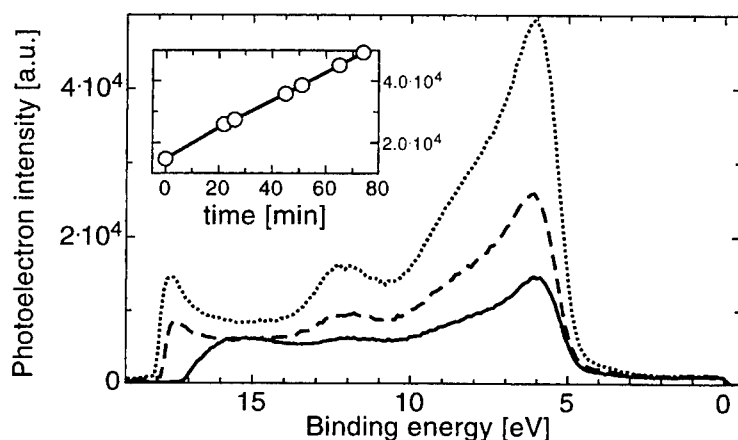


FIGURE 1: UPS measurement on the cathode surface of a device before it was operated for the first time (0 min, solid), after 22 min of operation at a bias voltage of 8 V (dashed), and after 74 min of operation at 8 V bias voltage (dotted). The inset shows the photoelectron intensity at the binding energy 6.1 eV versus time.

We interpret the increase in the intensity of the UPS spectrum as the effect of the slow oxidation of the Mg layer that takes place even in UHV because of the very reactive Mg. UPS is so sensitive that even a part of a monolayer of oxidized Mg at the surface already affects the photoelectron spectrum.

After a half day the Fermi edge is not anymore visible in the UPS spectra and the cathode surface turns completely into MgO (an insulator).

No sharp peak in the UPS spectrum, which could be related to organic molecules at the surface of the cathode, was observed. If  $\text{Alq}_3$  molecules could reach the surface of the Mg layer the signal would be drastically

changed. But we did not find any new peak or changes even after longer time.

This means the Mg cathode of an OLED is not destroyed by an intrinsic mechanism like diffusion of Mg into Alq<sub>3</sub>. The thin cathodes we used would be very sensitive to any changes which occur from the interface and grow towards the surface. From these experiments we can conclude that any interfacial changes taking place at the Mg/Alq<sub>3</sub> interface will be very localized, with a maximum extension lower than 35 nm, the thickness of the cathodes we used.

An additional feature that we observed in the UPS spectrum is a shift of the left edge of the spectrum, related to the slow electrons, when the device is running. While the oxidation of the Mg-cathode is still visible by UPS when the OLED is switched off, this shift in the spectrum only appears when the device is being operated. The left edge becomes sharper and moves by about 1 eV to the left if the current is flowing through the device.

The reason for this behavior is not clear yet. We propose two tentative explanations: (1) Because of the relative arrangement of cathode and ITO-anode on our sample, a deformation of the electric field of the negatively charged cathode can take place when the anode is on ground potential. This involves a higher UPS signal at the slow electron edge and shifts the position of the UPS spectrum to the left, depending on where on the cathode the photoelectrons are emitted from. (2) A non-homogeneous conduction at the cathode surface could lead to spatially inhomogeneous voltage drops over the cathode surface, which would lower the acceleration of photoelectrons, also producing a shift of the left edge of the UPS spectrum.

## 5. CONCLUSIONS

In conclusion, we could observe, for the first time to our knowledge, the changes in the UPS spectrum of the thin Mg cathode of a running OLED.

We found that no intrinsic degradation mechanisms can destroy even a 35 nm thin Mg-cathode. If there is an effect of the OLED operation on the Mg/Alq<sub>3</sub> interface, that this interfacial changes are limited to a thickness of less than 35 nm from the interface.



**Acknowledgments**

This work was supported by the Swiss Federal Institute of Technology (ETH) Zürich. The authors would like to thank Dr. Max Doebli for the thickness measurements using Rutherford Backscattering Spectroscopy.

**References**

- [1] C. H. M. Mare *et al.*, J. Appl. Phys. **84**, 4013 (1998).

## Influence of Hole Transporting Materials on the Emission of Organic LED

ZUGANG LIU, JOÃO PINTO, JORGE SOARES, ESTELA PEREIRA

*University of Aveiro, Department of Physics, 3800 Aveiro, Portugal*  
Email: zugang@fis.ua.pt

The electroluminescent (EL) characteristics of organic light emitting diodes (LED) with , N,N'-bis-(1-naphthyl)-N,N'-diphenyl-1,1'-biphenyl-4,4'-diamine (NPB), 4,4',4''-tris(3-methyl-phenylphenylamino) triphenylamine (m-MTDATA), or both of them as hole transport layer (HTL), and Alq as emissive layer have been investigated. It is found that the full width at the half maxim (FWHM) of electroluminescent (EL) emission band of device with m-MTDATA/Alq interface is 0.53eV at 14V driven voltage, much wider than 0.44eV of photoluminescent (PL) band of Alq film. The EL peak position of the devices with m-MTDATA/Alq interface is red shifted (maxim 0.2eV) and variant with the driven voltage, which is same as the previous results. A blue shift of 0.04eV has been observed in first time, to the best of our knowledge, in the EL emission of the device with NPB/Alq, however neither widening nor variation on driven voltage has been observed. When m-MTDATA completely contact with Alq in dip-coated film of their mixture, the similar phenomena such as red shift and widening have been observed in the PL emission too. The absorption of mixed film shows no new species appears when Alq and HTL materials contact closely.

**Keywords** organic; electroluminescence; hole transport material; exciplex

### 1. INTRODUCTION

Organic light emitting diodes (LED) have been widely studied in the past decade since Tang and his co-workers published their work (1, 2). They have shown a potential application in flat panel display and, as widely considered, will be in use in the near future. In addition to the advantages in fabrication and application, organic LED attracts a lot of physics and chemistry scientists to study its complex electroluminescent mechanism.

In organic LED, a hole transport layer (HTL), mostly a derivative of triphenylamine, is used to enhance the emission from the emissive electron transport layer, normally a chelate of tris-8-hydroxyquinoline aluminum (Alq). The HTL is believed to increase the hole injection from anode contact and to form an electron block barrier at the interface of the two organic layers to increase the recombination efficiency with the electron injected from cathode contact. 4,4',4''-tris (3-methyl-phenylphenylamino) triphenylamine (m-

MTDATA) (3,4,5), and N,N'-bis-(1-naphthyl)-N,N'-diphenyl-1,1'-biphenyl-4,4''-diamine (NPB) (6,7,8) are widely used as HTL due to their high glass transition temperature and stability.

When m-MTDATA was used as HTL in double layer devices, a yellow exciplex emission, generated from the excited state of Alq and the ground state of m-MTDATA, has been observed (9,10). But the influence of NPB on the electroluminescent (EL) emission of devices has not been reported, to the best of our knowledge. We found in devices with NPB/Alq contact, a clear blue shift comparing to the green emission of Alq, and a red shift in the devices with m-MTDATA/Alq contact. In PL spectra of dip coated films of mixed Alq and HTL material, similar emission have been observed in Alq/m-MTDATA mixture while no significant change has been observed in Alq/NPB mixture. This paper will report the changes of EL emission of the devices with NPB/Alq and m-MTDATA/Alq contacts and PL emission of films of mixed HTL and emissive material.

## II. EXPERIMENTAL

The devices are made according to the following steps. On a sufficiently cleaned ITO coated glass, in the same vacuum chamber, the organic HTL materials m-MTDATA (Syntec GmbH ST627) and NPB (Syntec GmbH ST16/7) are deposited on different zones separately. Then the emissive material Alq (synthesized by us) is deposited on top of the different HTL layers. The thickness of organic layers, measured and controlled by Sycon Instruments STM-100 thickness/rate monitor, are 40nm respectively. The deposition rate is about 0.2 nm/sec. The metal aluminum (200nm) is finally deposited on the Alq layer; thus two devices with different HTL are made on one substrate at almost the same conditions.

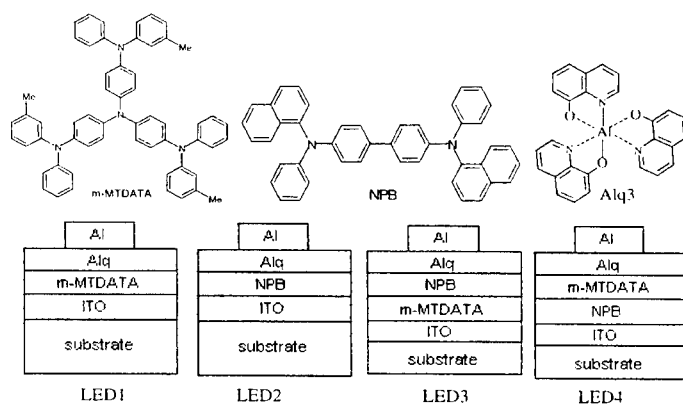


Figure 1: the molecular structures of materials and the diagrams of LED devices

The structures of two devices are ITO/m-MTDATA/Alq/Al (LED1) and ITO/NPB/Alq/Al (LED2) (see figure 1). For comparison, two triple layer devices with structure ITO/m-MTDATA/NPB/Alq/Al (LED3) and ITO/NPB/m-MTDATA/Alq/Al

(LED4) are made under similar condition. The LED devices are encapsulated with glass covers by epoxy adhesive in nitrogen atmosphere.

Single films of Alq, m-MTDATA, NPB, and bilayer films of m-MTDATA/Alq and NPB/Alq are vacuum deposited for measurement of photoluminescent and absorption spectra.

On the other hand, thin films of Alq, m-MTDATA, NPB, mixture of m-MTDATA and Alq (1:1 molecular), and mixture of NPB and Alq are dip coated on the quartz for measurement of the absorption and PL spectrum, too.

The photoluminescent (PL) spectra of the vacuum deposited films (40nm, same as that in the devices) and the dip-coated films are measured by a Czery-Turner SPEX 1704 spectrometer with a Hamamatsu 928 photo-multiplier, with excitation at 360nm. The electroluminescent (EL) spectra of devices are also measured by Czery-Turner SPEX 1704 spectrometer with a Hamamatsu 928 photo-multiplier, driving by a self-made direct power supply. The absorption spectra of the vacuum deposited films and dip-coated films are measured with a Shimadzu UV-2100 UV-visible recording spectrophotometer. All the measurements are carried out at ambient atmosphere and room temperature.

### III. RESULTS AND DISCUSSIONS

#### 1. Changes of EL Spectra of Devices with Different HTL

Figure 2 shows the EL spectra of the four LED's and also the PL of Alq single layer film. The LED1 with m-MTDATA as the HTL is greenish yellow and its emission band is much wider than the emission of Alq single layer film. The emission has the center peak at about 545nm (2.26eV) when driven at 14 Volts, the full width at half maximum (FWHM) of the emission being 0.53eV, wider than the 0.44eV of PL emission of Alq. The LED2 with NPB as the HTL gives green emission centered at 516nm (2.40eV), a blue shift comparing to the emission centered at 525nm (2.36eV) of PL of Alq single layer. The FWHM of emission of LED2 is about 0.44eV, almost same as that of an Alq single layer.

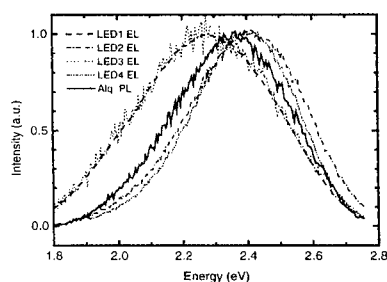


Figure 2. Electroluminescent spectra of four LED devices driven at 14 volts and PL spectrum of Alq film

To avoid the direct contact between m-MTDATA and Alq in LED1, we insert a NPB layer between them (LED3). The EL emission band is almost the same as that of LED2.

When we insert an m-MTDATA layer between NPB and Alq in LED2 to make LED4, we get an emission exactly same as that of LED1, as shown in figure 2.

From figure 2, one can see that the same emission come from the same HTL/EML interface. That means in these double layer devices, the emissions are from that interface and depend only on the HTL materials in contact with EML.

## 2. EL Spectrum Variation with the Applied Voltage

We found the EL spectra of the devices with m-MTDATA/Alq contact vary with driven voltage. It shifts from 570nm (2.17eV) to 545nm (2.28eV) when the driven voltage increases from 8V to 14 volts. On the other hand, the EL spectra of devices with NPB/Alq interface do not change their peak at 516nm (2.40eV) when increasing the applied voltage. Figure 3 shows the emissions of LED1 and LED2 at different driven voltage. For the device LED4 with NPB/Alq contacts, no significant change has been observed, too.

For the LED1, as discussed above, the wide emission band is composed of emission of bulk Alq layer near the m-MTDATA/Alq interface and exciplex emission at the same interface. When the applied voltage is increased, more holes and electrons are injected into the organic layers at two organic/electrode contacts, respectively. So, except the exciplex emission at the interface, more recombination will occur in the Alq bulk layer and hence emission in the bulk Alq layer increases.

In the LED2, the emission is generated mainly from the Alq layer near the NPB/Alq interface. No exciplex is observed and the center peak is insensitive to driven voltage. The origin of the 40meV shift to higher energy compared with the Alq PL requires further work

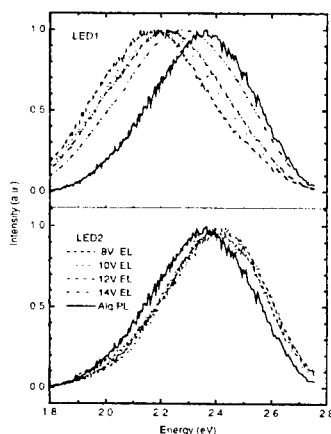


Figure 3. EL spectra of LED1 and LED2 at different applied voltage

## 3. PL Spectra of Mixture Films

To check the interaction between two HTL materials and Alq, we measured photoluminescent spectra of dip-coated m-MTDATA (D), NPB (N), Alq (A) films, m-MTDATA and Alq mixture film (m-MTDATA+Alq, namely D+A), and NPB and Alq mixture film (NPB+Alq, namely N+A), as shown in figure 4. We found that the emissions of both m-MTDATA and Alq are quenched and an emission band similar to the emission of LED1 is observed in m-MTDATA+Alq mixture film. For NPB+Alq mixture film, emission quench is also observed but the emission is similar to the emission of Alq film itself. One can see the spectra of m-MTDATA+Alq mixture films is a little wider than the Alq film and the center peak is changed from 520nm (2.38eV) of Alq film to 530 nm (2.33eV). It can be seen that the emission band of the mixed film is composed

of the emission band of Alq and the exciplex emission at m-MTDATA+Alq interface and the Alq layer.

The figure 4 shows also the PL spectra of the bilayer films that are the same as those in the bilayer devices. We can see that the bilayer films do not give any new emission except an emission band of HTL with a shoulder of emission of Alq at lower energy side. The bilayer film m-MTDATA/Alq shows a superposition of the band centered at 2.91eV corresponding to the emission of m-MTDATA and the band at 2.36eV corresponding to the Alq. The bilayer film NPB/Alq emits a main band with center peak at 2.88eV with a small shoulder at 2.36eV of Alq. When excited by photons with energy which only excite Alq (2.95eV), both bilayer films only emit a band centered at 2.36eV, which is same as the emission in the single layer Alq film. Thus the shift in EL to higher energy can not be connected with some new levels induced at the interface. So far we have not any explanation for this blue shift of the EL, and further study will be carried out.

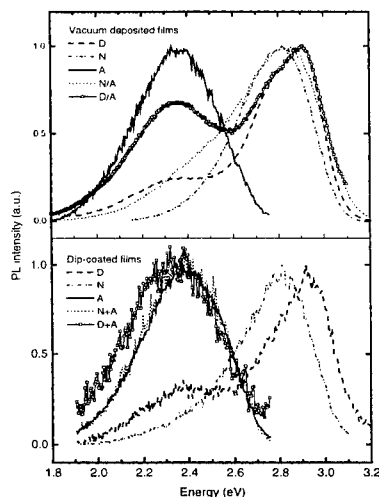


Figure 4. The photoluminescent spectra of the dip-coated films and the vacuum deposited films. The dip-coated films are those of m-MTDATA (D), NPB (N), Alq (A) and their mixture m-MTDATA+Alq (D+A) and NPB+Alq (N+A). The vacuum deposited films are single layer films of D, N and A, and the bilayer films of D/A and N/A.

#### 4. Absorption Spectra of the Mixture Films

We measured the absorption spectra of dip-coated films of the above mixtures of m-MTDATA+Alq, NPB+Alq, and evaporated bilayer films of m-MTDATA/Alq and NPB/Alq, as shown in figure 5. By fitting the absorption spectra of the bilayer films and the mixture films, we can see that no new emission band appears. However quenching in absorption at higher energy of both HTL and emissive materials in the mixture films is observed. This indicates that there is not any new species produced in the mixture. It is clear that, for the bilayer film, the absorption is a linear supposition of two components but for the mixture, however, only in the lower energy side, the absorption is the sum of those of the components. The absorption bands at higher energy side of both HTL and EML materials are quenched.

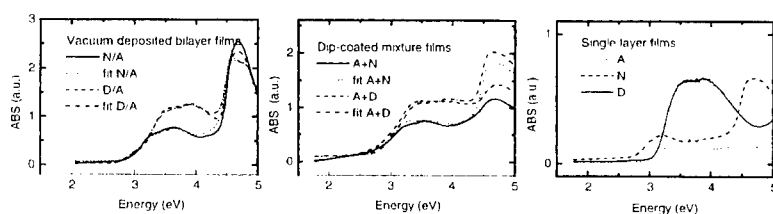


Figure 5. The absorption spectra of the dip-coated mixture films m-MTDATA and Alq (D+A), NPB and Alq (N+A), comparing with those of deposited bilayer films D/A and N/A. latter can be well fitted by simple superposition of absorption of the components.

#### IV. CONCLUSIONS

From the EL spectra of four organic LED devices, we concluded that the emission is generated at the heterojunction, namely the direct contact of Alq with hole transport material, such as the m-MTDATA/Alq contact in LED1 and LED3, and the NPB/Alq contact in LED2 and LED4. For the m-MTDATA/Alq contact, the exciplex emission is clearly observed in both EL and PL, while for the NPB/Alq contact, a blue shift is measured in EL but not in PL. The origin of the blue shift in the emission of devices with NPB/Alq contact has not been previously reported and is currently under further study. The absorption spectra of mixtures of HTL materials and Alq show that no new absorption appears, indicating that there is no new in the system.

#### Acknowledgements

This work is partially supported by Foundation for Science and Technology (FCT) of Portugal and by Foundation of Calouste Gulbenkian (FCG) of Portugal.

#### Reference:

1. C. W. Tang and S. A. VanSlyke, *Appl. Phys. Lett.*, **51**(12):913(1987)
2. C. W. Tang, S. A. VanSlyke and C. H. Chen, *J. Appl. Phys.*, **65**(9): 3610-3616(1989)
3. Y. Shirota, Y. Kuwabara, H. Inada, T. Wakinoto, H. Nakada, Y. Yonemoto, S. Kawami, and K. Imai, *Appl. Phys. Lett.*, **65**(7):807(1994)
4. C. Giebder, H. Antoniadis, D. D. C. Bradley, Y. Shitota, *Appl. Phys. Lett.*, **72**(19):2448(1998)
5. J. Staudigel, M. Stossel, F. Steuber, J. Simmerer, *Appl. Phys. Lett.*, **75**(2):217(1999)
6. Jianmin Shi, and C. W. Tang, *Appl. Phys. Lett.*, **70**(13):1665(1997)
7. H. Aziz, Z. Popovic, S. Xie, A. Hor, N. Hu C. Tripp, and G. Xu, *Appl. Phys. Lett.*, **72**(7):756(1998)
8. J. Kido and Y. Iizumi, *Appl. Phys. Lett.*, **73**(11):1457(1998)
9. K. Itano, H. Ogawa, and Y. Shirota, *Appl. Phys. Lett.*, **72**(6):636
10. C. Giebder, H. Antoniadis, D. D. C. Bradley, Y. Shitota, *J. Appl. Phys.*, **85**(1):608(1999)

## Probing space charge distributions in polymer LEDs by means of an electro-optic technique

F. MICHELOTTI<sup>a</sup>, S. BUSSI<sup>a</sup>, Z. BAO<sup>b</sup> and M. BERTOLOTTI<sup>a</sup>

<sup>a</sup>Istituto Nazionale di Fisica della Materia – Dip. Energetica, Via A. Scarpa, 16 I-00161 Roma Italy; <sup>b</sup>Lucent Tech., Bell Labs, 600 Mount. Avenue, Murray Hill, NJ, USA

### ABSTRACT

A single wavelength electro-optical reflection technique was used to study the creation of space charge distributions in an aluminium/polymer/indium tin oxide light emitting diode by monitoring the third order nonlinear optical response of the electroluminescent layer. The polymer is a derivative of poly(p-phenylene-vinylene) in which oxadiazole groups were grafted as side chains. The measured signal is strongly influenced by space charge distributions and by electro-static screening in the organic layer. The space charge distribution is the superposition of a stable one close to indium tin oxide, and of a slowly changing one due to carriers injected in the polymer film. Taking into account Debye-Hückel screening, with screening length  $\lambda=100\text{nm}$ , we estimated the density of the stable distribution to be  $\rho_0=1.5\cdot 10^{24}\text{ m}^{-3}$ , for a uniform distribution in a 110nm thick layer. The influence of carrier injection on the electro-optic signal results to be ten times smaller than that of stable charge.

**Keywords** electroluminescence; electro-optics; polymer; electroabsorption; OLED

### 1. INTRODUCTION

In the past few years, the applications of organic molecular and polymeric compounds in light emitting devices have drawn much interest<sup>1</sup>. Since the first observation of electroluminescence in a poly(phenylene-vinylene) (PPV) based device in 1989, a great number of papers appeared dealing with various PPV derivatives, charge injection from electrodes and device geometrical configurations<sup>2</sup>. However, it is not until recently that the mechanisms of charge injection, transport, and eventually trapping in the organic layers were shown to limit device performance. Many reports confirm the partially reversible creation of space charge (SC) distributions in organic devices upon application of a bias voltage<sup>3</sup>. There is not, however, consensus on the origin of such charges, that is whether they should be attributed to ions, trapped carriers or dipolar species. Very recently it was shown that charge transport and luminescence can be strongly influenced by ionic SC distributions in polymer LEDs<sup>4</sup>.



Here, we investigated a PPV derivative with electron-deficient oxadiazole sidechains covalently linked to PPV backbones (OXA1PPV) as shown in the inset of Figure 1. This molecular design strategy has been shown to improve the EL device performance for single-layer LEDs with air-stable Al cathodes compared to similar PPVs with electrically inactive alkyl sidechains<sup>5</sup>. The external quantum efficiency for OXA1PPV has been shown to be about ten times higher<sup>6</sup>.

## 2. EXPERIMENTAL

The OXA1-PPV was dissolved in 1,1,2-tetrachloroethane and spun on glass substrates previously coated with an indium tin oxide (ITO) transparent anode, with a sheet resistance of about  $20 \Omega/\square$ . The thickness of the OXA1-PPV films is  $h=285\text{nm}$ . The films were finally coated with an evaporated  $1500\text{\AA}$  thick aluminium cathode. The current/voltage characteristic was measured in dark, showing that charge transport follows a trap charge limited power law<sup>6</sup> with an exponent  $m=2\div 6$ . The creation of SC distributions leads to a hysteresis when cycling the bias voltage between positive and negative values, similar as what have been reported for other PPV derivatives<sup>7,8</sup>. Due to the relatively large thickness, electro-luminescence was not observed.

We used a polarisation sensitive single wavelength electro-reflectance experimental technique<sup>9</sup> in order to check the presence of SC distributions in OXA1-PPV. The technique is an ellipsometric evolution of the standard electro-reflectance<sup>10</sup>; it is more satisfying in selecting interface and bulk contributions than other common techniques, such as electro-absorption for example. The experimental set-up is sketched in Figure 1. A laser beam at  $\lambda=632.8\text{ nm}$  is impinging

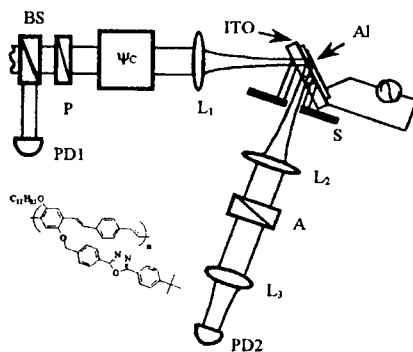


Figure 1 - Experimental set-up. (BS) beam splitter, (P) input polariser, (A) analyser, (C) voltage driven liquid crystal compensator, ( $L_1$ ,  $L_2$ ,  $L_3$ ) focusing optics ( $f_1=200\text{mm}$ ,  $f_2=70\text{mm}$ ,  $f_3=50\text{mm}$ ), (S) diaphragm used to extinguish multiple reflections from the glass substrate, (PD1, PD2) input and output silicon photodiodes. The input laser beam is produced by a low power He-Ne polarised laser. In the inset the chemical structure of the OXA1PPV is shown. Inset: chemical structure of OXA1PPV.

on the sandwich structure from the glass side, at an angle  $\alpha$ . Before incidence, the beam is polarised (P) with equal p and s components, whose relative phase  $\psi_c$  can be changed by means of the liquid crystal phase retarder (C). After reflection the beam is analysed by a cross polariser (A) and its power is detected by a silicon photodiode (PD2). Upon application of the voltage  $V(t) = V_{off} + V_{mod} \cos(\Omega t)$  to the electrodes, the reflected intensity can be modulated at  $\Omega$  and  $2\Omega$ , due to either a phase or an amplitude modulation of the p and s components. In the case of a disordered polymer, the modulation can be attributed to the bulk complex third order nonlinear response (Kerr electro-optic effect and electro-absorption) as well as to modulation of the reflectance of the ITO/polymer interface due to locally induced changes of the polymer refractive index<sup>8</sup>.

The average reflected power is given by:

$$P_{\alpha} = \frac{1}{4} |r_s|^2 P_0 \{ \tan^2 \Phi - 2 \tan \Phi \cdot \cos(\Psi_p + \Psi_s) \}, \quad (1)$$

where  $P_0$  is the input power,  $\Phi$  and  $\Psi_{ps}$  are defined by  $r_p/r_s = \tan(\Phi)e^{j\Psi_{ps}}$ , and  $r_{p,s}$  are the reflection coefficients for the p and s polarisations. Taking into account only bulk effects, the power modulation at  $\Omega$  and  $2\Omega$  upon application of  $V(t)$  is given by:

$$P_{\alpha}(\Omega) = A(\alpha) \cdot P_0 |r_s|^2 \cdot \Gamma_1 \cdot \{ \text{Re}(\tilde{\chi}^{(3)}) \cdot \tan(\Phi) \cdot \sin(\Psi_p + \Psi_s) + \text{Im}(\tilde{\chi}^{(3)}) \cdot [\tan(\Phi) - \cos(\Psi_p + \Psi_s)] \}, \quad (2)$$

$$P_{\alpha}(2\Omega) = \frac{1}{4} A(\alpha) \cdot P_0 |r_s|^2 \cdot \Gamma_2 \cdot \{ \text{Re}(\tilde{\chi}^{(3)}) \cdot \tan(\Phi) \cdot \sin(\Psi_p + \Psi_s) + \text{Im}(\tilde{\chi}^{(3)}) \cdot [\tan(\Phi) - \cos(\Psi_p + \Psi_s)] \}, \quad (3)$$

where  $\tilde{\chi}^{(3)}$  is the main third order susceptibility tensor component ( $z$  is the stacking direction) for the weakly anisotropic polymer film<sup>11</sup>.  $\Gamma_1 = \int_0^h E_s(z) E_m(z) dz$  and

$\Gamma_2 = \int_0^h E_m^2(z) dz$  are overlap integrals along the polymer thickness.  $E_m(z)$  is due to  $V_{mod}$ .

$E_s(z)$  is due both to  $V_{off}$ , to the  $V_{bi}$  given by the difference of the work functions  $\Delta\Phi$  of Al and ITO ( $V_{bi} = \Delta\Phi/e = -0.5V$ ) and eventually to charges in the OXA1PPV film. For a perfect and charge-free insulator  $\Gamma_1$  and  $\Gamma_2$  reduce to  $\Gamma_1 = V_{mod}(V_{off} + V_{bi})/h$  and

$\Gamma_2 = V_{mod}^2/h$  and  $E_m(z) = V_{mod}/h$ ,  $E_s(z) = (V_{off} + V_{bi})/h$ . Neglecting

multiple reflections<sup>9</sup> in the sandwich and in the low birefringence approximation:

$$A(\alpha) = \frac{2k_0}{n^2} \cdot \frac{\sin^2 \alpha}{\sqrt{n^2 - \sin^2 \alpha}}, \quad (4)$$

where  $k_0$  is the vacuum wave-number and  $n$  is the linear refractive index. Measurements performed for  $\alpha \in [20^\circ, 65^\circ]$  show that eqn. (4) is a first order approximation and that multiple-reflection interference effects cannot be neglected. However we overtook the problem by performing independent measurements at  $\Omega$  and  $2\Omega$  for the same  $\alpha$  and eliminating  $A(\alpha)$  from eqns. (2) and (3).

In Figure 2, we report ellipsometric measurements by plotting

$V_{\alpha}^{(2\Omega)}(\Omega; \Psi_c)$  versus  $V_{\alpha}(\Psi_c)$ , proportional to  $P_{\alpha}(\Omega; \Psi_c)$  and  $P_{\alpha}(\Psi_c)$ , measured

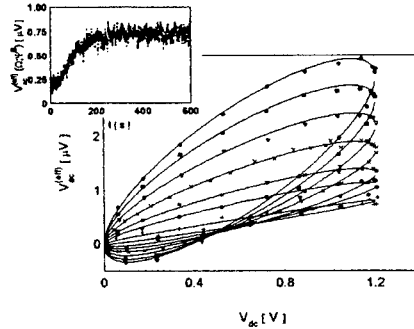


Figure 2 - Electro-optic measurements for a 285nm thick OXA1-PPV film. Data were obtained for  $V_{mod}=3V$ ,  $\alpha=30^\circ$ ,  $\Omega/2\pi=1680Hz$ ,  $T=T_{room}$  and for the following values of  $V_{off}$ : (●) -6V, (■) -4V, (▽) -2V, (×) 0V, (\* ) +2V, (○) +4V, (+) +6V. The solid lines are the fits with the Eqs. (1) and (2). In the inset the transient  $V_{\alpha}^{(2\Omega)}(\Omega; \Psi_c)$  signal time dependence is shown, when switching  $V_{off}$  from +7V to -7V. Inset: temporal dependency of the signal measured in one bias point.

respectively by a lock-in amplifier and a voltmeter connected to the photodiode, for several different  $\Psi_c$ . The curves were obtained for fixed values of  $V_{mod}=3V$ ,  $\alpha=30^\circ$ ,  $T=300\text{ K}$ ,  $\Omega/2\pi=1680\text{ Hz}$ ;  $V_{off}$  was scanned between  $-6V$  (uppermost curve) and  $+6V$  (lowest curve). The expected ellipse, as given by Eq.(1) and (2), is observed. The aperture of the ellipses is due to  $Re(\tilde{\chi}_{zz}^{(1)})$ , while the slope should be due to  $Im(\tilde{\chi}_{zz}^{(1)})$  bulk effects; in practice the slope signal is heavily affected by the modulation of the ITO/OXA1PPV<sup>1</sup> interface reflectivity, triggered by the Kerr effect and charge injection, which is difficult to model theoretically<sup>12</sup>. Fitting the ellipses one can get the value of their aperture, neglecting the slope contribution; as a matter of fact it is sufficient to measure the signals in the two bias points  $\Psi^{A,B}=(\Psi_{ps}+\Psi_c)=\pm\pi/2^\circ$ , and evaluate the quantities:

$$S_{Kerr}(\Omega) = \frac{V_{\alpha}^{(\Psi^A)}(\Omega, \Psi^A) - V_{\alpha}^{(\Psi^B)}(\Omega, \Psi^B)}{2V_{\alpha}} = \Lambda(\alpha) \cdot \frac{\tan \Phi}{1 + \tan^2 \Phi} \cdot \Gamma_1 \cdot Re(\chi_{zz}^{(3)}) \quad (5)$$

$$S_{Kerr}(2\Omega) = \frac{V_{\alpha}^{(\Psi^A)}(2\Omega, \Psi^A) - V_{\alpha}^{(\Psi^B)}(2\Omega, \Psi^B)}{2V_{\alpha}} = \Lambda(\alpha) \cdot \frac{\tan \Phi}{1 + \tan^2 \Phi} \cdot \Gamma_2 \cdot Re(\chi_{zz}^{(3)}) \quad (6)$$

in order to extract the information on  $\Gamma_1$ ,  $\Gamma_2$  and  $Re(\chi_{zz}^{(3)})$ .

In Figure 2 we observe that there is a signal for  $V_{off}=0$  and that it vanishes for  $V_{off}$  as high as about  $+7V$ , much higher than the  $-V_{bi}$  predicted by the Eq. (2) for a perfect and charge free insulator. Such result suggests that a very stable SC distribution  $\rho(z, t; V_{off})$  exists in the polymer film, giving rise to an additional  $E_{\rho}(z, t)$ . However such assumption is not sufficient as  $\Gamma_1=0$  for  $V_{off}+V_{bi}=0$ , in a perfect insulator and if  $\rho(z, t; V_{off})$  is slowly-varying with respect to  $V_{mod} \cos(\Omega t)$ . This last assumption is justified by transient electro-optic measurements and by measurements as a function of  $\Omega^3$ . As an example, in the inset in Figure 2 we report the measurement of  $V_{\alpha}^{(\Psi^A)}(\Omega, \Psi^A)$  as function of time, obtained by switching  $V_{off}$  from  $+7V$  to  $-7V$  at  $300K$ ; the dynamics, due to the assessment of a stationary  $\rho(z, \infty; V_{off})$ , show time-scales in the  $10^2\text{ s}$  range.<sup>14</sup>

It is then necessary to take into account an additional mechanism giving rise to the large offset. Supposing that the large amount of polarisable oxadiazole side-chains in the material gives rise to electrostatic Debye-Hückel screening with characteristic length  $\lambda$ , both the  $E_m(z)$  and  $E_s(z)$  profiles in the active film are distorted;  $E_m(z)$  is stronger close to the electrodes and acts as a weighting function for  $E_s(z)$  in  $\Gamma_1$ . In a simplified analytical model, considering a space charge distribution of thickness  $\delta$  close to ITO with an uniform density  $\rho(t; V_{off})$  and screening, we obtain:

$$\Gamma_1(t; V_{off}) = \kappa \frac{V_{mod}}{h} [V_{off} + V_{bi} + V_{DH}(t; V_{off})] \quad \text{and} \quad \Gamma_2 = \kappa \frac{V_{mod}^2}{h} \quad (7)$$

where:

$$V_{DH}(t; V_{off}) = \frac{\lambda^2 \rho(t; V_{off})}{\epsilon} \left( -\frac{\beta_2 + 1}{2\beta_1} + \frac{\beta_4}{\beta_1 \beta_3} \right), \quad \kappa = \frac{\beta_1^2 \beta_3}{4} \frac{h}{\lambda}, \quad \beta_1 = \frac{1}{\lambda(1 - e^{-h/\lambda})}$$

$$\beta_2 = [1 + e^{-h/\lambda} - e^{-\delta/\lambda} - e^{-(h+\delta)/\lambda}] \cdot \lambda \beta_1, \quad \beta_3 = 1 - e^{-2h/\lambda} + 2 \frac{h}{\lambda} e^{-h/\lambda},$$

$$\beta_4 = \frac{\delta}{\lambda} e^{-\delta/\lambda} + \frac{1}{2} e^{-(h+\delta)/\lambda} - \frac{1}{2} e^{-(h-\delta)/\lambda} + \frac{h-\delta}{\lambda} e^{-(h-\delta)/\lambda} + \frac{1}{2} e^{-\delta/\lambda} - \frac{1}{2} e^{-(2h-\delta)/\lambda}.$$

The Eqns.(7) show that the condition  $I_1=0$  can be shifted by  $V_{DH}$ , justifying what observed in Figure 2. In the model the  $\rho(t;V_{off})$  is the sum of a very stable  $\rho_0$ , due to fixed charges, and of a slowly varying  $\rho_{inj}(t;V_{off})$ , due to mobile charges injected in the film. A stationary  $\rho(\infty;V_{off})$  can be assumed if  $V_{off}$  is kept constant long enough to exhaust the transients. Such circumstance leads to the fact that when the  $S_{Kerr}(\Omega)$  vs  $V_{off}$  characteristic is measured (figure 3, (V)) the differential slope is changing during the scan (relaxed method), due to the variation of  $\rho(\infty;V_{bias})$  between adjacent stationary states, as observed in electro-absorption measurements too<sup>15</sup>. In order to deal with a constant SC distribution we performed the measurement in the following way (flash method): the sample is biased at  $V_{bias}$  and a stationary SC distribution  $\rho(\infty;V_{bias})$  is created in the film; the offset voltage is switched at fixed time intervals to  $V_{off}$  and kept at this level for the time of a measurement, which is sufficiently short to hinder relaxation; measurements are performed in the two bias points  $\Psi^{A,B}$  and are repeated for several values of  $V_{off} \in [-7V, +7V]$ . The dependence of  $S_{Kerr}(\Omega)$  on  $V_{off}$  is

shown in Figure 3 (■ and ●) for  $\alpha=50^\circ$  and for two different positive  $V_{bias}$  is now linear, as expected from eqn. (7). The relatively weak dependence of the zero crossing point on  $V_{bias}$  indicates that the effect of  $\rho_0$  is definitely larger than that of  $\rho_{inj}(\infty;V_{bias})$ . The curves approach the curve obtained with the relaxed method when  $V_{off}$  equates the fixed  $V_{bias}$  for each of them. When fitting data, the pre-factor in eq.5 can be obtained from an independent measurement of  $S_{Kerr}(2\Omega)$ ; as an example, in the inset of Figure 3, the measurement of  $S_{Kerr}(2\Omega)$  vs

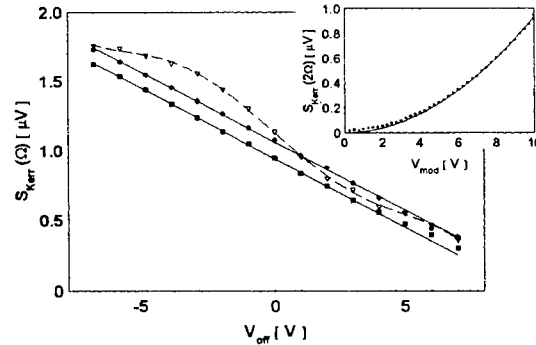


Figure 3 - Dependence of  $S_{Kerr}(\Omega)$  on  $V_{off}$  in a flash measurement. Data were obtained for  $V_{mod}=3V$ ,  $\alpha=50^\circ$ ,  $\Omega 2\pi=1680Hz$ ,  $T=T_{room}$  and for the following values of  $V_{bias}$ : (■) +3.5V, (●) +7V; the solid lines are the theoretical fits obtained with  $\delta=110nm$ ,  $\lambda=100nm$ , and respectively  $\rho_0=1.3 \cdot 10^{18} cm^{-3}$  and  $\rho_0=1.5 \cdot 10^{18} cm^{-3}$ . With (V) data obtained in a relaxed measurement are shown; each point is obtained waiting 20' after changing  $V_{off}$ . In the inset a measurement of  $S_{Kerr}(2\Omega)$  vs  $V_{mod}$  is shown for the same parameters settings, from which  $\Xi(\alpha)$  was extracted. Inset: quadratic dependency of the signal at  $2\Omega$ .

$V_{mod}$ , for the same  $\alpha$ , is reported; the parameter  $\Xi(\alpha) = A(\alpha) \frac{\tan \Phi}{1 + \tan^2 \Phi} \frac{Re(\chi_{xx}^{(1)})}{h} \frac{\kappa}{h}$  can be

estimated from the fit and introduced in Eq.5, that becomes  $S_{Kerr}(\Omega; \alpha) = \frac{h}{\kappa} \Xi(\alpha) I_1$ .

Assuming  $\delta=110nm$  and fitting data for three different  $\alpha$  ( $40^\circ$ ,  $50^\circ$ ,  $60^\circ$ ), we obtain  $\rho_0=(1.5 \pm 0.5) \cdot 10^{18} cm^{-3}$  and  $\lambda=100nm$ . The order of magnitude of the  $\lambda$  value estimated from the measurements is such that screening is weakly influencing  $S_{Kerr}(2\Omega)$  ( $\kappa \approx 1.06$  for  $\lambda=100nm$ ), although is changing dramatically the behaviour of

$S_{Kerr}(\Omega)$  as seen. Once  $\kappa$  is evaluated it is possible to work out a value for  $Re(\tilde{\chi}_{\text{eff}}^{(1)})$  from data reported in the inset in figure 3; we obtain  $Re(\tilde{\chi}_{\text{eff}}^{(1)}) = (4 \pm 1) \cdot 10^{-21} \text{ m}^3/\text{V}^2$  in good agreement with values found for other polymers of the PPV family<sup>7</sup>.

In conclusion we report here the interpretation of the electro-optic measurements on an oxadiazole-containing electroluminescent polymer films. We demonstrated that the large offset of the measurement is due to both the space charge distributions in the film and Debye-Hückel screening. A fixed charge distribution is created close to the ITO electrode giving rise to a strong counter field at the surface, of the order of  $10^8 \text{ V/m}$ , which can affect the electroluminescence efficiency. Once calibrated the experimental set-up, operating in the two bias points, it will be possible, in further investigations, to perform fast electro-optic measurements as a function of time and temperature in order to investigate dynamics of charge injection and ejection in the polymer layer.

## REFERENCES

- 1 Proceedings of the 2<sup>nd</sup> International Conference on Electro-Luminescence from Molecular Materials and Related Phenomena, Sheffield (UK), May 13<sup>th</sup>-15<sup>th</sup> 1999, D.D.C.Bradley (ed.), to be published on Synthetic Metals (2000).
- 2 J.H.Burroughes, D.D.C.Bradley, A.R.Brown, R.N.Marks, K.Mackay, R.H.Friend, P.L.Burn, A.B.Holmes, *Nature*, **374**, 539 (1990).
- 3 J.Yang, J.Shen, *J.Appl.Phys.*, **85** (5), 2699 (1999).
- 4 J.C.deMello, N.Tessler, S.C.Graham, R.H.Friend, *Phys.Rev.B*, **57** (20), 12951 (1999).
- 5 Z. Bao, Z. Peng, M. Galvin, E.A. Chandross, *Chem. Mater.*, **10** (5), 1201 (1998).
- 6 H.Eyring, D.Henderson, W.Jost, *Physical Chemistry an Advanced Treatise, Vol.IXA - Electrochemistry*, 506, Academic Press, New York (1970).
- 7 F.Michelotti, V.Taggi, M.Bertolotti, T.Gabler, H.H.Hörhold, A.Bräuer, *J.Appl.Phys.*, **83** (12), 7886 (1998).
- 8 C.Giebeler, S.A.Whitelegg, A.J.Campbell, M.Liess, S.J.Martin, P.A.Lane, D.D.C.Bradley, G.Webster, P.L.Burn, *Appl.Phys.Lett.*, **74** (24), 3714 (1999).
- 9 F.Michelotti, G.Nicolao, F.Tesi, M.Bertolotti, *Chem.Phys.*, **245** (1-3), 311 (1999).
- 10 M.Cardona, *Modulation Spectroscopy, Solid State Physics*, Vol.11, Academic Press, New York (1969).
- 11 P.N.Butcher, D.Cotter, *The Elements of Nonlinear Optics*, Cambridge University Press, Cambridge (1990).
- 12 P.A.-Chollet, G.Gadret, F.Kajzar, P.Raimond, *Thin Solid Films*, **242**, 132 (1994); Y.Levy, M.Dumont, E.Chastaign, P.Robin, P.A.-Chollet, G.Gadret, F.Kajzar, *Mol.Cryst.Liq.Sci.Techol.-Sec.B: Nonlinear Optics*, **4**, 1 (1993).
- 13 F.Michelotti, S.Bussi, M.Bertolotti, Z.Bao, manuscript in preparation.
- 14 See for example: H.Eyring, D.Henderson, W.Jost, *Physical Chemistry an Advanced Treatise, Vol.X-Solid State*, Academic Press, New York (1970).
- 15 C.Giebeler, S.A.Whitelegg, D.G.Lidzey, P.A.Lane, D.D.C.Bradley, *Appl.Phys.Lett.*, **75** (14), xxx (1999).

# IMPEDANCE SPECTROSCOPY OF $\text{AlQ}_3$ BASED ORGANIC LIGHT EMITTING DIODES IN ULTRA HIGH VACUUM

RUDI ONO, PAOLO LOSIO, IVAN BIAGGIO, AND PETER GÜNTER

*Nonlinear Optics Laboratory*  
*Swiss Federal Institute of Technology*  
*CH-8093 Zurich, Switzerland, <http://nlo-serv.ethz.ch/>*

The electronic properties of the organic layers and the interfaces in Organic Light Emitting Diode (OLED) structures were studied by impedance spectroscopy. To control the effect of gas contamination, the measurement was done in Ultra-High-Vacuum (UHV) and the results were compared with those measured in air. Impedance features probably related to a depletion region at the interface, which were observed in air, were not detected in UHV. The existence of atmospheric gas strongly influences the interface performance of OLEDs, contributing to the formation of an interfacial layer.

**Keywords:** OLED, Organic, Electroluminescence, Impedance Spectroscopy.

## 1. INTRODUCTION

Although remarkable progress has been achieved in recent years towards the optimization of the performance of Organic Light Emitting Diodes (OLEDs), the knowledge of the electronic properties of the organic layers and interfaces in the OLED structure is still insufficient.

In order to better understand the electronic properties of OLEDs, we use impedance spectroscopy, which allows the investigation of the frequency dependence of the complex impedance of the device. It also allows us to find the equivalent circuit of the individual OLEDs and study the existence of a depletion layer at the interface.

Our research goal is to study the electronic properties of OLEDs, to obtain information on the internal device structure as well as the behaviour of, e.g., the metal/organic interface. To this aim, we have grown the layered structure in a controlled way by molecular beam deposition in a Ultra High Vacuum (UHV, pressure below  $10^{-9}$  mbar). Since the UHV system is also equipped with an electrical measurement chamber,

we can measure the electrical characteristic of freshly fabricated devices which never entered into contact with any impurity gas. Thus we can truly exclude the effect of air/gas contamination.

In the following we present what we believe is the first impedance spectroscopy data on OLEDs which were both fabricated and characterized in a UHV environment.

## 2. EXPERIMENTAL

We fabricated single layer devices (ITO/Alq<sub>3</sub>/M, where M stands for Mg, Ag, or Ag/Mg) on a photolithographically patterned Indium Tin Oxide (ITO) glass substrate. Alq<sub>3</sub> was deposited onto ITO at a deposition rate of 0.3 nm/s. The thickness of the Alq<sub>3</sub> layer (80 nm) was controlled by a temperature stabilized quartz micro balance. The metal cathode (about 100 nm) was evaporated successively onto Alq<sub>3</sub>.

The samples were then contacted in the UHV system, and the impedance as a function of the frequency of the applied voltage was measured with a programmable impedance analyzer (Hewlett-Packard, HP 4129A). For all measurements, we applied an AC voltage of 0.1 V with various bias voltages and in the frequency range between 10 Hz and 10 MHz.

## 3. RESULTS AND DISCUSSION

Figure 1(a) shows the real part  $\text{Re}(Z)$  of the complex impedance  $Z$  of an ITO/Alq<sub>3</sub>/Mg device at different bias voltages. The dots represent the experimental data, and the solid curve a theoretical fit. The real-part of the complex impedance at low frequency decreases for increasing bias voltages, as expected. The instabilities observed at low ( $f < 1$  kHz,  $V < 8$  V) and high frequency ( $f > 100$  kHz) are typical of measurements performed in UHV. Similar instabilities at low voltages are also observed measuring electroluminescence in UHV. As the bias voltage increases above 8 V, the threshold voltage for LED operation is reached, and together with it, the maximum value of  $\text{Re}(Z)$  becomes frequency-independent ( $f < 1$  kHz). This corresponds to the start of carrier-injection at the electrodes. At bias voltages below 8 V the interface is supposed to play a more important role on the carrier accumulation and

injection. The strong frequency dependent of complex impedance at low frequency can be assigned to an interface behavior in UHV. As will be described later, this region appears as a second circuit formed by the interfacial region when the measurements are performed in air. This proves that the presence of atmospheric gases has a strong effect on the carrier injection at the interface.

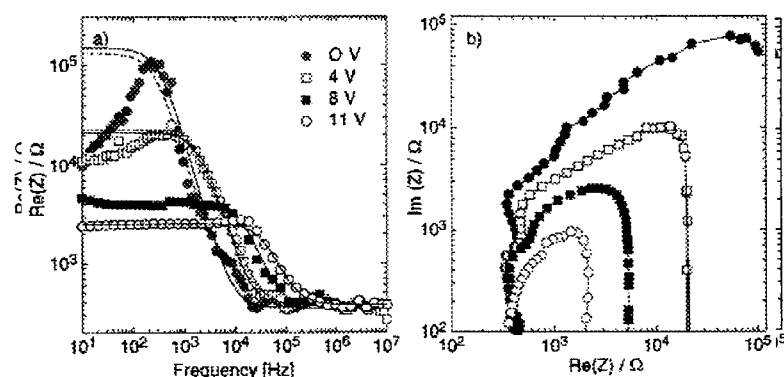


FIGURE 1: (a) Real part  $\text{Re}(Z)$ , and (b) Cole-Cole plot of the complex impedance  $Z$  of an ITO/Alq<sub>3</sub>/Mg device at different bias, measured in UHV. Solid curves and dashed curves represent a fit using the impedances calculated with 1 and 2 resistance-capacitance circuits in series, respectively. The amplitude of the ac modulation is 0.1 V, with a frequency range from 10 Hz to 10 MHz.

Figure 1(b) displays the Cole Cole plots (real-part of the impedance vs. imaginary part) of the same device, in a double logarithmic plot. The minimum  $\text{Re}(Z)$  value observed at high frequencies corresponds to a resistance  $R_s$  in series with the OLED (which could be assigned to an ohmic contact at the ITO/Alq<sub>3</sub> interface [1]). In this device,  $R_s$  is about 310  $\Omega$ . The maximum  $\text{Re}(Z)$  value at low frequencies corresponds to the sum of  $R_s$  and the OLED resistance ( $R_p$ ), which is bias dependent and is of the order of 100 K $\Omega$ . Although a model using 2 circuits gives a somewhat better fit at 0 bias voltage (Fig.1(a)), the Cole-Cole plot basically displays only one semicircle for this UHV measurement. The depletion region due to the energy level gap at the Mg/Alq<sub>3</sub> interface is supposed to have no strong effect leading to the establishment of a new circuit. In this environment, therefore, only a negligible interfacial capacitance is observed. The results (Fig.1(a)) show that the capacitance  $C_p$  of the bulk



layer is bias independent [2,3], and is about 3.65 nF.

When the device is brought to air, totally different results are observed. They are displayed in Figure 2(a). The complex impedance is stable in the air, from which one can tentatively conclude that the presence of atmospheric gases supports a smoother carrier injection at the electrodes. In contrast to the results in UHV, at low bias voltage we observe 2 similar structures in the real part plot, while only one of them remains when the bias voltage is increased. At a bias voltage lower than 3 V, the plots can be well fitted by an equivalent circuit containing 2 circuits in series, each with a resistance and a capacitance in parallel, plus a single resistance in series. The equivalent circuit is sketched in the inset. At high applied voltage ( $V > 8$  V), the results can be well fitted by using a single resistance and capacitance network. At bias voltages between 4 and 8 V, both models are applicable, but the model using 2 circuits still gives a better fit, as shown in Fig. 2(a). This observation can also be readily made with the Cole-Cole plot in Fig. 2(b), which clearly shows two semicircles at low bias voltage. One semicircle ( $f > 1$  kHz,  $\text{Re}(Z) < 10\text{K}\Omega$ ) can be assigned to the organic bulk layer, and it is also observable when the device is measured in UHV. The other semicircle, which is only detectable in air, is supposed to be due to the depletion region at the Mg/Alq<sub>3</sub> interface. It shows a strong dependence on bias voltage, and it allows an initial carrier accumulation, before injection into the Alq<sub>3</sub> layer.

From the above results it is clear that exposure to air strongly influence the interface performance. It may also give an answer to why the electroluminescence is stronger in air [4]. The depletion region at the interface can be explained in two different ways. A first possibility is the gap between the metal Fermi level of Mg and the lowest unoccupied molecular orbital (LUMO) of Alq<sub>3</sub>. When the two materials are contacted, this gap will lead to a carrier transfer from Mg to Alq<sub>3</sub>, causing an "energy band alignment" at the interface. Because of the influence of atmospheric gas at the interface, a Schottky barrier is well established, which will eventually appear as new impedance feature. The second possibility is related to an interfacial layer formed at the Mg/Alq<sub>3</sub> transition because of diffusion of Mg into the the Alq<sub>3</sub> layer [5,6], forming an Mg-doped Alq<sub>3</sub> layer at the interface. Atmospheric O<sub>2</sub> chemically reacts with Mg and Alq<sub>3</sub> and forms the interfacial Alq<sub>3</sub>-Mg-O<sub>2</sub> layer at interface.

To further elucidate what actually forms the depletion region at the interface, two devices were prepared. The first one used an Ag cathode

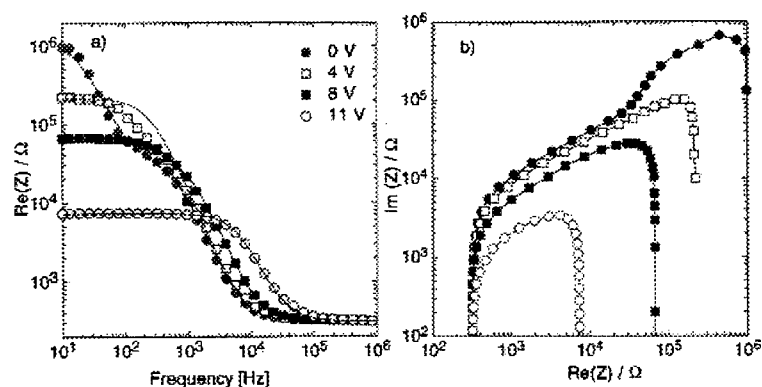


FIGURE 2: (a) Real part  $\text{Re}(Z)$ , and (b) Cole-Cole plot of the complex impedance  $Z$  of  $\text{ITO}/\text{AlQ}_3/\text{Mg}$  at different bias voltages, measured in air. Solid lines and dashed lines represent the fit of corresponding impedances using 1 and 2 resistance-capacitance networks in series, respectively. The inset shows this equivalent circuit.

(about 90 nm thick). Ag has a high chemical stability, it does not diffuse into  $\text{AlQ}_3$ , and has a higher work function than Mg, which could be expected to create a high interface barrier and to form a wide depletion region. For the second device, a thin (2 nm) Ag layer was deposited on  $\text{AlQ}_3$  before successively evaporation the Mg cathode (100 nm thick). Such an Ag layer effectively blocks diffusion of Mg into  $\text{AlQ}_3$ .

The measurement in UHV were very similar to those of the device with an Mg cathode, but the device with Ag cathode has a higher threshold voltage for electroluminescence, and the one with the inserted 2 nm Ag layer has a longer lifetime when measured in air [4]. The measurements in air are shown in Fig. 3. Both devices show only one semicircle in the Cole-Cole plot. This shows that the  $\text{Ag}/\text{AlQ}_3$  work function gap does not establish an interfacial region. Despite the presence of atmospheric gases at the  $\text{Ag}/\text{AlQ}_3$  interface, the unreactive Ag can not promote the creation of an interfacial layer, which results in a lower carrier accumulation at the  $\text{Ag}/\text{AlQ}_3$  interface. The insertion of a thin Ag layer efficiently hinders the inter-diffusion of Mg and  $\text{AlQ}_3$ , and it also does not lead to the formation of an interfacial layer in the air. In conclusion, we may suppose that the interfacial  $\text{AlQ}_3\text{-Mg-O}_2$  layer at the interface contribute to the appearance of interfacial impedance feature.

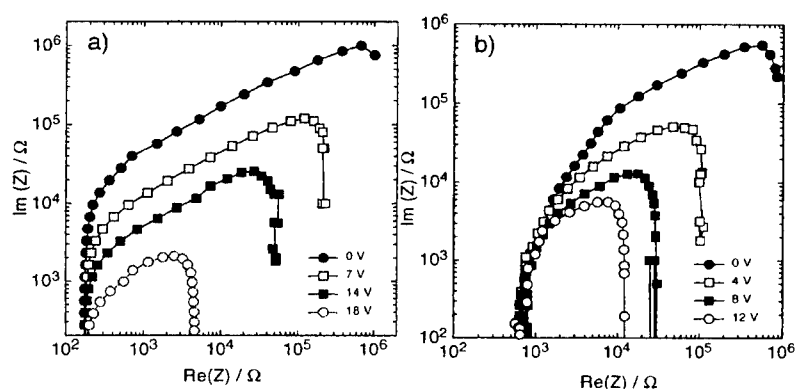


FIGURE 3: Cole-Cole plots in the complex impedance plane at different bias voltages for (a) ITO/Alq<sub>3</sub>/Ag, and (b) ITO/Alq<sub>3</sub>/Thin Ag/Mg. Both measurements were performed in air.

#### 4. CONCLUSIONS

We have presented impedance spectroscopical measurement performed on ultra-clean OLEDs grown and characterized in an UHV system. The results show an instability of the charge-injection behaviour in devices which never entered into contact with any atmospheric gas. The presence of impurity gases strongly influences the charge-injection performance at the electrode interfaces in OLEDs.

#### References

- [1] A. J. Campbell, D. D. C. Bradley, and D. G. Lidzey, *J. Appl. Phys.* 82, 6326 (1997).
- [2] C. Jonda and A. B. R. Mayer, *Chem. Mater.* 11, 2429(1999).
- [3] A. J. Campbell, D. D. C. Bradley, J. Laubender, and M. Sokolowski, *J. Appl. Phys.* 86, 5004 (1999).
- [4] M. Kiy, I. Gamboni, U. Suhner, G. Conradin, I. Biaggio, and P. Günter, *Synth. Met.* 111-112(2000), in print.
- [5] Y. Tao, A. Kündig, C. Cai, I. Gamboni, B. Müller, and P. Günter, "Inter-diffusion at Mg/Alq<sub>3</sub> interface", *Materials Research Society Spring Meeting*, San Francisco 1998.
- [6] A. Rajagopal and A. Khan, *J. Appl. Phys.* 84, 355 (1998).

## BLUE GREEN LIGHT-EMITTING ELECTROCHEMICAL CELLS BASED ON A COPOLYMER DERIVED FROM FLUORENE

OLIVIER STÉPHAN \*, YANN KERVELLA

Laboratoire de Spectrométrie Physique, Université Joseph Fourier  
Grenoble 1 and CNRS (UMR C5588), 140 rue de la physique, B.P. 87  
38402 Saint Martin d'Hères Cedex, France

A copolymer derived from fluorene has been synthesised using a fluorene monomer functionalised with poly(ethylene oxide)-like segments as comonomer in a poly(dihexylfluorene) main chain. Such material exhibits the three functions of luminescent, ion-solvating and ion-transporting material on the same main polymeric chain. Efficient blue-green polymer light-emitting electrochemical cells (LECs) based on this copolymer without the addition of an extra ion-supporting polymer such as poly(ethylene oxide) are reported, leading to threshold operating voltages close to the electrochemical gap of poly(fluorene).

**Keywords** Light-emitting devices ; Electroluminescence ; Fluorene

### INTRODUCTION

A significant new advance in the field of organic light emitting devices to obtain brightnesses and operating voltages suitable for commercial applications has been the discovery of light-emitting electrochemical cells [1,2]. In such systems, ionic species must be solvated within the active layer to provide the counterions necessary to achieve p-type and n-type doping of the electroluminescent conjugated polymer. As a result, an ionically conductive material, generally poly(ethylene oxide) (PEO) complexed by a lithium salt such as lithium triflate [2] is often

added to the polymer blend. Nevertheless in that case, phase separation that occurs between the ionic conductor and the non polar luminescent material remains the main problem to solve.

With this aim in view, we have synthesised a new monomer derivated from fluorene, functionalised with PEO-like segments : 2,7-dibromo - 9,9 - bis (7,10,13,16 - tetraoxaheptadecyl) fluorene, denoted dibromo-(BTOHF). It must be pointed out that the use of an alkyl spacer-arm between the fluorene units and the PEO-like segments prevents the twist of the conjugated repeating units from planar configuration which usually leads to a drop in fluorescence quantum yield. In addition, we are going on the assumption that the grafting of such side groups on the fluorene backbone avoids the need for a two-phase blend with an extra ion-supporting polymer.

The synthesis of the corresponding homopolymer, poly(BTOHF) was successful. Nevertheless, the resulting material was melted at ambient temperature due to its side groups. As a consequence, we investigate the co-polymerisation of the BTOHF moiety with the more simple 9,9-dihexylfluorene one, denoted DHF. The chemical structure of poly(DHF-co-BTOHF) copolymer is shown on Figure 1. It must be pointed out that such conducting copolymer exhibits the three functions of luminescent, ion-solvating and ion-transporting polymer on the same main polymeric chain.

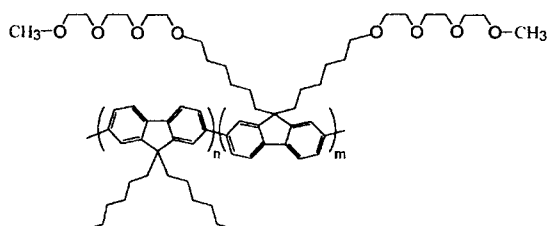


FIGURE 1 Chemical structure of the copolymer.

## EXPERIMENTAL

The copolymer was synthesised using the well-known dihalogenative polycondensation of the dibromo corresponding derivatives catalysed by a Ni(0) complex in N,N-dimethylacetamide (DMAc) starting with a

4:1 molar ratio for the comonomers as previously described [3]. Thin films were prepared by spin coating onto ITO-coated glasses. Metallic contacts were deposited onto the polymer layer by vacuum evaporation. A mask has been used to determine well-defined shape for the Al electrodes whose area is  $9 \text{ mm}^2$ . Photoluminescence and electroluminescence (EL) spectra were recorded with a 10 cm monochromator followed by an AsGa photomultiplier tube. For quantitative measurements, a calibrated Hamamatsu silicon photodiode, with a large surface collection area, was used. The distance between the sample and the detector was 1 mm.

## RESULTS AND DISCUSSION

The photoluminescence and electroluminescence spectra for chloroform solution of the copolymer and for LECs upon operation, shown on figure 2, display different spectral features, with a red shifted emission for electroluminescence.

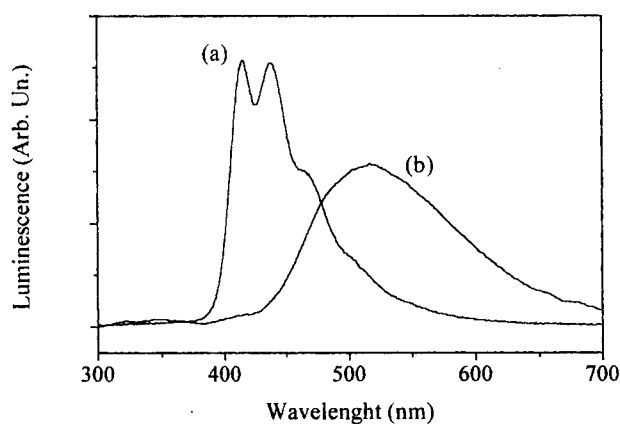


FIGURE 2 (a) Photoluminescence spectrum of poly(DHF-co-BTOH) in chloroform solution (excitation 365 nm) and (b) electroluminescence spectrum.

This is the result of interchain electron-hole recombination [4]. Indeed, it is now established that polyfluorenes-based materials generally develop additional broad red-shifted bands, located in the region of 500-600 nm, upon annealing or the passage of current. As a result, although the luminescence from isolated chains may be blue, taking its origin in intrachain recombination, for electroluminescence, the dominant band emission is in our case the yellow part of the spectrum leading to blue-green emission. Nevertheless, it must be pointed out that the electroluminescence spectrum shows only a very slight evolution upon device operation leading to constant blue-green emission.

First investigations on LECs were based on the use of the classical and simple device configuration : Indium-Tin-Oxide (ITO)/copolymer/aluminium. Thin films of poly(DHF-co-BTOHF) with typical thickness of 110 nm were prepared from 30 mg.ml<sup>-1</sup> cyclohexanone solution containing different amount of lithium trifluoromethanesulfonate. The admixed lithium salt provides the ionic conductivity necessary for the formation of the light-emitting p/n junction. All characterisations were run in a gloves box under inert atmosphere.

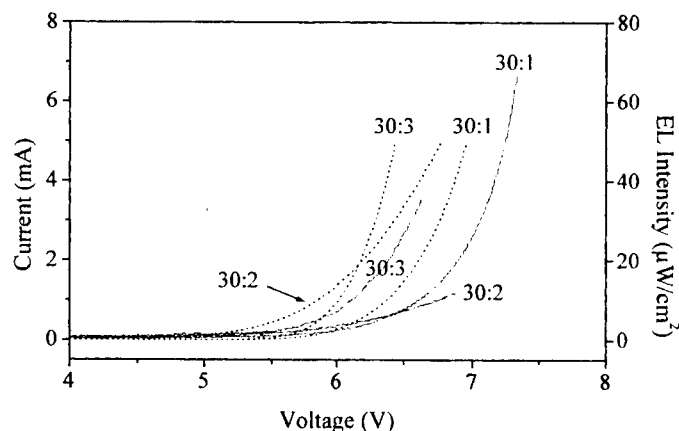


FIGURE 3  $I(V)$  and  $EL(V)$  (dashed lines) curves of "fresh" LECs for 30:1, 30:2, 30:3 copolymer and lithium-triflate weight ratios.

As shown by figure 3, in each case, the intrinsic ionic conductivity of the mixture copolymer and  $\text{LiCF}_3\text{SO}_3$  allows to obtain apparent threshold potential for electroluminescence (EL(V) curves) below 6 V. As a result, we assume that the devices are functioning like LECs since voltage higher than 25 volts must be applied when no salt is added to the active layer [3]. Furthermore, the salt proportion clearly affects the device performances. As expected, the lower threshold value, can be associated to the higher ionic conductivity. Indeed, assuming that the DHF : BTOHF ratio in the copolymer tracks the starting comonomer ratio, the 30 : 2 copolymer and lithium-triflate weight ratio correspond to an O : Li ratio close to 20 and it is well known that with regular PEO the best conductivities are reached for such rather low salt concentration [5].

When a voltage scan is performed between 0 and 6 Volts in one second on a "fresh" LECs, the apparent threshold voltage for EL(V) curve is around 5 V as shown on figure 3. Although the initial apparent threshold voltage is strongly dependent on the sweep rate, lowering when decreasing the scan rate, it is noteworthy that once the junction has been formed, for instance after an initial stress at 5 V for a few minutes, the subsequent scan exhibits lower threshold, at around 3.5 V. Figure 4 displays typical EL(V) curves as a function of time.

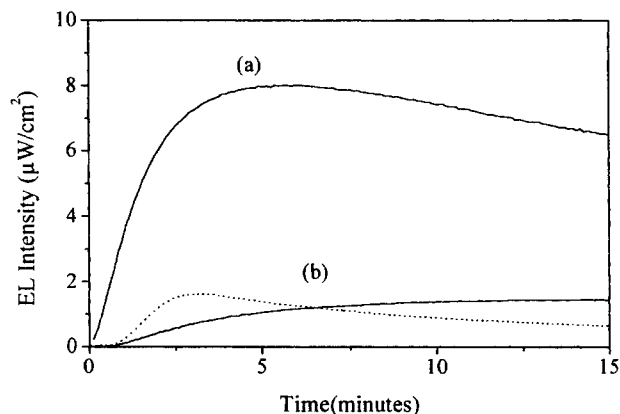


FIGURE 4 Evolution of EL(V) curves of a "fresh" LECs biased at + 5 V (a) and +3.5 V (b) (dashed line for LiTFSI).



Although the current is quite stable (curves not shown), the light intensity slowly increases with time. This initial increase can be associated to the growth of the p-type and n-type doped regions leading to electrons and holes recombinations. Under a constant voltage of 3.5 V, the emission intensity reaches a value close to  $1,5 \mu\text{W}/\text{cm}^2$  in approximately 15 minutes. Turn-on speed can be enhanced, as shown by figure 4 by increasing the operating voltage. Nevertheless the emission intensity is fastly decreasing, a lost of 50 % of its intensity occurring within 30 minutes at 5V. For initial voltages ranging from 10 to 15 V, the light emission is greatly increased but the lifetime is dramatically shortened leading to electrical breakdown within a few minutes. Another way to reduce the turn-on speed, as shown by figure 4, is to enhance the ionic mobility by using a lithium-trifluoromethylsulfonyl imide (Li-TFSI) salt, providing large delocalization of the negative charge in the salt and leading to enhanced ionic conductivity. However, if the response is faster, reaching maximum brightness of  $1,5 \mu\text{W}/\text{cm}^2$  in 2 minutes, after build-up of the p/n junction a slow luminescence decay is clearly observed.

## CONCLUSION

These preliminary results on electroluminescence of a copolymer derived from fluorene containing fluorene moieties functionalised by PEO-like segments, clearly show the interest of such a system in which ion conducting segments are incorporated into the poly(fluorene) main chain. LECs based on this new material are clearly demonstrated, leading to threshold operating voltage for electroluminescence close to the electrochemical gap of poly(fluorene).

## References

- [1] Q. Pei, G. Yu, C. Zhang, A. J. Heeger, *Science* **269** 108 (1995).
- [2] Y. Yang and Q. Pei, A. J. *Appl. Phys.* **81** (7) 3294 (1996).
- [3] O. Stephan, V. Collomb and J. C. Vial, M. Armand, *Synth. Met.* (2000) (in press).
- [4] G. Klärner, M.H. Davey, W.-D. Chen, J.C. Scott and R.D. Miller, *Adv. Mater.* **10** 993 (1998).
- [5] C. D. Robitaille and D. Fauteux, *J. Electrochem. Soc.* **133** (2) (1986)

## **Luminescent and Electronic Properties of End-Substituted Distyrylbenzene Derivatives**

YE TAO<sup>a</sup>, MARIE D'IORIO<sup>a</sup>, MAN SHING WONG<sup>b</sup>, ZHONG HUI LI<sup>b</sup>, ISABELLE LEVESQUE<sup>a</sup>, JENNIFER LAM<sup>a</sup>

<sup>a</sup>Institute for Microstructural Sciences, National Research Council of Canada, M-50 Montreal Road, Ottawa, Ontario, Canada, K1A 0R6;

<sup>b</sup>Department of Chemistry, Hong Kong Baptist University, Kowloon Tong, Kowloon, Hong Kong

The luminance and electronic properties of two distyrylbenzene derivatives with poly(alkyleneoxy) and multi-alkoxy end groups were investigated. The materials exhibit similar UV-visible absorption and photoluminescent properties in solution, but the emission wavelengths in solid thin films are quite different. The reduced red-shift in one of the distyrylbenzene derivatives when forming a solid thin film is attributed to the reduced interaction between the  $\pi$ -electrons of the neighboring molecules by the “bulky” or “spacer” end-groups formed by the methoxy and poly(alkyleneoxy) substituents.

**Keywords:** distyrylbenzene; organic; electroluminescence; OLED; photoluminescence; end-substitution.

### **INTRODUCTION**

Electroluminescence in conjugated polymers was first discovered in poly(*p*-phenylenevinylene) (PPV)<sup>1</sup>. Since then research efforts on polymer-based light emitting devices have increased dramatically, primarily due to their potential application in full color flat panel displays and the low fabrication costs associated with this technology. Poly(phenylenevinylene) (PPV) and its derivatives have been widely

used as emissive materials in polymer light emitting diodes (PLEDs). Conjugated polymers derive their semiconducting properties from delocalized  $\pi$ -electrons along the polymer chain. Therefore it is possible to modify the semiconducting properties of the polymer by adding different functional groups to the polymer structure thereby altering the extent of delocalization of the  $\pi$ -electrons. The knowledge of how different functional groups in the PPV structure affect its physical properties is very important for understanding the structure-property relationship in this material. However, a broad molecular weight distribution and the presence of blocks with different conjugation lengths in the polymeric material often complicate the issue. In this sense, oligo(phenylenevinylene) (OPV) type of material is ideal to use as a model system to study the structure-property relationship. Due to controllable and well-defined chemical structures, it is much easier to follow and correlate the physical properties of the OPVs with the molecular structures. In addition, many oligomeric materials can be thermally sublimed under high vacuum, allowing for the preparation of multilayer organic light emitting diode (OLED) structures and devices in an ultra-clean and well-controlled environment thus overcoming the uncertainties involved in wet processes.

For these reasons, several types of OPVs have been synthesized and their absorption, luminance and electronic properties<sup>2-4</sup> have been investigated. Wong *et al.*<sup>5</sup> have shown that solubilizing substituents such as polyalkyleneoxy and alkylsulfonyl groups incorporated at the ends of the  $\pi$ -conjugated skeleton of distyrylstilbene can improve the solubility without disrupting the co-planarity of  $\pi$ -conjugation backbone. We have found that substituents incorporated at the end of the conjugated main chain can shift the HOMO and/or LUMO level and thus alter the HOMO-LUMO energy gap of an oligomer. This provides a means to tune the energy gap leading to a change in optical and electronic properties of an oligomer<sup>6</sup>. The electroluminescent (EL) emission of these end-capped distyrylbenzene derivatives falls in the blue and blue-green region of the visible spectrum. However, when the materials were fabricated into solid thin films, the photoluminescent (PL) and EL emission underwent significant red-shifts as compared to the solution PL. This is certainly an undesirable effect for the EL devices, especially for blue OLEDs. The red-shifts occurring when forming solid thin films have been attributed to the increased interaction in the solid state between the  $\pi$ -electrons of neighboring molecules. Therefore, the key to overcoming this issue is to reduce the possible interaction among the

neighboring  $\pi$ -electrons. In this work, we report the use of non-conjugated methoxy groups to form "bulky" ends at the OPV molecules, to prevent or reduce the interaction of the  $\pi$ -electrons of the closely packed neighboring molecules, thus suppressing the red-shifts in PL and EL emission when forming solid thin films using OPVs.

## EXPERIMENTAL

The OPVs used in this work are 1,4-Bis{4-[2-(2-butoxyethoxy)ethoxy]styryl}benzene (OPV(1)-OR) and 1,4-Bis-4-{[2-(2-butoxyethoxy)ethoxy]-3,5,-dimethoxy}styrylbenzene (t-OPV(1)-OR). Their molecular structure and computer simulated geometry using the PM-3

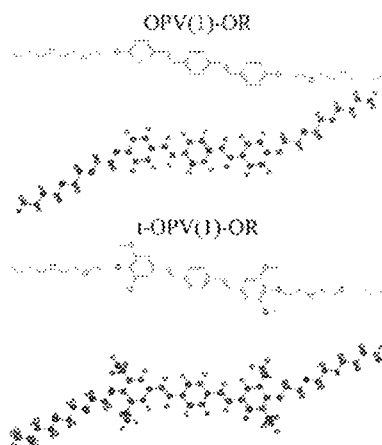


Figure 1 Molecular structures and computer calculated ground state molecular geometry of OPV(1)-OR and t-OPV(1)-OR.

method can be found in Wong *et al*<sup>5,7</sup>. In these two OPVs, the backbones are the same, but the t-OPV(1)-OR has extra methoxy groups attached to the 3,3'- and 5,5'-positions of the end-phenyl groups in its structure. A Spex Fluorolog-3 spectrometer, and a Cary 50 spectrometer were used for PL and UV-visible absorption measurements. For the solution spectra, the OPV concentration in chloroform was controlled to give out 0.05 absorbance in order to minimize the intermolecular interaction. The solid PL spectra were measured on thin films prepared by

vacuum deposition on quartz plates. Test OLEDs were prepared on commercial ITO coated glass substrates (Applied Films Corp.) with sheet resistances of 12  $\Omega$  per square, and an ITO thickness of  $\sim$ 120 nm. Before photolithographic patterning, the ITO substrates were cleaned using cleanroom soap, acetone, and isopropanol. The anodes were formed by chemical etching, and the patterned ITO substrates were treated in a UV ozone oven for ten minutes before loading into the

vacuum chamber. The device structures consisted of 50 nm TPD as a hole transport layer (HTL), 50 nm OPV as an emissive layer (EML), 20 nm PBD and 2 nm LiF as the hole blocking layer (HBL), and a thermally evaporated aluminum layer as a cathode. The thermal evaporation was carried out in an Edwards Auto 306 coater equipped with a cryo-pump, using either tungsten or molybdenum boats. All depositions were performed at high vacuum ( $2 \times 10^{-7}$  torr). A typical growth rate of  $2 \text{ \AA/s}$  was used and the substrates were held at room temperature. The active device area is  $1.0 \times 5.0 \text{ mm}^2$ . The devices were operated and characterized in air. The EL spectra and luminance were measured by using a Photo Research®-650 SpectraColorimeter.

## RESULTS AND DISCUSSION

The ground state molecular geometries of OPV(1)-OR and t-OPV(1)-OR were calculated by the PM-3 semi-empirical method. The results indicate that the end substitution do not disrupt the co-planarity of the  $\pi$ -conjugated backbone of the oligomers (Figure 1). Because of the co-planarity of the backbone and the long chain feature of the end-groups, the OPV(1)-OR is a rather flat molecule. Therefore the possibility of having strong interaction among the  $\pi$ -electrons of the neighboring molecules in the solid state is high. Adding methoxy groups

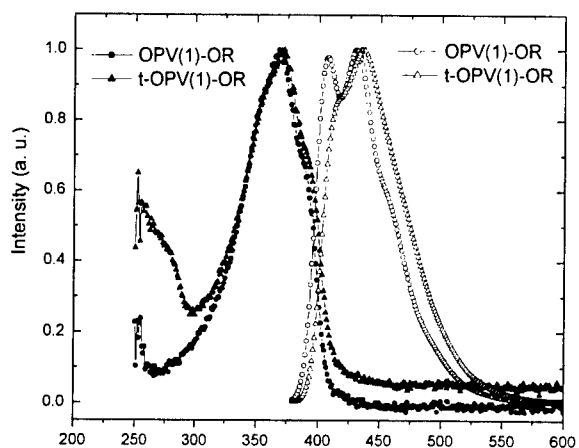


Figure 2 UV-visible absorption (filled symbols) and photoluminescence (open symbols) spectra of OPV(1)-OR and t-OPV(1)-OR in  $\text{CHCl}_3$ .

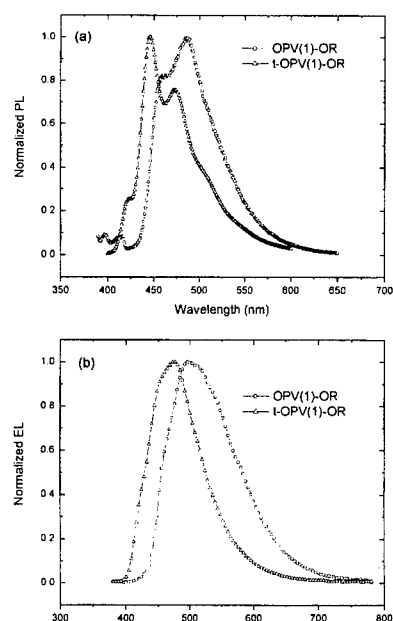


Figure 3. Thin film photoluminescence (a) and electroluminescence (b) spectra of OPV(1)-OR and t-OPV(1)-OR.

visible fine structures due to vibronic levels in the ground state. The 0-0 phonon emission peaks are at 408 and 416 nm for OPV(1)-OR and t-OPV(1)-OR respectively. The PL maxima are at 431 and 436 nm. The PL spectra show that in solution, the OPV(1)-OR has very similar or slightly shorter emission wavelength than the t-OPV(1)-OR.

The PL spectra measured from solid thin films of OPV(1)-OR and t-OPV(1)-OR are shown in Figure 3 (a). The 0-0 phonon emission peak is at 458 nm for OPV(1)-OR and 445 nm for t-OPV(1)-OR. The emission maxima are at 486 and 446 nm respectively. From solution to the solid state, the emission spectrum of OPV(1)-OR underwent a 50 nm red-shift, while that of t-OPV(1)-OR underwent a 29 nm shift (comparing the 0-0 phonon peaks). Clearly, the OPV(1)-OR underwent a much larger red-shift in the solid state than the t-OPV(1)-OR.

The EL emission spectra were measured from multilayer OLEDs using OPV(1)-OR or t-OPV(1)-OR as the emitting material. All devices showed typical rectifying behavior in their current-voltage characteristics. The turn-on voltage of these devices is around 4–5 V.

to the 3,3'- and 5,5'- positions of the OPV(1)-OR structure to form t-OPV(1)-OR molecule not only further increases the solubility of the material, but also forms two very "bulky" ends with the polyalkyleneoxy substituent at the 4, 4' positions at the molecule as shown by the molecular geometry in Figure 1. The UV-visible absorption and PL spectra of OPV(1)-OR and t-OPV(1)-OR in chloroform are shown in Figure 2. The UV-visible spectra of the two materials are very similar, with 0-0 phonon absorption peaks clearly visible at 390 nm, and 386 nm respectively. The absorption maxima are at 368 nm and 372 nm. The PL spectra of the two materials in chloroform are also very close, and the peak shapes are similar to that of PPV, with

The maximum luminance values reached so far for both materials are around 800 cd/m<sup>2</sup>. The EL spectra are shown in Figure 3(b). The EL spectrum of OPV(1)-OR is nearly identical to its thin film PL spectrum, indicating that the EL emission originates from the OPV(1)-OR layer, with peak position of 489 nm. The overall EL emission of t-OPV(1)-OR is also similar to its thin film PL spectrum, but the relative intensity of its 0-0 and 0-1 phonon peaks is quite different as compared to the PL spectrum. This might be due to the fact that in OLEDs, the injected charge carriers will drift forward in the emissive layer under the influence of the strong electric field. During the course of the drift they will adjust to those more energy favorable states (with lower energy), thus when they form excitons the lower energy component will be dominant. Despite the changes in the relative intensity of different components in EL emission spectra, it is obvious that the t-OPV(1)-OR has much smaller red-shift in its thin film EL spectrum. We attribute this reduced red-shift in the thin film PL and EL spectra of the t-OPV(1)-OR to the "bulky" end-groups formed by the methoxy and poly(alkyleneoxy) substituents of the molecule.

In summary, we have shown that "bulky" or "spacer" functional groups can be used to reduce or suppress the interaction between the conjugated backbones among closely packed neighboring molecules in the solid state. This can be useful in the design and modification of blue molecular light emitting materials.

## References

- 1 J. Burroughs, D. D. Bradley, A. R. Brown, R. N. Marks, K. Mackey, R. H. Friend, P. L. Burns, and A. B. Holmes, *Nature* **347**, 539 (1990).
- 2 S. Nakatsuji, K. Matsuda, Y. Uesugi, K. Nakashima, S. Akiyama, G. Katzer, and W. Fabian, *J. Chem. Soc. Perkin Trans. 2*, 861 (1991).
- 3 N. N. Barashkov, D. J. Guerrero, H. J. Olivos, and J. P. Ferraris, *Synth. Met.* **75**, 153 (1995).
- 4 A. Schmidt, M. L. Anderson, D. Dunphy, T. Wehrmeister, K. Muellen, and N. R. Armstrong, *Adv. Mater.* **7**, 722 (1995).
- 5 M. S. Wong, M. Samoc, A. Samoc, B. Luther-Davies, and M. G. Humphrey, *J. Mater. Chem.* **8**, 2005 (1998).
- 6 Y. Tao, A. Donat-Bouillud, M. D'Iorio, J. Lam, T. C. Gorjanc, C. Py, and M. S. Wong, *Synth. Met.* in press.
- 7 M. S. Wong, Z. H. Li, M. F. Shek, K. H. Chow, Y. Tao, and M. D'Iorio, Submitted to *J. Mater. Chem.*

# Transient photocurrent investigation of charge transport in electroluminescent organic thin films

A. TAPPONNIER, I. BIAGGIO, M. KIY, R. ONO, P. GÜNTER

*Nonlinear Optics Laboratory, Swiss Federal Institute of Technology  
CH-8093 Zurich, Switzerland, <http://nlo-serv.ethz.ch>*

We use transient photoconductivity induced by short light pulses to study the charge transport processes occurring in Alq3-based organic light emitting diodes (OLEDs) on different time-scales. From the temporal variation of the photocurrent transient, information on charge-carrier dynamics and trapping can be extracted.

**Keywords:** photoconductivity; organic LED; charge transport; dispersive transport; trap states

## 1. INTRODUCTION

Optimizing the performance of organic light emitting diodes (OLEDs) requires a deep knowledge of the electronic and transport properties of the material. Photocurrents induced by short light flashes can give information on the response time of the photoconductivity and thus on free-carrier lifetimes, the influence of deep and shallow traps, and the charge-carrier mobility, and they are sensitive to defect states in a manner similar to Time-of-Flight experiments [1] [2].

The aim of this work is to investigate the performance of transient photocurrents induced by short laser pulses as an investigative tool for the characterization of standard OLEDs, without the need for any specially prepared samples. Transient photocurrent investigations could thus offer complementary information to conventional tools such as electroluminescence and electrical characterisation [3].

## 2. TRANSIENT PHOTOINDUCED CURRENT MEASUREMENT

In pulsed photoconductivity measurements, a constant voltage is applied to an OLED, and the current transient induced by illumination with a



short laser pulses (Nitrogen laser pulses at  $\lambda_{ex} = 337.1$  nm with pulse duration  $< 1$  ns) is detected by measuring the voltage drop over a resistor. Fig. 1 shows the experimental setup and the equivalent electronic circuit.

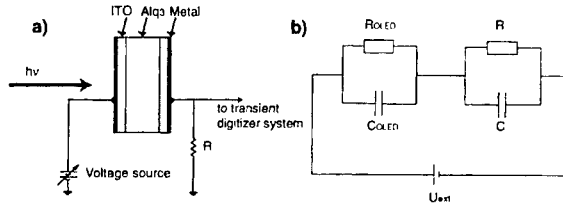


FIGURE 1: (a) Experimental setup for pulsed photoconductivity measurements. (b) Electronic circuit equivalent to the measurement system. The left part corresponds to the organic LED and the right part represents the oscilloscope and the cables with the measurement resistor  $R$ . The voltage is defined positive for positively biased anode (forward bias).

The response time of the detection system determines how far the detected signal mirrors the dynamics of the photocurrent induced by the short laser pulse. The circuit in Fig. 1 can be easily analyzed in a general way by assuming that at time zero the laser pulse induces a photoexcited charge carrier distribution at the interfaces and in the bulk of the sample which gives rise to a photoconductivity. We describe the arbitrary time evolution of the photoconductivity with a function  $\sigma_{ph}(t)$ , so that the OLED resistance is

$$R_{OLED}(t) = \begin{cases} R_{dark} = \frac{d}{S} \frac{1}{\sigma_0}, & t < 0 \\ \frac{d}{S} \frac{1}{\sigma_{ph}(t)}, & t > 0 \end{cases} \quad (1)$$

where  $d$  is the organic layer thickness and  $S$  the electrode area. The apparent conductivity  $\sigma(t)$  is in general given by the densities and mobilities of the photoexcited carriers:  $\sigma(t) = (e/d) \int_0^d \{ \mu_h(t, x) n_h(t, x) + \mu_e(t, x) n_e(t, x) \} dx$ . We assume  $\sigma_0 \ll \sigma_{ph}(t = 0)$ .

The current through the diode is the sum of the currents through the measurement resistor  $R$  and through the capacitor  $C$ . We consider the fact that the diode has a built-in capacitor  $C_{OLED}$  in parallel to a resistance  $R_{OLED}(t)$ . Using  $U$  for the voltage across the measurement resistor and  $U_{ext}$  for the applied voltage, Kirchhoff's law leads to:

$$\frac{U_{ext}}{R_{OLED}(t)} = U \left( \frac{1}{R} + \frac{1}{R_{OLED}(t)} \right) + (C + C_{OLED}) \frac{dU}{dt}. \quad (2)$$

While performing the experiment, the measured voltage is always of the order of some tens of millivolts, while the applied voltage is of the order of few volts. Therefore, we assume that  $R$  is negligible compared to  $R_{OLED}$ . Using  $C_{tot} = C + C_{OLED}$  and the detection time constant  $\tau_{RC} = C_{tot}R$ , equation (2) becomes

$$\frac{U(t)}{\tau_{RC}} + \frac{dU(t)}{dt} = \frac{U_{ext}}{C_{tot}} \left( \frac{S}{d} \right) \sigma_{ph}(t). \quad (3)$$

Using  $I = U_{ext}(S\sigma/d)$  for the current through the OLED, the general solution for the measured voltage is

$$U(t) = \exp(-t/\tau_{RC}) \left\{ U(0) + \frac{1}{C_{tot}} \int_0^t I(s) e^{s/\tau_{RC}} ds \right\}. \quad (4)$$

It is common to measure directly the relaxation of the photoinduced current by using a small measurement resistor  $R$  to decrease the response time  $\tau_{RC}$  of the detection system. However, although this method is the most straightforward to analyse the photocurrent signal, it is not possible to apply it in a simple way to OLEDs, which have a relatively large capacitance that tends to make  $\tau_{RC}$  large. Since we want to apply this method to standard OLEDs, we have to turn this fact into an advantage. This can be done when  $\tau_{RC}$  can be made much longer than the relaxation time of the photoinduced current, because for  $t/RC \ll 1$ , we can replace  $\exp(-t/\tau_{RC})$  with 1 in eq. (4) to obtain

$$U(t) = U(0) + \frac{1}{C_{tot}} \int_0^t I(s) ds. \quad (5)$$

Therefore, the detected signal is in this case proportional to the time integral of the current, *i.e.* the total charge emitted from the OLED. Its time-dependence is given by the rate at which charge is accumulated on the capacitor of the OLED, before it has the time to flow through the external circuit. If necessary, the dynamics of the photoinduced conductivity can then be found by numerical differentiation of experimental signal.

Eq.(4) means that the detected signal is the convolution of the real photocurrent with the response function of the detection system  $e^{-t/\tau_{RC}}$ . When  $\tau_{RC}$  tends to zero,  $U(t)$  is directly proportional to the real photoconductivity. On the other hand, in the limit where  $\tau_{RC}$  is infinite compared to the decay time of the photoconductivity, the detected signal is proportional to the time-integral of the photoconductivity.

Eq. (4) can also be easily solved for the special case where the photoconductivity is an exponential decay,  $\sigma_{ph}(t) = \sigma_0 \exp(-t/\tau)$ . Using  $R_0 = d/(S\sigma_0)$ , the solution of the differential equation (2) in the limit where  $R \ll R_{OLED}$  is then:

$$I(t) = \frac{U_{ext}}{R_0} \frac{1}{\tau_{RC}} \frac{e^{-t/\tau_{RC}} - e^{-t/\tau}}{1/\tau_{RC} - 1/\tau}. \quad (6)$$

### 3. RESULTS AND DISCUSSION

We apply the technique of Integrated Pulsed Photoconductivity, which was introduced above, to characterize OLEDs grown in our laboratory by molecular beam deposition in ultra-high vacuum. They consist of a transparent indium-tin oxide (ITO) layer, an organic layer ( $Alq_3$ ), and a top metal cathode (Mg). Initially, we chose mostly simple single-layer  $Alq_3$  devices in order to test the viability of this characterization method in a sample where the charge generation and transport occur in one material only. To avoid field distortions by the mobile space charge, a laser pulse of low intensity is used ( $30 \mu J$ ). The electrode area  $S$  of our OLEDs is  $18 \text{ mm}^2$ . A large measurement resistor was used to reach the  $t/RC \ll 1$  limit.

Fig. 2 shows the evolution of the total charge which comes out of the device as a function of time in an ITO/ $Alq_3$ /Mg OLED at room temperature. The signal consists of three regions. Initially, and until below  $1 \mu s$  after the generation of the charge carriers, charge is being emitted at its maximum speed (line with slope 1 in the figure), corresponding to a photoconductivity that is constant on that time scale. Then there is an intermediate part (between  $1 \mu s$  and  $5 \mu s$ ) where there is a decay in the speed of charge accumulation (corresponding to a decay in the photoinduced conductivity). This is characterized by a slope of the order of  $\sim 0.2$  in the log-log plot. A “kink” where this slope changes to a smaller value is observed at  $t \approx 10 \mu s$ , and afterwards there is then a long tail of charge emission, which lasts for about three decades. This very slow time dynamics is typical of samples where charge-transport is hindered by a multitude of defect levels which continually trap and thermally release the charge carrier, leading to the phenomena of dispersive charge transport. In this particular case, the data indicates that charge carriers are trapped at various impurity sites with a distribution of thermal

excitation energies and that some charge carriers are still emitted several milliseconds after excitation. Some electron and hole pairs excited by the UV illumination therefore escape recombination for a time as long as 10 ms. The corresponding photocurrent decay is strongly non-exponential, being more similar to a power-law.

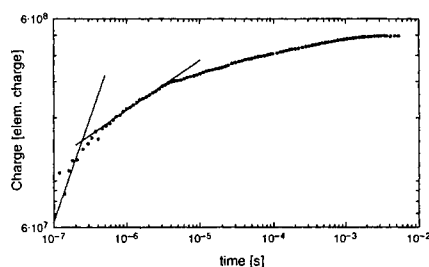


FIGURE 2: Log-log plot of the total charge emitted from an ITO/Alq<sub>3</sub> (300nm)/Mg structure at an electric field of  $2 \times 10^5$  Vcm<sup>-1</sup> after illumination with a short laser pulse. The two solid lines have slopes of 1 and 0.2, respectively.

The voltage dependence of the transient behavior is shown in Fig. 3a. The typical slopes of the lines is the same for all applied voltage, with the exception of the data taken with a voltage of 2.5 V. Note that the “kink” time at  $\sim 10 \mu\text{s}$  (vertical dashed line in the figure) does not change when increasing the electric field, only the amplitude of the signal becomes larger. Therefore, this time can not be attributed to a transit process. The two regions with different slopes in the log-log plot probably correspond to two different types of dispersive charge transport. One possible interpretation would be to associate them with the two types of charge carriers being affected by different trap-distributions. The total amount of charge generated in the device is observed to depend quadratically on the voltage, from which we conclude that the quantum efficiency for photoionization depends quadratically on the electric field. The sensitivity of this transient photocurrent technique to the presence of defect states was demonstrated above. To show an example of how it can be exploited to systematically study the presence of defect states in different types of organic layers, we present in Fig. 3b similar measurements in a two-layer devices with silver cathode. The difference is striking. In contrast to what was observed for the ITO/Alq<sub>3</sub>/Mg device, for these devices there is no long charge-emission tail indicative of a large distribution of defect

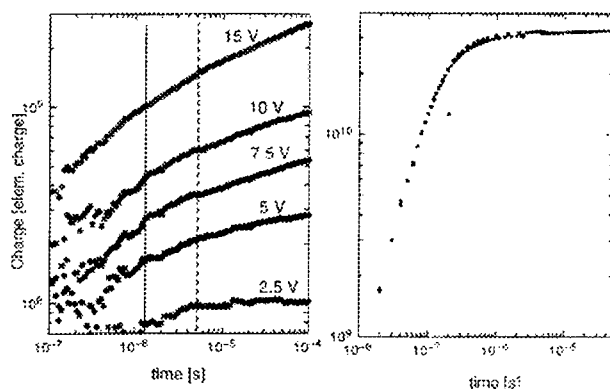


FIGURE 3: a) Electric field dependence of the transient photoconductivity of an ITO/Alq (300nm)/Mg organic LED. The applied voltage for each curve are indicated. b) Transient photoconductivity at an electric field of  $6 \times 10^5 \text{ Vcm}^{-1}$  in a double-layer ITO/NPB(40nm)/Alq(40nm)/Ag device.

states. On the contrary, at  $\sim 0.2 \mu\text{s}$  the typical slope of the charge accumulation curve changes from about 1 to about 0, which corresponds to a photocurrent decay which is more similar to a single exponential decay. This demonstrates the absence of defect states with a long excitation time in this device.

#### 4. CONCLUSIONS

In conclusion, we demonstrated that Integrated Pulsed Photoconductivity is a powerful tool to study charge transport and defect states in OLEDs. We demonstrated the sensitivity of this method to the presence of defect states and the fact that this method allows the study of electron-hole recombination and charge transport in the same devices where electroluminescence and other electronic properties are characterized.

#### References

- [1] R. G. Kepler *et al.*, Appl. Phys. Lett. **66**, 3618 (1995).
- [2] E. Lebedev *et al.*, Appl. Phys. Lett. **71**, 2686 (1997).
- [3] P. Ranke *et al.*, Appl. Phys. Lett. **71**, 1332 (1997).

## Injection and Transport of Carriers in Single Layer Light Emitting Device

ZUGANG LIU, JOÃO PINTO, HELENA NAZARÉ, and SHAOHONG XU\*

Physics Department, University of Aveiro, 3810 Aveiro, Portugal

\*School of Materials, Shanghai University Jiading Campus, Shanghai, 201800, China

In this paper we report the charge injection and transport mechanism in some single layer organic light emitting devices (LEDs) based on Alq<sub>3</sub> (tris-(8-hydroxyquinoline) aluminium). We measured the current voltage (I-V) and electroluminescent characteristics of devices with different cathode and anode. The anodes used were an aluminium doped zinc oxide ZnO:Al (AZO), ITO, and a semitransparent aluminium (Al) film. The cathodes were Mg:Ag and Al. It is shown that the hole is the majority carrier in Alq<sub>3</sub> single layer devices using ITO or AZO as the anode and Al or Mg:Ag as the cathode. The holes control the device current and the electrons control the electroluminescent efficiency of the devices. We also measured and fitted the I-V curves of four devices with an ITO/Alq<sub>3</sub>/Mg:Ag structure, but different thickness of Alq<sub>3</sub>. We found that the device current was bulk limited. In the lower applied field, it was controlled by both thermally generated charges and injected charges and in the higher field, by trapped charges.

**Keywords** organic; electroluminescence; injection; transport

### 1. INTRODUCTION

In an organic LED, there are three main steps in the electroluminescence process: the injection of holes and electrons from the two electrode contacts, the migration of the carriers in the organic layers, and the recombination of paired holes and electrons in the emissive layer. The injection and the transportation of the carriers are two of the most important factors that determine the efficiency of the organic LED.

There are two mechanisms proposed to describe the current voltage characteristics of the organic LED: injection limited current flow and bulk limited current flow (1). The proposed injection mechanisms are tunnelling injection or thermionic emission. The proposed bulk mechanisms are ohmic conduction or space charge limited current. In any case, the majority charge carrier in the device current is determined by the difference in the energy barrier between the two injection contacts.

Parker (2) and Davids (3, 4) have proved that the current in a single layer polymer LED was contact-limited. The bulk-limitation of the current has also been proved by Burrows' works (5-7) in a heterojunction structure TPD/Alq<sub>3</sub> bilayer device and by some other groups' works on the polymer devices (1,8,9).

Generally, Alq<sub>3</sub> was preferentially considered as an electron-transporting layer with a limited hole diffusion length of few hundreds of angstroms (10). However, whether a material is hole or electron transporting, depends on its oxidizability at the contact with the anode and its reducibility at the contact with the cathode (11). So, Alq<sub>3</sub> could be a hole conductor as well as an electron conductor, depending on the

amounts of the carriers injected in the hole and electron contacts. When Alq3 contacts with AZO or ITO, it is possible that the holes instead of electrons dominate the injection currents.

On the other side, whether the device current of an organic LED is contact limited or bulk limited should be determined as well by the mobility of the carriers in the organic layer as by the injection probabilities in the injection contacts. If there are lots of energy traps in an organic layer and the carrier mobility is very low, even though at a lower carrier injection (with a higher barrier), the device current should be controlled by the space charge or the traps limited space charge.

The majority carrier and the other characteristics of device current through the single layer Alq3 device are remained uncertain. That's why, in this paper, we study the injection mechanism, the nature of the majority carrier in the current, and the transport mechanism in single Alq3 layer device.

## II. EXPERIMENTAL

The organic material used in this work was Alq3, an aluminium chelate of 8-hydroxyquinoline. It was deposited by thermal evaporation in vacuum ( $10^{-6}$  torr) on the anode film (ITO or AZO) coated glass substrate. Here ZnO:Al (AZO) is deposited by r.f. sputtering. The cathodes used in this work were an aluminium and Mg:Ag (9:1) alloy, deposited on top of the organic layer by thermal evaporation. The thickness of the organic layer was monitored with a thin film thickness monitor using oscillating quartz crystal as the sensor. Measurements were carried out in air and at room temperature.

## III. RESULTS AND DISCUSSION

### 1. Current voltage characteristics of the devices with different electrodes

Using ITO, AZO and the semitransparent Al as anode, Al and Mg:Ag as cathode, six devices with a fixed thickness of 60 nm of Alq3 layer, were fabricated. Their structures are as follows: (a) AZO/Alq3/Mg: Ag, (b) AZO/Alq3/Al, (c) ITO/Alq3/Mg: Ag, (d) ITO/Alq3/Al, (e) Al/Alq3/Mg: Ag, and (f) Al/Alq3/Al.

Figure 1 shows the current voltage (I-V) curves at bias higher than 5 volts of the 6 devices with same thickness of organic layer and different anode and cathode. It is clear that the I-V curves can be divided into three groups based on the anode material. The AZO groups includes the curve (a) and (b), ITO group (c) and (d), and Al group (e) and (f).

This result implies that the holes are the majority carriers in ITO and AZO devices. Because for AZO and ITO device, changing cathode can't significantly affect the current through the device as changing anode does. When use Al as the anode, the hole injection can be neglected for its too high injection barrier, and the currents, which are dominated by electrons then, decrease a lot.

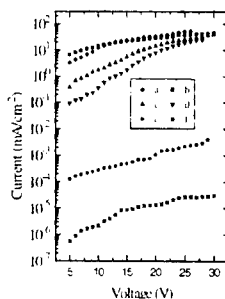


Fig. 1 I-V curves of the devices with AZO, ITO and Al as anode and Al and Mg:Ag as cathode

### 2. $\eta$ -V characteristics of the devices with same anode but different cathode

The luminance voltage characteristics of the devices with same anode (ITO) and different cathode (Al and Mg:Ag) have been measured and their electroluminescent (EL) efficiency ( $\eta$ ) voltage characteristics have been calculated and given in table 1.

Table 1. EL efficiencies of devices with ITO as anode, Mg:Ag and Al as cathodes

Voltage (V)	Al cathode			Mg:Ag cathode		
	I(mA/cm <sup>2</sup> )	L(cd/m <sup>2</sup> )	$\eta$ (%)	I(mA/cm <sup>2</sup> )	L(cd/m <sup>2</sup> )	$\eta$ (%)
14				4.1	31.4	0.25
17	3.36	2.67	0.02	9	39.3	0.14
22	11.75	5.74	0.02	19	55	0.09
28	25	7.85	0.01	33.75	68.2	0.06

It can be seen that there are very large differences of luminance between two devices, while the differences of currents of two devices are small. The difference of efficiency of the two devices is large too. We concluded that the electrons injected from the cathode/organic interface control the efficiency of these two devices, though they do not dominate the device current. The similar results have also been obtained in the devices with AZO as the anode. These results indicate, in another side, that the electrons in the single Alq3 layers of the devices with ITO or AZO as the anode are minority carriers and holes are majority ones.

### 3. Determination of the majority carriers

At higher bias, charge injection should be tunnelling and the current density will follow the Fowler-Nordheim equation. Assuming the energy barrier at the injection contact is a triangular barrier, the F-N equation can be written:

$$I = AF^2 \exp\left(-k \frac{\sqrt{\phi_i}}{F}\right) \quad \text{With} \quad k = \frac{8\pi}{3qh} \sqrt{2m^*} \quad (1)$$

Where  $A$  is a constant for a give material,  $m^*$  and  $q$  are the effective mass and the charge of the carrier concerned,  $h$  is the Planck's constant,  $F$  is the applied electric field, and  $\phi$  is the height of the energy barrier at the injecting contact.

Here, with same material Alq3 and same thickness, the injection current of all six devices and their dominating carrier should be determined only by the difference of the height of energy barrier ( $\phi$ ) at hole and electron injection contacts. By Kelvin method (12), we obtained the work function values of ITO, AZO, Al and Mg, as 5.0eV, 5.2eV, 4.3eV and 3.9eV. The highest occupied molecular orbital (HOMO) of Alq3 obtained from a cyclic voltammetry method (12) is 5.7eV and the lowest unoccupied molecular orbital (LUMO) obtained from the optical absorption band is 3.1eV. With these data, an energy diagram is drawn as figure 2. From figure 2, we obtained the values of energy barrier height for hole injection ( $\phi_h$ ) and for electron injection ( $\phi_e$ ) in different devices and shown them in table 2.

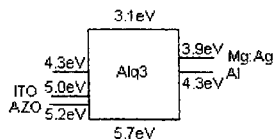


Figure 2. Energy diagram of devices

Table 2. The energy barrier heights in the devices

device	(a)	(b)	(c)	(d)	(e)	(f)
$\phi_h$ (eV)	0.5	0.5	0.7	0.7	1.4	1.4
$\phi_e$ (eV)	0.8	1.2	0.8	1.2	0.8	1.2



In the devices with AZO or ITO as the anodes, the hole injection barriers are lower than the electron injection barriers, and therefore we expect majority carriers in the device (a), (b), (c) and (d) to be holes. For the devices (e) and (f), with Al as the anode,  $\phi_e < \phi_h$ , and so the majority carrier will be the electrons.

#### 4. The relative hole and electron injection current

Considering device (d), as an example, we can roughly estimate the ratio of the hole and electron injection current. Taking  $F = 3 \cdot 10^6$  V/cm, assuming  $m_e^* = m_h^* = m_0$ , and with the barrier height  $\phi_h = 0.7$  eV and  $\phi_e = 1.2$  eV, we calculated the ratio of the hole current injected from the hole barrier at ITO/Alq3 interface and the electron current injected from the Alq3/Al interface,  $I_h / I_e$  as a value of the order of  $10^8$ . Much more holes are injected into the Alq3 layer than electrons.

From section 3, we know that the electrons injected from Alq3/Al dominate the device current of device (f) and the holes current injected from the ITO/Alq3 interface dominate the current of device (d). We can see from the figure 1, at electric field of  $3 \cdot 10^6$  V/cm, the device current ratio of device (d) and device (f) is about  $10^6$ . That ratio can be considered as the experimental ratio of hole and electron injection in the device (d), because the electron injection current of the device (d) and the device (f), according to the equation (1), should be approximately same. We noted a difference of 2 order of magnitude between the calculated ratio of the hole and electron injection current and the experimental device current.

For the ratio of hole injection in device (b) and device (d), the dominated injection for both devices, is calculated as 190 at  $3 \cdot 10^6$  V/cm electric field, compared with the experimental result 5, the difference is also of the order of  $10^2$ . The differences between the calculated results and the experimental ones imply that the device current does not exactly follow the F-N equation of injection current.

#### 5. I-F characteristics of the devices with different thickness of Alq3 layer

To determine the device current domination mechanism of the single Alq3 layer device, we made four devices with ITO as the anode and Mg: Ag as the cathode but different thickness of Alq3 layer, from 30nm, 60nm, 90nm, to 120nm. The I-V curves of these four devices and their current electric field (I-F) form are shown in figure 3. From the figure 3(b), one can see that the I-F curves of the devices are not coincided, which indicates again that the device current is not perfectly satisfied the F-N tunnelling injection. This is because, if the tunnelling injection dominates the current, the device current, according to equation (1), should be same at same electric field.

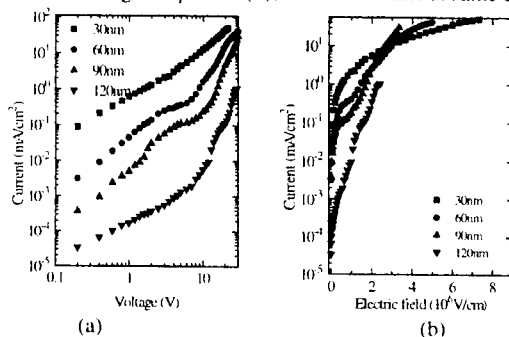


Fig.3 I-V (a) and I-F (b) curves of devices with different thickness of organic layer

### 6. Determination of the space-charge-limited device current

The effective mobility of hole and the electron in Alq3 are low and lots of energy traps exist in the film. So it is possible that the injected holes accumulate in the region near the anode/organic contact in the organic layer to form space charge distribution.

At low applied electric field, the amount of the thermally generated free charge is larger than that of the injected charge, the device current density is described by

$$I = q\mu_h n_0 \frac{V}{d} \quad (2)$$

Where  $q$  and  $\mu_h$  are the carrier charge and mobility of hole,  $n_0$  is the thermally generated background free charge density,  $V$  is the apply voltage, and  $d$  is the thickness of organic layer. So the device current depends on the voltage  $V$ . When the Fermi level of the hole lies below the hole trap energy, the device current is space-charge-limited

$$I = \left(\frac{9}{8}\right)\mu_h \epsilon \frac{V^2}{d^3} \quad (3)$$

Now the current is dependent on square of voltage  $V^2$ . When the applied field is increased, the quasi-Fermi level of the organic material increases and more hole traps are filled, resulting the decrease of the density of the empty traps and the increase of effective mobility of hole. In this case, the current should depend on a higher power of voltage, the trapped-charge-limited current should be

$$I \propto \left(\frac{V}{d}\right)^B \quad (4)$$

$B$  should be larger than 2.

From figure 4(a), we note that all the curves of four devices can be separated into two parts according to their slaps though the separating position are different for each curve. It seems that dividing the curves according with the applied electric field is more reasonable than with the voltage.

Setting  $1 \cdot 10^6$  V/cm as the separating point, we cut each I-F curve into two parts and plot  $I \sim (V/d)$  curves below and above  $1 \cdot 10^6$  V/cm in figure 4.

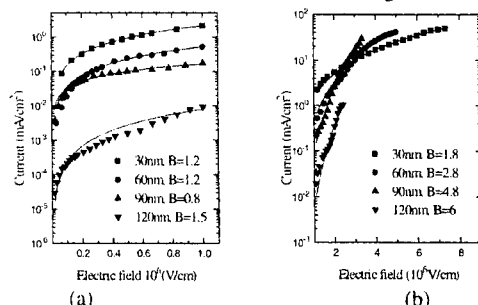


Fig. 4 The current field characteristics at low electric field (a) and high field (b)

We find that all these curves are of power law form, indicating the device currents are space charge limited. Using the power law relation  $I \propto (V/d)^B$ , we get the  $B$  values of four devices in two ranges of electric field. In the lower field, the values of  $B$  are less than 2, while larger than 2 in the higher field. We think that in the lower field, the device current is controlled by both thermally generated charges and

injected charges, so the  $B$  values are between 1 and 2 except the 90 nm device, which is out of expectation. Because our measurements are carried out in the room temperature and in ambient radiation, the quantity of thermally and even radically generated charges may be significant enough to be comparable with the injected ones. The different  $B$  may be arisen from the different trap density in the different thickness organic layers that are deposited in different times.

In the higher electric field, the traps are consequently filled by the injected charge, giving in the higher power law satisfactory rule. Some of the energy traps are formed from the roughness of the ITO and the diffusion of the metal electrode; the average trap density should decrease with the increase of the organic thickness. So, in trapped-charge-limited range, the order of the power law increases with the organic thickness.

#### IV. SUMMARY

By comparing the I-V curves of six devices with different anode and cathode and the  $\eta$ -V characteristics of two devices with same anode but different cathode, we indicated that in the Alq3 single layer devices with AZO or ITO as the anode and Al or Mg: Ag as the cathode, the hole is the majority in the device current and the electron is the minority which affects the EL efficiency of the devices. By comparing the I-F relation of the four devices with same anode and cathode but different thickness of Alq3 layer, we shown that the device currents are bulk-limited. In the lower applied electric field, the current is controlled by both thermally generated charges and injected charges, while in the higher field by the trapped ones.

#### Acknowledgements

This work is partially supported by Foundation for Science and Technology (FCT) of Portugal and by Shanghai Municipal Orient Star Program of China.

#### References:

- 1 A. J. Campbell, D. D. C. Bradley, and D. G. Lidzey, *J. Appl. Phys.*, **82**(12):6326(1997)
- 2 I. D. Parker, *J. Appl. Phys.*, **75**(3):1656(1994)
- 3 P. S. Davids, Sh. M. Kogan, I. D. Parker, and D. L. Smith, *Appl. Phys. Lett.*, **69**(15):2270(1996)
- 4 P. S. Davids, I. M. Campbell, and D. L. Smith, *J. Appl. Phys.*, **82**(12):6319(1997)
- 5 P. E. Burrows, and S. R. Forrest, *Appl. Phys. Lett.*, **64**(17):2285(1994)
- 6 Z. Shen, P. E. Burrows, V. Bulovic, D. M. McCarty, and S.R. Forrest, *Jpn. J. Appl. Phys.*, **35**:L401(1996)
- 7 P. E. Burrows, Z. Shen, V. Bulovic, D. M. McCarty, and S. R. Forrest, *J. Appl. Phys.*, **79**(10):7991(1996)
- 8 H. Antonidis, M. A. Abkowitz, and B. R. Hsieh, *Appl. Phys. Lett.*, **65**(16):2030(1994)
- 9 E. M. Conwell, and N. W. Wu, *Appl. Phys. Lett.*, **70**(14):1867(1997)
- 10 A. R. Brown, D. D. C. Bradley, J. H. Burroughes, R. H. Friend, N. C. Greenham, P. L. Burns, A. B. Holmes, and A. Kraft, *Appl. Phys. Lett.*, **61**:2793(1992)
- 11 D. V. Khrantchenkov, H. Bässler, and V. I. Arkhipov, *J. Appl. Phys.*, **79**(12):9283(1996)
- 12 Liu Zugang, Zhao Weiming, Ji Rongbin, Zhang Zhilin, Jiang Xueyin, Xue Minzhao, and Fang Bin, *J. Phys.: Condens. Matter* **8**:3221-3228(1996)

## NOTES FOR CONTRIBUTORS TO NONLINEAR OPTICS

As Gordon and Breach moves into the delivery of journals in electronic format, it becomes essential that authors prepare their manuscripts according to established specifications. The effectiveness of the search capabilities offered by electronic delivery will depend upon the care used by authors in preparing their manuscripts. Therefore, contributors are strongly encouraged to read these instructions carefully before preparing a manuscript for submission, and to check the manuscript for compliance with these notes before submitting it for publications.

Gordon and Breach online "offices" enable our authors to submit abstracts and full-text articles in virtually any file format, from anywhere in the world, at any time. Visit [http://www.gbhap.com/Nonlinear\\_Optics/](http://www.gbhap.com/Nonlinear_Optics/) to access a full range of internet author services.

### MANUSCRIPTS

Papers should be typed with double spacing and wide (3 cm) margins on good quality paper, and submitted in triplicate to any of the editors, or via a member of the Editorial Advisory Board. Submission of a paper to *Nonlinear Optics* will be taken to imply that it represents original work not previously published, that it is not being considered elsewhere for publication, and that if accepted for publication it will not be published elsewhere in the same form, in any language, without the consent of editors and publisher.

*Language:* English language is preferred, but French or German papers will be accepted if an English summary of 200–300 words is also supplied.

*Abstract:* Each paper requires an abstract of 100–150 words summarizing the significant coverage and findings. Non-English papers should have a similar abstract in the language, but must also contain an English-language abstract of 200–300 words.

It is a condition of acceptance by the editor of a typescript for publication that the publishers acquire automatically the copyright in the typescript throughout the world.

### FIGURES

All figures should be numbered with consecutive arabic numbers, have descriptive captions, and be mentioned in the text. Keep figures separate from the text, but indicate an approximate position for each in the margin.

*Preparation:* Figures submitted must be of a high enough standard for direct reproduction. Line drawings should be prepared in black (India) ink on white paper or tracing cloth, with all lettering and symbols included. Alternatively, good sharp photoprints ("glossies") are acceptable. Photographs intended for half-tone reproduction must be good glossy original prints, of maximum contrast. Clearly label each figure with the author's name and figure number; indicate "top" where this is not obvious. Redrawing or retouching of unusable figures will be charged to authors.

*Size:* The preferred width of submitted line drawings is 20 to 23 cm with capital lettering 4mm high, to accommodate reduction to single-column width. Photographs for halftone reproduction should be about twice the desired size.

*Color Plates:* Whenever the use of color is an integral part of the research, or where the work is generated in color, the journal will publish the color illustrations without charge to the authors. Reprints in color will carry a surcharge. Please write to the Editor for details.

### EQUATIONS AND FORMULAE

*Mathematical:* Mathematical equations should preferably be typewritten, with subscripts and superscripts clearly shown. It is helpful to identify unusual or ambiguous symbols in the margin when they first occur. To simplify typesetting, please use:

(1) the "exp" form of complex exponential functions; (2) fractional exponents instead of root signs; and (3) the solidus (/) to simplify fractions – e.g.  $\exp x^{1/2}$ .

*Chemical:* Ring formulae, and other complex chemical matter, are extremely difficult to typeset. Please, therefore, supply reproducible artwork for equations containing such chemistry. Long reaction sequences should be designated as "Schemes" and treated like figures; i.e. keep artwork separate from the text, indicate in the margin an appropriate position, and supply a separate list of scheme captions. Where necessary, individual chemical formulae can be identified with bold arabic numbers. Chemical equations referred to in the text should be indicated with arabic numbers set over to the right, and in parentheses.

*Marking:* Where chemistry is straightforward and can be set (e.g. single-line formulae), please help the typesetter by distinguishing between, e.g. double bonds and equal signs and single bonds and hyphens, where there is ambiguity. The printer finds it extremely difficult to identify which symbols

---

should be set in roman (upright) or italic or bold type, especially where the paper contains both mathematics and chemistry. Therefore, please *underline* all mathematical symbols to be set italic and put a wavy line under bold symbols. Other letters not marked will be set in roman type.

#### TABLES

Number tables consecutively with roman numerals, and give each a clear descriptive caption at the top. Avoid the use of vertical rules in tables. Indicate in the margin where the printer should place tables.

#### REFERENCES

References and notes are indicated in the text by consecutive superior arabic numbers in brackets. The full list should be collected and typed at the end of the paper in numerical order. Listed references should be complete in all details, but excluding article titles in journals. Authors' initials should precede their names; journal title abbreviations should conform to *Chemical Abstracts* style. Examples:

1. A. B. Smith and C.D. Jones, *J. Appl. Phys.* **34**, 296 (1965).
2. R. B. Brown, *Molecular Spectroscopy* (Gordon and Breach, New York, 1970), 3rd ed., Chap. 6. pp. 95–106.

#### FOOTNOTES

Authors are encouraged to minimize the use of footnotes. A footnote may include the designation of a corresponding author of the paper, current address information for an author (if different from that shown in the affiliation), and traditional footnote content. Information concerning grant support of research should appear in a separate Acknowledgments section at the end of the paper, not in a footnote. Acknowledgments of the assistance of colleagues or similar notes of appreciation also properly belong in an Acknowledgments section, not in footnotes.

Footnotes should be indicated in the text by the following symbols: \* (asterisk or star), † (dagger), ‡ (double dagger), ¶ (paragraph mark), § (section mark), || (parallels), # (number sign). Do not use numerals for footnote call-outs, as they may be mistaken for bibliographical reference call-outs or exponents. Type each footnote at the bottom of the typescript page on which its text call-out appears.

Footnotes within a table should be indicated by the same symbols listed above. Reinitialize symbol sequence within tables. Type footnotes to a table directly beneath the table.

It is assumed that, with the development of the World Wide Web (WWW), authors and/or the publisher will propose distribution of articles or parts of articles on the WWW. If the author knows the HTTP address of a referenced article on the WWW, this information should be added at the end of the reference. Please use the following style:

< www <http://www.blouk.com/article.html> >

where <http://www.blouk.com/article.html> is the HTTP address.

#### TEXT CALL-OUTS TO FIGURES, TABLES, SECTIONS, SCHEMES

Text call-outs to figures, tables and other elements are the basis for searching articles on electronic delivery. Therefore, proper designation of text call-outs to figures and other elements is essential to the success of electronic delivery. When referring to a figure, table or other element within an article, always call the element by its full name: "See Table 1", "Figure 1 illustrates...", "Refer to Scheme 1". Do not use ambiguous call-outs (for example, "I illustrates...") that do not clearly denote the element being referred to.

#### SUBMISSION OF ARTICLES ON DISK

The Publisher welcomes article submission on disk. Disk files should be submitted with the final hard copy manuscript. The disk file and hard copy must match exactly.

When typing the article, do not include design or formatting information. Type all text flush left, unjustified and without hyphenation. Do not use indents, tabs or multi-spacing. If an indent is required, please note it by a line space; also mark the position of the indent on the hard copy manuscript. Indicate the beginning of a new paragraph by typing a line space. Leave one space at the end of a sentence, after a comma or other punctuation mark, and before an opening parenthesis. Be sure not to confuse lower case letter "l" with numeral "1", or capital letter "O" with numeral "0". Distinguish opening quotes from close quotes. Do not use automatic page numbering or running heads.

Tables and displayed equations may have to be rekeyed by the typesetter from your hard copy manuscript.

Articles prepared on most word processors are acceptable. If equations and/or scientific symbols have been imported into the article from another program, please provide details of the program used and the procedures followed. If author-created macros have been used, please include them as well.

Illustrations that are available in an electronic format are acceptable; please supply them on a separate disk. Please clearly indicate on the disk the file format and/or program used to produce them, and supply a high-quality hard copy of each illustration as well.

If more than one disk is submitted, please number each disk. Please mark each disk with the journal title, author name, abbreviated article title and file names. Retain a back-up copy of each disk submitted and pack the disks carefully before shipping. Complete the Author Disk Submission form that appears at the back of the journal (forms also may be obtained from the publisher and journal editor in chief) and submit it with the disk and hard copy manuscript.

#### **SUBMISSION OF ANIMATION**

Author-supplied animation related to articles accepted for publication may be included in the on-line version of the journal in most forms. Such animation, in any format, should be submitted to the journal editor with the final manuscript after it has completed the refereeing process. Animation should be mentioned in the text. Indicate an approximate location for the animation call-out in the margin. The Publisher cannot guarantee inclusion of the animation on-line in case of format incompatibility or length. Please contact the Publisher to discuss other options with the Publisher prior to submission.

#### **PROOFS**

Authors will receive page proofs (including figures) by air mail for correction, which must be returned to the printer within 48 hours of receipt. Please ensure that a full postal address is given on the first page of the typescript, so that proofs are not delayed in the post. Authors' alterations in excess of 10% of the original composition cost will be charged to authors.

*Reprints:* 25 free reprints will be provided to the first-named author of each article. Additional reprints may be ordered by completing the appropriate form sent with proofs.

#### **PAGE CHARGES**

There are no page charges to individuals or to institutions.

---

## Disk Specifications

Journal name \_\_\_\_\_

Date \_\_\_\_\_ Paper Reference Number \_\_\_\_\_

Paper title \_\_\_\_\_

\_\_\_\_\_

Corresponding author \_\_\_\_\_

Address \_\_\_\_\_

\_\_\_\_\_

\_\_\_\_\_ Postcode \_\_\_\_\_

Telephone \_\_\_\_\_

Fax \_\_\_\_\_

E-mail \_\_\_\_\_

### Disks Enclosed (file names and descriptions of contents)

Text

Disk 1 \_\_\_\_\_

Disk 2 \_\_\_\_\_

Disk 3 \_\_\_\_\_

---

*PLEASE RETAIN A BACK-UP COPY OF ALL DISK FILES SUBMITTED.*

GORDON AND BREACH PUBLISHERS • HARWOOD ACADEMIC PUBLISHERS

---

**Figures**

Disk 1 \_\_\_\_\_

Disk 2 \_\_\_\_\_

Disk 3 \_\_\_\_\_

**Computer make and model** \_\_\_\_\_

**Size/format of floppy disks**

☐ 3.5"

☐ 5.25"

☐ Single sided

☐ Double sided

☐ Single density

☐ Double density

☐ High density

**Operating system** \_\_\_\_\_

**Version** \_\_\_\_\_

**Word processor program** \_\_\_\_\_

**Version** \_\_\_\_\_

**Imported maths/science program** \_\_\_\_\_

**Version** \_\_\_\_\_

**Graphics program** \_\_\_\_\_

**Version** \_\_\_\_\_

**Files have been saved in the following format**

Text: \_\_\_\_\_

Figures: \_\_\_\_\_

Maths: \_\_\_\_\_

---

*PLEASE RETAIN A BACK-UP COPY OF ALL DISK FILES SUBMITTED.*

**GORDON AND BREACH PUBLISHERS • HARWOOD ACADEMIC PUBLISHERS**



(Continued from inside front cover)

nonreceipt of issues will be honored if made within three months of publication of the issue. **See Publication Schedule Information** Subscriptions are available for microform editions; details will be furnished upon request.

All issues are dispatched by airmail throughout the world.

**Subscription Rates** Base list subscription price per volume: EUR 139.00.\* This price is available only to individuals whose library subscribes to the journal OR who warrant that the journal is for their own use and provide a home address for mailing. Orders must be sent directly to the Publisher and payment must be made by personal check or credit card.

Separate rates apply to academic and corporate/government institutions. Postage and handling charges are extra.

\*EUR (Euro). The Euro is the worldwide base list currency rate; payment can be made by draft drawn on Euro currency in the amount shown, or in any other currency within the eurozone at the euro-denominated rate. All other currency payments should be made using the current conversion rate set by the Publisher. Subscribers should contact their agents or the Publisher. All prices are subject to change without notice.

**Publication Schedule Information** To ensure your collection is up-to-date, please call the following number for information about the latest issue published: +44 (0) 118-956-0080 ext. 391; +1 973 643-7500 ext. 290; or web site: <http://www.gbhap.com/reader.htm>.

*Note:* If you have a rotary phone, please call our *Customer Service* at the numbers listed below.

*Orders should be placed through one of the addresses below:*

IPD Marketing Services  
PO Box 310  
Queen's House, Don Road  
St. Helier, Jersey  
Channel Islands JE4 0TH  
Telephone: +44 (0) 118-956-0080  
Fax: +44 (0) 118-956-8211

PO Box 32160  
Newark NJ 07102 USA  
Telephone: +1 800 545-8398  
Fax: +1 973 643-7676

Kent Ridge, PO Box 1180  
Singapore 911106  
Republic of Singapore  
Telephone: +65 741-6933,  
Fax: +65 741-6922

Yohan Western Publications Distribution Agency  
3-14-9, Okubo, Shinjuku-ku  
Tokyo 169-0072, Japan  
Telephone: +81 3 3208-0186  
Fax: +81 3 3208-5308

Enquiries can also be sent by e-mail: <[info@gbhap.com](mailto:info@gbhap.com)> and the world wide web: <http://www.gbhap.com>.

#### **Rights and Permissions/Reprints of Individual Articles**

Permission to reproduce and/or translate material contained in this journal must be obtained in writing from the Publisher.

This publication and each of the articles contained herein are protected by copyright. Except as allowed under national "fair use" laws, copying is not permitted by any means or for any purpose, such as for distribution to any third party (whether by sale, loan, gift, or otherwise); as agent (express or implied) of any third party; for purposes of advertising or promotion; or to create collective or derivative works. A photocopy license is available from the Publisher for institutional subscribers that need to make multiple copies of single articles for internal study or research purposes. Any unauthorized reproduction, transmission or storage may result in civil or criminal liability. Copies of articles may be ordered through SCAN, the Publisher's own document delivery service. SCAN provides customers with the current contents and abstracts to all Gordon and Breach and Harwood Academic journals. Please contact one of the addresses listed above to receive SCAN, or view current contents and abstracts directly on the Web at <http://www.gbhap.com>, and for ordering.

The Publisher is also a member of Copyright Clearance Center.

The Canada Institute for Scientific and Technical Information (CISTI) provides a comprehensive, worldwide document delivery service for Gordon and Breach/Harwood Academic journals. For more information, or to place an order for a copyright-cleared Gordon and Breach/Harwood Academic document, please contact Client Assistant, Document Delivery, CISTI, National Research Council Canada, Ottawa, Canada, KIA OS2 (Tel: 613-993-9251; Fax: 613-993-7619; e-mail: <[cisti.docdelnrc.ca](mailto:cisti.docdelnrc.ca)>).

**Voluntary Page Charges** The United States National Science Foundation has extended the allowance of page charge funds for payments to journals regardless of the Publisher's commercial status. Previously this was reserved for only nonprofit society-sponsored journals. Voluntary page charge payments are now accepted for this journal, and authors may elect to pay any amount up to a maximum of \$25.00 per page. Payments will be refunded in the form of a voucher at 100% value of total payment. This voucher can be used by the author or the author's university library for any product of service offered by the Publisher, and thereby can be used to supplement library funding.

**Article Vouchers** The principal author of each article will receive a voucher for his contribution in the amount of EUR 33.00 (USD 30.00, JAPAN YEN 3,400), which can also be used to purchase the Publisher's products directly or through university libraries, thereby reducing costs of publications to those authors supporting the journal.

This journal is sold CIF with title passing to the purchaser at the point of shipment in accordance with the laws of The Netherlands. All claims should be made to your agent or the Publisher.

Printed in Malaysia

November 2000